The Applicability of Sliding Block Analyses for the Prediction of Lateral Spreading Displacements

Andrew J. Makdisi

A thesis submitted in partial fulfillment
of the requirements for the degree of

Master of Science in Civil Engineering

University of Washington
2016

Committee:

Steve Kramer

Pedro Arduino

Joseph Wartman

Program Authorized to Offer Degree:
Civil and Environmental Engineering

University of Washington

Abstract

The Applicability of Sliding Block Analyses for the
Prediction of Lateral Spreading Displacements

Andrew Makdisi

Chair of the Supervisory Committee:
Research Advisor Professor Steve Kramer
Civil and Environmental Engineering

Liquefaction-induced lateral spreading deformations can pose significant risks to bridge pile foundations, underground utilities, and shallow foundation systems, particularly at sites in seismically active areas near embankments and levees, in close proximity to natural or man-made free faces. Current approaches for lateral spreading predictions, consisting primarily of empirical models and strain potential methods, largely neglect complex and critical factors that influence such deformations, such as nonlinear dynamic site response, dilation pulses, void redistribution, and water film formation, as well as complex two- or three-dimensional topographic effects. It has also been proposed by several researchers that lateral spreading predictions can be potentially approximated using Newmark-type rigid block analyses, with an appropriate reduction in the yield acceleration to account for soil liquefaction.

The appropriateness of the Newmark-type framework in lateral spread characterization was assessed in this study. Particular focus was placed on characterizing any potential structural biases inherent to the sliding block framework, including those related to the assumption of strain concentration along a discrete failure plane and rigid dynamic behavior, as well as practical issues related to the uncertainty in sliding block displacement predictions, and how the sliding block method compares to other approaches currently in use for predicting lateral spreading displacements. When evaluating solely the effects of the assumption of a discrete failure surface, sliding block analyses predicted displacements on the order of 30 to 70% lower than displacements predicted using simple dynamic analyses of a soil continuum. Further analyses showed that, when compared to both finite-element methods used for liquefaction modeling and established lateral spreading empirical models, sliding block methods largely failed to predict substantial deformations over a broad range of lateral spreading conditions, and have the potential to be highly un-conservative in characterizing lateral spreading hazards in general.

Contents

Acknowledgments

First of all, I would like to extend my sincerest gratitude towards Dr. Steve Kramer for his guidance and good humor over the past couple of years, and without whom this thesis would not have been possible. I have learned so much working with him over the past few years, and am truly grateful for the opportunity to have done so. I would also like to thank the rest of the geotechnical group at the University of Washington for their support and camaraderie. There were a lot of times when I felt like I was pretty far off the reservation while doing my research work, and someone in this group would either provide some insightful outside perspective, a well-timed joke, or would just drag me outdoors for a walk and some coffee to keep my sanity intact.

Finally, I have to thank my family and friends for their love and support - my mom Rima, and my sister Joy, in particular, and of course, my dad Faiz. Dr. Makdisi has been instrumental from afar during this whole process, always being there with words of support or advice, or some joke coming from that weird sense of humor of his. I cannot thank my dad enough for his guidance. Thanks again to all of the people mentioned here, and many others.

Chapter 1

INTRODUCTION AND OVERVIEW

Soil liquefaction during large earthquakes has resulted in numerous documented cases of extensive damage and loss of life over the course of the past half century, and is today regarded as a significant source of hazard in seismically active areas. Liquefaction is triggered when saturated, loosely deposited granular materials are subjected to strong, sustained ground shaking, such as that seen in large seismic events. The cyclic shear stresses imposed by strong ground shaking have the effect of increasing the porewater pressure within the loose soils, eventually resulting in a significant losses in stiffness and shearing resistance.

Soil liquefaction can have immense consequences. On flat ground, it can result in bearing failure (due to decreases in shear strength) or excessive settlements (due to vertical strains after pore pressures dissipate) of shallow foundations, and reduction in the capacity of deep foundation systems. In gently sloping ground, liquefaction can cause excessive lateral deformations of the ground surface, which can damage utility lines, shallow foundation systems, and deeper bridge pile foundations. In steep slopes, embankments, and dams, large landslides and flow failures can occur, potentially destroying large areas of land, and causing extensive damage.

The focus of this thesis is to investigate the liquefaction-related phenomenon of lateral spreading. Lateral spreading occurs at gently sloping sites, or sites near embankments or free-faces. Ground deformations related to lateral spreading tend to occur during ground shaking, when the cyclic shear stresses and the (relatively) low static shear stresses combine to produce plastic strains in the soil that lead to lateral soil movement. Sites that are situated along riverbanks, levees, and embankments are particularly prone to this type of ground failure, as they are often underlain by the type of loosely deposited, geologically young, granular material most susceptible to liquefaction, but generally lack the larger

magnitude of static shear stresses that have been known to cause flow failures in steeper environments.

Despite being the focus of a great deal of research over the last 40 years, lateral spreading deformations remain notoriously difficult to predict. It is an extremely complex process, and is highly sensitive to numerous mechanisms occurring both before and after the onset of liquefaction that are difficult to predict and observe directly. In particular, much of the difficulty lies in what occurs after liquefaction is triggered, where the effects of dilation pulses, void redistribution, and the geometry of the spreading mass can have complex effects on the dynamic response of the system and the permanent shear deformations in the liquefied material. A wide variety of methods and models that purport to characterize and predict lateral spreading hazards currently exist in practice. These methods can largely be grouped into two subcategories: empirical models based on multiple regression on a series of observed case histories, and laboratory-based models that predict the shear strain within the liquefied material as a function of its initial density, and then estimate permanent displacements by accounting for the thickness of liquefied material, and in some cases also accounting for site topographic effects.

Alternatively, it has been proposed that Newmark sliding block analyses can be used to predict lateral spreading displacements. In this approach, the lateral spread is modeled as a rigid block that slides relative to an inclined, frictional surface. While this model is attractive in its ability to capture the ratcheting-type deformations associated with lateral spreading, as well as at least some of the effects of ground motion variability on the response of the site, their results are extremely sensitive to the strength assigned to the soil. Sliding block-based models, as they pertain to lateral spreading predictions, have not been developed to the same degree that empirical methods or strain potential models have.

In this thesis, the concept of modeling a lateral spread as a rigid block is investigated in detail, particularly with respect to both its ability to predict accurate and precise lateral spreading displacements, as well as its utility in back-analyzing liquefied shear strengths from lateral spreading case histories. In addition to exploring the fundamental assumptions implied by the sliding block model and how they may differ from the actual system being emulated, the Newmark-based framework is also assessed relative to other methods currently in use for analyzing lateral spreading.

1.1 Objectives

- Review and discuss the applicability of the currently available methods used to characterize and predict lateral spreading.
- Investigate the practical issues pertaining to the general use of conventional sliding block analyses, and how these issues affect the applicability of such models within the context of lateral spreading.
- Characterize any potential structural biases inherent to using sliding block models to model lateral spread, particularly the assumption of a discrete failure surface in cases where liquefaction occurs in relatively thick strata.
- Assess the validity of using sliding block analyses to back-calculate liquefied shear strengths from lateral spreading case histories, particularly with respect to how liquefied shear strengths mobilized during lateral spreads compare to those mobilized during liquefaction flow failures.
- Assess how sliding block analyses predict lateral spreading displacements compared to other established methods for lateral spreading characterization.

1.2 Organization of Thesis

This thesis begins by reviewing the mechanics and fundamentals of liquefaction, as well as discussing the methods currently in use for analyzing liquefaction triggering, in Chapter 2. Chapter 3 focuses on liquefaction-related effects and hazards such as flow failures, vertical settlement, ground motion amplification, and lateral spreading. Chapter 4 reviews the current state of practice regarding seismic slope stability, and can be divided into two main sections, each pertaining to methods that evaluate sites on sloping ground within both inertial instability frameworks (such as limit equilibrium and sliding block analyses) and weakening instability frameworks (including empirical methods, strain potential models for lateral spreading displacements, and sliding block analyses accounting for reduced strengths). Chapter 5 discusses two lateral spreading databases. The first database was compiled and developed by Youd et al. (2002) to develop their empirical model. The second database was compiled by Olson and Johnson (2008) to develop a sliding block-based method to back-analyze shear strengths of liquefied soil at lateral spreading sites and predict future lateral spreading displacements. The two databases are compared and evaluated with respect to how well they represent a broader range of lateral spreading conditions. Chapter 6 focuses on some of the practical considerations pertaining to the

general use of sliding block analyses, including how the selection and application of ground motions, and the assumptions of a rigid failure mass and a discrete failure surface affect the accuracy of sliding block analyses for various seismic slope stability applications. Chapter 7 extends the concepts presented in Chapter 6 to the more specific context of lateral spreading, and explores the potential structural biases that sliding block analyses may introduce in modeling lateral spreading. Specifically, the sliding block-based methodology of Olson and Johnson (2008) is investigated within a probabilistic framework to characterize potential uncertainties inherent to both the back-calculation of shear strengths and forward-prediction of displacements procedures. Chapter 8 is a comparative study of three methods of predicting lateral spreading displacements, in which the analysis results of the 2002 Youd et al. and 2008 Olson and Johnson models are compared to the results of the finite-difference numerical model FLIP for a wide range of lateral spreading site and earthquake source conditions. Finally, the findings presented herein are summarized in Chapter 9, and conclusions are drawn about the applicability of sliding block analysis for the evaluation of lateral spreading displacements.

Chapter 2

FUNDAMENTALS OF SOIL LIQUEFACTION

2.1 Introduction

Among the most significant earthquake-related hazards is the occurrence of soil liquefaction in cohesionless, loosely deposited, saturated soils. As a loose sand is subjected to cyclic loading associated with ground motions, it tends to contract such a way that the total load acting on the soil is gradually transferred from the soil matrix to the pore water. In an undrained condition, as is usually the case with seismic shaking, this mechanism is accompanied by an increase in pore water pressure, which can result in large decreases in the effective stress, strength and stiffness of the soil mass. The term "liquefaction" is used to describe the soil deformations that occur as a result of these reduced strength properties.

Historically, the destructive effects of liquefaction were first widely observed during two earthquakes in the 1960s. The 1964 Niigata Earthquake was a magnitude 7.6 shock that is thought to have originated on a reverse fault some 50 km south of the Japanese city of Niigata. The overwhelming majority of structural damage from this earthquake is attributed to the bearing failure of shallow footings founded on young deltaic deposits that liquefied during ground shaking (Figure 2.1). The measured PGA within the city of Niigata was about 0.20g, which is generally not considered intense enough to cause extreme structural damage by itself. Also noteworthy was the collapse of the Showa Bridge (Figure 2.2), which was reported to have occurred some 70 seconds after the end of the recorded ground motions (Yoshida et al. 2007). It was later determined that the collapse of the simply supported bridge spans occurred as a result of lateral spreading of liquefied soils

near the banks of the Shinano River.

Figure 2.1: Collapse of tall buildings as a result of liquefaction-induced bearing failure during the 1964 Niigata Earthquake (USGS)

Figure 2.2: Collapse of the Showa Bridge, due to lateral spreading, during the 1964 Niigata Earthquake (USGS)

The Great Alaskan Earthquake, which also occurred in 1964, was and still is, the most

powerful recorded earthquake in North American history, registering a moment magnitude of 9.2. The shock, centered about 20 km north of the Prince William Sound, triggered numerous liquefaction-induced landslides in Anchorage, which was about 125 km west of the epicenter, causing damage to many building, private homes, and underground utilities in the city (Figure 2.3). The severity of these events, coupled with the relatively short time interval in which they occurred, helped identify liquefaction as a significant earthquake engineering consideration (Idriss and Boulanger 2008) and has since sparked the development of geotechnical earthquake engineering as a substantial subspecialty of engineering research.

Figure 2.3: Aerial view of the Government Hill landslide in Anchorage, Alaska; occurred during the 1964 Great Alaskan Earthquake (USGS)

2.1.1 Flow Liquefaction

Flow liquefaction is used to describe the phenomenon in which the initial static shear stress that the soil experiences (due to natural or cut slopes, retaining walls, etc.) exceeds the liquefied shear strength (also termed "residual shear strength") of the soil deposit. This generally leads to dramatic flow-like deformations with large magnitudes of displacement, such as those seen in Anchorage during the 1964 event. Additional examples of flow liquefaction will be discussed further in Section 2.2.

2.1.2 Cyclic Mobility

The somewhat less dramatic manifestation of liquefaction occurs when static shear stresses do *not* exceed the liquefied shear strength of the soil. This condition is known as *cyclic mobility*; deformations under this conditions are generally smaller than those seen in flow-like deformations, and occur incrementally during cyclic loading. In this case, deformations are driven by both static shear stresses and cyclic shear stresses imposed by ground shaking (Kramer 1996). Deformations associated with cyclic mobility are generally known as *lateral spreading*, and usually occur in very gently sloping grounds, or flat ground which may be within the general vicinity of a free face. The aforementioned Showa Bridge failure is a classic example of lateral spreading failure in which incremental displacements of the Shinano River deposits placed undue stresses and excessive deformations on the supporting bridge piles, causing the collapse of the simply supported spans. More cases of cyclic mobility will be explored in Section 2.2 as well.

2.2 Historical Liquefaction Cases

The destructive nature of liquefaction has been observed numerous times throughout the last century. Each case history is unique in the characteristics of the causative earthquake, local geologic conditions, and the effects of liquefaction on local infrastructure, and has provided researchers with a sizeable dataset in order to better characterize the liquefaction phenomenon. In addition to the 1964 Niigata and Great Alaska events, this section discusses several important case histories in order to illustrate the many ways in which liquefaction is manifested as a hazard. The mechanics of these hazards are discussed in greater detail in Chapter 3

1925 Santa Barbara, California

The magnitude 6.8 event occurred about 10 km south of Santa Barbara, and lasted about 20 seconds. In addition to the collapse of many buildings in the city center, this event is notable for the liquefaction-induced failure of the Sheffield Dam. Built in 1917, the earth-fill embankment dam experienced liquefaction in the soil at its center base. The deformations and reduced strength in the liquefied soil caused the collapse of the dam, which resulted in about 2 feet of flooding in Santa Barbara. While the damage due to the dam failure was relatively mild in terms of casualties and economic losses, Sheffield Dam remains the only dam in history to have failed due to soil liquefaction during an

earthquake.

1964 Niigata, Japan

In addition to the aforementioned damages due to bearing capacity failures and lateral spread, the Niigata event is particularly notable for the widespread ground subsidence that occurred in the city after the earthquake. USGS reports that about one-third of the city experienced ground settlement by as much as 2 meters. Once ground shaking terminate, liquefied strata will experience a dissipation of excess pore pressure towards the surface, which generally results in the densification of the liquefied material. This can cause excessive ground settlement, and in areas where bearing failure has not occurred, ground subsidence can be the dominant structural hazard.

1971 San Fernando, California

The San Fernando Earthquake of 1971 was a magnitude-6.6 event that occurred on a thrust fault in the foothills of the San Gabriel Mountains. Local intensity was classified as XI on the Modified Mercali Scale, which corresponds to "Extreme." The nearby Sylmar Juvenile Hall sustained extensive structural damage due to lateral spreading of the underlying thick alluvial deposits. In general, ground deformations in the City of San Fernando caused significant damage to underground gas, water, and other utility lines.

Perhaps the most spectacular effect of the earthquake may have been the near-catastrophic failure of the San Fernando Dam, a hydraulic-fill embankment structure located just southeast of Sylmar. The upstream face of the Lower dam, initially 140 feet high, slid into the reservoir, bringing the water level to within 5 feet of the lip of the dam (Figure 2.4). Overflow of the dam would have resulted in the inundation of an area consisting of about 80,000 residents. The residents were evacuated for fear of any aftershocks triggering further collapse of the dam. Later dynamic analyses of the dam (Seed et al. 1975) showed that a substantial zone of liquefaction developed in the base of the upstream shell of the lower dam, producing large downslope displacements and a significant decrease in the height of the downstream crest. However, a complete breach of the dam was averted due to the fact that deformations were generally restrained by considerably stronger sand on both the upstream and downstream side of the Lower dam.

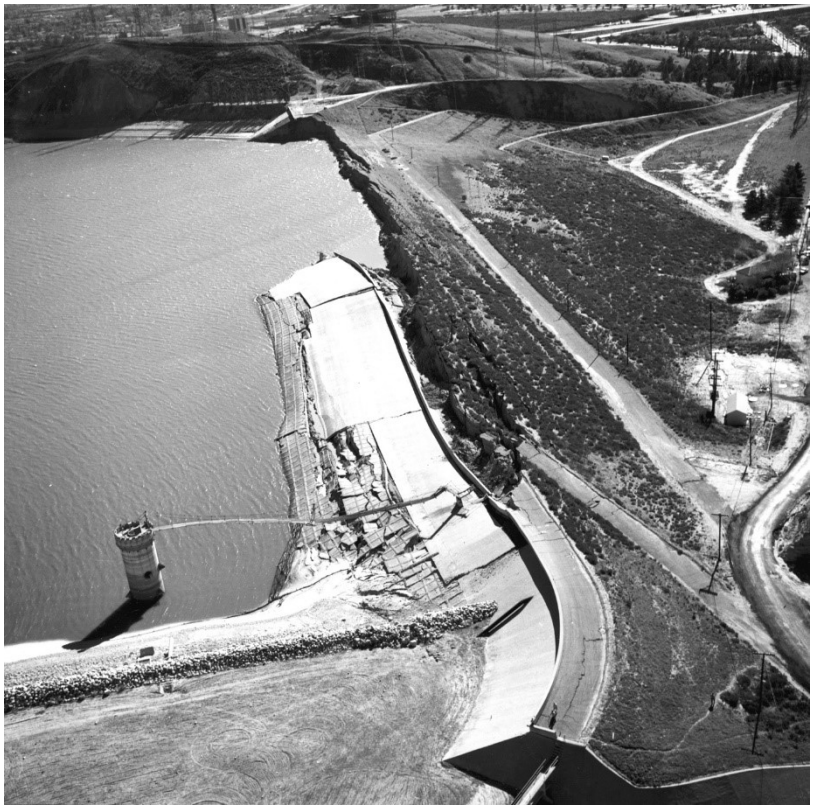

Figure 2.4: Liquefaction-induced failure of the Lower San Fernando Dam; downstream crest (USGS)

1989 Loma Prieta, California

In what may be the most famous earthquake in American history, a 6.9 magnitude shock occurred on October 17th at 5 P.M. local time, putting a halt to the San Francisco Bay Area's rush hour commute, as well as Game 3 of the 1989 World Series. The event was the result of a 35 km-long strike-slip rupture on the San Andreas Fault, originating about 60 km south of San Francisco. About 20 km away from the epicenter in Moss Landing, lateral spreading in soft beach deposits resulted in ground deformations of up to 1.5m, causing significant structural damage to the Monterey Bay Aquarium Research Institute and Moss Landing Marine Laboratory facilities (Figure 2.5). In San Francisco's Marina District, liquefaction-induced lateral spreading not only caused significant structural damage, but also induced ruptures in critical underground utility lines. The breaking of a gas main caused a large fire in the area (Figure 2.6), with emergency crews unable to utilize local water lines due to failure of the fire hydrant system in the area, which also occurred due to excessive ground deformations. Four people were killed as a result of the damage to the Marina District. The events in the Marina in particular highlighted the need for more robust critical infrastructure (i.e. underground utilities), and also provided an instructive

case study in local bedrock basin effects and soft-soil amplification of ground motions at long source-site distances.

Figure 2.5: Ground failure in Moss Landing, CA, due to lateral spreading, after the 1989 Loma Prieta Earthquake (USGS)

Figure 2.6: Fire erupts in the Marina District in San Francisco, CA after the 1989 Loma Pieta Earthquake, caused by rupture of gas and water utility lines due to lateral spreading.

1999 Chi Chi, Taiwan

The magnitude 7.6 earthquake in Taiwan caused an estimated $30 billion in damages and caused the deaths of over 2,400 people. A high density of ground motion sensors, coupled with the numerous cases of ground failure in the area resulted in what has been considered "the best set of data ever collected for an earthquake" (Monastersky 1999). Widespread liquefaction resulted in large differential settlements in shallow foundations, as well as structural damage to buildings due to bearing failure of liquefied soil. Lateral spreading was also a major hazard in the areas near the fault rupture, featuring large displacements along multiple rivers and creeks. Additionally, sand boils and sediment ejecta were observed throughout the affected area, a common surface manifestation of liquefaction (Figure 2.7). As mentioned previously, the dissipation of excess pore pressure after liquefaction occurs generally results in the upward flow of water towards the surface. In many cases, the upward-flowing water reaches and breaks through the surface, carrying sediments with it. In general, this phenomenon does not pose significant risk to infrastructure or human life. However, in the case of the Chi Chi earthquake, the widespread eruption of sand boils resulted in the filling in of a number of water wells with sediments, rendering them unusable for significant periods of time.

Figure 2.7: Sand boils erupting after the conclusion of the 1999 Chi-Chi, Taiwan Earthquake (USGS)

Summary

The aforementioned earthquakes, along with countless others in the past half century, highlighted the numerous potential hazards associated with soil liquefaction. The reduction in the strength of liquefied soils can lead to instability in steep slopes, resulting very

large soil deformations that can damage buildings, bury towns, and jeopardize embankment dams. In gentler slopes or slopes near free faces, smaller incremental deformations can damage and rupture critical underground utility structures, cause lateral extension of structural foundations, and place high lateral stresses on deep foundations, especially those near river banks or supporting bridge spans. The subsequent dissipation of excess pore pressures after liquefaction can result in intolerably high total and differential building settlements. In many cases, including the earthquakes discussed previously, the majority of ground shaking did not directly cause structural damage; rather it was indirect structural failure due to significant ground damage that cost many lives and billions of dollars in damage. Design of infrastructure in seismically active regions presents numerous challenges to the engineer, not the least of which is the evaluation of the potential for soil liquefaction, and the identification of the hazards that may occur as a result.

2.3 Mechanics of Liquefaction

The occurrence of liquefaction is fundamentally linked to the stress-strain behavior of cohesionless material when it is subjected to shear and the resulting interaction between the soil skeleton and pore water (Kramer 2009). The response of sand in to shear stress is dependent on a wide range of factors, including the grain-size characteristics of the sand, its depositional environment, and the characteristics of the induced stresses, such as magnitude and drainage conditions. This section explores how each of these factors affect the stress-strain response of sand, and in turn how stress-strain behavior provides a framework for understanding the mechanics of liquefaction as a whole.

2.3.1 Shearing Behavior of Granular Soils

At its most fundamental level, the response of sand to any type of shear load is dependent on its initial relative density or void ratio (D_R or e_0), the initial vertical effective stress acting on the soil (σ'_{v0}), the soil's stress history (OCR), and the depositional history that the soil has experienced. When a soil mass is subjected to deviatoric, or shear stress, it tends to undergo some form of volumetric change. An initially *loose* sand will generally experience a decrease in volume, known as *contraction*; while an initially *dense* sand will see an increase in its volume, termed *dilation*. Once the applied shear stress is large enough, the soil will reach a condition in which it is being continuously sheared at a constant shear stress without any further changes in its void ratio or effective stress. This condition is known as the *critical state* (Figure 2.8). Critical state can consist of a wide

range of volume and stress combinations; the critical void ratio and effective stress of a particular element of soil is dependent on the initial conditions of the soil and the manner in which the load is being applied (drained or undrained). All possible combinations of critical void ratio and critical effective stress for a given soil can be represented by the curve in Figure 2.8, known as the *critical state line*. In e-log(p') space, the CSL plots as a straight line.

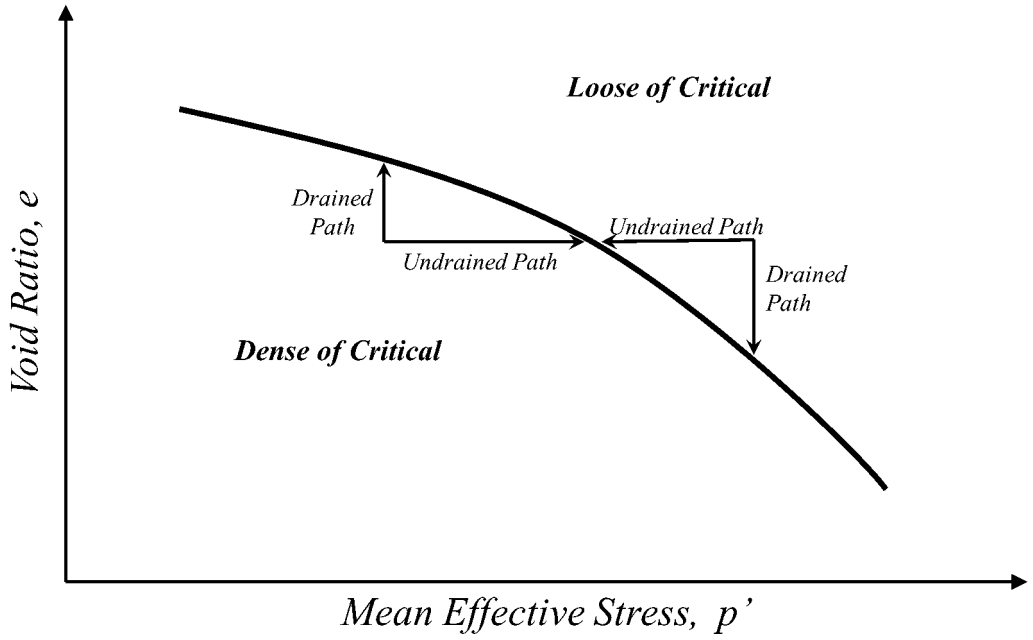

Figure 2.8: Illustration of the Critical State Line (CSL) in void ratio-effective stress space (after Idriss & Boulanger 2008)

Whether or not a soil is considered loose or dense is highly dependent on its initial relative density and effective stress. Thus, it is useful to examine the combined effects of D_R and σ'_{v0} by using both parameters to define the soil's initial *state*. By plotting e vs. σ'_{v0} or p' in Figure 2.8, the general response of the soil to shearing can be inferred by its position relative to the CSL. Soil states that plot below the CSL exhibit dilative behavior, and are considered *dense of critical*, while soil states that plot above the CSL will tend to contract, and are described as *loose of critical*. It is important to make the distinction between a material's relative density and its density relative to the solid state line. Close examination of Figure 8 shows that a soil can exist in a dense or very dense state ($D_R = 75\%$ or higher), but can still be considered loose of critical at very high confining pressures. This distinction is illustrative of the shortcomings in using solely absolute density measures in characterizing the response of sand to shear (Kramer, unpublished manuscript, 2014). The concepts of soil state and critical state can be extended to show that the behavior of sands is related to the proximity of the initial soil state to the critical state line (Been and Jeffries 1985). The *state parameter*, ψ, proposed by Been and Jeffries to represent this proximity, is defined, for a given p' as:

$$\psi = e - e_{cs} \tag{2.1}$$

where e and e_{cs} are the initial and critical state void ratios, respectively. Thus, it is

expected that soil states that are similar distances from the CSL will exhibit comparable responses to shear (Figure 2.9)

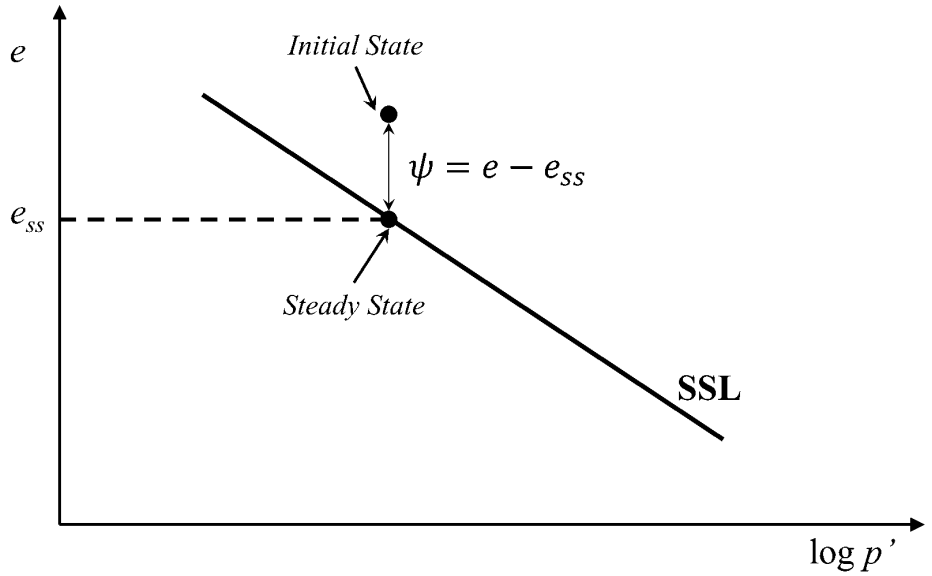

Figure 2.9: Illustration of the state parameter in relation to the Solid State Line (after Kramer, 1996)

Konrad (1988), found that normalizing the state parameter by (e_{max}–e_{min}) correlated better with dilatant shearing behavior. However, it is important to recognize that characterizing the state parameter of a particular soil requires determination of its maximum and minimum density as well as the determination of its critical state line. While these characteristics can be determined via careful laboratory testing, the inherent complexities of *in situ* deposits of sand render these types of tests both impractical and not particularly trustworthy (Idriss and Boulanger 2008). Alternatively, Boulanger (2003a) introduced the *relative state parameter*, ξ_R, which is defined as:

$$\xi_R = D_{R,CS} - D_R \tag{2.2}$$

where D_R is the current relative density, and $D_{R,CS}$ represents the relative density at critical state for a given sand. $D_{R,CS}$ is defined empirically, based on the work of Bolton (1986), as:

$$D_{R,CS} = \frac{1}{Q - \ln \frac{100(1+2K_0)\sigma'_{vc}}{3P_a}} \tag{2.3}$$

where σ'_{vc} is the effective overburden stress, K_0 is the coefficient of lateral earth pressure, P_a

is atmospheric pressure, and Q is a constant relating to the stress at which particle crushing becomes significant. Intuitively, Q depends on grain type; Bolton (1986) indicated that is approximately 10 for quartz and feldspar, 8 for limestone, 7 for anthracite, and 5.5 for chalk. Boulanger's relative state parameter can be related to the response of sand to shear without using complex and inefficient laboratory test procedures on a case-by-case basis. All that is required is the relative density and *in situ* confining pressure of the soil in question, as well as its granular composition. Boulanger (2003a) used cyclic triaxial and simple shear tests on Fraser Delta sand to show that there is an inverse relation between ξ_R and the ability of saturated sand to resist liquefaction when subjected to cyclic loading when $\xi_R < 0$. In other words, the closer D_R is to $D_{R,CS}$ the less dilative the soil is, and the less resistant it will be to generating excess pore pressures when subjected to undrained shear. Note that $D_{R,CS}$ contains a term that accounts for the in situ effective stress of the soil, thus $D_{R,CS}$ effectively characterizes the interaction between relative density and stress in relation to the critical state.

2.3.2 Monotonic Loading of Saturated Sands

As stated previously, the response of a sand to shear loading is dependent primarily on its relative density and effective stress. The combination of these factors relative to the critical state line determine whether the soil behaves in a contractive or dilative manner. Monotonic loading can be applied in two ways: drained or undrained, and the response of the soil will depend on which of these conditions applies.

Drained Shear

Lee and Seed (1967) performed drained triaxial tests on reconstituted Sacramento River Sand, in both loose ($D_R = 38\%$) and dense ($D_R = 100\%$) states, with varying confining pressures for each relative density. Because the loading is drained, no excess pore pressures are generated, meaning that the soil will undergo some change in volume. Thus, it is informative to examine the behavior of the sand in terms of both stress-strain response and vertical strain response (Figure 2.10).

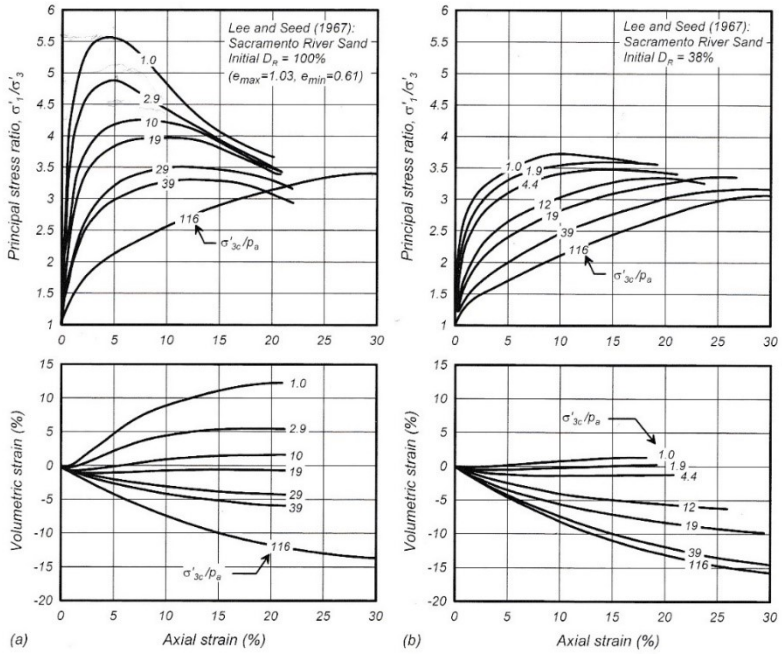

Figure 2.10: Results of monotonic drained triaxial tests on Sacramento River Sand (Idriss and Boulanger 2008, after Lee and Seed 1967))

The stress-strain curves for the $D_R = 100\%$ sand showed that at low confining stresses, the shear stress approaches a distinct peak at relatively low shear strains, followed by a rapid drop in shear stress to the critical state stress ratio. Conceptually, the rapid drop in stress corresponds to the initially dense particles finally being forced to ride up and over each other to accommodate the high shear stress. The accompanying plot of vertical strain shows that for the corresponding low confining stresses, the change in sample height is positive, indicating a dilative response. At intermediate initial confining stresses ($\sigma'_{3c}/p_a =$ 10 and 19), the volumetric strain is marginal, indicating that while there is some dilative and contractive response, respectively, the volumetric strains and maximum applied shear stresses are reached relatively quickly, i.e. at lower strains . In $e-p'$ space, the initial state of these samples would be much closer to the CSL than the other 5 test samples. The sample confined to the highest effective stress ($\sigma'_{3c}/p_a = 116$) showed a very large decrease in volume and no low-strain peak shear stress. Despite being a relatively dense sample at D_R=100%, this sample exhibit clear contractive behavior. Conceptually, the over-riding of particles at high stresses is made impossible by the very high confining pressure on the specimen. That is to say, dilative behavior, even for the densest possible soil, can be inhibited at high enough vertical effective stresses.

The D_R=38% specimen generally exhibited contractive behavior for almost all confining pressures, with the exception of the lowest possible ($\sigma'_{3c}/p_a = 1$), which only showed a slight increase in height (about +1% volumetric strain). We see that the maximum

shear stresses are generally lower in the looser specimen, and the magnitude of volumetric strains is much higher at comparable confining pressures. In this case, the looser particle arrangement indicates that the soil skeleton's resistance to shear will instead take the form of densifying into a more tightly-packed arrangement, rather than the riding up of particles over each other seen in the denser specimens. There is no distinct peak shear stress, and stress-strain response at low-to-intermediate strains is generally quite gradual.

Note that for all samples, regardless of initial state, the principal stress ratios (σ'_1/σ'_3) at large strains tended towards approximately the same value of 3.3. This value corresponds to the critical state stress ratio for the Sacramento River sand. Using this information, the *critical state friction angle*, ϕ_{cv} can be determined to be about 32°.

Undrained Shear

Undrained shear loading differs from drained loading in that the pore water is not allowed to drain from the specimen. The soil mass is in essence a closed system, meaning that there are no volumetric strains, and thus instead of a change in void ratio, the response of the soil mass to shear stress is manifested in the generation of excess pore pressures. Ishihara (1993) performed undrained triaxial shear tests on saturated Toyoura sand to examine the general response characteristics of granular material to undrained shear. The Toyoura sand was tested in three states of relative density: loose ($D_R = 16\%$), medium ($D_R = 38\%$), and dense ($D_R = 64\%$). At each relative density, the specimens were tested at a range of initial confining pressures. The results are summarized in Figure 2.11. Because undrained specimens undergo changes in pore pressure, and hence changes in their effective stresses, it is more instructive to pair the usual stress-strain plot with a plot of the stress path, or $q - p'$ plot, where q is the deviatoric stress, and p' is the mean effective stress.

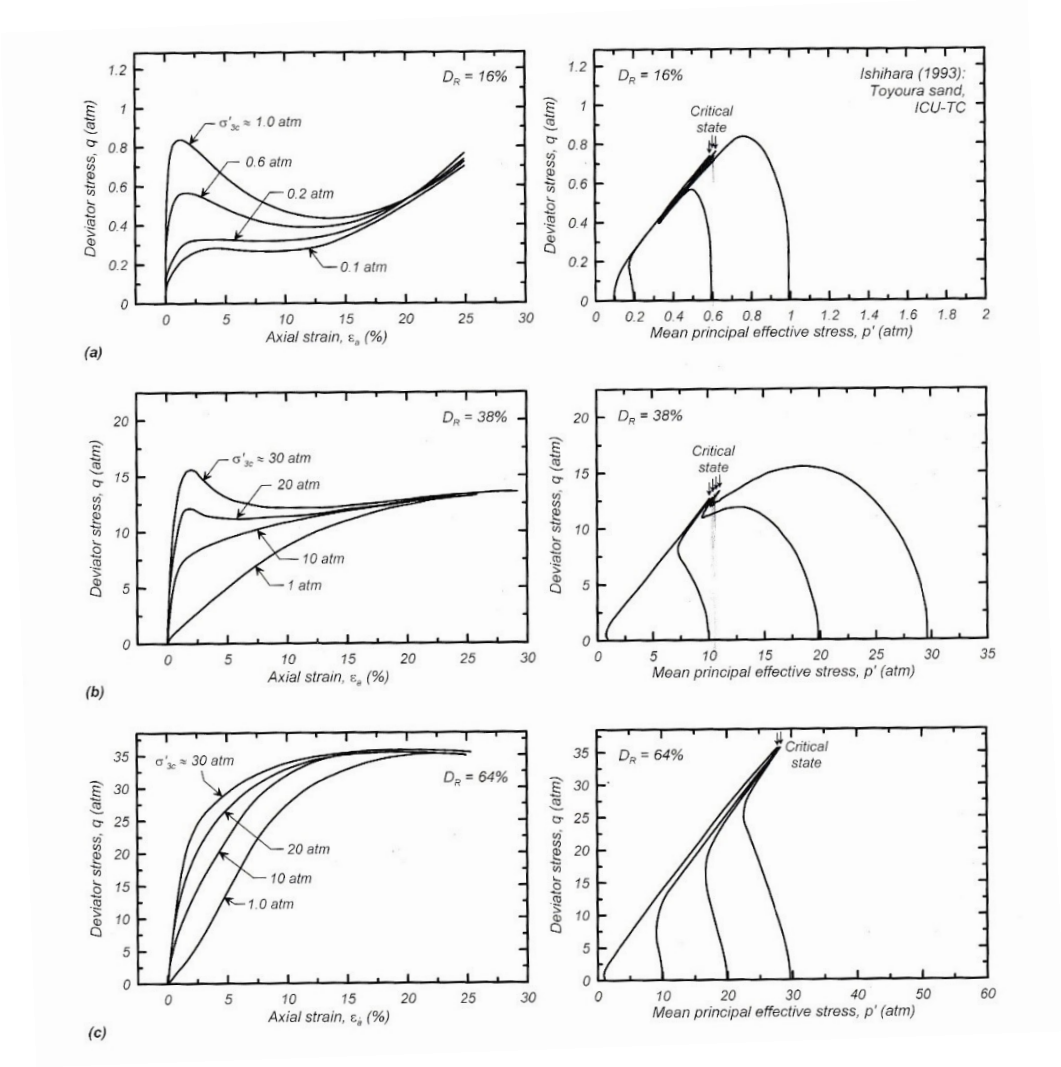

Figure 2.11: Results of monotonic undrained triaxial tests on Toyoura Sand (Idriss and Boulanger 2008, after Ishihara 1993)

Tests on the loose specimens ($D_R = 16\%$), which were consolidated to pressures between 0.1 and 1 atm, showed that in an undrained condition, the response at lower strains (less than 5%) of saturated sand is generally contractive in nature. We see a very sharp rise in shear stress at very low strains (less than 1%), followed by considerable post-peak softening (marked by an increase in pore pressure and associated decrease in p') in the specimens consolidated to σ'_{3c} greater than about 0.5 atm. At confining pressures lower than 0.5 atm, the post-peak strain softening is generally dampened by the lack of overburden stress. At larger strains (10-15%), all specimens tended to exhibit strain-hardening (i.e., dilative) response, which is marked by an increase in shear stress, decrease in pore pressure, and an increase in p'. It is notable that at large strains, all the loose specimens, regardless of their initial confining pressures, tended towards the same critical state strength. Additional examination of the stress path shows that the dilative response

at critical state occurred along the same line of constant stress ratio, q/p'.

Specimens that had been tested at medium density ($D_R = 38\%$) were able to be consolidated to much higher confining pressures (1 to 30 atm), and thus exhibited higher peak strains and a higher critical state strength than the looser specimens. Specimens consolidated to higher pressures (20 and 30 atm) showed slightly contractive behavior at lower strains and some post-peak softening response, while the lower-confined specimens (1 and 10 atm) showed strain-hardening response. Once again, all specimens tended towards the same critical state strength and stress ratio. All four dense specimens ($D_R = 64\%$) exhibited strain-hardening response, and reached a common critical state strength that was about 3 times higher than that of the $D_R = 38\%$-sand. This set of triaxial tests, as well as countless others, reveals a number of overarching principles that govern the behavior of sand in undrained shear. For soils of constant initial effective stress, denser soils will exhibit more dilative behavior (resulting in a decrease in pore water pressure, and increase in effective stress) (Figure 2.12); for constant relative density, an increase in the initial confining pressure will increase the contractive behavior of the soil (generating more excess pore water pressures) (Figure 2.13). It was also seen that sands at the same relative density will tend to converge toward the same critical state strength and same effective stress at large strains, regardless of their initial confining pressure. Finally, examination of the stress paths shows that the critical state stress ratio are all roughly the same (about 0.8), regardless of relative density. Hence, the characteristics of the critical state line are not dependent on depositional factors like density and effective stress, but rather more fundamental characteristics of the soil deposit, such as grain size distribution, angularity, and roughness.

Transitional Behavior

The results of Ishihara's undrained tests on Toyoura sand also allow for the examination of another important phenomenon that often occurs during undrained shear. A revisiting of the stress paths shows that the looser specimens, as well as the medium specimens consolidated to high stresses, underwent a transition from contractive to dilative behavior at some point during shearing. This point of transition has come to be known as *phase transformation*. Further tests on Toyoura sand (1993) in very loose states highlight this point of transition from contractive to dilative behavior (Figure 2.14).

The behavior of sand as it transitions from contractive to dilative is actually quite complex. As seen in Figure 2.15 (Kramer, unpublished manuscript), there are several states of interest during this transition, and thus several distinctions should be made

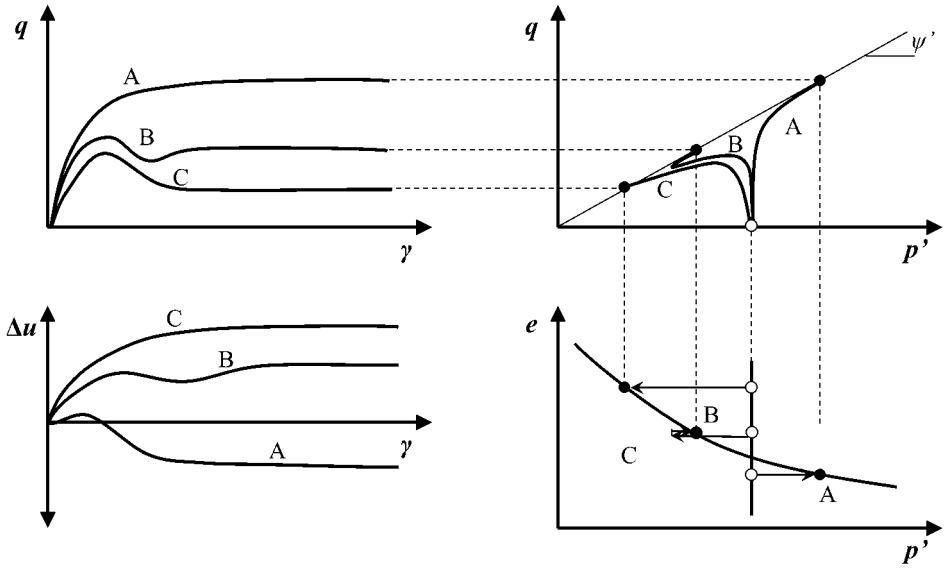

Figure 2.12: Idealized undrained response of sand with constant confining pressure and variable relative density (after Kramer, unpublished manuscript)

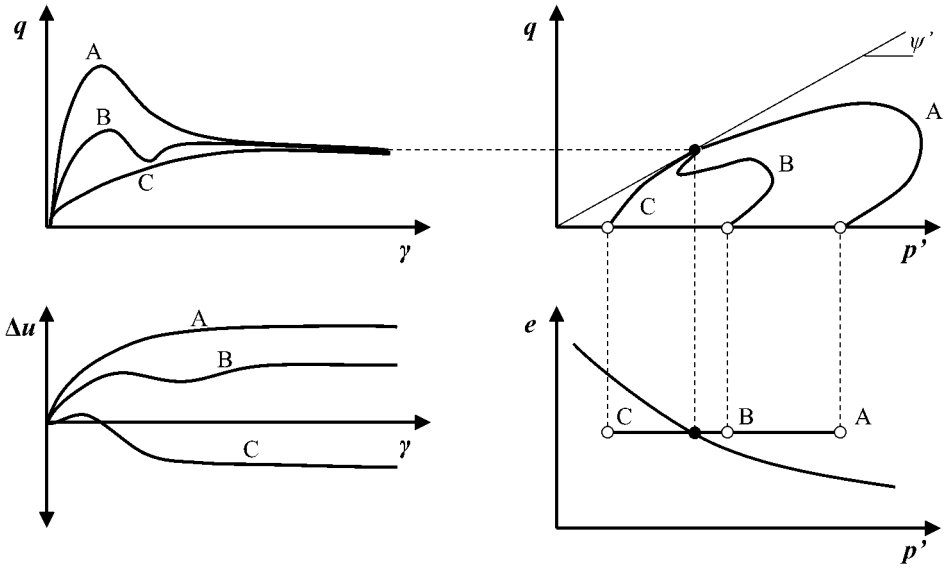

Figure 2.13: Idealized undrained response of sand with constant relative density and variable confining pressure (after Kramer, unpublished manuscript)

about what each state represents. It may seem intuitive to consider the point of phase transformation to be the point of minimum mean effective stress in $q - p'$ space (p'_{min}). However, the soil is in fact slightly contractive at this point, and the true point of phase transformation is instead defined by the point where the tangent to the stress path is parallel to the total stress path. Additionally, the local point of minimum shearing resistance after the onset of post-peak softening must also be distinguished, and is generally referred

to as the *quasi-steady state* (QSS) point. In loose sands that undergo post-peak strain softening as well as phase transformation, the QSS should be distinct from the *steady state of deformation* (SS), which is defined almost identically to the critical state of deformation previously discussed, with one additional condition: SS deformation occurs not only at constant effective stress, volume, and shearing resistance, but also at constant strain rate. The QSS also must be distinguished from the *ultimate steady state* (USS), which is defined as the soil's shearing resistance at very large strains (Yoshimine and Ishihara 1998).

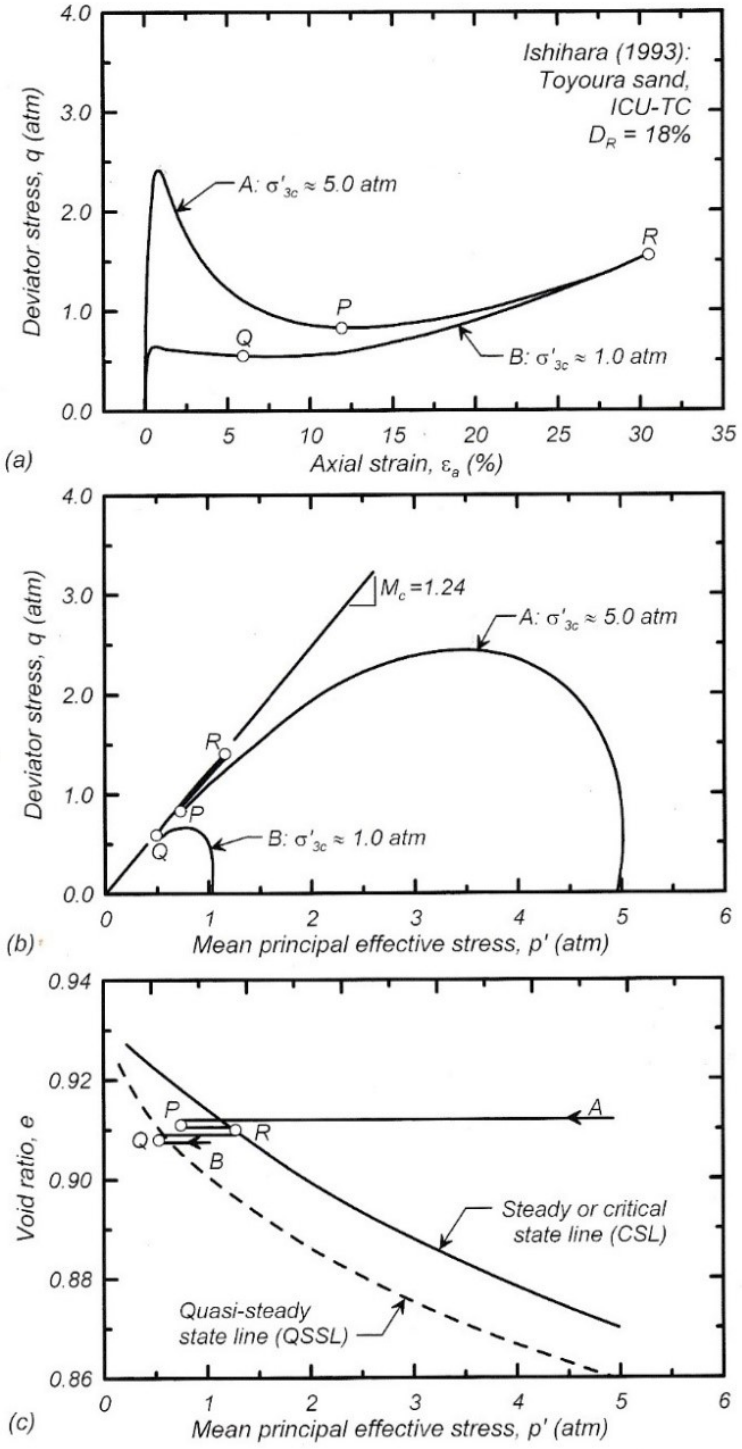

Figure 2.14: Illustration of phase transformation points, using the results of isotropically consolidated triaxial tests on initially loose Toyoura sand at different confining pressures (Idriss and Boulanger 2008)

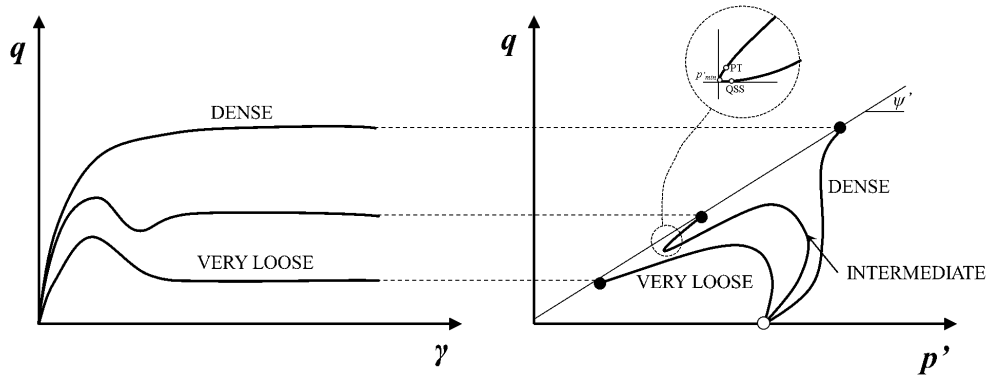

Figure 2.15: Illustration of phase transformation (PT), quasi-steady state (QSS), and minimum effective stress points in stress-strain and stress path space (after Kramer, unpublished manuscript)

2.3.3 Cyclic Loading of Sand

Generally, granular soils rarely exhibit undrained response under monotonic loading. The permeability of sandy soils is so high that any momentary excess pore pressures caused by an applied shear load are almost instantaneously dissipated through the relatively large pores of the soil mass. Unless there are significant impedances to drainage of water (such as clay layers or seams), the response of sand to a monotonic load (such as a structural footing or embankment) is modeled in terms of drained strength. However when dealing with rapid cyclic loading, such as those associated with earthquake-induced ground motions, excess pore pressure that is momentarily generated from a single loading cycle often does not have time to dissipate before the next loading cycle (generally a reversal of stress) occurs. It is for this reason that characterizing the undrained response of sand is critical in geotechnical earthquake engineering.

Drained Cyclic Loading

It is instructive to first examine the nature of drained cyclic behavior, since many of its features can be directly related to undrained cyclic loading (Idriss and Boulanger 2008). Figure 2.16 shows the results of a drained, strain-controlled cyclic simple shear test on Ottawa sand (Youd 1972). The general trend throughout the test is an incremental, ratcheting-type net contraction of the specimen. It can be seen that within a particular cycle, the specimen will initially contract after the reversal of the direction of stress. Once the horizontal strain reaches approximately zero, the behavior transitions from contractive to dilative (point D in Figure 2.16). In general, the contractive increments are of a larger magnitude than the dilative increments, resulting in accumulated net contraction.

The magnitude of the net contraction depends on a number of factors. Similar to monotonic loading, the degree to which the specimen will contract overall is dependent on both its initial density and effective stress. It also depends on the characteristics of the cyclic load being applied to it. Specifically, the larger the magnitude of the applied cyclic shear stress (and thus the greater shear strain the specimen undergoes), the greater the magnitude of contraction the sand will undergo. Of equal importance is the number of applied loading cycles; with each progressive cycle, the sand will accumulate more vertical strain, with the change in void ratio becoming smaller with each cycle.

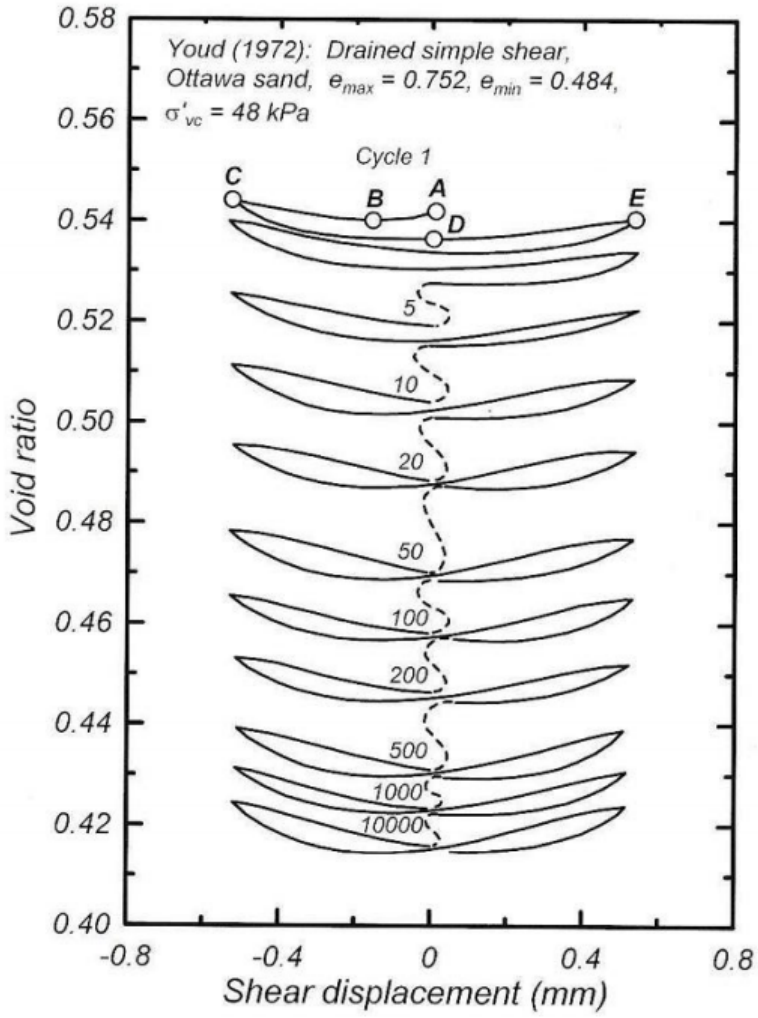

Figure 2.16: Results of a drained cyclic shear test on dry Ottawa Sand (Idriss and Boulanger 2008, after Youd 1972)

Undrained Cyclic Loading

The characteristics of drained cyclic loading introduced in the previous section can be applied in a similar fashion to characterize the response of sand to undrained cyclic loading.

In the undrained case, the net contraction, as well as the alternating contractive and dilative behavior seen throughout a single drained loading cycle, is manifested through changes in pore pressure, rather than volumetric strain. These concepts are classically illustrated by the results of an undrained cyclic triaxial test on Sacramento River sand in Figure 2.17 (Boulanger and Truman 1996). The specimen used for this test was a medium-dense clean sand that was anisotropically consolidated to an initial static shear stress ratio ($q/2p'_c$) of about 0.1. We see that with each progressive harmonic loading cycle, the specimen experiences an increase in pore pressure due to incremental contraction similar to that seen in the drained cyclic loading. As the pore pressure increases, the effective stress decreases, and the specimen moves towards the left in stress path space. In stress-strain space, the sand initially deforms along the same curve throughout the first several cycles, exhibiting relatively small decreases in stiffness.

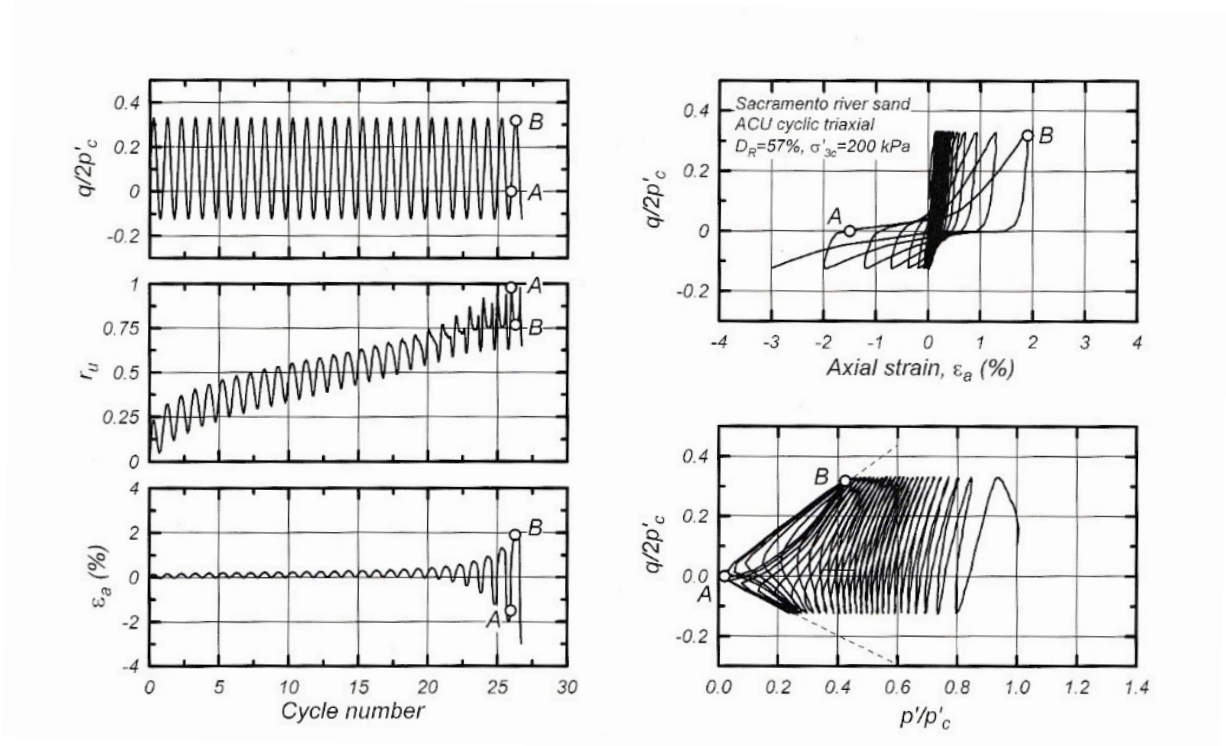

Figure 2.17: Results of a drained cyclic shear test on dry Ottawa Sand (Idriss and Boulanger 2008, after Youd 1972)

However, as the specimen approaches the failure envelope in stress path space, we see larger decreases in effective stress within each cycle, and increasingly flatter stress-strain hysteresis loops, indicating significant softening of the soil mass. Finally, at about the 27th loading cycle, the effective stress has been reduced to zero (Point A), resulting in the onset of liquefaction. At this point, the total stress in the sample is completely accounted for by the pore water pressure, and thus a large reduction in stiffness occurs, as evidenced by the very flat curve as the specimen is loaded from point A to point B.

The accompanying plots of excess pore pressure ratio ($r_u = \delta u/\sigma'_{3c}$) and shear strain show that while the pore pressure increase is relatively consistent throughout the loading sequence, the shear strains are relatively small up until just a couple of cycles before the onset of liquefaction. It is also important to note that when the specimen reaches the failure envelope during a particular loading cycle, it will suddenly dilate within that same cycle before the stress reversal occurs. This effect is perhaps better illustrated in the schematic of the behavior of liquefiable soil in Figure 2.18 (Boulanger and Ziotopoulou 2012). In stress path space, the sequence of dilation occurs along the same slope as the failure envelope, and the subsequent cycles after the onset of liquefaction seem to indicate that the system has stabilized somewhat. However, the accompanying stress-strain curve shows that even though the stress path appears to be stable, the shear strain amplitudes continue to increase with subsequent cycles. These seemingly contradictory results can be resolved by noting that this softening is unrelated to the reduction in effective stresses, and is more a result of the softening of the fabric of the soil (Kramer 2009).

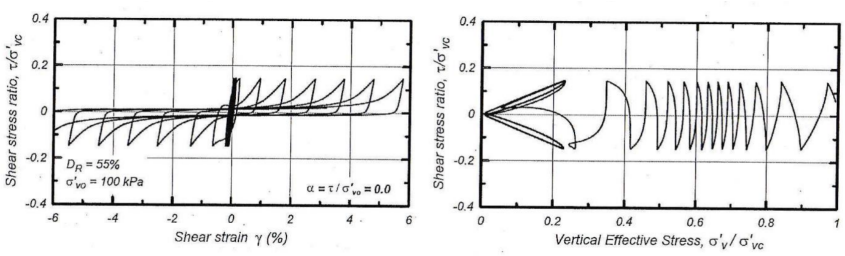

Figure 2.18: Idealized stress-strain and stress path response of liquefiable soil subjected to harmonic cyclic loading (Boulanger and Ziotopolou 2012)

2.3.4 Factors Affecting Pore Pressure Generation

There are numerous factors that can affect the rate at which excess pore pressures are generated during cyclic loading. These factors are generally related to the soil grain characteristics, the soil's initial state, and the characteristics of the applied cyclic load.

Soil Plasticity

Pore pressure generation is directly related to how sensitive a soil's response is to its current state of stress. Purely frictional soils such as sands and gravels derive all of their strength from their effective stress. Thus, frictional soils will exhibit increasingly large strains as their effective stress moves towards zero during cyclic loading. This results in flatter stress-strain hysteresis loops, and more rapid stiffening during dilation (Figure 2.19). More cohesive soils, such as silts and clays, tend to still exhibit some strength

even at low effective stresses, and thus are less contractive and less sensitive to reductions in effective stress during cyclic loading. When comparing the cyclic responses of the frictional soil (PI=0) and cohesive soil (PI=26) in Figure 2.19, we see that the stress path of the cohesive soil tends to stabilize at a higher effective stress than the frictional soil. Furthermore, comparison of the stress-strain curves indicates that the reduction in stiffness is considerably smaller in the higher plasticity material, and the variation in stiffness during a single cycle is much lower. The result is much "fatter" stress-strain hysteresis loops, which indicates a larger rate of dissipated energy during cyclic loading. In other words, while cohesive certainly may soften significantly during cyclic loading, they do not liquefy in the same manner that frictional soils do, and are generally more resistant to cyclic shear stresses.

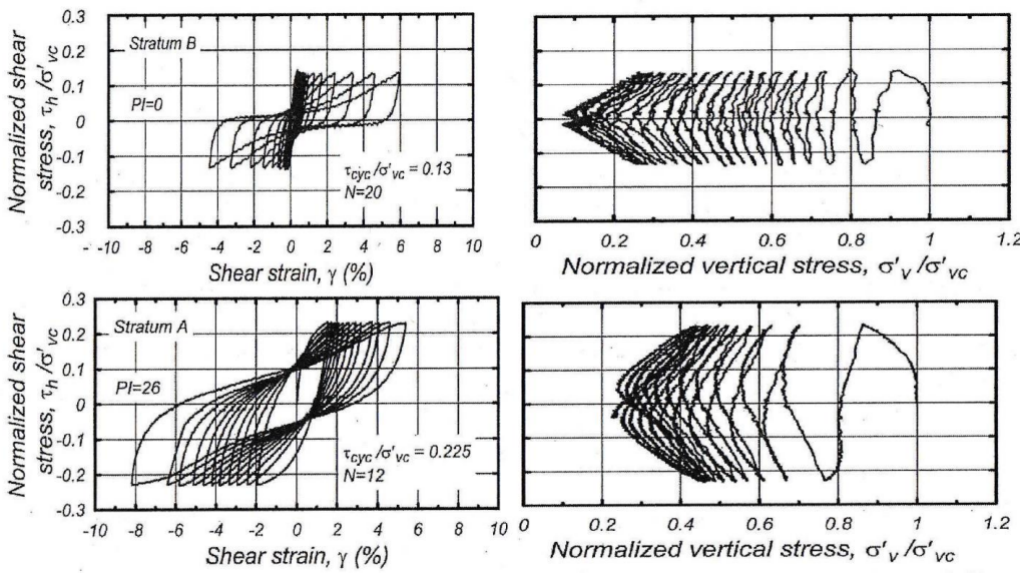

Figure 2.19: Effects of plasticity on undrained stress-strain response and pore pressure generation. (Kramer 2009)

Amplitude of Cyclic Loading

In general, the rate of pore pressure generation is directly related to the amplitude of cyclic shear stress imposed on the soil. Figure 2.20 shows a schematic comparison of the response of a soil subjected to cyclic shear strains of 15 kPa (Specimen A) and 20 kPa (Specimen B). Specimen B experienced much larger reductions in effective stress on a per-cycle basis than Specimen A, and reached liquefaction in just 7 cycles, compared to 23 for Specimen A.

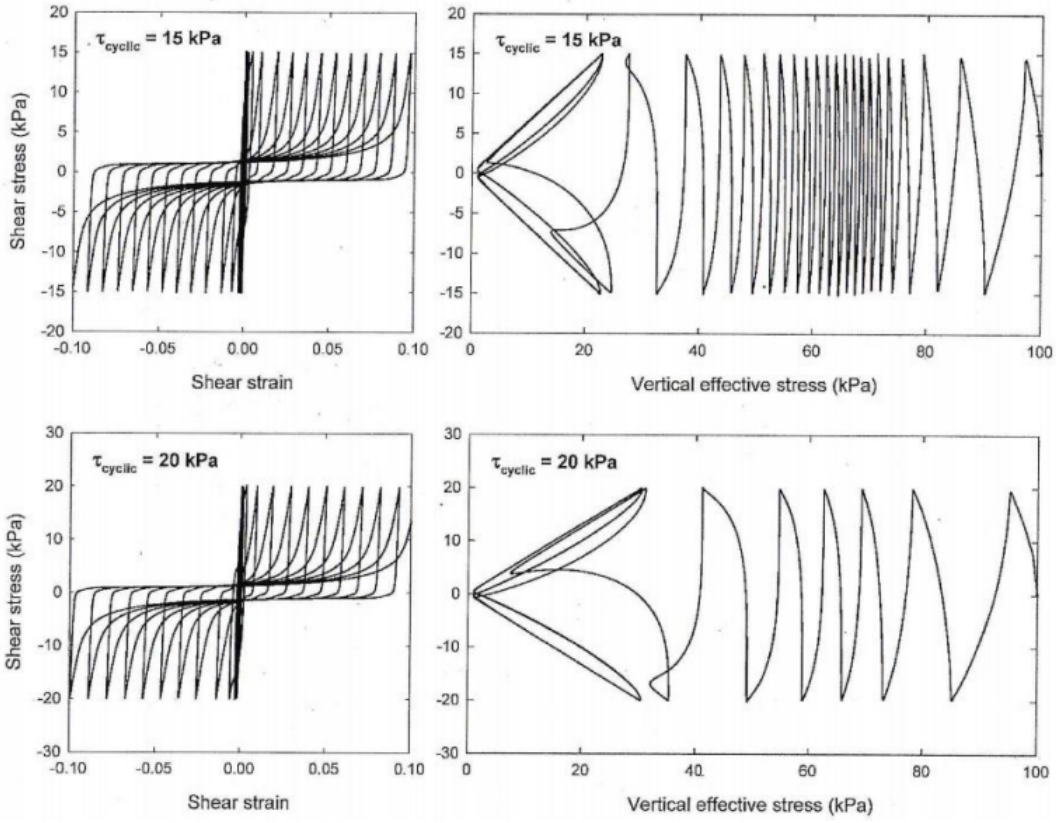

Figure 2.20: Effects of cyclic load amplitude on undrained stress-strain response and pore pressure generation. (Kramer 2009)

Initial Relative Density

As discussed previously, the initial relative density of the soil directly influences how contractive or dilative the soil's response to shearing will be. In a single cycle, a looser soil can be expected to experience a larger reduction in effective stress than the same soil in a denser state would, due to the fact that a looser material is further from the critical state line in e-p' space. Thus, when subjected to the exact same cyclic loading, the looser material will reach liquefaction in fewer cycles. These effects are illustrated schematically in Figure 2.21. Specimen A, which had an initial relative density of 40%, reached liquefaction in just 14 cycles. Specimen B was prepared to 50% relative density, and required 38 cycles to reach liquefaction.

Initial Effective Stress

Also discussed previously was the tendency for large confining stresses to inhibit dilative behavior, or amplify contractive behavior in soil. Thus, all other factors being equal, we

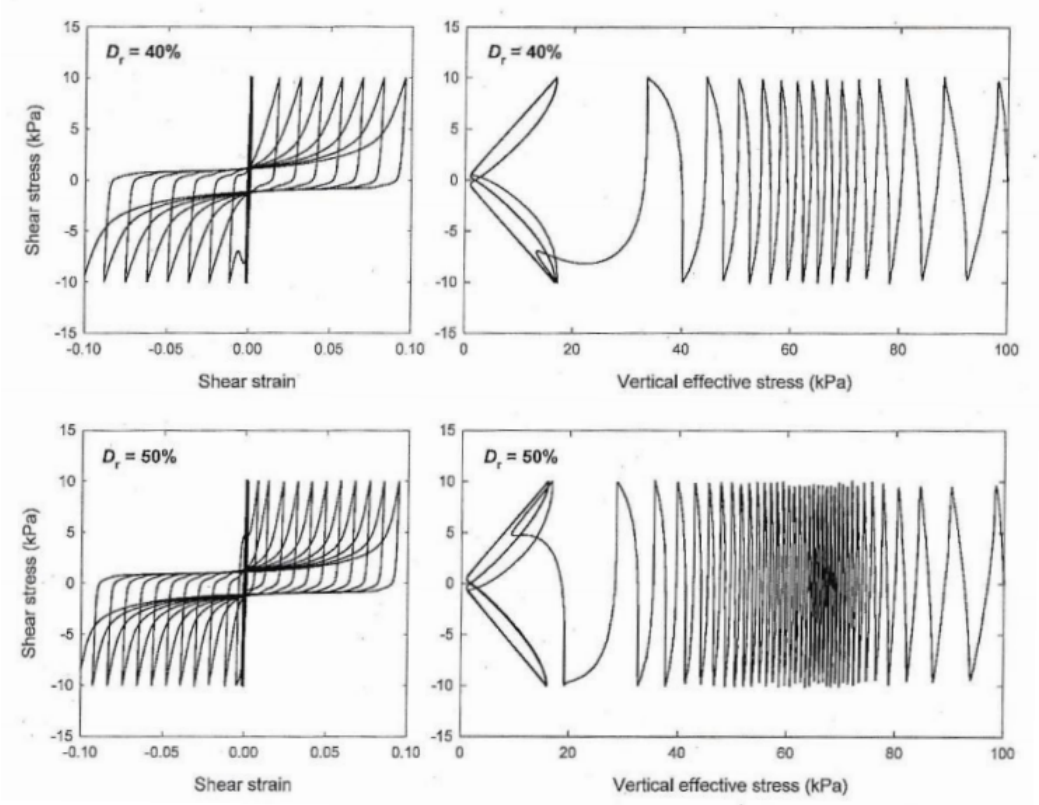

Figure 2.21: Effects of initial relative density on undrained stress-strain response and pore pressure generation. (Kramer 2009)

can expect that a specimen of sand consolidated to a higher initial effective stress will experience a larger reduction in effect stress upon shearing than a specimen consolidated to a lower effective stress. As a result, when subjected to cyclic shear, the specimen at higher confining stresses is expected to generate excess pore pressures at a faster rate, and will require fewer cycles to liquefy. The schematic plots in Figure 2.22 confirms these trends; Specimen A was consolidated at $D_R = 60\%$ to 100 kPa, while Specimen B had the same density, but was consolidated to 200 kPa. Specimen B reached liquefaction in 15 uniform loading cycles, while Specimen A reached liquefaction in 22 cycles.

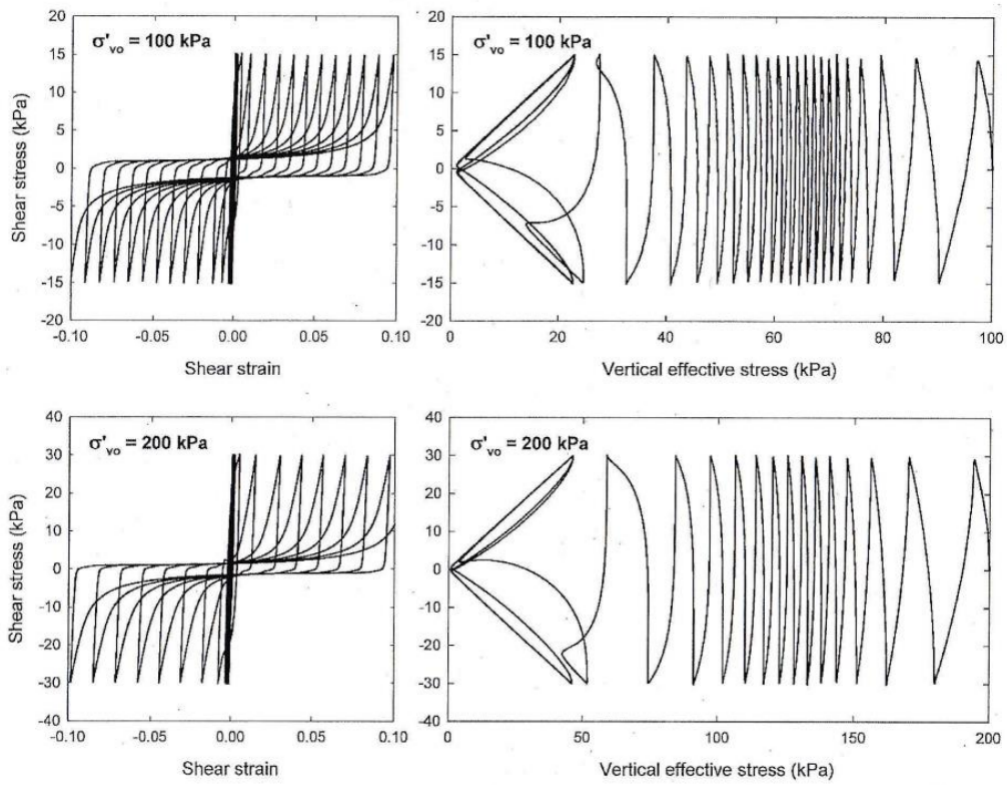

Figure 2.22: Effects of vertical effective stress on undrained stress-strain response and pore pressure generation. (Kramer 2009)

Initial Static Shear Stress

Soil in sloping ground is subjected to an initial static shear stress prior to any earthquake shaking. In very loose soils, the existence of a static shear stress usually results in lower liquefaction resistance, i.e. fewer loading cycles required to reach initial liquefaction. In medium dense to dense soils, however, the existence of static shear stress can actually increase liquefaction resistance. Increases in pore water pressure generally occurs at points of zero shear stress in the material, when the soil particles begin to reorient themselves. During cyclic loading, these zero shear stress instances occur during reversals in stress, at the moment in which the sign of the shear stress is changing. For soils subjected to high enough static shear stresses, such a reversal in shear stress may not occur during cyclic loading, and thus pore pressure generation may be somewhat inhibited. In many cases, liquefaction may not occur because the zero effective stress condition is not reached.

2.4 Analysis of Liquefaction Triggering

Two main conditions must be satisfied for liquefaction to occur. First, the soil deposit must be sufficiently susceptible to liquefaction, i.e. it must exist in an environment such that the soil will exhibit contractive behavior when sheared. Secondly, the seismic load must be significant enough to cause the soil to contract to the point of zero effective stress. This will require a combination of load amplitude and number cycles that will would be sufficient to trigger liquefaction. Thus, it is the task of the engineer to accurately identify and characterize the likely loading demands placed on the soil, and in turn the soil's ability to resist liquefaction. There have been multiple different approaches to analyzing the triggering of liquefaction. The most common is the cyclic stress-based approach, which will be discussed in detail in this section. Other methods have also been explored by researchers, such as methods based on the relationship between cyclic shear strains and pore pressure generation, as well as methods based on dissipated strain energy. Whatever the method used, the overall theme is consistent. The soil deposit in question must first be evaluated for susceptibility, and the characteristics of the expected seismic load must be accurately determined.

2.4.1 Liquefaction Susceptibility

Classification of liquefaction susceptibility requires a thorough understanding of the geologic history of the site, detailed information about its subsurface stratigraphy and hydrogeologic features, and an accurate characterization of the grain-size characteristics and stress state of the potentially liquefiable soil in question. The propensity of a soil deposit to liquefy can be characterized, at least on a first-level basis, by considering four basic criteria of liquefaction susceptibility.

Historical Criteria

A common misconception surrounding liquefaction is the belief that it effectively densifies the affected soil deposit, thus making it more resistant to liquefaction in the future. The reality is that while *densification* of individual soil particles may occur on a local scale, what is actually occurring throughout the general soil deposit is better described as a *redistribution* of individual soil particles. That is to say, if a particular zone of a liquefied soil deposit has densified, then another zone has loosened. There is more than sufficient evidence to support this mechanism, as there are numerous instances where liquefaction has been observed to have occurred in the same soil deposit in multiple earthquakes, most

recently in Christchurch, New Zealand during the 2010-2012 sequence of large earthquakes.

The most obvious method of historical characterization of liquefaction is a simple review of literature concerning liquefaction case histories at or near the site in question. However, detailed documentation of liquefaction has only been in practice for about the last half century or so, which makes up a very small portion of the geologic time scale that a practicing engineer is interested in. Furthermore, post-earthquake liquefaction reconnaissance is generally limited to examining the evidence of surface liquefaction, such as sand boils, other sediment ejecta, lateral spreading, ground cracks, and ground subsidence. The absence of all of these phenomenon does not completely rule out the occurrence of liquefaction. In absence of surface evidence, subsurface investigations into historical liquefaction, commonly known as *paleoliquefaction investigations* can be effective in revealing particular subsurface geologic features that point to historical liquefaction. In general, evidence of the flow of liquefied sand, such as subsurface dikes and sills, can provide sufficient evidence of liquefaction in a particular deposit (Figure 2.23). Paleoliquefaction can be a valuable, first-level method in identifying a soil deposit as being potentially liquefiable.

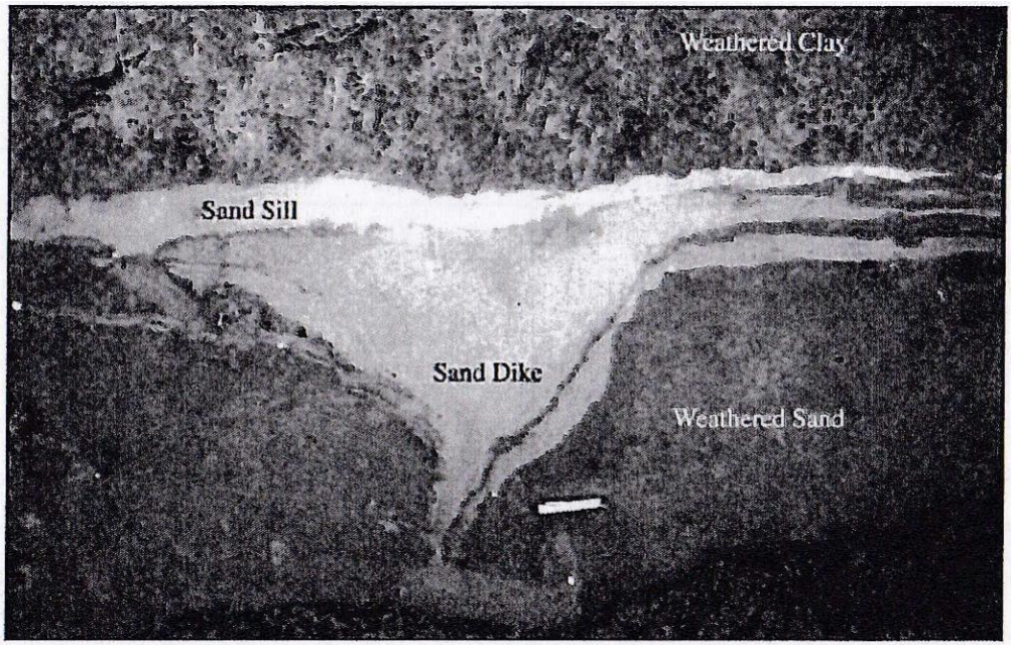

Figure 2.23: Profile view of a sand dike that occurred as a result of the flow of liquefied sand in Missouri. (Kramer 2009)

Geologic Criteria

The next level of characterization involves identifying soils deposited via particular geologic processes that are associated with potentially liquefiable material. The depositional processes of interest are any modes that separate out particles into layers of uniform gra-

dation, cause settlement of particles in loose configurations, and result in smoother and more rounded individual grains. This points primarily towards many water-borne modes of deposition, such as fluvial and colluvial, and to a lesser degree, alluvial deposits. Saturated aeolian deposits have also been observed to liquefy (Kramer 1996). It has also been observed that geologically younger deposits, primarily Holocene-aged, are more likely to liquefy than their Pleistocene predecessors. This is generally due to the fact that Holocene deposits are usually closer to the ground surface, and thus are likely to be less dense than Pleistocene soils. Additionally, younger deposits are less likely to have undergone geologic aging processes, such as cementation, that would increase their resistance to imposed shear stresses.

Sites with high ground water levels are also more susceptible to liquefaction. It is for this reason, as well as those outlined above, that hydraulic fills are especially suspect when evaluating a site's susceptibility to liquefaction. It has been remarked that there is hardly a more effective way to manufacture a liquefiable soil than via the method of hydraulic filling. This method was favored in the construction of embankment dams and artificial reclamation projects for decades before liquefaction became a well-known seismic hazard, due to its speed and ease of material transport from quarry to site. However, the process of hydraulic filling fulfills nearly every criterion outlined in this section. It involves the deposition of coarse-grained, purely frictional material in a water; it usually occurs in sites where high groundwater conditions are present; and it is obviously very young geologic material with very low density. Armed with this knowledge, it should come as no surprise that many observed cases of liquefaction have occurred at sites where artificial fill has been placed in order to reclaim land, such as in Dagupan city in the 1990 Luzon, Philippines earthquake; or to build large embankment dams, as was the case in the Lower San Fernando Dam discussed in Section 2.2. In particular, the failure of the San Fernando Dam in 1971 forced state government agencies throughout the western United States to re-evaluate the seismic stability of their many embankment dams, resulting in large-scale retrofit projects that are still continuing to this day.

Compositional Criteria

It is also important to consider soils that, at a fundamental level, are likely to exhibit high volume change behavior when subjected to cyclic loading. This requires a detailed evaluation of the grain-size characteristics of the soil deposit in question. Particle size is of utmost importance; a wide range of grain sizes and soil classifications can be susceptible to liquefaction, from nonplastic silts to coarse sands. Even finer gravels can potentially liquefy in situations where drainage might be impeded by an impermeable layer, such as

a clay or silt seam. It is also important to consider particle shape; rounded particles tend to slide past each other more easily, meaning that a soil deposit of rounded particles (as is seen in water-borne depositional environments) will be less resistant to applied shear stresses, and thus more susceptible to liquefaction. Finally, it is important to recognize the influence of grain-size distribution on liquefaction susceptibility. Well-graded soil deposits are generally denser, due to the presence of smaller particle sizes residing in what would be void spaces in a uniformly-graded soil skeleton. This results in a tighter-interlocked structure that is more resistant to shearing deformations, and thus less susceptible to liquefaction.

State Criteria

Finally, as discussed in Section 2.3, an understanding of the soil deposit's current state of stress in relation to its critical state line will also provide key information about its liquefaction susceptibility. Knowing the soil's initial relative density and *in situ* effective stress, and using an empirical or laboratory-based relationship to determine the relation of its state to the critical state line will allow the engineer to determine how contractive or dilative a particular soil deposit would be under undrained loading. Once a site has been identified as potentially susceptible using the criteria outlined above, the task now turns towards identifying sources of seismicity, characterizing the expected seismic demand on the soil deposit, and estimating the resistance of that soil deposit to liquefaction under the expected conditions.

2.4.2 Cyclic Stress-Based Approach

The cyclic stress-based approach is the most common way practicing engineers evaluate liquefaction potential. While several different stress-based methods have been developed by different researchers, they all have the same essential framework: a deterministic evaluation of cyclic stresses due to earthquake loads is compared to the cyclic resistance of the soil deposit in question. The result is a calculated factor of safety against liquefaction:

$$FS_{liq} = \frac{CRR}{CSR} \tag{2.4}$$

where CRR is the cyclic resistance ratio, or the capacity of the soil to withstand cyclic stresses; and CSR is the cyclic stress ratio, which is the demand load being placed on the soil.

Estimation of Earthquake-Induced Cyclic Stresses

The cyclic stress ratio (CSR), the demand parameter of interest in this factor-of-safety analysis, is theoretically represented by Equation 2.5 below, and is simply the ratio of the induced cyclic stress to the vertical effective stress:

$$CSR = \frac{\tau_{cyc}}{\sigma'_{v0}} \tag{2.5}$$

Practically speaking, the cyclic shear stresses induced by seismic activity can be primarily attributed to vertically-propagating horizontal shear waves (or SH-waves). The uncertainty then lies in finding a method for relating the estimated loading parameter to an induced cyclic shear stress. Seed and Idriss (1971) devised a simplified procedure for liquefaction evaluation that involves using the peak ground acceleration (PGA), which continues to be used in practice today.

Initially, the maximum induced shear stress at any depth for a rigid body, $((\tau_{max})_r$, can be calculated simply by multiplying the PGA, in units of g, by the total stress at a given depth:

$$(\tau_{max})_r = (\gamma z)a_{max} = \sigma_v a_{max} \tag{2.6}$$

However, the assumption of a rigid body is not generally applicable to a column of potentially liquefiable soil, which generally behaves as more of a compliant or deformable column. Thus, we can expect that the peak ground acceleration seen at the surface actually decreases with depth. Idriss (1999) and Golesorkhi (1989) used nonlinear site response analyses to show that, in a practical manner, the reduction of acceleration in the soil column is primarily a function of earthquake magnitude (M) and depth (z). Those analyses resulted in a depth reduction coefficient, r_d, which is illustrated in Figure 2.24 .

It is also important to note that earthquake time histories generally consist of many cycles, with a wide range of acceleration amplitudes. The demand energy induced by seismic shaking can be approximated as a series of uniform loading cycles; thus, the peak ground acceleration, which can often be the result of a single large pulse, is not the best representation of the earthquake demand energy. Seed and Idriss chose to represent the applied cyclic shear stresses as 65% of the peak value, which is known as the *equivalent uniform value*. By applying the reduction factors due to depth and the equivalent uniform cycles, the applied cyclic shear stress at a given depth can be represented by:

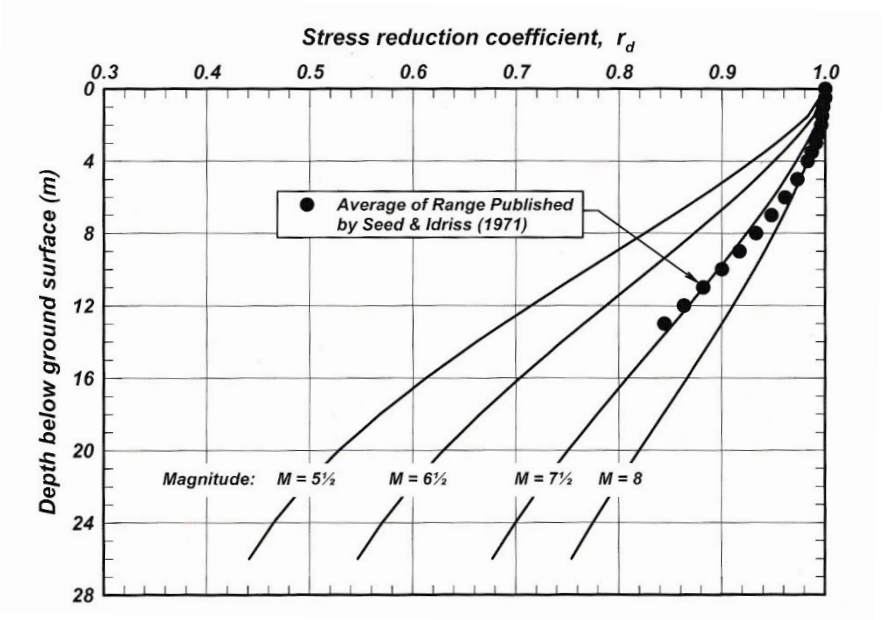

Figure 2.24: Variation in the stress reduction coefficient with respect to depth and magnitude (Idriss 1999)

$$\tau_{cyc} = 0.65 r_d \sigma_{vc}(a_{max}) \tag{2.7}$$

Finally, the CSR is modified to a value associated with a consistent earthquake magnitude ($M = 7.5$), using a magnitude scaling factor (MSF). The need for a magnitude scaling factor arises from the fact that cyclic resistance of soil is dependent on the number of *equivalent* loading cycles. An equivalent loading cycle is considered to be any exceedance of 65% of the PGA in a given time history; the number of loading cycles has been found to be most closely related to earthquake magnitude. The relationship between MSF and moment magnitude has been explored by multiple researchers, with the most prominent relationships summarized in Figure 2.25. Thus, CSR can be expressed as:

$$CSR = 0.65 a_{max} \frac{\sigma_{vc}}{\sigma'_{vc}} \frac{r_d}{MSF} \tag{2.8}$$

Overall, order to estimate the CSR, one must be able to characterize the subsurface profile of the site in question in order to determine the distribution of total and effective stresses with depth, and the expected magnitude and PGA due to a particular seismic event.

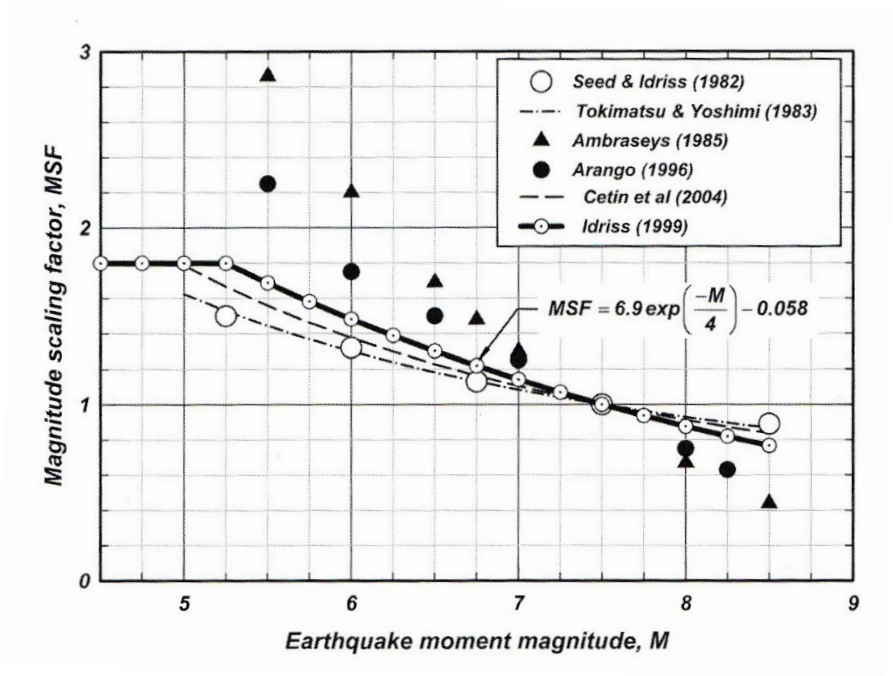

Figure 2.25: Multiple relationships showing the variation of magnitude scaling factor with moment magnitude (Idriss and Boulanger 2008)

Estimation of Cyclic Resistance

As discussed previously, the resistance of soil to liquefaction is largely dependent on its *in situ* relative density as well as other environmental factors such as geologic age, cementation, and soil fabric. Many or all of these characteristics are extremely difficult to preserve in taking samples for laboratory testing. Particularly in coarser granular samples, collapse of the soil fabric is a very common side effect of field sampling, and simply reconstituting the specimen to its *in situ* relative density does not guarantee the same arrangement of particles. While laboratory tests for cyclic resistance are useful for research purposes, such as isolating particular variables in their relation to cyclic resistance, they are not nearly as useful for practicing engineers on a case-by-case basis.

Instead, the current state liquefaction triggering analysis is centered on the results of *in situ* testing, in particular the Standard Penetration (SPT) and Cone Penetration Tests (CPT). Results from SPT were the first that were used in developing liquefaction correlations, due to the abundance of SPT data and the relative ease involved in conducting the SPT. As technology has improved, however, the CPT has grown in prominence, due to its ability to measure penetration resistance continuously and with more reliability. The tradeoff is that the newer CPT correlations for liquefaction are based on a much smaller database, and often rely on converting SPT-based penetration resistance to CPT

resistances, which introduce a significant amount of uncertainty into the process. In practice, it is most useful to employ both testing methods at a particular site in order to obtain a more complete characterization of site conditions and establish a basis for comparison of liquefaction triggering analyses.

SPT

The standard penetration test involves measuring the density, strength, or resistance of the soil by subjecting it to impact from a 140-lb. hammer in free fall from a height of 30 inches. The SPT-resistance, known as the N-value, is simply the number of hammer blows required to drive the sampler through 12 inches of soil, after an initial 6-inch seating drive. The raw N-value is then corrected to a standardized value by multiplying by correction factors related to the energy delivered to the sampler by the hammer (normalized to 60% of theoretical maximum); and factors related to the sampling apparatus, including the borehole diameter, rod length, and the usage of sample liners. Applying these correction factors to the raw N-value results in a standardized N-value, known as N_{60}.

Within a given soil profile, the SPT N-value generally increases with increasing confining pressure (and thus increasing depth). This has little to do with the actual density of the soil being tested; for the purposes of liquefaction correlation, this would make comparison of samples from different sites difficult. To avert this issue, a correction factor for overburden stress (C_N) is then applied to the standardized N_{60} to obtain $(N_1)_{60}$. Multiple relationships for C_N have been proposed, with most showing that C_N is a function of the relative density of the soil, which is in turn estimated from $(N_1)_{60}$. This implicit relationship requires some basic iterative solutions for calculating $(N_1)_{60}$.

Finally, a correction is applied for materials with significantly high fines contents. In order to be applicable to the liquefaction triggering correlations presented in the next section, penetration resistances must be adjusted to reflect those of equivalent clean sands. The relationship between fines content and the clean sand correction, $\delta(N_1)_{60}$, is shown in Figure 2.26. The penetration resistance value used in liquefaction triggering analysis is then:

$$(N_1)_{60,cs} = (N_1)_{60} + \Delta(N_1)_{60} \tag{2.9}$$

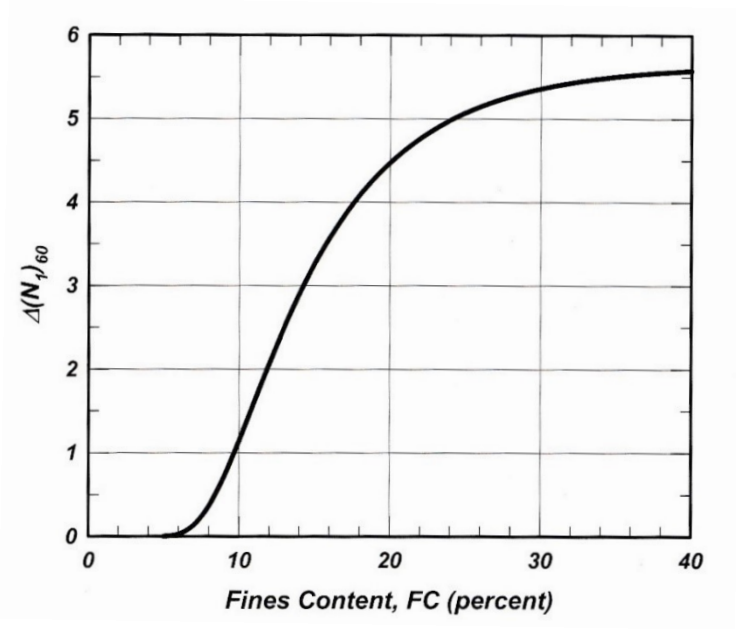

Figure 2.26: Relationship between fines content of liquefiable material and equivalent clean-sand SPT-resistance correction (Idriss and Boulanger 2008)

CPT

The cone penetration test generally involves pushing a 35.7-mm-diameter conical penetrometer into the ground at a constant rate (2 cm/sec is standard, but the rate may vary according to the needs of the engineer). Electronic transducers within the cone record penetration resistances at the tip of the cone, behind the tip, and along the sleeve at relatively short length intervals (usually 2 cm). Additionally, a pore pressure transducer can also be utilized to characterize the soil's behavior as contractive or dilative.

The tip resistance, q_c, is the most important parameter from CPT for the purposes of liquefaction triggering correlations. Similar to N_{60}, q_c is also normalized for overburden correction, and additionally divided by atmospheric pressure to obtain q_{c1N}. An equivalent clean sand correction is also used to arrive at a final CPT resistance value, denoted as $q_{c1N,cs}$.

Both CPT and SPT methods have their advantages and disadvantages. SPT is generally considered to be the more crude method of site characterization. Repetitive, high-impact penetration from a relatively complex hammer system introduces myriad uncertainties into the testing process. The corrections used to standardized SPT resistances carry some inherent uncertainty as well. SPT is, however, relatively cheap, easy to administer, and yields good samples for soil classification, if nothing else. CPT provides for a more continuous method of sampling, where the high frequency of data points for penetra-

tion resistances paints a clearer picture of the site's subsurface characteristics. However, no sample is obtained in a CPT, and thus nearby complementary borings are usually required for samples. Additionally, the CPT generally has issues penetration large particle layers (gravels, rocks), or very stiff layers (cemented sand). It is also important to note that, despite the improved stratigraphic resolution, the cone tip does experience a zone of influence as it is being pushed through the soil. The size of the zone of influence is dependent on the relative density of the material (Idriss and Boulanger 2008). This can impact its ability to detect thin layers due to the zone of influence from the previous layer "smearing" the thin underlying layer - in other words, the conical tip never actually feels the effects of the thin seam of material. This issue can generally be resolved by applying a thin-layer correction factor for thin seams of sand (Youd et al. 2001).

Liquefaction Triggering Correlations

Case histories in which potentially liquefiable material was subjected to strong ground motions have been compiled by several researchers. Using SPT and/or CPT data, each case was plotted against the CSR for its event. Each case was classified as "Liquefaction", "No Liquefaction", or "Marginal Liquefaction" having occurred; the boundary separating liquefaction and non-liquefaction cases represents the liquefaction triggering curve. Different researchers used varying methodologies and frameworks to determine CSR, thus there is some level of uncertainty in liquefaction triggering correlations. The SPT and CPT-based correlations are presented in Figure 2.27 and Figure 2.28.

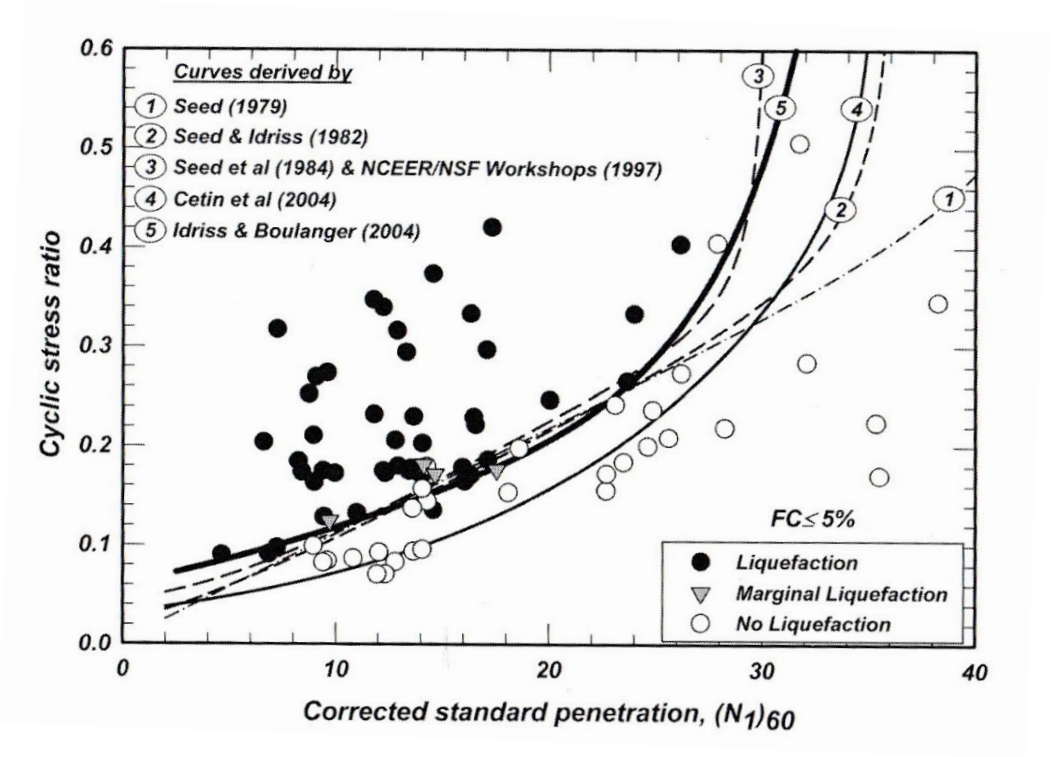

Figure 2.27: Liquefaction curves for SPT-based penetration resistances (Idriss and Boulanger 2008)

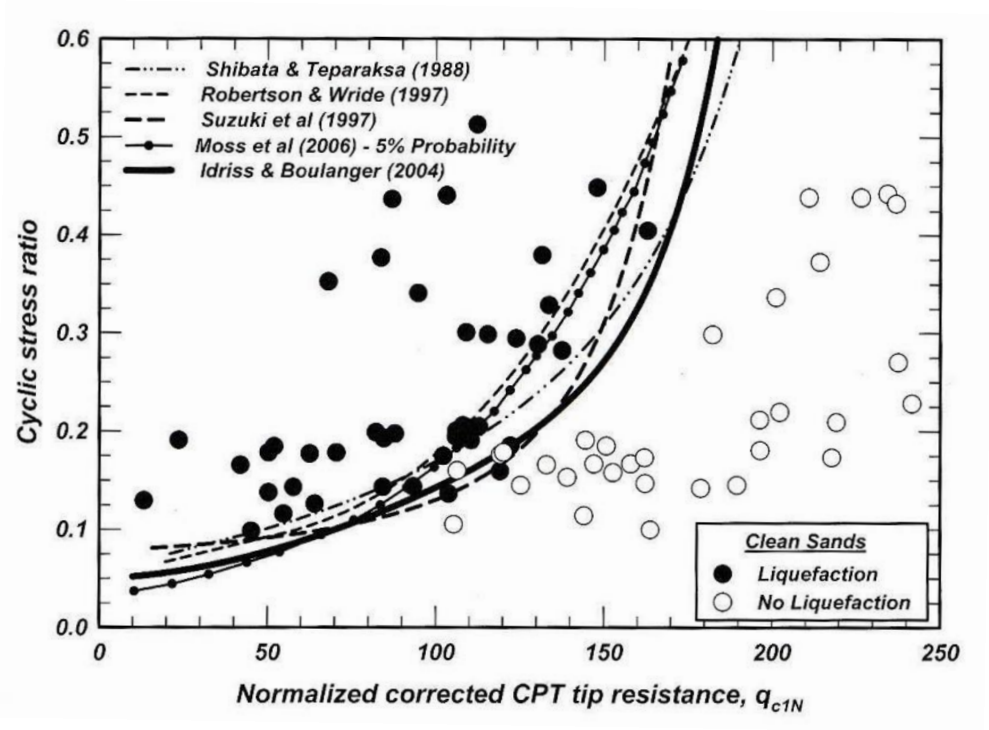

Figure 2.28: Liquefaction curves for CPT-based penetration resistances (Idriss and Boulanger 2008)

The derived correlations for SPT and CPT penetration resistances are represented by the following equations (Idriss and Boulanger 2008):

$$CRR_{\sigma=1tsf} = \exp\left[\frac{(N_1)_{60,cs}}{14.1} + \left(\frac{(N_1)_{60,cs}}{126}\right)^2 - \left(\frac{(N_1)_{60,cs}}{23.6}\right)^3 + \left(\frac{(N_1)_{60,cs}}{25.4}\right)^4 - 2.8\right] \tag{2.10a}$$

$$CRR_{\sigma=1tsf} = \exp\left[\frac{q_{c1N,cs}}{540} + \left(\frac{(q_{c1N,cs}}{67}\right)^2 - \left(\frac{q_{c1N,cs}}{80}\right)^3 + \left(\frac{q_{c1N,cs}}{114}\right)^4 - 3\right] \tag{2.10b}$$

Note that the CRR determined from these triggering correlations is based on a standard reference effective stress (1 atm), and thus in order to be applied on a case-by-case basis, an overburden stress correction factor (K_σ) is utilized. Idriss and Boulanger (2004) showed that K_σ is a function of the *in situ* effective stress and the relative density:

$$K_\sigma = \min\left\{1.0, \quad 1 - C_\sigma \ln\frac{\sigma'_{v0}}{p_a}\right\} \tag{2.11}$$

where

$$C_\sigma = \frac{1}{18.9 - 2.55\sqrt{(N_1)_{60,cs}}}, \quad (N_1)_{60,cs} \leq 37 \tag{2.12}$$

Summary

The simplified procedure for determining the factor of safety for liquefaction on a deterministic level can thus be summarized as follows:

1. Using various site characterization methods, determine subsurface conditions at the site in questions.
2. Using the general guidelines for liquefaction susceptibility, identify the layer(s) of potentially liquefiable material, and divide into sufficiently small sublayers (0.5-1.0m

thick is generally adequate).

3. Determine the earthquake magnitude for the event in question, and estimate the associated peak ground acceleration

4. Calculate *CSR* using Equation 2.8, taking care to appropriately correct for depth reduction factors in each sublayer and apply the magnitude scaling factor.

5. Using SPT and/or CPT test results for the subsurface profile, assign appropriate penetration resistances (N_{60} or q_c) for each sublayer, and correct the penetration resistances for overburden stress and fines content.

6. Using Equation 2.10 , determine $CRR_{\sigma=1}$, and correct once again for overburden using Equation 2.12.

7. Use Equation 2.4 to calculate the final factor of safety for each sublayer. It is generally standard practice to plot the variation in FS_{liq} with depth for the profile.

Probabilistic Application of the Simplified Method

At its most basic level, Idriss and Boulanger's simplified procedure is a deterministic method; the engineer selects one particular event magnitude and estimates the resulting PGA using one or more ground motion prediction equations (GMPEs). However, it requires only a relatively simple leap in logic to characterize the cyclic stresses at a particular site in a probabilistic manner. A probabilistic seismic hazard analysis (PSHA) can be used to generate an array of pairings of magnitude and peak ground acceleration (Baker 2008). Each pairing, associated with a particular probability of occurrence, can be used to calculate the *CSR*, which will have the same probability of occurrence associated with it. The result is, instead of a single *CSR* representing a single event, a probability distribution of *CSR*s that reflects the recurrence of seismic events in the region of interest, the diversity of seismic sources, and the uncertainty associated with predicting ground motion attenuation for each particular case.

From a cyclic resistance standpoint, probabilistic liquefaction correlations have also been developed (Toprak et al. 1999, Cetin et al. 2004), representing the relationship between *CRR* and $(N_1)_{60}$ as a probability distribution, rather than a single curve (Figure 2.28). This, combined with the PSHA outlined above, allows the engineer to adequately account for a great deal of the uncertainty associated with the cyclic stress-based method for evaluating liquefaction triggering potential.

Despite the wide usage and plethora of literature dealing with cyclic stress-based

methods for analyzing liquefaction, it is at its core a highly uncertain method for evaluation of liquefaction potential. The relationship between cyclic stresses and pore pressure generation is dependent on myriad factors, each associated with a significant level of uncertainty. This uncertainty is reflected in the liquefaction triggering curves seen in Figure 2.29. The methods used to establish these correlations are diverse, relying on different frameworks, interactions between variables, and statistical methods of evaluation. Thus, alternative methods have been explored by numerous researchers in an attempt utilize stronger and more direct relationships for the generation of excess pore pressure.

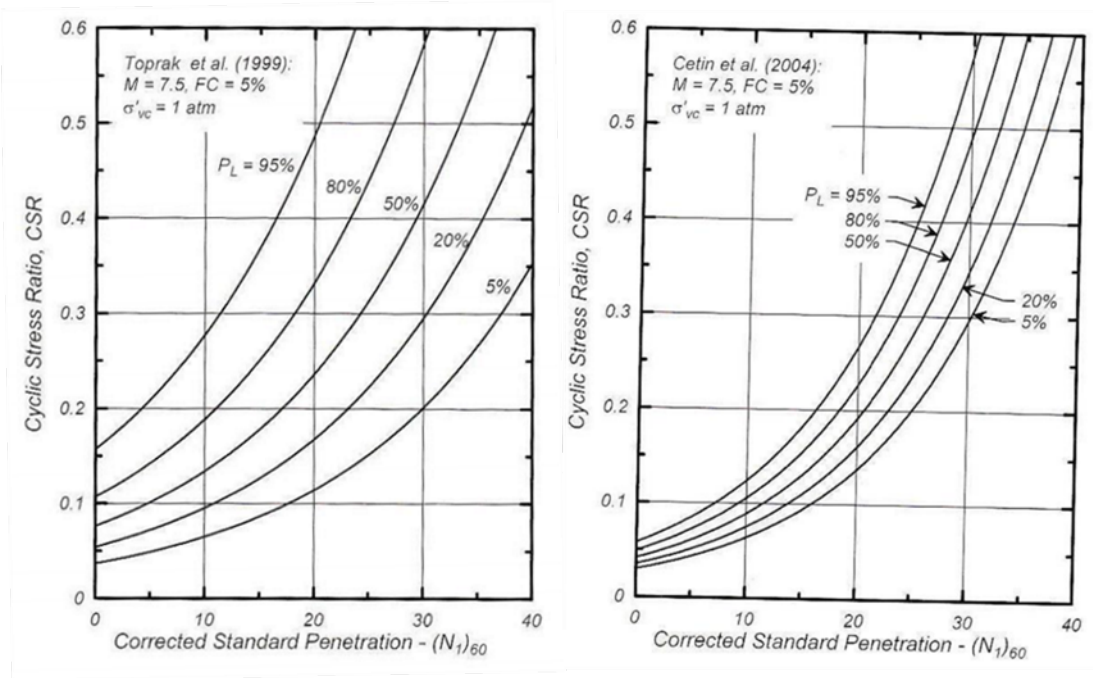

Figure 2.29: Probabilistic liquefaction correlations for SPT resistances from a) Toprak et al. (1999) and b) Cetin et al. (2004). Curves are for clean sand, 7.5-magnitude, and atmospheric pressure. (Idriss and Boulanger 2008)

2.4.3 Strain-Based Evaluation of Cyclic Loading Behavior

Using the results from a series of strain-controlled cyclic undrained triaxial tests on various sands, Dobry (1985) showed that the pore pressure generation has a relatively unique relationship to the amplitude of cyclic shear strain (Figure 2.30). This narrow band in which r_u plots versus cyclic strains in Figure 2.30 is applicable to a wide variety of sand types, number of loading cycles, and initial relative densities and confining pressures. It has been observed that r_u generally reaches 100% at around 0.3-1.0% cyclic shear strain. Zeghal and Elgamal (1994) used data obtained from the Wildlife Array during the 1987 Superstition Hills Earthquake, where liquefaction had been observed. The Wildlife Array consisted of downhole accelerometers and pore pressure transducers, allowing for

the determination of both shear stress and shear strain time histories, along with the time history for pore pressure generation; at various depths. Analysis of this data found that pore pressure generation occurred at a cyclic shear strain of about 0.04%, which is in good agreement with the concept that excess pore pressure generation should theoretically begin at around the volumetric cyclic threshold shear strain of about 0.01-0.02% (Idriss and Boulanger 2008).

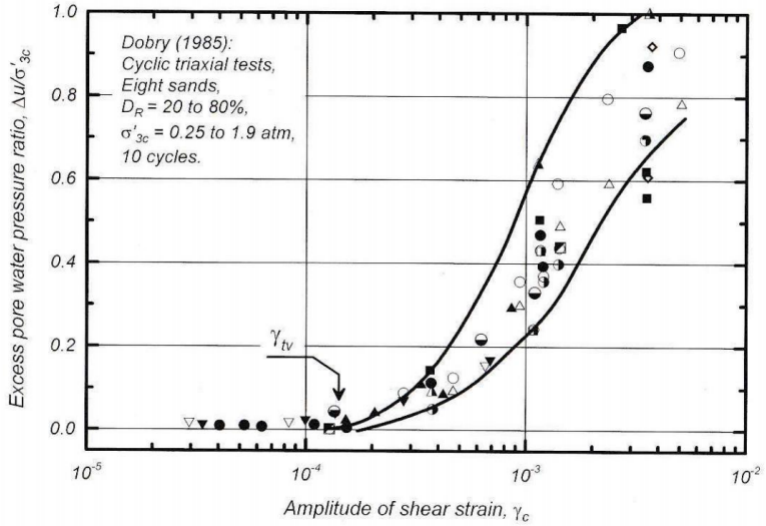

Figure 2.30: Relationship between excess pore pressure generation and shear strain amplitude, based on laboratory test methods (Idriss and Boulanger 2008, after Dobry 1985)

Despite its strength, the relationship between cyclic strain and pore pressure generation is difficult to implement in practice, largely due to the fact that it requires estimating the cyclic strains imposed on the soil by a design ground motion. This involves first determining the applied cyclic stress, along with the stiffness (or shear modulus) and modulus reduction behavior of the soil. The engineer is essentially tasked with modeling the cyclic stress-strain response of the soil. The considerable uncertainty involved in this procedure, coupled with the relative lack of literature concerning the subject, is the main reason that the stress-based method remains preferred in practical earthquake engineering.

The strain-based relationship for pore pressure has instead been best utilized in the formulation of numerical models. There are numerous models in development and available in industry that can model pore pressure generation and evaluate liquefaction potential with an adequate degree of reliability. Generally, these numerical models use some sort of material property relationship to model the cyclic stress-strain behavior of the soil; commonly used are equivalent linear models, cyclic nonlinear models, or advanced constitutive models. These codes then utilize the unique relationship between pore pressure generation and cyclic shear strain to calculate the change in pore pressure (and thus change in effective stress) for each time step during a loading sequence. Adjustments are then made

to the soil stiffness due to the change in effective stress before response in the next time step is calculated. This general framework provides an adequately reliable way to evaluate liquefaction potential from an alternative standpoint. While the use of numerical models generally is not a stand-alone method in practice, it provides an excellent comparison to stress-based methods. It is, however, a much more computationally intense method, especially if the engineer wishes to evaluate for liquefaction potential in a probabilistic framework.

2.4.4 Analysis of Liquefaction Potential Using Energy-Based Methods

The dissipated energy in undrained cyclic loading has also been shown to correlate closely with excess pore pressure generation in sand or silt (Idriss and Boulanger 2008). Davis and Berrill (1998, 2001) examined this relationship using records from two downhole arrays: Lotung (Taiwan) during a ground motion known as "Event 16", and Sunamachi (Japan) during the Chiba-Toho-Oki Earthquake. Using similar methods from Zeghal and Elgamal (1994) for determining stress and strain at the sampling locations and interpolating throughout the depth profile, the dissipated energy was determined by integrating the stress-strain loops for both horizontal components of motion, then summing up the dissipate energies to obtain a total value (D).

Next, three different relationships were proposed to relate D and pore pressure generation (p): linear, power law, and exponential. The linear law was used in the Lotung and Sunamachi studies, and the calculated pore pressure time histories were compared to the actual pore pressure histories recorded by the downhole piezometers at each array (Figure 2.31). The calculated and recorded pore pressures showed relatively good agreement for the Lotung array, save for the apparent presence of signal noise in one of the recording instruments. The differences between recorded and calculated pore pressures at the Sunamachi array were slightly larger, particular after about 25 seconds, when the actual recorded pore pressures began to dissipate. This effect was also seen in the Lotung array, but to a lesser degree. This suggests that the recorded time histories were affected by the drainage of excess pore pressures, and that site conditions at the Sunamachi array provided for more enhanced drainage, leading to the larger divergence in recorded and calculated pore pressure. Thus, it would seem that dissipated energy can in fact provide a reasonable approximation of pore pressure generation, provided that the calculated pore pressures are adjusted for drainage at each time step, which is certainly a reasonably simple phenomenon to model in parallel. Similar to strain-based concepts, however, this sort of dissipated energy-based method requires a reasonable estimate of the stress-strain behavior at each time step, with all the same uncertainties inherent to such an estimation.

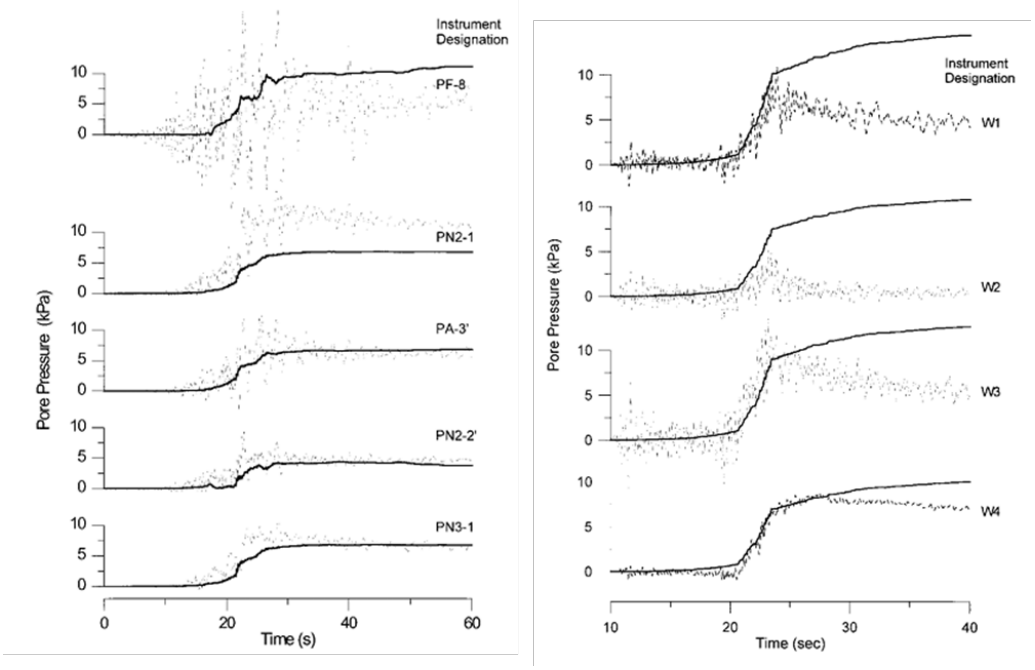

Figure 2.31: Measured and calculated pore water pressure time histories at the a) Lotung and b) Sunamachi downhole arrays (Davis and Berrill 2008)

Baziar et al. (2011) proposed an evolutionary approach to strain energy-based assessment of liquefaction potential. Similar to a factor of safety-type analysis, this method is based on comparing the energy content of an earthquake, or the "demand energy," with the amount of dissipated energy required for the soil to reach liquefaction, or "capacity energy" (Davis and Berrill 1982). The model for predicting the capacity energy of soil was based on statistical regression of parameters relating to both the soil state and the soil type itself. Using a multigene Genetic Programming framework based on a dataset consisting largely of laboratory-based cyclic tests. Genetic Programming is a biologically-inspired tool used to recognize patterns in statistical data, and in this case, produce an explicit relationship between soil/state variables (vertical effective stress, relative density, median grain size, coefficient of uniformity, and fines) and capacity energy. More detailed information on genetic programming can be found in Koza (1992). The demand energy is estimated through slightly more traditional means, either by reconstructing and integrating stress-strain loops, or double-integration of interpolated predicted acceleration records. For the latter method, the means by which the interpolation is achieved (linear or trigonometric) is expected to introduce variations in demand energy prediction (Baziar 2011), in addition to the same uncertainties inherent to prediction of cyclic strains.

2.4.5 In Situ Effects of Excess Pore Pressure Generation

It has been established that the generation of excess pore water pressures during an earthquake will result in a hydraulic gradient, and thus the dissipation of excess pore pressures should be expected to occur over time. The flow of water, coupled with often complex heterogeneities in soil masses, can create significant spatial variability in patterns of resulting strength loss and deformation of the soil. Many of these *in situ* effects are very difficult to model and account for in analyzing a site for liquefaction potential, and are certainly not replicated in traditional laboratory tests (with the exception of centrifuge tests).

One of the key considerations in site investigations is the type of material that overlies the potentially liquefiable stratum, and how it might be affected by the upward flow of water as excess pore pressures are dissipated. Upward flow of water into an overlying dense, granular material could result in significant increases in pore pressure in that layer (particularly if there is an impermeable layer overlying the dense material). This can cause liquefaction in a material that had previously been considered too dense to liquefy through traditional means of cyclic stress.

On the other hand, the presence of an impermeable overlying layer such as fine silt or clay can act as a barrier to upward-flowing water, forming *water films* at the layer boundary (Figure 2.32). The water films may eventually dissipate through other means (horizontally, and eventually through a weak point in the impermeable material). In the meantime, however, this redistribution of voids and grains within the liquefied material can result in potentially very weak zones of soil near the top of the layer, and denser zones of soil near the bottom. In sloping grounds, the weak zones may be of particular significance, as they can serve as slip surfaces, resulting in large deformations in the ground above the layer boundaries. Centrifuge tests from Malvick et al. (2008) support this concept that the presence of a water film at an impermeable boundary can result in significant post-shaking deformations in sloping ground (Figure 2.33).

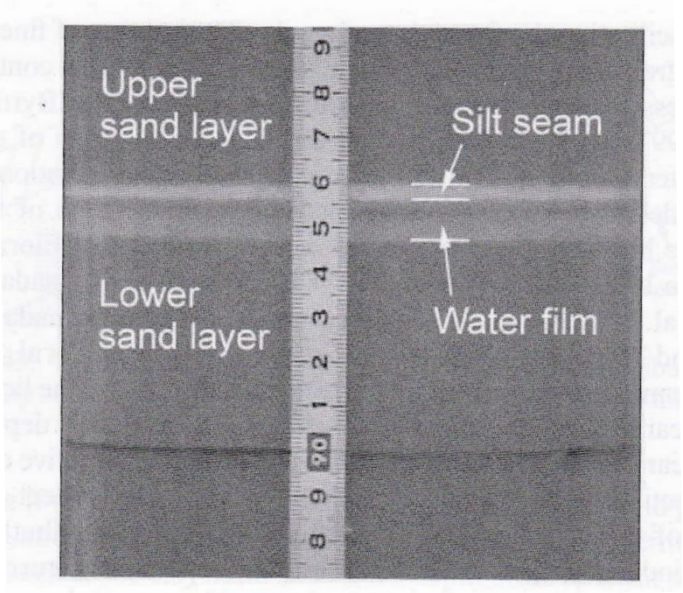

Figure 2.32: Water film formation due to the presence of a silt seam in a column of liquefied sand (Kokusho 1999)

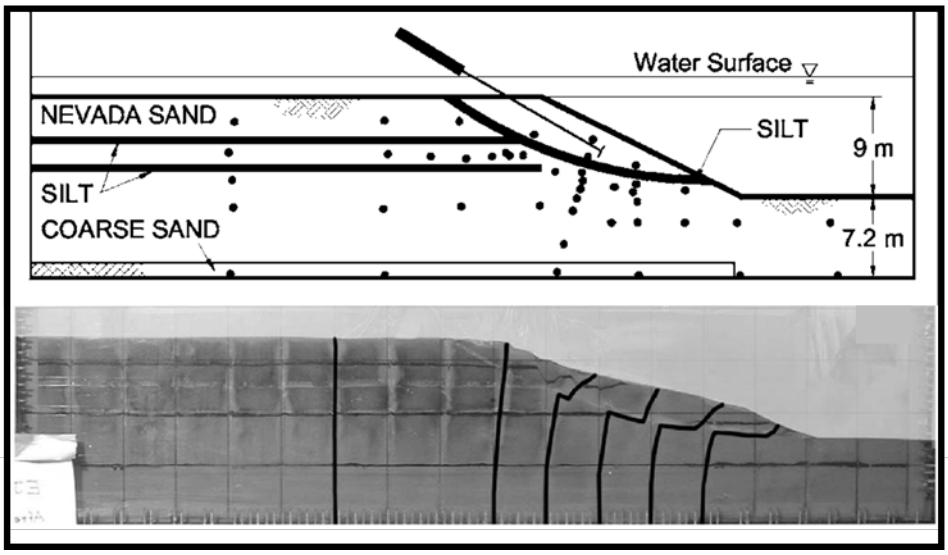

Figure 2.33: Centrifuge test results showing large localized shear deformations at an impermeable silt boundary above liquefied sand (Malvick et al. 2008)

Thus, it is not generally sufficient for the practicing engineer simply to establish the potential for pore pressure generation during an earthquake without also characterizing the likely result of pore pressure dissipation both during and after shaking. It is for this reason that accurate, thorough site investigations are imperative, not just in establishing which materials are potentially liquefiable, but also detecting strata that may impede or be affected by the resulting upward flow of water. Once again, the combined use of SPT

and CPT methods can achieve this goal; CPT provides for high-resolution stratigraphic characterization, while SPT sampling provides soil classification of such layers, allowing engineers to characterize, among other things, the hydraulic properties of the soils of interest.

2.5 Summary

It has been shown in this chapter that soil liquefaction is significant issue that must be accurately characterized when assessing seismic hazards at a project site or in particular region. Liquefaction generally occurs in loose, saturated, cohesionless soils that have been subjected to strong ground shaking. The susceptibility of a particular soil to liquefaction is dependent on whether it is expected to contract or dilate under undrained shear. Classification of grain type, grain-size distribution, historical evidence of liquefaction, and a knowledge of the historical mode of deposition of the soil are fundamental first-level assessments that must be made in order to determine the liquefaction susceptibility of a material. Once a material has been deemed to be susceptible, characterization of local seismicity is critical in determining whether levels of ground shaking are expected to be high enough to cause liquefaction to occur. Finally, correlations between *in situ* relative density and the expected applied cyclic stresses are used to determine the factor of safety for liquefaction in a cyclic stress approach. Alternative methods can be used, including strain-based and energy-based evaluations, or nonlinear or equivalent linear numerical models that combine site response analyses with material models that predict stress-strain behavior and subsequent pore pressure generation. Depending on the relative cost of the project, multiple methods can be used in conjunction to verify or refine the prediction of liquefaction potential.

It must be noted that the current methods used to evaluate liquefaction susceptibility and its introduce a significant level of uncertainty into liquefaction analysis on a site-by-site basis. The database of observed case histories is still relatively small, and suffer from varying levels of completeness in site characterization. Furthermore, most methods generally utilize a single measure of ground motion intensity (PGA), while attempting to account for duration by incorporating a design earthquake magnitude. The issues pertaining to excess pore pressure dissipation, impeded drainage, and void redistribution have not been thoroughly characterized in research to date, and thus current practice is ill-equipped to deal with these kinds of site effects, other than simply using more conservative estimates.

One of the ways in which these issues have been accounted for is through evaluation

of liquefaction potential through a more probabilistic framework. By evaluating local seismicity in a probabilistic sense, by generating a probability distribution of seismic events, rather than a single deterministic event, and using probabilistic liquefaction correlations or parametric analyses, much of the uncertainty that is inherent in liquefaction analysis can be accounted for.

Chapter 3

LIQUEFACTION-RELATED EFFECTS AND HAZARDS

3.1 Introduction

It has been established that liquefaction can lead to significant reductions in shear strength in susceptible sands and silts. The consequences of such a loss in strength are quite diverse, and depend on the nature of the earthquake-induced ground motions, the properties of the soil before the event occurred, the subsurface conditions at the site, the ground surface site topography, and the presence of nearby structures. The hazards related to liquefaction have briefly introduced in Section 2.2, and analysis of the potential for these consequences requires the ability to characterize the losses in shear strength in the liquefied soil, and the resulting deformations (or in some cases bearing failure) that may occur as a result. Four main consequences of liquefaction are discussed in this section: loss of shear strength, amplification of ground motions, vertical settlement, and lateral spreading.

3.2 Loss of Shear Strength - Flow Failures

Under static, stable conditions, the *in situ* shear stresses that exist under sloping ground surfaces obviously do not exceed the shear strength of the soil – otherwise, large downslope displacements would be expected to occur. However, in post-earthquake conditions in which soil has liquefied the static shear stresses *may* exceed the new, liquefied shear strength of the soil, resulting in what are known as *flow failures*. Flow failures can occur during ground shaking in truly undrained conditions, when soil liquefies and significant

losses in shear strength occur. Flow failures have also been observed to occur in post-earthquake conditions when excess pore pressures result in the flow of water into looser soils that subsequently liquefy, or when upward-flowing water meets an impermeable barrier, creating a very weak slip surface on which large deformations can occur.

Evaluation of the potential for flow failures thus relies on the ability of engineers to predict the likely residual strengths in liquefied soil. Building on the early work of Castro (1969), Poulous (1985) used results from laboratory tests to develop the concept of the steady state of deformation, in which a soil is being sheared at constant volume, constant shearing resistance, constant effective stress, and constant strain rate. Because these conditions are rarely all met in the field, the term residual strength has also been used to describe the strength of a liquefied soil. Under controlled laboratory conditions, the shearing resistance at steady state is considered to be the residual strength of the soil (Kramer and Stewart 2017, in preparation), but the strength mobilized in the field may be different than the steady state strength. The residual strength of the soil was found to be strongly related to the soil's relative density. This relationship renders the use of laboratory testing of field samples on a case-by-case problematic, since traditional field samples of granular materials are prone to unacceptably high levels of disturbance. Frozen sampling, an alternative technique, has proven to be much more effective in obtaining quality field samples that preserve both the *in situ* relative density and the natural soil fabric. However, frozen sampling is generally very expensive, extremely difficult, and requires considerable time to be performed correctly. Thus, the use of frozen sampling techniques is usually limited to use in academic research.

3.2.1 SPT-Based Correlations for Residual Shear Strength

Seed (1987) developed an SPT-based approach to evaluating the potential for flow slide failures by compiling a database of observed flow-slide case histories that were back-calculated to determine the residual shear strength, or S_R. The procedure used subsurface data from the flow failures, along with the slope geometry prior to the slide, material properties in the embankment, and the spatial extent of the slide to calculate the apparent residual strength of the liquefied material (Kramer and Stewart 2017, in preparation). Seed and Harder (1990) updated the original procedure with added case histories, producing the relationship shown in Figure 3.1. It is important to note that the range of residual shear strength values for a given SPT resistance is quite large, although the authors recommend that the lower bound be used as a point of conservatism. The method suffers from considerable uncertainty, stemming from both the methods used to determine the residual shear strength for each case, and a relatively limited sample size.

The back-calculation procedure involves a pre-earthquake static stability analysis of the embankment or slope, with shear strengths assigned to each layer of soil, and the shear strength of the suspected zone of liquefaction held as unknown (Idriss and Boulanger 2008). The residual shear strength can then be calculated by setting the factor of safety for slope stability equal to 1. The residual shear strength can also be calculated using the deformed post-earthquake geometry. Generally, the differences between the two residual shear strengths can be quite significant, which has resulted in methods for interpolating between the two estimates that account for inertial forces, changes in geometry, and strength losses due to other site effects.

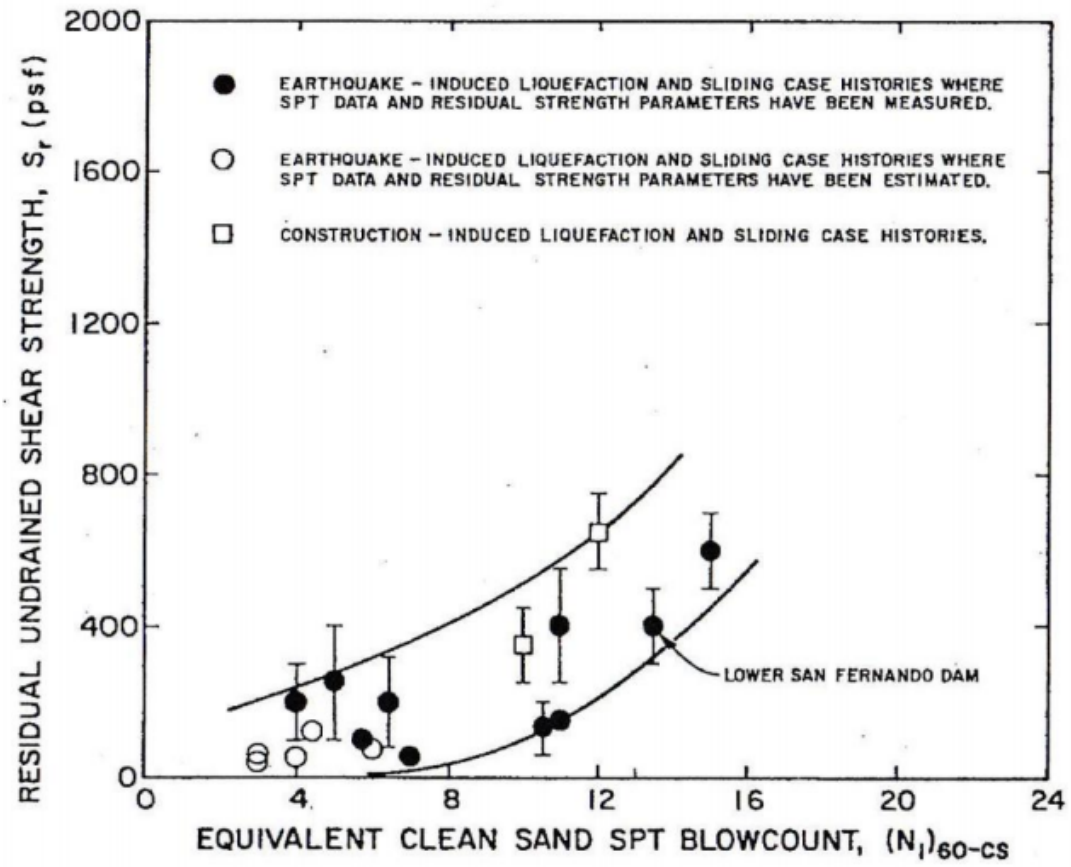

Figure 3.1: Relationship between back-calculated residual strengths and SPT-resistance for 17 case histories (Seed and Harder 1990)

A large source of uncertainty from this method stems from the post-earthquake site characterization, particularly determining penetration resistances in deformed soil masses. It is likely that post-earthquake flow sliding will have resulted in a significant amount of intermixing of soils that had previously been well-stratified in pre-earthquake conditions. This effect is illustrated in Figure 3.2, where the post-earthquake SPT data for the San Fernando Dam shows considerable scatter involved in determining the representative mean SPT resistances in the downstream shell.

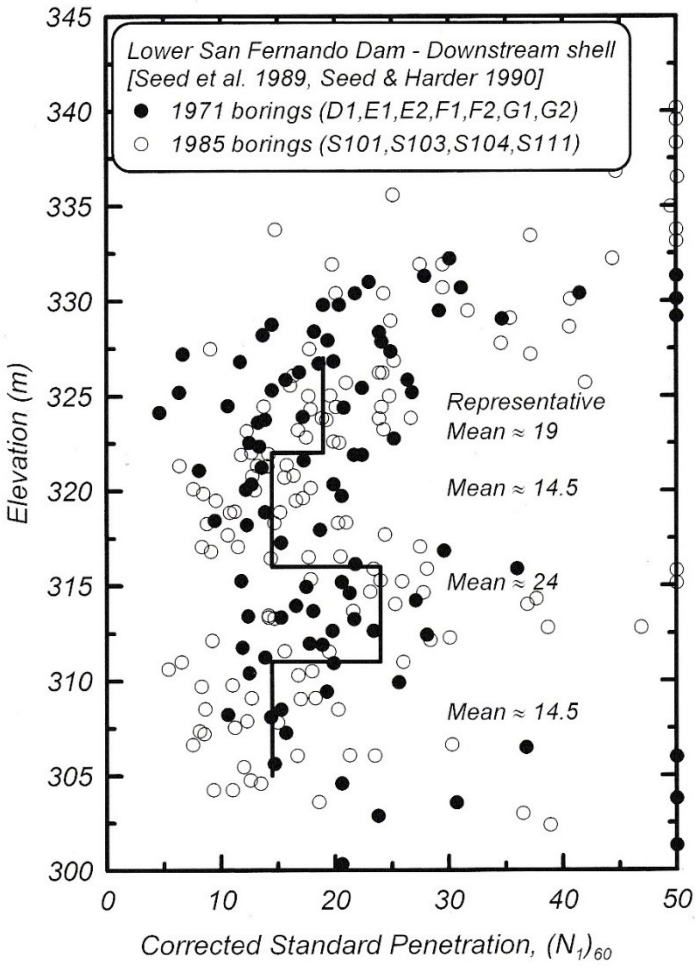

Figure 3.2: SPT data from downstream shell of Lower San Fernando Dam (Idriss and Boulanger 2008, after Seed et al. 1989 and Seed and Harder 1990)

Idriss (1999) refined the Seed and Harder model by adjusting the case history database, and representing the correlation as a single best-fit exponential curve (Figure 3.3), with the uncertainty represented for each case by error bars. The $S_r - (N_1)_{60}$ (with S_r in atm) correlation can then be closely approximated as:

$$S_r = 0.0239 \exp\left[0.16(N_1)_{60,cs}\right] \quad \leq 0.5 \tag{3.1}$$

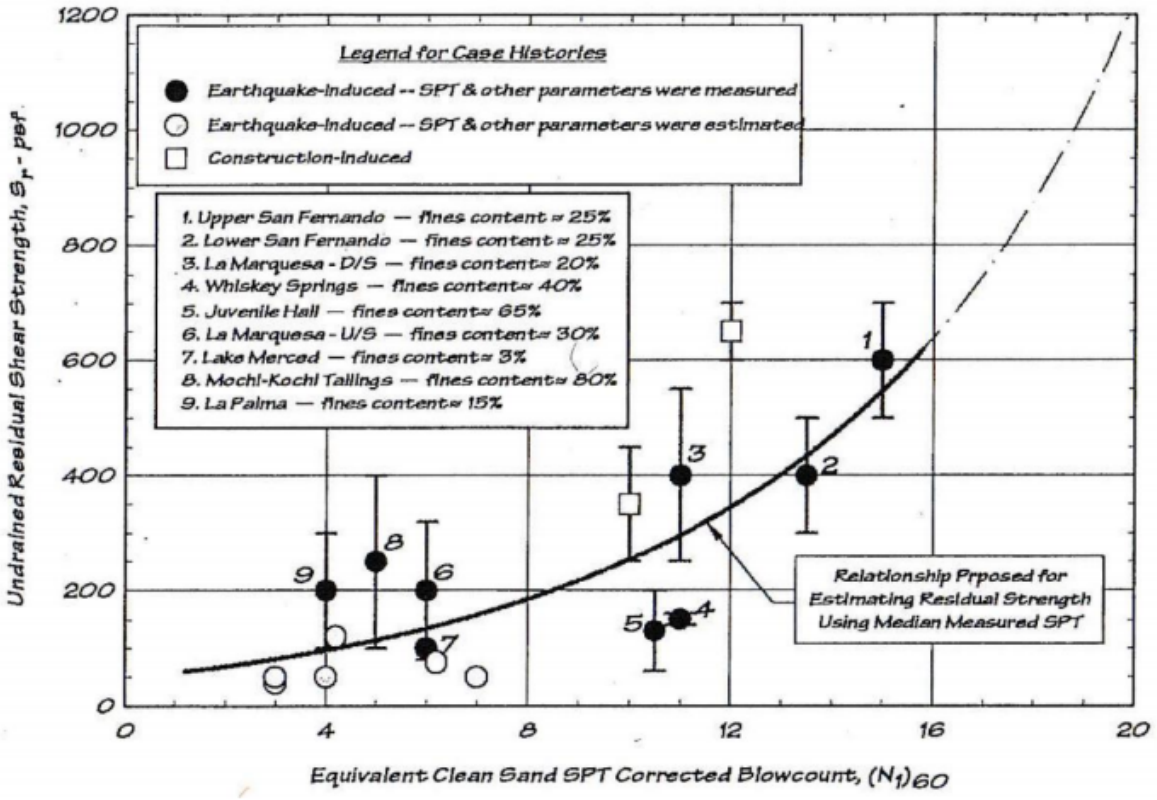

Figure 3.3: Relationship between residual shear strength and SPT resistance represented as a single curve with error bars for each case history (Idriss 1999)

3.2.2 SPT-Based Correlations Using Normalized Strength Ratios

The correlation between S_r and penetration resistance is logically sound. As the initial relative density increases, it has been shown that in undrained/cyclic shear, the critical state strength of the soil should increase as well. However, a stronger correlation may exist between in situ relative density (represented by SPT resistance) and the *normalized residual strength ratio* (S_r/σ'_v). The advantages to using normalized strength ratios stem from the fact that the residual strength is a function primarily of initial relative density, which is in turn a function of initial overburden pressure. Thus, using (S_r/σ'_v) takes advantage of the dependence of residual strength on both relative density and overburden pressure. Olson and Stark (2002) used these concepts to develop a normalized strength model that accounts for the influence of effective overburden pressure on the rate of increase in residual strength with relative density; the relationship is shown in Figure 3.4 .

Idriss and Boulanger (2007) revised this model by refining the case history database to include only cases that were considered to be sufficiently documented, and grouping the case histories by the relative confidence in the site data (in terms of penetration resistance and site geometry) (Figure 3.5). Their model also allows for the evaluation of residual

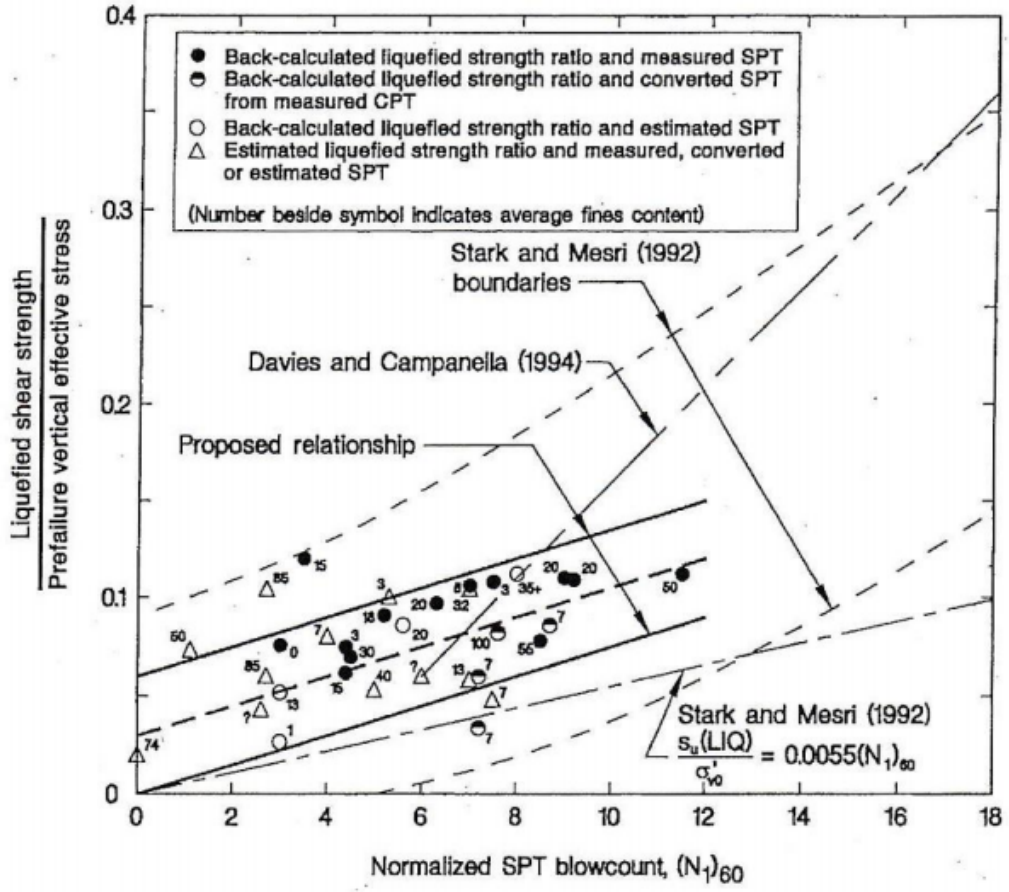

Figure 3.4: Relationship between the normalized residual shear strength ratio and SPT resistance (Olson and Stark 2002)

shear strength for cases in which the effects of void redistribution may be expected to be significant, i.e. if there exists an impermeable barrier above the liquefiable material. The lower bound curve in Figure 3.5 is used to represent the effects of void redistribution, which is expected to result in a much lower residual shear strength in the liquefied material. Note the complete absence of data for void redistribution conditions, and the existence of just one case history for $(N_1)_{60}$ greater than about 13. Both of the curve extrapolations, therefore, are not based on any real case history data, but rather engineering judgment and concepts of critical state soil mechanics. Furthermore, the relationship between void redistribution and strength loss has not been fully explored on a physical level, and there is little documentation of its occurrence in any of the existing case histories. However, the effects of void redistribution are expected to be greater in initially looser material, and thus the two curves in Idriss and Boulanger's model would therefore be unlikely to be the same at low resistance values.

Kramer and Wang (2004) developed a model that incorporates concepts from both the

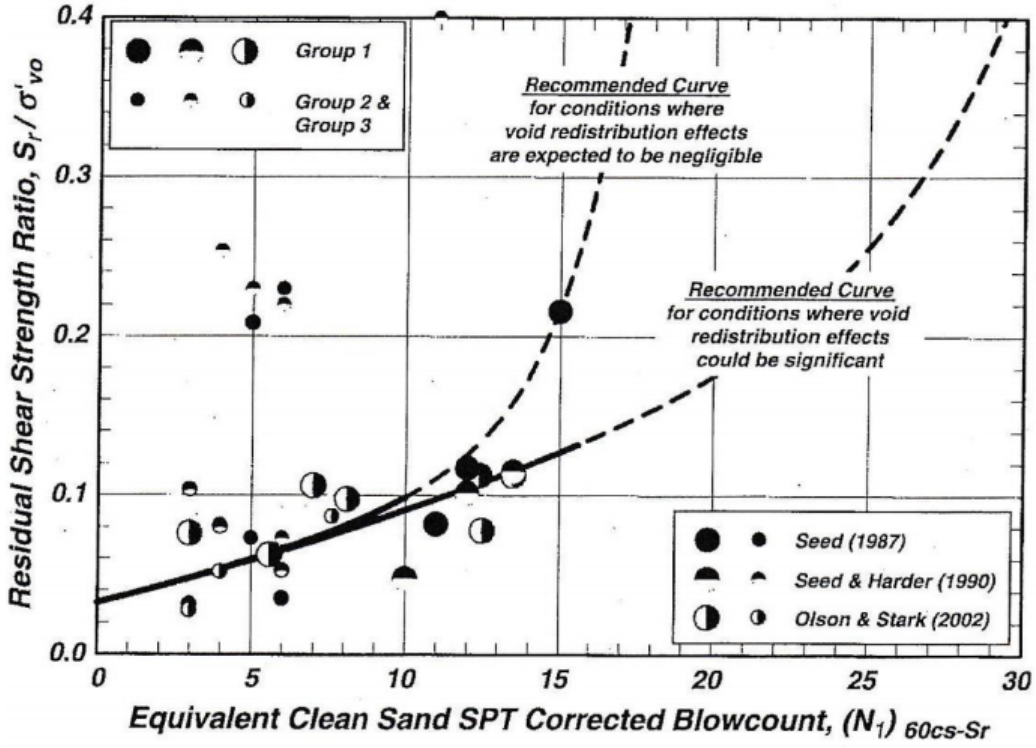

Figure 3.5: Relationship between the normalized residual shear strength ratio and SPT resistance, with curve for cases where redistribution effects could be significant (Idriss and Boulanger 2007)

classical residual strength and normalized shear strength ratio models (Figure 3.6). This "hybrid" method models the variation of residual strength due to both SPT resistance and effective overburden pressure without the added constraint of proportionality between S_r and σ'_v (Kramer, unpublished manuscript). While Figure 3.6 presents the relationship in a deterministic form, the model can also be formulated probabilistically:

$$S_r(P) = \exp\left[\overline{\ln S_r} + \Phi^{-1}(P)\sigma_{\ln S_r}\right] \tag{3.2}$$

where P is the probability of non-exceedance,

$$\overline{\ln S_r} = -8.444 + 0.109\overline{N} + 5.379\sigma_{\ln S_r} \tag{3.3}$$

and $\sigma_{\ln S_r}$ is a function of the coefficients of variation of N and σ', the mean residual shear strength, and the mean SPT resistance.

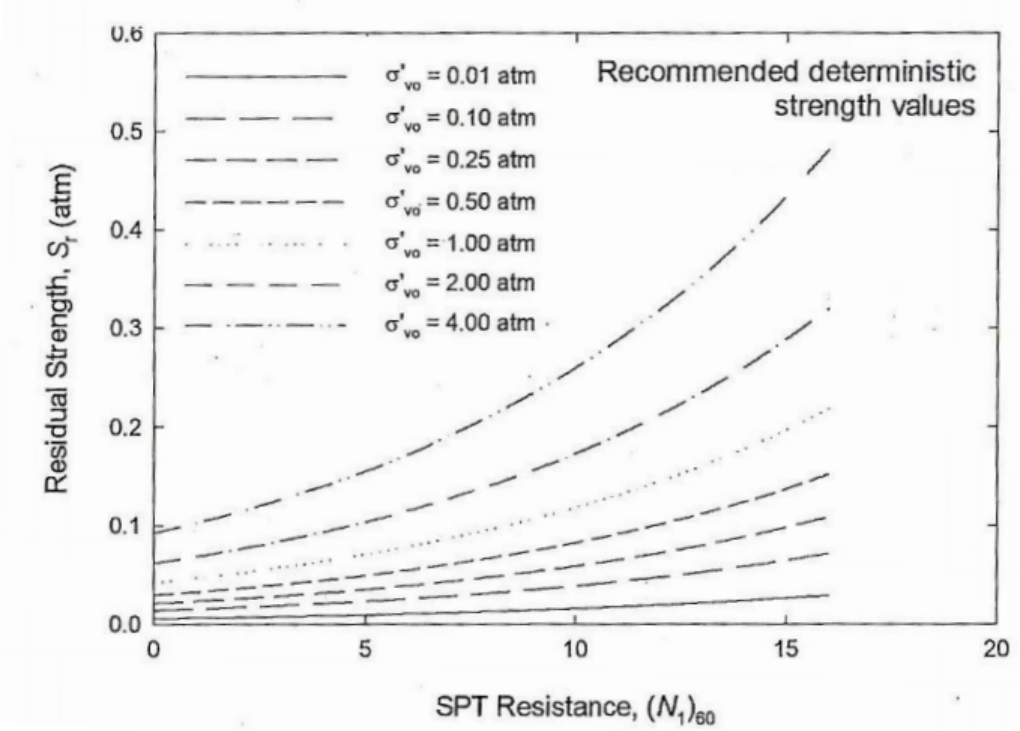

Figure 3.6: Hybrid model for relating residual shear strength with SPT resistance for various effective stresses. (Kramer and Wang 2007)

3.3 Ground Motion Amplification

If liquefaction occurs early enough during the time history of a ground motion, the decrease in stiffness of the liquefied material can have a significant effect on the propagation of stress waves at the site, thus altering the amplitude, frequency content, and (to a certain degree) the significant duration of the ground motion at the site.

It is instructive to briefly discuss the factors that affect the manner in which stress waves propagate through layered media. Consider the layered soil profile shown in Figure 3.7. Material C is the bedrock for this site; material B represents a dense, granular material; and material A is the loose, surficial sandy deposit that is considered liquefiable. Thus, we see a general density gradient as depth decreases, as well as a stiffness gradient.

3.3.1 Effects on Amplitude

As a propagating stress wave, here referred to as the *incident* wave reaches a particle boundary (assuming vertically propagating SH-waves), the wave will split into two components: one is a *transmitted* wave that passes through the next material, the other is a

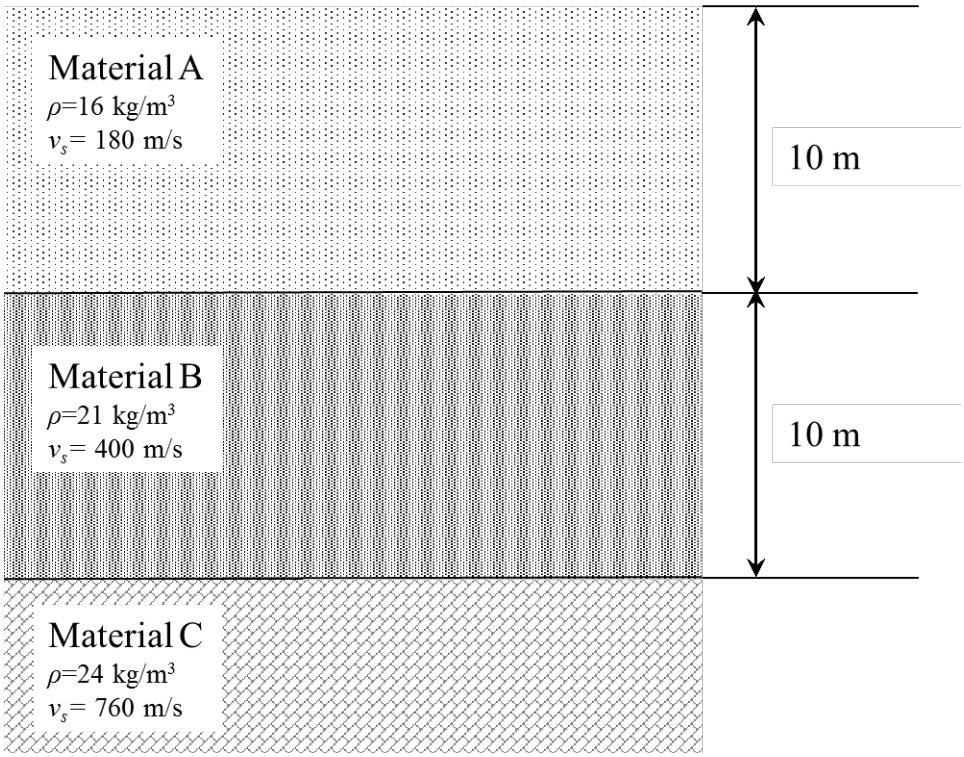

Figure 3.7: Idealized soil profile, with a surficial layer of liquefiable material

reflected wave that propagates back through the initial medium. Both of these waves will have a different stress amplitude than that of the incident wave. The change in amplitude is controlled by the *impedance ratio* between the two materials, which is described by:

$$\alpha_z = \frac{\rho_2 v_2}{\rho_1 v_1} \tag{3.4}$$

where ρ_2 and $v_2 2$ are the density and shear wave velocity of the second material, with the subscript "1" denoting the initial material through which the incident wave passes. The amplitude of the transmitted shear wave, A_t, can then be related to the impedance ratio and the incident shear wave amplitude, A_i, by:

$$A_t = \frac{2}{1 + \alpha_z} A_i \tag{3.5}$$

Based on the material properties of the soil profile in Figure 3.7, we can expect that the amplitude of the incident stress wave will increase as it approaches the ground surface. The impedance ratio between materials C and B, $\alpha_{z,CB}$ is 0.46 and the impedance ratio between materials B and A, $\alpha_{z,BA}$ is 0.34. We then can expect that the incident stress

wave will be amplified by a factor of about 1.4 in material B. By the time the original stress wave travels through material A and reaches the ground surface, it will have been amplified by an overall factor of 2.0. However, if material A liquefies at some point during ground shaking, it will likely experience a significant loss in stiffness, which will be reflected mostly in the shear wave velocity. Thus, if we assume that vs decreases from 180 to 100 m/s in material A after liquefaction occurs, the incident stress wave will instead be amplified by a factor of 2.3 at ground surface.

3.3.2 Effects on Frequency Content

Aside from the amplification effects of liquefaction, the softening of liquefied soil can also have a considerable effect on the ground motion frequencies that are expected to produce the largest shear wave amplitudes. Much like any solid material, soil masses have a resonant frequency that depends on their stiffness and mass. A mass that is vibrating at its resonant frequency, or any higher modes of its resonant frequency, can be expected to experience the maximum amplitude of motion. For soil masses, this resonant frequency is usually expressed in terms of the *natural period*, T_0:

$$T_0 = \frac{4H}{v_s} \tag{3.6}$$

where v_s is the shear wave velocity of the soil, and H is the thickness of the layer of interest. Considering again the soil profile in Figure 3.7, the initial natural period of the surficial layer of material A is about 0.22 seconds. Once again assuming that the soil liquefies during ground shaking and its shear wave velocity drops to 80 m/s, the surface ground motions will be altered by the lengthening of the natural period to 0.5 seconds. Thus, we can expect that longer-period ground motion components will be amplified at sites where liquefaction has occurred.

3.3.3 Discussion

The manner in which amplifications and changes to frequency content of ground motions occur at liquefaction sites is highly dependent on the initial density, position, and pervasiveness of the liquefiable material at a given site (Greenfield, personal communication). A classic example comes from the Treasure Island site, which liquefied during the 1989 Loma Prieta earthquake. The site consists of thick surficial deposits of initially very loose sand, which was found to have liquefied about 13 seconds after the beginning of ground

shaking. When the ground motions at the site are compared with those recorded at the adjacent Yerba Buena Island (Figure 3.8), which is a natural rock outcrop, we see that the two response spectra are quite similar until just before liquefaction occurs. After the onset of liquefaction, ground motions at Treasure Island are significantly amplified at all periods, with a noticeable development of a spectral acceleration spike at a period of 1.4 seconds.

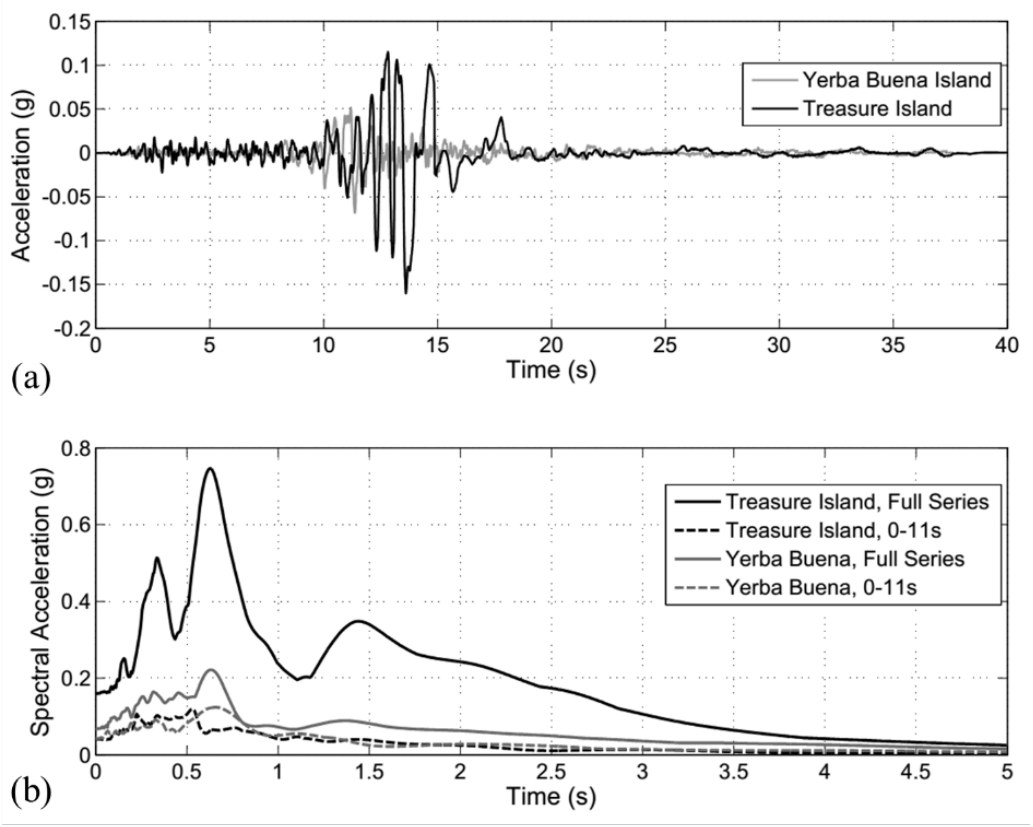

Figure 3.8: Ground motion (a) acceleration time histories and (b) response spectra for Treasure Island and Yerba Buena Island, from the 1989 Loma Prieta Earthquake

Another interesting case history comes from Kushiro Port, which liquefied during the 2003 Tokachi Oki earthquake in Japan. The site, which experienced liquefaction about 30 seconds after the start of ground shaking, consisted primarily of a deep deposit of dense sand, with occasional thick layers of silt and gravel (Greenfield, personal communication). A comparison of downhole and surface acceleration records and response spectra (Figure 3.9) at the port site reveals several interesting characteristics.

First, note several acceleration spikes occurring up to 15 seconds after the onset of liquefaction, known as *dilation pulses*. These pulses tend to occur when the liquefied material dilates at very high strains within a stress cycle, and the resulting increase in stiffness (see Figure 2.17) actually results in amplification at *higher* frequencies. Thus, we see both extreme amplification in the expected longer period range (due to the low-

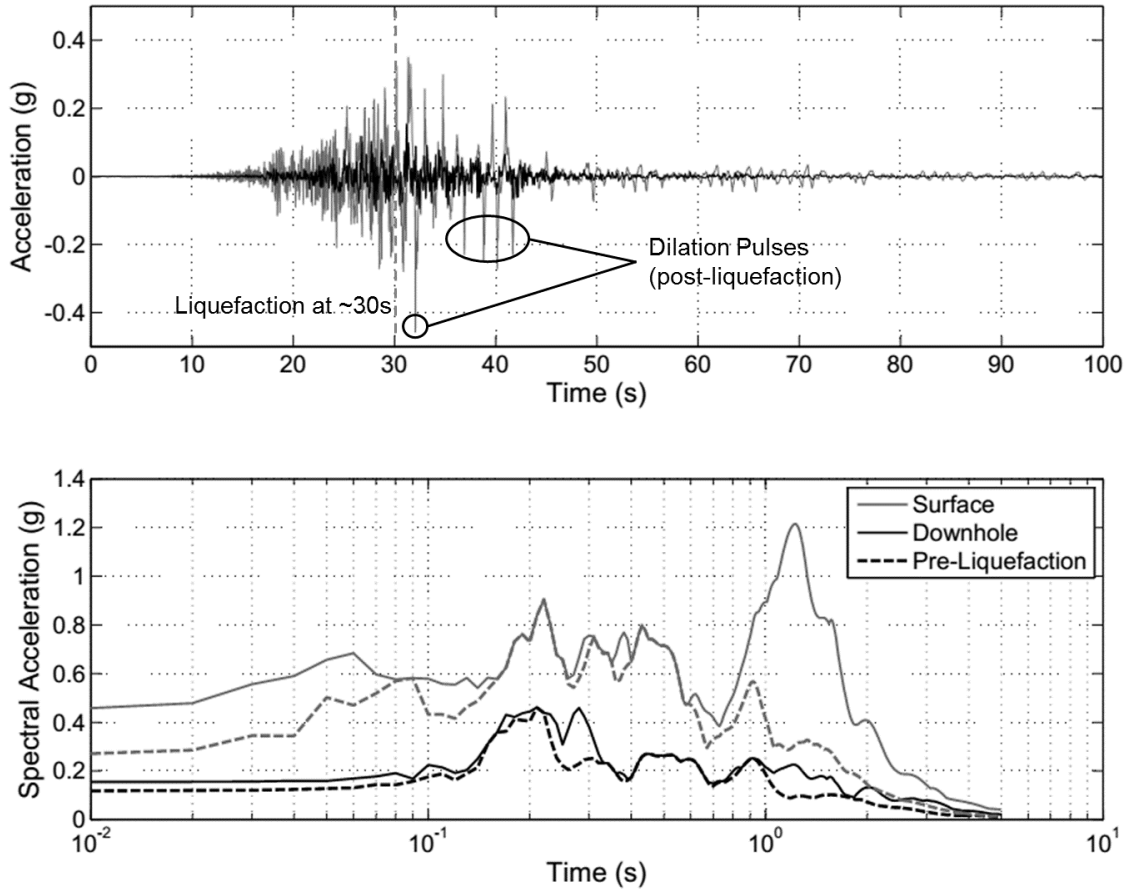

Figure 3.9: Downhole and ground (a) surface acceleration time histories and (b) response spectra for Yushiro Port site, from the 2003 Tokachi Oki Earthquake

frequency dilation pulses) and significant amplification in the short period range (due to the stiffening of liquefied material at the end of the dilation pulses). The intermediate range of the spectrum (approximately 0.1 to 1.0 seconds) tends to see very little amplification from these two competing phenomena.

3.4 Lateral Spreading

Lateral spreading is a particularly significant consequence of liquefaction, due in large part to the relative difficulty involved in detecting the potential for it to occur, characterizing the degree to which it occurs, and its associated hazards. Lateral spreading, as stated previously, can occur at gently sloping site or on level sites in the vicinity of a free face. For the purposes of this study, a *free face* is simply a topographic condition where the ground slope changes from relatively gentle or flat to suddenly much steeper. This is often

seen in man-made cuts, natural slopes, or any sort of embankment that borders a body of water.

In Section 2.1, two different types of liquefaction – flow liquefaction and cyclic mobility – were introduced and discussed. Flow liquefaction, which generally manifests as large, rapid deformations of relatively steep slopes, occurs when the *in situ* static shear stresses exceed the residual or liquefied shear strength of the soil. Since the liquefied shear strength is generally a function of initial relative density, it follows that for flow liquefaction to occur, the slope must be large and steep enough to impose significant static shear stresses, and the soil must initially be loose enough to experience a reduction in strength to a level below the imposed static shear stresses. Thus, flow liquefaction is driven by *static* shear stresses. On the other hand, cyclic mobility occurs when the static shear stresses have *not* exceeded the liquefied shear strength of the soil. This requires relatively low static shear stresses and a soil sufficiently dense such that its liquefied shear strength exceeds the imposed static shear stresses. Cyclic mobility is then a phenomenon which is driven by *cyclic* shear stresses. Deformations related to cyclic mobility almost always occur *during* ground shaking, and tend to occur as a combination of the permanent strains that result from the inelastic response of liquefied material to ground shaking, and the deformations that occur during increments of time in which the ground acceleration imposes a shear stress that, when combined with the static shear stress, temporarily exceeds the liquefied shear strength of the soil.

Cyclic mobility is the liquefaction mechanism that drives lateral spreading. The soil involved in lateral spreading is generally loose enough to liquefy and at the same time initially too dense to develop larger, flow-like deformations. Despite this distinction, deformations due to lateral spreading can be quite significant; field observations from earthquakes in Chi-Chi (1990), Edgecumbe (1987), and Imperial Valley (1979) included lateral displacements as high as 3 or 4 meters. These sort of deformations can impose serious structural demands on building foundations, underground utilities, and earth retention structures.

3.4.1 Lateral Spreading Hazards

Lateral spreading deformations frequently cause damage to structures and facilities located near waterfronts. In these areas, soils are more likely to have been deposited via waterborne modes in an environment with a high groundwater table, meaning that more soil is saturated at shallow depths. Developed waterfront areas are also often underlain by artificial fill placed in land reclamation; some of the more vintage methods used to place

hydraulic fill, as stated in Section 2.4.1, can be particularly problematic, as they generally have replicated the very same natural processes that result in liquefiable natural material. From a topographic standpoint, regions that are near bodies of water also tend be on ground that slopes towards the water, or near free-face embankments with static shear stresses that can drive lateral spreading.

Lateral spreading deformations have high potential to damage foundations and buried utilities. For buildings founded on shallow footings, such as the facilities in Moss Landing during the 1989 Loma Prieta event (Section 2.4.1), large, irregular, permanent ground deformations downslope or toward a free face can result in significant structural damage to building columns due to differential displacement of the supporting footings. Lateral spreads can also impose high stresses on underground utility lines; less flexible installations can be prone to extremely costly rupture, such as in the Marina District during the 1989 Loma Prieta earthquake. One of the most significant structural hazards, however, stems from the damage to bridge foundations caused by large lateral deformations. Bridges are often supported by deep foundation elements such as driven piles or caissons, and are generally subjected to a higher level of seismic hazard than structures on land. Bridge piles nearest to an embankment may be particularly susceptible to extensive damage in the event of a large earthquake. The 1964 Niigata Earthquake (Figure 2.2), 1987 Edgecumbe Earthquake (Figure 3.10), and 1990 Luzon Earthquake (Figure 3.11) resulted in extensive and costly damages to major bridge systems after their bridge supports were subjected to excessive loading due to large lateral displacement at their respective riverbanks.

3.4.2 Ground Motion Effects

The three main components of earthquake ground motions are amplitude, frequency content, and duration. Significant lateral displacements induced by cyclic mobility occur during a given ground motion. This usually results in momentary, ratcheting downslope displacements, rather than the relatively continuous downslope displacement associated with flow-like liquefaction events. During a particular cycle of acceleration, the magnitude of downslope movement depends on how large the cyclic shear stress induced in the soil is, and at what frequency the pulse is occurring. Naturally, a ground motion time history with more cycles of large stresses will result in the accumulation of larger downslope strains in the liquefied soil, and thus a larger permanent displacement. As a result, lateral spread deformations are heavily dependent on both the amplitude and duration of the ground motion that the site is being subjected to.

Frequency content also has a significant inffluence on lateral spread deformations. As

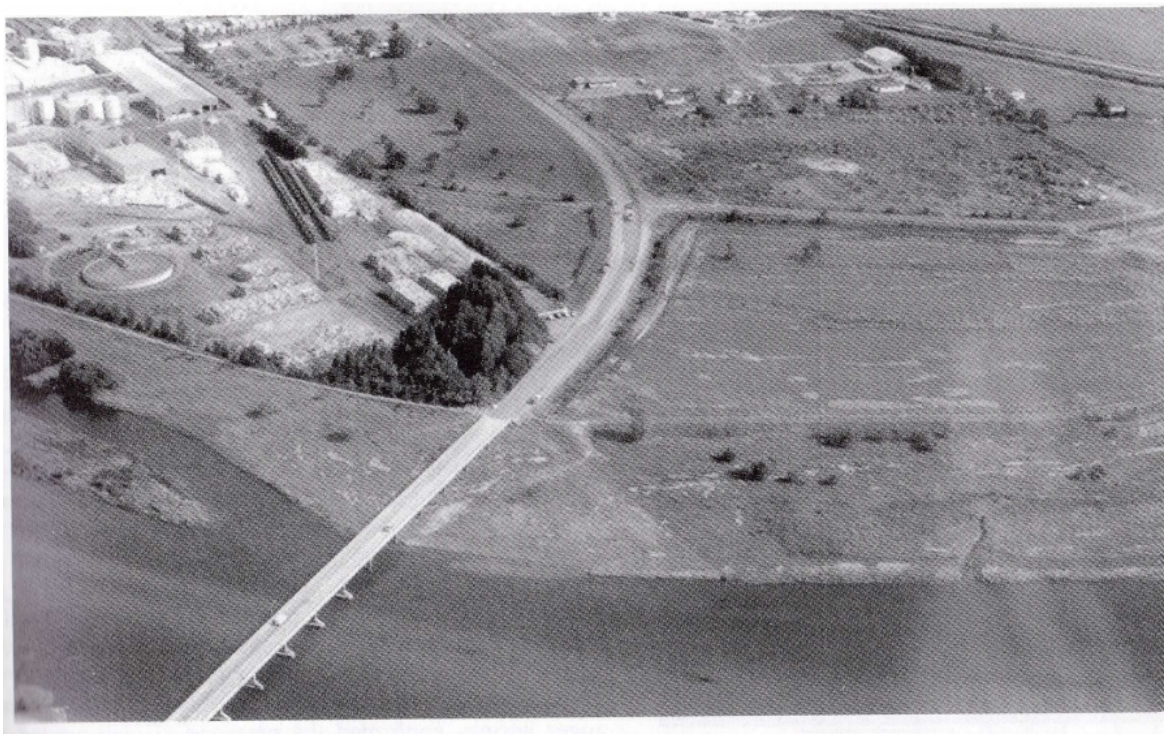

Figure 3.10: Aerial view of Landing Road Bridge site, looking northwest. Ground cracks near the bridge abutment, extending a 300m inland, are marked by lighter-colored sand ejecta. (Berrill et al., 2001)

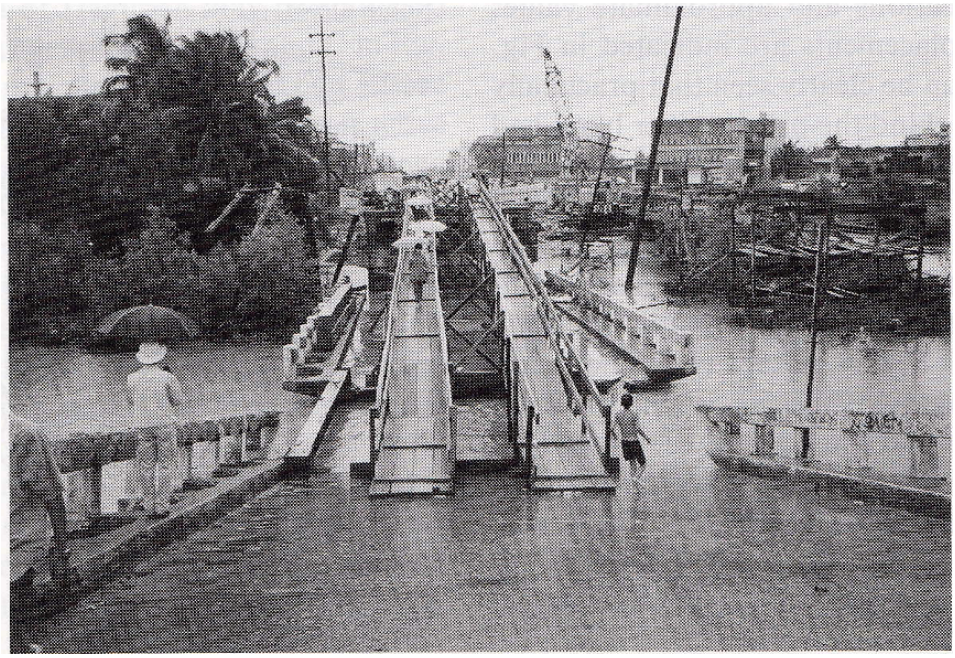

Figure 3.11: Collapse of the Magsaysay Bridge in Dagupan, Philippines. (Ishihara et al., 1993)

discussed in Section , ground motions with a frequency content close to the characteristic site period will be amplified to the maximum extent possible at the site. For sites that

have experienced liquefaction, and thus a lengthening of their characteristic site period, motions with longer-period characteristics can cause significant amplifications at the site. Longer-period motions generally can occur in large-magnitude earthquakes, at sites that are relatively far away from the source. High-frequency waves have shorter wavelengths, and thus are more likely to dissipate when traveling long distances and passing through complex layered media. Thus, longer-period stress waves are more likely to reach a distant site, provided that the fault rupture at the source must release sufficient energy to produce stress waves with large enough amplitudes to withstand damping over long distances. It is for these reasons that long-period site amplification is usually only considered in situations where the design earthquake is expected to be quite large, and the site of interest is at a considerable distance (upwards of about 70 km).

The characteristics of the input ground motion control the magnitude of the imposed cyclic shear stress on the liquefiable soil. Similar to the methods discussed in Chapter 2 for evaluating how cyclic shear stresses influence the onset of liquefaction, the very same stresses that occur after liquefaction influence how often and how much the ground is expected to displace downslope or towards a free face. Hence, characterization of the amplitude, frequency content, and duration of the expected ground motion at the site in question is an important step in evaluating the potential for lateral spreading.

3.4.3 Effects of Ground Surface Conditions

Lateral deformations are influenced not only by the cyclic shear stresses, but also by the existing static shear stresses. As stated previously, τ_{st} , within the scope of lateral spreading, results from ground conditions that favor displacement in a particular direction. The most obvious example of this condition is in sloping ground, where the magnitude of τ_{st} is dependent on the ground slope angle. In the case of a free face, such as near an embankment or retaining wall, the larger static shear stresses occur at locations closer to the free face. The larger the initial static shear stress, the more likely it is that a cycle of shear stress will exceed the liquefied shear strength, thus causing significant permanent shear strains. In other words, for the same ground motion and subsurface strata, sites on steeper sloping ground will experience larger deformations, and sites with free faces will experience larger deformations closer to the free face. Thus, it is critical that ground slope conditions are thoroughly characterized at the site, and that the site's proximity to any sort of free face is adequately accounted for.

3.4.4 Effects of Subsurface Conditions

Finally, the amount of shear strain that occurs in a given cycle of stress depends on how large the combined shear stresses (cyclic and static) are in comparison to the liquefied shear strength. As was established in Section 3.2, the residual shear strength of liquefied soil depends primarily on the initial *in situ* relative density of the liquefiable soil. The relative density has already been established in the initial evaluation of liquefaction potential using SPT- or CPT-based test methods, and the penetration resistance can be utilized again in the evaluation of lateral spread. The potential for impeded drainage boundaries, which can further reduce the residual strength of the liquefied material by creating local sliding surfaces via the formation of water films, is also an important factor.

The thickness of the liquefiable layer also has a large influence on permanent lateral displacements. A thicker liquefiable layer indicates that a larger amount material is undergoing shear strain, which results in a larger accumulation of strains at the ground surface. In addition to properly evaluating the vertical extent of the liquefiable material, it is also important to recognize the role its horizontal extent plays in contributing to lateral spread hazard. Consider the two profiles shown in Figure 3.12. The first profile features a liquefiable layer that extends toward a nearby free face. The second profile features a layer of the same liquefiable material with the same thickness, but one which does not reach the free face; it is instead bounded by dense material at the free face. If the profiles are subjected to the same ground motion, Profile A would be expected to experience larger deformations towards the free face, as material contributing to the deformations is allowed to extend and deform freely. Deformations in Profile B, while perhaps not insignificant, would be suppressed somewhat by the dense, nonliquefiable material bounding it to the right. In fact, this exact sort of subsurface condition was seen in the near-failure of the Lower San Fernando dam in 1971 (Section 2.2). Catastrophic failure of the dam was averted in part due to the fact that deformations of the liquefied sand were restrained to some degree on both the upstream and downsteam sides of the lower dam by much denser sand that did not liquefy.

Thus, when the potential for lateral spreading exists, it is important to thoroughly characterize the subsurface conditions at the site both vertically and horizontally. This may involve more borings than a conventional site investigation might require, especially near the free face and outside of the building footprint, in order to determine the extent of the liquefiable material and to be able to predict how lateral deformations might manifest. A more detailed discussion some of the approaches to predicting lateral spreading deformations is presented in Section 4.3.1.

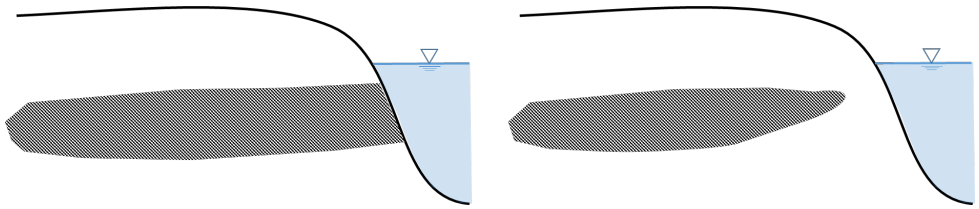

Figure 3.12: Subsurface profiles comparing sites with liquefiable material extending to the open free face, and a liquefiable layer constrained by dense material closer to the free face

3.4.5 Summary

Fundamental to any evaluation of lateral spreading hazards is a reliable estimation of the ground motion characteristics that the site is expected to experience, a thorough characterization of the subsurface conditions with particular respect to the extent and thickness of liquefiable material, and a complete understanding of the dominant topographical features of the site. The next section discusses the various approaches used to estimate lateral spread displacements. While they may vary significantly in approach, methodology, and ideology, they all share common threads, and thus require rigorous attention to detail concerning the factors detailed above.

3.5 Settlement

It has been observed in numerous earthquakes that liquefied soil may undergo significant levels of vertical strain. Vertical ground deformations that occur after liquefaction are generally termed *earthquake-induced settlements*, and generally are completed after excess pore pressures are dissipated. In level-ground conditions, excess pore pressures generated during ground shaking result in a decrease in effective stress in the liquefied soil. Once these excess pore pressures eventually dissipate, the soil will return to its previous effective stress, but in a denser state. This concept is simply an extension of the drained cyclic shearing behavior outlined in Section 2.3.3. Whereas liquefaction is evaluated in terms of undrained shear, post-liquefaction settlement effects can be viewed in a drained framework. An initially loose sand will contract after excess pore pressures dissipate, resulting in volumetric strains. The occurrence of earthquake-induced settlements can cause excessive settlements in shallow foundations, damage to bridge approaches, and downdrag loads on deep foundation systems (Kramer 2009).

There are several complications to evaluating the potential for vertical reconsolidation settlement induced by liquefaction. The volumetric strain induced following liquefaction is not simply controlled by the consolidation properties of the soil and the dissipation of

excess pore pressures; in fact, cyclic loading of a soil that has liquefied generally produces significant changes to the soil's fabric, leaving it more compressible than its original state (Kramer 2009). The volumetric strain associated with cyclic drained shear depends on both the initial relative density of the soil, and the peak amplitude of cyclic shear strain. The peak shear strain has been found to be especially useful in capturing the effects of the breakdown of the soil's fabric. Most methods for prediction of volumetric strains are based on these two factors: *in situ* relative density, in the form of SPT- or CPT-based correlations; and peak shear strain, generally represented by cyclic stress ratio. These correlations are based on either laboratory test results, or field observations of vertical settlement. The combined database of laboratory tests and case histories is relatively small, so there is considerable uncertainty involved in the usage of the methods discussed in this section.

Tokimatsu and Seed (1987)

The model proposed by Tokimatsu and Seed is probably the most widely-used method for estimate liquefaction-induced settlement in the United State. It was based on the concept that post-liquefaction volumetric strains are dependent on initial relative density and peak shear strain, supported primarily by laboratory tests. Peak shear strain was related to *CSR*, and relative density was related to SPT resistance. The relationship between volumetric strain, SPT resistance, and *CSR* is shown in Figure 3.13. Note that for high cyclic stress ratios, which correspond to stronger levels of ground shaking, the volumetric strains reach a limiting value for a given SPT resistance. The estimated volumetric strain (ε_v) can then be used to calculate the vertical settlement. Similar to calculating consolidation settlement, this is usually achieved by dividing the soil profile into discrete sublayers, and calculating the vertical settlement in each sublayer:

$$\Delta H = \sum_{i=1}^{n} (\varepsilon_v)_i \Delta z_i \tag{3.7}$$

where $(\varepsilon_v)_i$ is the vertical strain of the ith sublayer, and Δz_i is the thickness of sublayer i.

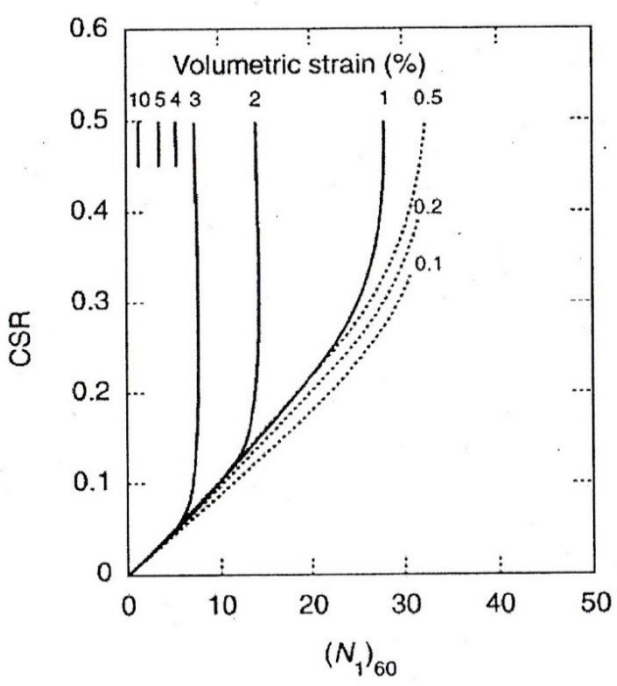

Figure 3.13: Relationship between volumetric strain, CSR, and SPT resistance used in evaluating liquefaction-induced settlement (Tokimatsu and Seed 1987)

Ishihara and Yoshimine (1992)

Ishihara and Yoshimine used similar methodology to Seed and Tokimatsu, in which the volumetric strain is estimated for discretized sublayers in a soil profile and used in Equation 3.10. The correlation for volumetric strain (Figure 3.14) is instead based on relative density (or SPT/CPT resistance) and factor of safety against liquefaction. As discussed in Section 2.4, FS_{liq} is a function of both the peak cyclic shear stress due to ground shaking and the relative density of the soil, so the model accounts twice for relative density. The range of 0 to 2 for FS_{liq} thus allows for the estimation of volumetric strains for excess pore pressures generated in cases where liquefaction does not occur. Note that for FS_{liq} ¿ 1.0, the volumetric strains are generally quite small (as high as 3%), but overall not insignificant, particularly if differential settlement of shallow foundations is of concern.

Wu and Seed (2006)

Wu and Seed's 2006 model is of the same framework as the two previously discussed methods. It is, however, based purely on cyclic simple shear tests performed on a single type of sand. By varying the density of the sand, Wu and Seed were able to isolate the

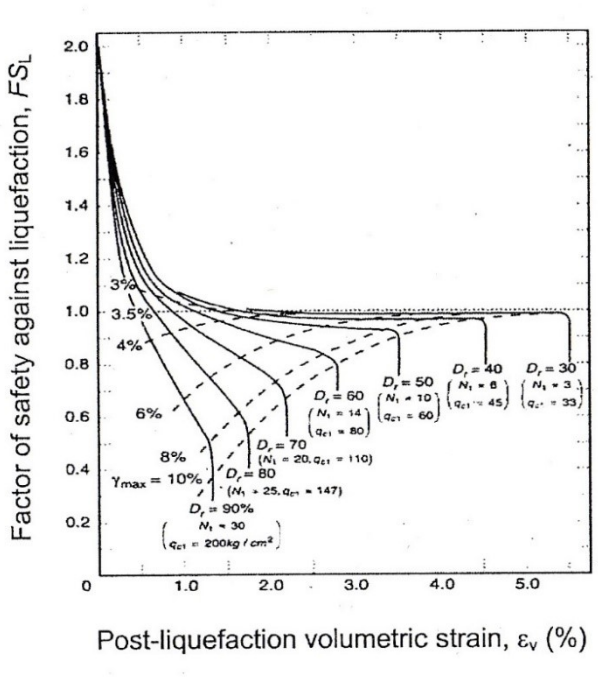

Figure 3.14: Relationship between volumetric strain, FS_{liq}, and relative density (Ishihara and Yoshimine 1992)

effects of relative density on volumetric strain and develop a correlation between the two for varying *CSR*. The correlations were then calibrated to field observation case histories, and the correlation for clean-sand SPT-resistance was developed in Figure 3.15. The volumetric strain is similarly computed for discretized sublayers. Note that volumetric strain contours in Wu and Seed's correlations do not reach limiting strains as prevalently at higher *CSR* values than Seed and Tokimatsu's correlations.

Shamoto et al. (1998)

Shamoto et al. proposed an alternative framework, which is also based on laboratory results, involving the estimation of a *maximum* amount of residual volumetric strain, which is then used to calculate a value known as the *ground settlement potential*, or D_s. The residual volumetric strain ($\varepsilon_{v,r}$) is calculated using the relationship between shear stress ratio (τ_{av}/σ'_z), which is equivalent to *CSR*, and adjusted SPT N-value, N_a (Figure 2.45). N_a is a fines-adjusted SPT resistance value based on the Japanese standard SPT N-value, N_1.

$$N_a = N_1 + \Delta N_f \tag{3.8a}$$

$$N_1 = 0.833(N_1)_{60} \tag{3.8b}$$

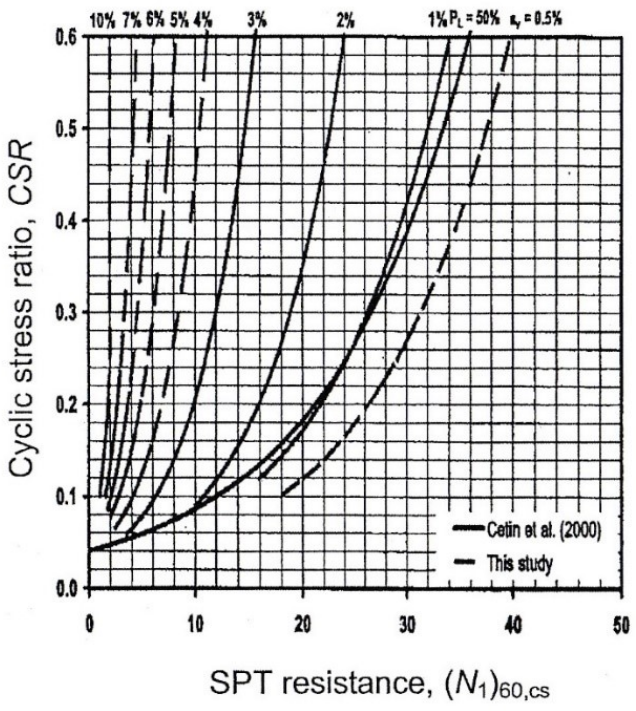

Figure 3.15: Relationship between volumetric strain, CSR, and relative density (Wu and Seed 2006)

$$N_a = \begin{cases} 0 & FC \leq 5 \\ FC - 5 & 5 < FC \leq 10 \\ 0.1FC + 4 & FC \geq 10 \end{cases} \tag{3.8c}$$

Once the adjusted N-value is calculated, the residual volumetric strain potential, $(\varepsilon_{vr})_{max}$ can be determined using one of the three plots in Figure 3.16, depending on the fines content in the liquefiable soil. The residual volumetric strain potential is interpreted as the *maximum* strain that the liquefied soil can be expected to experience (Kramer). When calibrated against existing case histories of field observations, the expected settlement was found to be about 84 percent of the maximum settlement potential. Similar to the methods developed by Tokimatsu and Seed, this model is usually applied by discretizing the soil profile and evaluating strain potential in each sublayer. Thus, the expected settlement for a given sublayer can be calculated as:

$$\Delta H = \Delta z 0.84 (\varepsilon_{vr})_{max} \tag{3.9}$$

$$\Delta H = \sum_{i=1}^{n} 0.84 (\varepsilon_{vr})_{max} \Delta z_i \tag{3.10}$$

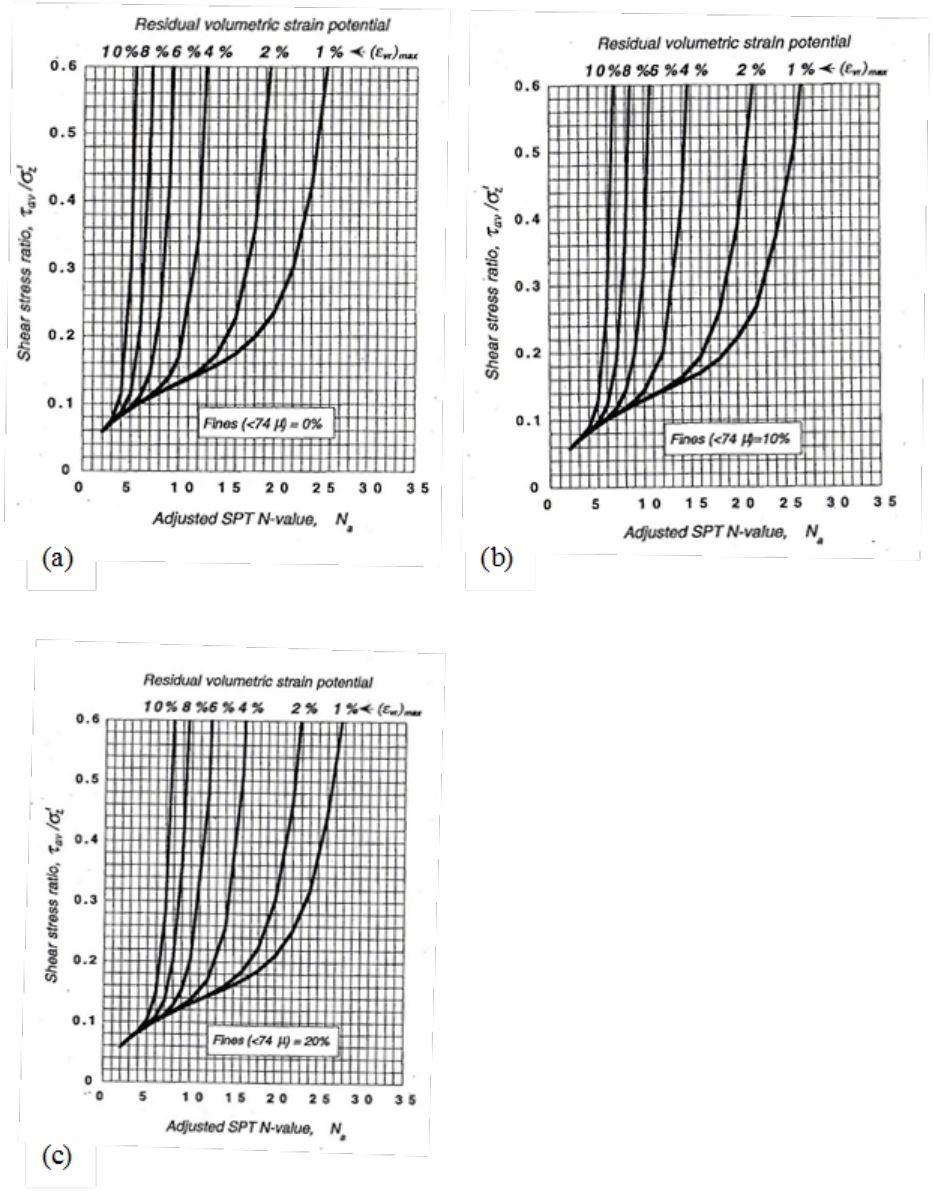

Figure 3.16: Relationship between volumetric strain, *CSR*, and adjusted SPT resistance for sand with fines content of a) 0%, b) 10%, and c) 20% (Shamoto et al. 1998)

3.6 Summary

The analysis of liquefaction susceptibility at a particular is only the first step in most geotechnical earthquake engineering applications. Equally critical to the process is the subsequent evaluation of the potential effects and hazards associated with the onset of liquefaction. This requires accurate characterization of the thickness of the liquefiable layer, ground surface topography, and groundwater conditions. Special attention should also be paid to the flow of excess pore pressures, and if there exists the possibility of impeded drainage due to an impermeable barrier. The effects of liquefaction on ground motions at the surface can be quite significant, and must also be considered; amplification of stress waves can result in larger-than-predicted ground accelerations, and longer-period motions due a lengthening of the characteristic site period. In steep slopes where the liquefiable material is initially quite loose, the possibility of flow liquefaction must be considered, and thus predicting the liquefied shear strength of the soil becomes critical. In more gently sloping sites or sites near free faces, the hazard of lateral spread becomes more prominent, and usually requires an evaluation of the soil properties and thickness of the liquefiable layer, site topography, and an accurate estimation of the expected ground motion characteristics. Potential vertical settlement of the ground must also be characterized, and is primarily based on accurately characterizing the initial relative density of the liquefiable material.

In Section 2.4.2, a brief discussion was presented regarding the evaluation of liquefaction triggering in a probabilistic fashion. This framework can be similarly extended to the characterization of liquefaction-related effects. If liquefaction triggering-related indices such as FS_{liq}, CSR, CRR, or clean sand-corrected penetration resistances are characterized via probability distributions, the subsequent liquefied shear strengths and vertical and/or horizontal deformations can similarly be evaluated probabilistically. The multitude of models and methods for predicting liquefaction and its effects allows the engineer some versatility, and can help establish a range of possible outcomes and estimates, rather than a single estimate. Probabilistic- and performance-based geotechnical earthquake engineering represents the cutting edge in earthquake engineering; it can account for the uncertainty inherent to seismology and soil liquefaction, and provides developers with more applicable and useful assessments of hazard in terms of property damage and losses. Thus, a significant portion of research moving forward should be geared toward performance-based concepts and probabilistic methods to characterize liquefaction.

Chapter 4

EVALUATION OF SEISMIC SLOPE STABILITY

4.1 Introduction

Landslide hazards are a highly visible result of the constantly evolving nature of landscapes. They occur in both natural and man-made slopes, and can be influenced by geologic, seismic, meteorological, and anthropogenic factors. Slopes exists in varying states of stability, which generally depend on how the driving forces of the potential failure mass compare to the internal strength of the material comprising the slope. Slope stability can be affected by long-term factors such as uplift of the earth's crust (due to convergence of tectonic plates) or erosion processes, as well as short-term variations in the slope conditions such as those caused by a period of particularly heavy rainfall, or a large seismic event.

Earthquake-induced landslides are a critical component of the design process in seismically active areas. Assessment of seismic slope stability requires detailed knowledge of the slope geometry, material properties, and phreatic surfaces of the landform, as well as the ground motion characteristics expected at the site. This chapter introduces two different forms of seismic slope instability, inertial instability and weakening instability, and discusses the various approaches used by engineers to evaluation these phenomena.

4.2 Inertial Instability

Earthquake ground motions produce vertical and horizontal forces that, combined with the static weight of the failure mass, can significantly increase the driving normal and shear stresses along potential failure surfaces, thus reducing the overall stability of the slope. This is known as inertial instability, in that the stability is affected solely by changes in the driving stresses, while the strength of the material is generally assumed to be unchanged during ground shaking. The methods discussed here that assess inertial stability do so by first characterizing the static driving stresses and internal strength of the slope of interest, and then by making assumptions about how earthquake loads affect the overall driving stresses.

4.2.1 Pseudo-static Analysis

One of the widely-utilized methods for evaluating seismic slope stability is a relatively straightforward extension of the limit equilibrium analysis (LEA) of static slope stability (Duncan et al., 2014). For a given potential failure mass and corresponding failure surface, the LEA assesses the stability by determining the forces and moments exerted by the mass on the plane, and the resulting strength of the material along the plane required to maintain equilibrium. This required shear strength is then compared to the actual available shear strength of the material along the plane to calculate the factor of safety for slope stability, FS (Figure 4.1).

$$FS = \frac{\tau_{avail.}}{\tau_{static}} \tag{4.1}$$

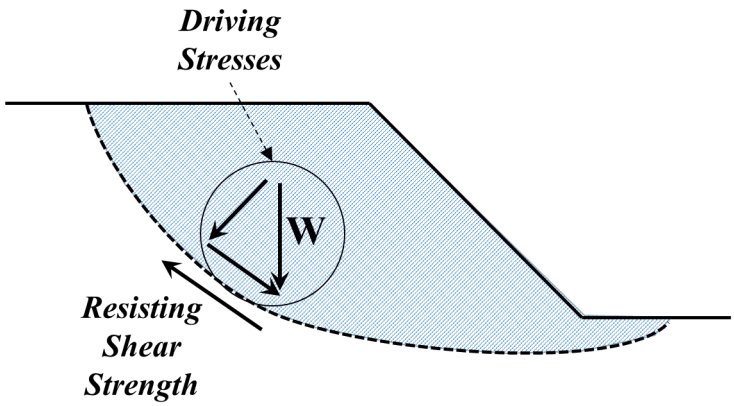

Figure 4.1: Illustration of the forces acting on a potential failure plane, used to evaluate the static factor of safety in limit equilibrium slope stability analyses

Pseudo-static analyses extend the LEA framework by adding an additional horizontal (and sometimes vertical) seismic force to the limit equilibrium calculation. The horizontal seismic force is expressed as a function of the weight of the failure mass (W) and the intensity of ground shaking:

$$F_h = \frac{a_y}{g} W \tag{4.2}$$

where a_y and g are the pseudo-static and gravitational accelerations, respectively. The ratio of the two accelerations is often denoted as the seismic coefficient, k_h (Figure 4.2). The factor of safety for pseudo-static slope stability can be expressed as:

$$FS = \frac{\tau_{avail.}}{\tau_{static} + \tau_{dyn.}} \tag{4.3}$$

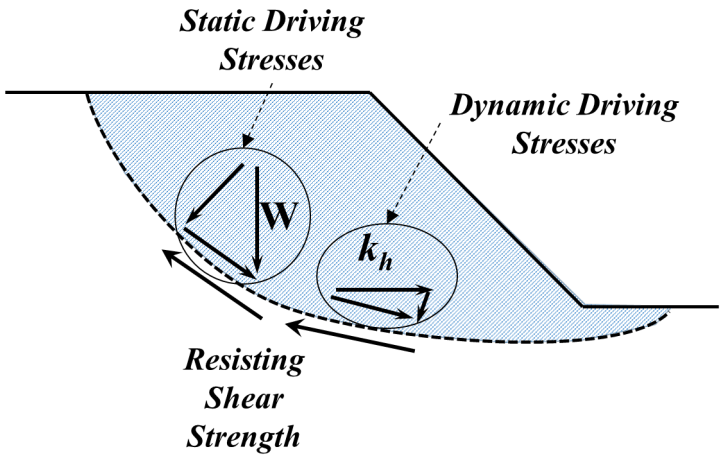

Figure 4.2: Illustration of the static and dynamic forces acting on a potential failure plane, used to evaluate the pseudo-static factor of safety in limit equilibrium slope stability analyses

Practical Considerations

The selection of an appropriate seismic coefficient is a critical component to effectively applying the pseudo-static LEA. If actual slopes truly behaved as rigid systems, a_h would be simply defined as the maximum ground acceleration, which corresponds to the maximum horizontal seismic force expected to be experienced by the mass. However, actual slopes and embankment dams do not behave in this manner, and the dynamic response of the system must be accounted for, leading to a_h values that are significantly lower than .

Various recommendations have been made over the past 60 years, each accounting for the dynamic response (as well as the criteria for acceptable deformations) in a different manner. As a result, a relatively wide range of design a_h values exist in literature. Terzaghi (1950) and Seed (1979) suggested that a_y can be as low as 0.1. Hynes-Griffin and Franklin (1984) recommended a value of about 0.5 times the PGA; this value generally corresponds to about 3 feet of displacement in dams, which was considered to be an acceptable criteria.

Furthermore, considerable attention must be paid to the characterization of the available shear strength of the soil along the failure plane. The LEA assumes that factor of safety for slope stability is constant along the failure surface; that is, the shear strength is assumed be mobilized at the same rate at all points on the failure surface (Kramer, 1996). The resulting mechanical behavior is thus assumed to be rigid-perfectly plastic. In reality, however, many soils tend to exhibit strain-softening tendencies, where differences between peak and residual shear strengths can be quite significant (Figure 4.3). In slopes where these types of soils are featured, it is often found that the peak shear strength may be reached only at a particular point or segment on the failure plane. Once the peak stress is reached and the soil strength is reduced to its residual value, the stresses are then redistributed to adjacent soils, which subsequently may reach their peak stress. This process is known as *progressive failure*, which has been observed in cases when the factor of safety, having been computed using the peak shear strength, was significantly greater than 1.0. As a result, it is generally more reliable to conduct LEA analyses using residual strengths, rather than peak strengths, when strain-softening soils are present.

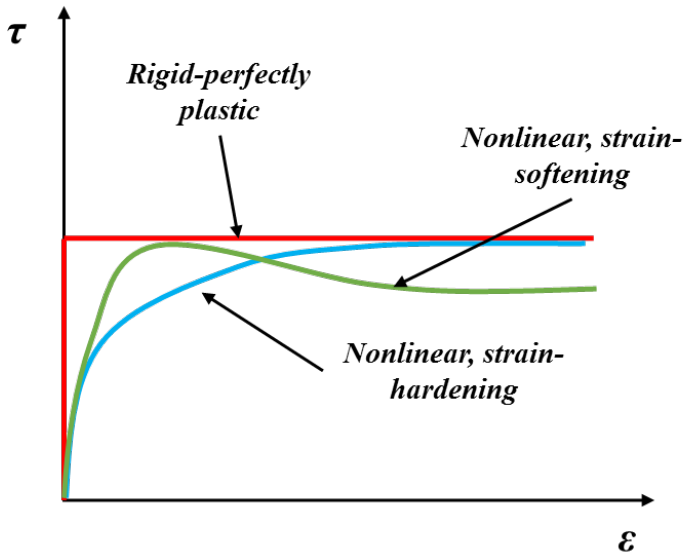

Figure 4.3: Comparison between rigid-perfectly plastic, nonlinear strain-hardening and strain-softening stress-strain behavior

Limitations

The LEA provides a relatively simple and straightforward way to characterize the stability of slopes for both static and seismic cases. However, its ability to assess the actual hazards related to the slope failures is limited, as it has no way of characterizing the actual permanent deformations that can be expected to occur *after* failure occurs. Furthermore, the pseudo-static application of the LEA accounts for seismic loading in a very crude manner. By using a single scalar value (k_h) to represent the effects of ground shaking, the pseudo-static method fails to capture all of the complexities associated with the observed dynamic responses seen in real slopes and embankment dams. Finally, by assuming that the factor of safety is related to the initial shear strength of the soil, pseudo-static analyses do not account for the effects of earthquake-induced changes in pore water pressure within the slope. High intensity ground motions, which generally tend to feature numerous cycles of significantly high shear stresses, can result in significant changes to the pore pressure, and subsequently the strength of the soil within the slope, even if liquefaction is not ultimately triggered. This mode of instability, due to the weakening of the soil along potential failure planes, will be discussed in greater detail in Section 4.3.

4.2.2 The Yield Acceleration

A variation of the pseudo-static analysis method detailed in the previous section is to instead consider a stable slope under static conditions and, knowing its factor of safety, determine the magnitude of horizontal force required to reduce FS to 1.0 and trigger slope failure. In earthquake engineering applications, this force manifests as a horizontal acceleration, and is known as the *critical* or *yield acceleration* (a_y). Newmark (1965) presented a simplified procedure for determining a_y (in units of g) as a function of the static factor of safety and the inclination angle, β, of an infinite slope:

$$a_y = (FS - 1)\sin\beta \tag{4.4}$$

For very shallow slopes subjected to strong ground shaking, it may also be of interest to determine the yield acceleration at which the site might fail in the upslope direction; the horizontal yield acceleration in the upslope direction can be determined via:

$$a_{y,u} = \frac{\tan\theta + \tan\beta}{1 + \tan\theta\tan\beta} \tag{4.5}$$

where

$$\tan\theta = \frac{a_{y,d} + \tan\beta}{1 - a_{y,d}\tan\beta} \tag{4.6}$$

and $a_{y,d}$ is the downslope yield acceleration determined in Equation 4.4

4.2.3 Sliding Block Analysis

In order to obtain a more concrete assessment of the seismic performance of slopes, earth dams, and levees, analysis methods that provide actual estimates of permanent deformations are generally more desirable that the pseudo-static method, which simply provides an index of the stability. Newmark (1965) proposed one such method, known as the *sliding block analysis*, based on modeling the site and potential failure mass as a block sliding on an inclined surface (Figure 4.3). In its most basic form, the sliding block method models the strength of the deforming soil using a coefficient of friction between the block and the sliding surface. Based on the slope of the surface and the friction coefficient, a critical acceleration can be used to represent the level of acceleration required to produce slip of the block relative to the plane. The inclined base is then subjected to a bedrock ground motion, and the block displaces relative to the inclined surface whenever the base acceleration exceeds the yield acceleration.

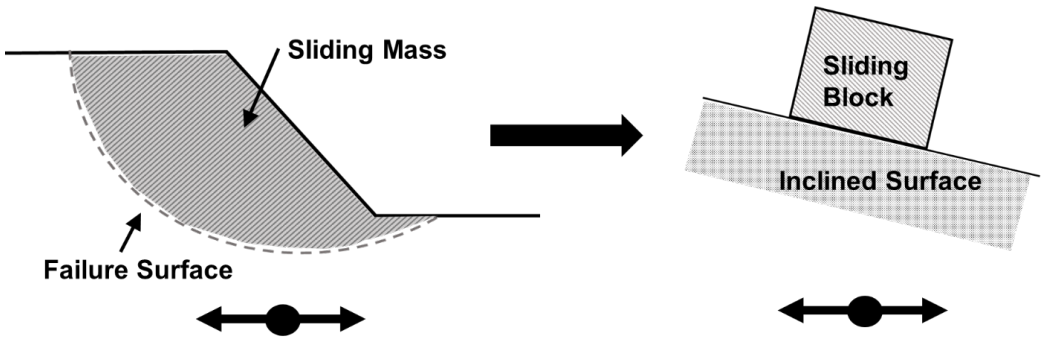

Figure 4.4: Idealization of a slope subjected to ground shaking as a rigid block on a frictional surface

During a time increment when the ground acceleration exceeds the yield acceleration, the relative displacement between the block and surface can be obtained by double-integrating the relative acceleration. This concept can be extended to a full ground motion, with multiple instances of yield acceleration exceedance (Figure 4.5).

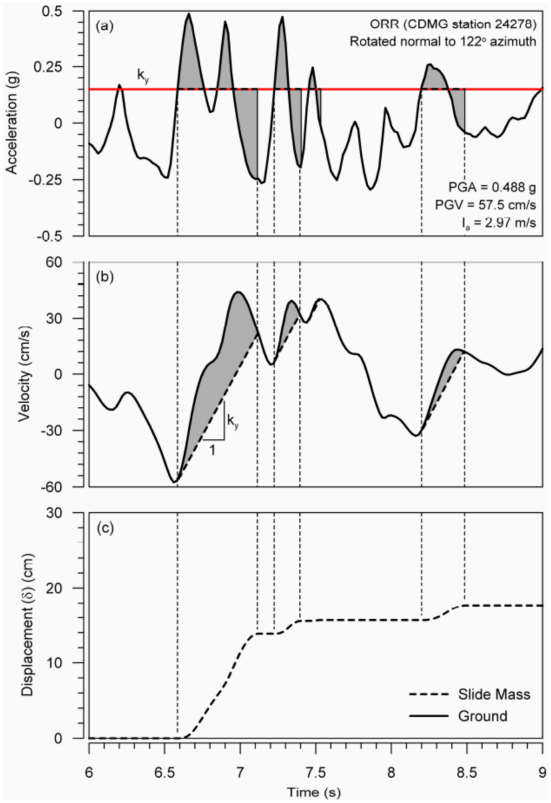

Figure 4.5: Illustration of the relative displacement calculation for Newmark sliding block analyses (Wartman)

Assumptions and Limitations

The use of Newmark's method makes several key assumptions about the system being modeled that must be addressed here. Firstly, the simplification of such potentially complex soil systems as large slopes, embankment dams, and levees as a rigid block on a planar surface can result in dynamic behavior that is largely inconsistent with that observed in actual earth structures. The rigid block model assumes that the potential failure mass moves uniformly as a single entity, i.e. that the displacement experienced at the failure plane will be the same as that experienced at the crest of the slope. However, real slopes and embankment dams tend to exhibit far more complex dynamic behavior.

Consider a hypothetical embankment, with a uniform shear stiffness (represented by its shear wave velocity v_s), subjected to ground shaking at its base. If the frequency of the input ground motion is very low, then the wavelength λ of the input motion will be relatively long. If the longer wavelength is roughly comparable to the height of the embankment, then we can expect that its response will be relatively uniform (Figure 4.6a). However, if the predominant frequency of the input motion is very high, corresponding

to a shorter wavelength relative to the height of the embankment, we can expect that its dynamic behavior will feature significant out-of-phase response (Figure 4.6 b). Thus, the reliability of the assumption of rigid mass movement is highly dependent on the frequency content of the input ground motion, as well as the stiffness characteristics and dimensions of the site of interest.

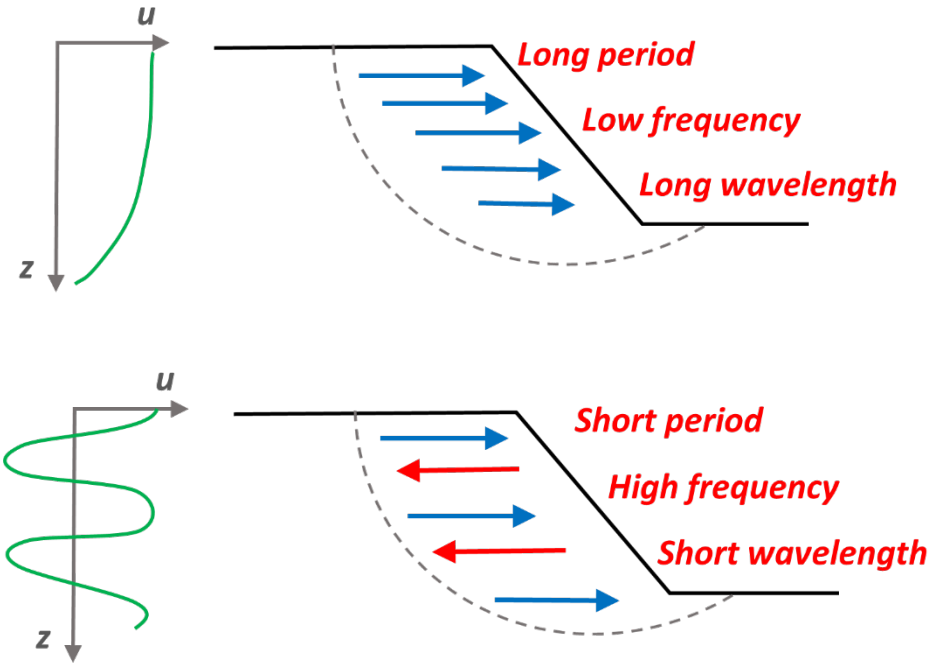

Figure 4.6: Comparison of the effects of (a) low frequency content and (b) high frequency content ground motions on the dynamic response of an idealized earth embankment

Another assumption inherent to Newmark sliding block analyses relates to the behavior of the soil at the failure surface. Much like limit equilibrium analyses, sliding block procedures assume rigid-perfectly plastic behavior along the failure plane. The failure mass remains motionless relative to the base until the yield acceleration is exceeded, after which the mass begins to slide relative to the plane, and the sliding resistance along the failure surface remains constant, i.e. it does not degrade with time or level of displacement. This idealization of stress-strain behavior is largely inconsistent with behavior observed in actual soils (particularly soft cohesive soils and loose granular soils), which generally exhibit some level of nonlinear strain-hardening or strain-softening response to shear stress (See Figure 4.3). For materials with very low stiffness such as liquefied soil, a significant amount of shear strain can be induced in the material before the available shear strength is mobilized. The shearing resistance of soil can also be rate-dependent, which is not reflected in the rigid-perfectly plastic sliding block mechanism, or be influenced by factors such as dilation due to phase transformation behavior.

4.2.4 Summary

The methods presented in this section have seen wide use in engineering practice since their introduction, and deal with the issue of seismic slope stability primarily by considering the inertial effects of ground motions on slopes. The pseudo-static limit equilibrium analysis assesses the stability of slopes by extending the traditional LEA to account for seismic loading via an additional horizontal force (the seismic coefficient). While the pseudo-static method provides an index value that indicates the likelihood of slope failure in the event of an earthquake, it does little to indicate what the actual effects of potential slope failure might be. The Newmark sliding block method is based on similar assumptions to the LEA (such as rigid-perfectly plastic soil behavior, and rigid movement of the failure mass), but is able to estimate permanent displacements and utilizes ground motion characteristics in a more complete manner.

It is important to note, however, that these methods for evaluating inertial instability have inherent structural biases rooted in the assumptions about the behavior of real slopes upon which they are based. Rarely do large earth structures move as a single coherent mass in response to dynamic excitation at their base; the dynamic complexity of the response of earth structures is well-recognized by the earthquake engineering community, and can be evidenced by the wealth of literature concerning reliable estimates of k_h in pseudo-static analyses (Terzaghi 1950, Seed 1979, Marcuson 1981, Hynes-Griffin and Franklin 1984), as well as the emergence of compliant sliding block methods since the late 1970s, which are discussed in greater detail in Section 4.2.4. Equally as critical is the assumption about the rigid-perfectly plastic stress-strain behavior of the soil, which is known to differ from actual soil behavior, as well as the inherent assumption that the only source of seismic slope instability is inertial. The assumption that the competence of the material comprising earth structure, determined *a priori*, does not change throughout the process of ground shaking is also inconsistent with what has been observed in numerous case studies over the past half-century; as a result, the pseudo-static LEA and Newmark analyses fail to capture a critical component of seismic slope stability, related to the reduction of strength that many soils experience during strong ground shaking.

4.3 Weakening Instability

When medium dense to loose granular soils and soft cohesive soils are subjected to strong ground shaking, excess pore pressures develop in response to undrained loading, often leading to significant reductions in the soils' ability to resist shearing deformations. When

the excess pore pressure buildup becomes significantly large, these reduced shear strengths can be exceeded by the static and dynamic shear stresses imposed on the soil, leading to potentially large shear strains and lateral deformations. As discussed previously in Section 2.1, this phenomenon can occur in two different ways. Flow liquefaction occurs when the soil is initially under relatively high static shear stresses, and experiences a reduction in strength such that it drops below the initial static stress, resulting in large flow-like deformations. Cyclic mobility occurs in somewhat milder topographical conditions, where initial static shear stresses are relatively low, and it is the combination of these shear stresses and the dynamic shear stresses from the ground motions that cause the soil to weaken and undergo lateral deformations. The remainder of this section focuses on the effects of cyclic mobility, and the methods used to characterize and predict permanent lateral spreading deformations.

4.3.1 Lateral Spreading

The methods used to evaluate lateral spreading deformations can be divided into four main categories. Fundamental to any evaluation of lateral spreading hazards is a reliable estimation of the ground motion characteristics that the site is expected to experience, a thorough characterization of the subsurface conditions with particular respect to the extent and thickness of liquefiable material, and a complete understanding of the dominant topographical features of the site. While the various methods discussed herein may vary significantly in approach, methodology, and ideology, they all share common threads, and thus require rigorous attention to detail concerning the factors detailed above. The main approaches to characterizing lateral spreading can be grouped as follows:

- Procedures based on experimental data that relates some measure of the liquefied soil's initial density and the expected peak cyclic stress to an associated shear strain. These relationships can be used to estimate the shear strain likely to develop in liquefiable soil with respect to depth at a site of interest and integrate the strains throughout the depth to obtain an estimate of permanent lateral deformation.
- Empirical correlations based on field observation case histories, laboratory tests, or results from nonlinear dynamic analyses using advanced constitutive models. These models use input parameters related to the earthquake, site, and soil characteristics as predictor variables to estimate an expected displacement prediction.
- Methods that model the lateral spreading mass as a rigid or compliant block sliding on an inclined frictional plane (See Section 4.2.3).

- Numerical methods, specifically nonlinear dynamic analyses, coupled with material models that can simulate pore pressure generation and pore water dissipation. These types of analyses can be computationally intensive and very time consuming, often requiring input data that is not commonly available.

Each of these approaches have resulted in a plethora of models that utilize different methodologies and are based on different types of datasets. Thus, for a given site, multiple models can be utilized in order to establish a range of possible displacements. This is an effective way to account for uncertainty in analysis of lateral spreading; each model that will be discussed herein has inherent limitations based on its methodology and dataset, and thus has the propensity to predict outliers for certain situations. By using multiple models, these outliers can be identified and addressed, and resulting in a more accurate evaluation.

4.3.2 Empirical Approach

A common approach to modeling lateral spreading focuses on using statistical regression of lateral spread case histories to develop equations for predicting permanent displacements. In general, these methods establish a correlation between permanent lateral displacements and a set of predictive variables such as ground motion intensity, characteristics of the liquefiable material, and site topography. Different empirical methods draw on different types of databases, usually either data from observed case histories of lateral spreading or from rigorous numerical analyses, and can differ in the predictive variables used and the statistical methods used to perform regression of those variables.

Youd et al. (2002) Model

One of the most commonly used empirical models, initially introduced by Youd and Bartlett in 1992, is based on a large database of lateral spreads that occurred in Japan and the western U.S. The model was updated and refined in 2002, and the Youd et al. (2002) will be referred to herein as the Youd model. The form of Youd's multilinear regression (MLR) equation for predicting lateral spreading displacements is:

$$\begin{aligned}\log D_H =& b_0 + b_1 M_w + b_2 \log R* + b_3 R + b_4 \log W + b_5 \log S \\ &+ b_6 \log T_{15} + \log 100 - F_{15} + b_8 \log D50_{15} + 0.1mm\end{aligned} \tag{4.7}$$

Table 4.1: Description of predictor variables, and their recommended ranges of applicability, used in Youd et. al (2002) MLR equation for predicting lateral spreading deformations

Parameter	Description	Range of Applicability
M_w	Moment Magnitude	6.0-8.0
R	Source-site distance	–
$R*$	Modified source-site distance	–
W	Free-face ratio (%)	1-20 %
S	Ground slope angle (%)	0.1-6 %
T_{15}	Cumulative thickness of liquefiable material with $(N_1)_{60} < 15$	1-15m
F_{15}	Average fines content of liquefiable material with $(N_1)_{60} < 15$	See Figure 4.8
$D50_{15}$	Average mean grain size of liquefiable material with $(N_1)_{60} < 15$	See Figure 4.8

where the predictor variables are summarized in Table 4.1

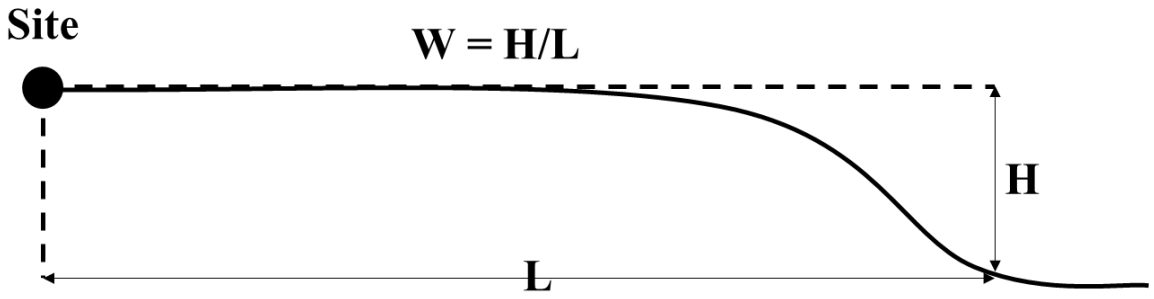

Figure 4.7: The free face ratio parameter, W, as defined by Bartlett & Youd (1992)

The coefficients for each case are summarized in Table 4.2. Note that the coefficients for the ground motion and soil parameters are identical for both cases, with the only differences being the coefficients that control the ground slope and free face ratio, as well as the b_0 values.

Table 4.2: Regression coefficients for the empirical model for lateral spread displacement prediction proposed by Youd et al. (2002).

Model	b_0	b_1	b_2	b_3	b_4	b_5	b_6	b_7	b_8
Ground Slope	-16.213	1.532	-1.406	-0.012	0	0.338	0.54	3.413	-0.795
Free Face	-16.713	1.532	-1.406	-0.012	0.592	0	0.54	3.413	-0.795

Table 4.1 also summarizes the recommended ranges of applicable values for each input parameter. It should also be noted that the model is generally only applicable for liquefiable material up to depths of about 15 m below ground surface. The recommended ranges of use of Youd's model are based on a combination of the limits of the sample data employed in the statistical regression, and the physical constraints of the system that the model is attempting to replicate. For instance, very few of the 484 case histories were used in this statistical regression had earthquake magnitudes greater than 8.0, and thus it would be a significant extrapolation to attempt to apply the model to a design scenario for magnitude 8.5 event. Similar constraints apply to the soil parameters $D50_{15}$ and F_{15} (Figure 4.8). On the other hand, the restriction on free face ratio usage is based on more physical limitations. Displacements at or near the free face may be subjected to the effects of rotational failures of slump blocks, gravitational effects that may induce flow failures, or other localized instabilities (Bartlett & Youd, 1992). These types of ground failures tend to be influenced by mechanics outside the framework of lateral spreading, and thus extrapolation of Equation 4.7 for use in cases with free face ratios of greater than 20% should be done with extreme caution, or alternative measures altogether should be used (Youd et al., 2002).

The observed displacement for each case history is plotted against the displacement predicted by the Youd empirical model in Figure 4.9. Franke & Kramer (2014) computed the standard deviation of $\ln D_H$ from the Youd model to be 0.464, and the large majority of the data plots within a factor of two of the predicted vs. actual displacements. This is considered to be sufficient predictive power for most routine engineering applications (Youd et al., 2002). When applying Equation 4.7 in engineering practice, utilization of Figure 4.9 can be useful in gaining a better understanding of the range of possible displacements that may be observed at the site in question, rather than simply using a single estimate of lateral displacement.

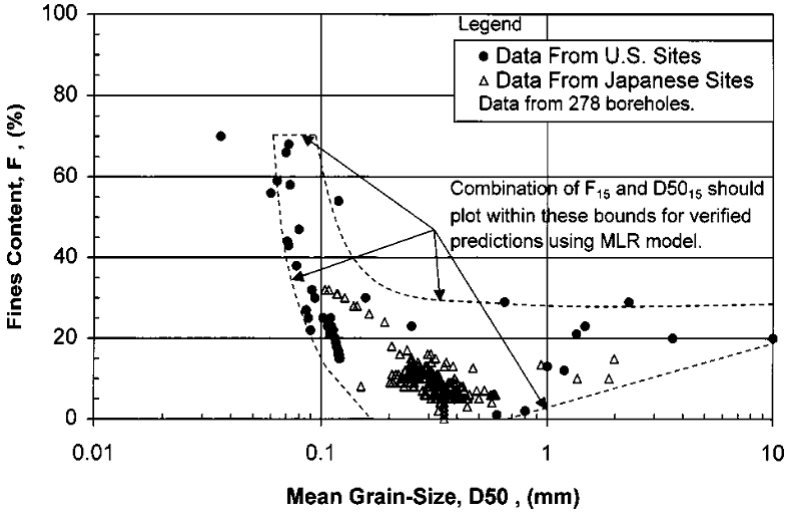

Figure 4.8: Recommended range of applicable combinations of fines content and grain size of liquefiable material for utilization of Youd et al. (2002) empirical model

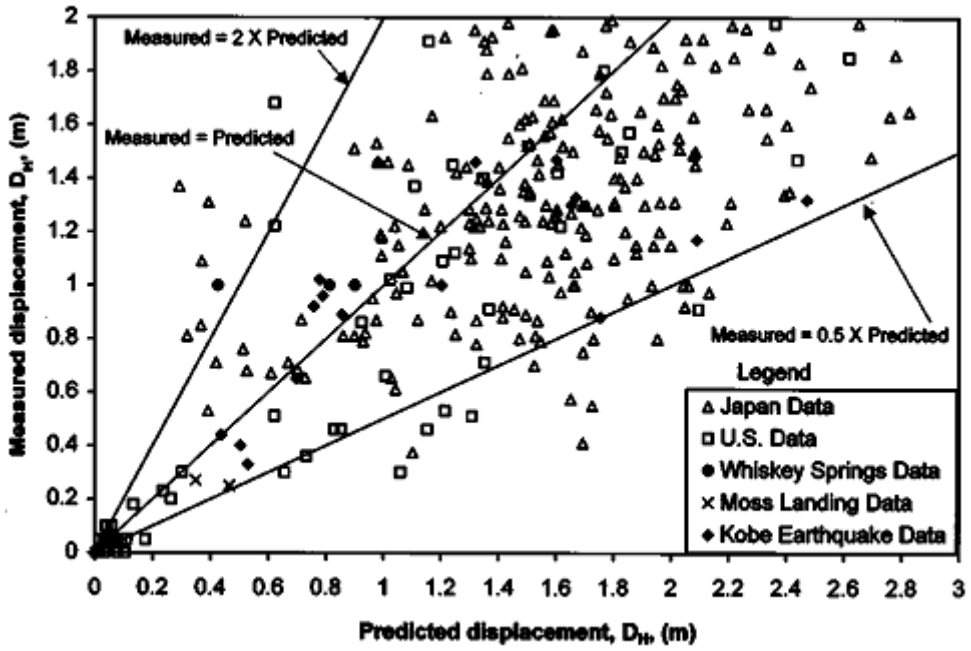

Figure 4.9: Predicted vs. observed displacements for the database used in multilinear regression of Youd et al. empirical model (Youd et al. 2002)

Practical Considerations

The Youd model has seen widespread use in industry, and is one of the primary methods used for evaluating lateral spreading in engineering practice (Kramer 2008). It is, however, limited particularly by issues with its implementation of the T_{15} parameter. By establish-

ing a binary cutoff of $(N_1)_{60} < 15$ for materials that contribute to lateral spreading, the model neglects to account for exactly how lateral deformations are influenced by relative density. The model will implicitly assume, for instance, that a site with a layer of liquefiable material of $N = 15$ will contribute the same magnitude of shear strains and lateral deformations as a site underlain by the same amount of a much looser material ($N = 4$). Hence, the model may be subject to inaccuracies in predicting lateral displacements for sites underlain by very loose material. Furthermore, the use of the T_{15} parameter also implies that soils with N-values larger than 15 do not mobilize significant shear strains at all. Even in conditions without any static shear stress, sands with corrected standard penetration resistances above $N = 15$ can still reach significant shear strains at large (but still realistic) magnitudes of cyclic stress (Idriss & Boulanger, 2008). The model therefore does not capture the influence of initial relative density on cyclic shear strain. In doing so, it can be subject to significant under-predictions of lateral spread deformations for very loose as well as medium dense sands.

Other Empirical Methods

Alternative empirical models have also been proposed by various researchers for predicting lateral spreading displacements. Rauch and Martin (2000) developed a model using multiple linear regression of data from 71 lateral spread case histories; they divided the predictor variables of their model into three components. The "regional" component is comprised of four earthquake loading parameters: moment magnitude, source-to-site distance, peak ground acceleration, and significant duration. The "site" component consists of three parameters related to the topographic conditions: the maximum horizontal length of the slide, the average slope across the lateral spreading area, and (if necessary) the height of the free face. The "geotechnical" component consists of two depth parameters: the average depth to the zone of minimum factor of safety for liquefaction, and the average depth to the top of the liquefied soil. Several issues about the parameters used by Rauch and Martin are worth noting. First, the dataset of 71 cases is relatively limited, particularly when compared to the nearly 500 cases used by Youd et al., resulting in somewhat narrow ranges in the data values used to fit the model. Secondly, the four regional parameters are not entirely independent of each other; although there appeared to be no evidence of multicollinearity in the model, concern still exists over whether the model is over-fitted. Finally, the geotechnical component of the model is fairly limited in that it focuses only on where the liquefiable material is located, and makes no attempt to account for the characteristics of the material itself, such as initial density or fines content, or the magnitude of FS_{liq}.

Kramer and Baska (2006) developed an empirical model based on the regression of a series of nonlinear analyses, using an advanced constitutive model that had the capability to capture the mechanics and effects of pore pressure generation in liquefiable soil. This model, referred to herein as "KB06", was then calibrated to field data for lateral spreading. The KB06 model has some similarities with Youd's model, particularly in the manner in which loading and topographical factors are represented, but differs considerably in the way the liquefiable soil is represented. Kramer and Baska decided to account for the effects of initial relative density and depth in a continuous manner, rather than the step function model (N less than 15) used in Youd's equation, using the *equivalent thickness parameter*, which is a continuous function of SPT resistance and depth. This means that the predicted displacements vary smoothly with $(N_1)_{60}$, which is more closely representative of how shear deformations are manifested in soil mechanics. The fact that the equivalent thickness parameter also varies with depth of sublayer captures the principle that soils that liquefy at larger depths develop smaller lateral strains.

The other conceptual difference between KB06 and the models proposed by Youd and Rauch and Martin is that it is not based solely on pure statistical regression. The Kramer and Baska model uses the basic mechanics of liquefaction and lateral spreading to establish the general form of a predictive relationship, and uses field observations to calibrate that relationship. In this way, the model attempts to accurately capture the mechanics that drive liquefaction and lateral spreading. Thus, it is more likely to be better equipped to predict instances of lateral spread than a model that is based solely on a limited number of field observations that have happened in the past (Kramer 2009).

4.3.3 Strain Potential Approach

One approach to evaluating lateral spread deformations is based on the concept that the permanent lateral deformation (LD) can be estimated by discretizing a layer of liquefiable soil into small sublayers, determining the shear strain (γ) in each sublayer due to the expected cyclic shear stress, and integrating the shear strains through the entire depth of liquefiable material:

$$LDI = \int_0^{z_{max}} \gamma dz \tag{4.8}$$

Ishihara and Yoshimine (1992) used cyclic undrained laboratory tests on clean, reconstituted sand specimens at varying relative densities to develop a relationship between the factor of safety for liquefaction and maximum shear strain developed during cyclic loading

(Figure 4.10). Note that as FS_{liq} decreases to less than unity, the maximum shear strains increase rapidly for loose materials ($D_R < 70\%$). For denser materials, the increase in shear strains is more gradual as the factor of safety decreases. Dense sands require much more intense levels of shaking in order to liquefy, and for very high cyclic stresses, the magnitude shear strains will depend more on the amplitude of stress than the initial density of the material. Also note that for low FS_{liq} and D_R, the maximum shear strains tend towards limiting values. Figure 4.11 shows these limiting shear strains as they relate to relative density, which is represented by clean sand penetration resistance, $(N_1)_{60,cs}$. Idriss and Boulanger (2006) represented the results of Ishihara and Yoshimine's correlations in terms of the parameters established in their simplified procedure for evaluating liquefaction potential, CSR and $(N_1)_{60,cs}$ (Figure 4.12)

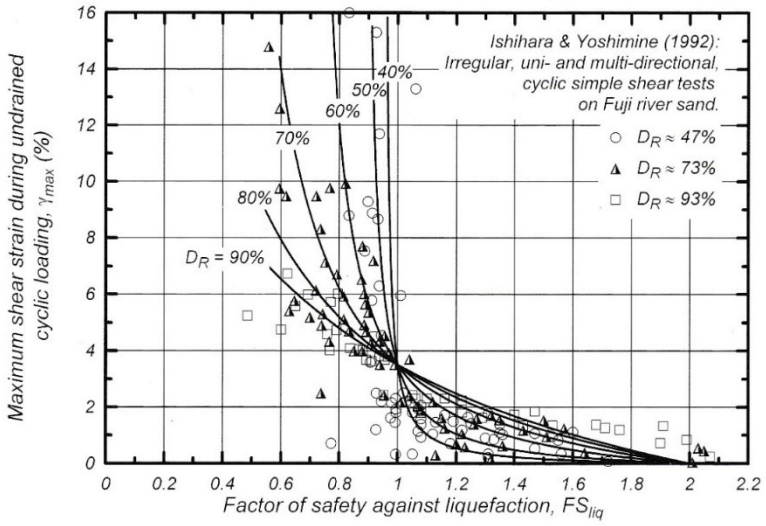

Figure 4.10: Results of cyclic simple shear tests on Fuji river sand of varying density, and correlation between maximum cyclic shear strain and factor of safety of liquefaction. (Idriss & Boulanger 2008, after Ishihara & Yoshimine 1992)

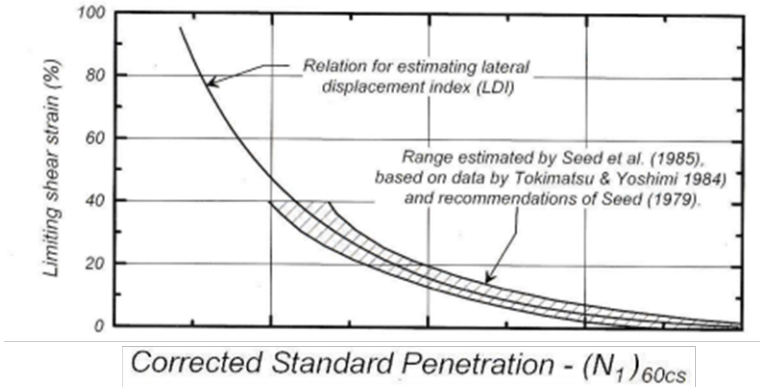

Figure 4.11: SPT-based liquefaction correlation for limiting shear strain, with $M = 7.5$ and $\sigma'_{vc} = 1$ atm (Idriss & Boulanger, 2008)

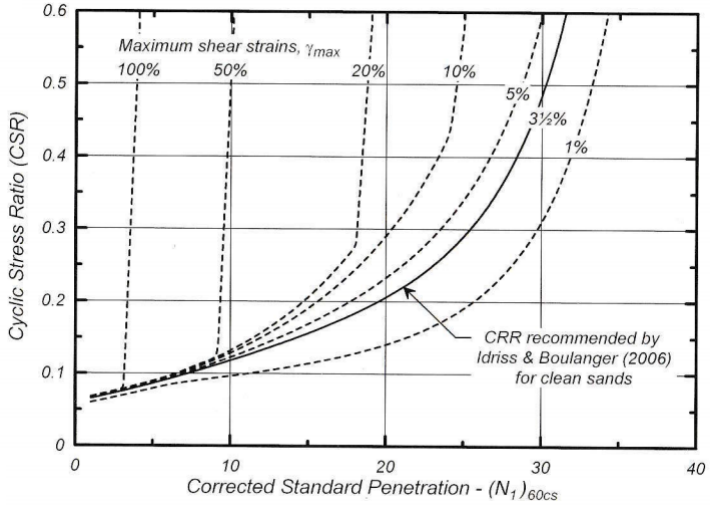

Figure 4.12: SPT-based liquefaction correlation for maximum shear strain, with $M = 7.5$ and $\sigma'_{vc} = 1$ atm (Idriss & Boulanger, 2008)

Similar correlations for maximum shear strain have been developed by Tokimatsu and Asaka (1998), and Wu (2002). A comparison between the three shear strain potential models for 50%, 20% and 5% maximum shear strain is shown in Figure 4.13. The scatter between the three methods is quite significant. For instance, for a clean sand-corrected N-value of 15, a peak shear strain of 20% would be estimated to be reached for CSRs of 0.2, 0.22, and 0.35; using the correlations proposed by Ishihara and Yoshimine (1992), Tokimatsu and Asaka (1998), and Wu (2002), respectively. Thus, considerable uncertainty is involved in using these simplified methods and generalized relationships to evaluate lateral displacements (Idriss and Boulanger 2008).

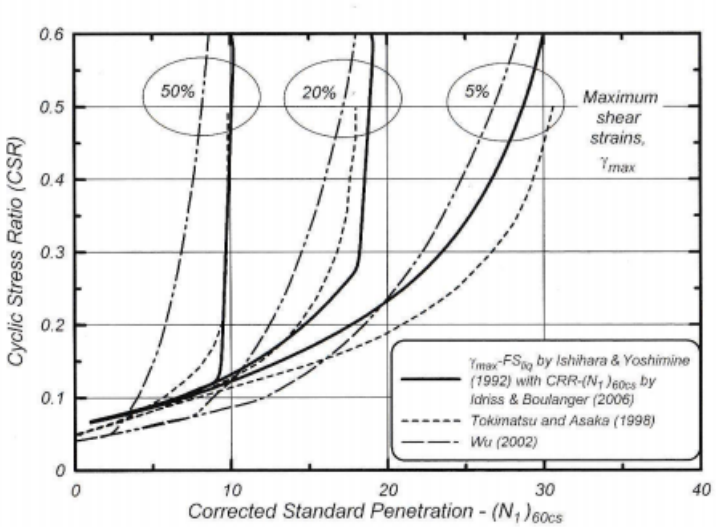

Figure 4.13: Comparison of CSR-$(N_1)_{60,cs}$ correlations for maximum shear strain (Idriss and Boulanger 2008)

Practical Considerations

It is important to recognize that the laboratory-based models that relate shear strain potential to relative density and cyclic shear stress do so without any consideration of static shear stresses; the laboratory tests upon which they were based involved no application of initial shear stresses. Thus, a fundamental component that influences lateral spreading, ground surface conditions, isn't accounted for in using these methods. The relationships discussed in this section were developed to evaluate strain potential in soils at level-ground sites. At present time, there is no clearly established, experimentally verified link between shear strain response of soils with no static shear stress to the response of soils in sloping ground or near a free face. Zhang et al. (2004) developed a model within the same framework that does account for topographic effects. 291 displacement measurements from 13 case histories were analyzed by calculating the level-ground lateral displacement index for each case, using CPT- and SPT-based correlations to estimate FS_{liq} and Figure 4.10 to estimate the cyclic shear strain, and comparing the calculated LDI with the actual observed displacements. The difference between the two displacements LD/LDI was then correlated to topographic parameters for sloping sites, sites with free faces, and sites with both.

Another issue not accounted for in shear strain potential models is the variation of maximum shear strain with depth. This is especially important for sites near a free face. Chu et al. (2006) found that soils deforming laterally toward a free face of at least 3 m in height (H_{ff}) generally did not deform significantly below a depth of about $2H_{ff}$. Below this depth, the liquefied soil is considered to be confined sufficiently against shear strains (Idriss and Boulanger 2008) and will not contribute significantly to lateral spreading. Sites near free faces have the added complication of the spatial variability of shear strains with respect to the distance from the free face. The closer an element of soil is to a free face, the larger the static shear stress will be, and hence the lateral deformations will decrease with distance behind the free face. Youd et al. (2002) confirmed this hypothesis by analyzing several case histories of lateral spreading where observed displacements were recorded at multiple locations at a particular free face site. The variability in lateral displacements was found to depend on the ratio of the distance from the free face (L) to the depth to the bottom of the liquefied layer (H). The following approximate guidelines were established for reducing the maximum displacement at the free face (LD_0) with respect to L/H:

$$LD/LD_0 \approx 0.5, L/H \approx 5 - 20 \tag{4.9a}$$

$$LD/LD_0 \approx 0.2, L/H \geq 20 \tag{4.9b}$$

It should be noted that these reduction guidelines are approximate, and can only be applied for sites where little spatial heterogeneity exists. The thickness of the liquefiable layer should be relatively consistent, and the presence of liquefiable material should persist continuously towards the free face. Other issues related to spatial variability must also be taken into account. Variations in both the thickness and density of liquefiable material are quite common at a given site, and thus it is necessary to evaluate the potential lateral deformations at all boring locations to determine the extents of the lateral spread zone. For instance, analysis of a boring log performed 50 meters from a free face may indicate that extensive lateral deformations are possible. However, if none of the borings taken along the waterfront or closer to the free face indicate that lateral spreading is possible, then it would be reasonable to conclude that the deformations from the first boring could be restricted by denser or non-liquefiable material at the waterfront, and thus lateral spreading hazards are unlikely to be significant. Deformations very close to the free face are may also be affected by local instabilities unrelated to lateral spreading. In such cases, predicted lateral spreading deformations can be significantly lower than what was actually observed.

The importance of evaluating the potential for lateral spreading in a spatial sense comes about as a result of another important issue that must be considered when using strain potential methods. These methods implicitly assume that the maximum potential shear strain is reached at all points in the liquefiable material. This may not always be the case, as described in the example above. Overall, there can be significant uncertainty and bias involved in using shear strain potential correlations to evaluate lateral spread. Shear strains can be significantly over-predicted in cases where the maximum shear strain is not reached (due to spatial heterogeneities that restrict lateral movement), or significantly under-predicted in sites where nontrivial static shear stresses are imposed on the soil. Furthermore, significant uncertainty exists in using the three correlations discussed in this section. Thus, even with a thorough characterization of site conditions at and below the ground surface, there is limited justification for the use of shear strain potential models as standalone methods for predicting lateral displacements.

4.3.4 Sliding Block Approach

It has also been proposed by several researchers that lateral spreads can potentially be modeled using Newmark sliding block analyses. Castro (1987) used sliding block analyses to analyze the Heber Road lateral spread from the 1979 Imperial Valley event, and Baziar et al. (1992) also suggested its applicability in predicting lateral spreading displacements, with the caveat that characterizing the post-liquefaction residual shear strength

could be potentially problematic. The concept is based on the fact that lateral spreading deformations are primarily driven by repeated cycles of dynamic shear stresses, and may exhibit the same ratcheting-type deformations as a rigid block on a frictional surface when subjected to an input ground motion.

Olson and Johnson (2008) Method for Analyzing Lateral Spreads

Olson and Johnson (2008) developed an intriguing method to model lateral spreading displacements using a framework that combines sliding block analyses with a pseudo-static LEA component. The authors back-analyzed 39 cases of lateral spreading using this combined procedure to estimate the liquefied (or mobilized) shear strength ratio $s_u(mob)/\sigma'_{v0}$ for each case. In a similar framework to the back-analyses performed on liquefaction flow failures by Olson and Stark (2002), the authors reviewed existing literature on each case history and used subsurface test data on the liquefied material for each case history to select a representative mean, upper bound, and lower bound SPT and CPT penetration resistance values for the material that liquefied in each case history. Their work was presented only in a technical paper, and the level of detail in the descriptions of portions of their procedures and data were affected by limits on the length of the publication. No thesis or dissertation presenting complete, detailed descriptions is available. The authors Olson and Johnson will be referred to herein as "O&J".

The back-analysis procedure used to determine the mobilized shear strength of the liquefied material consisted of two distinct components. First, sliding block analyses were used to estimate a yield acceleration for the laterally spreading mass. A ground motion suite of about 20 acceleration time histories was compiled for each case history, based on the magnitude, rupture mechanism and site stiffness. All of the motions were then scaled to the observed or estimated PGA at the site. The motions were then used as inputs to a series of one-way sliding block analyses for a range of yield accelerations. The median relationship between a_y and D_H was then used to determine the yield acceleration for the observed displacement at the site (Figure 4.14). O&J also reported 25th and 75th percentile values of the yield acceleration for each case.

Once the yield acceleration was determined for a particular case history, the authors used a series of pseudo-static slope stability analyses to relate the yield acceleration to the shear strength of the soil. Using the available site data for each case, a soil profile of the lateral spread was generated in a slope stability program. Then, using pseudo-static analyses, the authors varied the strength of the liquefiable material and determined the corresponding horizontal acceleration required to decrease the factor of safety to unity (i.e.

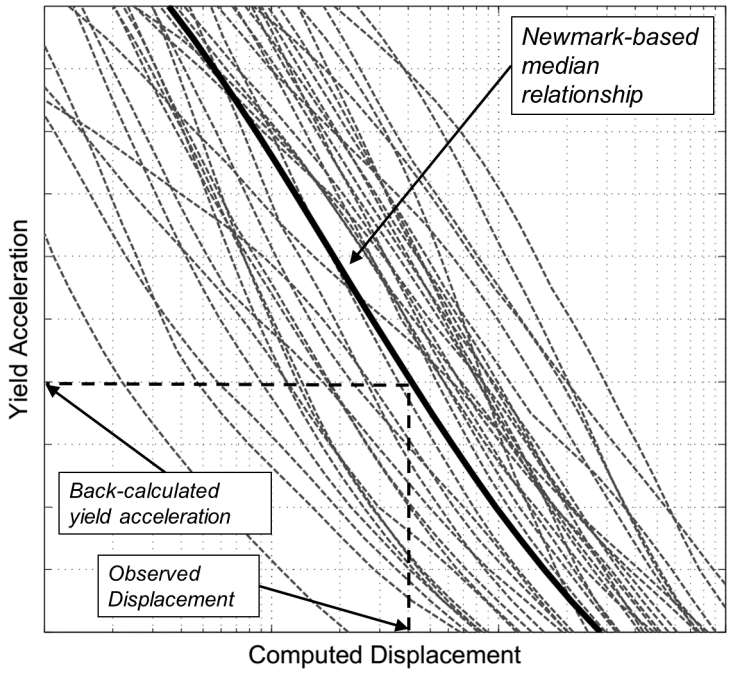

Figure 4.14: Schematic illustrating the determination of the yield acceleration, based on observed lateral spread displacement and median relationship between a_y and sliding block displacements for a suite of ground motions

cause failure) for each strength value, thus developing a relationship between yield acceleration and mobilized shear strength ratio (Figure 4.15). The mobilized shear strength ratio for each case was taken as the value corresponding to the yield acceleration determined from the sliding block analyses. The pseudo-static analyses were carried out in a purely deterministic manner; no uncertainty regarding soil parameters, groundwater conditions, or site topography was accounted for. A schematic of the full framework used by O&J to determine the mobilized shear strength ratio is illustrated in Figure 4.16.

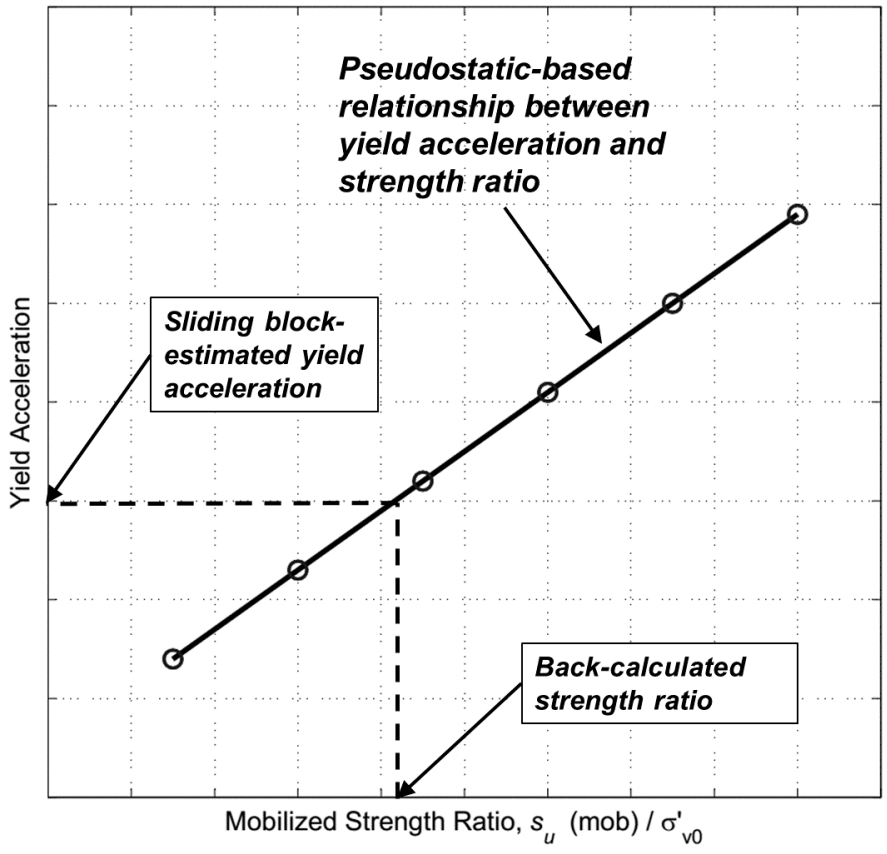

Figure 4.15: Determination of mobilized shear strength ratio of liquefied soil, using a pseudostatic-based relationship between yield acceleration and shear strength of liquefied material.

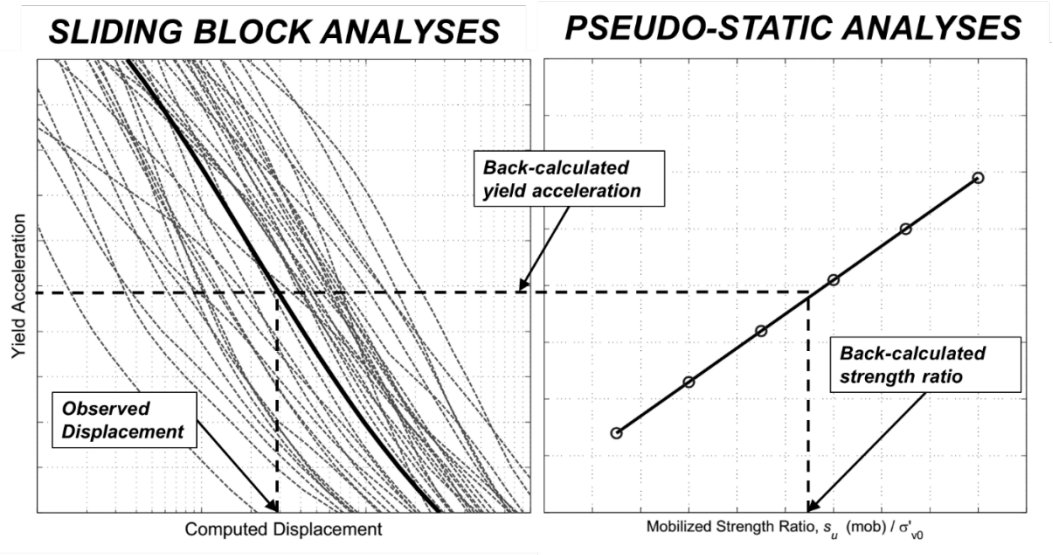

Figure 4.16: Schematic of full back-analysis framework for determining mobilized shear strength ratios from liquefaction-induced lateral spreads

An actual example of the back-analysis procedure is shown in Figure 4.17 for the Juvenile Hall lateral spread that occurred during the 1971 San Fernando Earthquake. The left-hand axis shows the sliding block displacements as a function of yield acceleration. The observed lateral displacement at Juvenile Hall was 1.52 m, which, based on the median relationship between a_y and D_H, corresponds to a yield acceleration of 0.02 g (note that the 25th and 75th percentile relationships indicates back-calculated a_y values of 0.008 and 0.03 g, respectively). Superimposed on the results of the sliding block analyses are the results of the multiple pseudo-static slope stability analyses. The LEA computations for this particular case produced a linear relationship between the mobilized strength ratio and yield acceleration for $FS = 1$. Thus, the given back-calculated yield acceleration of 0.02 corresponds to a mobilized strength ratio of 0.049. Using the 25th and 75th percentile values of a_y corresponded to mobilized strength ratios of 0.04 and 0.06, respectively.

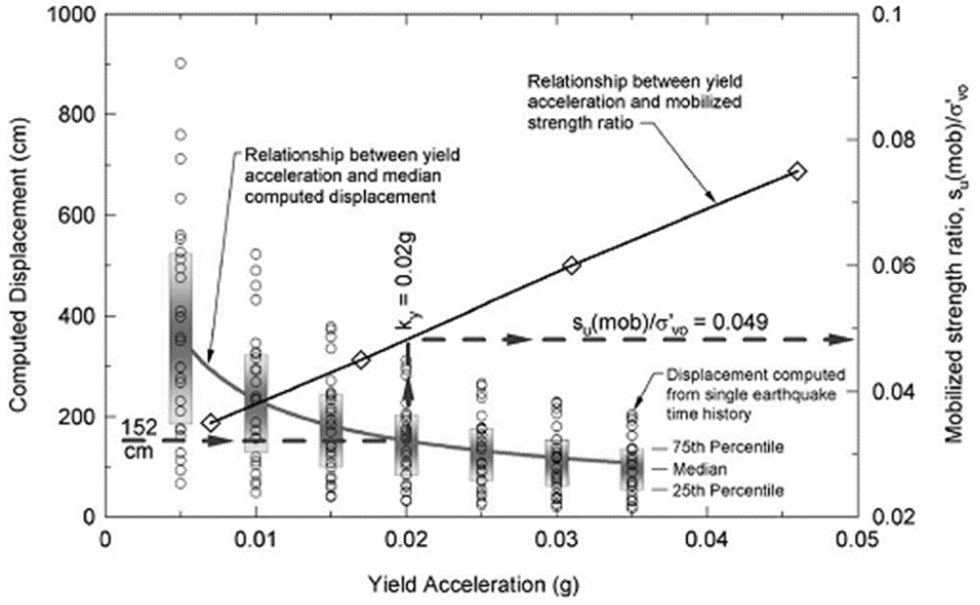

Figure 4.17: Relationship between yield acceleration and permanent displacement plotted along with the relationship between yield acceleration and mobilized shear strength ratio (Olson & Johnson, 2008)

The back-calculated mobilized shear strength ratios for each case history were then plotted against their representative SPT and CPT resistances, and compared to the corresponding flow failure data from Olson and Stark's analyses (Figure 4.18). Olson and Johnson then concluded that the strength ratios back-calculated lateral spreads were consistent with the strength ratios calculated from liquefaction flow failures, based on the fact that most of the 39 lateral spread case histories plotted within the lines of the linear relationship proposed by Olson and Stark for flow failures:

$$\frac{S_r}{\sigma'_0} = \begin{cases} 0.03 + 0.0143(q_{c1}) \pm 0.03, & q_{c1} \leq\sim 6.5MPa \\ 0.03 + 0.0075(N_1)_{60} \pm 0.03, & (N_1)_{60} \leq\sim 12 \end{cases} \tag{4.10}$$

The authors additionally proposed an extension of the penetration resistance bounds of Equation (4.10) based on the addition of the new lateral spreading data points:

$$\frac{S_r}{\sigma'_0} = \begin{cases} 0.03 + 0.0143(q_{c1}) \pm 0.03, & q_{c1} \leq\sim 10MPa \\ 0.03 + 0.0075(N_1)_{60} \pm 0.03, & (N_1)_{60} \leq\sim 16 \end{cases} \tag{4.11}$$

The correlations in Equation 4.11 can be used in a practical setting to estimate lateral spreading displacements by using the original Newmark sliding block procedure in

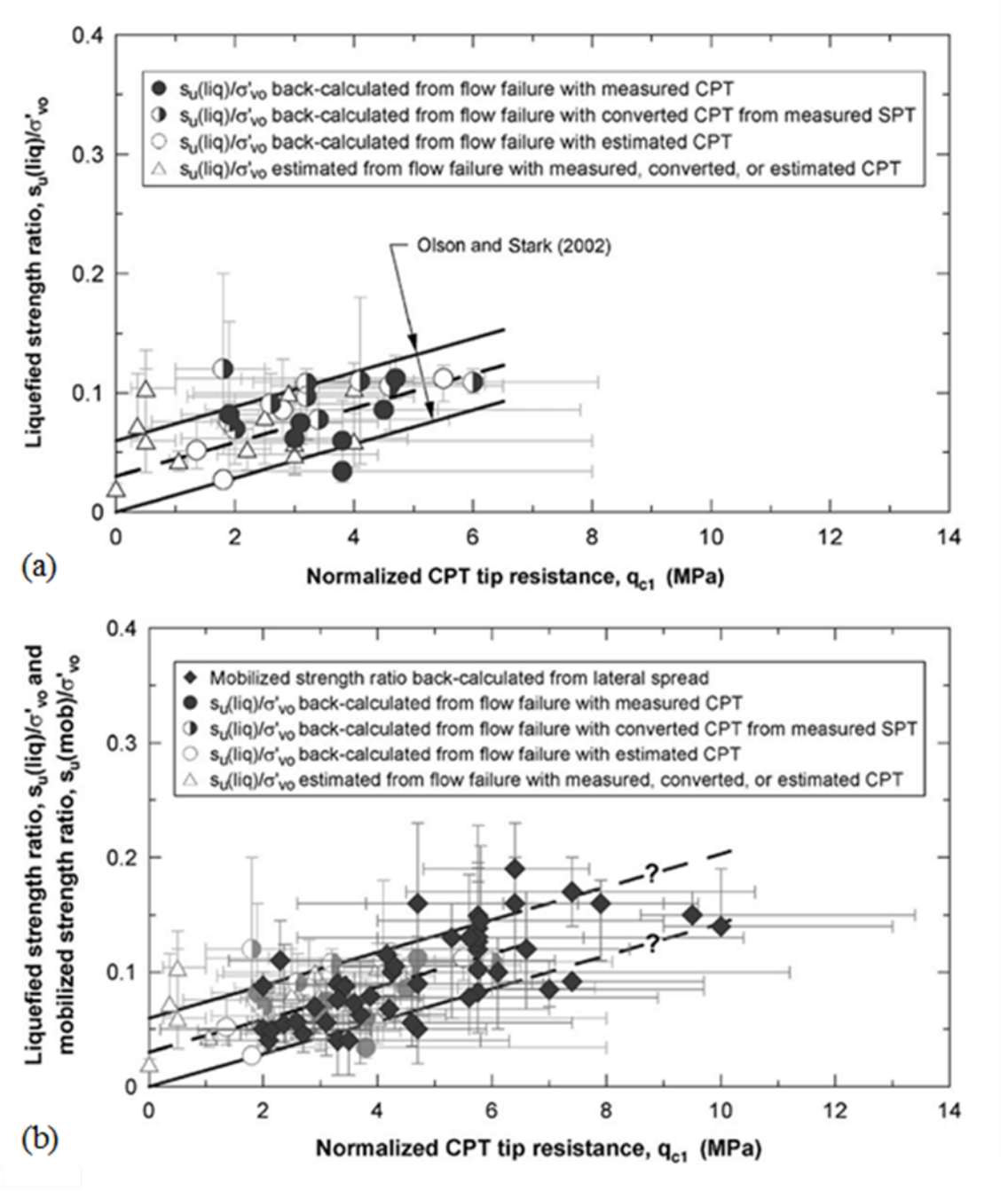

Figure 4.18: Relationships between CPT tip resistance and a) liquefied shear strength ratio back-calculated from liquefaction flow failures (Olson and Stark 2002) and b) mobilized strength ratio back-calculated from lateral spreads (Olson and Johnson 2008) plotted against the bounds from Olson and Stark's linear correlation. (Olson and Johnson 2008)

conjunction with a pseudo-static analysis, which can be utilized for both free face and ground slope cases:

1. Use subsurface data to generate a site profile in terms of both penetration resis-

tances (either SPT or CPT), and traditional slope stability analysis parameters (unit weight, friction angle, and cohesion).

2. Using Spencer's Method, determine the location of the likely failure surface within the liquefiable material. Failure surfaces that may pass through weak, but non-liquefiable materials, can be avoided by generally by forcing the failure surfaces to pass through certain zones, in this case, the liquefiable material. Most current slope stability software is equipped with this capability.

3. Determine the SPT or CPT resistance value from the layer through which the failure surface passes, and use Equation 3.11 to determine the mobilized shear strength ratio.

4. Perform a pseudo-static analysis to determine the yield acceleration for the shear strength determined in Step 3.

5. Perform Newmark sliding block analyses using a suite of ground motions that match the design earthquake for the yield acceleration determined in Step 4 to obtain an estimate of the mean permanent displacement.

Discussions

Two separate discussions of the O&J paper examined some of the components of the analysis that may warrant further consideration. Moss and Hollenback (2011) primarily addressed the uncertainties involved in characterizing penetration resistances for each case. 29 of the 39 case histories analyzed by the authors contained both CPT and SPT data; however, the remaining 10 cases had only one of the two, or even neither of the two (two of the Luzon cases were characterized primarily by Swedish cone tests). For these cases, the authors relied on correlations that converted between SPT and CPT, or Swedish cone to SPT to CPT. These correlations are generally based on data from the comparison of different tests performed in the same strata, and are not without significant scatter. The discussers analyzed the uncertainty in these conversion equations, and found that converting from N_{60} to q_c (uncorrected for overburden stress) for sands introduces a coefficient of variation (C.O.V.) of about 40% to the estimate of the CPT resistance. Furthermore, the two-step conversion from Swedish cone resistance (SWS) to SPT to CPT resistance introduces a C.O.V. on the order of about 120% (Figure 4.19).

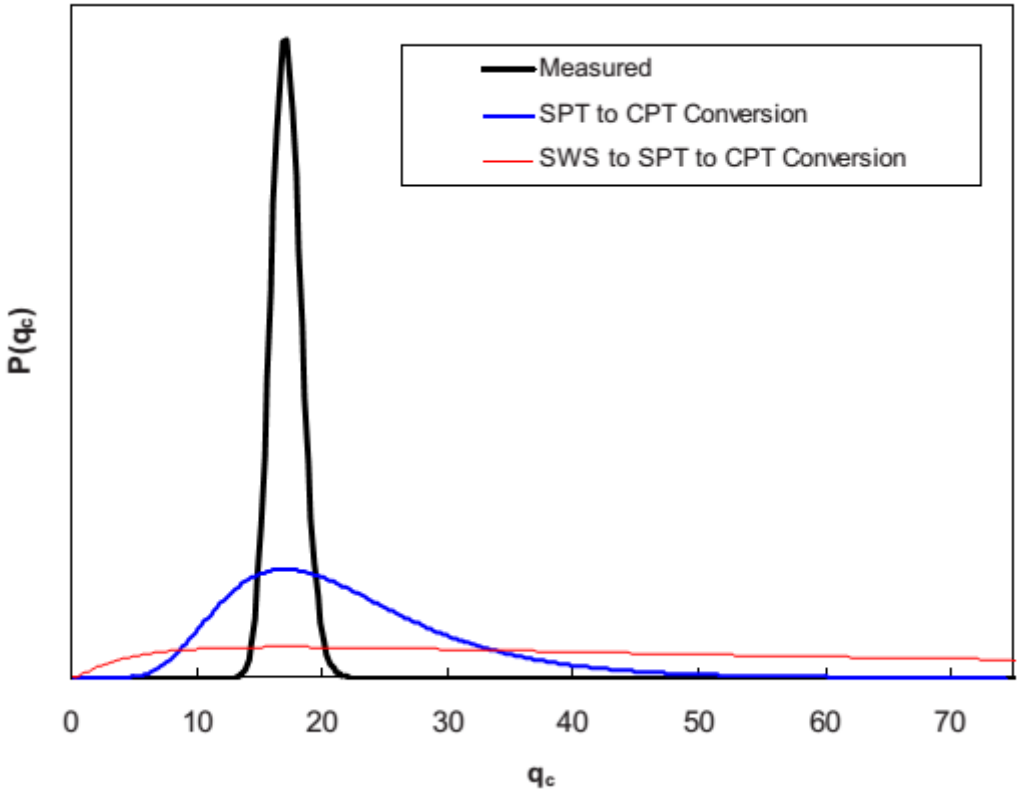

Figure 4.19: Comparison of the probability distributions between the determination of CPT resistance by direct field measurement, conversion from SPT resistance, and two-step conversion from Swedish Cone to CPT (via SPT) (Moss and Hollenback, 2011)

Park and Kutter (2011) examined the uncertainties in the correlation equations themselves that were developed by Olson and Johnson (2008) and Olson and Stark (2002). Analysis of the correlations between mobilized shear strength (as well as mobilized shear strength ratio) and SPT resistance for the lateral spread, flow slide (rigorous and simplified), and flow side (kinetic) datasets revealed coefficients of correlation (R^2) of between 0.11 & 0.6, with an R^2 of 0.42 for the lateral spread dataset (Figure 4.20). These values suggest that the correlation between the back-calculated mobilized/liquefaction shear strength ratios and *in situ* penetration resistances is not particularly strong.

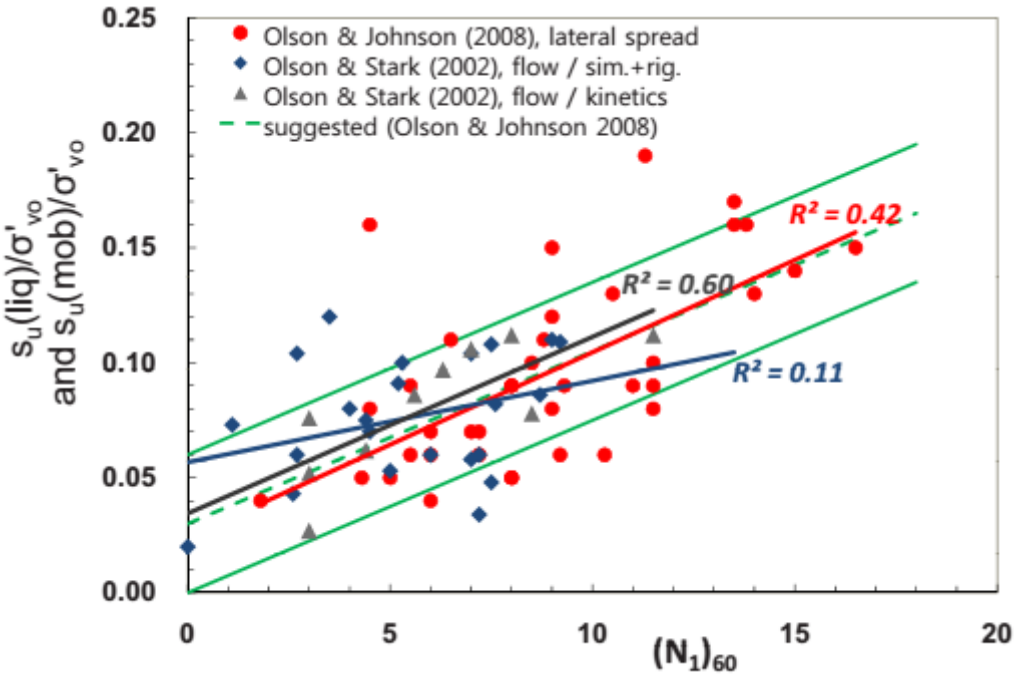

Figure 4.20: Analysis of scatter in relationships between $(N_1)_{60}$ and shear strength ratio for both flow failure cases and lateral spread cases (Park and Kutter, 2011)

The discussers also highlighted some of the uncertainties inherent in the back-analysis procedure used to determine the mobilized strength and yield accelerations for each case. Considerable qualitative judgment was involved in selecting a failure surface, determining the representative vertical effective stress within the liquefiable layer, and characterizing the strength properties and unit weights of the nonliquefiable soils above the failure surface. Furthermore, the selection of appropriate individual lateral spread displacement values can be quite complex, especially at free face sites where displacements vary with respect to the distance from the free face. Other spatial variations in displacement levels occur due to localized variations in soil properties and topographic features, which make the application of a Newmark-based analysis framework (which requires a single estimate of yield acceleration) slightly more problematic.

4.3.5 Summary

Numerous, diverse developments in the characterization and prediction of lateral spreading have occurred over the last 30 years. Certain research efforts have focused on the mechanics of how shear strains develop in liquefied soils, with a number of laboratory-based relationships relating maximum shear strain potential with various representations of cyclic resistance and cyclic stress such as relative density, $(N1)_{60,cs}$, and the factor of safety for liquefaction. Empirical models have also seen wide use in recent years, with sev-

eral models proposed that use varying types and sizes of datasets, and different methods for representing the various source, site, and geotechnical factors that tend to influence lateral spreading displacements. Most recently, we have seen the emergence of an intriguing Newmark-based method for modeling liquefaction-induced lateral spreading deformations, where the ratcheting-type deformations associated with cyclic mobility are modelled using a rigid block sliding on a frictional, planar surface.

Each of these methods involve characterization of the ground motion characteristics, site geometry, and characteristics of the liquefiable soil in order to provide reasonable estimates for the permanent lateral spreading displacement. The utilization of these methods, however, should be done with a strong understanding of the potential aleatoric and epistemic uncertainties and biases that may exist. This variability stems from the assumptions and simplifications that the model makes, as well as the scatter involved in developing a correlation between the input parameters and predicted displacement.

4.4 Concluding Remarks

Some of the deadliest earthquakes in recorded history have featured massive landslides. There are numerous instances of slopes that were previously marginally stable failing in spectacular and dramatic fashion during or after ground shaking. In many of the largest seismic events, the majority of deaths and economic costs were attributed directly to the triggering of landslides (Kramer, 1996). Earthquake-induced ground shaking can trigger landslides via two distinct mechanisms. Ground shaking can de-stabilize slopes by increasing the driving stresses along potential failure planes (inertial instability), thus affecting the force and moment equilibrium and decreasing the factor of safety. Ground motions can also generate excess pore pressures in the soil, weakening it to the point where slope failure occurs to some combination of the initial static stresses and the earthquake-induced dynamic stresses (weakening instability).

There exists a diverse array of methods to deal with the issue of earthquake-induced landslide hazards. Methods that deal with the inertial component of slope instability, such as the pseudo-static limit equilibrium analysis and Newmark sliding block method, are relatively simple to implement and can often produce reasonable assessments of the factor of safety and permanent displacements, respectively. They do, however, make several simplifying assumptions, particularly with respect to the dynamic response of the system and the stress-strain response of the soil to ground excitation, introducing structural biases that can affect the reliability of their implementation. Alternative methods exist that place additional focus on the instability caused by weakening of soils, and are geared toward

the prediction of flow failures and lateral spreads. These models, such as Youd's empirical model, the various shear strain potential models presented in Section 4.3.3 , and the Newmark-based model proposed by Olson and Johnson, are effective in that they combine the effects of inertial and weakening instabilities; but still contain inherent structural biases and uncertainties that can also affect their reliability.

The methods discussed here should be implemented only with a strong understanding of the potential aleatoric and epistemic uncertainties and biases that may exist. This variability stems from the assumptions and simplifications that the model makes, as well as the scatter involved in developing a correlation between the input parameters and predicted displacement. A geotechnical model is far more powerful if its limitations are quantified. Rather than producing a single estimate of permanent displacement, which implies significantly more knowledge than any geotechnical engineer has about lateral spreading, or even providing a range of estimated displacements, the most useful way a complex phenomenon such as lateral spreading can be characterized is through some sort of probability distribution of the displacements. This allows a developer or structural engineer to evaluate seismic risk more completely, and is the cornerstone of performance-based design.

Chapter 5

LATERAL SPREADING CASE HISTORIES

5.1 Introduction

When a series of historical case studies is used to develop and empirical model, examination of the dataset is critical in assessing the overall reliability of the model itself. The quality of a dataset generally will depend on the number of case histories it contains, the quality of the data collected from each case history; the reliability and robustness of the model upon which it is based will further depend on the range of the regression variable data that the database represents. Within the context of lateral spreading, empirical models should be based on case history datasets that represent wide ranges of earthquake source and ground motion characteristic parameters, site topographies, and characteristics of the liquefied material. In this chapter, these database components are discussed in greater detail, and the case histories from two empirical lateral spreading prediction models, Youd et al. (2002) and Olson & Johnson (2008), are evaluated for how well they represent the range of conditions under which lateral spreading occurs and their applicability in predicting future lateral spreading deformations.

5.2 General Considerations

The database developed by Youd et al. (2002), and used to develop the MLR equation for the prediction of lateral spreading displacements (See Equation 4.7) is comprised of 484 cases of observed lateral spreading displacements from the 1906 San Francisco, 1964

Alaska, 1964 Niigata, 1971 San Fernando, 1979 Imperial Valley, 1983 Nihonkai-Chubu, 1983 Borah Peak, 1987 Superstition Hills, 1989 Loma Prieta, and 1995 Kobe earthquakes. This database has been used by many researchers, and has loong been considered to represent the range of conditions under which lateral spreading failures typically occur. The lateral spreading database employed by Olson and Johnson in their back-analysis procedure is considerably smaller; 39 case histories were used to develop their model. Only six case histories were featured in both databases.

5.2.1 Observed Displacements

Many lateral spreading sites feature multiple ground cracks, often with varying widths that indicate different magnitudes of displacement. This is often seen at sites near free faces, where the static prefailure shear stresses increase with proximity to the free face, resulting in larger lateral spreading deformations (Section 4.3.3). Youd et al. accounted for sites with varying displacement magnitudes by considering them as distinct case histories. For instance, 18 vectors of varying displacement were record at the lateral spread at Juvenile Hall that occurred during the 1971 San Fernando earthquake, each of which are accounted for as separate data points in Youd's case history database.

For many of their case histories, Olson and Johnson reported the full range of observed displacements at the site (which were often quite wide), along with the representative displacement value used in the Newmark-type sliding block analyses that were performed to determine the yield acceleration. This value could have either referred to a specific displacement vector location (particularly at free face sites), or simply been a representative (e.g., mean or median) value; the actual locations are not explicitly identified by O&J. For some cases, the location that a specific displacement value was referring to was not clearly identified; for others, it could generally be inferred from the source literature. The cases where the location of the reported displacement vector is unclear are discussed more specifically in their respective sections.

5.2.2 Ground Motion Characteristics

The two models differ significantly in the manner in which they account for seismic loading. Olson and Johnson's model requires the selection of ground motions for the Newmark-type sliding block analyses were based on identifying the rupture mechanism, moment magnitude, peak ground acceleration, and soil classification in the upper 30 m for each site. It should be recognized that several of the sites in the database were not near ground

motion recording stations, and thus PGA estimates were made based on either data from the nearest ground motion recording stations, ground motion prediction equations, site response analyses, or the USGS or equivalent ShakeMap for that event. Furthermore, site stiffness classifications are based on the average shear wave velocity in the upper 30 m of the site, or v_{s30} . The ability to reliably estimate the site classification depends on the depth to which subsurface data is available as well as whether or not vs is directly measured or calculated using penetration resistance correlations. Sites where these uncertainties are prominent, as well as any other discrepancies in PGA or magnitude estimates, will be discussed. The Youd model accounts for source effects in a much simpler fashion, by using moment magnitude and source-site distance as predictor variables. This eliminates a significant source of uncertainty from the process of compiling case history data, in that site PGA is not considered explicitly, but rather implicitly as a function of M_w and R, which can be determined with significantly more accuracy and precision. However, magnitude and distance provide an incomplete description of the transient, dynamic loading that leads to lateral spreading.

5.2.3 Site Characterization

Both the Youd and O&J models rely on thorough site characterization procedures to determine the surface topography, subsurface lithography, and soil properties. For Youd's model, the case history databased was developed by analyzing sites with respect to their ground surface dimensions (and subsequently classifying them as "ground slope" or "free face" site), identifying the vertical extent of liquefied material, the liquefied material with $N < 15$, and grain-size properties of that particular subset of the liquefied material. The O&J model relied on site characterization to develop their pseudo-static LEA models, and to select representative penetration resistances to plot with the back-calculated strength ratios.

Ground Surface Topography

Application of the Youd model requires an estimate of either the ground slope inclination and/or the dimensions of the free face to be used as direct inputs to the MLR equation, while O&J's model requires a similar characterization to be used in the pseudo-static LEA analyses. For sites with lateral spread on a ground slope, information about the slope angle was either obtained directly from the source (i.e. a direct presentation of the ground slope angle), inferred from subsurface cross sections, or in some cases, inferred from elevation contour maps. Free face cases tended to be slightly more uncertain, as it was often unclear

whether the elevation of the free face toe shown in many of the soil profiles was accurately reported or estimated by the original investigators.

Penetration Test Interpretation and Estimation of Soil Properties

As stated previously models also require interpretation of SPT and/or CPT data for their implementation. In the case of Youd's model, reliable characterization of the SPT N-value in the liquefiable material is critical in determining the cumulative thickness, average fines content, and average median grain size parameters. O&J's model may rely even more heavily on the interpretation of penetration test data, as the selection of a representative penetration resistance was critical in their conclusion that flow failure and lateral spreading strength ratios are coincident. It should be noted that all methods of subsurface characterization carry some level of uncertainty in terms of spatial variability, in terms of geometry and/or material properties, of strata identified by penetration tests. This uncertainty can be reduced by increasing the spatial frequency of tests and pairing SPT and CPT tests together at a particular location.

5.2.4 Selection of Failure Surface and Penetration Resistance

Addtionally, two components of the Olson and Johnson back-analysis procedure that are highly dependent on case history interpretation must be discussed. The assumption of a single failure surface may be somewhat inconsistent with the actual mechanics of lateral spreading (Section 6.6.2, and have the potential to result in underpredicted lateral spreading displacements for thick, liquefiable material when sliding block analyses are used to model the spread. Other issues within the analysis framework used by O&J could potentially introduce uncertainty into their correlations between $(N_1)_{60}$ and mobilized strength ratio. The selection of a single failure surface is an essential step in employing a Newmark-type sliding block analysis to relate yield acceleration to mobilized shear strength. However, for sites where lateral deformations result from distributed strains within multiple layers of liquefied material at different depths; the assumption of a single, discrete, planar failure surface diverges significantly from the actual mechanism driving lateral deformations at that site.

The selection of a representative value of $(N_1)_{60}$ and q_{c1} for each case also involved significant uncertainty. O&J generally included a wide range of penetration values in their estimates, especially for thicker layers of liquefied material; the mean value for each case was often directly in the middle of this range, despite the fact that the failure surface

is usually assumed, based on most slope stability analysis methods, to pass through the zone of weakest material if a continuous zone of weak material existed. An alternative methodology would be to select a lower representative penetration resistance than the median, if not the minimum value altogether (Wride et al., 1999).

For instances where SPT or CPT data was unavailable, the authors used the following relationship to convert between SPT and CPT resistance:

$$q_c/N_{60} = 0.5 \tag{5.1}$$

where q_c is in MPa, and both penetration resistances are uncorrected for overburden resistance. This is a very approximate relationship, one that does not reflect the influence of grain size in converting between SPT and CPT resistances (Figure 5.1). Any conversion between SPT and CPT resistances involves an added level of error (Salgado 2008), which does not appear to have been accounted for by the authors. Equation 5.1 implies that the mean grain size of the material is about 0.2 to 0.3 mm for all case histories examined.

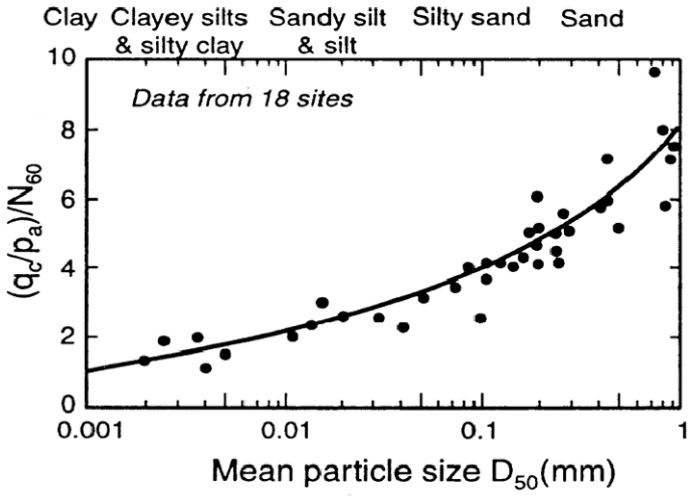

Figure 5.1: Relationship between SPT N-value, CPT qc, and mean grain size (Robertson et al. 1983)

5.2.5 Summary

The database compiled by Youd et al. (2002) is widely considered to be reliable and representative of lateral spreading conditions. This is due in large part to the sheer size of the database, along with the fact that it contains multiple deformation vectors for the same spread, thus capturing the effects of site topography (specifically, the variation of displacement with distance from a free face). The Olson and Johnson database is

considerably smaller; as a result, inconsistencies and systematic misinterpretations may have an outsized influence on the results of the back-analysis procedure. In Section 5.4, the O&J database is analyzed and examined, with particular attention paid to some of the sources of uncertainty discussed above and their potential effects on the back-analysis procedure.

5.3 Youd et al. (2002) Database

The initial database of lateral spreading case histories was compiled by Bartlett and Youd in 1992. Youd, Hansen, and Bartlett (2002) provided three modifications to the database. The first adjustment was to the observed ground deformations from the 1983 Nihonkai-Chubu, Japan earthquake, which were originally estimated to be 1.9 times larger than the field displacements reported by Hamada et al. in 1986. The second modification was to remove data from sites where displacements were affected by boundary conditions. Since the intent of the Youd model is to predict displacements of unimpeded lateral spreads, displacement vectors from eight sites that included some form of buttressing of the slope face were excluded from the database. Finally, the database was updated to include lateral spreading displacements from three more earthquakes: 1983 Borah Peak, 1989 Loma Prieta, and 1995 Kobe. The lateral spreading sites are summarized in Table 5.1

Table 5.1: Earthquake and lateral spread sites used in Youd et al. (2002) *MLR* analyses (adapted from Youd and Bartlett 1992 and Youd et al. 2002)

Earthquake	Lateral Spread Site	Reference
1906 San Francisco	Coyote Creek	Youd and Hoose (1978)
1906 San Francisco	Mission Creek Zone	Youd and Hoose (1978)
1906 San Francisco	Salinas River	Youd and Hoose (1978)
1906 San Francisco	South of Market St.	Youd and Hoose (1978)
1964 Alaska	Bridges 141.1, 147.4, 147.5, 148.3 on Matanuska and Knik Rivers	Bartlett and Youd (1992b); McCulloch and Bonilla (1970)
1964 Alaska	Bridges 63.0, 63.5, 64.7 on Portage Creek and Twenty-Mile river	Bartlett and Youd (1992b); McCulloch and Bonilla (1970)
1964 Alaska	Bridge 629 on Placer River	Bartlett and Youd (1992b); McCulloch and Bonilla (1970)
1964 Alaska	Bridge 605A on Snow River	Bartlett and Youd (1992b)
1964 Alaska	Bridges 3.0, 3.2, 3.3 on Resurrection River	Bartlett and Youd (1992b); McCulloch and Bonilla (1970)
1964 Niigata, Japan	Several lateral spreads in Niigata	Hamada et al. (1986)
1971 San Fernando, Calif.	Jensen Filtration Plant and Juvenile Hall	O'Rourke et al. (1992b); Bennett (1989); Youd (1973)
1979 Imperial Valley, Calif.	Heber Rd. and River Park	Bennett et al. (1984); Dobry et al. (1992)
1983 Borah Peak, Idaho	Whiskey Springs and Pence Ranch	Andrus and Youd (1987); Andrus et al. (1991)
1983 Nihonkai-Chubu, Japan	Several lateral spreads in Noshiro	Hamada et al. (1986)
1987 Superstition Hills	Wildlife Instrument Array	Holzer et al. (1989); Youd and Bartlett (1988)
1989 Loma Prieta, Calif.	Moss Landing, Sandholdt Rd.	Mejia (1998); Boulanger et al. (1995)
1995 Kobe, Japan	Port and Rokko Islands, Osaka Bay	Hamada et al. (1995)

5.4 Olson and Johnson (2008) Database

The database employed by Olson and Johnson consisted of 39 case histories of lateral spreading from 12 earthquakes that occurred between 1971 and 2003. Six of the earthquakes occurred in California, with the rest occurring in Idaho, New Zealand, the Philippines, Iran, Taiwan, and Turkey. Displacements ranging from 15 cm to 6 m were observed in events ranging from magnitude 6.5 to 7.6, with peak ground accelerations between 0.18 and 0.84 g. This section examines each case history, using the literature sources cited by the authors, to provide a qualitative assessment of the conditions that existed in the analyses performed by O&J

5.4.1 1971 San Fernando

The 1971 San Fernando Earthquake was an M_w-6.6 reverse rupture faulting event originating in the foothills of the San Gabriel Mountains in southern California. A peak ground acceleration of 0.4 g to 0.6 g was assumed for the site. At San Fernando Valley Juvenile Hall, lateral spreading displacements of about 1.5 m were observed in the southwest direction, on a 1.5°ground slope, over an area of about 1.2 km in length (Figure 5.2) extending northeast from the upper Van Norman Lake. Based on the mean prefailure effective stress reported by O&J (115 kPa) and their final estimates of mobilized strength ratio, it can be interpreted that their analysis was based on a displacement point located roughly at the No. 10 SPT boring (Figure 5.3).

Various researchers have performed back-analyses and presented their estimates of representative N-values for the site. Most estimates (Seed 1987, Davis et al. 1988, Bennett 1989, Seed and Harder 1990) are in good agreement with the estimates made by O&J. Stark and Mesri (1992) estimated a significantly higher $(N_1)_{60}$ of about 8 bpf, while Wride et al. (1999) estimated an $(N_1)_{60}$ of about 1.5, based on the "weakest link" methodology discussed in Section 5.2.3

Figure 5.2: Aerial view the Juvenile Hall lateral spreading feature (Youd 1973)

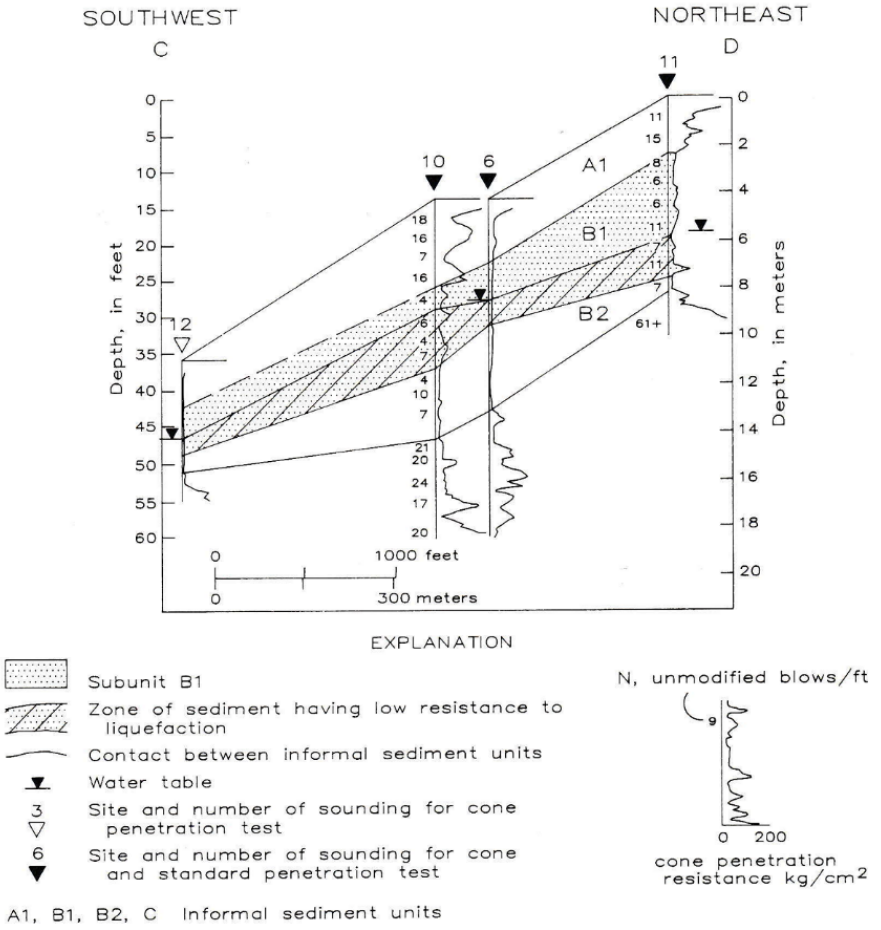

Figure 5.3: Subsurface cross section of the Juvenile Hall lateral spreading feature (Bennett 1989)

5.4.2 1979 Imperial Valley

The 1979 Imperial Valley Earthquake was an M_w-6.5 event epicentered just south of the U.S.-Mexico border, about 30 km south of El Centro, CA. The event triggered liquefaction-induced lateral spreading at the Heber Road site about 1.6 km northeast of the Imperial Valley fault rupture, in an area about 100 m long and 160 m wide. Observed displacements were in the range of 1.2 to 4.2 m; O&J selected a representative displacement of 2.3 m, possibly corresponding to a vector of observed displacement on the northern edge of the canal closer to Heber Road (Baziar et al. 1992., after Youd and Bennett 1983) (Figure 5.4). The ground surface at the site is nearly flat, and it has been well-established that the static driving stresses at the site were due to a 2-meter deep natural depression just south of the canal in Heber Dunes County Parks (Baziar 1992, Davis et al. 1988).

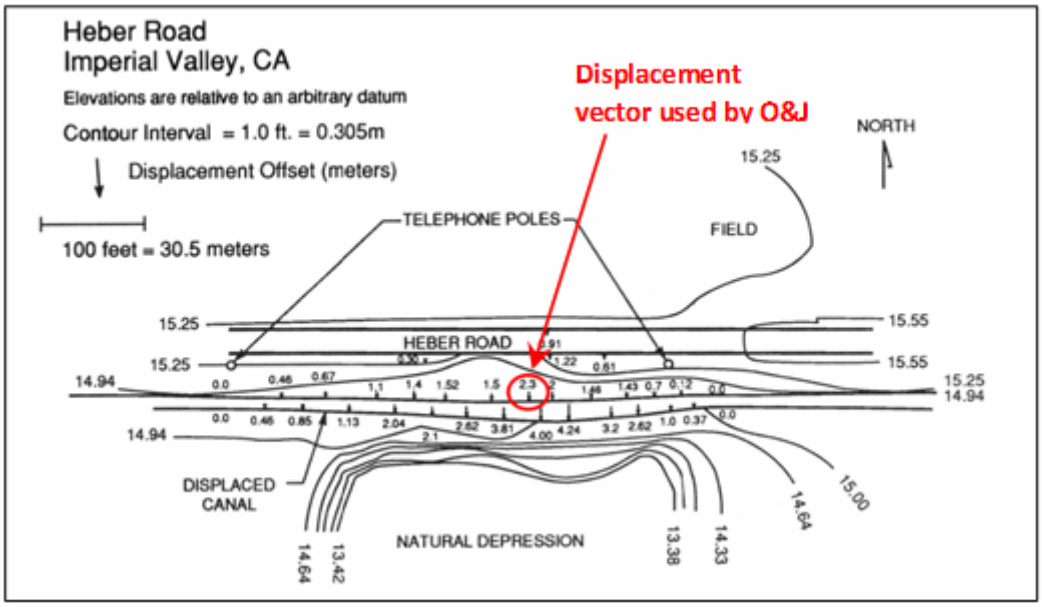

Figure 5.4: Plan view of observed displacement at Heber Road site (Bennett et al. 1981)

The original site investigation performed by Bennett et al. (1981) showed that an approximately 4-m thick layer of natural channel deposits consisting of very loose, very fine sand and silty sand, found between about 1.5 m and 5.5 m below ground surface, liquefied during the 1979 earthquake, causing lateral displacements in the southern direction towards the natural depression (Figure 5.5).

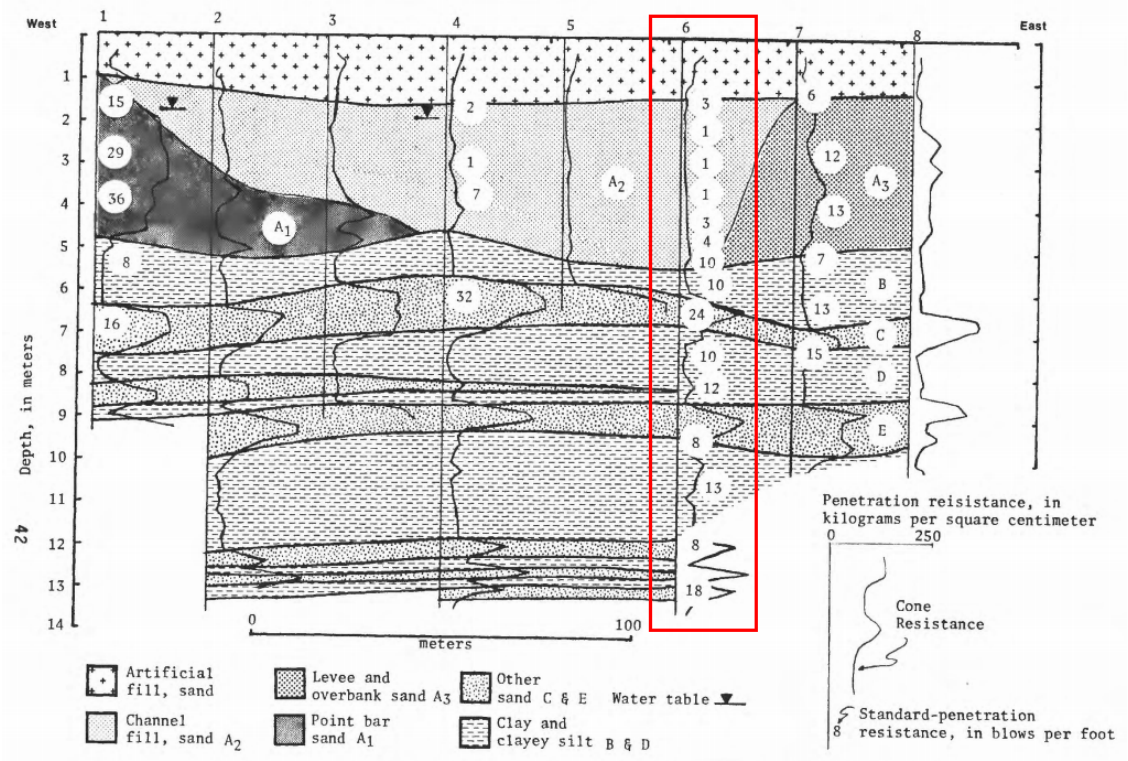

Figure 5.5: East-west profile of south side of Heber road (Bennett et al. 1981); Unit A2, a deposit of channel fill sand, was determined to have liquefied, causing the lateral spread.

Most early analyses of the Heber Road site conservatively assumed a *PGA* of 0.8 g (Youd and Bennet 1983, Castro 1987, Baziar et al. 1992), based on ground acceleration recordings at the Bonds Corner station, about 10 km southeast of Heber Rd. O&J, however estimated a *PGA* of 0.47 g in their Newmark-based analyses, possibly based on the results of a SHAKE analysis performed by Castro (1995) for the Heber Rd site, using the Bonds Corner motion as the input motion. Baziar et al. (1992) presents four ground motion recording stations considered to be near the Heber Road site, including Bonds Corner (Table 5.2). The other three ground motion stations recorded much more moderate shaking intensities, with the *PGA* at those stations between 0.25 g and 0.32 g. Additionally, the USGS Shakemap for 1979 Imperial Valley (Figure 5.6) indicates that the *PGA* at Heber Rd may have been in the range of 0.3 to 0.5 g. It is possible, although unclear, if O&J selected their *PGA* based on the USGS data. Furthermore, using NGA ground motion prediction equations (GMPE) yields a median *PGA* estimate of 0.25 g, with a standard deviation range of 0.16 to 0.41 g.

Table 5.2: Ground motion data from 4 sites closest to Heber Rd. lateral spread from 1979 Imperial Valley event (after Baziar et al. 1992)

Name	Site Geology	Epicentral Distance (km)	Horizontal PGA (g)	Duration (sec)
Meloland	Alluvium	18	0.32	6.0
Holtville	Alluvium	20	0.30	7
Calexico	Alluvium	15	0.28	10.8
Bonds Corner	Alluvium	6	0.81	13.2

Further examination of the Bonds Corner ground motion records (Greenfield 2014, personal communication) reveals that the Bonds Corner site likely had been subjected to liquefaction of its underlying alluvial deposits (Figure 5.7). There does not appear to be any surface evidence or documentation of liquefaction at the site, and Castro (1995) classified the underlying material as "dense alluvium," presumably justifying the use of the ground motion record at Bonds Corner an appropriate base input motion for the dynamic response analysis at Heber Road. However, changes in the frequency content of the ground motion, which can be visualized through the use of the adjusted PGA show significant nonlinear softening of the alluvium beginning at about 5 seconds, followed by the full onset of liquefaction at about 8 seconds. Based on this data, use of the Bonds Corner motion as a reliable representative motion for the Heber Road Site as well as a bedrock input motion for Castro's 1995 SHAKE analysis is difficult to justify; its *PGA* seems unnaturally high given the other strong motion data for the 1979 Imperial Valley event, and it appears to be significantly influenced by dynamic effects resulting from nonlinear soil behavior and pore pressure generation at the site.

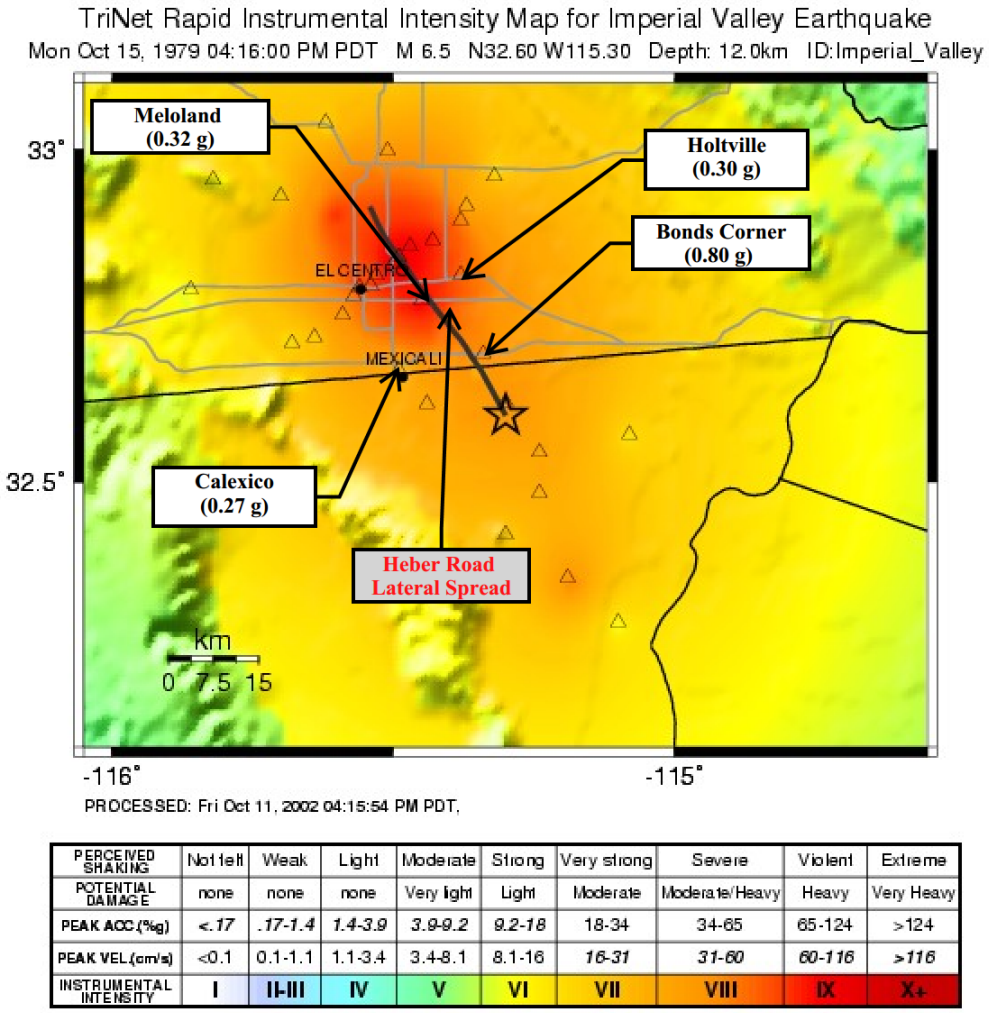

Figure 5.6: USGS Shake Map for the 1979 Imperial Valley earthquake, with locations of Heber Rd. site and closest ground motion stations shown.

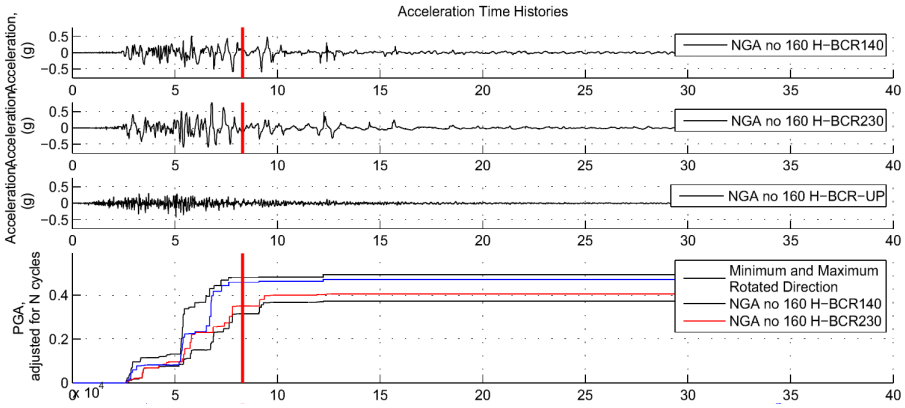

Figure 5.7: Analysis of ground motion accelerograms from Bonds Corner; 3 components of acceleration, and adjusted PGA for N cycles is shown. (Greenfield, personal communication)

5.4.3 1983 Borah Peak, Idaho

The Borah Peak earthquake is the largest seismic event to have been recorded in the state of Idaho. It was an M_w-7.3 normal fault rupture event in the western foothills of the Lost River Mountain Range, east of Thousand Springs Valley in southeast Idaho. Olson and Johnson listed the moment magnitude for Borah Peak in their analyses as 6.9, which was actually the Richter magnitude for this event. At the Whiskey Springs site, less than 2 km from the epicenter, liquefaction of gravelly deposits resulted in lateral spreading displacements of about 0.6 to 1.2 meters in the southwest direction in an area about 2.1 km long and 75 m wide.

Estimates of peak ground acceleration in the Thousand Springs Valley are relatively uncertain. Due to the remoteness of the epicenter and affected areas, very few ground motion recording stations captured significantly strong ground accelerations. Andrus and Youd (1987) used liquefaction opportunity analyses to estimate a *PGA* of about 0.4 to 0.6 g, which corresponds with the range given by O&J, who used a representative *PGA* of 0.45 g. Jackson and Boatwright (1987) used two methods, aftershock *PGA* ratios and complex spectral ratios to arrive at an estimate between 0.35 and 0.65 g for near-field areas. A combination of PEER NGA ground motion prediction equations predicted a mean *PGA* of about 0.6 g for this event, however with very high uncertainty.

Andrus and Youd (1987) performed SPT, CPT, Becker Penetration Tests (BPT), drill hole sampling, trenching, and SASW tests to characterize the site. The slope geometry is relatively well-defined; a slope angle of 11.5°can be inferred from the subsurface profile of the lateral spread (Figure 4.5.8). The investigation found that the "C1" stratigraphic unit, which varied from about 1.2 to over 2 m thick, consisting of saturated silty gravel, had liquefied during ground shaking. It should be noted that only two SPT borings were performed in the liquefiable material, at the southwest and northeast extents of the slide area. Wride (1999) noted that N-values proposed by several researchers for this site are based on a combination of the relatively sparse SPT data and conversions from BPT and CPT data, which carry significant uncertainty.

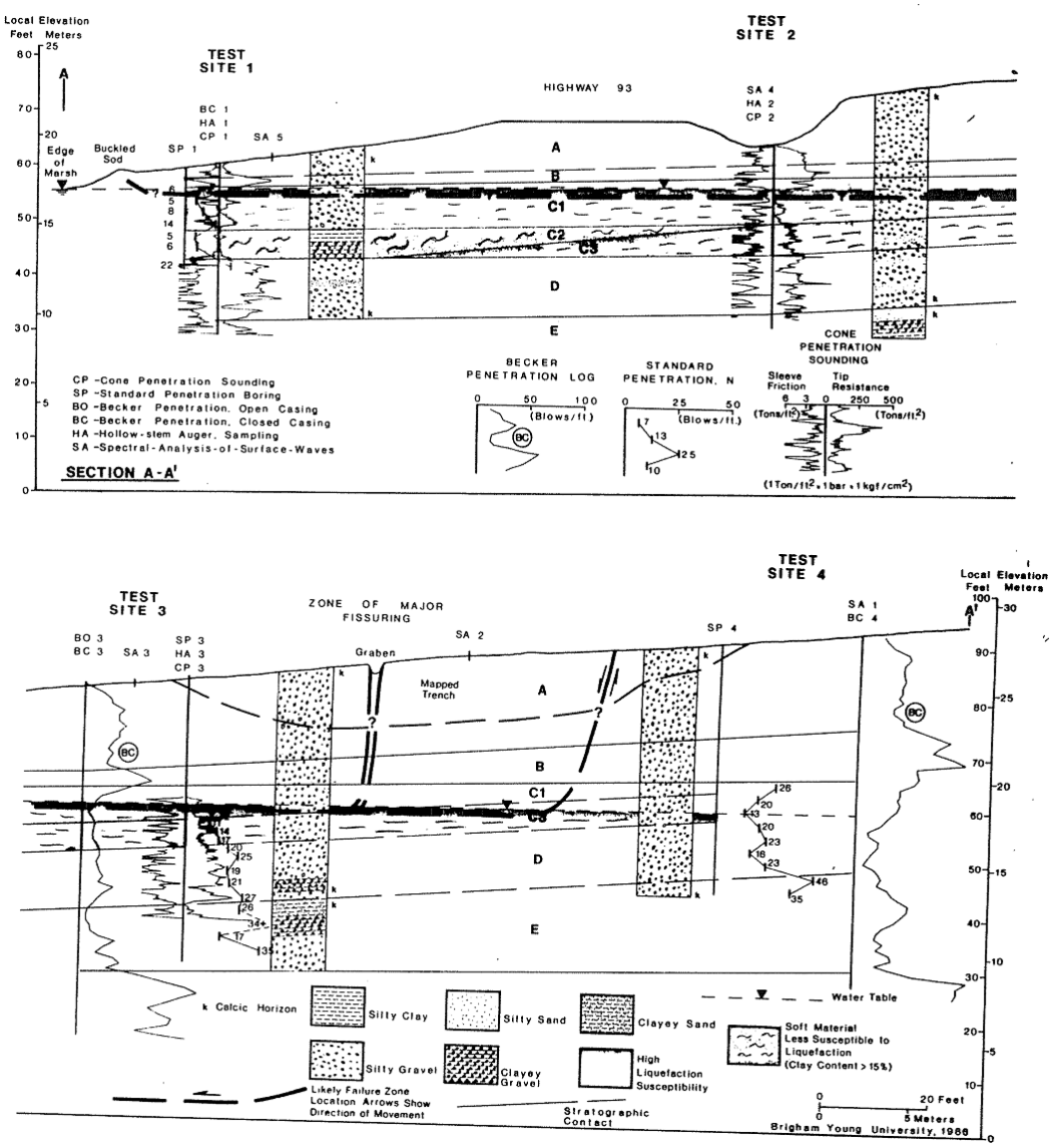

Figure 5.8: Subsurface profiles of the Whiskey Spring lateral spread; (a) southwest and (b) northeast extents (Andrus and Youd, 1987)

5.4.4 1987 Edgecumbe, New Zealand

The March 2nd, 1987 earthquake that struck the Bay of Plenty region on the north island of New Zealand was an M_w 6.5 event that occurred due to a normal fault rupture of the complex faulting mechanism in the Whakatane Graben. Widespread liquefaction was observed in the town of Whakatane, at the mouth of the Whakatane River. The estimated level of ground shaking in Whakatane was about 0.28 g (Christensen 1995), possibly based on contoured ground motion maps for the event. Lateral spreading at three sites in Whakatane, all about 10 km from fault rupture, was analyzed by Olson and

Johnson.

James St. Loop

Lateral spreading displacements of 0.75 to 3.0 m were observed in the westward direction towards the banks of the Whakatane River; O&J chose a representative displacement of 1.0 m. Christensen (1995) noted that the accuracy of the displacement data at the James St. Loop site, which was based on photogrammetric measurements, was compromised by dense vegetation near the riverbank. Ground cracks indicated significant scatter in both magnitude and direction of displacement at the site. Eight CPT tests were performed on the right bank of the river, producing two subsurface profiles (Figure 5.9. O&J do not indicate which profile was used in their pseudostatic analyses; Section AA indicates that a single 4 m-thick layer of soil liquefied, while Section BB shows more discontinuities in liquefied soil, suggesting that multiple layers may have contributed to lateral deformations. The selection of a representative N-value, in the absence of SPT data, was based on Equation 5.1. No mean grain sizes were reported by Christensen for the liquefied material; however, the site's close proximity to the Whakatane Pony Club implies that a $D50$ of 0.25 mm may be a rational estimate for James St. Loop. Thus, the use of Equation 5.1 would produce a reasonable conversion from CPT to SPT resistance for this particular site.

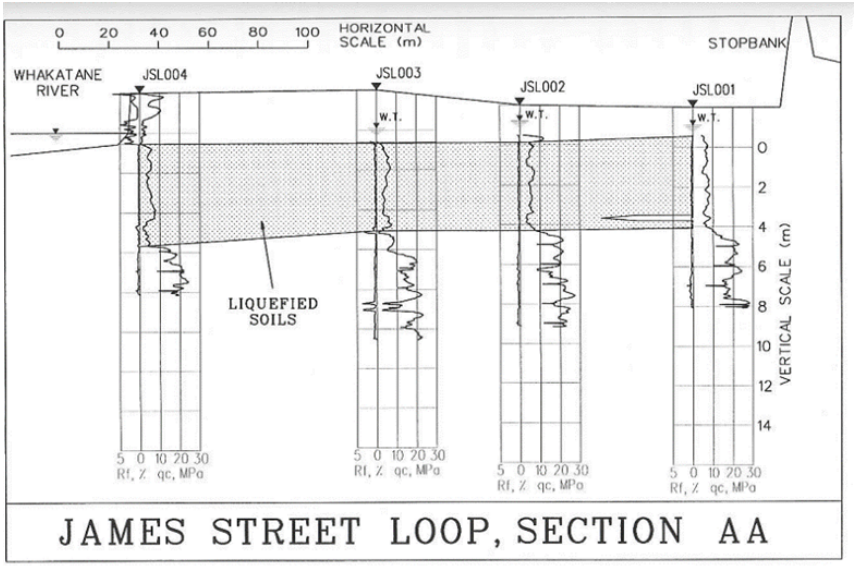

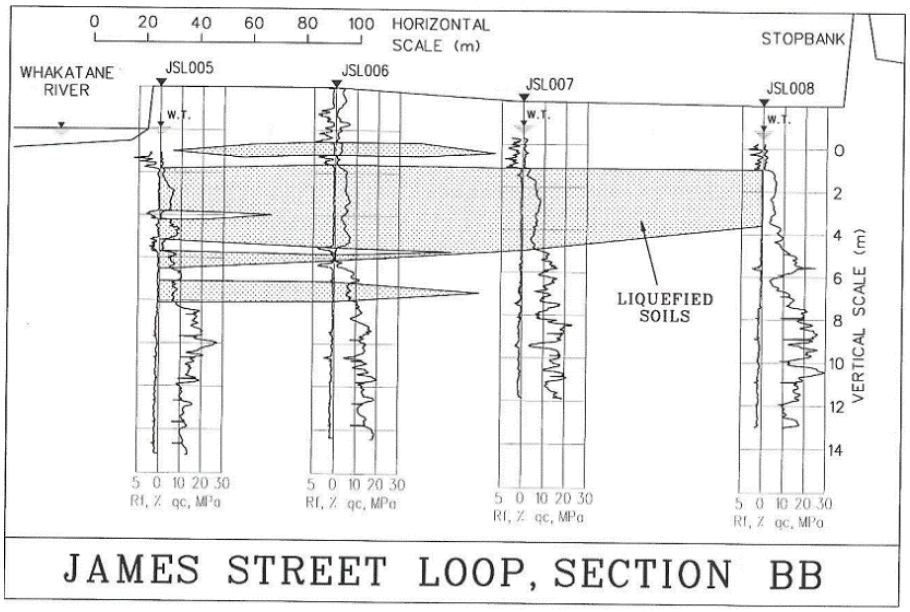

Figure 5.9: Subsurface profiles (a) AA and (b) BB of the lateral spread at James St. Loop, towards the Whakatane River (Christensen 1995)

Whakatane Pony Club

Ground displacements measured at the Whakatane Pony Club were also based on photogrammetry, and were very inconsistent in terms of both magnitude and direction (Figure 5.10). This is possibly due the site's proximity to both the Awatapu Lagoon and the Whakatane River, as well as the relatively low reliability of photogrammetric measurements. O&J reported a representative displacement of 1.0 m at the site, possibly corresponding to a northward displacement vector towards the Awatapu Lagoon. Exami-

nation of subsurface profiles in that area (Figure 5.11) showed that the liquefied soils were erratically distributed, with 3 or 4 possible planes of sliding. Furthermore, the mechanism for lateral spread is somewhat unclear, as deformations were reported to have occurred on level ground, and there is little information on the depth of the lagoon or dimensions of any free face.

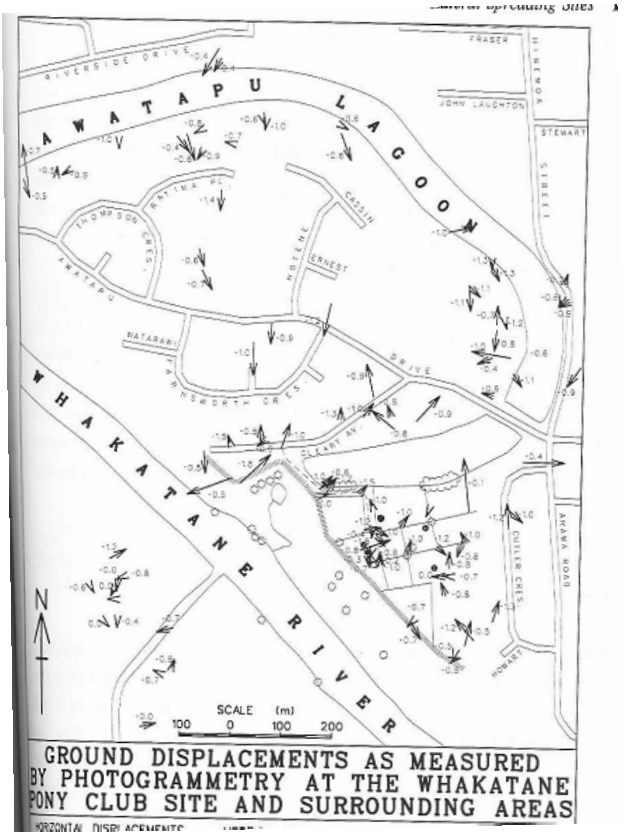

Figure 5.10: Relationship between volumetric strain, CSR, and SPT resistance used in evaluating liquefaction-induced settlement (Tokimatsu and Seed 1987)

Landing Road Bridge

At the Landing Road Bridge site, lateral spread deformations of 0.5 to 2.0 m towards the riverbank imposed lateral forces on pile foundations supporting the bridge that were close to ultimate capacity (Berrill et al. 2001). O&J selected a displacement of 1.5 m to use in their analyses, although neither the location of or justification for that value was presented. Based on results from 13 CPTs and 1 SPT boring performed at the site, it was determined that a 4-6 m-thick layer of loose, clean sand liquefied at the left bank of the river, causing lateral displacements and significant structural damage at the north abutment of the bridge.

The liquefied sand appears to be mostly homogeneous below the northern abutment, although a discontinuity was detected in CPT borings at the toe of the stopbank in Section A-A (Figure 5.12), extending behind the stopbank for about 80 m. The geometric

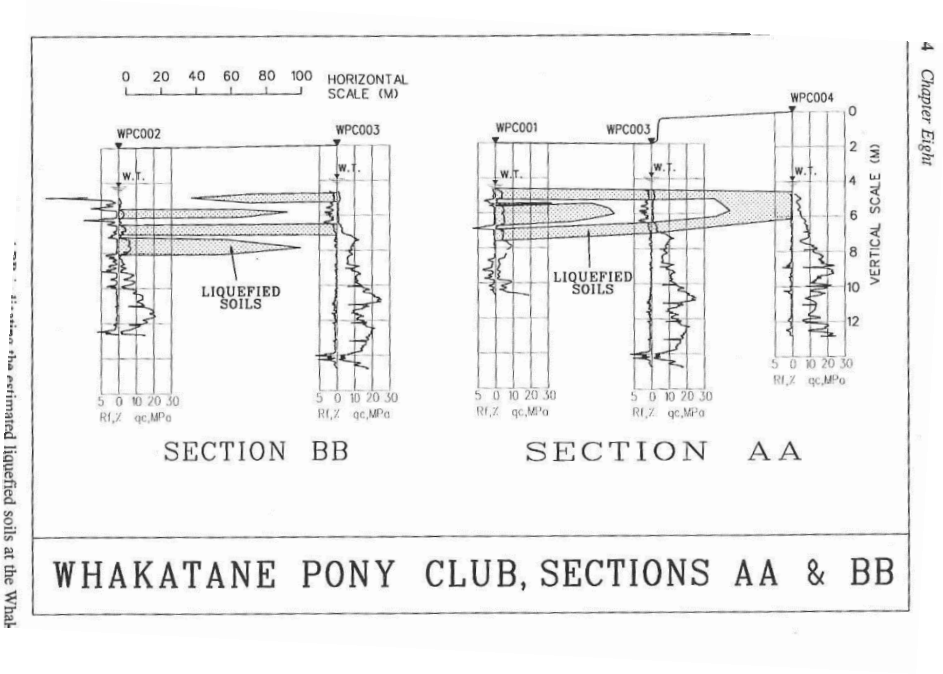

Figure 5.11: Subsurface profiles AA and BB of the lateral spread at the Whakatane Pony Club, towards the Awatapu Lagoon (Christensen 1995)

constraints of the slide are somewhat unclear. Berrill et al. (2001) indicated that the determination of free face dimensions was impossible for the site due to the fact that the pre-earthquake depth of the channel was unknown. However, the profile view of the bridge shows reasonable detail of the slope geometry that likely contributed to the slide, although it is unclear whether the ground surface dimensions are pre- or post-earthquake.

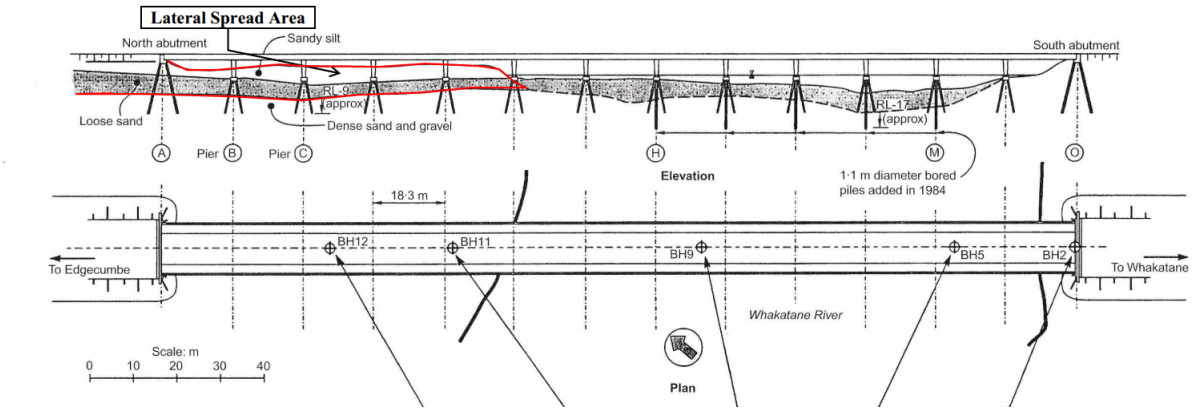

Figure 5.12: Plan and profile view of the Landing Road Bridge (pre-construction); depth of channel is approximate (Berrill et al. 2001)

5.4.5 1987 Superstition Hills

Perhaps one of the best laboratories for liquefaction is the Wildlife Site in southern California. During the $M_w = 6.6$ 1987 Superstition Hills earthquake, an array of ground motion recording equipment and pore pressure transducers captured key data when a 3 m-thick layer of loose, saturated sand liquefied at the site. A *PGA* of 0.21 g was recorded at the site, about 25 km from the fault rupture, which is the same value reported by O&J in their analyses. Moderate lateral displacements of about 20 cm towards the 1.74 m-high free face at the Alamo River were observed on nearly level ground (Figure 5.13), with O&J reporting a representative displacement of 0.18 m in their pseudo-static back-analysis for the site. O&J's estimates of the prefailure vertical effective stresses are on the order of 14 to 33 kPa. This indicates that they analyzed the mobilized strength ratio of only the silty sand that was directly below the Alamo River channel; the western extent of the liquefied layer, which experienced prefailure effective stresses of approximately 30 to 70 kPa, was not analyzed, despite clear evidence from the pore pressure array (Holzer et al. 1989) that liquefaction did occur in this particular stratum at least 25 meters west of the river channel.

The first instrumental array was installed in 1982, and in 1984, Bennett et al. performed a geotechnical investigation of the site. SPT and CPT data were paired for 4 boring locations, all within 50 m of the free face. The amount of subsurface data, along with well-characterized ground surface and ground water conditions, makes the 1987 liquefaction event at Wildlife Array one of the best-documented cases of liquefaction and lateral spreading to date; aside from inherent scatter in SPT and CPT resistance data, there was very little uncertainty in the site characterization and ground motion data for the Wildlife site. However, O&J's estimates for the CPT and SPT resistances in this material are significantly lower than the data reported by Bennett et al. (1984) (Table 5.3), possibly due to their aforementioned possible focus on the material directly below the bottom of the river channel, rather than the material closer to the instrumental array. It should be noted that no subsurface data appears to exist for the material below the channel, and thus the source of O&J's penetration resistance estimates is not entirely clear.

Table 5.3: SPT and CPT resistances for liquefied silty sand at the Wildlife Array, as interpreted from Bennett et al. (1984) in this report, and as reported by Olson and Johnson (2008)

SPT/CPT Data (Bennett et al. 1984)				SPT/CPT Data (as reported by O&J)			
Parameter	Mean	Mean-1 Std. Dev.	Mean+1 Std. Dev.	Parameter	Mean	Mean-1 Std. Dev.	Mean+1 Std. Dev.
CPT q_{c1} (Mpa)	7.2	3.9	10.5	CPT q_{c1} (Mpa)	3.3	1.8	6.7
SPT $(N_1)_{60}$	4.9	2.5	7.3	SPT $(N_1)_{60}$	8	5	1

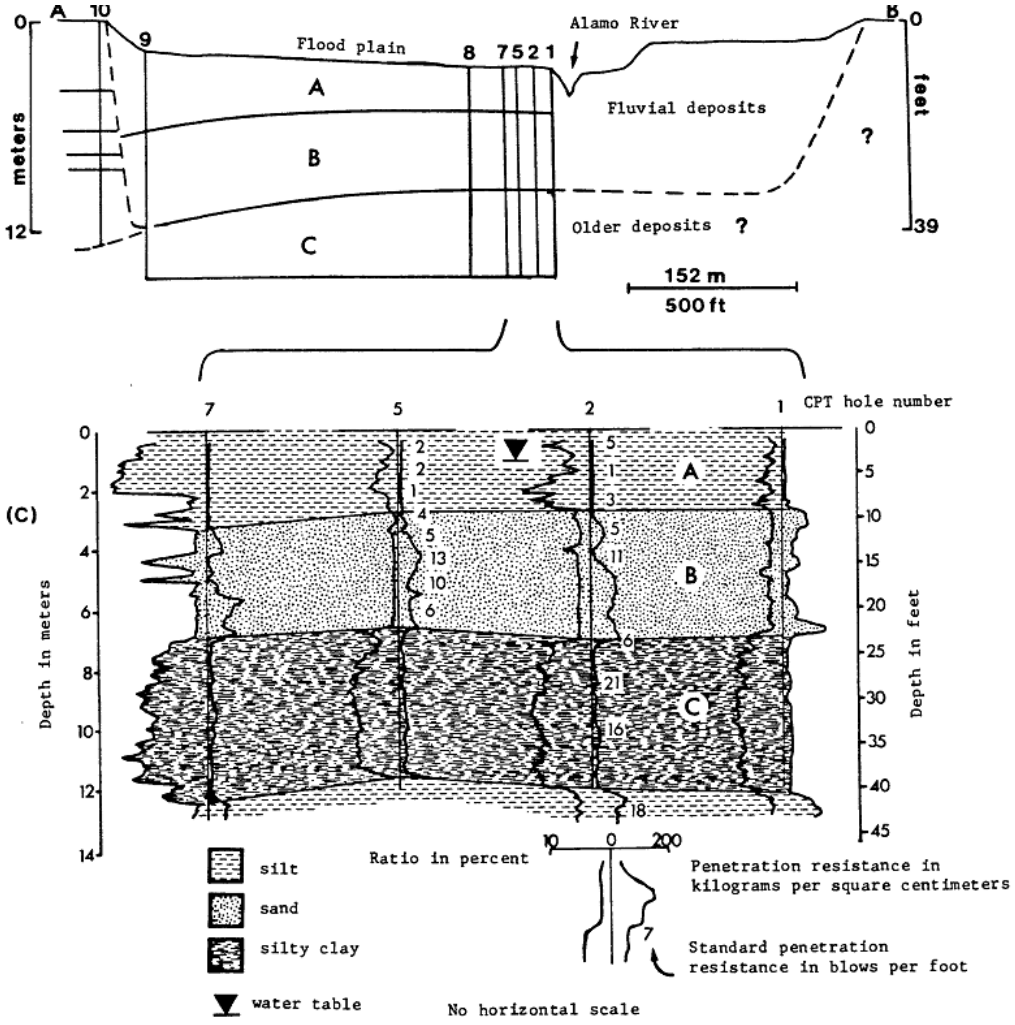

Figure 5.13: Subsurface profile at Wildlife Array; soil unit B was determined to have liquefied during the 1987 Superstition Hills Earthquake (Bennett et al. 1984)

5.4.6 1989 Loma Prieta

The M_w-6.9 Loma Prieta event occurred as the result of a large strike-slip rupture of the San Andreas Fault. The rupture originated in the Santa Cruz Mountains, and caused widespread liquefaction at sites throughout the coastal region of northern California, including the Marina district in San Francisco, Moss Landing in the Monterey area, several farmland sites east of Santa Cruz, and on Treasure Island between Oakland and San Francisco. Olson and Johnson identified ten cases of lateral spreading to be analyzed within their framework.

Moss Landing

Four of the lateral spread study sites were located on Monterey Bay at Moss Landing, about midway between the cities of Santa Cruz and Monterey, about 21 km from the San Andreas fault rupture. Peak ground accelerations in Moss Landing were estimated to be between 0.25 and 0.35 g. No recorded ground motion data for the sites was available, but based on numerical simulations that showed that bedrock accelerations at the site would have been about 0.15 g and the application of the relationship by Idriss for site amplification, a 0.25 g median estimate was presented by Boulanger et al. (1997), and was used by Olson and Johnson in their analyses.

At Building 4 of the Monterey Bay Aquarium Research Institute (MBARI), lateral displacements of about 0.3 m toward the Moss Landing Harbor were determined based on data from a slope indicator (SI-2) installed 15 m inland from the harbor (Figure 5.14). Deformation data from SI-2 showed that almost all lateral strain occurred between 2 and 4.5 m below ground surface, corresponding to a layer of loose, poorly graded sand, with interbedded layers of clayey silt (Figure 5.15a) that liquefied during ground shaking. It is not clear exactly how pervasive the clayey silt is at Sandholdt Rd., but it is possible that lateral deformations could have occurred in multiple layers.

At Building 3 of MBARI, 25 cm of displacement was observed based on deformation data from another slope inclinometer (SI-5). It was determined that the deformations toward the harbor were largely due to large lateral strains in saturated, loose sand at depths of about 4 to 6 m below ground surface (Figure 5.15b) (ground water was estimated at about 3 m below ground surface). Analysis of the loose sand shows that it liquefied during ground shaking (Boulanger et al. 1997). The loose sand layer was relatively homogeneous, with no evidence of the interbedded clayey silt seen about 150 m to the southwest at SI-2. The free face dimensions of the harbor appear to be well-defined in

the soil profiles for both MBARI sites, however the actual depth of the free face was not specified in the literature.

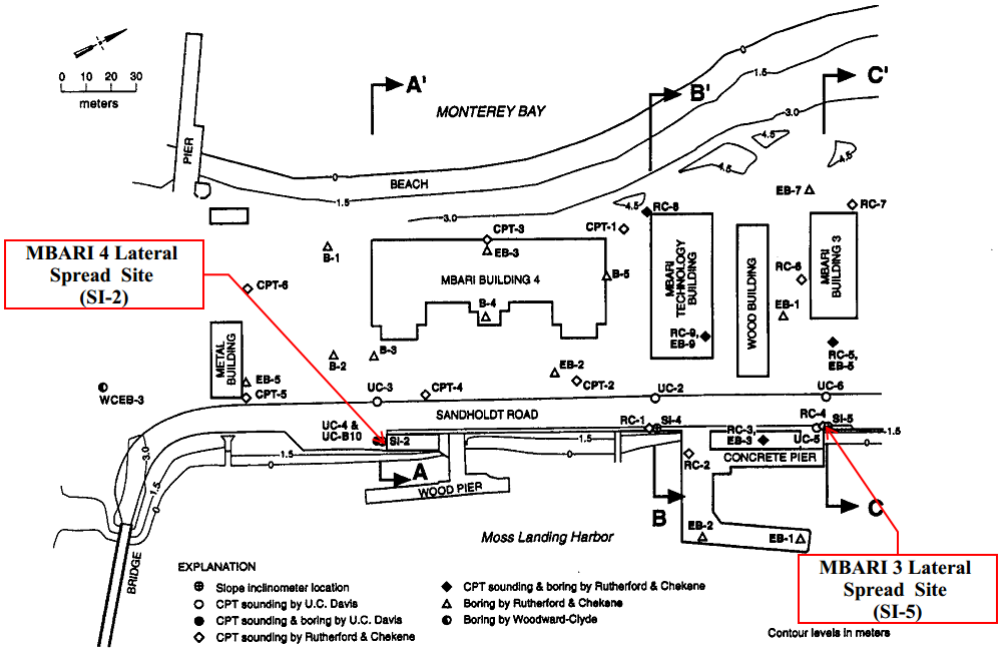

Figure 5.14: Site plan for Monterey Bay Aquarium Research Institute (MBARI), showing penetration test and slope inclinometer locations (Boulanger et al. 1997)

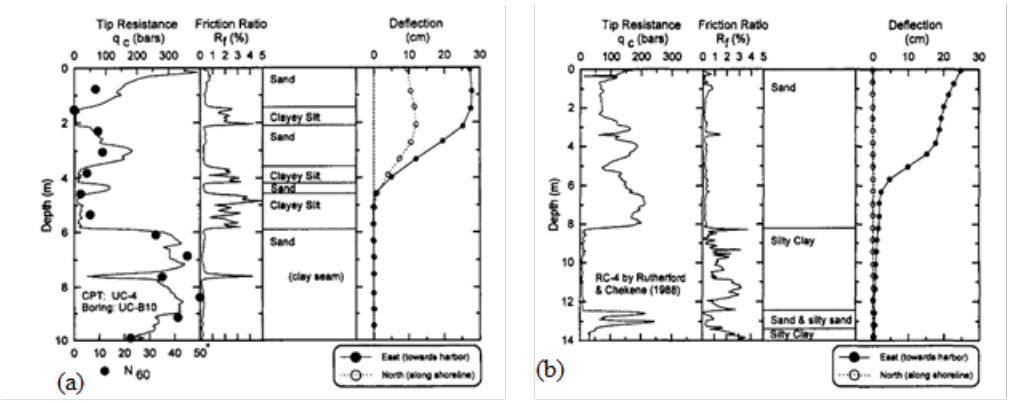

Figure 5.15: Lateral deformation and penetration resistance data at MBARI site from a) SI-2 and b) SI-5 (Boulanger et al. 1997)

The Moss Landing Marine Laboratory (MLML) building, which is located on the Moss Landing spit, experienced significant extension due to lateral spreading of the spit in both the eastward and westward directions. The liquefaction at the spit occurred in loose, saturated beach sand deposits (Figure 5.16). The eastward spread consisted of a displacement of about 0.8 m on level ground towards Old Salinas River, and occurred largely due to liquefaction of an approximately 1.5 m-thick layer of sand, about 2 to 3.5 m below ground surface (Mejia 1998). Subsurface investigations at the eastern portion of

the site showed significant heterogeneity at those depths, with clay and clayey silt also prominently featured. Thus, the spatial extent of the liquefiable material contributing to the eastward spread is somewhat uncertain. Furthermore, the geometry of the slide is somewhat unclear with respect to the dimensions of the free face; the location of the bottom of the channel is not indicated in any of the profiles provided by researchers (Boulanger et al. 1997, Mejia 1998), although it may have been inferred from the elevation contour map of the site plan.

The westward spread was characterized by about 0.6 to 0.8 m of displacement towards Monterey Bay, due to liquefaction in approximately 2-2.5 feet of the loose beach sand. It appears that the beach sand is more homogeneous on the western side of the site. O&J did not, however, specify which displacement location they based their analysis on for the westward spread. Displacements at the northwest corner of the site occurred in the proximity of a free face, while the displacements in the southwest portion occurred on a more consistent ground slope. Slope stability analyses for mobilized shear strength may have yielded significantly different results for the two geometric profiles. In general, Olson and Johnson's estimates of the representative $(N_1)_{60}$ in liquefied material differed significantly from those reported by Mejia (1998) for the four lateral spread sites in Moss Landing (Table 5.4)

Table 5.4: Comparison of estimates of $(N_1)_{60}$ by Olson and Johnson (2008) and Mejia (1998) for liquefied sand deposits at Moss Landing.

Case No.	Site	Olson & Johnson Estimates		Mejia (1998) Estimates	
		Mean	Range	Mean	Range
8	MBARI Bldg 4, Sandholdt Rd (SI-2)	16.5	15.1-17.1	10	8-12
9	MBARI Bldg 3, Sandholdt Rd (SI-5)	15	10-20	20.5	20-21
10	MLML Bldg., Eastward Spread	11	10-16	17	16-18
11	MLML Bldg., Westward Spread	11.5	10-16	17.5	16-19

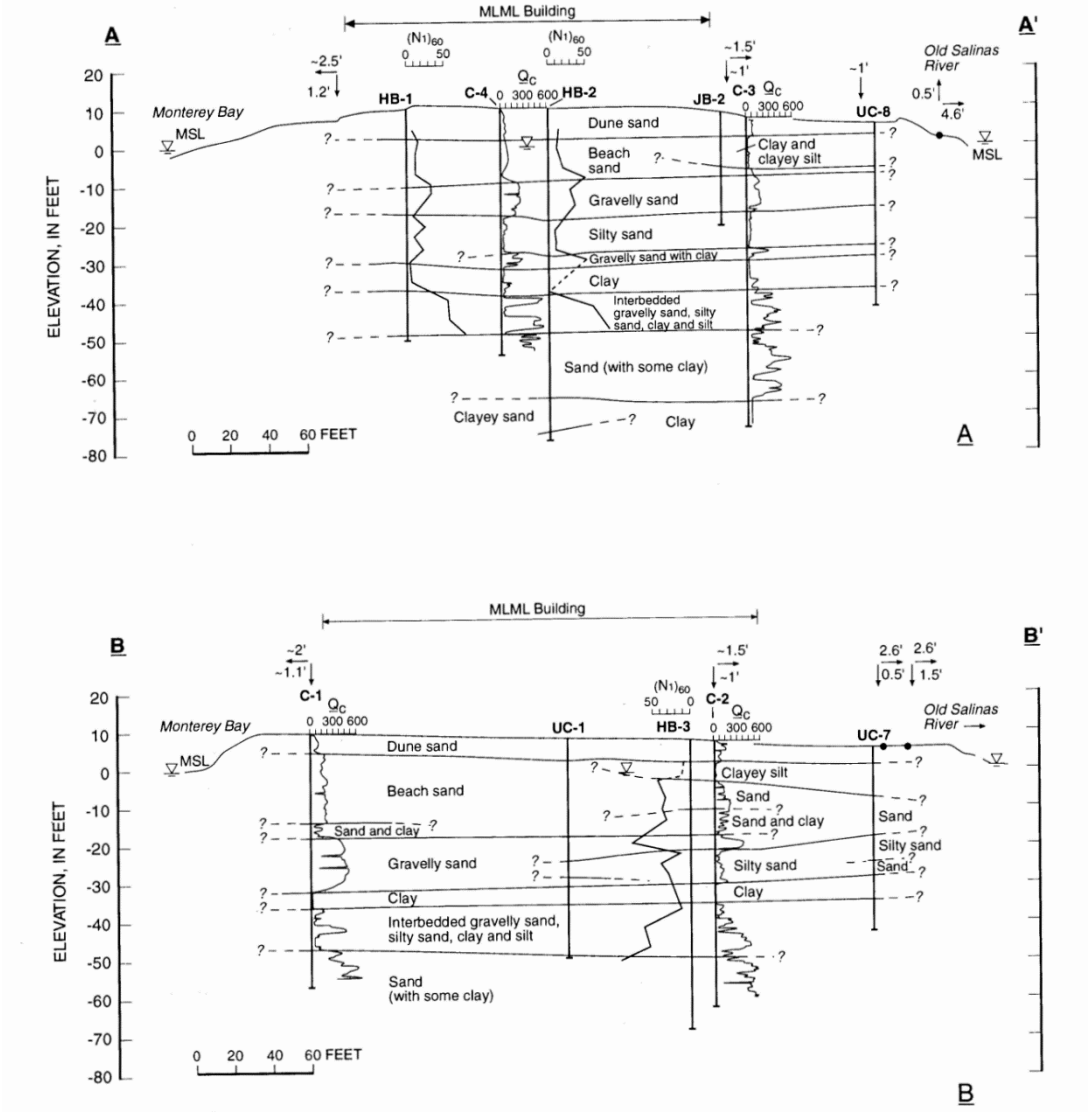

Figure 5.16: Subsurface profiles for the Moss Landing spit, with vertical and lateral deformation vectors (Mejia 1998)

Miller and Farris Farms

Four farm sites were also observed to have experienced significant lateral deformation in the areas near Watsonville and Castroville. Two sites in Watsonville, about 10 km from the nearest fault rupture, experienced moderate lateral displacements toward the Pajaro River channel (Figure 5.17). The site experienced an estimated peak acceleration of about 0.36 g, possibly based on USGS Shakemap data.

At Miller Farm, about 12 to 45 cm of northward ground displacements were observed in a spread area extending up to 200 m from the Pajaro River channel; Olson and Johnson selected 16 cm as the representative displacement value for their analyses. Farris Farm, on

the northern side of the channel, experienced a wider range of observed displacements; a range of 24 to 82 cm was observed, with the authors selecting a representative displacement of 30 cm. Liquefaction analyses by Holzer et al. (1994) showed that loose sand deposits of approximately 4 to 6 m thick liquefied south of the river channel, causing the northward spread towards a relatively mild free face (Figure 5.18). SPT sampling and reported stratigraphy appear to indicate that the sand layer was mostly homogeneous, although a wide range of penetration resistances were reported within the layer: $(N_1)_{60}$ values ranged between 7 and 21, and q_{c1} values ranged between 2.6 and 10.4 MPa. The geometry of the site was characterized thoroughly, although it was reported that ground water elevations at the site tended to vary by about 1.5 m in a given year. Holzer et al. (1994) estimated a slightly higher range for the $(N_1)_{60}$ of the liquefied material (12-24 bpf) than that estimated by O&J (19 to 16 bpf) at Farris Farm, possibly due to the interpretation of different boring logs as representative of the liquefied material.

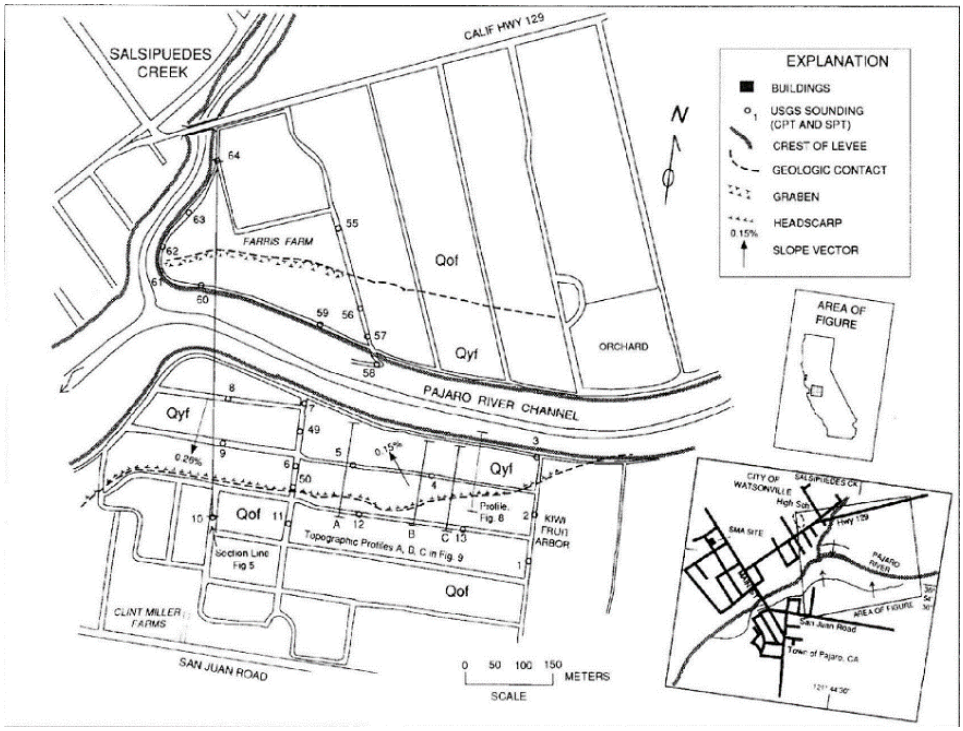

Figure 5.17: Site map of Miller and Farris Farms lateral spread site in Watsonville, CA (Holzer et al. 1994)

Sea Mist and Leonardini Farms

Two more farmland sites in Castroville, about 27 km from the nearest fault rupture, experienced lateral displacements of up to 2 m towards the Salinas River on sloping ground. Estimates of peak ground acceleration at the site are varied for the site; Charlie et al. (1998) estimated a PGA of about 0.16 g, possibly based on recordings from a site about

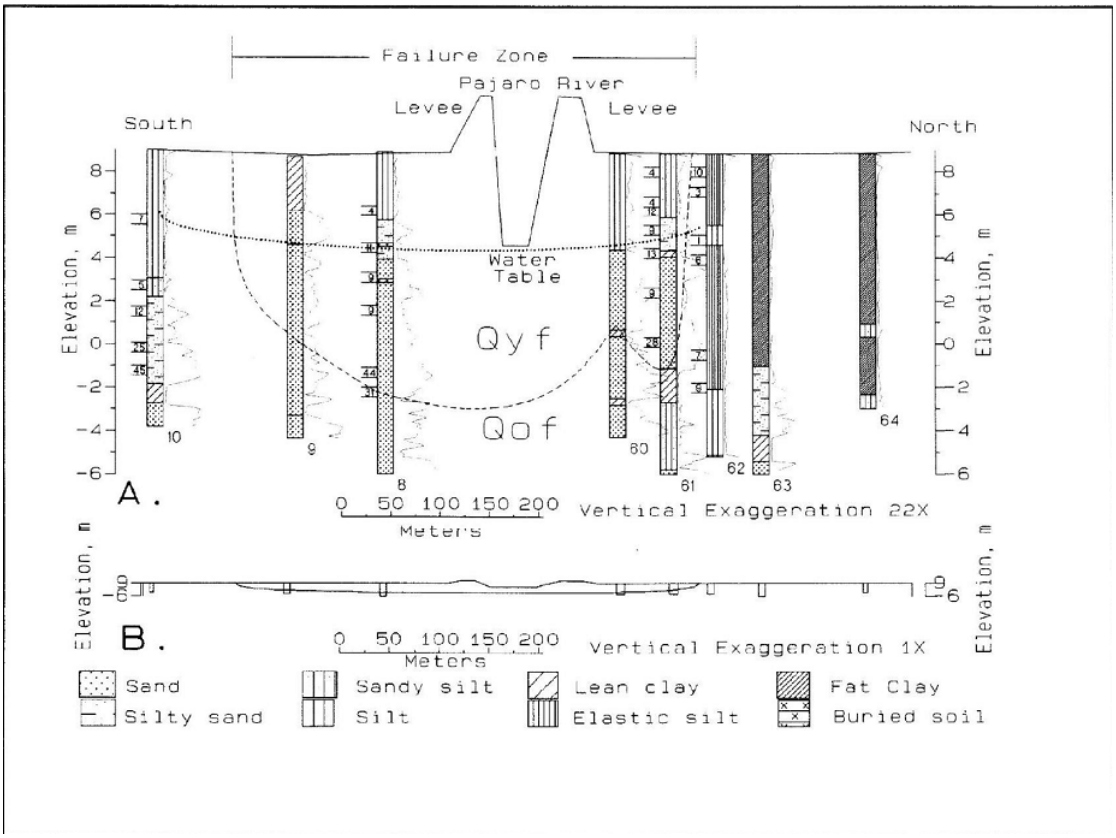

Figure 5.18: Subsurface profile of Miller and Farris Farms lateral spread site, with vertical exaggeration and actual scale shown. (Holzer et al. 1994)

15 km away in Salinas. Olson and Johnson estimated 0.21 g, which may reflect the softer site and Castroville's closer distance to the fault rupture than Salinas.

At the Leonardini Farm site (Figure 5.19), displacements of 0.17 to 2.0 m were observed towards the Salinas River channel. SPT, CPT, and piezovane tests showed that a layer of loose, saturated silty fine sand, about 1 m thick, liquefied during ground shaking. The material that liquefied was in the upper portion of a larger stratum of silty sand that extended from about 2 to 8 m below ground surface, with an increasing density with depth. The gradual slope geometry of the site was well-characterized by investigators (about 0.4%), and ground water level estimates varied by less than 0.5 m.

The Sea Mist Farm site, which lies about 400 m to the north of Leonardini Farm, experienced a mean of 0.47 m (0.23 to 0.71 m) of displacement towards the Salinas River channel. Subsurface profiles for the site were not readily available, however, a site grade of about 1.5% could be inferred based on ground surface elevation data from the boring logs for the site. Based on liquefaction analyses (Charlie et al. 1998) and subsurface data (Bennett and Tinsley 1995), it is likely that liquefaction occurred in about 2.5 m of loose

sand, which was found in Boring no. 30. The horizontal extent of this material is uncertain, however; Boring no. 31, which was about 50 m closer to the river channel, showed very heterogeneous silty sand and sand with silt at similar depths, which theoretically could have also liquefied, but is likely a different stratigraphic unit. The penetration resistances, grain size, and fines content were only reported by O&J for this silty sand unit, implying that their analyses were based on a soil profile generated by Boring no. 31. However, sand boil and ground crack mapping appear to indicate that most liquefaction effects occurred further away from the river channel, closer to Boring no. 30, for which only CPT data is available.

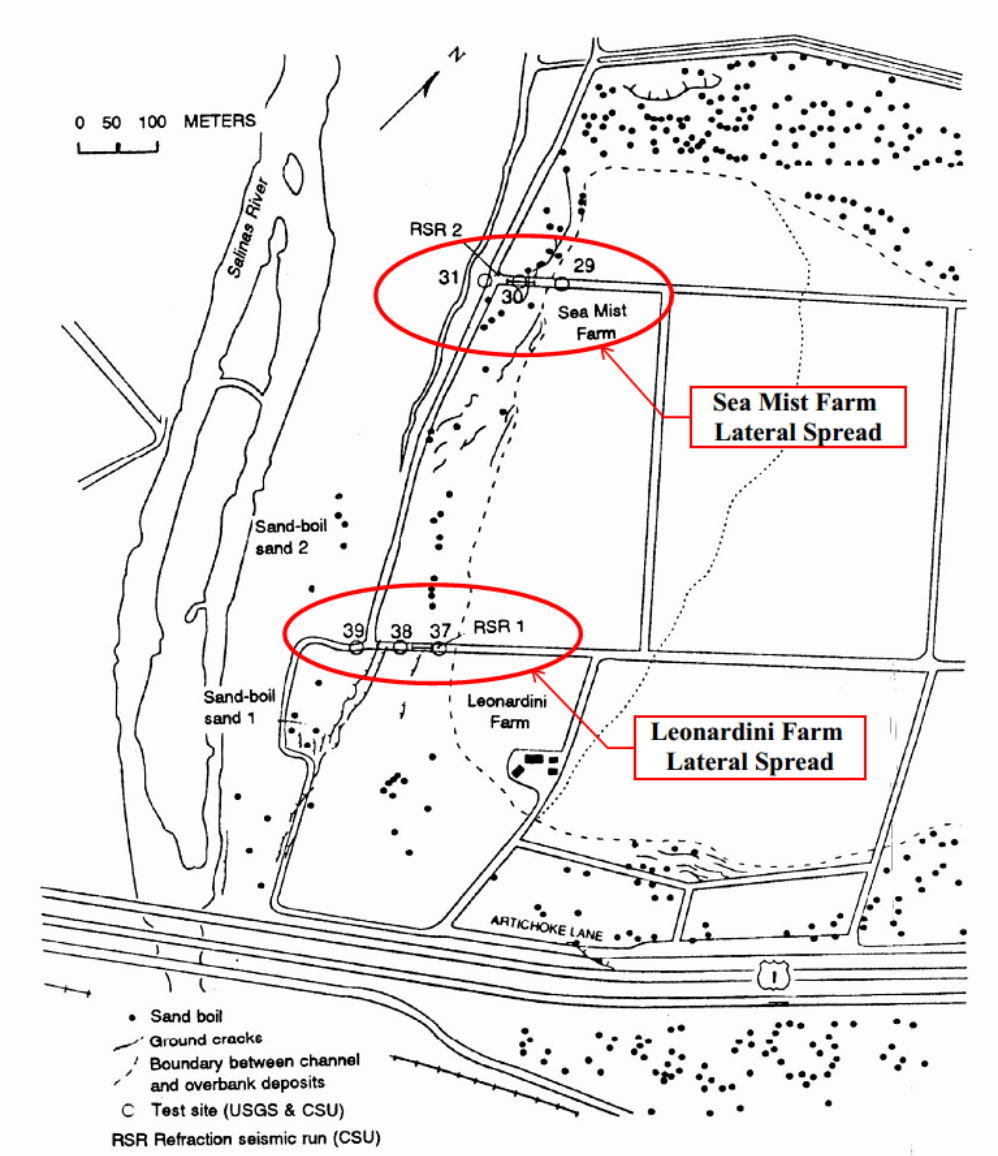

Figure 5.19: Map of Leonardini and Sea Mist Farms Lateral spread site, with boring locations. (Charlie et al. 1998)

Marina District, San Francisco

The St. Francis Yacht Club in San Francisco's Marina district sustained significant structural damage due to lateral deformations of 0.3 to 0.6 m toward the San Francisco Bay. Shaking in the Marina district, which was heavily damaged despite being some 85 km north of the fault rupture, was assigned a modified Mercalli intensity (MMI) of IX. A peak ground acceleration of 0.16 g was estimated by O&J. A similar *PGA* was recorded on Treasure Island, a site that also featured liquefaction of fill; both sites are approximately 80 km from the Loma Prieta rupture, and both sites have and estimated v_{s30} of less than 200 m/s.

The St. Francis Yacht Club sits on the St. Francis Spit, which is comprised of about 4 m of artificial fill placed above beach deposits of sand and silty sand. The spit is about 61 m long in the north-south direction, and is supported by rubble seawalls on both sides. The subsurface data for the spit is relatively sparse; two SPT borings were performed by Harding Lawson and Associates in 1977 (only one directly below the site), with large scatter in SPT resistances. It is somewhat difficult to ascertain exactly which material below the yacht club liquefied during ground motions. It is likely that the bottom 2 m of fill (below the water table) liquefied, which would have been the only material that would have contributed to such large lateral deformations. The underlying beach sand and silty sands were described as medium dense and loose to medium dense, respectively.

Furthermore, the presence of the seawall to the north of the site would have complicated the application of a pseudostatic limit equilibrium analysis. The pile-supported seawalls, by design, imposed significant lateral restraint on the St. Francis Spit, and would need to be accounted for in a slope stability analysis as a high-strength, dense material-type, such as coarse gravel. If the failure surface were controlled such that it was forced to pass through the liquefiable layer as well as the seawall, than a psuedostatic analysis would effectively capture the relationship between the liquefied shear strength of the fill and the yield acceleration of the failure surface. However, if the failure surface was assumed to be circular, this would increase the inclination of likely failure surface, forcing it to pass *under* the toe of the seawall. Thus, a very small portion of the thin layer of liquefied fill would actually be represented in the failure surface (Figure 5.20), and the yield acceleration of the slide would be relatively insensitive to variations in the shear strength of the liquefied material. Thus, the validity of this particular case history as a data point is dependent on how the pseudostatic analysis was performed by the authors; the nature of that analysis is currently unknown.

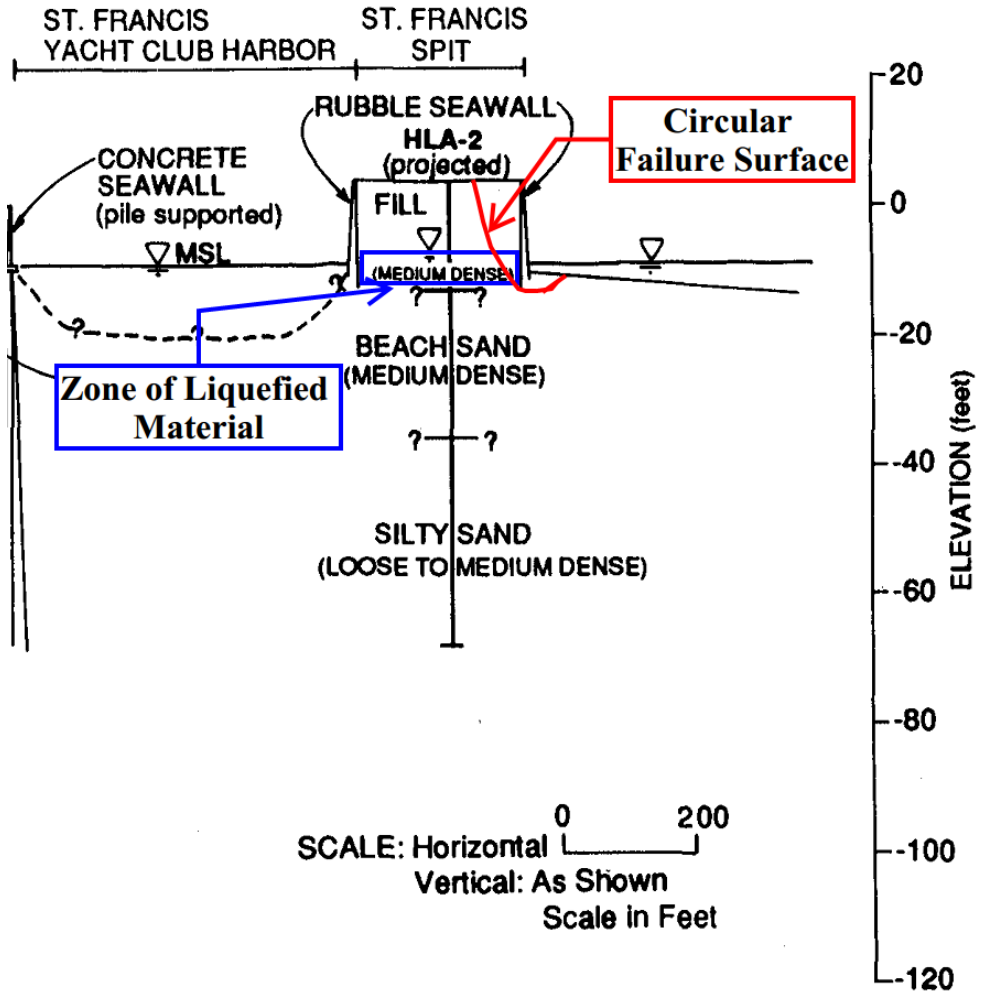

Figure 5.20: Site profile of the St. Francis Yacht Club harbor (horizontal exaggeration) (Taylor et al. 1992); liquefied fill and possible circular failure surface are indicated

Treasure Island, San Francisco Bay

Treasure Island was constructed in 1937 as a World's Fair site. The island, which sits adjacent to a natural rock outcrop, Yerba Buena Island, was built up using hydraulic fill within a perimeter dike around the outside edge of the island. During the 1989 Loma Prieta event, widespread liquefaction occurred in the fill, causing significant lateral spreading displacements along the perimeter of the island. Ground motions on Treasure Island were recorded, measuring a peak ground acceleration of 0.16-0.17 g, indicating that, similar to the Marina district, significant soft-site amplification effects had occurred despite it being about 80 km north of the fault rupture. At 4th St. and Avenue N. in the eastern portion of the island, about 10 to 30 centimeters of lateral displacement had been observed. Sub-

surface investigations by Hryciw et al. (1998) showed that the eastern corner of the island was underlain by about 12 m of the loose saturated fill and the spread occurred towards a free face buttressed by rock fill. The slope geometry appears to be well-characterized, and SPT data from the site shows that the fill that likely liquefied (generally below an $(N_1)_{60}$ of 15) was about 5 to 6 m thick (Figures 5.21 and 5.22)

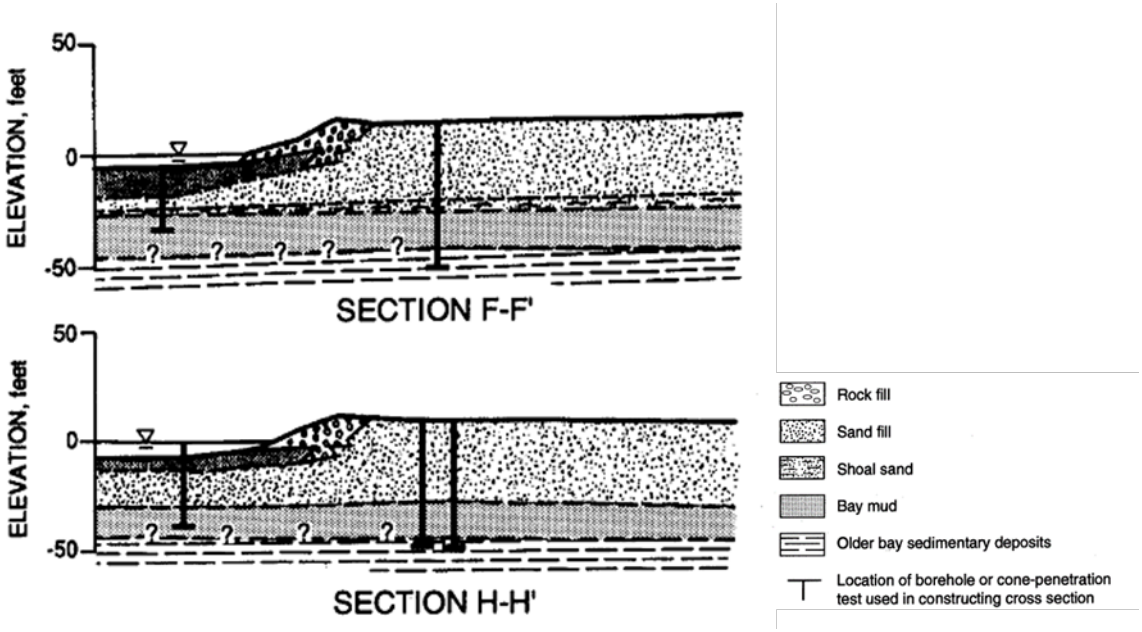

Figure 5.21: Profiles of lateral spread sections near 4th St. & Avenue N on Treasure Island, showing stratigraphic units (Power et al. 1998)

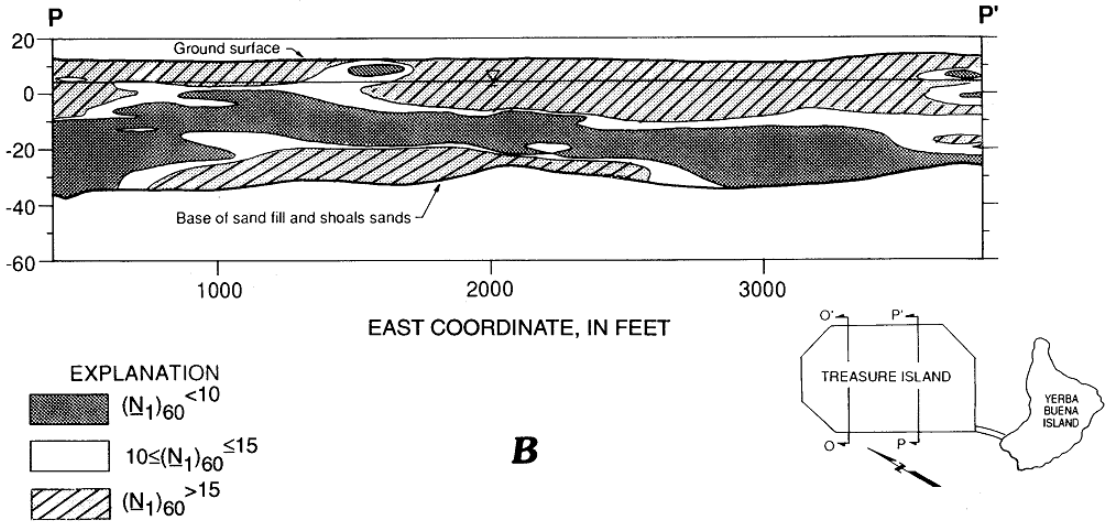

Figure 5.22: Profile of sand fill SPT data across the south side of Treasure Island (Power et al 1998)

5.4.7 1990 Luzon, Philippines

The M_w-7.8 event in the Philippine archipelago was caused by a 110 km-long rupture of the northernmost edge of the left-lateral striking Philippine and Digdig faults. The result was massive damage to a 20,000 km^2 area on the main Philippine island. The city of Dagupan, about 65 km west of the fault rupture, experienced widespread liquefaction of sandy deposits near the mouth of the Pantal River, causing large building settlements, bearing failure of shallow foundations, and large lateral ground deformations at the riverbanks. Almost all building damage was caused by liquefaction and ground failure, and peak accelerations in areas of the city that did not liquefy were estimated to be about 0.18 g (Tokimatsu et al 1994).

The historically complex meandering pattern of the Pantal River had resulted in about 5 to 10 m of pervasive loose silts and sands that generally featured two modes of deposition. During the 1990 Luzon event, liquefaction occurred in both old channel deposits and point bar deposits (Figure 5.23). The resulting lateral displacements (Figure 5.24) along the current river channel were observed to be quite large (from 2 to 6 meters) and very destructive. Small houses along the riverside area were torn apart, and trees were completely uprooted in a zone extending up to about 50 m from the riverbank. This level of displacement and damage is not usually seen in cases of lateral spreading, leading Ishihara (1993) to conclude that the displacements had probably occurred as a result of flow-type liquefaction, and *not* cyclic mobility-based lateral spreading. Thus, there does not seem to be a strong link between applying a Newmark-type sliding block analysis to characterize deformations in Dagupan in terms of a yield acceleration.

It should also be noted that subsurface investigations in Dagupan were conducted using primarily SPT and Swedish cone tests. SPT data was more sparse, and thus the $(N_1)_{60}$ and CPT q_{c1} values reported by Olson and Johnson may be subjected to a significant of uncertainty due to extrapolation of sparse SPT data and conversions between Swedish cone penetration values and SPT and CPT resistance values (Moss and Hollenback 2009).

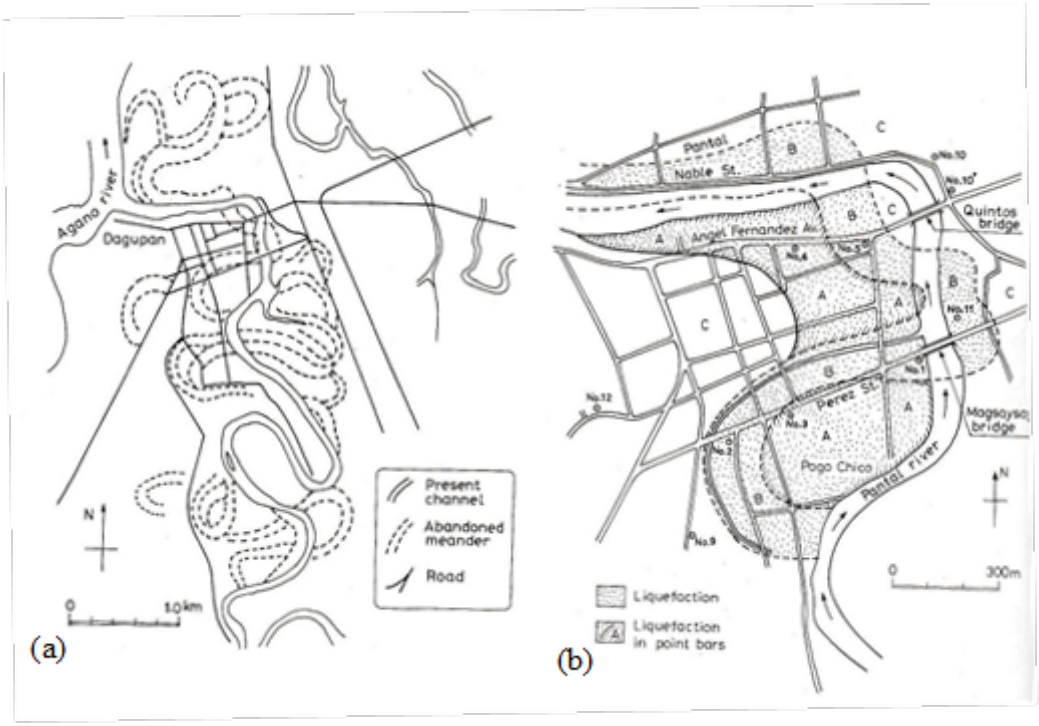

Figure 5.23: a) Historical meandering pattern of Pantal River near Dagupan, and b) Visualization of liquefaction in point bar deposits (unit A) and abandoned channel deposits (unit B) (Ishihara 1993))

5.4.8 1990 Manjil, Iran

The 1990 Manjil earthquake was a highly destructive, magnitude-7.4 event that originated in the Alborz Mountains in Iran, southwest of the Caspian Sea. The earthquake destroyed three major cities and over 700 smaller villages in northwest Iran, killing 40,000 people and causing over $200 million in damage. In the town of Rudbaneh, about 65 km southeast of the fault rupture, liquefaction was observed in loose alluvial deposits, resulting in lateral spreading of about 0.8 to 2.0 meters towards the Heshmat Rud Canal. The ground motions in Rudbaneh were of a particularly long duration (about 30 s of significant ground shaking), with an estimated *PGA* of about 0.17 g. Yegian et al. (1995) used the results of 3 SPT borings near the canal to characterize the spread geometry and subsurface conditions at the canal (Figure 5.25). There appears to be some uncertainty in the actual depth of the canal itself, however, as Ishihara's analyses of the spread (1992) are based on a canal depth of about 4 m, while Yegian analyzed the residual strength of the soil for a free face height of about 15 m. Unsurprisingly, this discrepancy led to distinct differences in strength estimates by each investigator; Ishihara estimated a mobilized shear strength ratio of 1.6 kPa, while Yegian's estimate was 21.2 to 28.7 kPa. O&J, who estimated a mean mobilized shear strength ratio of 13.3 kPa, did not state which free face height was used in the

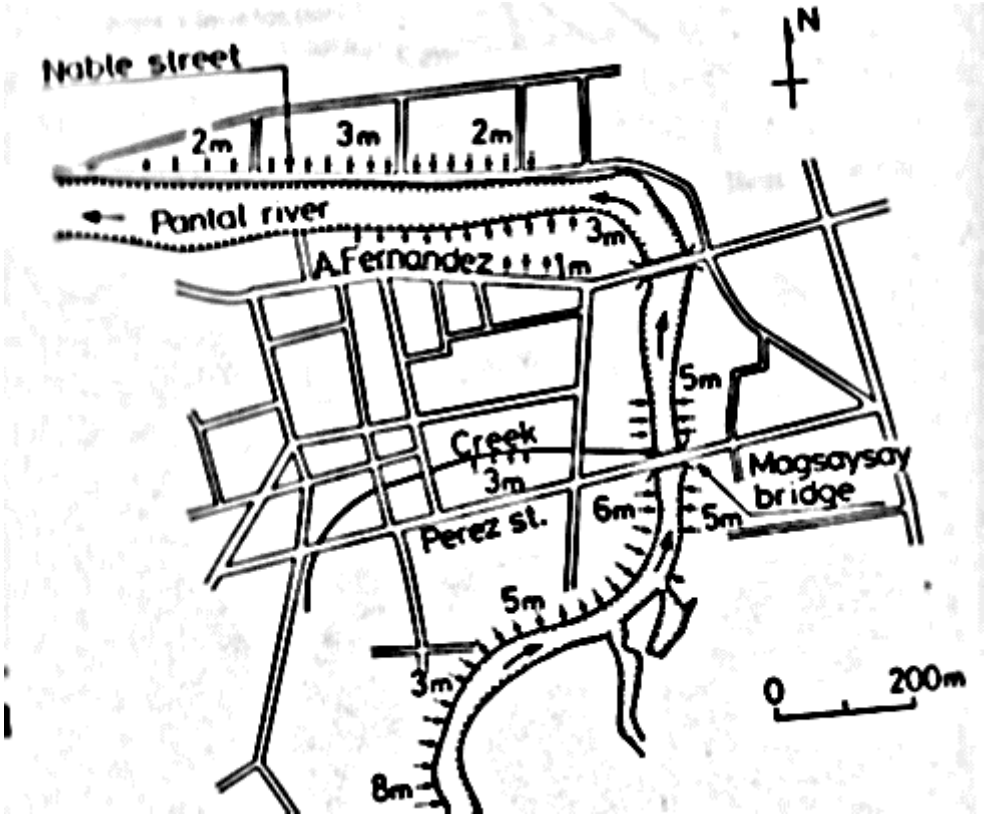

Figure 5.24: Deformation patterns and magnitudes along the Pantal River after the 1990 Luzon Earthquake (Ishihara 1993)

pseudostatic limit equilibrium analyses. In the absence of CPT data, it is presumed that O&J used the SPT-CPT conversion in Equation 5.1 to obtain equivalent q_{c1} values for their correlations. For the median grain size reported for the liquefied sand in Rudbaneh (0.25 mm), using the correlation from Robertson et al. (1983) would result in a mean q_{c1} of about 6.7 MPa, rather than the 4.3 MPa estimated by the authors.

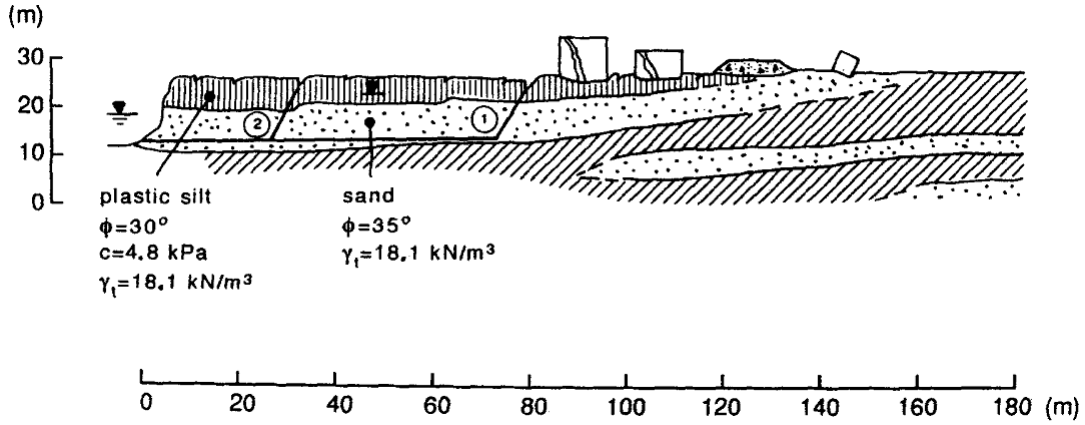

Figure 5.25: Cross section of the lateral spread towards the Heshmat Rud Canal in Rudbaneh, Iran. (Yegian et al. 1995b)

5.4.9 1994 Northridge

The 1994 Northridge earthquake, despite its relatively moderate moment magnitude (6.8), caused very high intensity ground motions in the southern California area and liquefaction at several near-fault sites. The liquefaction was found to have occurred on gently sloping ground, in 8 to 12-meter thick Holocene alluvium, that had been loosely deposited by sediment-laden floodwaters.

Balboa Boulevard

At the Balboa Blvd. site, which lies about 2.5 km north of the fault rupture, a peak ground acceleration of about 0.84 g was estimated by Holzer et al. (1998), based on ground motion recordings at a station 2.3 km east of the site. While this high PGA is relatively consistent with local PGA contour maps of the event, ground motion characteristics can exhibit a high degree of variability at near-fault sites. A lateral spread was observed to have occurred over a 1 km-long-by 0.5 km-wide zone on a 1.6% grade. Based on aggregate measurements of ground crack widths, the displacement at the site was estimated at about 0.5 m in the southward direction. Liquefaction analyses by Holzer et al. (1998) showed that liquefaction occurred in fluvial deposits consisting of silt and silty sand, with $(N_1)_{60,cs}$ in the range of 17-25 blows per foot. The fluvial deposits, along with other geologic materials at the site, were found to have a mean fines content of about 57% and a clay content of about 18%, but to be quite heterogeneous, with relatively low plasticity of fines. Based on the subsurface profile in Figure 5.26, a single, distinct layer of liquefiable material may have been difficult to identify for the purposes of a pseudostatic analysis to determine the mobilized shear strength.

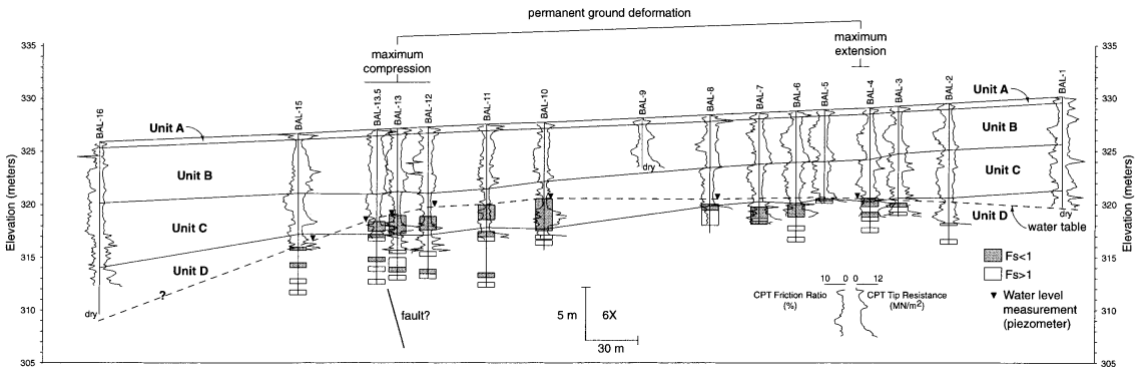

Figure 5.26: Cross section of the lateral spread at Balboa Blvd, showing FS_{liq} for all potentially susceptible material (Holzer et al. 1998)

Wynne Avenue

The Wynne Avenue site, which sloped at about 1.3% within the surface projection of the reverse fault rupture, experienced about 10-20 cm of displacement in the southern direction over a 150 m-long-by-12 m-wide area. Near-fault *PGA* estimates, especially those within the rupture plane, were highly variable; a *PGA* of 0.51 g was estimated at Wynne Ave, based on ground motion records from a site about 1.7 km to the southeast. However, it should be noted that peak accelerations as high as 0.94 g were recorded at other nearby sites, and that Balboa Blvd, which was further away from the fault rupture, experienced an estimated peak acceleration of 0.84 g. It was determined that liquefaction occurred in two distinct layers of Holocene silty sand (Figure 5.27). The C1 unit, which is thicker and more pervasive across the spread area, was likely the major contributor to the slide.

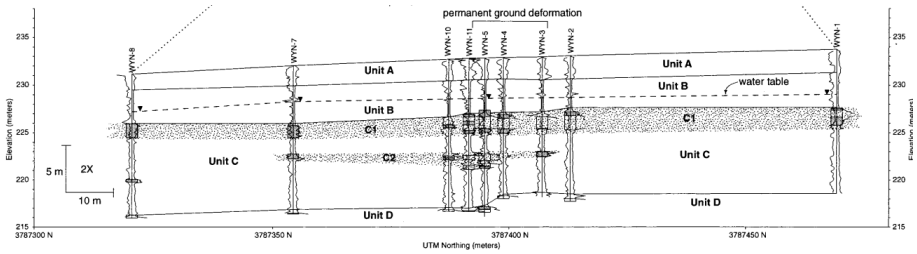

Figure 5.27: Cross section of the lateral spread at Wynne Ave showing FS_{liq} for all potentially susceptible material (Holzer et al. 1998)

Potrero Canyon

At Potrero Canyon, about 22 km NNW of the epicenter, about 10-20 cm of lateral ground deformations towards the Potrero canyon floor were observed. A *PGA* of about 0.43 g was estimated at Potrero Canyon, based on ground motions recorded about 3.8 km east of the site. Two subsurface profiles, each based on six soundings were generated for the site (Holzer et al. 1998), and ground slope conditions were well-characterized. It is somewhat unclear, however, which profile was used by O&J for their pseudostatic analysis, and the pervasiveness of the liquefied alluvium is relatively inconsistent. The CPT data indicates significant heterogeneity (Figure 5.28), and thus the assumption a single failure plane for the spread would introduce a significant level of uncertainty to the back-calculated mobilized shear strength of the soil and yield acceleration for this case.

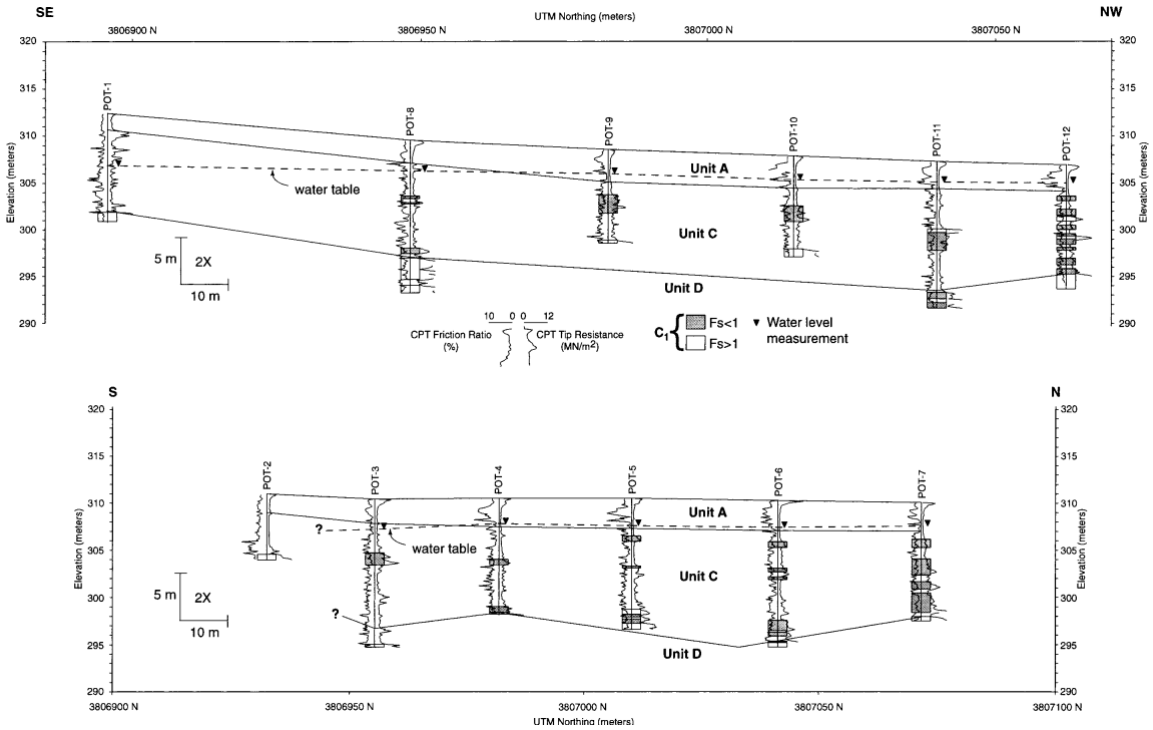

Figure 5.28: Cross section of the lateral spread at Potrero Canyon showing FS_{liq} for all potentially susceptible material (Holzer et al. 1998)

5.4.10 1999 Chi-Chi, Taiwan

The M_w 7.9 Chi-Chi earthquake resulted from a massive reverse fault rupture that caused extensive ground damage due to both surface faulting and liquefaction in the near-fault region. Liquefaction and lateral spreading in young, Holocene alluvium was observed and investigated by Chu et al. (2006) at several sites in two cities, Wufeng and Nantou, both within 1 km of the fault rupture.

Wufeng

At the Ger-Niao-Ken Creek in the city of Wufeng, four instances of lateral spreading were observed at three sites (C, C1, and B) within 0.5 km of the nearest surface fault rupture (Figure 5.29). The depth of the creek varied between 3 and 4 m below ground surface, and liquefaction occurred in about a 2 to 4m-thick layer of silty sand, starting at about 3 to 4m below ground surface. The peak ground acceleration at the site was estimated to be about 0.67 g, based on records at a site about 0.5 km to the north, although it should be noted that the near-fault nature of these sites indicates that there is high spatial variability in estimating the true PGA.

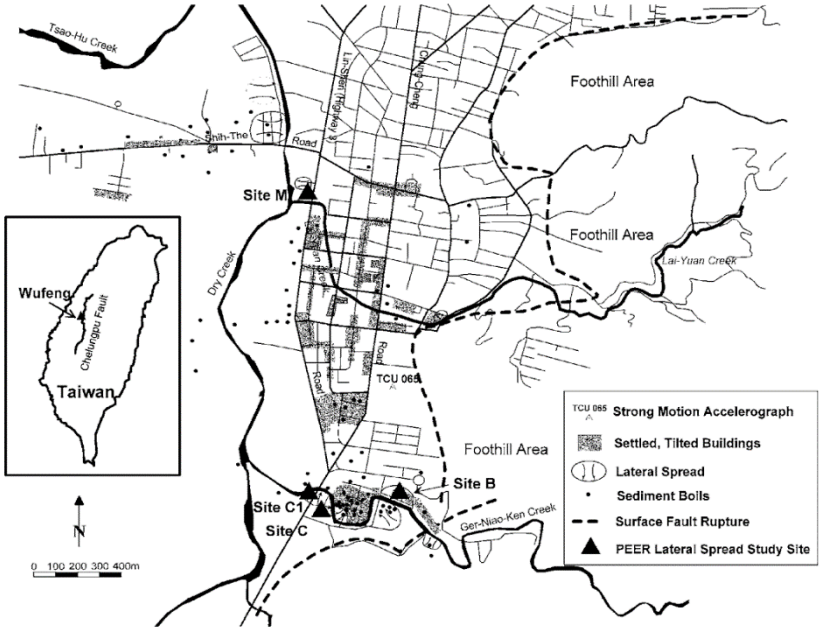

Figure 5.29: Map of Wufeng lateral spread sites with respect to 1999 Chi-Chi fault rupture (Chu et al. 1999)

Displacements at the spreading sites were measured based on ground cracks and thoroughly mapped with respect to distance from the edge of the creek (Figure 5.30). In general, displacements decreased gradually with distance from the free face, as is expected for lateral spreading at such sites (Barlett and Youd 1992). For each case, O&J used the maximum displacement vector (closest to the free face) for their sliding block analyses to determine the yield acceleration for the site. This approach can be somewhat problematic in modeling lateral spreading, as ground displacements close to embankments may be influenced more by localized instabilities at steep free faces, rather than by the mechanisms that drive lateral spread deformations. The empirical model for lateral spreading proposed by Bartlett and Youd (1992), and later Youd et al. (2001) accounts for this limitation by recommending that free face ratios (ratio of the height of the free face to the distance from the fee face) of no more than 20% be used in their model. All five cases at Wufeng are above this 20% threshold (Table 5.5) to varying degrees.

Table 5.5: Observed displacements and free face ratios of case histories used by Olson and Johnson (2008) at study sites in Wufeng (from Chu et al. 1999)

Case No.	Wufeng Site	Observed Displacement (m)	Free Face Ratio, H/L (%)
28	C (A-A')	2.05	49.9
29	C (B-B')	0.49	21.2
30	C1	1.24	57.7
31	B	2.96	31.3
32	M	1.62	23.7

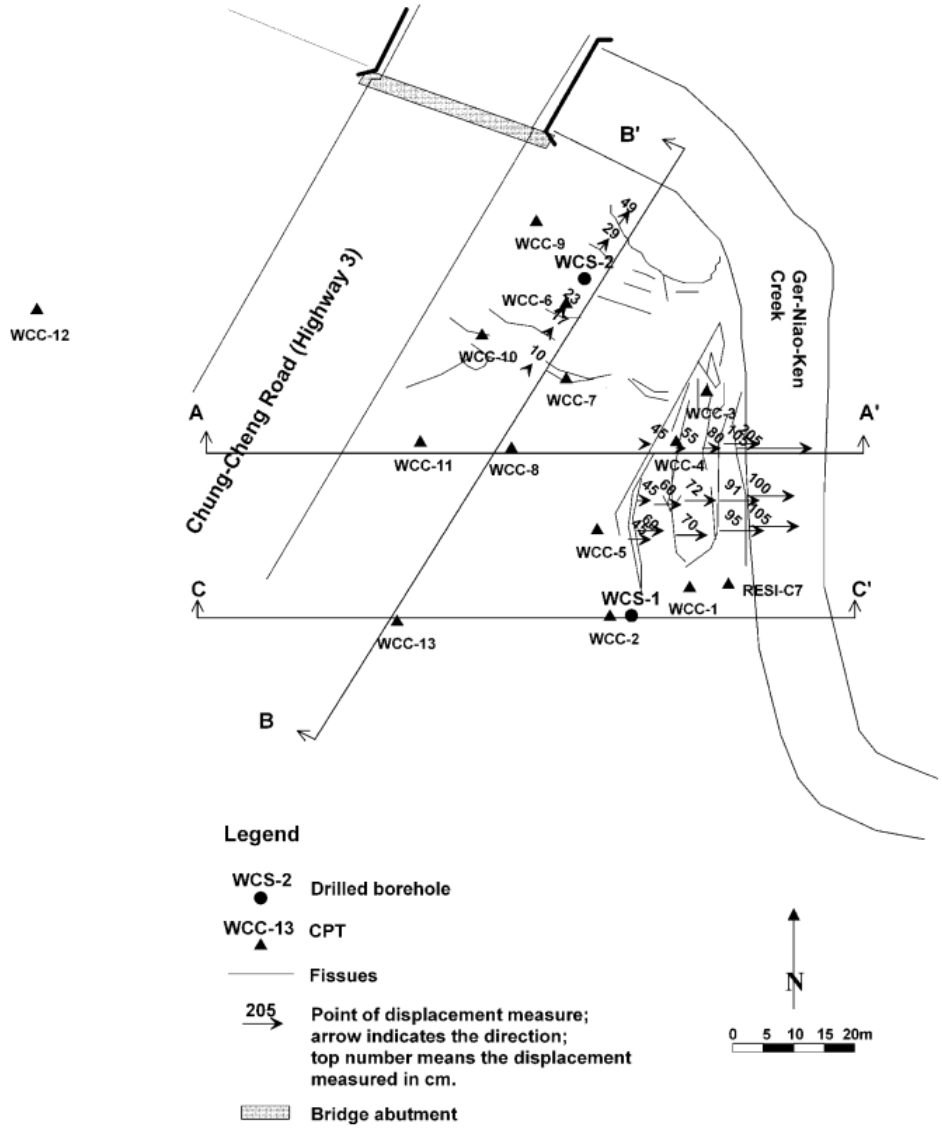

Figure 5.30: Map of observed displacements and test locations at Wufeng, Site C (Chu et al. 1999)

Note that for the A-A' profile, the increase in displacements is fairly gradual as we move closer to the free face; however, the displacement magnitude increases by a factor of nearly two between the second-closest (free face ratio of 37%) and closest displacement vectors (50% free face ratio) (Figure 5.31).

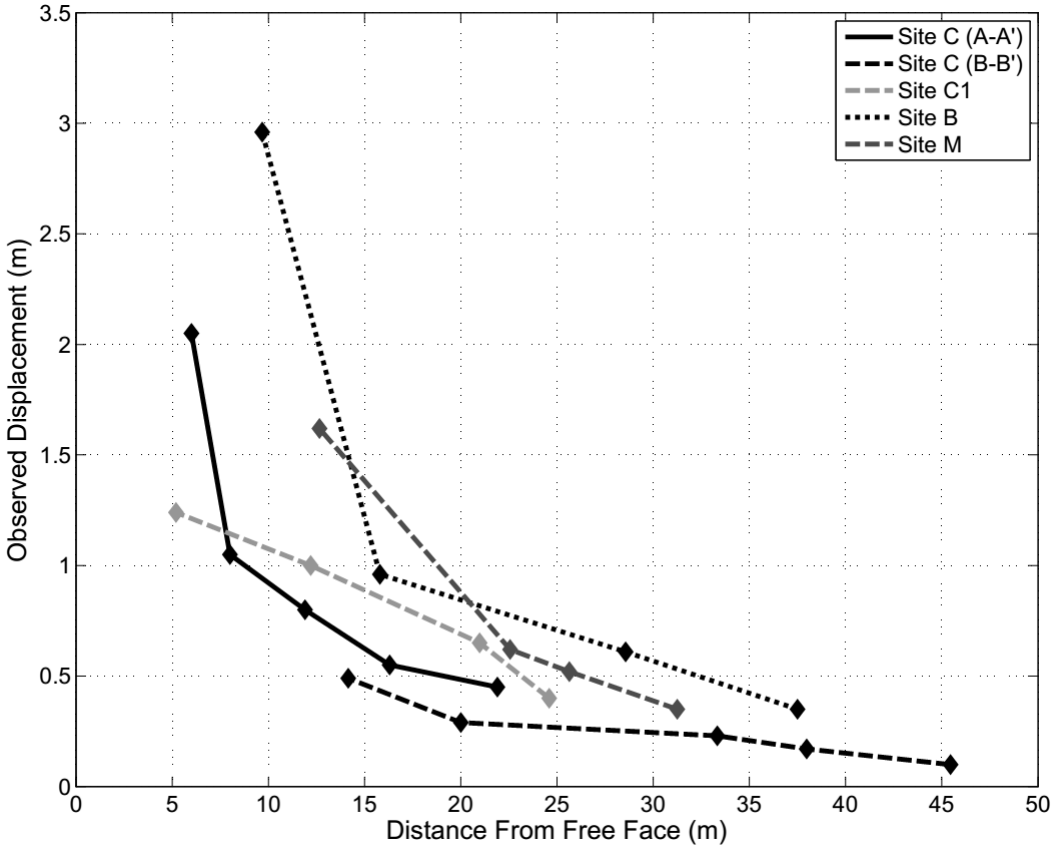

Figure 5.31: Variation of observed displacement with respect to distance from free face for Chi Chi lateral spreading site. Displacement vectors where free face ratio exceeds 20% are circled)

A fourth site (Site M) was investigated for lateral spreading towards Lai-Yuan Creek. A displacement of 1.62 m was observed on sloping ground of about 1.1% grade about 13 m from the edge of the 3-m-deep creek. The free face ratio for this particular displacement point was 23.1%, which is slightly above the upper limit recommended by Youd above which local instabilities are expected to be significant, but still may be moderate enough to produce reasonable estimates of the yield acceleration. It is likely that about a 2.5 m-thick layer of loose silty sand liquefied during ground shaking, however the SPT and CPT data for the site is quite sparse (only two N-values were recorded in the silty sand near the displacement vector), and somewhat variable (a range of 5-18 blows per foot was estimated for the liquefied material).

Nantou

In Nantou city, about 0.6 km from the nearest fault rupture, lateral displacements were observed in an alluvial floodplain west of the Miao-Lo River. The site PGA was estimated

to be about 0.39 g, with the nearest recording station about 0.6 km west of the site (further from the fault rupture) recording a *PGA* of about 0.42 g. The spread was likely driven by static shear stresses from the combination of the 3 to 3.5 m-high embankment at the edge of the river and the 3.8%-grade sloping ground in the floodplain. Liquefaction was found to have likely occurred in about 2-3 m of silty sand deposits near the surface. Displacements at the site were estimated to be about 25 cm; however, the mapped displacements were not based on any direct measurements of the ground, but rather on interpretation of aerial photos taken at the site coupled with interviews from local sources. Thus, the reported displacements for Nantou are considered less reliable than those mapped at Wufeng.

5.4.11 1999 Kocaeli, Turkey

The 1999 Kocaeli earthquake that struck northwest Turkey was an M_w 7.4 event that occurred on the North Anatolian fault, causing about 145 km of surface rupture just south of the Black Sea. Similar to the Chi-Chi event, the Kocaeli earthquake caused liquefaction at many near-fault sites, in the region around Sapanca Lake. Much of the region south of the lake is blanketed in Holocene-era deposits of fine-grained sands and silts, many of which liquefied during ground shaking.

Hotel Sapanca

At the Hotel Sapanca site, lateral displacements of 20-30 cm were observed as far as 100 m from the shoreline of Lake Sapanca (Figure 5.32, Cetin et al. 2002). The estimated *PGA* for the site was approximately 0.35 to 0.45 g, based on event-specific attenuation relationships and site response analyses (Cetin et al., 2002). Deformations accumulated to as high as 2.0 m at the shoreline, although it is possible that some of that deformation resulted from local instabilities involving a seawall. Most of the lateral spread area is on a ground slope of about 4-5% grade; ground cracks were measured to be between 10 and 50 cm in width across the site, with no discernible relationship between lateral displacement and distance from the sea wall (Figure 5.33).

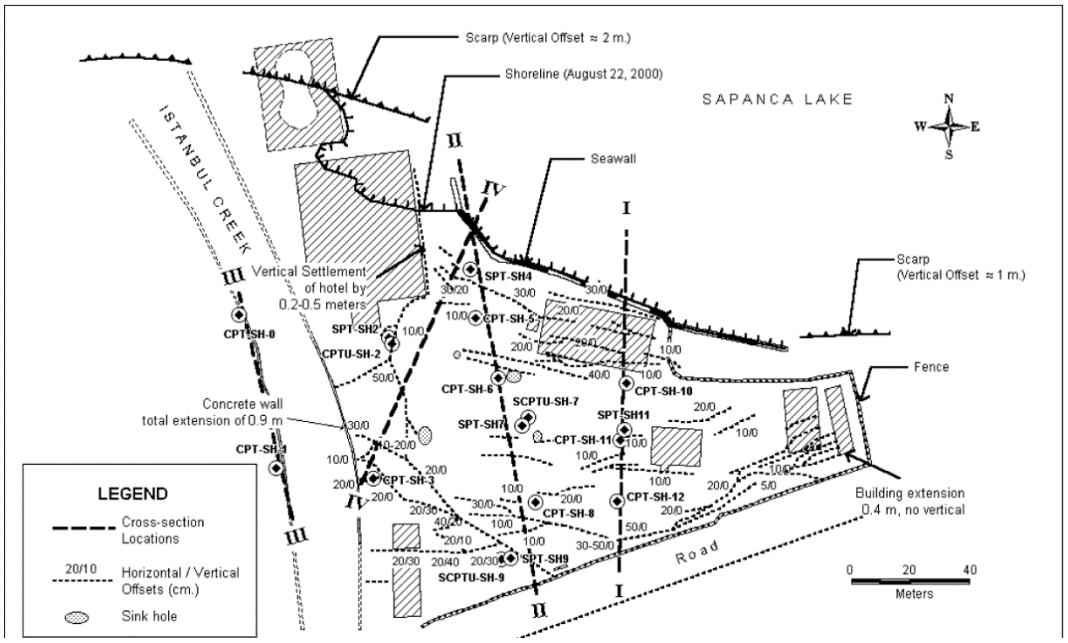

Figure 5.32: Map of ground cracks and subsurface investigation locations at Hotel Sapanca (Cetin et al. 2002)

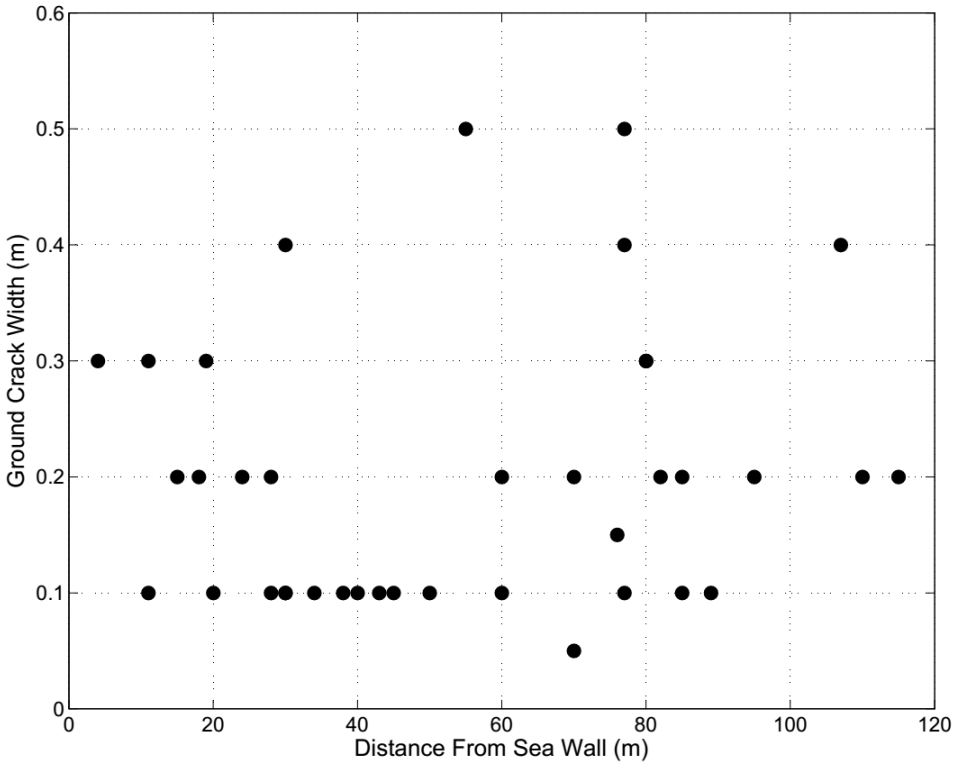

Figure 5.33: Variation of ground crack width with respect to distance from sea wall at Hotel Sapanca lateral spreading site.

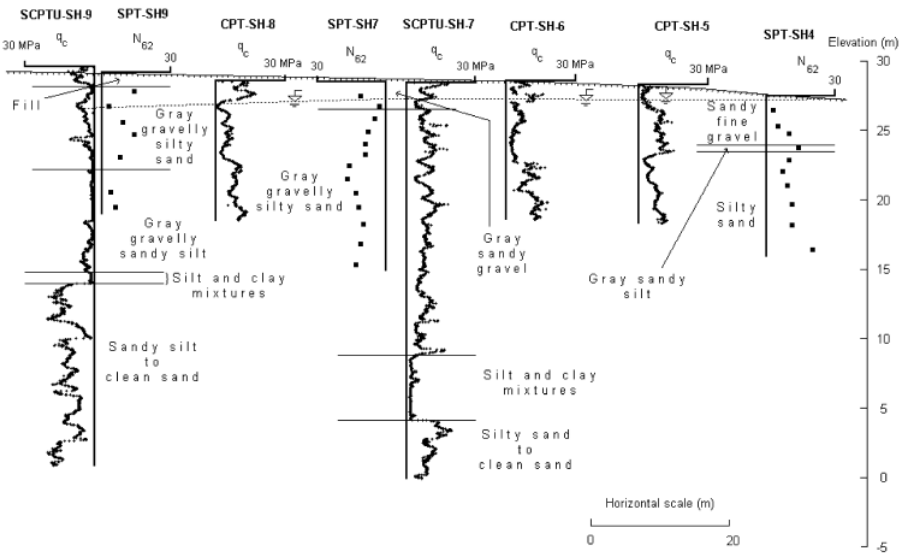

Figure 5.34: Cross section II-II at Hotel Sapanca (Cetin et al. 2002)

Analyses by Cetin et al. (2002) showed that liquefaction likely occurred in a 10 m-thick layer of silty sand, with occasional interbedded lenses of silt (Figure 5.34). The material grades coarser and increases in gravel content nearer to the shoreline, with scattered $(N_1)_{60}$ values between 8 and 20, approximately.

Police Station

Three more lateral spread sites along the coast of the Izmit Bay were evaluated by the Cetin et al. (2004b). In the town of Golcuk on the eastern shore of the Izmit Bay, ground deformations at the Police Station site were estimated to be as high as 2.4 m, based on accumulation of ground cracks (Figure 5.35). The geometry of the spread can be inferred from Cetin's application of Youd et al.'s 2001 empirical model and the elevation contours from the map of the site. The spread was generally treated as a free face by Cetin et al., as evidenced by the general increase in ground crack widths with respect to the shoreline, with a value of 8% for the free face ratio. The ground slope at the site varies between 10 and 15% (Figure 5.36), which may be steep enough to induce flow failures in the liquefiable soil (Youd et al. 2002), and cause localized variations in lateral displacements.

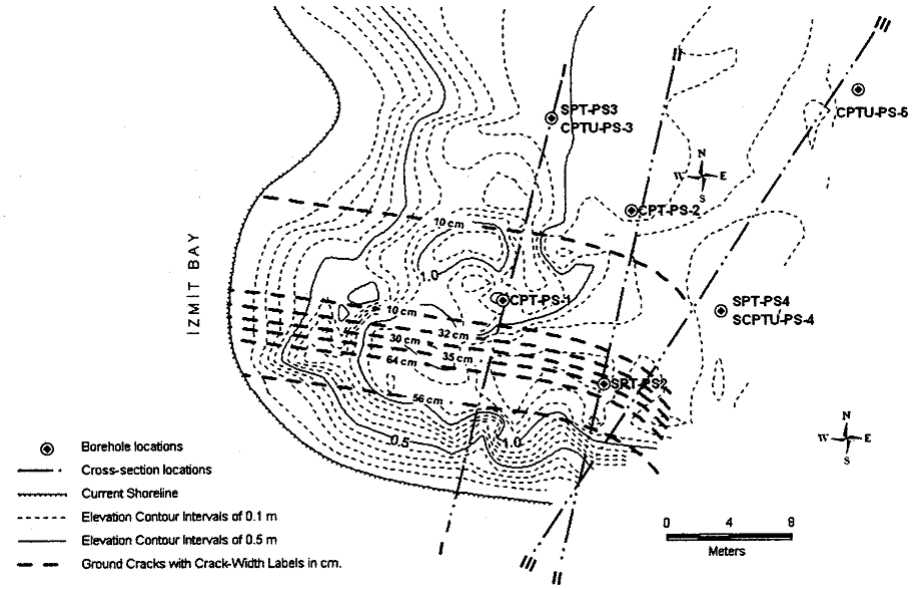

Figure 5.35: Map of ground cracks and penetration test locations at the Police Station site in Golcuk (Cetin et al. 2004b)

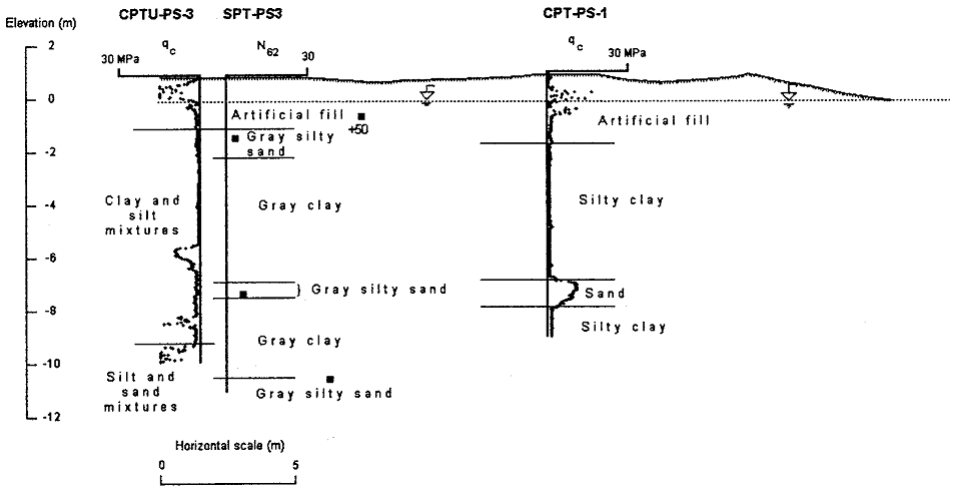

Figure 5.36: Cross Section I-I of Police Station site (Cetin et al. 2004b)

The subsurface conditions at the site were considered to be relatively laterally consistent (Cetin et al. 2004b). The site was blanketed by about 1.5 to 2.0 m of artificial fill consisting of poorly graded gravelly sand. Underlying the fill were two distinct layers of loose silty sand, encountered at depths of about 2.0 m and 8.0 m, each approximately 1.5 to 2.0 m thick, and separated by about 4.0 m of silty clay. Cetin's application of the method for calculating lateral strains from Shamoto et al. (1998) indicates that liquefaction and significant lateral displacements could have occurred in the artificial fill, and both underlying layers of silty sand. Thus, the determination of a single, discrete failure plane for this particular site would be subject to some uncertainty. Furthermore, the grain-size characteristics reported by Olson and Johnson for the liquefied material are inconsistent

with those reported by Cetin et al. (2004b). O&J reported a D50 of 0.13 mm, with a fines content of 36% for the liquefied material. The source of these estimates is unclear; the mean grain size of 0.13 mm was not evident in any of the material analyzed by Cetin et al., while the fines content of 36% matches the silty sand found in SPT-PS3, which is located about 20 m from the shoreline, and about 8 m inland from the 0.1 m-wide ground fissure. Grain size data for the silty sand closer to the shoreline, at SPT-PS2, was reported by Cetin as D50=1.6mm and FC=12%. SPT-PS2, however, is located at the 35 cm displacement location, and no grain-size information is available at the actual shoreline, where the accumulated 2.4 m displacements used by O&J in their analyses occurred.

Soccer Field

At the Soccer Field site about 8.5 km east of Golcuk, ground shaking with an estimated 0.4 g peak acceleration caused lateral ground deformations up to about 30 m from the Izmit Bay shoreline. The deformations ranged from 10 cm at the furthest extent of the spread, to a maximum of about 1.2 m within 10 m of the shoreline (Figure 4.37). The maximum displacement value at the site was used by O&J in their analyses. The profile of the site shows that displacements occurred on level ground toward a free face at the shoreline, and although the depth to the bottom of the free face is not clear in the cross section, Cetin's application of Youd's method indicated a free face ratio of 15% at SPT-SF6, which indicates a free face height of about 0.75 m.

Liquefaction at the soccer field site occurred in a 2-3 m-thick layer of silty sand, about 1 m below ground surface. CPT data at the site shows significant variation in tip resistance throughout the layer, indicating some heterogeneity in the liquefied material. Furthermore, only one SPT N-value was recorded for the silty sand, thus there is a high level of uncertainty to the determination of a representative penetration resistance of the liquefiable layer. No grain size data was reported by O&J, despite the fact that Cetin et al. reported a median grain diameter of 0.074 mm and fines content of 52% for the silty sand at SPT-SF6.

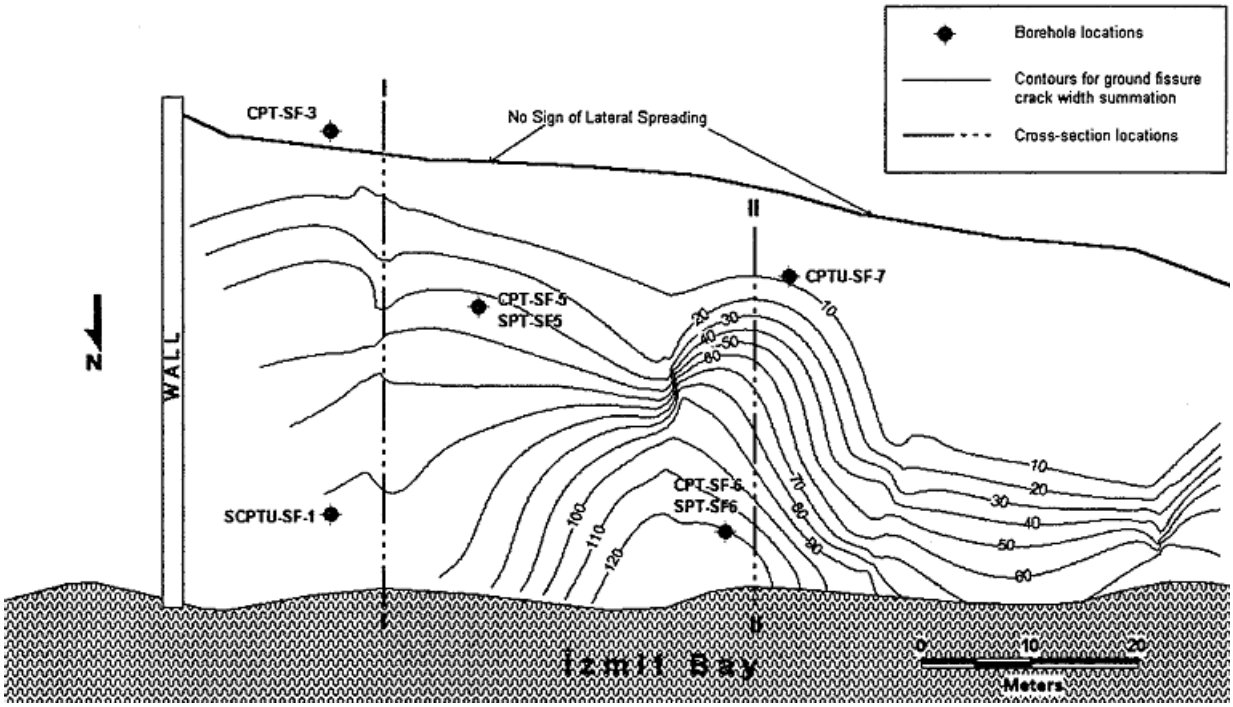

Figure 5.37: Map of ground cracks and penetration test locations at the Soccer Field site (Cetin et al. 2004b)

Yalova Harbor

At the Yalova Harbor site, lateral ground deformations accumulated to about 30 cm at the face of the harbor (Figure 5.38), about 5 km from the nearest fault rupture. The site was estimated to have experience a *PGA* of about 0.3 g, possibly based on USGS Shakemap estimates. Liquefaction occurred in a 5-7 m-thick, relatively homogeneous layer of silty sand, found at about 1 m below ground surface. The subsurface cross section produced by Cetin et al. indicates that lateral spread occurred on flat ground, toward a free face of approximately 3-4 m high. The 30-cm displacement contour chosen by O&J was at a maximum distance of 3 m from the free face; this would result in a free face ratio of 75-100%, calling into question whether the 30 cm displacement was due to actual cyclic mobility, or more to some degree of local instability at the free face.

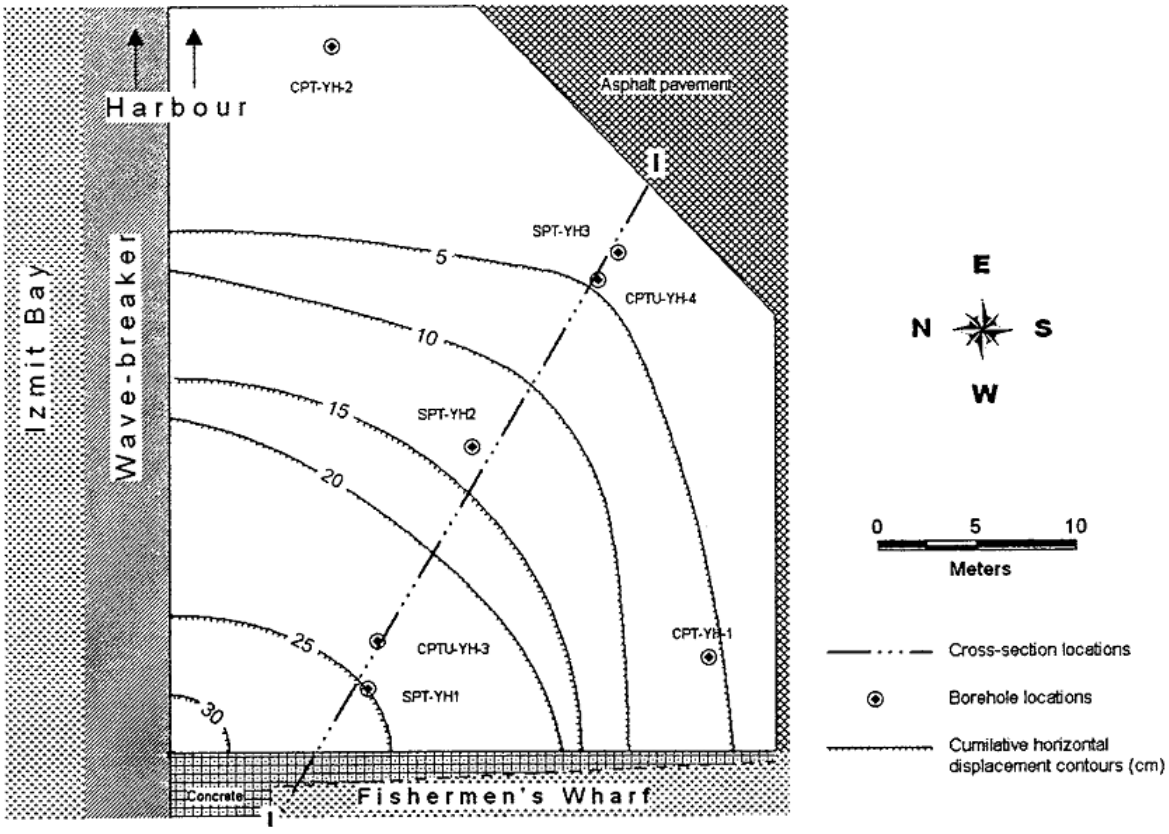

Figure 5.38: Map of ground cracks and penetration test locations at the Yalova Harbor site (Cetin et al. 2004b)

5.4.12 2003 San Simeon, CA

The 2003 San Simeon earthquake was an M_w 6.5 event that occurred with a reverse faulting mechanism in the complex Oceanic and Nacimiento fault zones of southern California. It has also been shown that the Hosgri and San Simeon fault zones may also have played a key role in the fault rupture. In Oceano, about 63 km southeast of the fault rupture, liquefaction and lateral spreading occurred in artificial fill and eolian sand deposits. Peak ground accelerations were unexpectedly high in Oceano, estimated between approximately 0.18 and 0.32 g. It is probable that local site amplification played a role in the relatively high ground motion intensities.

Holzer et al. (2004) conducted a site investigation in Oceano (Figure 5.39), and determined that two main deposits liquefied during the San Simeon event: artificial fill, which consisted of loose, clean fine sands; and clean eolian sand deposits. The investigation was conducted using only CPT soundings, and the equivalent N-values reported for lateral spreads at Norswing Drive and Juanita Avenue were determined by Olson and Johnson using the approximate conversion of Equation 5.1.

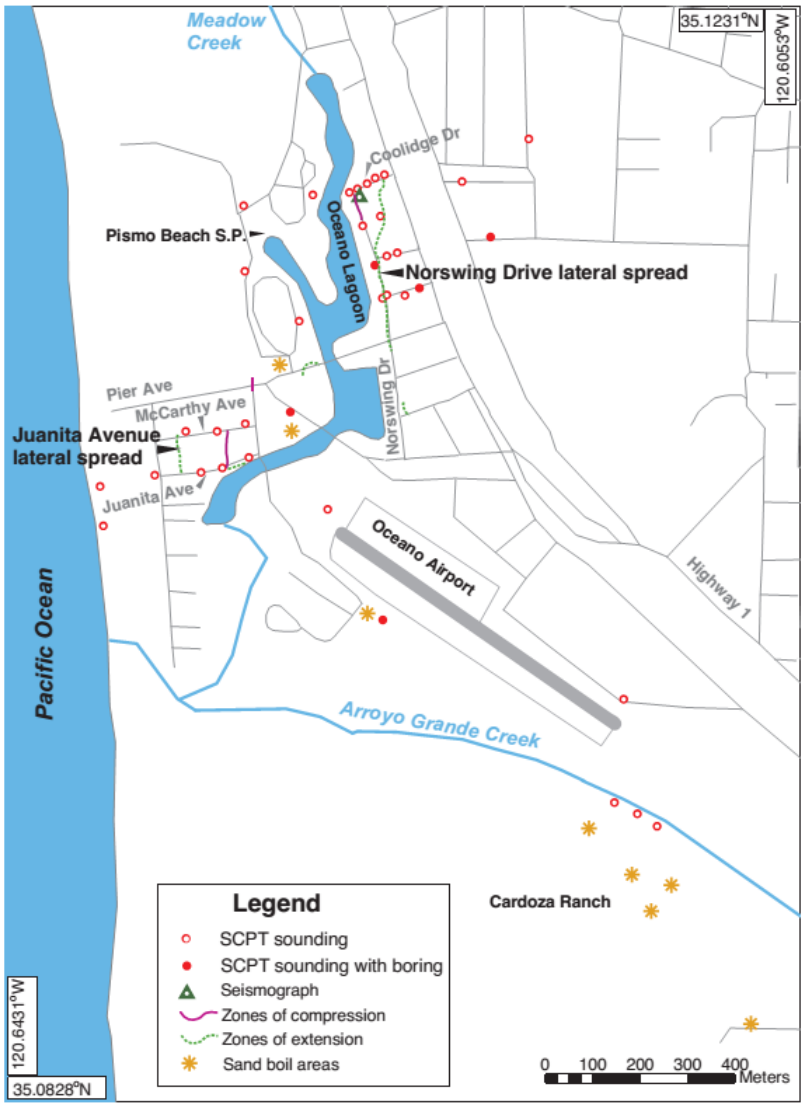

Figure 5.39: Map of lateral spread and subsurface investigation sites in Oceano, after the 2003 San Simeon earthquake (Holzer et al. 2004))

At Norswing Drive, lateral displacements of approximately 0.2 to 0.3 m, towards the Oceano Lagoon, were observed. The geometry of the spread was well-defined, it is clear that the deformations were driven by a combination of sloping ground (approximately 5% grade) and a free face ratio of about 3% at the edge of the lagoon. It was determined that liquefaction had likely occurred in about 3-5 m of eolian sand, as well as about 1 m of the artificial fill closer to the surface. Within about 100 m of the edge of the creek, the eolian sand and fill are separated by a thin layer of clayey marsh deposits (Figure 5.40). Thus, it is possible that there were multiple failure planes on which the lateral spread at Norswing Dr. occurred.

At Juanita Avenue, 0.2 to 0.3 m of lateral displacements were observed in the eastward direction. The spread occurred on essentially flat ground; it is likely that the spread was driven by static stresses from the 2% ground slope at the western extent of the spread,

just to the east of a sand dune (Figure 5.41). Based on CPT resistance (Holzer et al. 2004), liquefaction was determined to have occurred in an approximately 2 to 7 m-thick layer of artificial fill and eolian sands. Unlike the spread at Norswing Dr., no marshland deposits existed at the site to separate the two liquefiable strata.

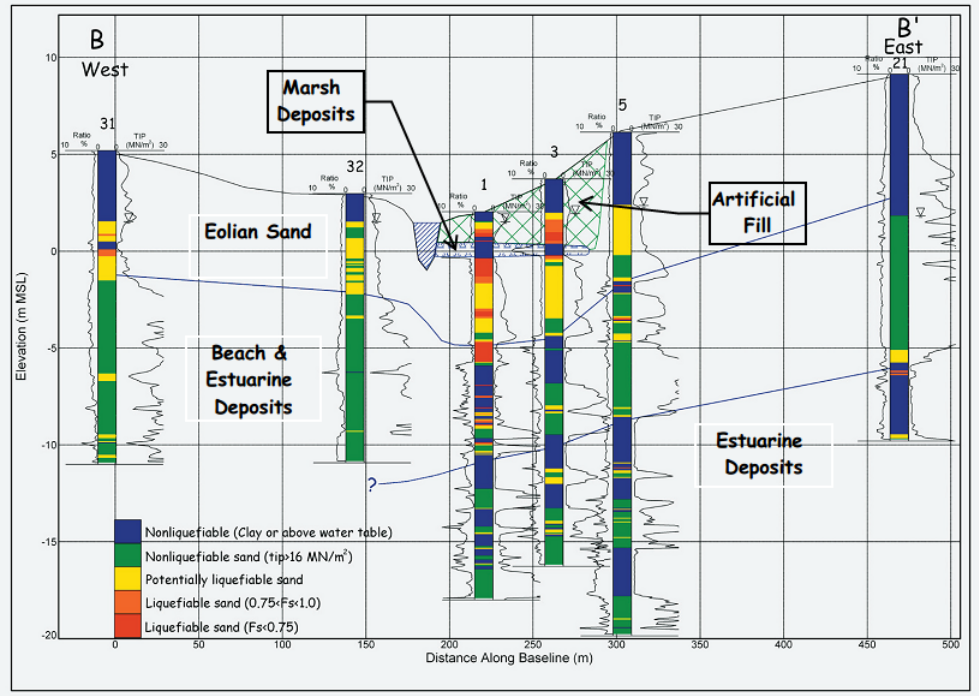

Figure 5.40: Profile of lateral spread at Norswing Dr, with liquefaction factors of safety for M = 6.5 and PGA = 0.25 g (after Holzer et al. 2004)

5.4.13 Summary

The potential sources of bias and uncertainty for each case as they pertain to the back analysis procedure are summarized in the Appendix. The effects of these biases and uncertainties on the final estimates of mobilized shear strength and penetration resistances are further discussed in this section.

Selection of Representative Displacements

In several cases (such as the Wufeng Sites and Yalova Harbor), O&J selected the maximum displacement vector closest to the free face for use in their sliding block analyses. In these cases, the free face ratio, W, was significantly above the 20% limit recommended by Youd et al. (2002) for use in analysis of lateral spreads. Youd argues that at locations with very high free face ratios, displacements are influenced by mechanisms outside of lateral spreading, such as slumping or rotational ground failures, as well as possibly flow

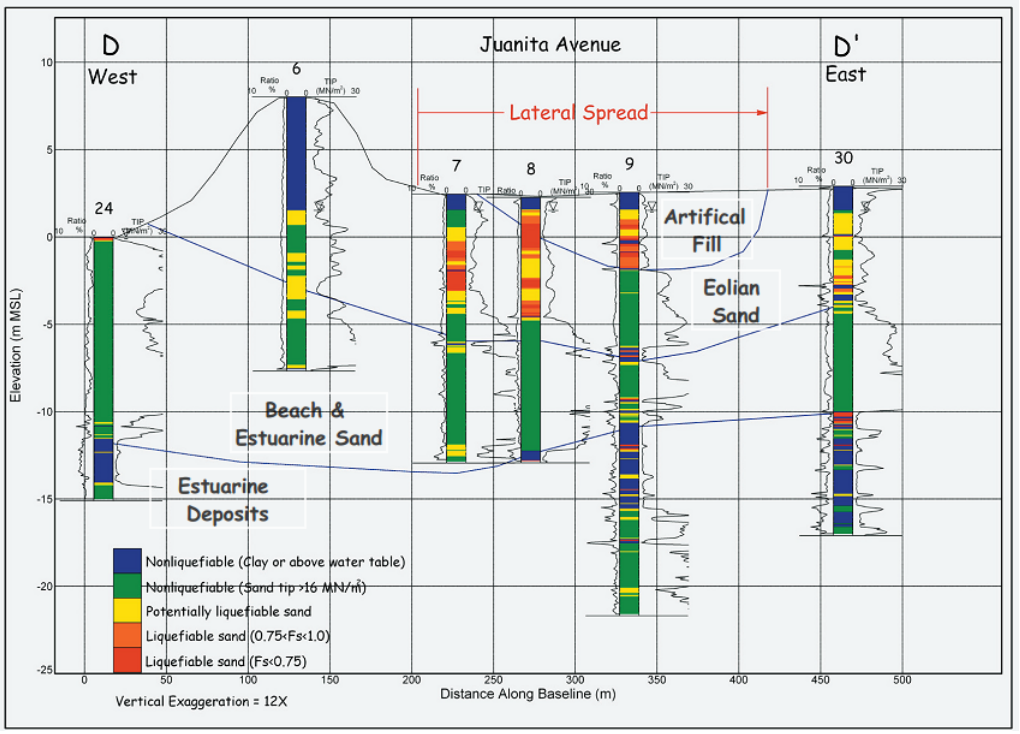

Figure 5.41: Profile of lateral spread at Norswing Dr, with liquefaction factors of safety for $M = 6.5$ and $PGA = 0.25$ g (after Holzer et al. 2004)

liquefaction. Thus, the higher observed displacement may result in under-prediction of the sliding block yield acceleration for the lateral spread, resulting in a lower estimate of the mobilized shear strength ratio of the liquefied material.

The use of an "accumulated" displacement, that is, the sum of the observed ground crack widths at the site, may also have biased and introduced unnecessary uncertainty into the back analysis procedure, particularly for ground slope cases. For the Hotel Sapanca Site (Section 5.4.11, the 2.0 m of accumulated displacement used by O&J is difficult to justify; if the lateral spread were instead modeled as an infinite slope with 10-50 cm of deformation, rather than a single 2.0 m displacement vector at the seawall, it would likely result in a more reliable characterization of the case history.

Selection of Representative Liquefied Stratum

In order to reliably apply Olson and Johnson's back-analysis framework, determining the layer of liquefied stratum primarily responsible for the lateral spreading manifestation is critical. It enables both the specification of a reasonable failure surface for pseudo-static analyses and the selection of a representative penetration resistance. For many cases

featuring clear strata of homogeneous clean sand, this process is relatively straightforward. However, for cases where the subsurface profile is largely heterogeneous, determining a single failure surface (and thus, a clear penetration resistance), can be a highly uncertain process. Green et al. (2014) defined this *critical layer* for liquefaction cases as the layer believed to have been primarily responsible for the surface manifestation of liquefaction. For lateral spreading cases, Green et al. posited that the critical layer is often relatively thin; as the thickness increases or relative density decreases, the magnitude and extent of lateral spreading should increase. Despite this general guideline, Green et al. implied that significant judgment should be used on a case-by-case basis, taking into account the topographic conditions at the site, as well as the lateral extent of the liquefied stratum relative to the lateral spread area.

As discussed earlier, there were often significant discrepancies between the author's estimates of penetration resistances and those given by the original investigators for each case history. Some of these discrepancies may due to high uncertainty in estimates of rated SPT hammer energy in some of the older tests performed. SPT borings performed in the 1970s and 1980s were less standardized, and a variety of samplers and hammer mechanisms were used without indication of the exact specifications in the published boring log. Thus, various researchers may use different energy corrections to estimate final $(N_1)_{60}$ values for a particular boring record, as we can see with cases like the Juvenile Hall (Section 5.4.1) and Whiskey Springs (Section 5.4.3) lateral spreads.

For sites where SPT and CPT data are abundant, further complications stem from the concept that selection of a representative penetration resistance is subject to the interpretation of different test measurements at the same site. Various researchers may weigh data from multiple boring logs equally, place more emphasis on data from a particular boring log, or may focus on a single boring log altogether in estimating a representative penetration resistance for the liquefied soil. This type of uncertainty was evident in the Moss Landing, Farris Farm, and Sea Mist Farm case histories (Section 5.4.6; where significant scatter in penetration resistances between boring logs and uncertainties in horizontal spatial extent of liquefied strata resulted in inconsistent, wide-ranging estimates of penetration resistances between different researchers.

Finally, as discussed in Section 5.2.4, the selection of a representative penetration resistance, particularly from a wide range of values, is highly dependent on the interpretation of the individual. One may select the mean of all the N-values in the liquefied stratum, the middle of the range of values, the most commonly occurring value (if there is one), or the minimum value. Alternatively, it may be reasonable to utilize the continuous and less uncertain nature of the CPT tip resistance data to estimate a representative q_{c1},

then use a correlation, such as that proposed by Robertson et al. (1983), to convert to an equivalent $(N_1)_{60}$ (while taking into account the uncertainty inherent to this conversion).

Aside from the complications involved in selecting a single failure surface at sites where multiple layers of liquefiable materials exist (Section 5.2.4), an equally critical component to the pseudostatic back-analysis process is determining how the weakest failure plane was selected for each case history. Most slope stability analysis programs run automated factor-of-safety analyses on a wide range of potential failure surfaces to determine the most likely plane of failure. In back-analyzing liquefaction-induced lateral spreads, however, the failure surface must be assumed to pass through the liquefied layer. For many cases, this failure mode may automatically be determined by the search algorithm itself, provided that the strength of the weak layer is set low enough by the user. Complications, however, arise for sites where a free face is reinforced by a sea wall, riprap slope, or any other type of reinforcement.

For these sites, such as the St. Francis Yacht Club and Treasure Island (Section 5.4.6), an automatic search algorithm may instead estimate a plane of failure that passes under the toe of the slope, and not necessarily through a significant portion of the liquefied material, if the sea wall is accurately modeled and sufficiently strong. This would result in an inaccurate relationship between yield acceleration and mobilized shear strength, one that is relatively independent of the shear strength of the weak layer (Figure 5.42), since only a small portion of the failure plane actually passes through the weak layer.

In these cases, the failure plane must be manually forced by the program user to pass through both the weak layer *and* the reinforced sea wall, the latter of which could be replaced by a representative resisting force. This would, in effect, maintain an accurate failure surface, and account for the smaller lateral deformation that the restricting seawall likely provided for each case. While most programs do indeed contain this capability, it is presently unclear whether it was utilized by Olson and Johnson in their analyses.

5.5 Comparison of Olson & Johnson (2008) and Youd et al. (2002) Databases

To evaluate whether the smaller dataset used by Olson and Johnson is representative of the broader and more definitive database from Youd, the 39 case histories were evaluated in terms of the site and source parameters identified by Youd as the key contributors to lateral spreading displacements:

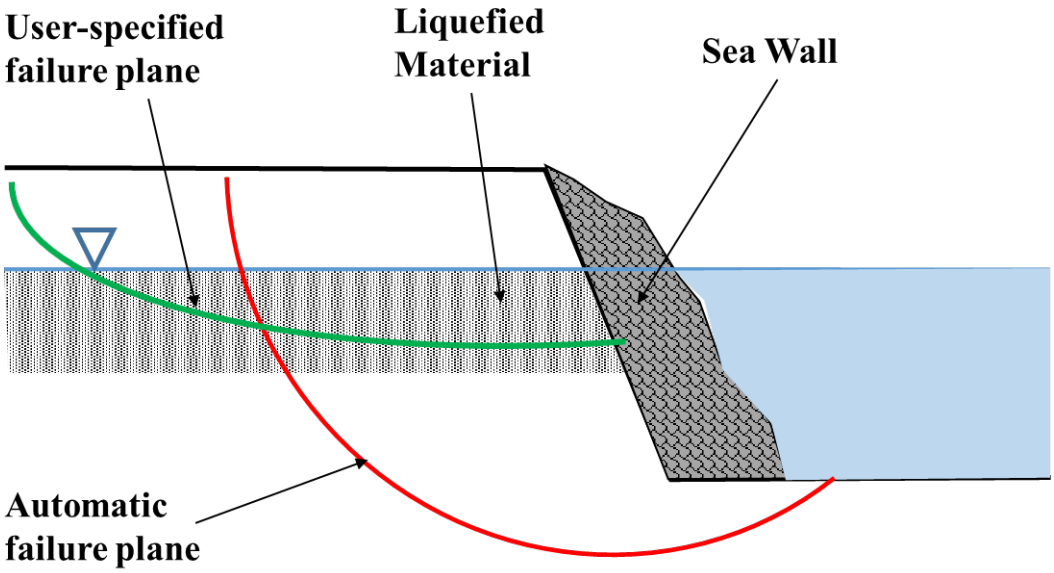

Figure 5.42: Comparison between hypothetical user-specified failure surface for lateral spreading conditions and automatically-generated failure surface in a general slope stability program for a typical site with a reinforced free face.

- Moment Magnitude, M_w
- Source-site distance, R
- Free face ratio, W
- Ground slope gradient, S
- Thickness of liquefied material with $N < 15, T_{15}$
- Fines content of liquefied material with $N < 15, F_{15}$
- Median grain size of liquefied material with $N < 15, D50_{15}$

In theory, any database assembled for these purposes should contain cases that represent a uniform distribution over a wide range of each of the variables. For each parameter, the values represented by both databases were compared to each other via their normalized histograms, means, and standard deviations. The O&J database was also evaluated in terms of the limits of applicability for each parameter, as recommended by Youd et al.

5.5.1 Results

For each significant parameter, comparisons are made by examining the histograms of parameter values for both the O&J and Youd databases. The mean value and standard deviation of each parameter are also presented.

Earthquake Souce Parameters

The two databases contain similar distributions of earthquake magnitude (Figure 5.43). With the exception of two 1906 San Francisco sites in Youd's dataset, both databases are within the recommended range of earthquake magnitudes (6.0 to 8.0). Examination of the source-site distance data (Figure 5.44) show that Youd's database is significantly influenced by the data from the 1964 Niigata and 1983 Nihonkai-Chubu sites, which account for 371 out of the 484 data points used in the multilinear regression. The lateral spreading sites for these two events were 21 and 27 km from the fault rupture, respectively. Thus, with over 75% of the cases represented by these two cases, the distribution of source-site distances in Youd's database is highly concentrated at its median of 21 km. The O&J database shows a broader and more uniform lognormal distribution of source-site distance values about its geometric mean of about 9 km.

Site Topography

The two databases differ significantly in terms of their distributions of free face ratios (Figure 5.45). The O&J database features significantly more lateral spreading cases that occurred very close to the free face, and thus the mean free face ratio (23%) is much higher than the 8% mean free face ratio seen in Youd's case histories. Furthermore, over 60% of O&J's free face cases feature values of W that are significantly higher than the upper limit of 20% recommended by Youd et al.

Examination of the ground slope cases (Figure 5.46) showed that Youd's database heavily emphasizes lateral spread sites with very gently sloping ground; nearly 80% of the cases surveyed by Youd et al. involved ground slope inclinations of less than 1%. O&J's database only included 10 ground slope cases in total, with three out of the 10 cases exceeding the recommended ground slope grade of 6%.

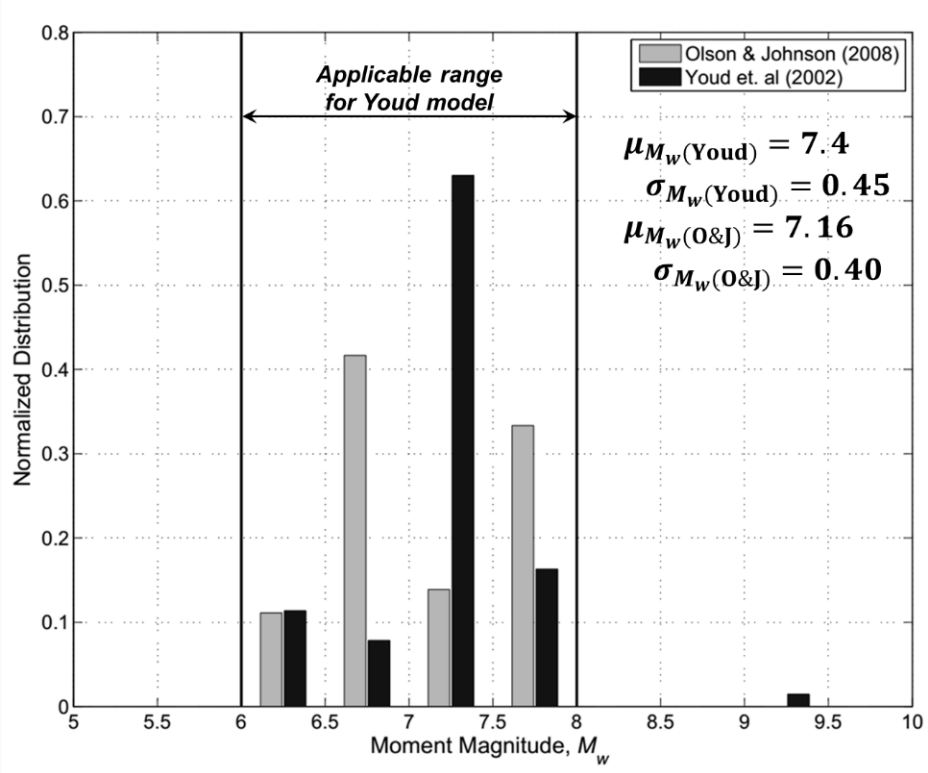

Figure 5.43: Normalized histograms of moment magnitude for the Youd et al. (2002) and Olson and Johnson (2008) databases.

Liquefied Soil Characteristics

Comparison of the distributions of T_{15} values (Figure 5.47) shows that the O&J database case histories generally represent the lower two-thirds of the range of T_{15} values that were examined by Youd et al. (1 to 15m) The fines content data (Figure 5.48) shows that Youd's database has a lower average F_{15} value and contains a higher proportion of clean-sand cases than O&J's database, which features a significant proportion (about 25%) of cases that have fines contents above 20%, and covers a broader range of fines contents.

Plotting F_{15} against $D50_{15}$ for both datasets (Figure 5.49) shows that the liquefied soil parameters in O&J's case histories reasonably approximate the larger dataset used by Youd et al. The geometric mean of the grain sizes are comparable, and the O&J database actually represents a more broad distribution of fines contents and grain sizes. Furthermore, only four O&J cases lie outside the boundaries of applicability.

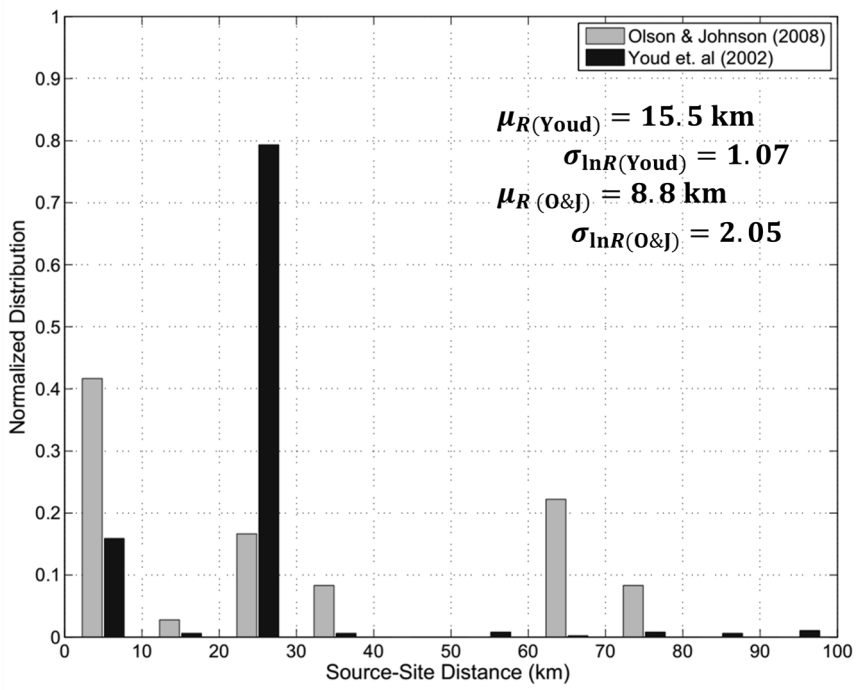

Figure 5.44: Normalized histograms of source-to-site distance for the Youd et al. (2002) and Olson and Johnson (2008) databases. Mean and standard deviations are presented assuming R is lognormally distributed

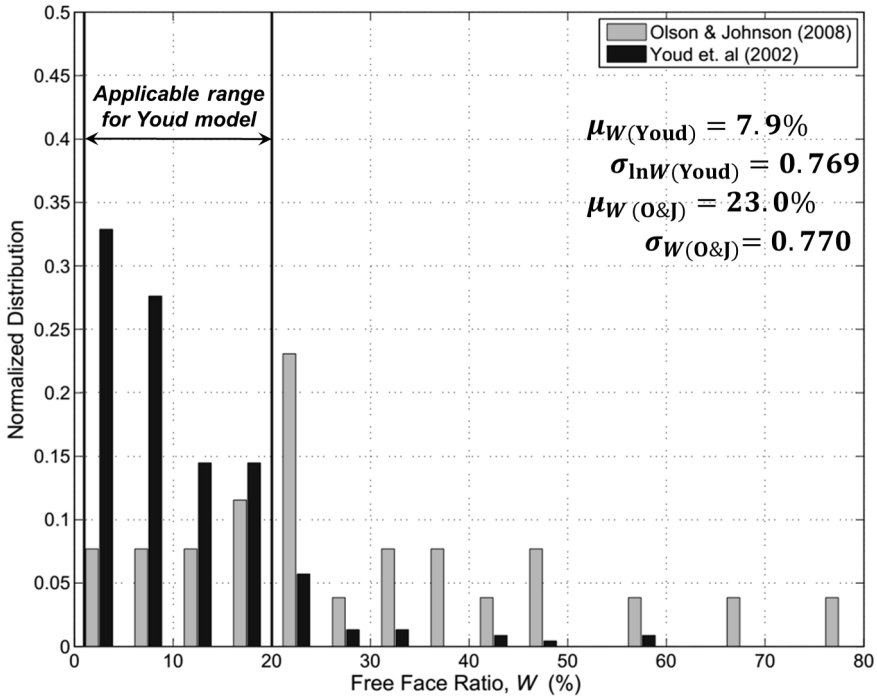

Figure 5.45: Normalized histograms of free face ratio for the Youd et al. (2002) and Olson and Johnson (2008) databases. Mean and standard deviations are presented assuming W is lognormally distributed

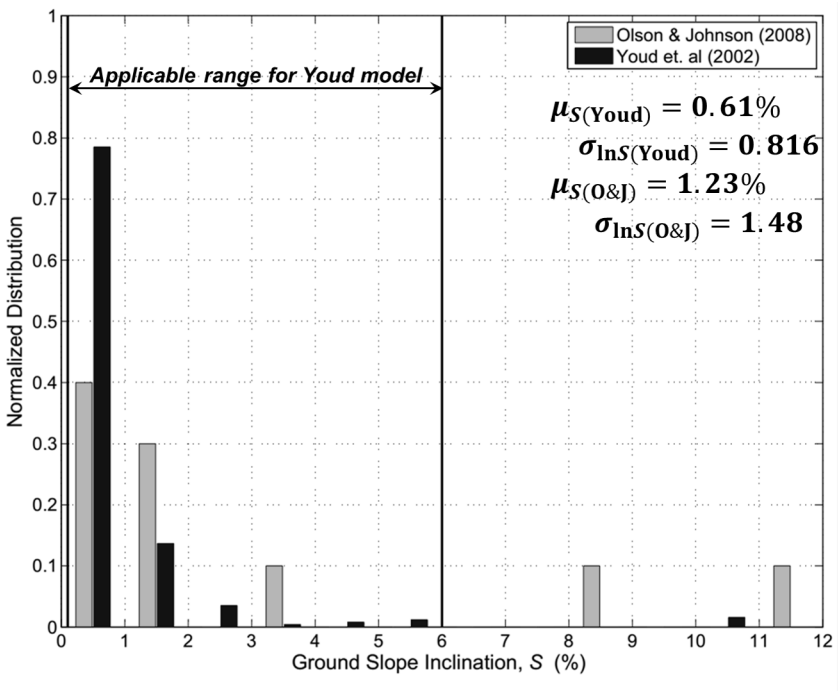

Figure 5.46: Normalized histograms of ground slope inclination angle for the Youd et al. (2002) and Olson and Johnson (2008) databases. Mean and standard deviations are presented assuming S is lognormally distributed

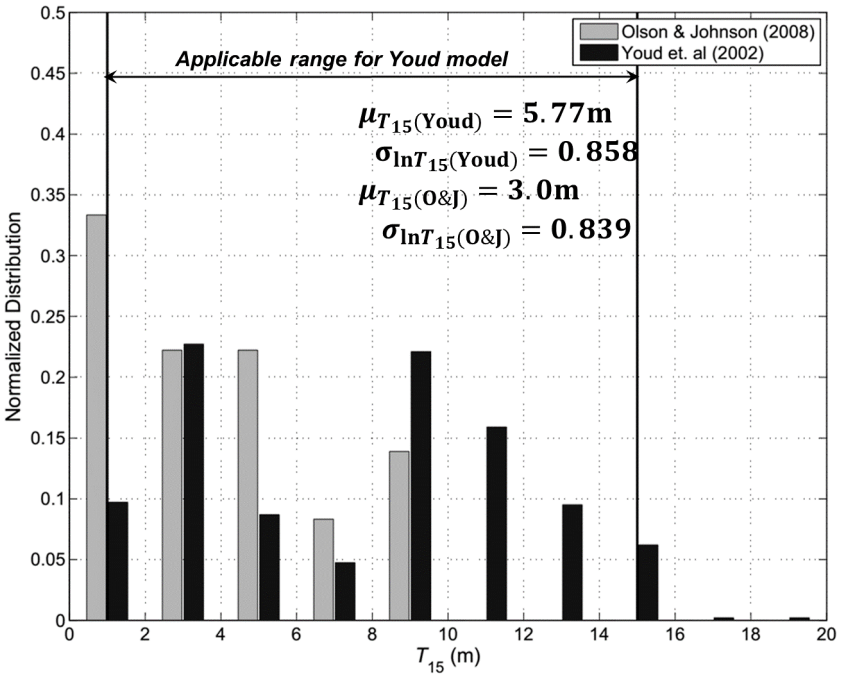

Figure 5.47: Normalized histograms of thickness of liquefied strata with $N_{SPT} < 15$ bpf for the Youd et al. (2002) and Olson and Johnson (2008) databases

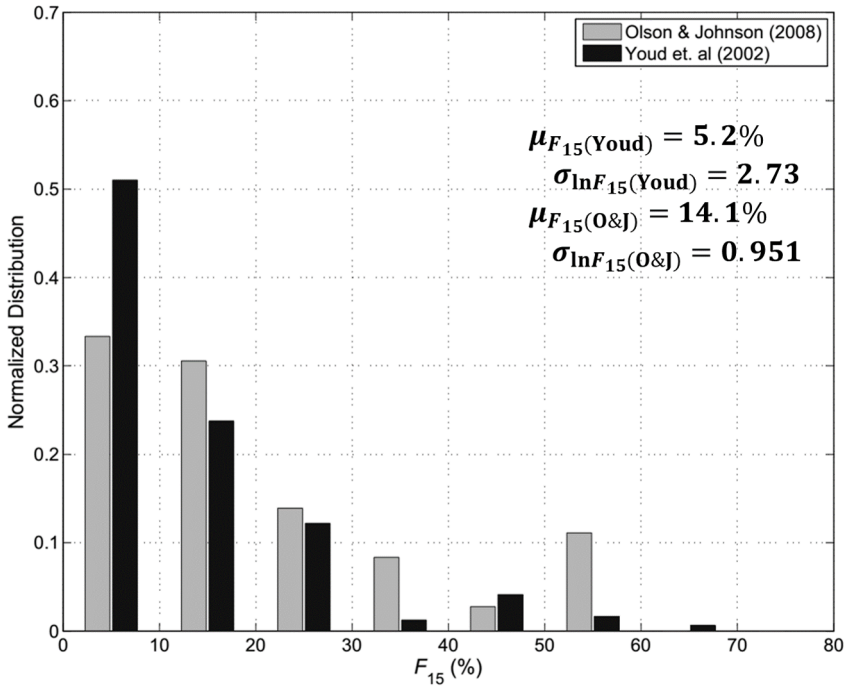

Figure 5.48: Normalized histograms of thickness of liquefied material with $N_{SPT} < 15$ bpf for the Youd et al. (2002) and Olson and Johnson (2008) databases. Mean and standard deviations are presented assuming S is lognormally distributed.

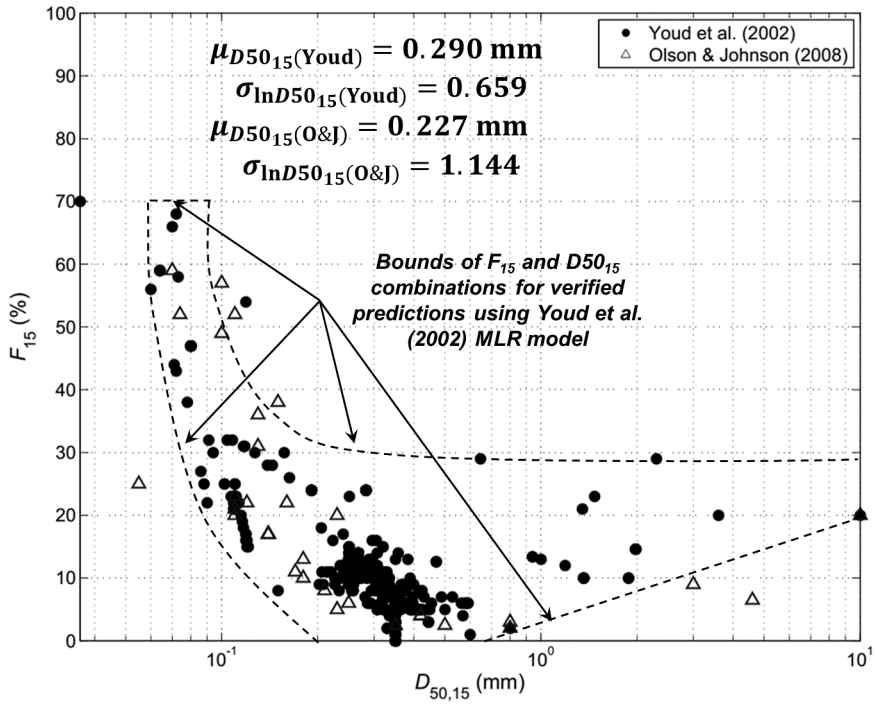

Figure 5.49: Combinations of grain size and fines content for both Youd et al. (2002) and Olson and Johnson (2008) datasets; bounds of verified predictions for MLR model included (after Youd et al., 2002)

5.5.2 Summary

The means and standard deviations of both databases for each parameter are summarized in Table 5.6 and visualized using the box-and-whisker plots in Figure 5.50. Additionally, the Z-test score between the two distributions is computed and shown for each parameter. The Z-test is a technique used to test whether or not two samples belong to the same population; in this case, the population refers to the various parameters associated with lateral spreading sites, as defined by Youd's 2002 model. The Z-test score for a given parameter x is calculated using the mean and standard deviations of the two databases:

$$Z = \frac{\mu_{x,1} - \mu_{x,2}}{\sqrt{\sigma_{x,1}^2 - \sigma_{x,2}^2}} \tag{5.2}$$

Generally speaking, two samples belong to the same distribution if the absolute value of their Z-test score is less than 2. Based on the values shown in Table 5.6, the distributions from both the Youd and O&J databases appear to coincide for each parameter. One caveat, however, is that the distributions for the free-face ratio and ground slope inclination were assumed to be lognormal. In reality, they may actually have some upper-bound truncations

that coincide with Youd's defined upper-limits for lateral spreading deformations, possibly at or slightly higher than the 20% and 6% recommended values for W and S, respectively. Both databases have distinct characteristics that lead to potential biases. The Olson and Johnson database, due to its relatively small number of data points, is much more subject to gaps in otherwise consistent distributions of source and site parameters. The Youd et al. database, because of its heavy reliance on the 1964 Niigata and 1983 Nihonkai-Chubu cases, is biased towards both the moment magnitudes and source-site distances from these cases, which otherwise display consistent distributions in their site parameters.

The O&J database, despite having significantly fewer data points, represents near-fault, intermediate, and distal sites in a relatively consistent distribution, and may in fact be a more realistic database in terms of source-site distance than Youd's database. However, of the 36 cases with known topographic dimensions, 19 of them feature ground slope angles or free face ratios that are greater than the limits recommended by Youd. For free face ratios above 20%, lateral displacements can be influenced heavily by local instabilities, such as rotational slumping, ravelling, or toppling ground failure near an embankment.

The two databases differ slightly in terms of the characteristics of the liquefied material. Compared to Youd's database, the O&J database generally represents a smaller range of thinner liquefied layers, comprised of slightly coarser sands with higher fines contents. The O&J database also contains four cases with combinations of mean grain size and fines content that are outside the range of the Youd's database (see Figure 5.49), as well as three cases with T_{15} values thinner than the 1 m lower limit (See Table 4.1).

Overall, 22 of the case histories analyzed by O&J feature at least one parameter that falls outside the limits recommended by Youd et al., most common of which are the free face ratio and combination of fines content and mean grain size. The fines content and grain size parameter constraints are generally defined by the range of soil characteristics in the case histories used by Youd et al. for MLR regression. In other words, while extrapolating Equation 4.7 for use in cases whose soil parameters lie outside the applicable range should be done with caution, it does not necessarily imply that the predicted lateral spreading displacements could not have occurred in soils outside the $F_{15} - D50_{15}$ range.

However, the cases in which the free face ratios significantly exceeded the 20% upper limit may present the most significant potential concern. Many of the cases Olson and Johnson analyzed involved ground cracks or inclinometers that had free face ratios greater than 20%, and as discussed earlier, displacements at these close distances can be heavily influenced by mechanisms other than lateral spreading. If we additionally consider sites with ground slopes about the 6% upper limit, then a total of at least 16 of the cases were

back-analyzed using the sliding block framework that may diverge significantly from the mechanisms under which displacements at the site manifested.

Table 5.6: Summary of Z-test scores, mean and standard deviation for each parameter in both Youd and Olson and Johnson databases

Parameter	Z-Score	Youd		Olson and Johnson	
		Mean	Std Dev.	Mean	Std Dev.
M_w	0.363	7.4	0.5	7.2	0.4
R (km)	0.244	15.5	1.07	8.8	2.05
W (%)	-0.979	7.9	0.769	23	0.77
S (%)	-0.420	0.61	0.816	1.23	1.48
T_{15} (m)	0.538	5.8	0.858	3.0	0.839
F_{15} (%)	-0.588	5.2	2.73	14.1	0.951
$D50_{15}$ (mm)	0.171	0.29	0.659	0.23	1.14

5.6 Concluding Remarks

In this chapter, the lateral spreading database used to develop the Olson and Johnson (2008) procedure for predicting lateral spreading displacements was analyzed and compared to the larger and more definitive database compiled by Youd and Bartlett (1992) and Youd et al. (2002). In doing so, not only were important conclusions drawn about how the O&J database represents the conditions under which lateral spreading typically occurs, but significant conclusions were also made about how reliably the database was applied to the Olson and Johnson back-analysis procedure that was used to develop their model.

It is important to note that the Youd and O&J models were developed using significantly different methodologies, and thus we cannot expect their databases to be completely compatible with each other. The use of multiple linear regression for Youd's model allows for the use of a massive database of lateral spreading vectors. The O&J model is based on a far more rigorous back-analysis method, requiring site-specific information that is not always available; time constraints would not allow for such a method to be applied to nearly 500 case histories. Even so, the both methods do purportedly predict lateral spreading displacements, and ideally should be based on comparable conditions.

With that in mind, there are several significant key differences between the two databases that should be discussed here. Firstly, it must be noted that Youd's database relies overwhelmingly on data from two sites; displacement vectors from the 1964 Niigata and 1983 Nihonkai-Chubu events account for over three quarters of the case histories in that database. Furthermore, it should be noted that Youd's database used multiple

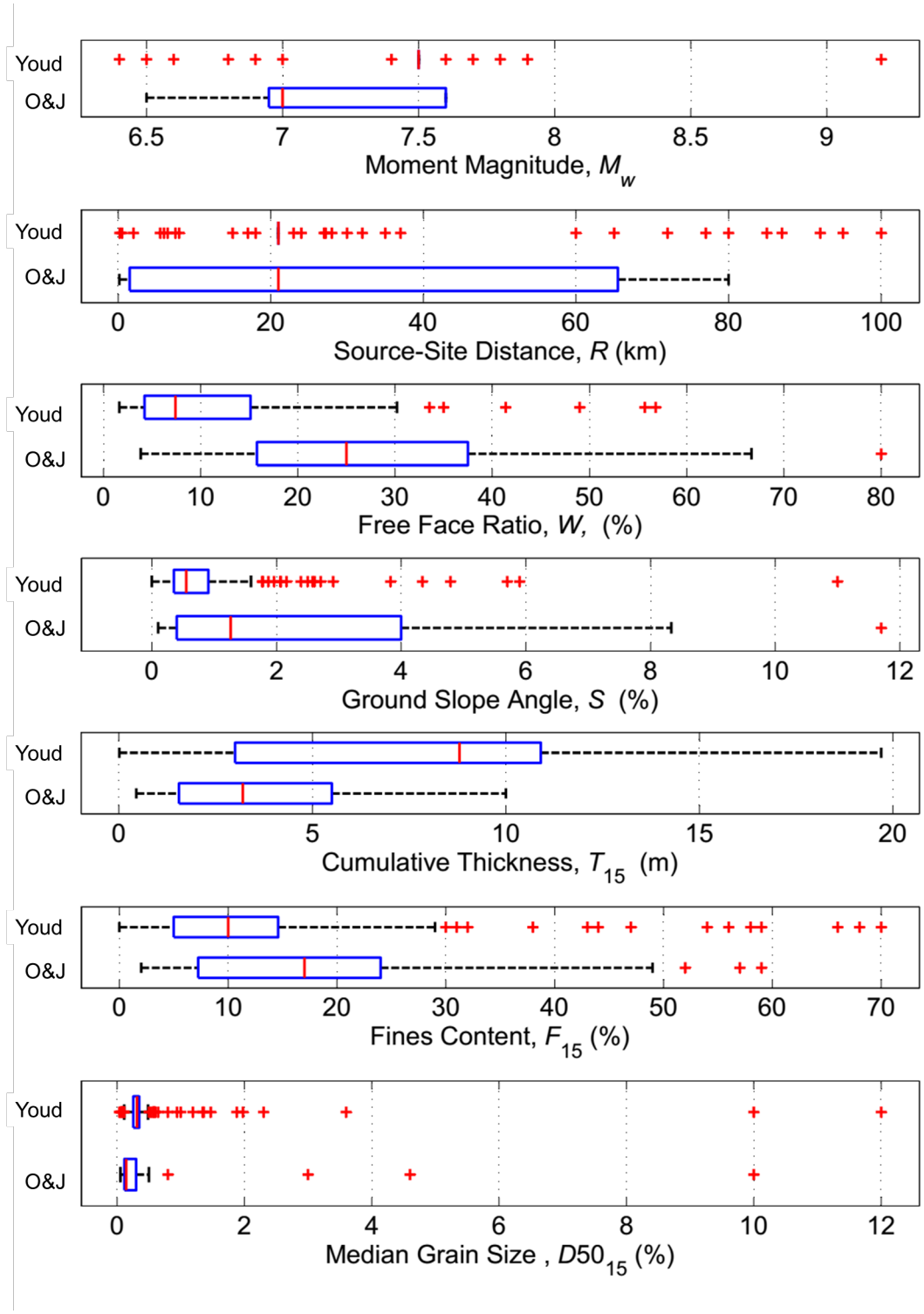

Figure 5.50: Comparison of box-and-whisker plots between O&J and Youd databases, with respect to Youd et al. (2002)*MLR* parameters

vectors from the same spreading sites as separate case histories, implying that they are independent data points when they in fact are most likely highly correlated with each other.

Olson and Johnson's database is far more balanced in this respect. Secondly, a significant number of the case histories from O&J's database feature free face ratios that are significantly higher than 20%. As stated previously, at free face ratios above 20%, static shear stresses are potentially high enough such that cyclic mobility-and thus, lateral spreading-is not the only deformation mechanism in the soil. An argument can be made that over half of O&J's lateral spreading database may not even represent the mechanism of lateral spreading. This is largely a result of the authors' decision to select a single representative displacement value at sites with a range of observed ground crack widths; often, the representative value was taken as the maximum displacement with the highest free face ratio. Furthermore, the six cases from the 1990 Luzon earthquake in Dagupan were explicitly described as likely flow failures by the primary investigators (Ishihara, 1993). These factors raise the question of whether the Olson and Johnson database is truly representative of the conditions under which lateral spreading displacements normally occur.

There are also some points of discussion about the O&J database as it pertains to the application of their back-analysis procedure. As discussed in Section 5.4.13, there are a few components of the back-analysis procedure that are highly sensitive not only to the quality of the data, but also to the actual site conditions themselves. First, uncertainties and inconsistencies in estimating the site PGA were present in a number of the cases analyzed, thus likely resulting in wide scatter or biased estimates of the sliding block-based yield acceleration. The vertical and horizontal extents of the liquefied material also play a significant role in how consistent the inherent assumptions of the sliding block and pseudo-static models are with the actual mechanisms experienced at the site. Specifically, the assumption and subsequent selection of a single plane of failure along which the strains are concentrated would have been difficult to implement in at least five of the 39 cases. Finally, the difficulties inherent in selecting a representative penetration resistance to plot against the back-calculated strength ratios have been well-documented by numerous researchers, and were no less conspicuous in the case histories analyzed here.

Chapter 6

GENERAL ISSUES IN CONVENTIONAL SLIDING BLOCK ANALYSES

6.1 Introduction

The Newmark framework for evaluating seismic slope stability (see Section 4.2.3) has seen wide usage in geotechnical earthquake engineering over the past few decades. It relatively simple and quick to implement, and can provide a reasonable assessment of the stability of a site on sloping ground or near a free face, as well as a range of potential displacements a site might experience in the event of an earthquake. The sliding block analysis method is a significant improvement over pseudo-static limit equilibrium analyses in both its ability to estimate actual slope displacements, and its more complete implementation of the effects of ground motion characteristics.

There are a few different ways the sliding block method can be implemented in a practical setting. Firstly, it can be used in a case-specific manner, where a suite of ground motions is obtained based on the ground motion characteristics of a design seismic event. There are a few different strategies that can be employed to obtain a suite of ground motions for this purpose; one of the most popular, known as the "NGA Method", will be discussed in Section 6.2. The other common way that the sliding block method is utilized is via a classification of models developed by numerous researchers, known as *sliding block models*. These models are based on the statistical regression of a large volume of Newmark analyses, and generally predict sliding block displacements as a function of

the yield acceleration (see Section 4.2.2) and some combination of various ground motion characteristic parameters. These models are introduced and discussed further in Section 6.4.

As with any method that involves a simplification of the system it intends to model, it is instructive to examine some of the ways in which a sliding block model differs from an actual site subjected to strong ground shaking. To that end, some of the issues inherent to conventional sliding block analyses are discussed herein; specifically, the basic assumptions of a rigid mass and deformation along a discrete failure surface and their effects on predicted displacements are examined. Additionally, other issues related to the manner in which sliding block analyses may be applied, such as the directionality and dimensionality of the input ground motion and the restriction of sliding to a single direction are discussed as well. Finally, the uncertainty inherent in using multiple ground motions to characterize the permanent deformation expected at a site is also discussed.

6.2 Ground Motion Selection

In order to establish a relationship between observed lateral displacements and sliding block-generated yield accelerations for a particular site and a particular seismic event, a suite of ground motions must be obtained. The ground motion suite should be sufficiently large so that outlier ground motions should not have an outsize impact on the central tendency of the sliding block results. A reliable ground motion suite should also contain ground motions that have characteristics similar to ground motions that would be produced by the design earthquake at the site of interest. Thus, establishing criteria for how ground motions should be selected is a critical component in employing the sliding block method. An optimal search criteria is one that is not particularly restrictive, but still manages to find motions with compatible intensity, frequency content, and duration parameters for the source and site conditions of interest.

6.2.1 The NGA Ground Motion Selection Method

A commonly-used criteria for selecting ground motions, which will be referred to as the "NGA Method", often utilized by researchers and practitioners, is to generate a target spectrum for a particular combination of site characteristics and earthquake parameters. The target spectrum can be generally estimated by using ground motion prediction equations (GMPEs). GMPEs are empirical models, based on the regression of a vast amount of ground motion data, which use predictor variables such as the magnitude and geometry of

the fault rupture, different measures of source-site distance, and site stiffness parameters to predict the expected intensity and frequency content of ground motions at the site of interest. The resultant output is a smoothed response spectrum, which can be used as a target spectrum for comparison to the response spectra of a large number of potential candidate motions.

Target Response Spectrum

The NGA approach is generally employed by taking the average response spectrum from four 2014 NGA West-2 GMPEs: Abrahamson, Silva, and Kamai (2013); Boore, Stewart, Seyhan, and Atkinson (2014); Campbell and Bozorgnia (2014); and Chiou and Youngs (2014). GMPEs are almost always used for forward-prediction analyses, where the researcher or practitioner wishes to make a future prediction about displacements at a site where a particular seismic event is yet to occur.

GMPEs are also used extensively in back-analysis procedures, where sliding block analyses may be used at sites where permanent displacements occurred during a seismic event, in an attempt to assess the strength of the failed material. In the relatively rare cases where actual ground motion data is available at the site in question, however, the target spectrum can be based on the deconvolution of surface motions to a bedrock-type response spectrum; in the even rarer cases when downhole accelerations are available, the target spectrum can be derived directly from these downhole motions.

Once the target spectrum is determined, an initial set of "candidate" ground motions may be obtained, often comprising of motions that may have a similar magnitude, rupture mechanism, source-site distance, and/or site stiffness to the design case. Each candidate acceleration time history is then converted to the frequency domain using a fast Fourier transform (FFT) to obtain its response spectrum. A range of scaling factors are then applied to the ground motion; for each scaling factor the scaled response spectrum is compared to the target spectrum using the mean-square error (*MSE*) between the two spectra:

$$MSE = \frac{1}{n_T} \sum_{i=1}^{n_T} [\hat{S}_a(T_i) - S_a(T_i)]^2 \tag{6.1}$$

where n_T is the number of time period points for which S_a, the spectral accelerations, are being compared. The optimal scaling factor for that particular ground motion corresponds to the minimum *MSE*. The optimally-scaled candidate motions are then selected based on

minimum *MSE* for Newmark sliding block analyses.

Practical Considerations

The NGA West GMPEs were developed quite rigorously from a large database of ground motions, and are used throughout academia and industry to predict ground motion characteristics. It should be noted, however, that a significant amount of uncertainty exists in the use of these equations. The Wildlife Instrument Array site in Imperial Valley during the 1987 Superstition Hills Earthquake provides a convenient example of this. The site and source parameters (Table **??**), which have been thoroughly documented, can be used as inputs to the four GMPEs to obtain the estimated mean response spectrum, along with the +/- one standard deviation spectra, for the site. The spectral accelerations are lognormally distributed, with a standard deviation ($\sigma_{\ln S_a}$) of about 0.55. This level of scatter is quite significant, corresponding to an estimated *PGA* between about 0.08 to 0.23 g.

Table 6.1: GMPE input parameters for Wildlife Array site,1987 Superstition Hills Earthquake

Moment Magnitude	6.5
Faulting Style	Strike-slip
$R_{rup}, R_{jb}, R_x, R_{y0}$ (km)	26, 26, 26 , 2
v_{s30} (m/s)	208
F_{RV}, F_{NM}, F_{HW}	0, 0, 1
Dip angle (degrees)	90
z_{tor}, z_{hyp} (km)	0, 9
$z_{1.0}$ (m), $z_{2.5}$ (km)	20, 5
Rupture Width (km)	12

The mean, upper-bound, and lower-bound target spectra correspond to a relatively wide range of ground motion spectral intensities; while the target spectrum is usually taken to be the mean GMPE-estimated spectrum, it is often helpful to make sure the scaled ground motion spectra fall within the upper- and lower-bound target spectra as well. It is also useful to compare actual downhole accelerograms taken from the site during the 1987 Imperial Valley event to the GMPE target spectra (Figure 6.1. The rotated "d50" record, which is obtained from the two orthogonal horizontal component records. It is clear that the actual record largely falls within the standard deviations for

nearly the entire range of periods, although there is some long-frequency spectral intensity that isn't predicted by the GMPEs.

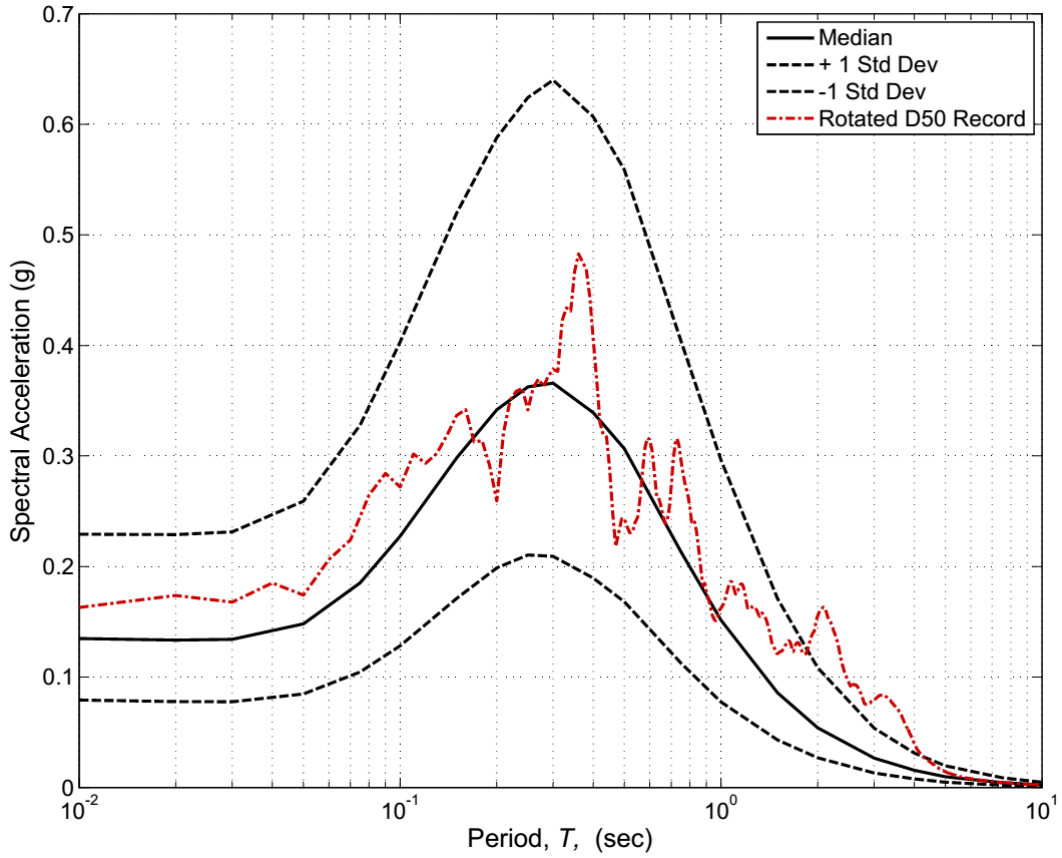

Figure 6.1: GMPE-estimated response spectra plotted with rotated "d50" spectrum from downhole ground motion records at the Wildlife Instrument Array site from the 1987 Superstition Hills earthquake.

6.3 Directionality and Dimensionality of Ground Motions

Another important component of the Newmark sliding block analyses has to do with the manner with which ground motions are applied to the sliding block. Recorded ground motions generally have three components: two orthogonal horizontal components, and a vertical component. It is up to the practitioner to decide which of these components to include in the sliding block analysis (i.e., how *dimensionality* effects are accounted for), and how the direction of the components should relate to the direction of the slope itself (known as *directionality*). Kramer and Lindwall (2004) considered both of these factors and their effects on computed sliding block displacements.

6.3.1 Ground Motion Characteristics

When ground motion records are obtained and applied to sliding block or other types of dynamic analyses, the vertical component of the motion is often not considered. Furthermore, the horizontal components may be considered as separate components, and evaluated individually based on how well they might fit certain ground motion selection criteria (see Section 6.2). It has often been assumed that vertical accelerations (a_v) are roughly two-thirds the magnitude of horizontal accelerations (a_h), and that horizontal components do not differ significantly between themselves. At large source-site distances, these assumptions general hold true.

However, at near-field sites, these assumptions are not always consistent with what has been observed in ground motion records. It has been found that a_v/a_h can vary significantly with magnitude, distance, site stiffness, and frequency, and can increase to greater than unity for near-field sites at short periods. Additionally, differences between near-field horizontal components can be quite significant as well, with fault-normal components observed to feature significantly higher amplitudes than fault-parallel motions. Rupture directivity can also have effect on ground motion characteristics; sites that lie towards the propagation of the fault rupture can have significantly different amplitudes, frequency contents, and durations than sites that site "behind" the fault rupture.

6.3.2 Dimensionality

Kramer and Lindwall (2004) (referred to herein as "K&L") identified four approaches to considering the dimensionality of ground motions as they apply to the sliding block procedure (Figure 6.2). The simplest approach is to consider the recorded motion as parallel to the inclined plane, known as a *pseudo-tangential* motion. A layer of complexity can be added by resolving the vertical and horizontal components in the downslope direction, obtaining a *true tangential* motion. The third approach is to consider the motion in two dimensions by applying both the horizontal and vertical motions to the plane, known as the *true two-dimensional* approach. The fourth approach is to additionally consider the second horizontal component, and apply all three component motions to the sliding block, thus creating a *true three-dimensional motion.*

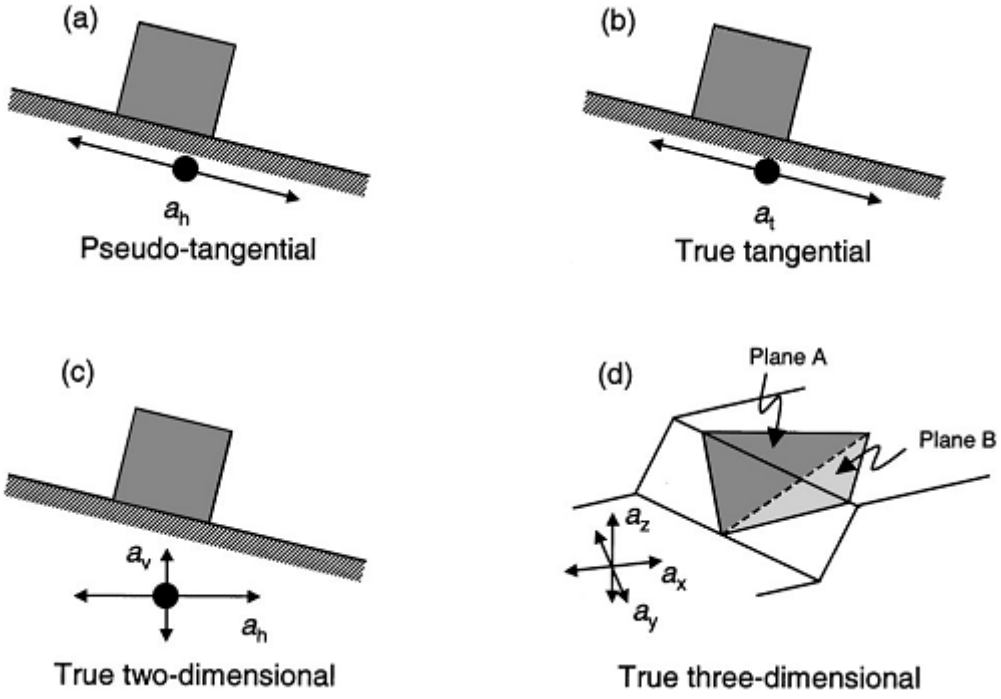

Figure 6.2: Illustration of various approaches in considering ground motion components for application to Newmark sliding block analyses (Kramer and Lindwall 2004)

K&L applied all four motion types to a range of slope inclination angles and static factors of safety. Using the results from the true 2-D motions as the "actual" displacement, K&L defined the *displacement ratio* as the ratio of the computed displacement using the pseudo-tangential and true tangential motions to the actual computed displacement obtained using the true 2-D motions. The displacement ratios for each of the first three motion types were plotted against slope inclination (Figure 6.3a) and factor of safety (Figure 6.3b) for purely frictional and purely cohesive slopes.

For relatively flat slopes below about 10°, the effects of using single component motions instead of multiple component motions are negligible. For steeper slopes where the shearing resistance is purely frictional, single-component analyses tend to significantly under-predict sliding block displacements for slopes whose strength is purely frictional; the displacement ratios decrease with both increasing slope inclination and increasing frictional strength. For slopes where the shear strength is primarily cohesive, the pseudo-tangential analyses actually *over-predict* the sliding block displacements for increasing slope inclination and increasing cohesion. Unsurprisingly, the true tangential analyses for cohesive slopes produced the same results as the true 2-D analyses, due to the fact that the addition of vertical stresses do not affect the cohesive strength.

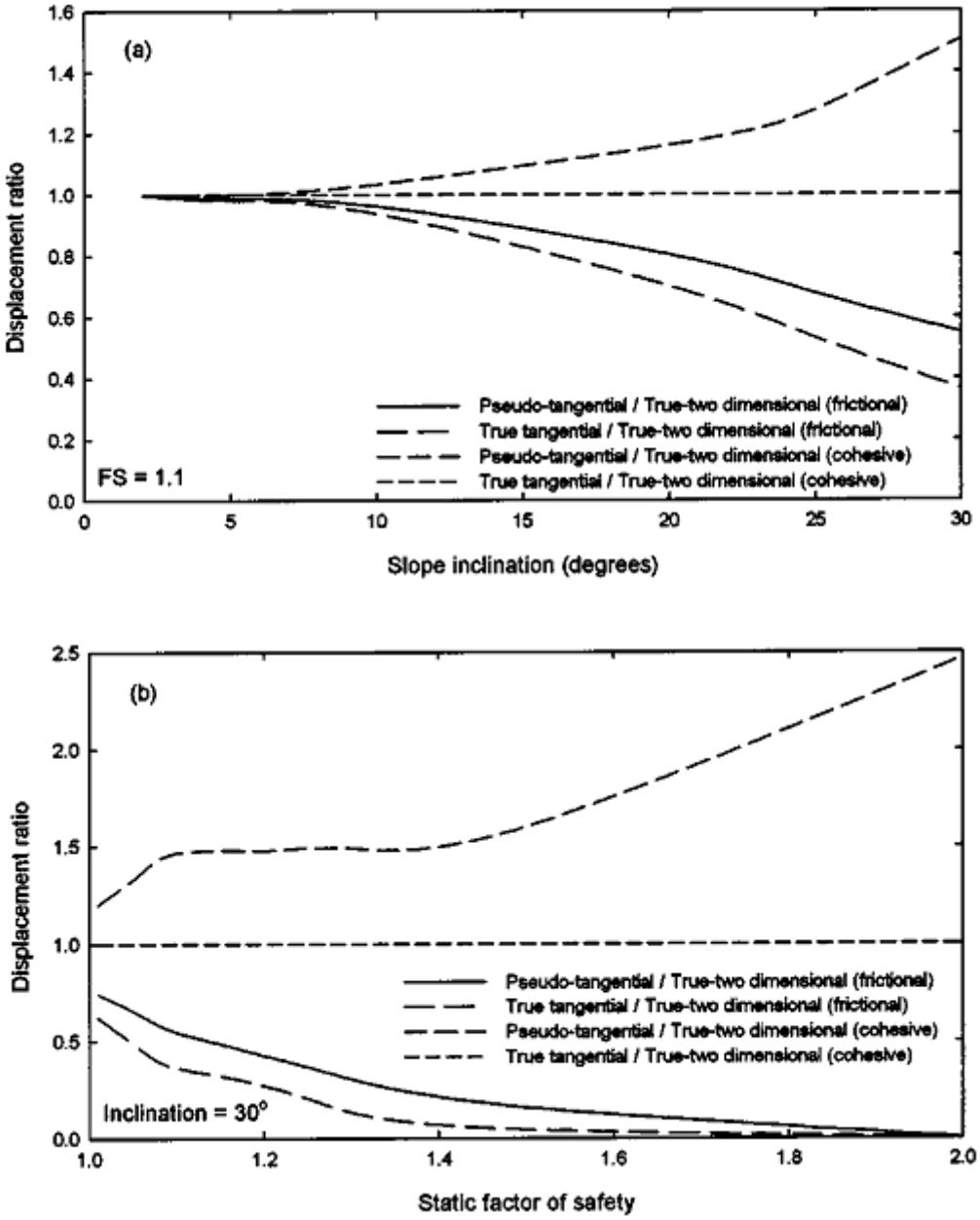

Figure 6.3: Variation of displacement ratio, with respect to (a) slope inclination and (b) static factor of safety, for Newmark analyses performed with psuedo-tangential, true tangential, and true two-dimensional ground motions (Kramer and Lindwall 2004)

6.3.3 Directionality

In practical settings, the use of single-component input ground motions in sliding block analyses inherently assumes that the ground motion direction is coincident with the dip direction of the slope of interest. However, it is obvious that slopes can dip in practically any direction, and that a given slope is unlikely to be oriented in the same direction as a single

component motion. Given that actual ground motions are three dimensional in nature, Kramer and Lindwall (2004) additionally examined the effects of azimuthal slope orientation on the computed, permanent sliding block displacements. K&L performed Newmark analyses on a three-dimensional wedge, and isolated the effects of azimuthal variability by repeating the 3-D analyses for a given ground motion by rotating the recorded motion in one-degree increments. The results of analyses for two 1994 Northridge motions, the Sylmar Hospital (SYH) and Los Angeles 116th St. School (LAS) are summarized in Figure 6.4.

The results suggest that significant azimuthal variability exists in the computed displacements; the variability is greater in near-field sites (such as SYH) than distal sites (LAS), as evidence by the azimuthal variability of the ground motion characteristics from the two sites (Figure 6.5). This result should not be surprising, given that directionality effects are more significant in near-field sites than in distal ones. K&L determined that the azimuthal variability was greater in slopes with higher yield accelerations, due to the fact that stronger slopes may only see permanent displacements for a small range of azimuths. K&L also found that the average displacement computed from the two recorded components is generally smaller than the average displacement computed for all possible azimuths over a wide range of conditions. This difference is greater for cohesive than frictional shearing resistances, and increases with decreasing yield acceleration.

6.3.4 Summary

Computationally, simplest assumption to make when conducting Newmark sliding block analyses is that the as single, horizontal ground motion component, applied in the same direction as the slope dip, can produce reliable, or at the very least conservative estimates of the permanent displacement. In some cases, this assumption may be a sound one and may not have any adverse effects on the reliability of the sliding block analyses. However, the results of Kramer and Lindwall's analyses show that site conditions exist in which the manner of ground motion application can have a significant effect on computed displacements.

From a standpoint of ground motion dimensionality, it has been shown that steep slopes (with inclination angles greater than about 10-15°) comprised primarily of frictional material may not be suitable for sliding block analyses that utilize single-component motions. More reliable estimates can be obtained by applying two-dimensional motions that account for both vertical and horizontal accelerations to these cases. A natural extension of this issue is the consideration of *how*, the horizontal components of ground motions

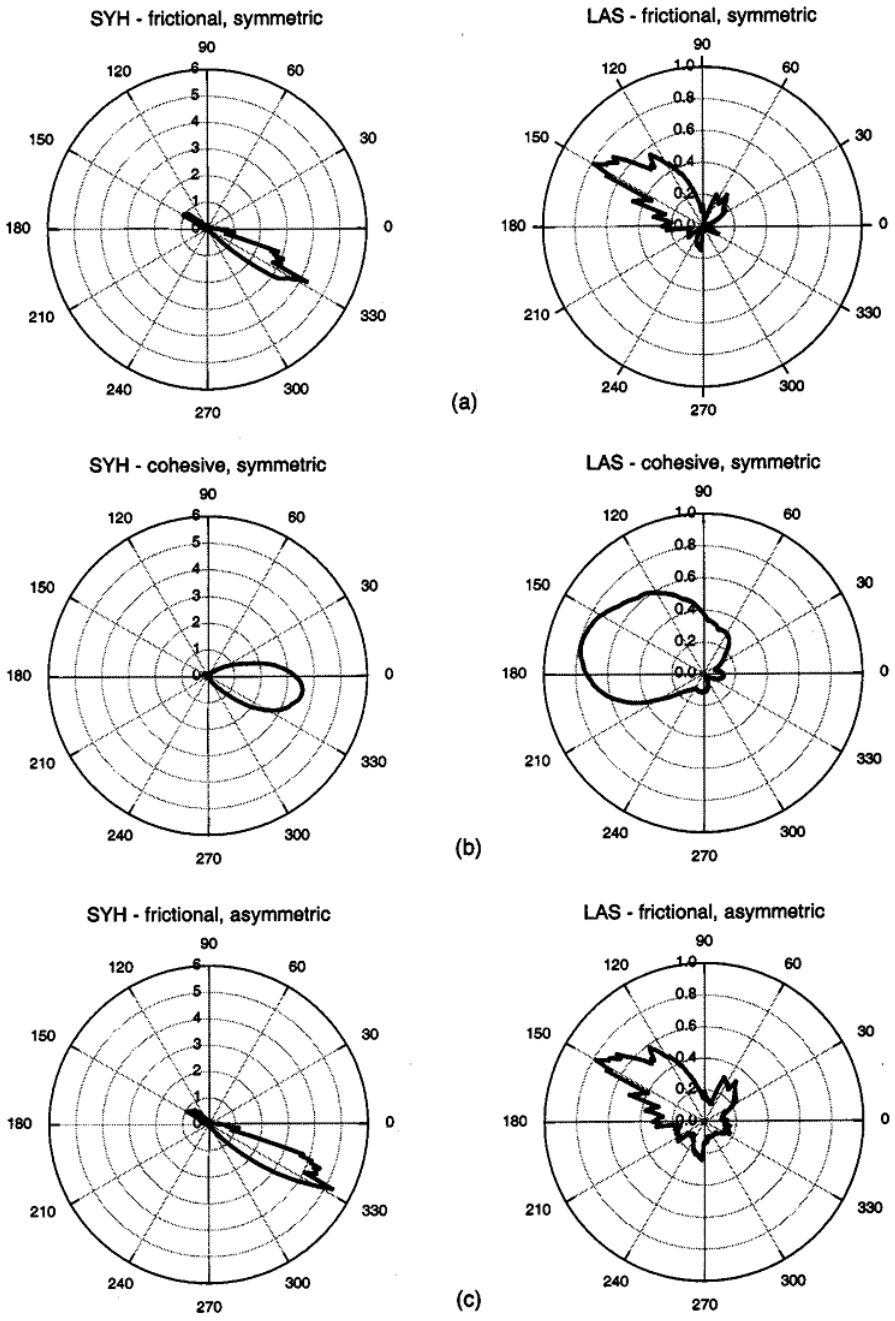

Figure 6.4: Variation of computed displacement (in cm) with respect to azimuth, for Sylmar Hospital and 116th St. School for (a) frictional and (b) cohesive symmetric wedges, and a (c) frictional asymmetric wedge (Kramer and Lindwall 2004)

should be accounted for, if at all. The issue of directionality can be significant at any location, but is particularly problematic at near-field sites, where issues such as directionality and directivity can play a large role in how permanent displacement estimates are obtained. Near-field sites, particularly those with more competent underlying soil, can have extremely high azimuthal variations in computed displacements. Whether or not a

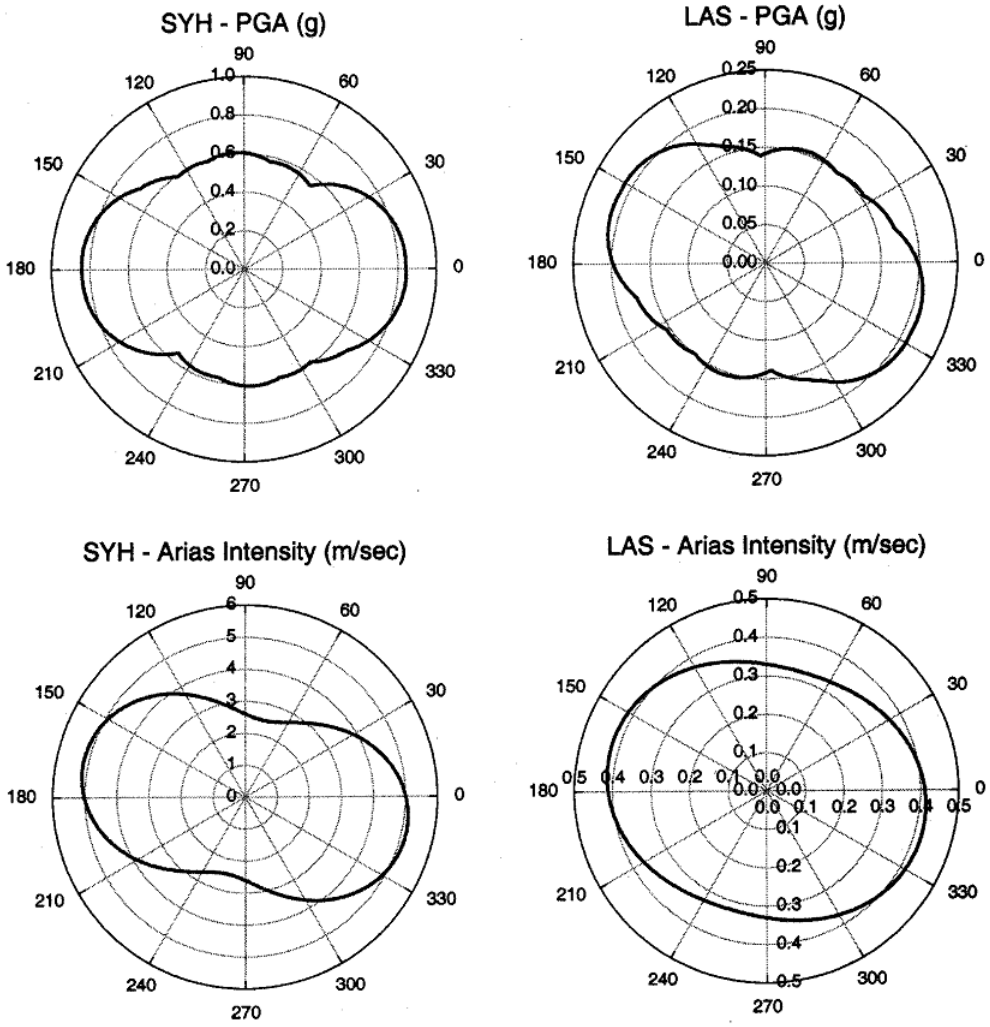

Figure 6.5: Variation of *PGA* and Arias intensity with respect to azimuth, for Sylmar Hospital and 116th St. School ground motions from the 1994 Northridge earthquake (Kramer and Lindwall 2004)

recorded component happens to be on the conservative or unconservative site is subject to almost pure randomness. Furthermore, an increasingly common method of accounting for directionality is to simply take the average of the computed displacements from the two horizontal components. This, however, has been shown to be a consistently unconservative practice, when compared to the average displacements obtained when all azimuthal directions are considered.

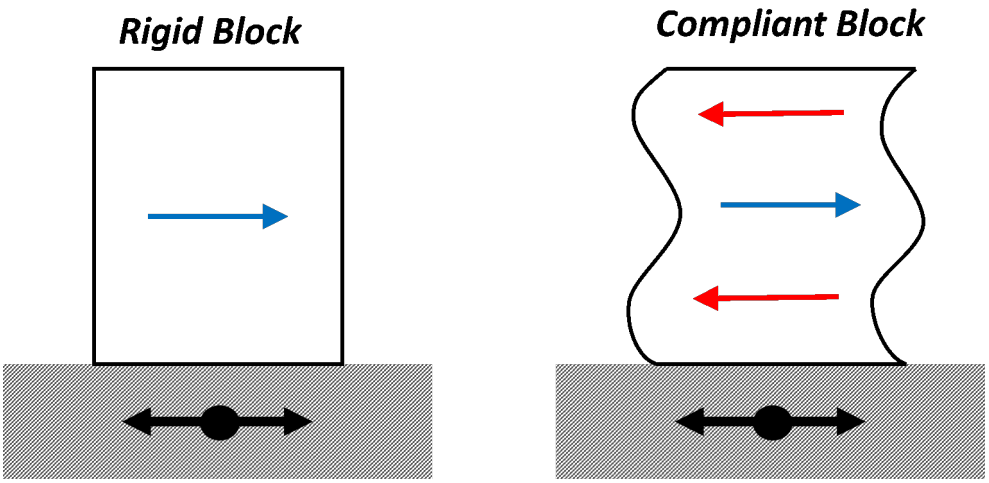

Figure 6.6: Schematic of rigid and compliant blocks subjected to short-wavelength (high-frequency) shaking.

6.4 Rigid and Compliant Block Models

As discussed in Section 4.2.3, the displacements computed using the sliding block method depend on the yield acceleration of the slope (which is dependent on the slope inclination and soil strength) and amplitude, frequency content, and duration of the input ground motion. In Sections 6.2 and 6.3, the sliding block methods was discussed within the framework of how it may be applied on a case-by-case basis. In this section, empirical models based on large sets of Newmark analyses consisting of a wide range of ground motion characteristics are introduced and discussed. Newmark-based empirical models can be generally classified as either *rigid* or *compliant* block models. Rigid block models have seen wide usage over the last 30 years; numerous models have been proposed, each with slight variations in the ground motion datasets used and the predictor variables (particularly with respect to ground motion characteristics) used to develop their relationships.

Recognizing some of the inconsistencies between the assumption of rigid block-type motion and the dynamic response of real slopes (See Section 4.2.3, various researchers have developed Newmark-type models that account for the so-called "compliance" of the sliding mass (Figure 6.6). Compliant block models can be developed via either a decoupled procedure, where the analysis of the dynamic response is separated from the sliding block analysis, and fully-coupled procedures, where the dynamic and sliding block responses are computed simultaneously. These models generally account for site compliance by making some sort of comparison between the frequency content of the input motion and the natural period of the slope.

As with any empirical model based on regression of a finite set of data, the models and relationships presented herein contain some measure of scatter and hence their application for the prediction of seismic slope displacements will have some uncertainty associated with them. The uncertainty in each model introduced herein will be discussed and characterized.

6.4.1 Rigid Block Models

Most rigid block models use as their inputs some measure of the ground motion (e.g., *PGA*, significant duration, arias intensity, magnitude, source-to-site distance) and the yield acceleration, a_y. Ambraseys and Menu (1988) formulated one of the earlier models that predicted horizontal displacements as a function of the ratio between yield acceleration and peak ground acceleration (a_{max}):

$$\log D = b_1 + \log\left[\left(1 - \frac{a_y}{a_{max}}\right)^{b_2}\left(\frac{a_y}{a_{max}}\right)^{b_3}\right] \tag{6.2}$$

The regression coefficients for Equation 6.2 were based on a database of 50 ground motions from 11 earthquakes. Jibson (2007) performed regression on the same form of the equation with a larger database consisting of 2,270 ground motions from 30 events. The coefficients and standard deviation from regression of both databases (Table **??**), as well as a comparison of the two relationships between permanent displacement and a_y/a_{max} (Figure 6.7) are presented below. The median displacements predicted by Jibson (2007) are lower than those predicted by Ambraseys and Menu (1988), but the uncertainty is considerably higher.

Table 6.2: Regression coefficients for the rigid block models of the form of Equation 6.2, from Ambraseys and Menu (1988) and Jibson (2007)

Model	b_1	b_2	b_3	b_4
Ambraseys and Menu (1988)	0.9	2.53	-1.09	0.3
Jibson (2007)	0.215	2.341	-1.438	0.51

Jibson (2007) also developed an original model that utilizes Arias intensity (I_a) as a more complete parameter in characterizing the effects of ground motion amplitude and duration on sliding block displacements:

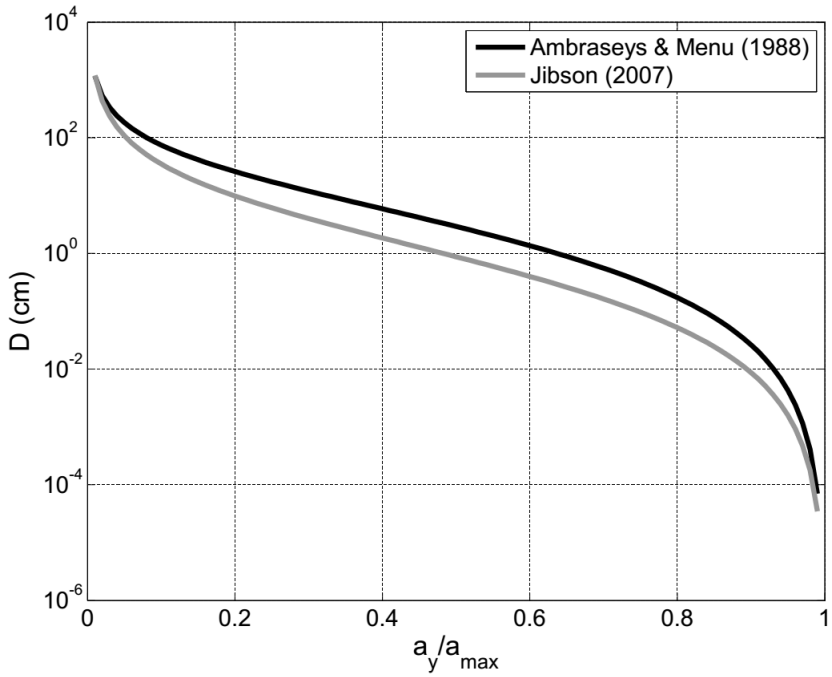

Figure 6.7: Relationship between D and a_y/a_{max} from Equation 6.2, based on databases from Ambraseys and Menu (1988) and Jibson (2007)

$$\log D = 2.401 \log I_a - 3.481 \log a_y - 3.230; \quad \sigma_{\log D} = 0.656 \tag{6.3}$$

Further work by Jibson in 2007 also saw the development of an improved prediction equation that characterizes ground motion duration and amplitude as peak ground acceleration and moment magnitude, respectively:

$$\begin{aligned} \log D = & -2.710 + \log \left[\left(1 - \frac{a_y}{a_{max}} \right)^{2.335} \left(\frac{a_y}{a_{max}} \right)^{-1.478} \right] + 0.424 M_w \\ \sigma_{\log D} = & 0.656 \end{aligned} \tag{6.4}$$

Rathje and Saygili (2009) found that a model based on peak ground velocity (instead of magnitude) and peak ground acceleration yielded improved ground displacement predictions:

$$\ln D = -1.56 - 4.58\frac{a_y}{a_{max}} - 20.84(\frac{a_y}{a_{max}})^2 + 44.75(\frac{a_y}{a_{max}})^3 - 30.5(\frac{a_y}{a_{max}})^4 - 0.64\ln a_{max} + 1.55\ln v_{max} \quad (6.5a)$$

$$\sigma_{\ln D} = 0.405 + 0.524\frac{a_y}{a_{max}} \quad (6.5b)$$

All the models discussed here use the same method for computing the yield acceleration, specifically, using the shear strength along the critical failure surface and the slope geometry. The difference with the models lies in the methods used to characterize ground motion parameters and the ground motion databases used to compute the sliding block displacements. We have seen that using PGA, I_a, M_w, PGV, or some combination thereof can yield equations that make reasonable predictions of lateral displacements. It was determined (Kramer 2009) that the dispersion of the PGA-PGV model by Rathje and Saygili is significantly lower than the dispersion from models that employ any combination of peak ground acceleration, Arias intensity, or moment magnitude. This indicates that the PGA-PGV model is more efficient in predicting ground displacements.

6.4.2 Compliant Block Models

Several compliant block models have been developed as a means to account for the less restrictive condition in which the mass of soil above the sliding surface does not deform uniformly with depth. For large soil masses that experience some softening of soil due to nonlinearity (resulting in a longer natural period), the rigid block assumption may cause under- or over-prediction of downslope displacements. Compliant block analyses attempt to capture the dynamic effects of a flexible column of soil being subjected to excitation at its base in order to evaluate both deformations in steeper, embankment slopes and shallower, lateral spreading failures.

Makdisi and Seed (1977) formulated a relationship between permanent slope displacements and a_y, a_{max}, the natural period of the slope (T_0), and earthquake magnitude (Figure 6.8). The relationship was obtained via a decoupled procedure in which the dynamic response of soil mass (average accelerations) was computed using Chopra's procedure (1966), and the computed average accelerations of the sliding mass used as inputs into a sliding block analysis. The dataset for the Makdisi and Seed procedure consisted of real and hypothetical dams that were subjected to both real and synthetic ground motions. While this procedure has seen wide use for a few decades in practice, and has been

viewed as a seminal work in geotechnical earthquake engineering (Kramer 2009), there are a few practical considerations that should not be overlooked with this procedure. Referring again to Figure 6.8, we see that slope displacements are predicted by determining a characteristic site period for trapezoidal embankments, yield acceleration, and design earthquake magnitude and peak ground acceleration. However, the bands of constant magnitude are quite large; given that $u/(a_{max}T_0)$ is plotted on a logarithmic scale, a significant amount of scatter is likely to be involved in making predictions based on this relationship. When coupled with the fact that the dataset upon which this model is based is relatively small and the uncertainty in the relationship was never formally evaluated, Makdisi and Seed's procedure should be used with some measure of caution in current practice, and generally in conjunction with newer models that incorporate a larger dataset and some manner in which uncertainty can be quantified.

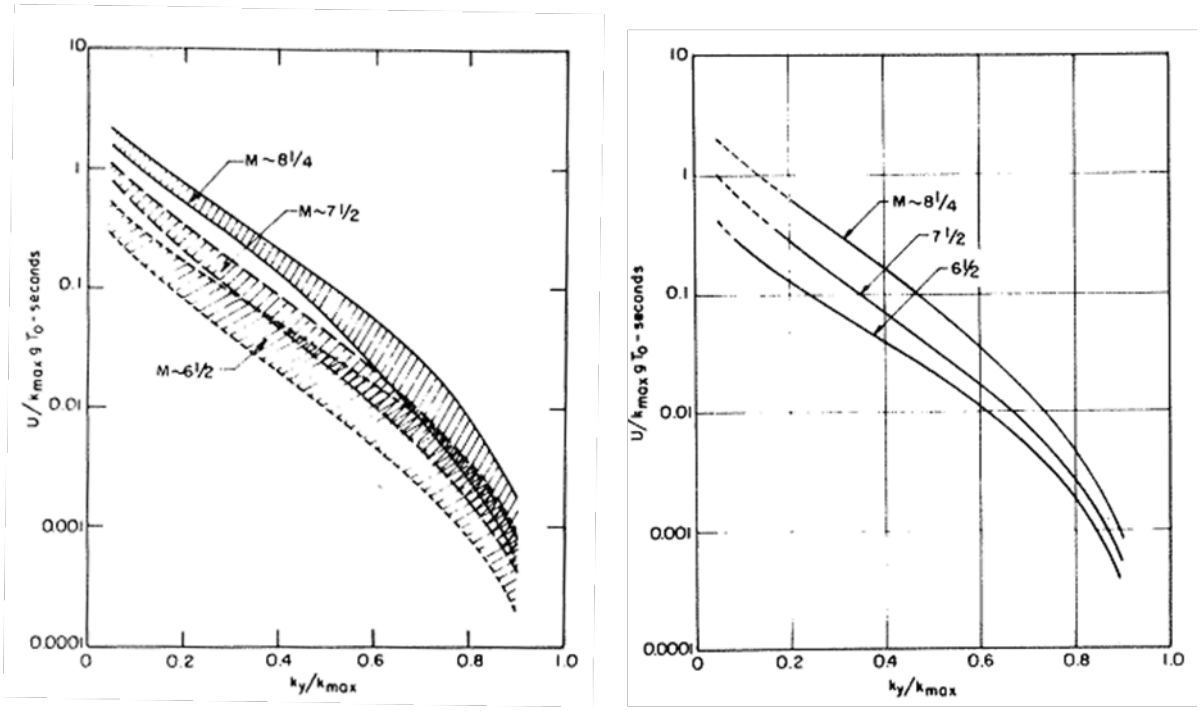

Figure 6.8: Variation of normalized permanent displacement with yield acceleration; a) summary of all data b) average variation (Makdisi and Seed 1977)

Kramer and Smith (1997) introduced a modified Newmark analysis that replaced the simple rigid block with a two-mass system connected by two springs and a viscous dashpot (Figure 6.9). The upper mass was taken as the generalized mass of the compliant slope and the stiffness of the spring was selected to match the fundamental frequency of the potentially unstable soil. Analyses using this model showed that while decoupled analyses generally tend to estimate conservative displacements for shallow, stiff slopes, they can potentially produce unconservative displacement estimates in deeper or softer failure masses such as landfills. Thus, in many cases, the effect of permanent displacements on

the dynamic response of the failure mass can be significant, and are not accounted for by decoupled procedures.

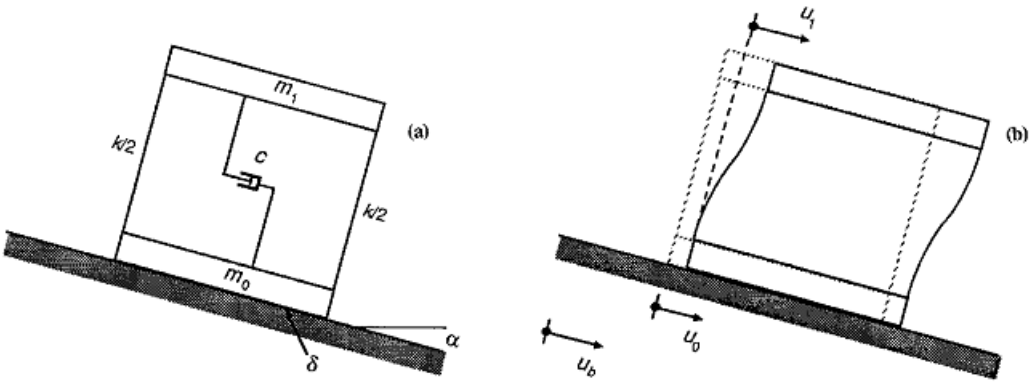

Figure 6.9: Schematic of the modified Newmark model (Kramer and Smith, 1997)

Rathje and Bray (2000) further showed that the decoupled approximation could be potentially unconvservative in cases with high-intensity ground motions, sites with low a_y values, larger a_y/a_{max} ratios, and high ratios of site period (T_s) to mean input ground motion period (T_m). Wartman et al. (2003) further emphasized the significance of the tuning ratio (T_s/T_m) in assessing the applicability of rigid block or decoupled methods. Based on the results of soil column tests, the authors concluded that rigid block analyses were unconservative when the predominant period was equal to or slightly higher than the natural period of the site, and that the decoupled procedure of Makdisi and Seed (1978) can be overly conservative for tuning ratios less than about 2.

Bray and Travasarou (2007) developed a fully-coupled, nonlinear stick-slip sliding block model, and by subjecting it to 688 ground motions, found that compliant block displacements had a stronger relationship to a longer site period than the initial characteristic period. The inclusion of this longer site period thus can help account for nonlinear softening in the response of the soil mass. The intensity measure employed in this model is the degraded spectral acceleration, $S_a(1.5T_0)$, where T_0 is the initial low-strain characteristic site period. The median displacement (greater than 1 cm) can be computed as:

$$\begin{aligned}\ln D = &-1.10 - 2.83 \ln a_y - 0.33(\ln a_y)^2 + 0.56 \ln a_y \ln S_a(1.5T_0) + \\ &+ 3.04 \ln S_a(1.5T_0) - 0.244(\ln S_a(1.5{T_0}^2 + 1.50T_0 + 0.278(M-7)\end{aligned} \tag{6.6}$$

The probability of exceeding some allowable displacement d_{all} can then be determined via:

$$P[D > d_{all}] = (1 - \tilde{p})P\left[1 - \Phi(\frac{\ln d_{all} - \ln D}{\sigma_{lnD}}\right] \tag{6.7}$$

where $\sigma_{l \ln D} = 0.66$, Φ is the standard normal cumulative distribution function, and $\tilde{p}$ is the probability that $D \leq 1$ cm, which is calculated by:

$$\tilde{p} = 1 - \Phi[-1.76 - 3.22 \ln a_y - 0.484 \ln_{a_y} + 3.52 \ln s_a(1.5T_0)] \tag{6.8}$$

6.4.3 Summary

The progression in the development of sliding block models over the past four decades conveniently reveals some of the ways in which the more simplified sliding block methods may be unreliable or unconservative. The reliability of rigid block and decoupled methods is best examined in terms of the tuning ratio (T_s/T_m); it has been demonstrated that rigid block analyses have the tendency to produce unconservative estimates when the predominant period of the input ground motion is nearly equal to or slightly higher than the natural period of the site (i.e. for tuning ratios close to unity). Decoupled procedures, such as the seminal model proposed by Makdisi and Seed in 1977 provided a significant improvement over the traditional rigid block model, but still show tendencies for unconservativism in deeper, softer slopes (corresponding to very long natural periods), and can produce conservative estimates for tuning ratios less than about 2.

The sliding block-based displacement models presented in this section are all based on statistical regression of Newmark-type analyses. The predictive equations differ in the way they model the failure mass (rigid or compliant), and the predictor variables used to account for ground motion intensity (PGA, PGV, I_a, M_w). These differences affect the amount of uncertainty associated with each predictive relationship. Those that use more predictive variables in a more complex model will have lower dispersion in their displacement predictions. The uncertainties associated with each model, it should be noted, are solely attributed to aleatoric uncertainty associated with the ground motions, or scatter associated with statistical regression, and do not account for the uncertainties associated with those factors that affect the determination of the yield acceleration of the block, namely, the ground slope geometry and strength parameters of the soil.

6.5 Comparison of One-way and Two-way Sliding Specifications

Another issue related to the implementation of sliding block analyses is related to whether or not the block is allowed to slide freely in the upslope direction. In the simplest of cases, all that is needed to predict displacements from a Newmark analysis is the horizontal yield acceleration, which can be determined for a particular site using Newmark's simplified procedure. However, at sites with more shallow slopes, displacement predictions can be made more accurate by allowing sliding to occur in the upslope direction, which requires the specification of the ground slope angle. However, in practice, Newmark analyses are often implemented using the one-way restriction, with little consideration of whether or not upslope displacement is likely to happen; the commonly-used sliding block program SLAMMER (Jibson and Jibson) maintains one-way sliding as its default setting, and includes an option for the user to specify upslope displacement and a slope angle, if needed. In this section, the site conditions under which the one-way restriction differs significantly from the actual two-way displacement behavior are evaluated, and the effects of the one-way sliding assumption on the prediction of permanent displacements is characterized.

Displacement in the downslope direction is controlled by the downslope yield acceleration, $a_{y,d}$, which can be defined here by:

$$a_{y,d} = \tan\phi - \beta \tag{6.9}$$

where ϕ is the friction angle between the block and plane and β is the ground slope inclination angle. Theoretically, the block should also be free to slide in the upslope direction, and the yield acceleration in the upslope direction can be calculated by:

$$a_{y,u} = \frac{\tan\phi + \tan\beta}{1 + \tan\phi\tan\beta} \tag{6.10}$$

It is convenient to define ratio of the downslope yield acceleration to upslope yield acceleration as simply:

$$\frac{a_{y,d}}{a_{y,u}} = \frac{\tan\phi - \tan\beta}{\tan\phi + \tan\beta} \tag{6.11}$$

Figure 6.10 illustrates how this ratio varies with respect to both ground slope angle and soil friction angle. For steeper ground slope inclinations, the upslope yield acceleration increases rapidly relative to the downslope yield acceleration, and it can be safely

assumed that permanent displacements will be largely controlled by the downslope yield acceleration. However, as the ground slope inclination approaches zero (level-ground conditions), $a_{y,d}/a_{y,u}$ approaches unity, and the block becomes more likely to slide equally in either direction. This effect is especially noticeable in materials with higher strengths; as the friction angle increases, steeper slopes are required in order for displacements to be controlled by just the downslope yield acceleration.

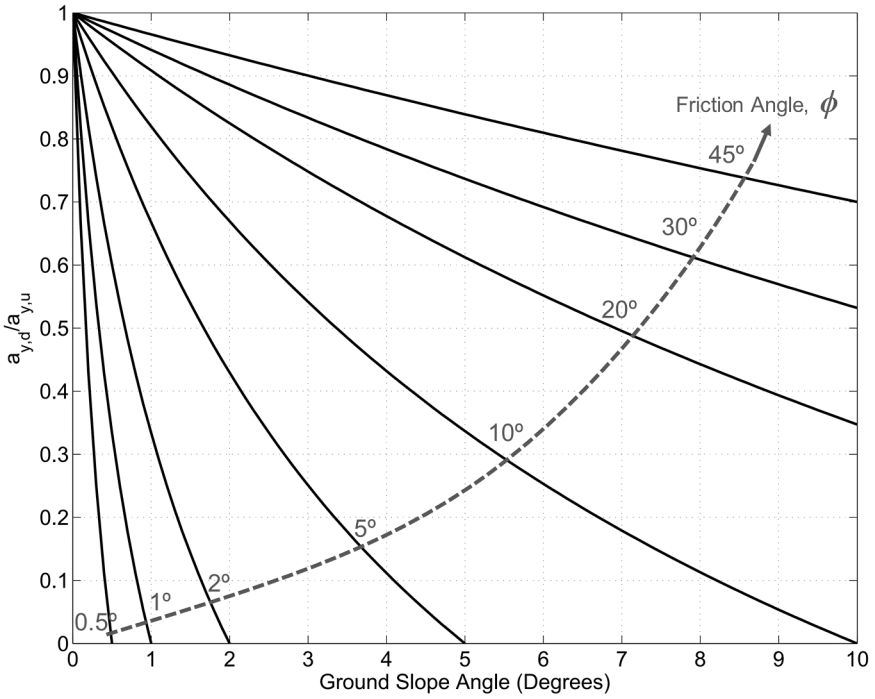

Figure 6.10: Variation in upslope yield acceleration relative to downslope yield acceleration with respect to strength and ground slope inclination

6.5.1 Procedure

In order to determine how the one-directional sliding restriction affects the the reliability of displacement predictions, a series of sliding block analyses were performed with and without the one-way sliding restriction for a series of ground slope angles. A suite of 90 ground motions, spanning a wide range of magnitudes and source-site distances (Appendix B), was used in these analyses. The ground motion records were obtained (Astaneh-Asl, personal communication) by generating GMPE target response spectra for a site with a v_{s30} of 760 m/s and a strike-slip rupture mechanism. The earthquake magnitude and distance varied according to the bins summarized in Table B.1. For each bin of magnitude and distance, ground motions were searched for and ranked according to how closely they matched the GMPE-generated target spectrum. The five closest-matching motions were used for each bin; 10 additional near-fault motions were included in the ground motion

suite.

For each value of a_y/a_{max}, the geometric mean of the displacements determined from the 90 input ground motions was calculated for each ground slope angle. The *displacement error* ($\Delta D_{1,2}$) and *displacement ratio* (r_D) between the two methods, are defined as:

$$\Delta D_{1,2} = D_{1-way} - D_{2-way} \tag{6.12a}$$

$$r_D = \frac{D_{1-way}}{D_{2-way}} \tag{6.12b}$$

Table 6.3: Moment magnitude and source-site distance bins used to formulate target spectra for the generation of the suite of ground motions for PSNL dynamic analyses and Newmark sliding block analyses.

Moment Magnitude	Distance (km)
$6.5 < M_1 < 7.0$	$0 < R_1 < 10$
$7.0 < M_2 < 7.5$	$10 < R_4 < 20$
$7.5 < M_3 < 8.0$	$20 < R_3 < 40$
$M_4 > 8.0$	$40 < R_4 < 80$

Since negative (upslope) displacements and zero-displacement results were prevalent, the geometric mean was calculated using a weighted average (Habib, 2012). The full set of N values (in this case, $N = 90$) is divided into positive, negative and zero-valued subsets. The geometric mean of each subset is then calculated via:

$$G_+ = \left(\prod_{i=1}^{N_+} X_i^+ \right)^{1/N_+} \tag{6.13a}$$

$$G_- = -\left(\prod_{j=1}^{N_-} |X_j^-| \right)^{1/N_-} \tag{6.13b}$$

where N_+ and N_- are the number of positive and negative values in the set, respectively, and X^+ and X^- are the values in the positive and negative subsets, respectively. The weighted geometric mean for the entire set is then determined by:

$$G = \frac{N_+}{N} G_+ + \frac{N_-}{N} G_- + \frac{N_0}{N} G_0 \tag{6.14}$$

where G_0 is the geometric mean of the zero-valued subset, which is, simply zero, thus eliminating the third term in Equation 6.14

6.5.2 Analysis and Results

The displacement error and displacement ratio between the one-way and two-way analyses are plotted against a_y/a_{max} for a range of shallow slope inclination angles in Figure 6.11. For small slope angles, generally 1.0°or smaller, the predicted displacements for the one- and two-way sliding assumptions tend to diverge significantly. For values of a_y/a_{max} below about 0.2, displacement estimates can differ by 10 cm or more, and at very low a_y/a_{max} (below about 0.05), displacements can differ by over 0.5 m for ground slopes below 0.5°. Ground slope angles above about 2°generally have two-way estimates that are consistent with the one-way assumption. Errors of only 3-4 cm manifest at very low values of a_y/a_{max} (below about 0.03) for $\beta = 2°$, and are practically negligible at higher ground slope angles for the full range of a_y/a_{max}.

6.5.3 Summary

When sliding block analyses are used to predict permanent slope displacements, the restriction of the sliding can have potentially significant impacts on the reliability of the displacement predictions, depending on the site conditions. For sites on nearly flat or very gently sloping ground, the one-way sliding restriction tends to predict much higher horizontal deformations than the more accurate assumption of sliding in both directions. At sites underlain by relatively competent material, for for ground motions of relatively low intensity (thus corresponding to high a_y/a_{max} values, this over-prediction is significantly magnified by the fact that many sliding block analyses may only predict a few instances of relative block motion, thus exacerbating differences between the two sliding assumptions. Thus, for these types of cases, it appears that the one-way sliding restriction as at the very least a conservative assumption, if not overly so, from a forward-prediction standpoint.

6.6 Assumption of Discrete Failure Plane

In addition to the various issues discussed in this chapter related to the actual application of the Newmark sliding block procedure, it is also important to examine some of the structural biases related to some of the assumptions that the sliding block model makes. The assumptions of a rigid response to dynamic input and rigid-perfectly plastic behavior

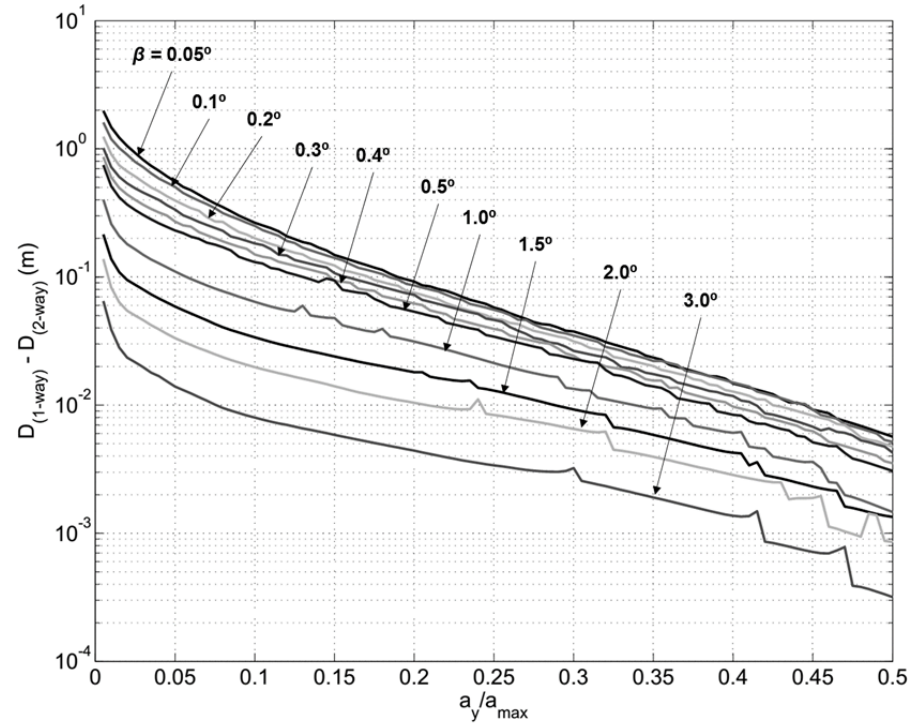

(a)

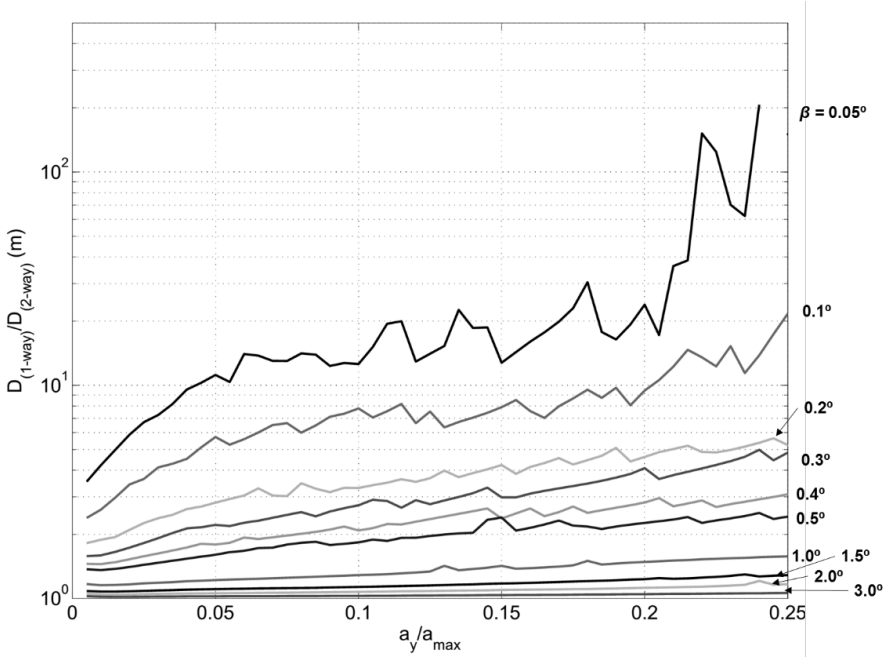

(b)

Figure 6.11: a) Error and b) ratio between sliding block displacement predictions obtained from the one-way and two-way sliding conditions for a series of slope inclination angles

of failure surface were briefly introduced in Section 4.2.3, with a more detailed treatment of the issue of mass compliance in Section 6.4. However, the assumption of a discrete, planar

failure surface may also be inconsistent with the conditions observed at certain sites, and could potentially lead to biased estimates of displacement, affecting the reliability of the Newmark-based analysis framework. If we first consider a site underlain by mostly competent material, with the exception of a relatively thin layer of weak soil or a bedding plane, it may be reasonable to assume that this weak stratum will account for most or all of the deformations that may occur during ground shaking, and thus the sliding block simplification may closely match the conditions observed at the site. However, if we consider a series of sites where the hypothetical weak material is more and more prevalent, it may be expected that the cyclic strains imposed by ground shaking will be distributed at multiple points throughout the weak layer, not just at a single interface (Figure). At sites like these, it is possible that the sliding block analyses may not fully capture the dynamics and deformation behavior that we would expect to observe.

In this section, the assumption that deformations are concentrated along a discrete failure plane is tested for sites like the ones described above. A series of Newmark-type sliding block analyses are performed for a series of gently-sloping sites, with varying ground slope inclination angles, soil strengths, and weak layer thicknesses; and compared to the results of a corresponding set of non-linear dynamic analyses performed for the same sites. The predicted displacements and dissipated energies calculated for each analysis method are compared to evaluate how, and under what conditions, Newmark-type sliding block analyses may be inconsistent with the actual behavior observed at these types of sites.

6.6.1 Analysis Framework

Subsurface Profiles

A series of 108 subsurface profiles were generated for the dynamic analyses (Figure 1), each with different combinations of thickness of the weak soil layer, strength of the weak layer, and ground surface slope angle (Table 1). A typical profile consisted of 3 m of very dense sand. This surficial layer is underlain by the layer of weak material, in which the deformation was expected to occur. This layer was modelled as frictionless, with generally very low cohesion. The cohesion in each weak sublayer was determined according to:

$$c = c_0 + c_1 \sigma'_v \tag{6.15}$$

where c_0 and c_1 correspond to each of the three strength classifications in Table 6.4. The stress-dependent term in Equation 6.15 was used in order to avoid numerical "base-

isolation" effects. Attempts to run dynamic analyses constant-cohesion soil profiles produced an effect where failure in the lowest sublayer would result in the transmission of almost no energy into the overlying weak sublayers, which is not consistent with what has been observed empirically to occur in laterally spreading soil. The constant cohesion term (c_0) was included so that the pseudostatic factor of safety for slope stability would not be uniform throughout the weak sublayer. This ensures that the factor of safety, and thus the yield acceleration, is minimal in the lowest weak sublayer for the purposes of modeling the soil profile as a sliding block, with its base at the bottom of the weak layer. In order to obtain consistent strain profiles, the weak layer was divided into 8 to 10 sublayers when possible, with thicknesses shown in Table 6.4; for layer thicknesses less than 1.0 m, a sublayer thickness of 0.1 m was used. The weak layer is underlain by another layer of very dense sand of varying thickness, which is directly above a rigid base of bedrock.

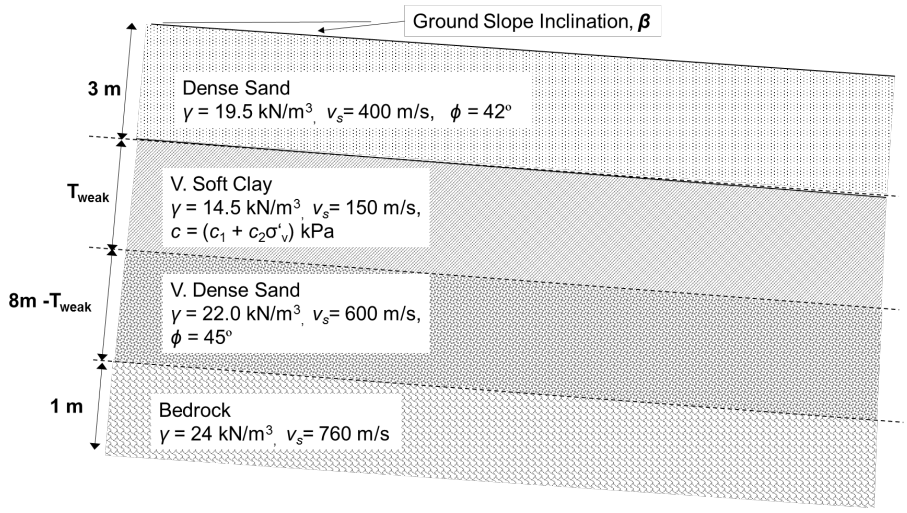

Figure 6.12: Representative soil profile used in PSNL total stress analyses (not to scale)

Table 6.4: Summary of variable soil profile parameters

Weak Layer Thickness (m)	Weak Sublayer Thickness (m)	Ground Slope Angle	Weak Layer Cohesion (kPa)
0.1	0.1	0.5°	$0.5 + 0.06\sigma'_v$
0.2	0.1	1.0°	(Low)
0.3	0.1	2.0°	
0.5	0.1	3.0°	$1.0 + 0.08\sigma'_v$
1.0	0.1		(Medium)
2.0	0.2		
3.0	0.3		$1.5 + 0.10\sigma'_v$
4.0	0.4		(High)
5.0	0.5		

Slope Displacement Models

Dynamic analyses of the soil profile as a continuum were performed using the ProShake Non-Linear (PSNL) total stress model. In order to isolate the effects of thick layers of weak material on rigid block displacement predictions, the weak layer was modelled using a linear material model with 1% damping. The selection of this simple model in a total stress framework was motivated by two factors. Firstly, an effective stress analysis (using loose, saturated sand as the weak material) could potentially affect the differences between

PSNL and Newmark displacement predictions, primarily as a result of complications due to liquefaction-related phenomena. Secondly, even within a total stress framework, a material model that allows for cyclic strain-induced stiffness degradation (e.g. the Vucetic-Dobry model for fine-grained material) could result in further disparity between rigid-block and continuum analyses which would obscure the effect of increased layer thickness that was the original focus of these analyses. The overlying and underlying dense sand layers were modeled using the upper-bound curve of the Seed and Idriss (1970) model for sand, and the bedrock was modeled by the linear 2% damping model.

In order to apply the sliding block model to the profiles outlined above, the horizontal yield acceleration in both the downslope ($a_{y,d}$) and upslope directions ($a_{y,u}$) is required. $a_{y,d}$ can be determined from the factor of safety for pseudostatic slope stability (Jibson 1993):

$$a_{y,d} = (FS - 1)\sin\beta \tag{6.16}$$

where β is the ground slope inclination angle. The factor of safety each weak sublayer i, for an infinite slope condition with no groundwater is:

$$FS_i = \frac{c_i + \sigma_{v,i}\cos^2\beta\tan\phi_i}{\sigma_{v,i}\cos\beta\sin\beta} \tag{6.17}$$

where σ_v is the total stress, ϕ is the friction angle, and c is cohesion in the soil sublayer of interest, respectively. For a frictionless ($\phi = 0$) material in the weak layer, Equation 6.17 simplifies to:

$$FS_i = \frac{c_i}{\sigma_{v,i}\cos\beta\sin\beta} \tag{6.18}$$

The horizontal yield acceleration used in for the sliding block analyses corresponds to the sublayer with the minimum factor of safety, which, in the case of the soil profiles modeled here, was found at the bottom of the weak stratum. Thus:

$$a_{y,d} = \left(\frac{c_i}{\sigma_{v,i}\cos\beta\sin\beta} - 1\right)\sin\beta \tag{6.19}$$

For relatively shallow slope conditions subjected to strong shaking analyzed herein, the rigid block will also tend to slide in the upslope direction, and thus the horizontal

yield acceleration in the upslope direction can be determined using Equation 6.19 and

$$a_{y,u} = \frac{\tan\phi + \tan\beta}{1 + \tan\phi\tan\beta} \tag{6.20}$$

where

$$\tan\phi = \frac{a_{y,d}}{1 - a_{y,d}\tan\beta} \tag{6.21}$$

The horizontal yield accelerations for the downslope and upslope directions were then used as inputs in Newmark analyses (see Appendix) to obtain sliding block displacement time histories, which were then compared to the corresponding PSNL-generated time histories.

Distribution of Strains

The degree to which shear strains were distributed throughout the soil profile in the continuum analyses was assessed by first determining the magnitude of strain in each layer, and normalizing that strain to the total magnitude of strain experienced by the entire soil profile:

$$\gamma_{norm,i} = \frac{|\gamma_i|}{\sum_{i=1}^{N}|\gamma_i|} \tag{6.22}$$

where $gamma_i$ is the total magnitude of strain in sublayer layer i, and N is the total number of sublayers of weak material. This allows for a convenient way to assess the degree to which any sublayer contributes to the overall relative displacement experienced at the ground surface of the soil profile. The standard deviation of the normalized strain was then calculated for each soil profile, and then compared to the maximum standard deviation of strain for that profile, $\sigma_(\gamma, max)$. The maximum standard deviation can be derived by considering the normalized strain profile of a case in which all of the strain occurs in a single sublayer. The mean and variance of the normalized strain for a profile with N sublayers are:

$$\mu_\gamma = \frac{1}{N}\sum_{i=1}^{N}\gamma_{norm,i} = \frac{1}{N} \tag{6.23}$$

$$\sigma^2_{\gamma,max} = \frac{1}{N}\sum_{i=1}^{N}(\gamma_{norm,i} - \mu_\gamma) = \frac{1}{N}\sum_{i=1}^{N}\left(\gamma_{norm,i} - \frac{1}{N}\right) \tag{6.24}$$

For a profile in which all of the strain is concentrated in a single sublayer, $\gamma_{norm,i}$ will equal 1 in the sublayer where the strain is occurring, and zero in the rest (N-1) of the sublayers. Equation 6.24 can be re-written as:

$$\begin{aligned}
\sigma^2_{\gamma,max} =& \frac{1}{N}\left[\sum_{i=1}^{N-1}\left(-\frac{1}{N}\right)^2 + \left(1-\frac{1}{N}\right)^2\right] \\
=& \frac{1}{N}\left[\frac{N-1}{N^2} + \frac{(N-1)^2}{N^2}\right] \\
=& \frac{1}{N}\left[\frac{N^2-N}{N^2}\right] \\
=& \frac{N-1}{N^2}
\end{aligned} \tag{6.25}$$

The maximum standard deviation of the normalized strain for a profile with N sublayers is then:

$$\sigma_{\gamma,max} = \sqrt{\frac{N-1}{N^2}} \tag{6.26}$$

The *strain distribution parameter*, η, for the displaced soil profile can be defined as:

$$\eta = 1 - \frac{\sigma_{\gamma,norm}}{\sigma_{\gamma,max}} \tag{6.27}$$

An η value of 1 corresponds to a profile with a perfectly uniform distribution of strains throughout all sublayers, while a value of zero represents the case where all of the relative displacement at the ground surface results from strain in a single weak sublayer (Figure 6.13).

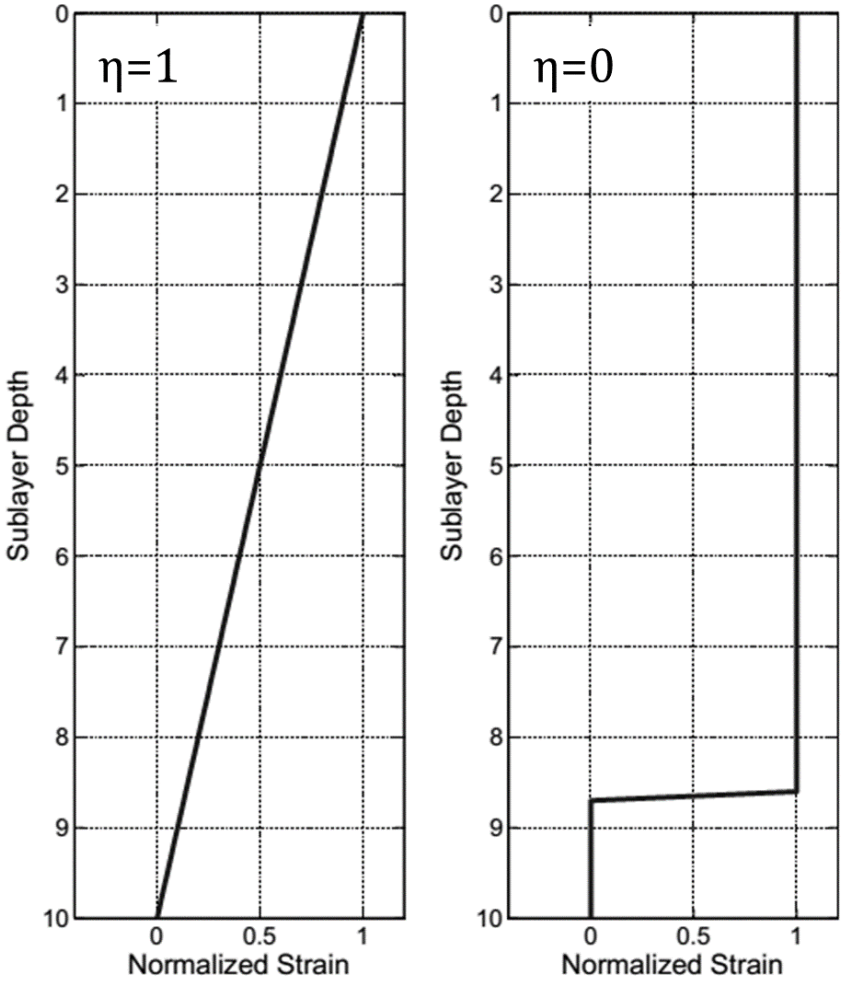

Figure 6.13: Idealized strain distribution profiles, illustrating cases where shear strains are distributed uniformly throughout the depth of the weak layer and concentrated in a single sublayer

Dissipated Energy

In addition to comparing permanent deformations, it is also useful to examine the differences between the work done, or energy dissipated, by the rigid block and continuum systems as they are subjected to the same ground motion. For the continuum system, we consider a column of soil, on sloping ground, with a layer of weak material (Figure 6.14).

The total stress experienced at the base of the soil column of height H is:

$$\sigma = \rho g H \cos\beta \tag{6.28}$$

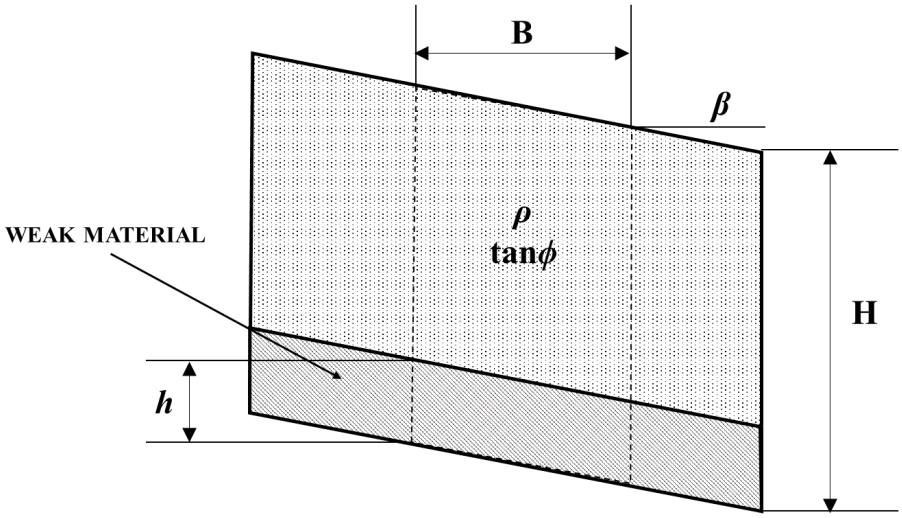

Figure 6.14: Schematic drawing of a soil column of total height H modelled as a continuum, with a weak layer of thickness h at its base.

The maximum shear stress that the material in the weak layer will experience is then simply a function of the shear strength of the soil ($\tan_\phi$, for the purposes of this derivation) and the total normal stress:

$$\tau_{max} = \sigma \tan \phi = \rho g H \cos \beta \tan \beta \tag{6.29}$$

The energy dissipated in a single stress-strain for an elastic-perfectly plastic material (Figure 4) is calculated by determining the area under the stress-strain curve:

$$w = \tau_{max} \gamma_p \tag{6.30}$$

where γ_p is the plastic strain. The total energy dissipated is determined by integrating w over the thickness of the weak layer. Substituting Equation 6.29 in to Equation 6.30 and integrating with respect to h, we obtain the final expression for the dissipated energy in the continuous soil column:

$$W_c = \int_0^z w dz = \rho g H \cos \beta \tan phi \gamma_p h \tag{6.31}$$

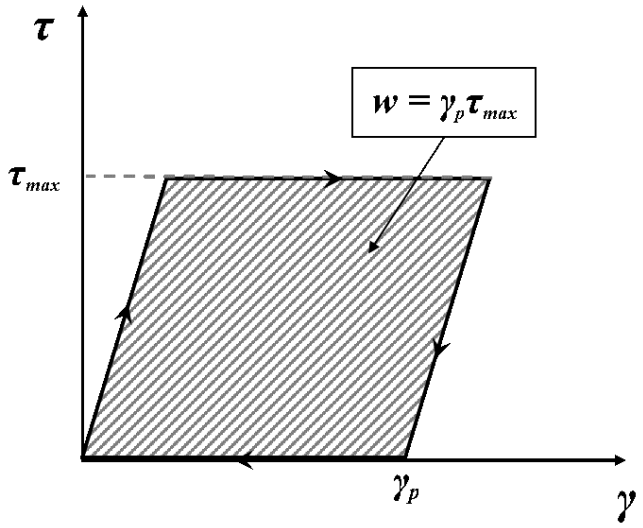

Figure 6.15: Calculation of dissipated energy from the stress-strain response of an elastic-perfectly plastic material

For comparison, the equivalent sliding block model is shown in Figure 6.16 , with the same dimensions and material properties as the continuous soil column.

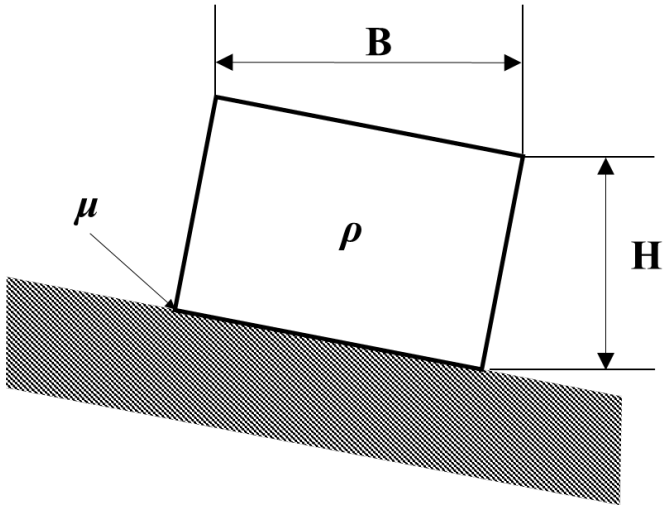

Figure 6.16: Schematic drawing of the sliding block representation of a deforming soil mass

The strength of the sliding block system is represented by the coefficient of friction between the block and the sliding plane, μ. For the sake of direct comparison to the soil column, the frictional coefficient can be expressed as $\mu = \tan\phi$. The normal force acting on the sliding plane by the block is:

$$N = Mg\cos\beta = \rho BHg\cos\beta \tag{6.32}$$

The maximum shear force that can be applied to the block before it begins to slide is thus:

$$T_{max} = \mu N = \rho BHg \cos\beta \tan\phi \tag{6.33}$$

The force-deformation behavior of the sliding block is rigid-perfectly plastic, and in a similar fashion to the soil column, the energy dissipated in a single shear stress cycle can be determined from the area under the force-deformation curve (Figure 6.17):

$$W_N = T_{max}\delta_p = \rho BHg \cos\beta \tan\phi \quad \delta_p \tag{6.34}$$

where δ_p is the permanent deformation mobilized along the frictional interface.

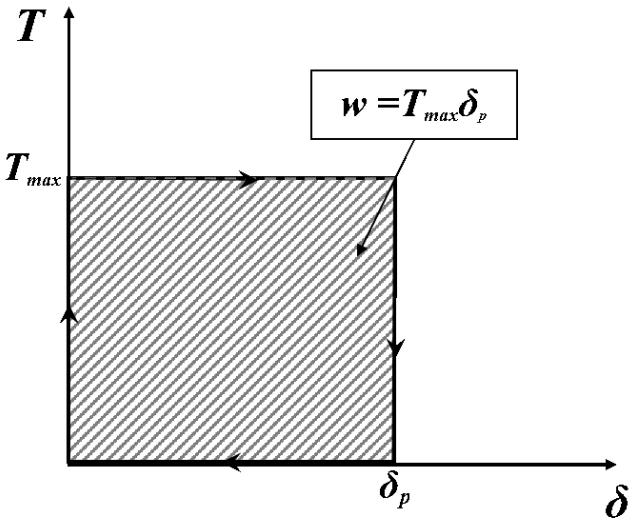

Figure 6.17: Calculation of dissipated energy from the stress-strain response of a rigid-perfectly plastic material

The total dissipated energies of the two models can be compared by setting Equations 6.31 and 6.34 equal to each other and simplifying the expression (assuming the width of the sliding block to be unity):

$$\rho gH \cos\beta \tan\phi \gamma_p h = \rho BHg \cos\beta \tan\phi \quad \delta_p \tag{6.35}$$

$$\gamma_p h = \delta_p \tag{6.36}$$

To examine the validity of the discrete failure plane assumption, the results of PSNL-based continuum analyses were compared to corresponding Newmark-based sliding block analyses for a wide range of ground slope inclinations, weak soil strengths, and thicknesses of weak layers (see Table 6.4). By examining discrepancies in the permanent displacements as well as dissipated energies between the two models, it was possible to characterize the accuracy of the discrete layer assumption as it relates to the various site conditions.

The suite of 90 ground motions were used as inputs for the comparative analyses. The ground motion records were obtained (Astaneh-Asl, personal communication) by generating GMPE target response spectra for a site with a vs30 of 760 m/s and a strike-slip rupture mechanism. The earthquake magnitude and distance varied according to the bins summarized in Table 2. For each bin of magnitude and distance, ground motions were searched for and ranked according to how closely they matched the GMPE-generated target spectrum. The five closest-matching motions were used for each bin; 10 additional near-fault motions were included in the ground motion suite.

6.6.2 Consistency Between Continuum and Sliding Block Analyses for Thin Weak-Layer Profiles

The Newmark and PSNL analyses were initially performed on the 0.1 m-thick soil profiles, the purpose of which was to establish a baseline between PSNL and Newmark analyses for the thinnest weak layer possible given computational constraints. In theory, as the thickness of the weak layer in the continuum profile approaches zero, the results of the rigid block and dynamic continuum analyses should converge to the same value. However, due to numerical limitations, the thinnest layer that could be modelled in PSNL for these purposes was 10 cm. Thus, some differences between the two methods of analyses were observed in both the predicted displacements and the dissipated energies for these "thin-layer" profiles.

Comparison of Displacements

For direct comparison between the rigid block and continuum analyses, it is useful to plot the displacements obtained from each method against each other in logarthmic space, and compare their relationship to the idealized "one-to-one" line, as is shown in Figure 6.18 for the "low strength" soil profiles. In general, we see that the displacements computed from the Newmark analyses (D_N) are relatively consistent with those computed from PSNL (D_C in the upper end of the displacement range. For moderate to lower displacements,

the Newmark analysis tends to under-predict the displacements. As the ground slope inclination increases, we see that the displacements at which the two analyses start to converge increases, from a value of about 10 cm for $\beta = 1.0°$, to a value of about 1 m for $\beta = 3.0°$.

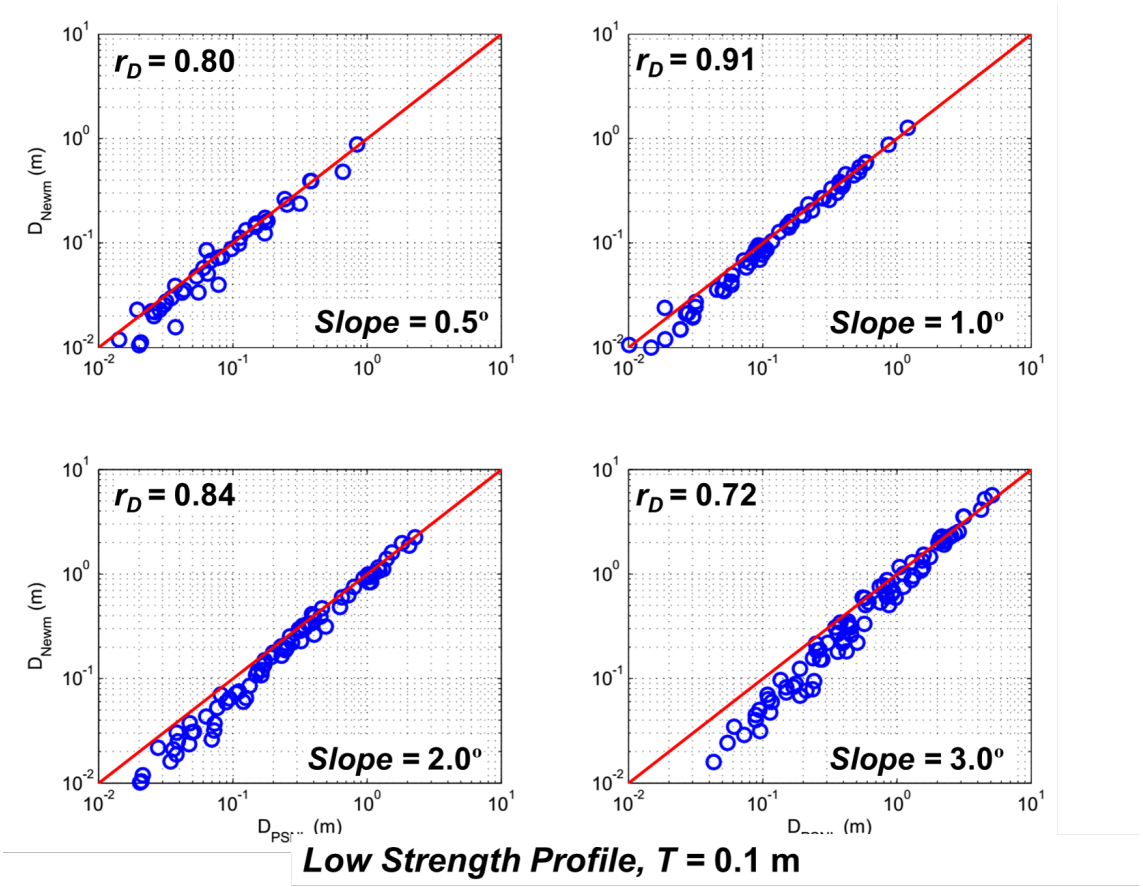

Figure 6.18: Comparison of Newmark- and PSNL-generate displacements, compared with the "one-to-one" line, for a site featuring a "low-strength", 0.1 m-thick layer

The overall difference between the two analyses for a given set of site conditions is best represented by defining the *median displacement ratio*, r_D, which is the ratio of the median computed displacement from the set of Newmark analyses to the median displacement obtain from the corresponding set of PSNL analyses (after Kramer and Lindwall 2004):

$$r_D = \frac{D_{N,median}}{D_{C,median}} \tag{6.37}$$

The displacements obtained from PSNL (D_C) are taken as the baseline for comparison due to the fact that they are based on dynamic, finite-difference analyses, and thus would be considered to be more accurate than the rigid block simplification upon which the Newmark analyses are based.

For the four low-strength cases in Figure 6.18, r_D is between about 0.8 and 0.9 for the more gently sloping site (0.5° to 2°), but begins to drop off sharply when the ground slope angle exceeds 2°, down to a value of about 0.7 for $\beta = 3°$.

Comparison of Dissipated Energies

Another useful comparison to make is to generate a similar plot of the dissipated energies obtain from the Newmark (W_D) and PSNL analyses (W_C, which were determined for each analysis method using Equations and (Figure 6.19). The first thing to notice is that the dissipated energies are more consistent with each other for the thin-layer cases than the displacement are. This is largely due to the fact that the computed displacements are not as strongly correlated with each other, particularly in cases with low slope angles, due to the fact that the mass can generally move in two directions. Comparing the dissipated energies for each case serves then as a convenient proxy for the absolute displacement of the sliding mass. In a similar manner to the computed displacements, the dissipated energies are more consistent at higher values, and tend to diverge (with Newmark analyses under-predicting the W) at the lower end of the range. This point of divergence once again occurs at much higher values of W as the slope angle increases.

The two methods can be compared by taking an analogous *median work ratio*, r_W, which is determined in a similar manner to the median displacement ratio (6.37). Examining the r_W values for the low-strength cases, a similar trend of decreasing values is seen as the ground slope angle increases. Significant drop-offs occur when β increases from 0.5 to 1° and from 2 to 3°.

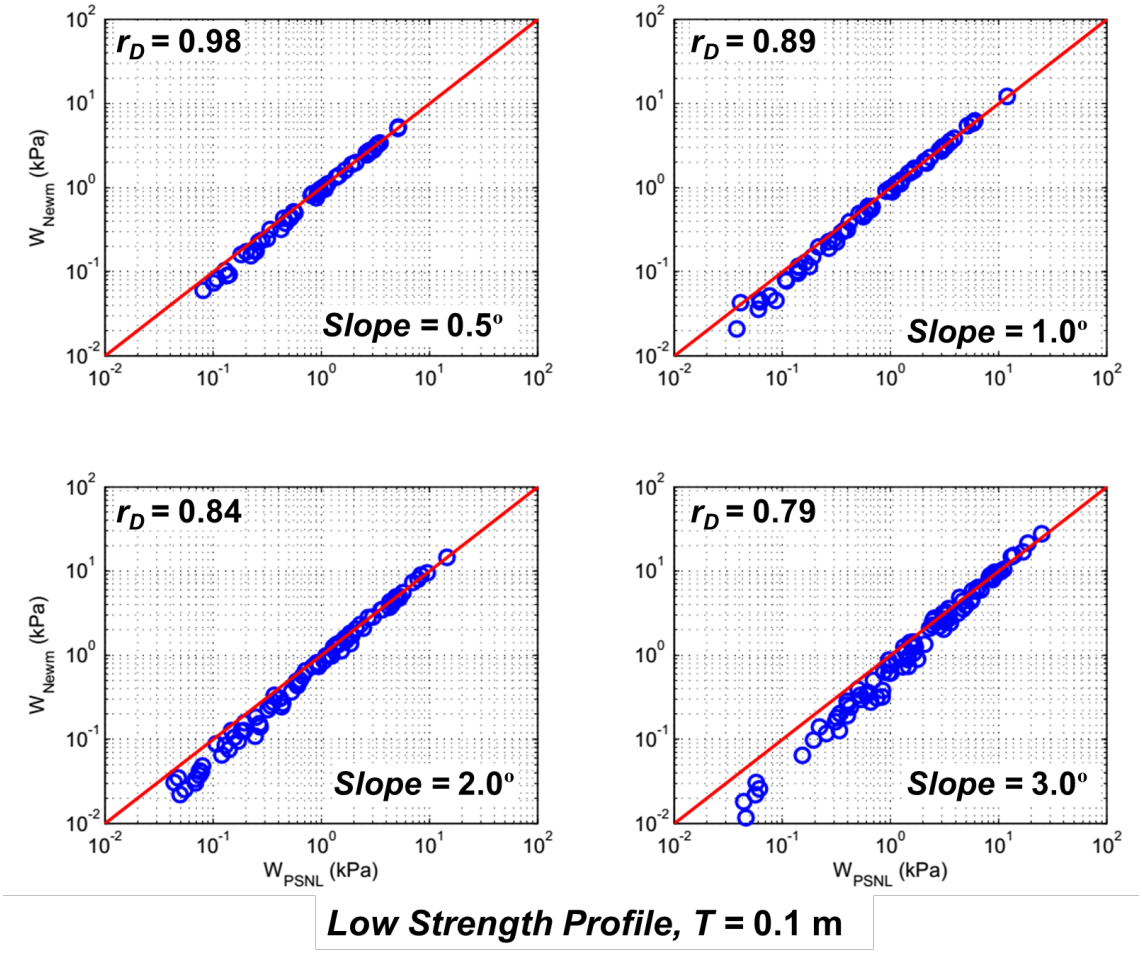

Figure 6.19: Comparison of Newmark- and PSNL-generate dissipated energies, compared with the "one-to-one" line, for a site featuring a "low-strength", 0.1 m-thick layer

Comparison of Work-Displacement Relationships

A third strategy for evaluating the rigid block and continuum analyses is to compare their respective relationships between work and displacement. If the permanent displacement is plotted against total dissipated energy for each set of analyses in logarithmic space (Figure 6.20, it is clear that, for the 0.1 m-thick thin layer cases, the Newmark and PSNL data coincide almost perfectly, particularly at higher slope angles (as the effects of two-directional sliding become less significant).

Additionally, taking advantage of the clear linear relationship between $\log W$ and $\log D$ in Figure 6.20, the data can be fit to a simple linear model to develop a relationship between W and D for both the Newmark and PSNL analyses. For example, for $\beta = 2°$, the equations are:

$$\ln D_N = 0.8329 \ln W_N - 2.0691 \tag{6.38a}$$

$$\ln D_C = 0.8007 \ln W_C - 2.0179 \tag{6.38b}$$

The displacements generated from the best-fit equations for each case ($D_{N,f}$ and $D_{C,f}$) can be then compared to each other via the *mean work-displacement ratio*, $r_{D,W}$, which takes the same form as Equation 6.37. For each of the thin-layer low-strength cases, $r_{D,W}$ is very close to unity, which suggests the work-displacement relationship for the rigid block case is consistent with that of the continuum case.

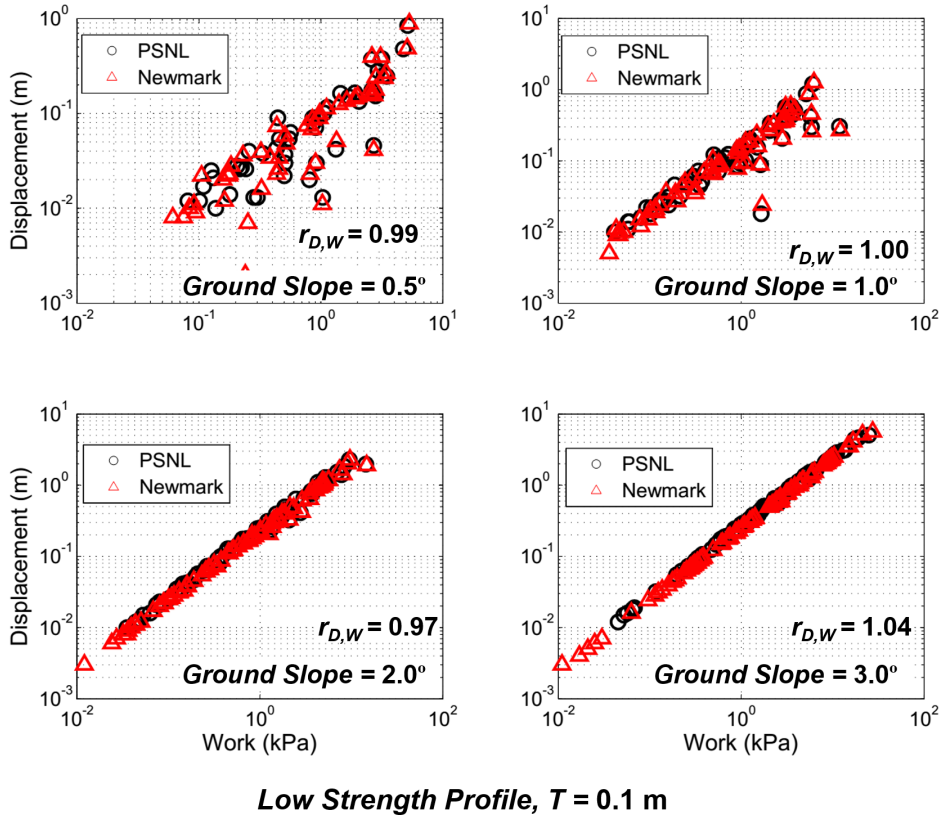

Figure 6.20: Relationships between dissipated energy and displacement, from Newmark and PSNL analyses, for a site featuring a "low-strength", 0.1 m-thick layer

Comparison of Yield Acceleration-Displacement Relationships

Finally, the relationship between normalized yield acceleration (a_y/a_{max}) and displacement, which is commonly seen in analyzing the results of sliding block analyses, can be utilized here to compare the Newmark and PSNL analysis results for the thin-layer pro-

files. The $a_y/a_{max} - D$ plot is particularly useful because it allows the results of profiles of all strengths and ground slope angles to be analyzed in the same dataset, as opposed to evaluating the displacement, work, and work-displacement ratios for individual profiles. The yield acceleration is dependent on both strength and ground slope inclination, and thus serves as a useful variable for examining the how the combined effects of static shear stress and strength of the weak material might affect the consistency between the rigid block and continuum assumptions. The $a_y/a_{max} - D$ data from each set of analyses is plotted and fitted to the Newmark-based empirical model of Saygili and Rathje (2009) (Figure 6.21):

$$\ln D = \beta_1 + \beta_2\left(\frac{a_y}{a_{max}}\right) + \beta_3\left(\frac{a_y}{a_{max}}\right)^2 + \beta_4\left(\frac{a_y}{a_{max}}\right)^3 + \beta_5\left(\frac{a_y}{a_{max}}\right)^4 + \beta_6\left(\frac{a_y}{a_{max}}\right)^5 \quad (6.39)$$

The coefficients are summarized in Table 6.5 for each case. Comparing the two curves (Figure 6.22) shows a similar trend seen the comparison of displacements, specifically that the two methods are quite consistent at very low yield accelerations, but tend to diverge significantly as a_y/a_{max} increases. In this context, the two methods can be once again compared, in terms of the fitted displacement values, via the *mean yield acceleration-displacement ratio* ($r_{D,ay}$), which is determined in similar fashion to $r_{D,W}$. For all cases of strength and ground slope, $r_{D,ay}$ was 0.69 for the 0.1 m-thick weak layer profile. In other words, if the data from both the Newmark and PSNL analyses are fit using Saygili and Rathje's 2009 model, the displacements computed using Newmark analyses are on average about 30% lower than the "actual" displacements computed from PSNL.

Table 6.5: Regression coefficients obtained by fitting Newmark and PSNL displacement data to Saygili and Rathje's 2009 equation

Coefficient	Newmark	PSNL
β_1	-2638	-1918.2
β_2	3776.7	2619.9
β_3	-1933.7	-1309.3
β_4	454.5	315
β_5	-64.3	-50.4
β_6	2.3	2

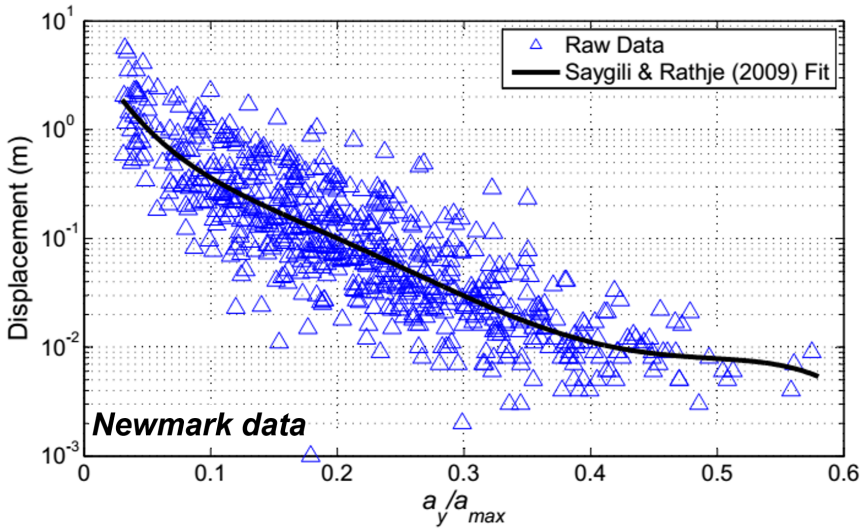

(a)

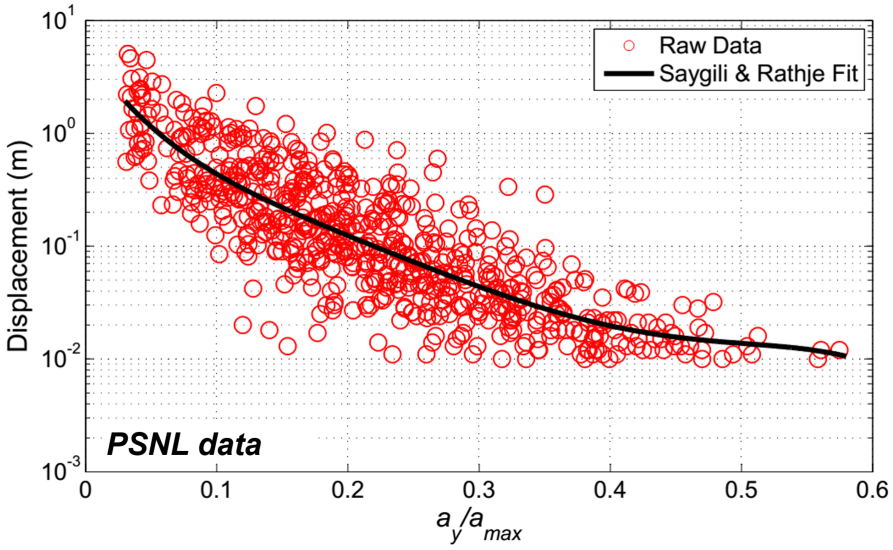

(b)

Figure 6.21: Displacements from (a) Newmark and (b) PSNL analyses, plotted against normalized yield accelerations for all strength and ground slope sites with 0.1 m-thick weak layer

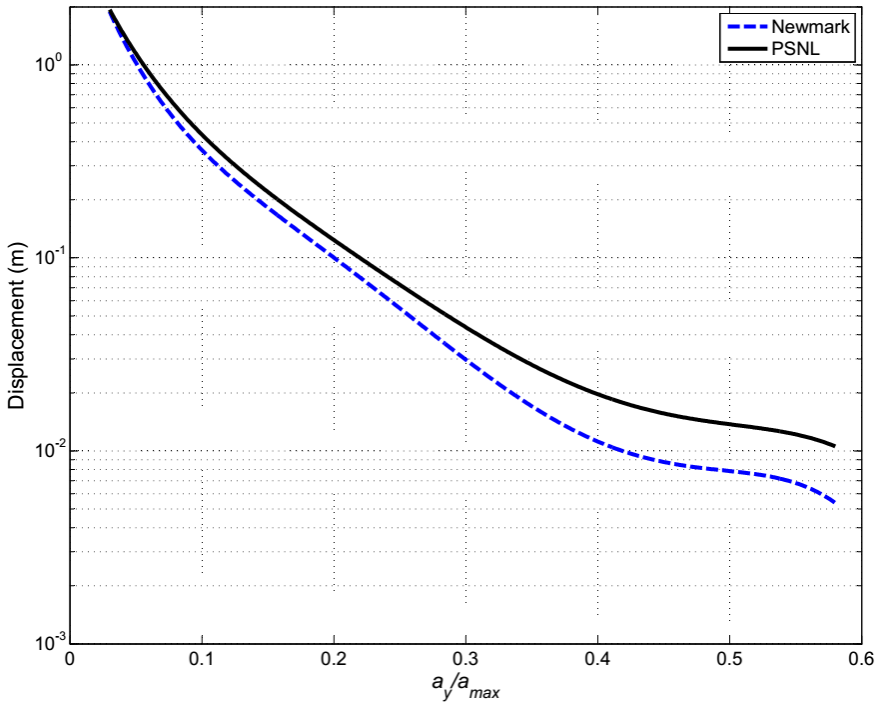

Figure 6.22: $D-a_y/a_{max}$ curves, fitted to the Newmark-type empirical model of Saygili and Rathje (2009), from Newmark and PSNL displacement data

Summary

The median displacement, median dissipated energy, and mean work-displacement ratios are summarized for each of the 12 thin-layer sites in Table 6.6. Similar trends exhibited in the low-strength profile are observed in the medium- and high-strength sites, specifically, the general decrease in both r_D and r_W with respect to increasing slope inclination, and the particularly significant decrease in the same ratios at $\beta = 3°$. As expected, dissipated energy ratios were more consistent between the two methods, particularly at lower slope angles when upslope displacements were significant. The work-displacement relationships, however, yielded the most consistent results between the Newmark and PSNL analyses, and, more importantly, were insensitive to strength or ground slope inclination. Overall, it was found that the median displacement ratio for all 12 cases was about 0.80, and the median dissipated energy ratio was 0.85. These results are not unexpected; as stated earlier, if the strains within the weak layer are integrated over its 10 cm thickness, significant displacements can certainly be expected to occur. The values summarized in Table 6.6, as well as the overall median displacement, median dissipated energy, and median yield-acceleration displacement (0.69) ratios were used as baselines of comparison for the results of the analyses on profiles with thicker sublayers.

Table 6.6: Summary of median displacement, median dissipated energy, and median work-displacement ratios for the 12 thin-layer cases

Soil Strength Classification	Slope Angle (degrees)	r_D	r_W	$r_{D,W}$
Low ($S_u = 4.05$ kPa)	0.5	0.89	0.95	0.89
	1.0	0.85	0.83	0.93
	2.0	0.80	0.84	0.92
	3.0	0.69	0.77	0.94
Medium ($S_u = 5.74$ kPa)	0.5	0.95	0.98	0.95
	1.0	0.87	0.92	0.85
	2.0	0.91	0.90	0.91
	3.0	0.74	0.77	0.93
High ($S_u = 7.42$ kPa)	0.5	0.84	0.92	0.86
	1.0	0.95	0.98	0.98
	2.0	0.86	0.94	0.88
	3.0	0.82	0.85	0.90

6.6.3 Example Analysis Case

In order to more closely examine how rigid block and continuum analyses diverge as the thickness of the weak layer increases and strains begin to distribute throughout the weak layer, an example set of analyses on a single site with varying weak layer thicknesses is presented here. The low-strength, 2.0° slope site was subjected to a single input ground motion (Figure 6.23 , Table 6.7). For each of the nine weak-layer profile thicknesses, the input motion was applied to Newmark and PSNL analyses, and the resulting displacement and work time histories from the two methods were compared, along with the distributions of displacement with respect to depth.

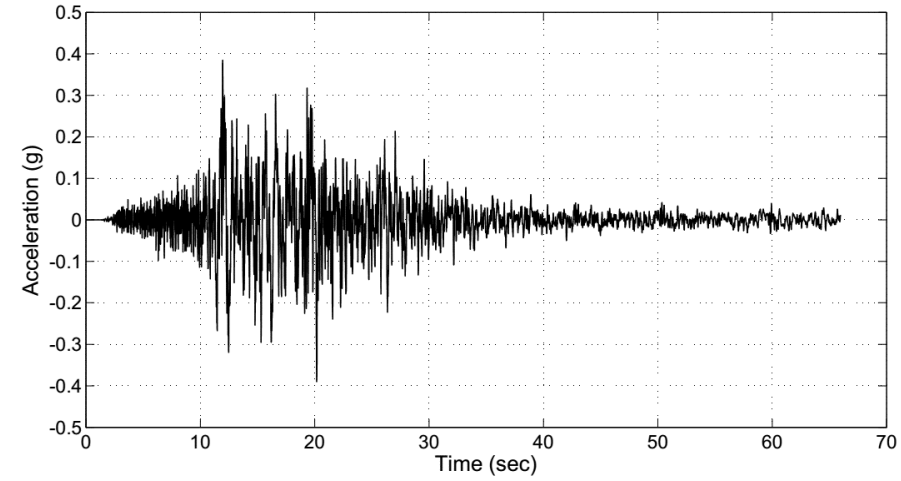

(a)

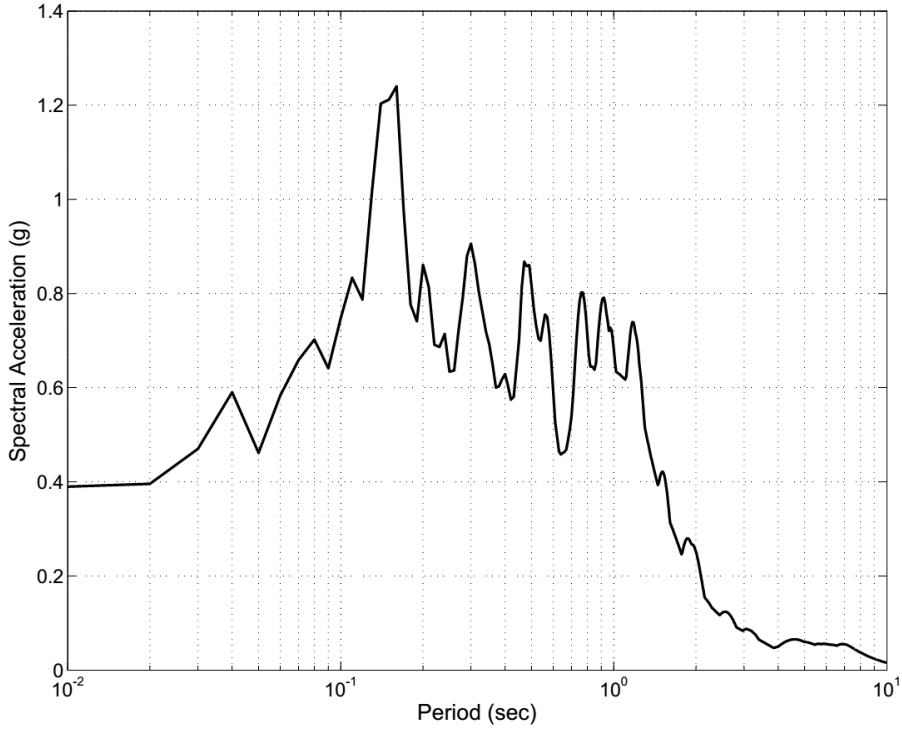

(b)

Figure 6.23: (a) Acceleration time history and (b) response spectrum of ground motion used in demonstration analyses

Table 6.7: Ground motion characteristics of input motion used in demonstration analyses

Parameter	Value
PGA (g)	0.385
PGV (m/s)	0.457
Arias Intensity (m/s)	3.481
Significant Duration (s)	34.1
Predominant Period (s)	0.16

Results and Discussion

The final displacements and dissipated energies for each method, along with the resulting displacement and work ratios, are summarized in Table . Additionally, for the profiles with T_{weak} greater than 0.1, the strain distribution parameter is also included. For the thin-layer case, the final displacements and dissipated energies for the Newmark and PSNL analyses are nearly identical, showing good consistency with each other. As the weak layer increases in thickness, we see a corresponding decrease in the displacement ratio; for this particular case, the two analyses are within about 10% of each other for layer thicknesses up to about 2.0 m, before diverging significantly to the final r_D value of 0.78 for $T_{weak} = 5.0$ m. If the changes in r_D are examined with respect to the distribution of strains, it becomes clear that the divergence between predicted displacements is influenced heavily by η. The PSNL and Newmark analyses were within about 10% of each for this case while η remained at or below about around 0.35, and began to diverge significantly once the strain distribution jumped to above 50% for the 3.0 m-thick case. The difference between the dissipated energies follows a similar general trend, however r_W is far less sensitive to changes in weak layer thickness or strain distribution.

The depth profiles of final displacement obtained from the PSNL analyses, can be compared to an "implied" displacement profile based on the Newmark analyses where the entire displacement is assumed to occur in the bottom of the weak sublayer (Figure 6.24). Examination of the implied Newmark profile (denoted by the dashed line) rshows that the sliding block discrete layer assumption managed to capture the strain behavior in the lower portions of the weak layer reasonably well in this case, particularly in the deepest two or three weak sublayers. However, when strains and displacements are allowed to occur in the weak material above these deep sublayers, the rigid block assumption results in significantly more unconservative displacement estimates.

The displacement and dissipated energy time histories are also presented and compared for each analysis method (Figures 6.25, 6.26, 6.27, 6.28). Examination of the time histories, shows, unsurprisingly, that deviations between the two methods occur in a ratcheting-type manner, particularly at instances where very large pulses in the input ground motion are occurring. These large excitations at the base of the soil profile appear to be significant enough to cause the resulting stress waves to propagate through the weak layer without damping out when large deformations occur in deeper weak sublayers.

It should be noted that the example analysis presented here is representative of a "best-case scenario", where the Newmark and PSNL analyses coincide perfectly for the thin-layer cases, and see only moderate (although not insignificant) divergences for thicker sublayers. The more representative scenario, as was shown in the results of the thin-layer analyses (see Section 6.6.2), is that the sliding block analysis under-predicts the continuum dynamic model by about 20% on average for the thin-layer cases. The expectation is therefore that, when compared to the best-case scenario presented here, lower displacement ratios at $T_{weak} = 0.1$ m will correspond to lower displacement ratios for thicker profiles, resulting in even unconservativism in the discrete failure plane assumption.

Table 6.8: Summary of displacement, work, and strain distribution results for the nine low-strength, 2.0˚ ground slope soil profiles.

Weak Layer Thickness (m)	Displacement (m)			Work (kPa-m)			Strain Dist. Parameter, η
	Newm.	PSNL	r_D	Newm.	PSNL	r_W	
0.1	1.17	1.17	1.00	5.63	5.60	1.00	0.00
0.2	1.18	1.21	0.98	50.78	5.79	1.00	0.80
0.3	1.18	1.21	0.98	5.93	6.02	0.99	0.23
0.5	1.20	1.25	0.96	6.22	6.37	0.98	0.30
1.0	1.22	1.31	0.93	6.97	7.38	0.94	0.36
2.0	1.26	1.37	0.92	8.38	9.18	0.91	0.23
3.0	1.28	1.48	0.87	9.79	10.70	0.91	0.50
4.0	1.30	1.64	0.80	11.21	12.38	0.91	0.54
5.0	1.32	1.69	0.78	12.62	14.02	0.90	0.60

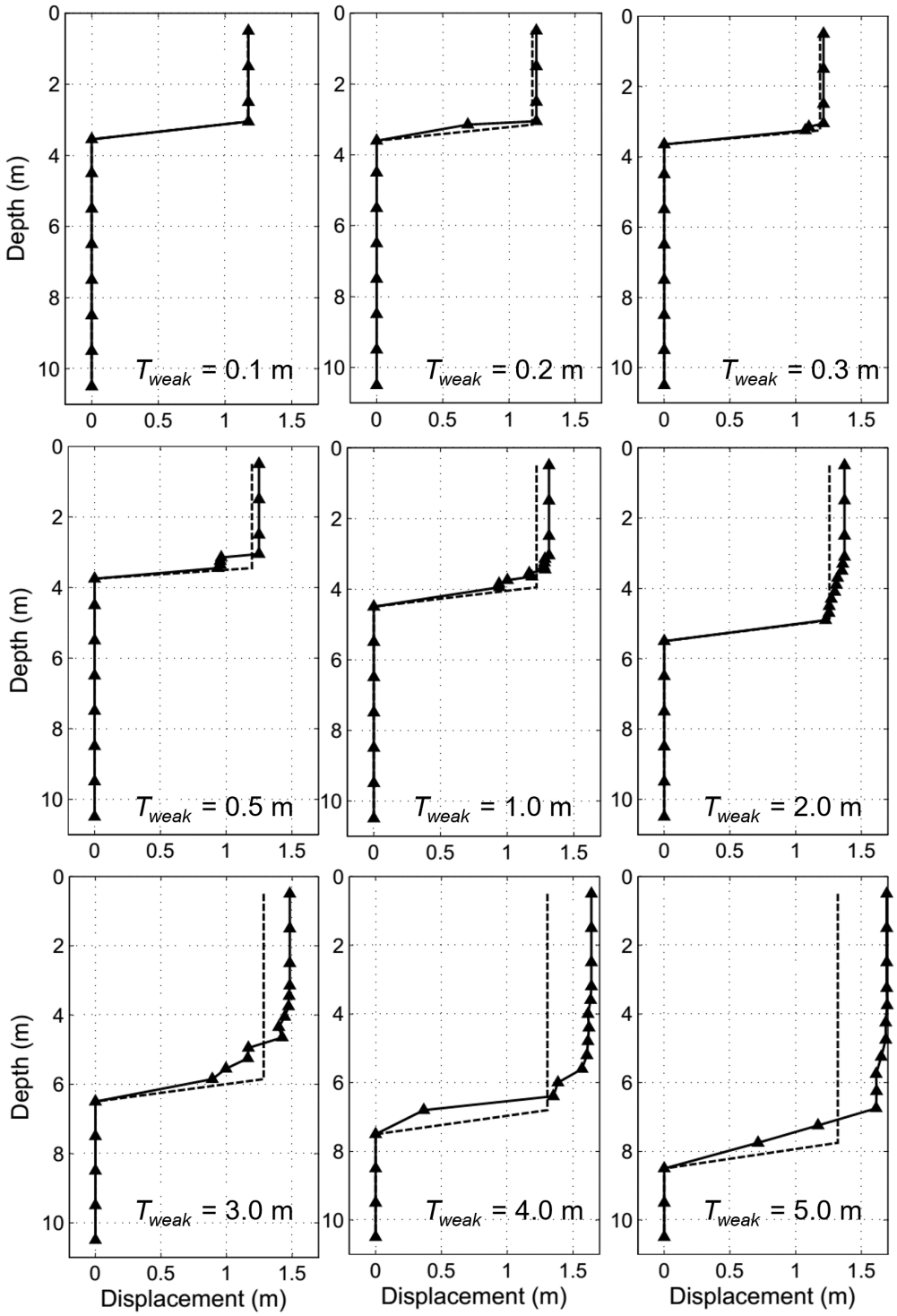

Figure 6.24: Final permanent displacement depth profiles, obtained from PSNL analyses, for the nine low-strength, 2.0˚ ground slope soil profiles; "implied displacement profiles from Newmark analyses are included as dashed lines

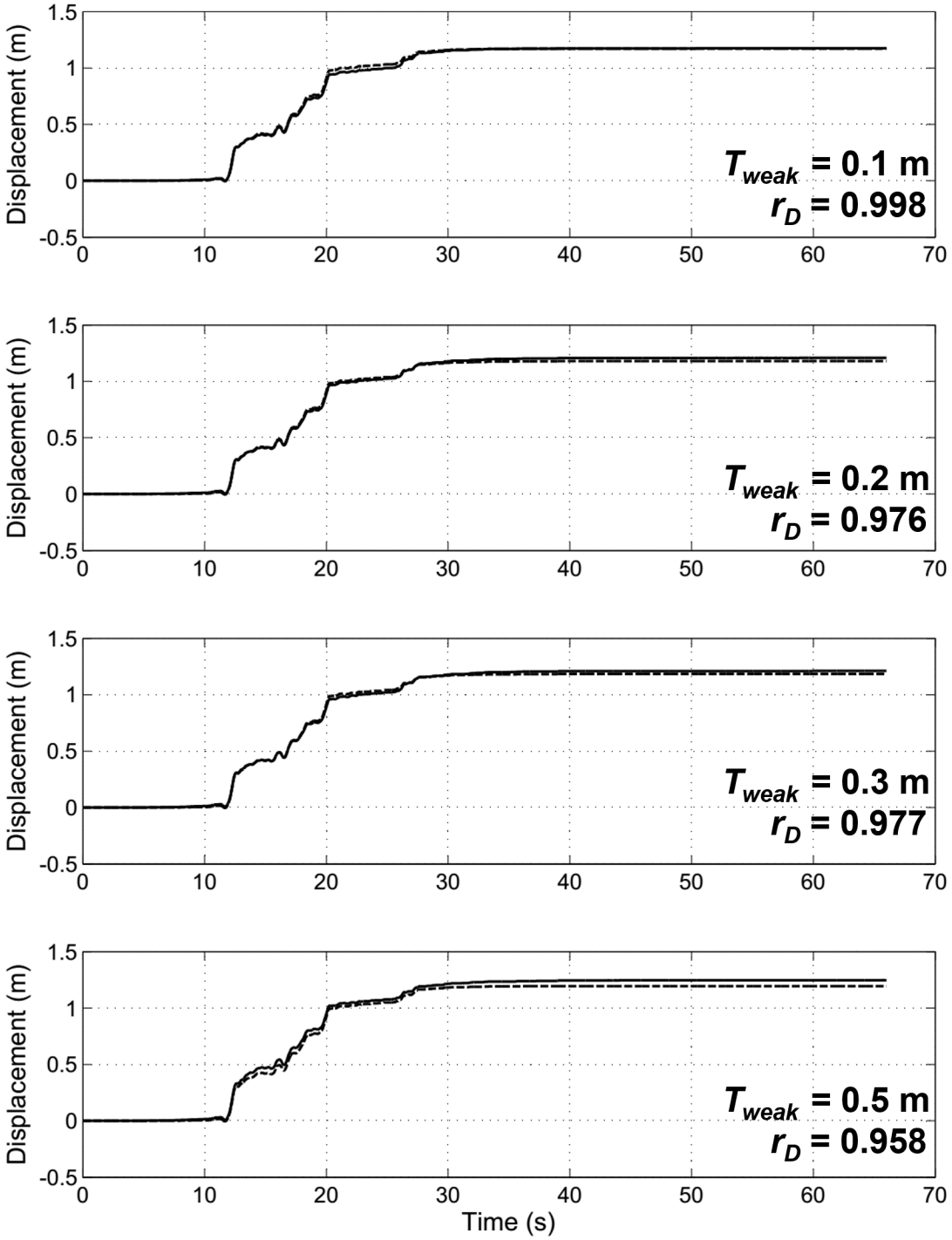

Figure 6.25: Displacement time histories for the 0.1, 0.2, 0.3, and 0.5 m-thick low-strength, 2.0° ground slope soil profiles; obtained from PSNL analyses (solid line) and Newmark analyses (dashed line)

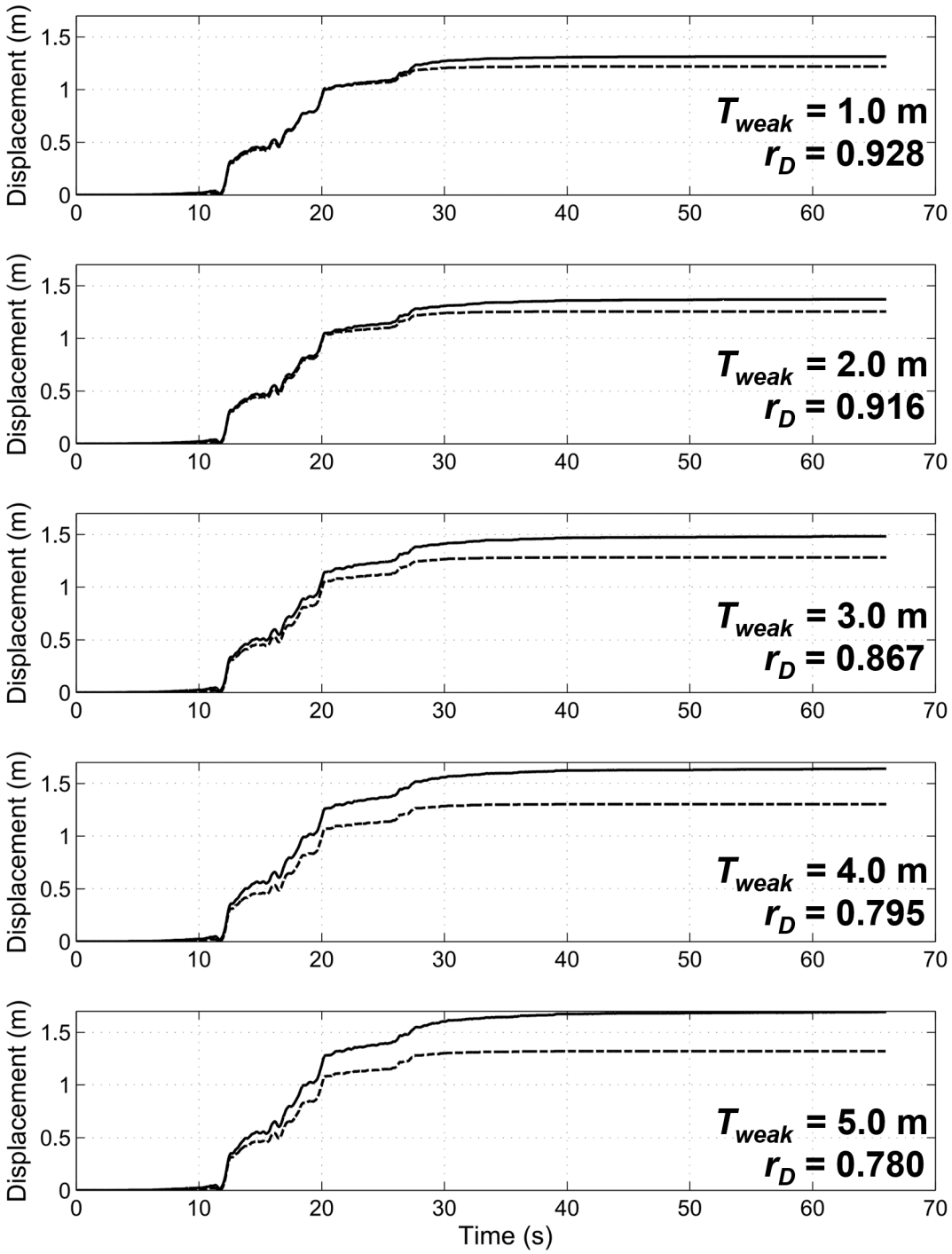

Figure 6.26: Displacement time histories for the 1.0, 2.0, 3.0, 4.0, and 5.0 m-thick low-strength, 2.0° ground slope soil profiles; obtained from PSNL analyses (solid line) and Newmark analyses (dashed line)

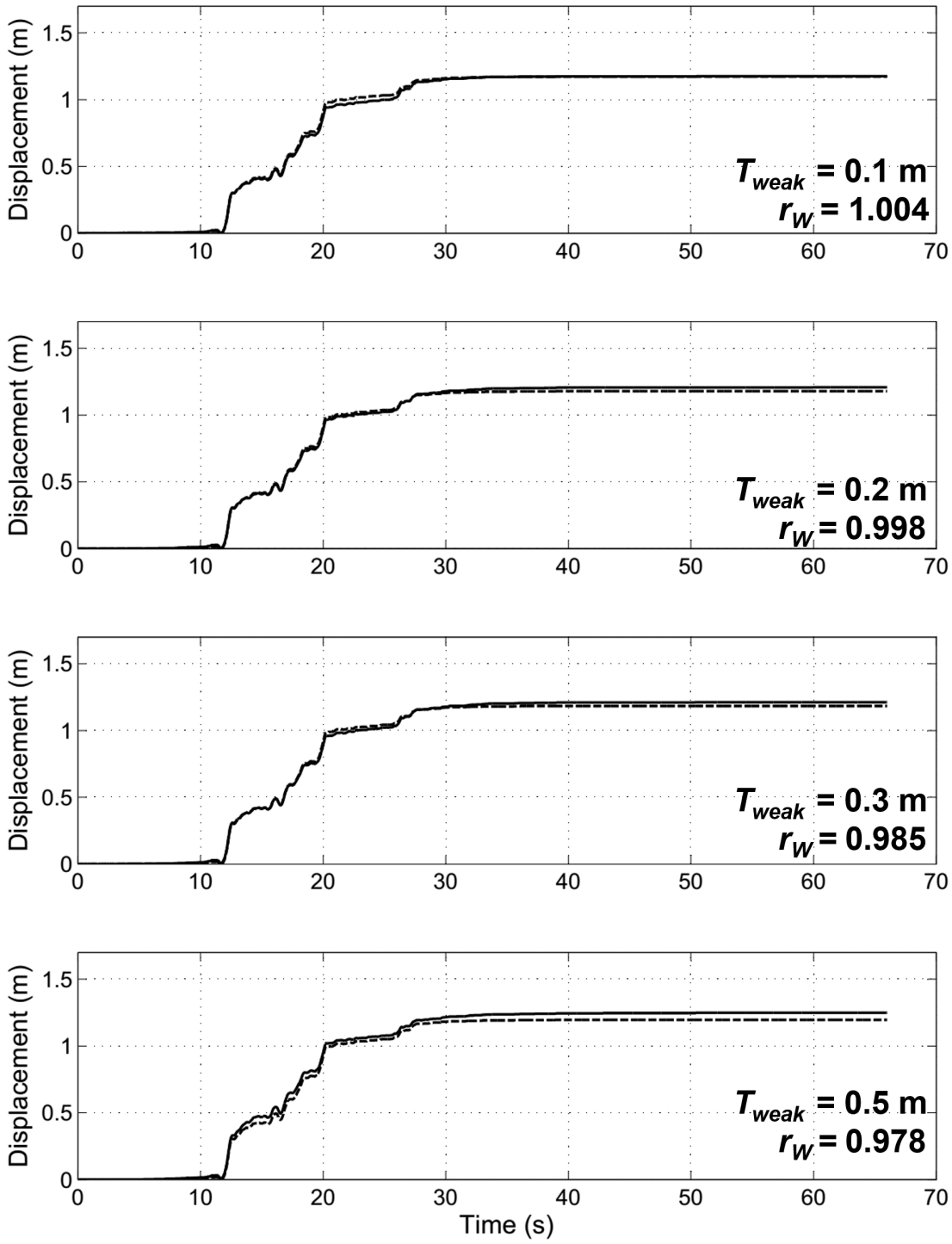

Figure 6.27: Dissipated energy time histories for the 0.1, 0.2, 0.3, and 0.5 m-thick low-strength, 2.0° ground slope soil profiles; obtained from PSNL analyses (solid line) and Newmark analyses (dashed line)

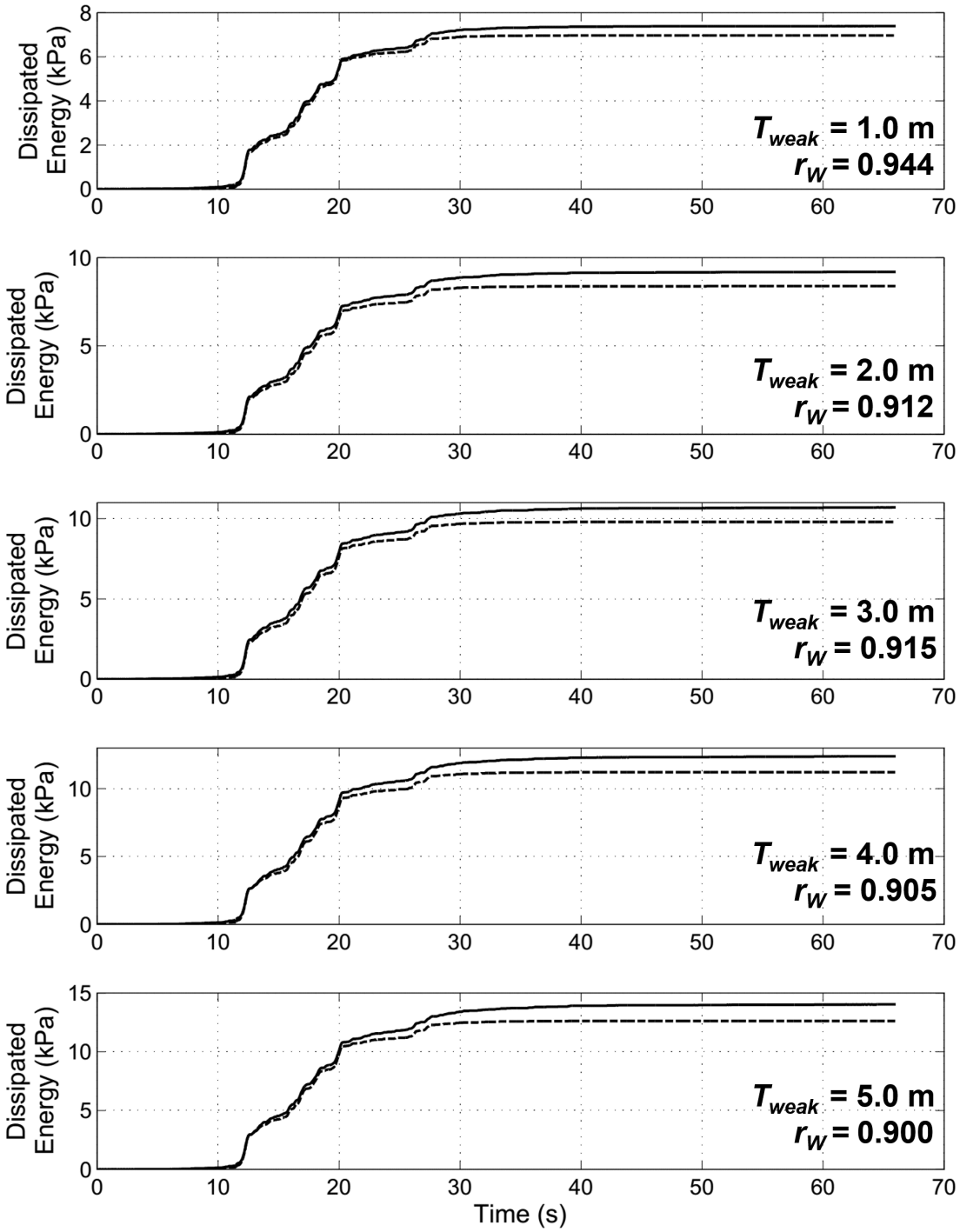

Figure 6.28: Dissipated energy time histories for the 1.0, 2.0, 3.0, 4.0, and 5.0 m-thick low-strength, 2.0° ground slope soil profiles; obtained from PSNL analyses (solid line) and Newmark analyses (dashed line)

6.6.4 Full Analysis Results and Discussion

The full set of Newmark and PSNL analyses consisted of applying 90 ground motions to a total of 108 different soil profiles (representing the range of ground slope angles, soil strengths, and weak layer thicknesses outlined in Table 6.4), resulting in a total of 9720 analyses. From this initial dataset, cases where the PSNL-computed displacement (D_C) was less than 1 cm were removed. For each case, the final permanent displacement and dissipated energy values were recorded for both the Newmark and PSNL simulations, with the strain distribution parameter η additionally obtained from each PSNL result. The data was analyzed largely in terms of median values of the displacement ratio (r_D) and work ratio (r_W), with a focus on how each of the site effects (weak layer thickness, ground slope, and soil strength) affected the distribution of strains, and thus the differences between the Newmark- and PSNL-based analyses.

Relationship between Strain Distribution and Displacement/Work Ratios

Primarily, a general relationship can be characterized between how well strains are distributed in the continuum analyses, and how this distribution influences the divergence between the continuum and sliding block analyses. Figure 6.29a shows, despite a significant amount of scatter in the full set of data, a clear general trend of decreasing displacement ratio with increasing strain distribution. In other words, when strains are more distributed throughout the weak layer, the Newmark-based analyses increasingly under-predict the corresponding displacements obtained via the finite difference continuum analyses. For example, the median r_D for all cases where η is between 0.50 and 0.6 was about 0.71. Conversely, cases where most of the strains occur in one or two sublayers (generally at the bottom of the weak stratum) tend to see better agreement between the Newmark and PSNL analyses. A similar trend is seen in the relationship between η and the work ratio r_W (Figure 6.29b), and with significantly less scatter than what is observed in the displacement data. This is largely due to the fact that the displacement analysis data features sliding in two directions; significantly less scatter exists when considering dissipated energy.

Effects of Thickness of Weak Layer

The influence of T_w on the consistency between sliding block and continuum analyses can be evaluated, in a broad sense, by considering the relationship between T_w and the displacement and work ratios (Figures 6.30 and 6.31) for all ground slope and strength

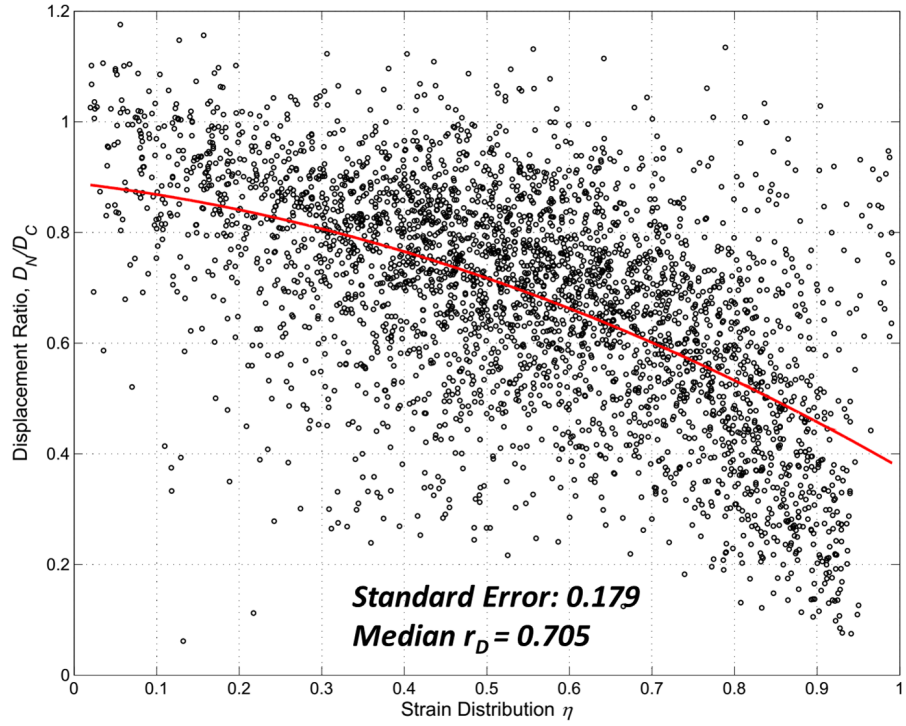

(a)

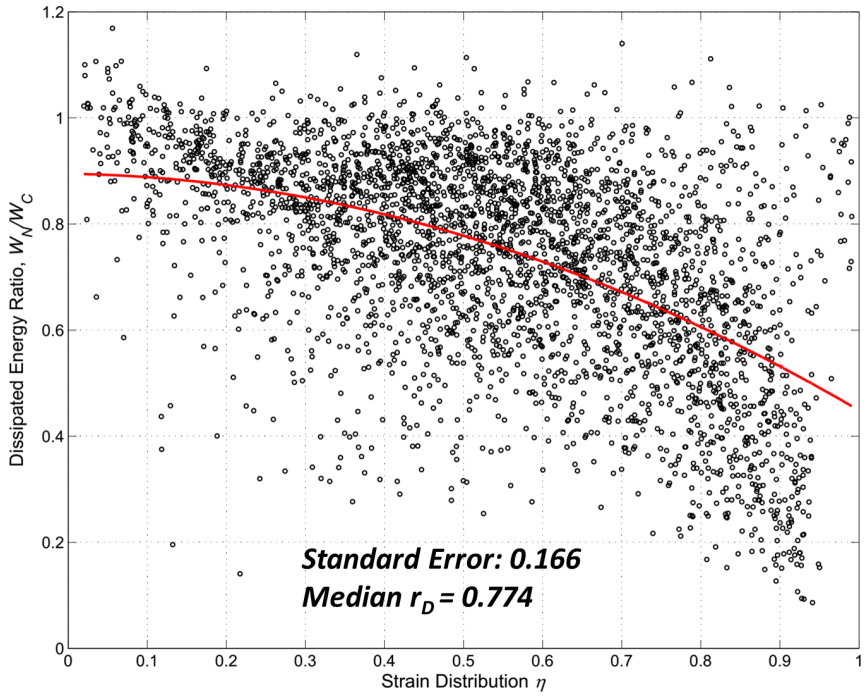

(b)

Figure 6.29: Relationships between (a) Displacement ratio and strain distribution parameter and (b) Work ratio and strain distribution parameter, based on data obtained from a series of computations using Newmark- and PSNL-based analyses on all ground slope and soil strength cases

cases. The plot of median displacement ratio against T_w in Figure 6.30a shows a rapid decrease in r_D of about 20% from its initial value of 0.8 as the thickness increases from 0.1 to 1.0 m. The divergence between the Newmark and PSNL displacements increases at a rate of approximately 5% per 1.0 m thereafter; at $T_w = 5.0$ m, the sliding block analyses predicted displacements that were, on average, about 55% lower than their corresponding PSNL analyses. Similar behavior is observed in the relationship between the work ratio and weak layer thickness (Figure 6.31), albeit with the overall magnitudes of r_W about 7% higher than r_D for all cases.

The effects of weak layer thickness can also be examined by comparing the Newmark- and PSNL-based computed displacements in the $D_H - a_y/a_{max}$ framework discussed in Section 6.6.2 (see Figures 6.21 and 6.22). For each value of T_w, the results of the sliding block analyses were plotted against a_y/a_{max}, and then fit to the form of Saygili and Rathje's sliding block model. The process was repeated with the corresponding PSNL data. By plotting the $r_D - a_y/a_{max}$ curves for each weak layer thickness, the divergence between the two methods can be characterized with respect to both the weak-layer thickness and the magnitude of displacement.

Examining the displacement ratio curves (Figure 6.32), we see that r_D is very sensitive to small changes in the thickness of the weak layer when T_w is less than 1.0 m, across the full range of yield accelerations. At low yield accelerations (or high displacement magnitudes), r_D is naturally higher across all layer thicknesses, ranging from 0.6 at $T_w = 5.0$ m to greater than 0.9 m for the thin-layer case. At intermediate to high values of a_y, the displacement ratios are generally much lower (less than 0.6 for all T_w), due to the lower overall displacement magnitudes, for which small to moderate differences between the Newmark and PSNL analyses will still produce high r_D values.

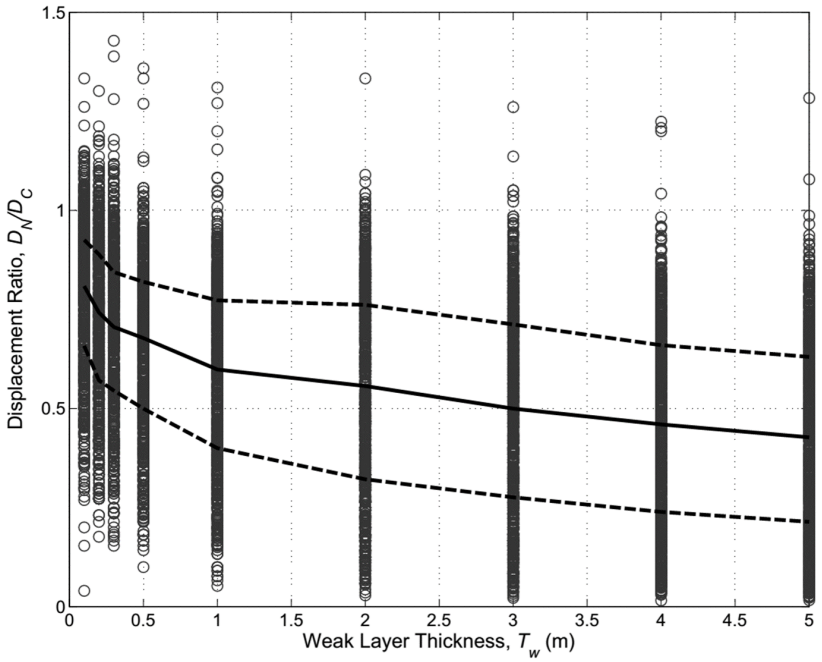

Figure 6.30: Relationship between displacement ratio and weak-layer thickness, based on data obtained from a series of computations using Newmark- and PSNL-based analyses on all slope and soil strength cases

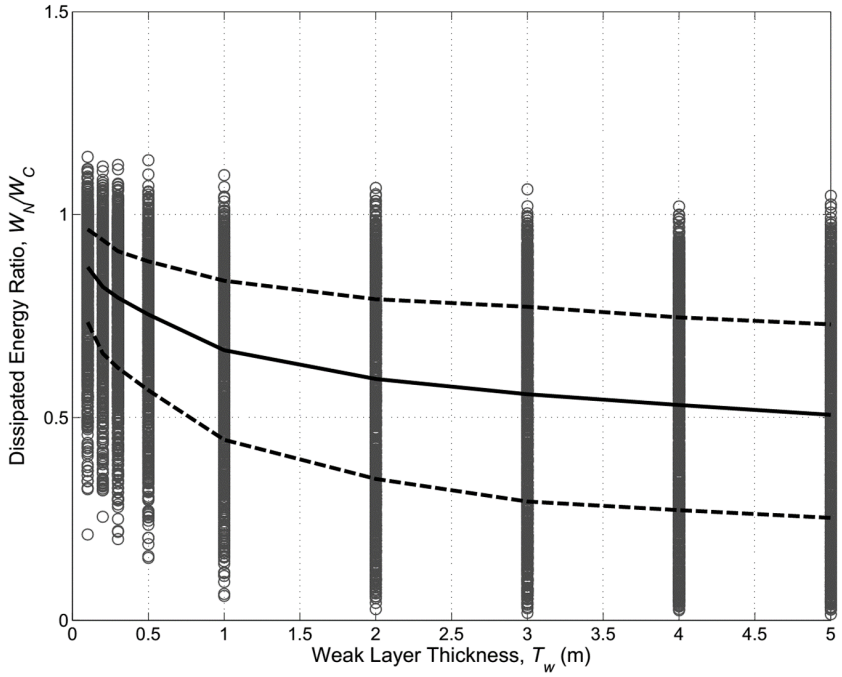

Figure 6.31: Relationship between dissipated energy ratio and weak-layer thickness, based on data obtained from a series of computations using Newmark- and PSNL-based analyses on all slope and soil strength cases

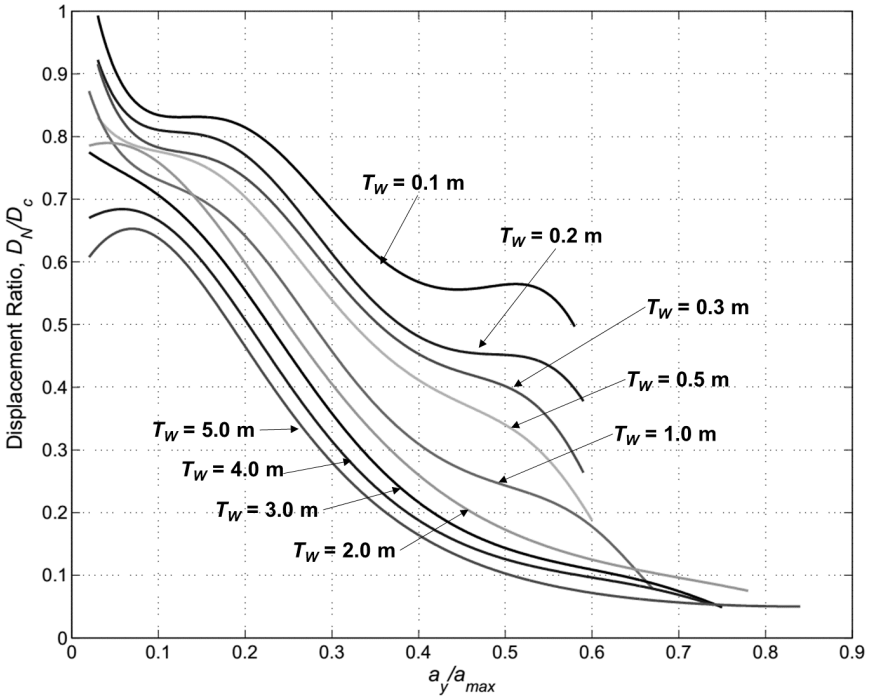

Figure 6.32: Displacement ratio curves for full range of T_w values,obtained by fitting to the Newmark-type empirical model of Saygili and Rathje (2009)

Effects of Ground Slope Inclination

The effects of ground slope inclination were examined by splitting the median ratio curves in Figures 6.30 and 6.31 into contours of ground slope angle (Figures 6.33 and 6.34). Based on these contours, a clear inverse relationship between r_D and slope angle exists in profiles with $T_w \leq 0.5$ m. For these types of sites, the discrepancy between the sliding block and continuum analyses increases for larger values of β. However, the sensitivity of both the work and displacement ratios to ground slope angle appears to be insignificant for sites with T_w greater than 0.5 m. There is no clear relationship between r_D or r_W and ground slope angle for these sites, and the curves for $\beta = 0.5°$, 2.0° and 3.0° are all within about 2% of each other. The behavior of the $\beta = 1.0°$ is somewhat intriguing, as it consistently plots about 5-10% below the rest of the curves for the thicker profiles.

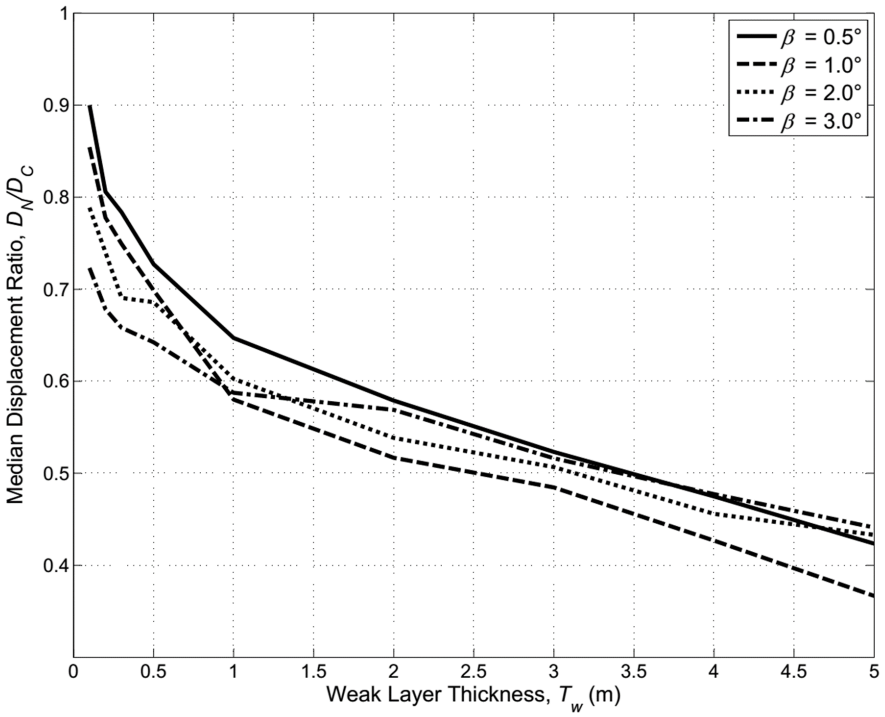

Figure 6.33: Relationship between displacement ratio and weak-layer thickness, for the range of ground slope angles analyzed

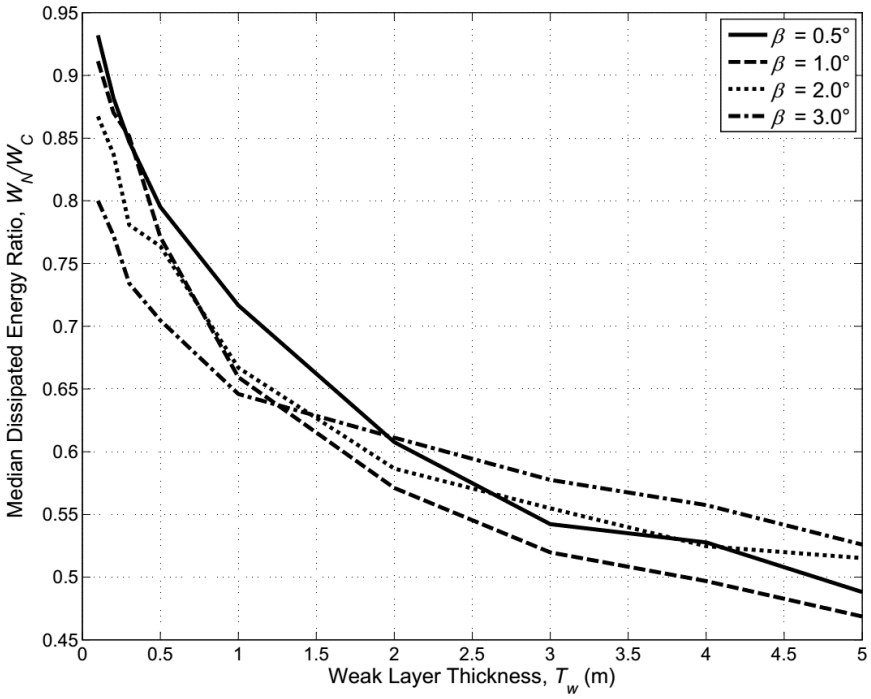

Figure 6.34: Relationship between dissipated energy ratio and weak-layer thickness, for the range of shallow ground slope angles analyzed

The source of this apparent discrepancy can be explained by examining the η–T_w curves for the same ground slope contours (Figure 6.35. It is clear that the permanent shear strains distribute much more evenly with depth in 0.5° and 1.0° profiles across the full range of weak-layer thicknesses. As was shown in Figure 6.29, better distribution of strain generally correlates to lower displacement and work ratios. While this effect is apparently largely mitigated in the 0.5° case due to back-sliding effects, the 1.0° sites do not benefit from the same counteracting effect. and thus plot much lower in $r_D - T_w$ space. Note that the counteracting effect of back-sliding is eliminated when r_W is considered, and both the shallower sites plot below the 3.0° curve at larger values of T_w.

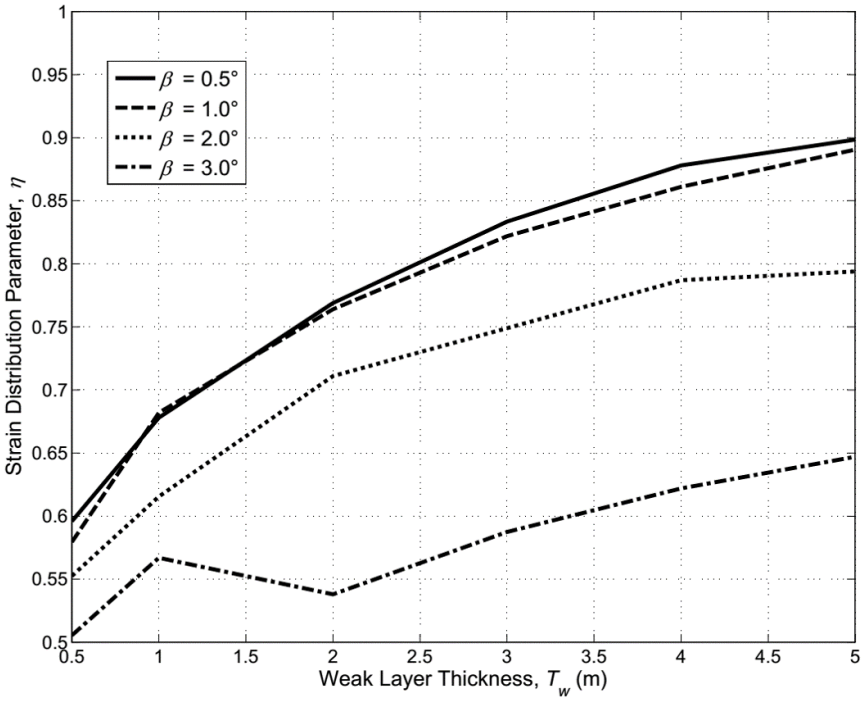

Figure 6.35: Relationship between strain distribution and weak-layer thickness for the range of shallow ground slope angles analyzed

Effects of Weak-Layer Strength

The $r_D - T_w$ and $r_W - T_w$ data are also presented as contours corresponding to the three soil strength classifications outlined in Table 6.4. Based on the curves shown in Figure 6.36, the displacement ratio generally decreases as the strength in the weak layer increases. This dependence becomes more pronounced as the thickness of the weak layer increases; the three curves are within about 5-8% of each other for $T_w \leq 0.5$ m, and about 10-15% of each other when T_w is larger than 0.5 m. These effects are far more pronounced when the data is considered with respect to dissipated energy (Figure 6.37); the three curves are within about 1-4% of each other when the weak layer is 0.5 m thick or smaller, and about 15-20% apart when T_w is 1.0 m or higher.

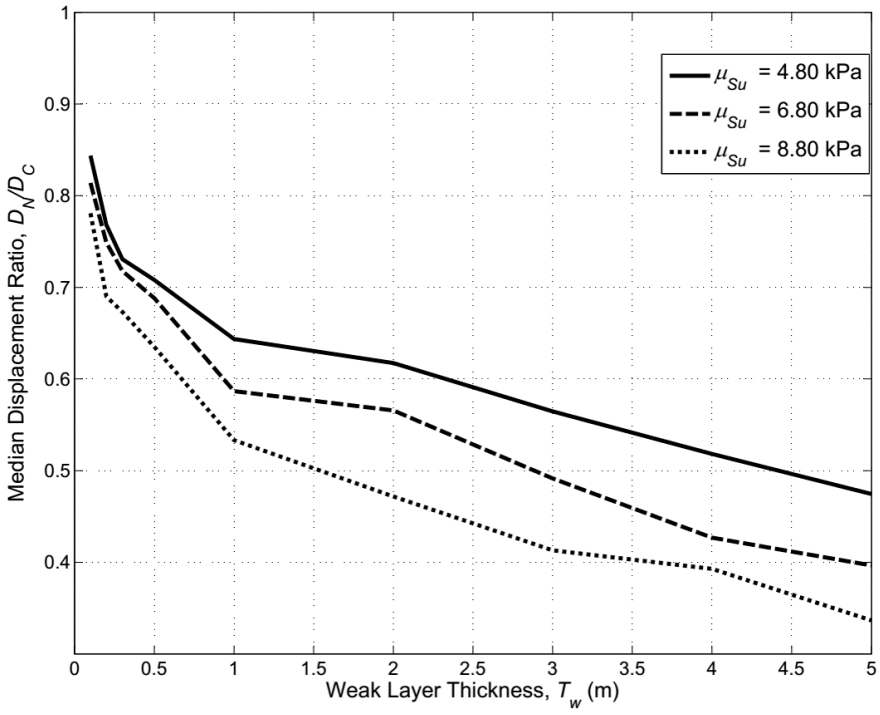

Figure 6.36: Relationship between displacement ratio, weak layer thickness, and weak layer soil strength

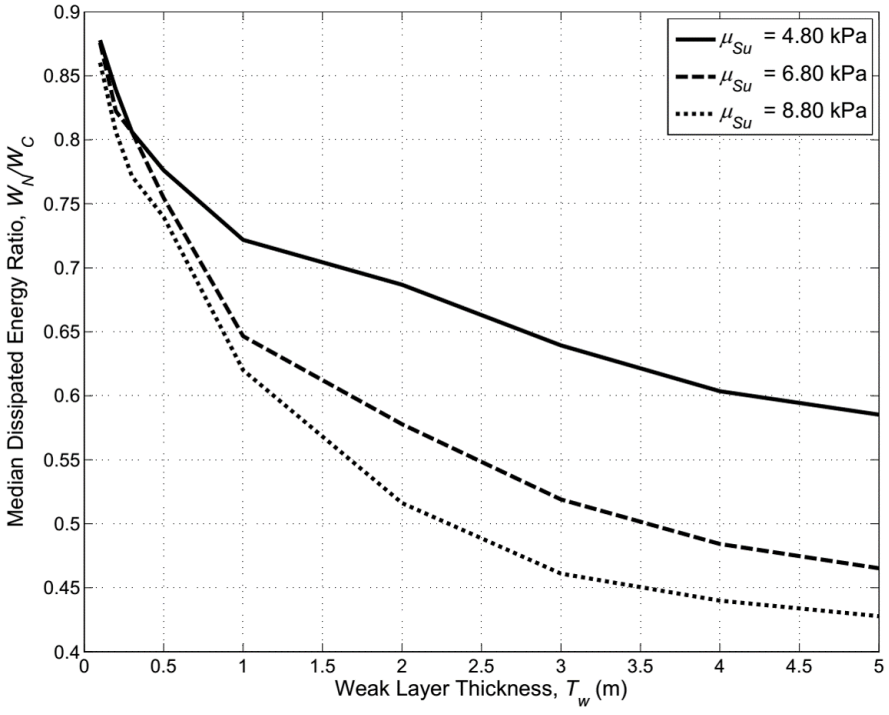

Figure 6.37: Relationship between dissipated energy ratio, weak layer thickness, and weak layer soil strength

This inverse relationship between r_D and strength can be explained in part by considering that r_D is generally lower for high displacement magnitudes, and that the higher-strength soil profiles would have been expected to produce generally lower displacement values. Indeed, the median PSNL-based displacements for the "Low", "Medium", and "High" strength soil profiles were 20.4 cm, 11.0 cm, and 8.4 cm, respectively. Another factor in the $r_D - S_u$ relationship is how the distribution of strains throughout the weak layer is affected by the strength of the weak-layer material. It is clear from Figure 6.38 that soil profiles with higher strengths see a better distribution of strains over a wide range of site conditions. This phenomenon has some physical basis, as stronger material will see lower strains and fewer instances of failure, thus dissipating less energy and allowing stress waves to propagate upwards through the weak stratum without being significantly damped.

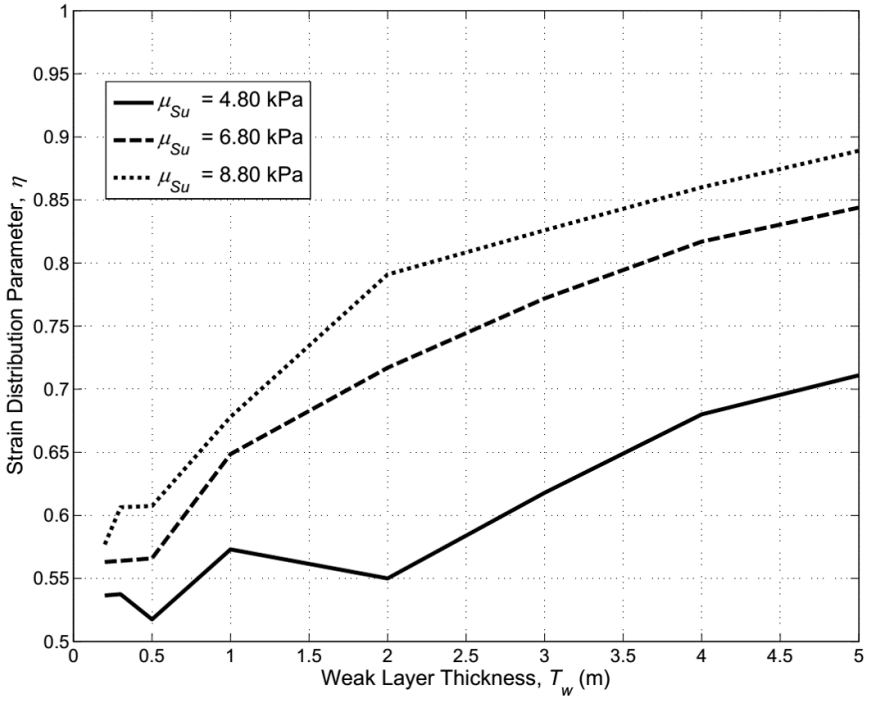

Figure 6.38: Relationship between strain distribution, weak layer thickness, and weak layer soil strength

6.6.5 Summary and Conclusions

In this section, the Newmark sliding block framework was investigated in relation to how reliably it can predict displacements at sites where deformations are expected to be distributed throughout a layer of weak material. A series of hypothetical soil profiles, with varying weak-layer thicknesses, shallow ground slope angles, and soil strengths, were subjected to the dynamic finite-difference total stress model PSNL to simulate the "actual" response of the soil profiles. The results from the PSNL analyses were compared to equivalent Newmark sliding block analyses on the same soil profiles. Displacements, dissipated energies, and the work-displacement relationships obtained using each method were compared, and general trends were evaluated with respect to the thickness of the weak layer, ground slope angle, and soil strength.

The results for all 108 soil profiles are summarized in Appendix C. Overall, the results indicated that the Newmark sliding block analysis tends to significantly under-predict displacements when compared to continuum dynamic analyses for sites where weak material exists over a broad range of conditions. It was shown that even when the weak layer is as thin as 10 cm, rigid block analyses tended to predict displacements that were on average about 25% lower than the actual displacements. Differences in displacements between the two methods increased rapidly with increasing weak-layer thickness. At sites where deformations occurred in 0.5 m-thick layers, Newmark-based displacement predictions were about 40% lower than their PSNL counterparts on average, with displacement ratios decreasing by about 5% for every 1.0 m increment of weak-layer thickness for sites where T_w was 1.0 m or greater.

The relationship between dissipated energy (or work) and displacement, which was seen to be far more consistent between the two analysis methods ($r_{W,D}$ was about 90% or higher for all sites) for thin weak layers and relatively independent of soil strength or ground slope angle, also exhibited a significant, albeit less dramatic decrease as the weak layer thickness was increased. In other words, the sliding block analyses generally predicted slightly lower displacements (by less than 10%) for the same amount of work done than the continuum dynamic analyses for the thin-layer cases. However, this discrepancy increased significantly as the thickness of the weak layer was increased.

The reliability of the Newmark analysis in modeling displacements in these types of sites is also dependent on other site factors such as ground slope inclination and material strength. It has been shown that, for site where deformations occur in relatively thin layers (less than about 0.5 m), the displacement and dissipated energy ratios are highly sensitive to changes in ground slope angle, with sliding block analyses diverging further

from dynamic continuum analyses as the ground slope inclination increases. It was also found that the ratio of Newmark- to PSNL-based displacements was generally lower for sites with higher soil strengths, particularly when weak-layer thicknesses were greater than 1.0 m.

Fundamentally, the ability of the Newmark analysis to model displacements at sites where weak layers are of a significant thickness lies in the level of strain distribution that occurs in these types of strata. It was shown (see Figure 6.29) that as the strain distribution parameter increases, the accuracy of the sliding block simplification decreases, and does so particularly rapidly when η is greater than about 0.7. Thus, sites where greater strain distribution might be expected to occur, such as sites with thicker weak layers, on shallower ground, and with higher soil strengths, may be even less suitable for modelling using Newmark analyses.

It should be noted that a great deal of variability exists in all of the data obtained in these analyses. Much of this can be attributed to the record-to-record variability from the suite of 90 ground motions used, which were selected intentionally to include a broad range of ground motion characteristics. The amplitude, frequency content, and duration characteristics of the input ground motion may have a significant influence over how the strains are distributed throughout the weak layer, and thus how well the sliding block analysis can model a continuum soil column. Even so, the central tendencies of the displacement and work ratios presented here suggest that structural biases are rather significant in using a rigid-block model that assumes a discrete failure surface. The results of these analyses have shown that the Newmark analysis is highly unconservative in predicting displacements at site where distributed deformations may occur, even for relatively thin weak-layer cases and shallow sloping ground conditions.

6.7 Summary

In this chapter, several important issues pertaining to the use of Newmark sliding block analyses to predict earthquake-induced slope deformations were examined in detail. Practical considerations, potential sources of bias (structural and otherwise), and sources of uncertainty were investigated, and their potential effects on sliding block-based displacement predictions were characterized. The first component that was examined is the selection and usage of ground motion time histories as inputs to a sliding block analyses. Customarily, ground motions are selected on the basis of how well they match a specific target spectrum, and can be optimally scaled to match that spectrum. The target spectrum is often based on careful consideration of site and source characteristics, and is usually de-

termined using empirical ground motion prediction equations. Despite the relative success and ease of implementation of this type of selection method, significant record-to-record variability is still a large source of uncertainty in the application of sliding block analyses.

Once ground motions are selected, the next consideration relates to *how* they are applied to the sliding block. Kramer and Lindwall (2004) noted that a single ground motion record from a seismograph will usually include three orthogonal components: two horizontal, and one vertical. The manner in which these components are accounted for – they can be applied in a pseuo-tangential, true tangential, or true two-dimensional manner – can significantly impact the sliding block results. Kramer and Lindwall found that in shallower slopes less than about 10°, ground motion dimensionality had little impact. For steeper slopes, using a single component of ground motion can significantly under-predict displacements in frictional materials. Another factor explored by Kramer and Lindwall was the orientation of the ground motion relative to the orientation of the slope. For near-fault sites, this azimuthal variation can be quite significant, and oftentimes simply taking the geometric mean of the two horizontal component motions (as is often done in practice) can in fact produce unconservative estimates of the permanent sliding block displacement.

Another practical consideration that may affect sliding block analysis results is the specification of the sliding direction of the block. In many cases, the yield acceleration is simply specified in the downslope direction, and the practitioner assumes that no upslope displacement will occur at the site. A simple set of analyses showed that this assumption is only valid for sites with inclinations steeper than about 20°; for sites on shallower ground, significant displacement can occur in the upslope direction, and the assumption of one-way sliding may be overly conservative in predicting permanent displacements.

It is also pertinent to examine some of the simplifications that the sliding block method makes, and how they might introduce some biases into the seismic design process. Sliding block models have evolved significantly over time, and can presently be classified as rigid, de-coupled, or fully-coupled, with the latter two classified as "compliant" block models. It has been well established that slopes rarely behave in a completely rigid manner under dynamic loading; Wartman et al. (2003) showed that the assumption of a rigid mass can be unconservative when the site period is nearly equal to the predominant or mean period of the input ground motion. The de-coupled model, which presents a significant improvement over the rigid block model from a structural standpoint, may also be slightly unconservative at sites with deep, soft slopes. All of the models presented in this chapter were developed using some form of empirical data, and thus are all inherently uncertain. Therefore, these models should be utilized with a characterization of the aleatory uncertainty, within a

probabilistic framework.

Finally, the biases inherent to the assumption of a discrete plane along which deformations are concentrated were also characterized. It was found that for sites where deformations might be expected to occur in a relatively thick stratum of weak material, the simplification of ductile failure of a rigid sliding block along a frictional surface is severely unconservative. For many sites underlain by deposits of weak material that are as thin as approximately half a meter, sliding block analyses can under-predict permanent deformations by nearly 35%, and become even more unconservative as the weak stratum increases in thickness.

The Newmark sliding block model can be a powerful tool for the practicing engineer to use in characterizing seismic slope stability. It is computationally easy to implement, and has the benefit of a large volume of research efforts to supplement its utility. It is important, however, to recognize the various ways in which the model may be overly conservative or, more dangerously, unconservative. A thorough characterization of the uncertainty is a necessary and practical step to take when using sliding block analyses. It is also important to understand what the model does and does not represent; it is an analytical model that simulates a rigid block, deforming in a ductile manner, on a frictional surface. Thus, the more the site of interest differs from this idealization, the less reliable the sliding block model may be in accurately modelling the site's seismic stability.

Chapter 7

APPLICATION OF SLIDING BLOCK ANALYSES TO LATERAL SPREADING

7.1 Introduction

The applicability of sliding block analyses to general seismic slope stability problems has been widely established and well-documented. It provides an improvement upon the pseudo-static limit equilibrium by better representing earthquake loading, and providing an actual estimate of the seismically-induced displacement, rather than a simple index of stability. More recently (Olson and Johnson 2008), the applicability of sliding block analyses has been extended to evaluate a special case of weakening seismic slope stability: liquefaction-induced lateral spreading. The ability of rigid block analyses to accurately capture the mechanisms prominently featured in lateral spreading has not been documented, however, and thus the mobilized strength ratios back-calculated by Olson and Johnson, as well as the lateral spreading displacements their procedure purports to predict, have not been thoroughly evaluated with respect to any potential biases and uncertainties inherent to rigid block assumption.

This chapter can be roughly divided into two parts. First, the general issues relevant to sliding block analyses that were discussed in Chapter 6 are examined within the context of lateral spreading, specifically Olson and Johnson's framework. The issues of ground motion selection, dimensionality, and directionality, and their effects on O&J's use of sliding block analyses are examined. Furthermore, the structural biases related to the rigid

mass and discrete failure plane assumptions are discussed in how they may affect O&J's estimates of the back-calculated yield acceleration and mobilized strength ratio. The second portion of this chapter consists of repeating the back-analysis and forward-prediction framework proposed by Olson and Johnson in a completely probabilistic framework for two of the case histories from their database. Uncertainty due to the ground motion selection process, record-to-record variability, soil and site parameters, and *in situ* penetration resistances, are all accounted for in an effort to quantify the precision with which the back-calculated mobilized shear strengths and predicted displacements can be calculated using the O&J method.

7.2 Ground Motion Selection

The "NGA Method" for selecting ground motions as inputs to a sliding block analysis (see Section 6.2) is based on the principle of developing a "target" response spectrum that reflects the source, path, and site characteristics of interest, and selecting a suite of scaled ground motions that best match it. The methodology employed by Olson and Johnson for selecting ground motions differedsignificantly from the NGA method. To develop a sliding block-based relationship between the observed displacement and back-calculated yield acceleration for their case histories, O&J used the following search criteria to generate suites of at least 20 ground motions for each case history:

- Same rupture mechanism (e.g., strike-slip fault)
- Moment magnitude (M_w within approximately $\pm 5\%$ of the event M_w
- Peak ground acceleration within approximately $\pm 30\%$ of the PGA recorded or estimated at the site
- Identical site classification, based on v_{s30} (Table 7.1)

Each ground motion was then scaled by a constant factor to match the recorded or estimated PGA at the site. Of the 39 case histories, 17 can be considered to have had "high-quality" estimates of PGA; that is, the estimates were based directly on data from nearby ground motion recording stations, or from event-specific attenuation relationships. 14 cases can be considered to have lower quality ground motion data, where PGA estimates were inferred from USGS shake maps or equivalent ground motion contour maps, GMPEs, or some other method of inference. Finally, eight cases, including the six cases from the Luzon earthquake, were considered to have poor or no ground motion data. In cases where

ground motion data was not widely available, O&J did not specify exactly how their *PGA* estimates were obtained. For the purposes of this discussion, the aforementioned criteria will be referred to as the "OJ08 Method".

Table 7.1: Caltrans/NEHRP soil profile types (Wair et al. 2008)

Site Classifiaction	Soil Profile Designation	v_{s30} (m/s)	SPT N-value	Undrained Shear Strength (kPa)
A	Hard Rock	> 1500	-	-
B	Rock	760 to 1500	-	-
C	Very Dense Soil and Soft Rock	360 to 760	> 50	> 100
D	Stiff Soil	180 to 360	15 to 50	50 to 100
E	Soft Soil	180	< 15	< 50

There are some significant differences between the NGA and OJ08 methods for selecting ground motions. First, the NGA GMPE-based method uses significantly more factors to characterize the earthquake and site conditions for each case history. In addition to earthquake magnitude and faulting mechanism used in both methods, the NGA method also includes factors such as source-site distance, hanging wall factors, fault dip angle, depth to rupture, and rupture width. Furthermore, the site stiffness is accounted for in a continuous manner, using v_{s30} as a GMPE input, rather than as a way to classify the site into discrete bins; a site with a v_{s30} of 180 m/s may have a significantly different earthquake response to one with v_{s30} of 360 m/s, yet using the OJ08 criterion, ground motions from sites spanning that range of v_{s30} are treated and classified similarly. The procedures also differ in how they scale the ground motions. The OJ08 method scales to the single *PGA* value that is observed or estimated to have occurred at the site, while the NGA method seeks to produce ground motions that match a wider range of periods by scaling to match an entire target spectrum.

In order to analyze how the different selection criteria might affect the $D_H - a_y$ relationship, three lateral spreading sites were subjected to sliding block analyses using ground motions obtained by both the OJ08 and NGA selection criteria. The Wildlife Array (Case 7) and Moss Landing (Cases 8-11) were ideal cases to isolate and evaluate the effects of using different ground motion selection criteria. The Wildlife site is a particularly reliable case, due to the availability of both downhole and surface acceleration time histories from

the 1987 Superstition Hills earthquake; the NGA motions for this site were thus based on a target spectrum obtained from the downhole ground motions (see Figure 6.1). The Moss Landing spread was an ideal case for which GMPEs could be used to generate a target spectrum; the site was about 25 km from the Loma Prieta fault rupture, and thus near-fault uncertainty involved in using GMPEs to predict the *PGA* as well as estimating the actual site *PGA* based on ground motion contour maps is reduced significantly. Furthermore, the GMPE-predicted *PGA* is relatively close to the documented estimates for Moss Landing, and thus potential bias in ground motion intensity that would occur as a result of the *PGA*-scaling used in the OJ08 method was significantly suppressed.

7.2.1 Analysis Procedure

Using the online ground motion database from PEER NGA West-2, a suite of 20 ground motions for each case was generated based on the O&J criteria, as summarized in Table 7.2. The NGA ground motion suite for Moss Landing was obtained by first estimating the target response spectrum using the GMPEs discussed in Section 6.2; the GMPE input variables are summarized in Table 7.3. The target response spectrum for the Wildlife case history was obtained using the downhole array accelerograms as described in Section 6.2. The target spectra are plotted in Figure 7.1. Note the relative smoothness of the Moss Landing target spectrum, which was generated from empirical predictive relationships, compared with the target spectrum obtained from the real ground motions recorded at the Wildlife Array. Scaled ground motions were obtained by minimizing the mean squared error of their response spectra relative to the target spectrum, as described in Section 6.2, and the 20 ground motions with the lowest *MSE* were selected for Newmark sliding block analyses.

Table 7.2: Ground motion search parameters using Olson and Johnson selection criteria

Earthquake	Site	Rupture Mechanism	M_w (±5%)	*PGA*, g (±30%)	Site Classification
1987 Superstition Hills	Wildlife Array	Strike-Slip	6.5 (6.2-6.8)	0.21 (0.15-0.27)	*D* (Stiff Soil)
1989 Loma Prieta	Moss Landing	Strike-Slip	7.0 (6.6-7.4)	0.25 (0.15-0.32)	*D* (Stiff Soil)

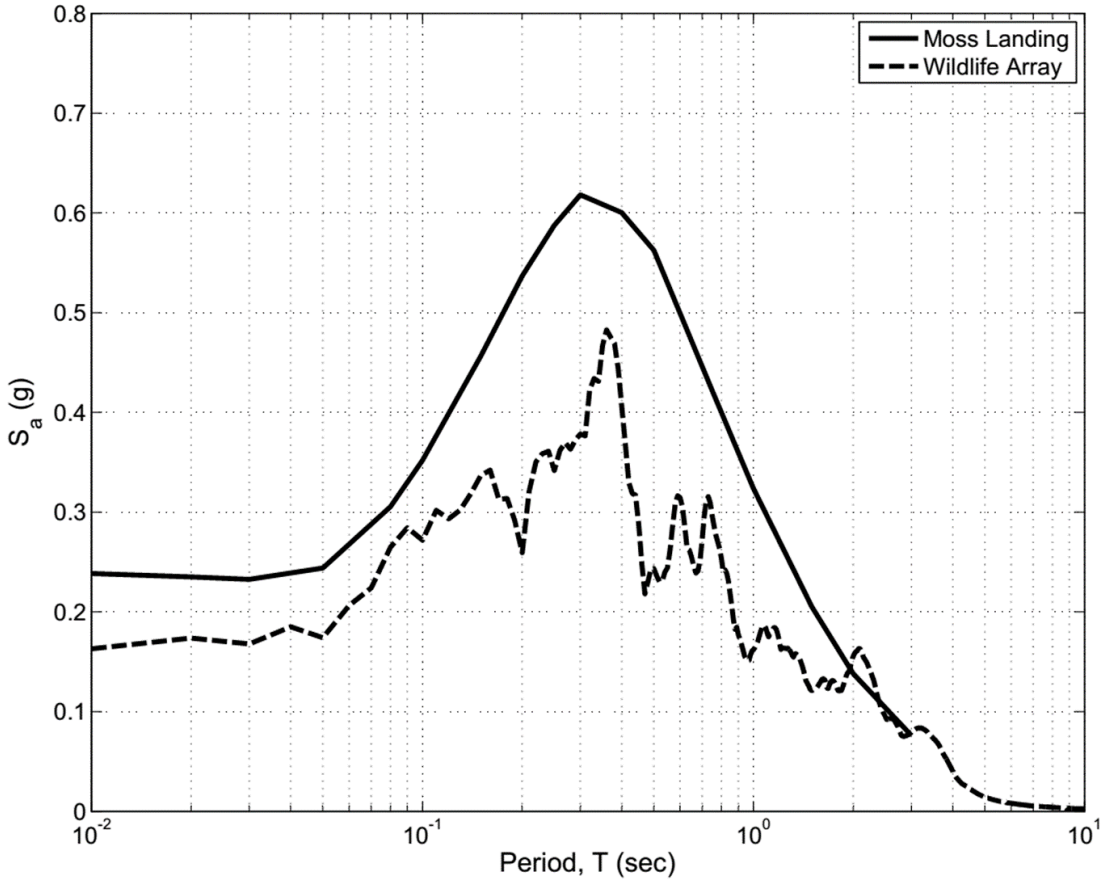

Figure 7.1: Target response spectra for lateral spreading sites at Moss Landing (1989 Loma Prieta) and the Wildlife Array (1989 Superstition Hills)

Table 7.3: Summary of GMPE input values for lateral spreading sites at Wildlife Array (1987 Superstition Hills), and Moss Landing (1989 Loma Prieta)

1989 Loma Prieta, Moss Landing	
Moment Magnitude, M_w	7.0
Fault Type	Strike-Slip
Source-Site Distances (R_{rup}, R_{jb}, R_x, R_{y0}) (km)	17, 16, 21, 0
Site Shear Wave Velocity, V_{s30} (m/s)	205
Fault Factors (F_{RV}, F_{NM}, F_{HW})	0, 0, 1
Dip Angle (degrees)	70
Rupture Depths (Z_{tor}, Z_{hyp}) (km)	1.5, 17.5
Depths to $V_s = 1$ and 2.5 km/s ($Z_{1.0}$, $Z_{2.5}$) (km)	0.06, 2
Rupture Width (km)	18
Estimated PGA (g) ($\pm$ 1 standard deviation)	0.238 (0.145-0.393)
Observed PGA (g)	0.250

7.2.2 Results and Discussion

Comparison of Ground Motion Characteristics

The scaled ground motion suites obtained using each selection criteria were characterized by determining the PGA, PGV, PGA/PGV ratio, mean period (T_m) (Rathje et al. 1997), significant duration (T_d), and Arias intensity (I_a) for each ground motion. The central tendency and scatter for each ground motion parameter can be visualized using the box-and-whisker plots in Figure 7.2.

These results indicate that the NGA selection method generally yields suites of acceleration records that have more consistent ground motion characteristics, with the only obvious exception being for PGA, which is uniformly scaled in O&J's method to a single value, thus generating no PGA scatter in the OJ08 ground motion suites. The reasons for these differences are relatively straightforward. Generally speaking, the NGA method provides consistency over a broad range of frequencies, while the OJ08 method considers motions with respect to the single PGA value. In this sense, the OJ080 method does not account for the frequency content of ground motions, which is an important component of ground motion characteristics.

The NGA method's use of GMPEs is far more selective and restrictive in terms of site and source characterization than the OJ08 method of using four source and site search criteria. More specifically, as discussed earlier, v_{s30} is accounted for in a continuous manner by the NGA GMPE-based method, and thus the sites from which ground motions were obtained tended to have a narrower distribution of stiffnesses for the Moss Landing case history. It is also useful to examine the response spectra from each suite of response spectra (Figures 7.3 and 7.4), particularly the mean and plus/minus one standard deviation spectra. It is clear that the NGA method of selecting motions based on a target spectrum generally resulted in a suite of ground motions that had more consistent frequency contents, and overall more similar characteristics. In other words, the more restrictive selection method generally results in a more homogeneous set of ground motion records.

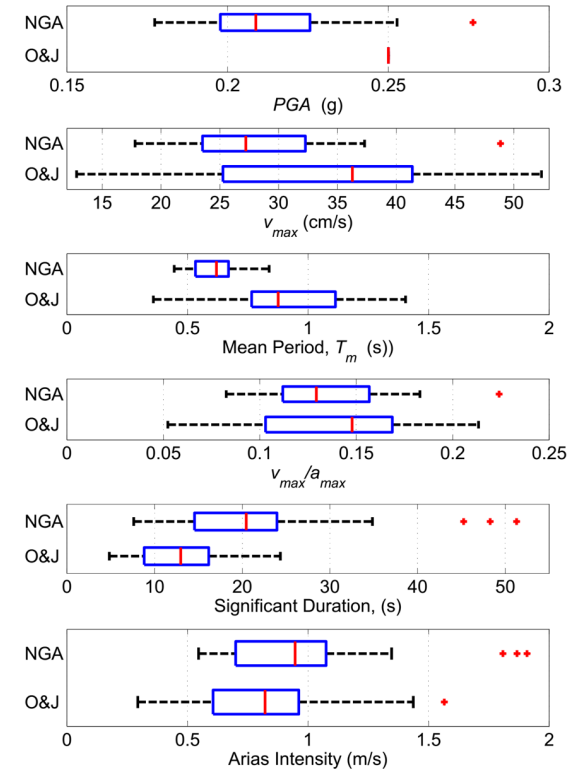

(a)

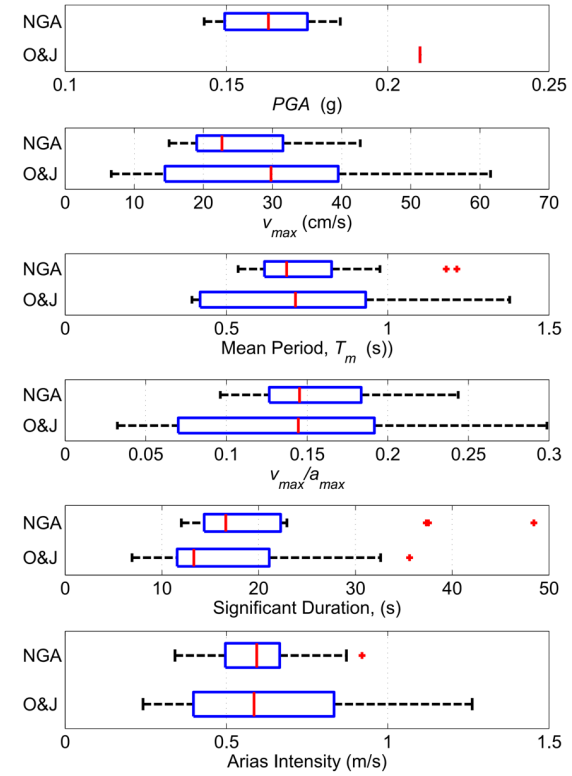

(b)

Figure 7.2: Box-and-whisker plots of OJ08- and NGA-generated ground motion suite characteristics for the (a) Moss Landing and (b) Wildlife Array sites

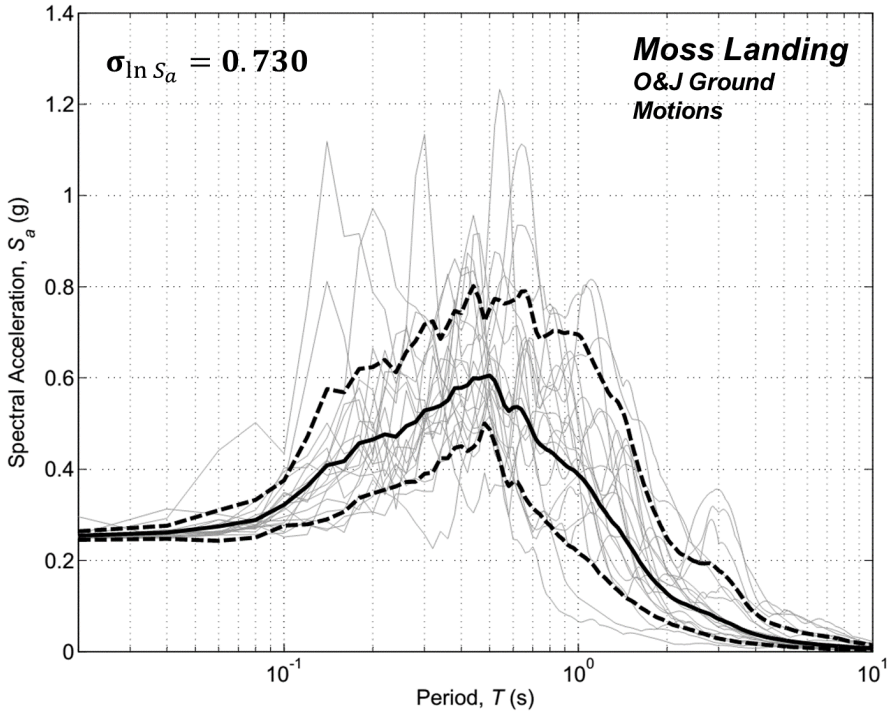

(a)

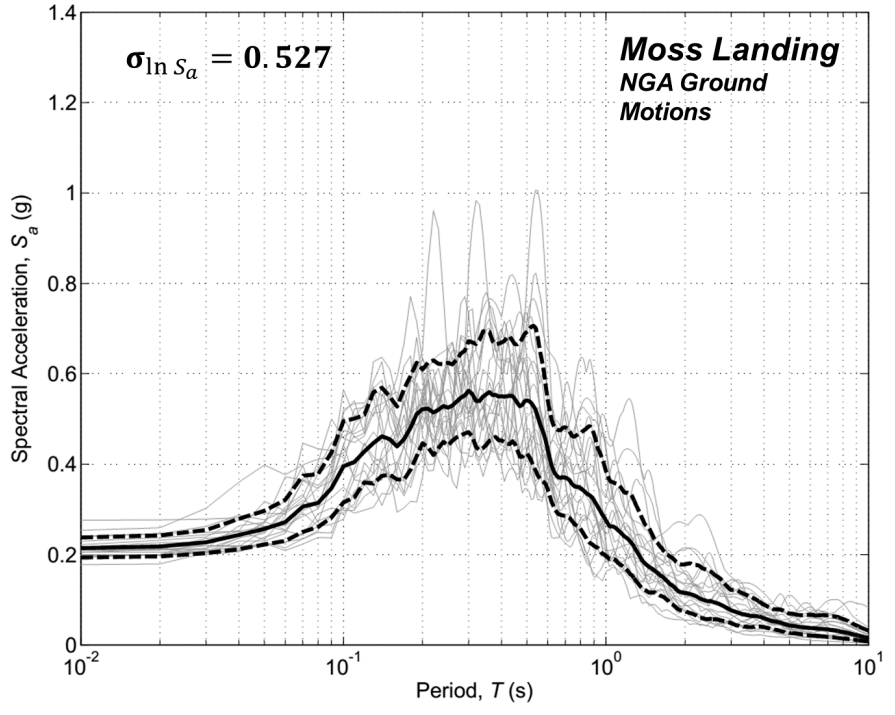

(b)

Figure 7.3: Response spectra from ground motion suites for the Moss Landing site, plotted with median and ± one standard deviation spectra, obtained via (a) the OJ08 method and (b) NGA method using a GMPE-based target spectrum.

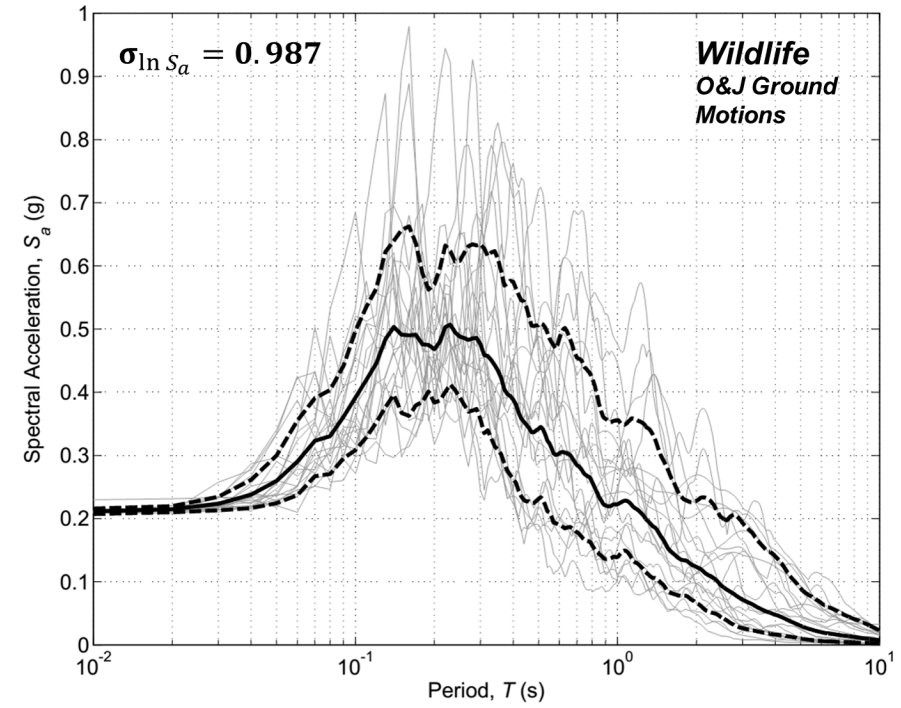

(a)

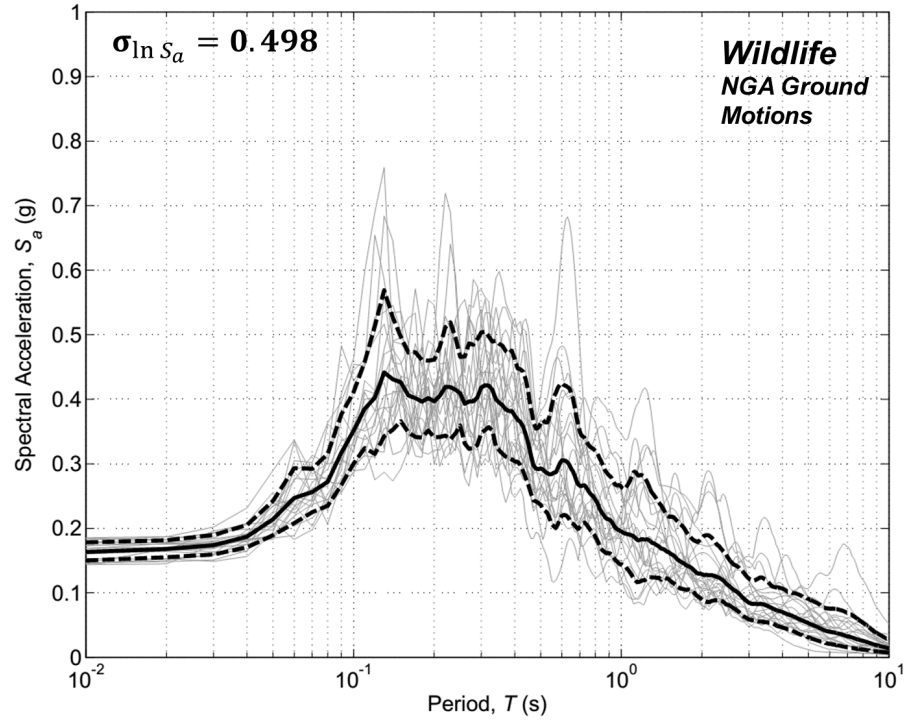

(b)

Figure 7.4: Response spectra from ground motion suites for the Wildlife Array site, plotted with median and ± one standard deviation spectra, obtained via (a) the OJ08 method and (b) NGA method using a GMPE-based target spectrum.

Bias and Uncertainty in Predicted Displacements

The sliding block analysis results in Figure 7.5 show that the relationships between a_y and D_H that were obtained using the OJ08 selection criteria differ significantly from those obtained using the NGA method. For both the Moss Landing and Wildlife Array case histories, the motions developed using the OJ08 selection criteria tended to predict significantly higher displacements throughout nearly the entire range of yield accelerations, with the only exception being at very low values of a_y for the Moss Landing curves, where the steeper NGA curve predicts slightly higher displacements.

The source of this bias becomes clear when the ground motion intensities for each of the suites are compared (see Figure 7.2); the OJ08 ground motion suites averaged significantly higher peak velocities and accelerations, durations, and Arias intensities than the corresponding NGA suites. For both cases, this was largely due the way the ground motion suites are scaled using each method. In particular, the OJ08 method relies heavily on estimating the peak ground acceleration, and thus any misinterpretation of site ground motion data can lead to significant errors in the scaling process. For the Wildlife case, the *PGA* reported by Olson and Johnson (presumably the value to which the ground motions were scaled) was 0.21 g. However, that value was obtained from the measured ground surface acceleration time history, and occurred *after* the onset of liquefaction, likely as a result of a dilation pulse (Figure 7.7). A more reasonable *PGA* estimate, taken from the downhole acceleration data, is closer to 0.17 g, resulting in a scaling factor error of about 20%.

The target spectrum scaling factors used for the NGA ground motion suite were, on average, about 42% lower than they would have been had the motions been scaled to *PGA*. For the Moss Landing case, the observed (0.25 g) and GMPE-estimated (0.24 g) were much closer; however, NGA scaling factors were still 17% lower on average than the PGA-scaled values.

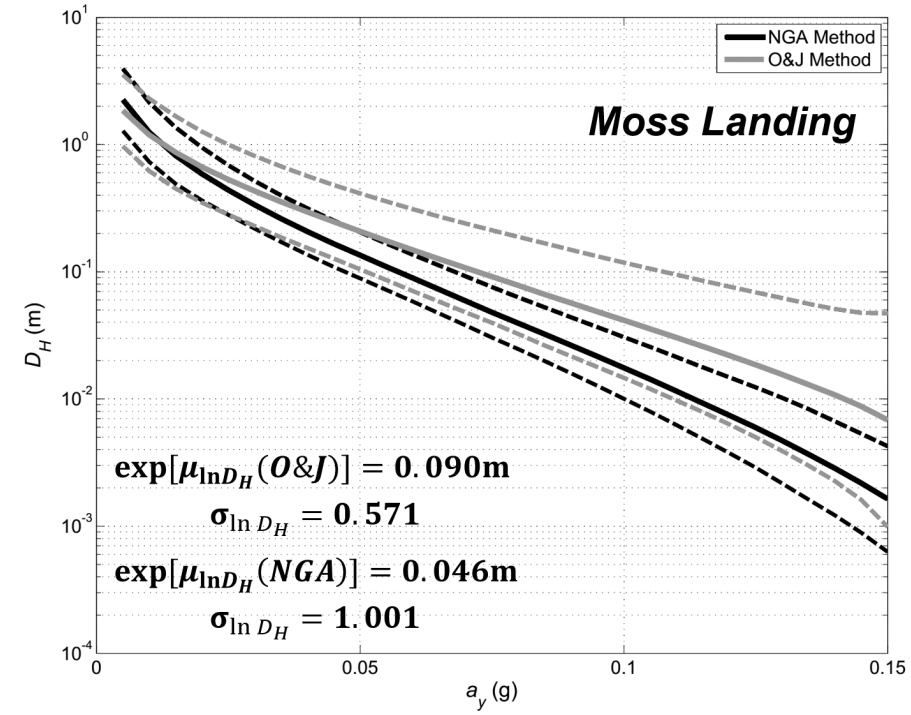

(a)

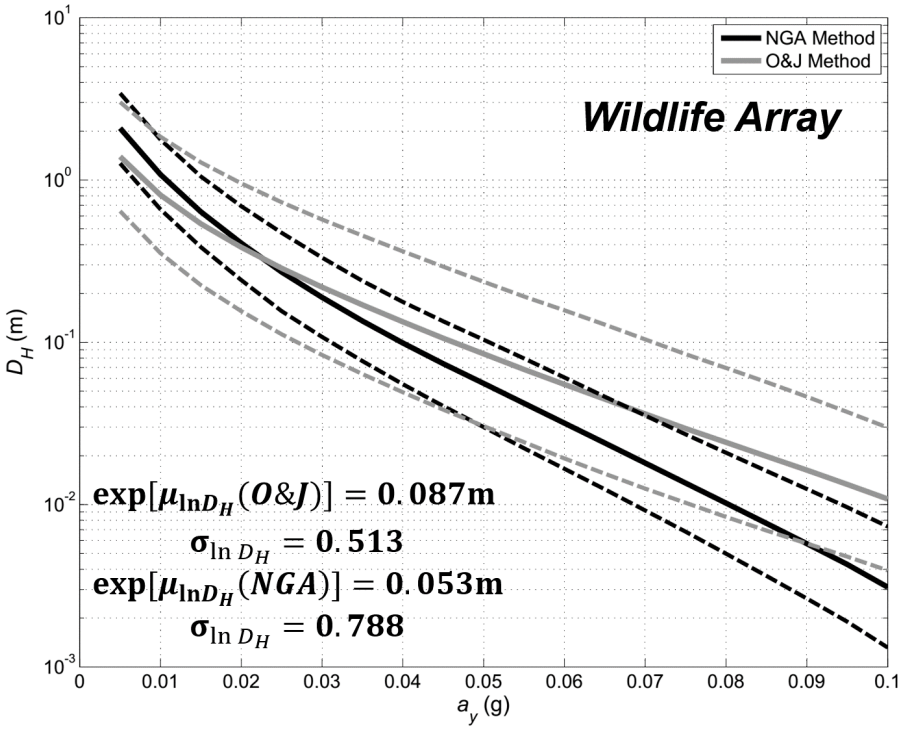

(b)

Figure 7.5: Sliding block-based relationship between yield acceleration and permanent displacement, using ground motions obtained by the OJ08 and NGA methods, for the (a) Wildlife Array and (b) Moss Landing lateral spreading sites

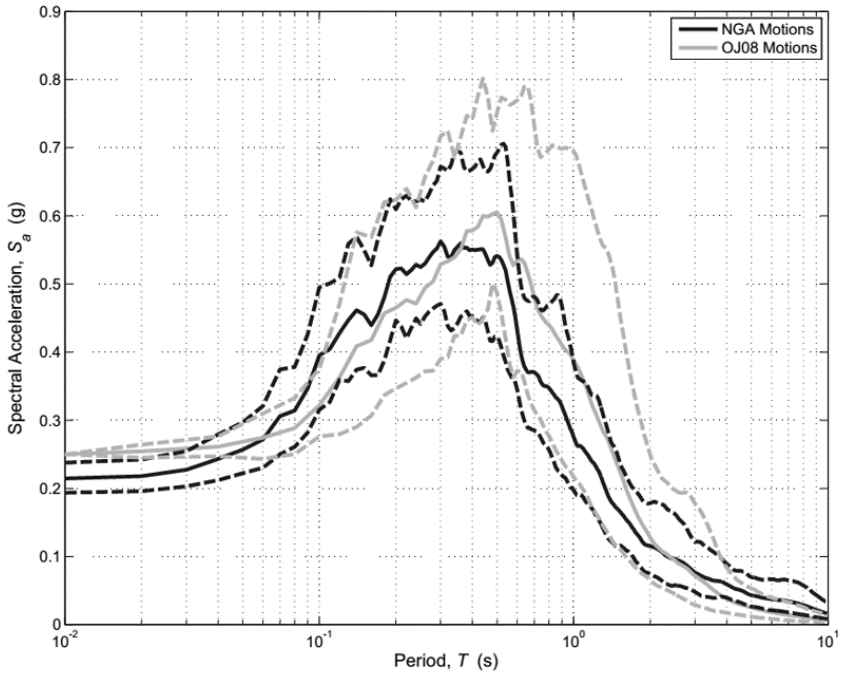

(a)

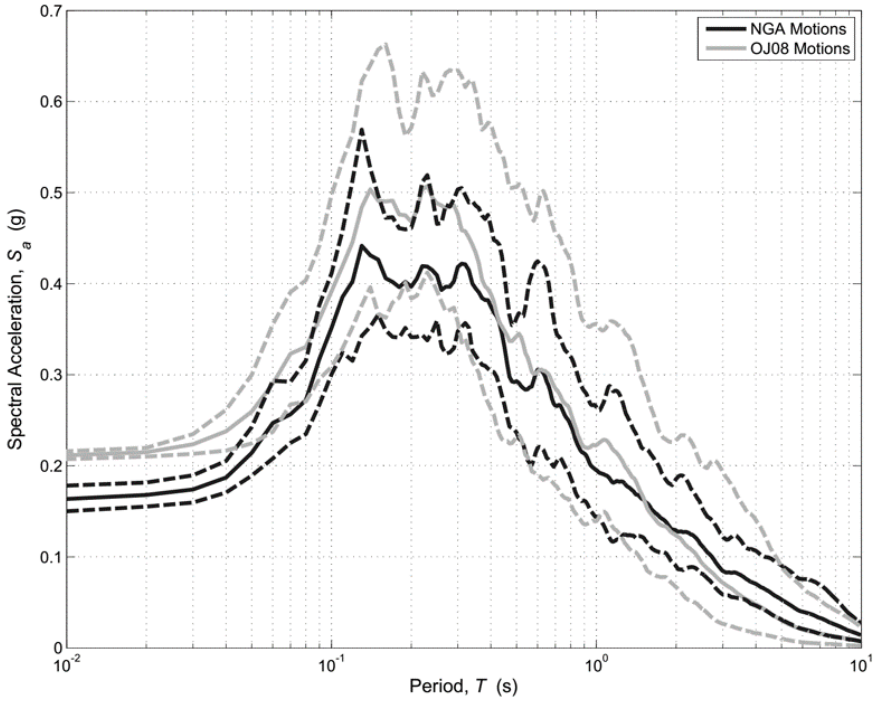

(b)

Figure 7.6: Comparison of median, 84th, and 16th percentile spectra for ground motions obtain using NGA and OJ08 selection methods, for (a) Moss Landing and (b) Wildlife case histories

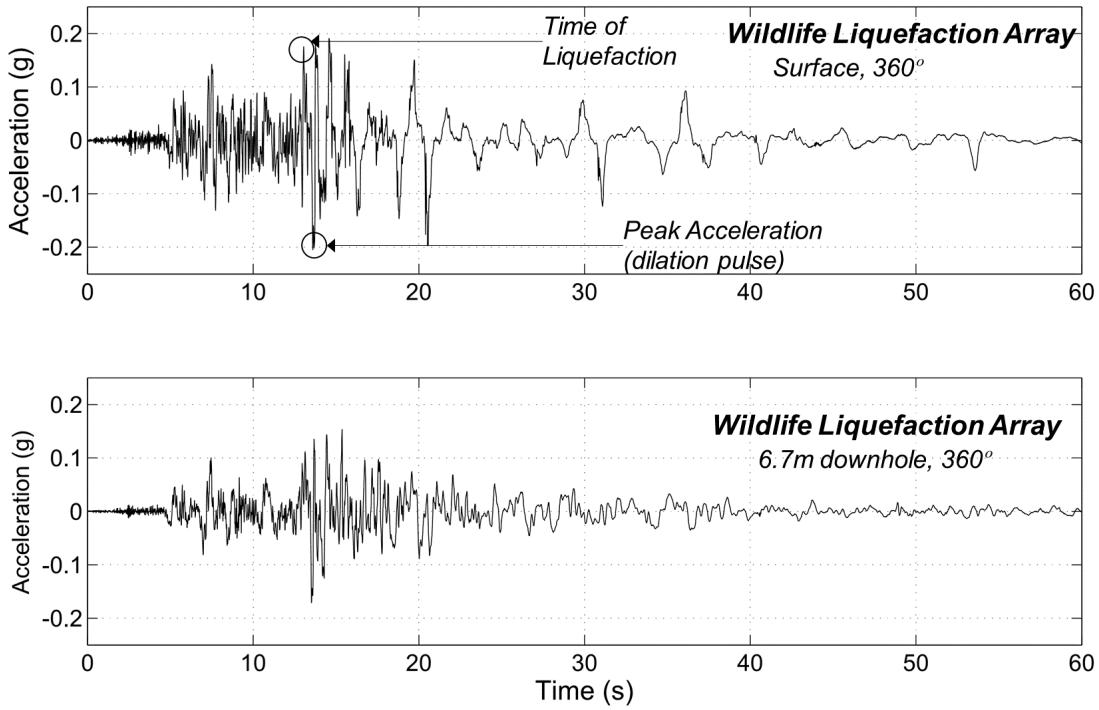

Figure 7.7: Comparison of downhole and surface acceleration time histories from the 1987 Superstition Hills earthquake at the Wildlife Liquefaction Array

The importance of scaling ground motions to a full target spectrum, rather than a single value of peak ground acceleration, can be evaluated by analyzing how sliding block displacements are correlated to spectral accelerations. A series of sliding block analyses were performed from the suite of 90 ground motions that span a wide range of magnitudes and source-to-site distances. Spectral accelerations for each motion were determined using an FFT-based response spectrum at 5% damping, and for a given period T, the spectral accelerations were plotted against the permanent displacements in log space (Figure 7.8). Linear regression was then used to determine a best fit line, and the correlation coefficient between the logarithms of spectral acceleration and displacement, $\rho_{\ln D, \ln S_a}$ were calculated. For the example shown in Figure 7.8, we see that the peak ground acceleration, represented here by $S_a(T = 0.01s)$, is correlated to permanent sliding block displacements at $\rho = 0.66$, where a value of unity implies perfect correlation, and a value of zero implies no correlation.

This procedure was repeated for the full range of periods to obtain a relationship between period and the correlation coefficient between $S_a(T)$ and D_H (Figure 7.9). It is clear from the figure that while PGA and D_H are correlated to a certain extent, displacements and spectral accelerations are much more closely correlated for periods between about 0.4 and 2 seconds. Referring back to the response spectra for the ground motion suites obtained for the Moss Landing and Wildlife sites (see Figures 7.3 and 7.4), we see

that while the OJ08 criteria produced ground motions with similar low-frequency characteristics, their spectral accelerations at the longer periods (where displacements are much more closely correlated) are much more variable than the NGA ground motion suites.

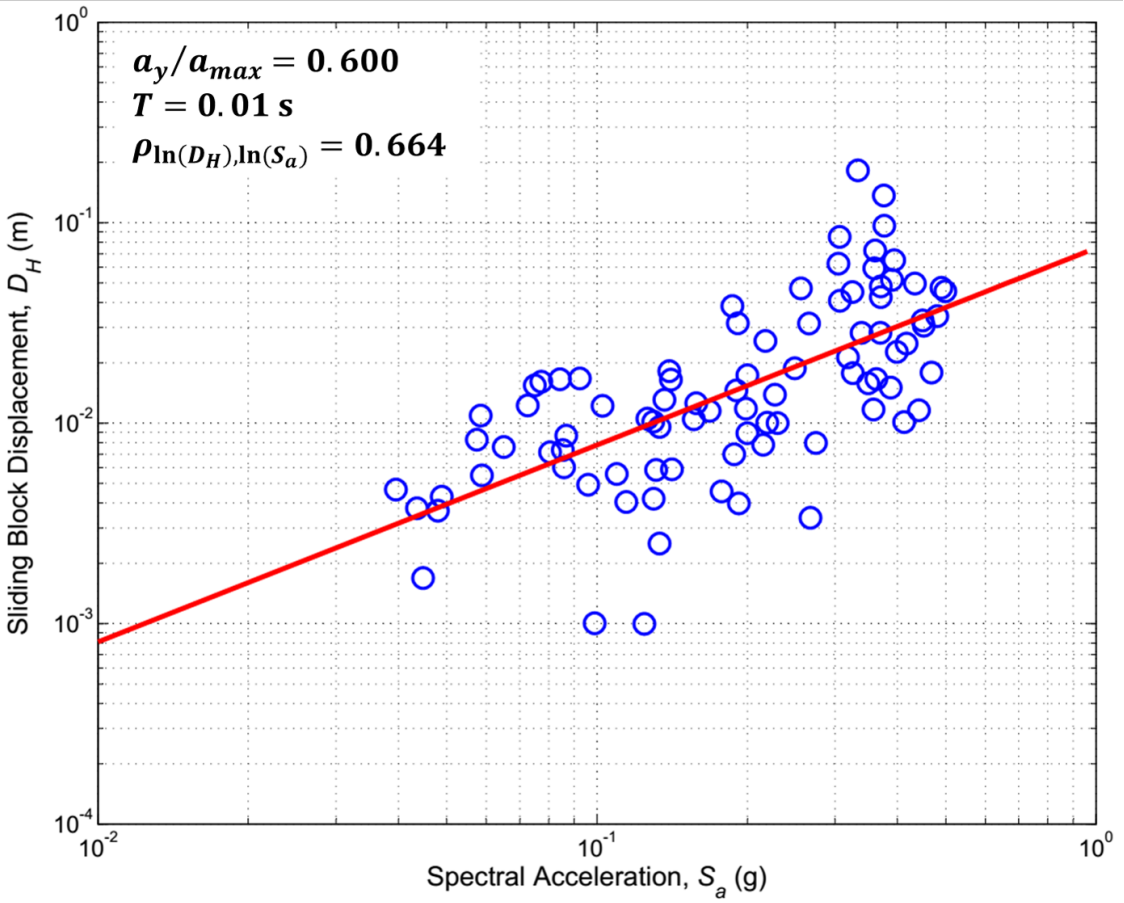

Figure 7.8: Determination of the correlation coefficient between the logarithms of spectral acceleration at $T = 0.01$ s and permanent displacement, using sliding block analyses from a suite of 90 ground motions at $a_y/a_{max} = 0.6$

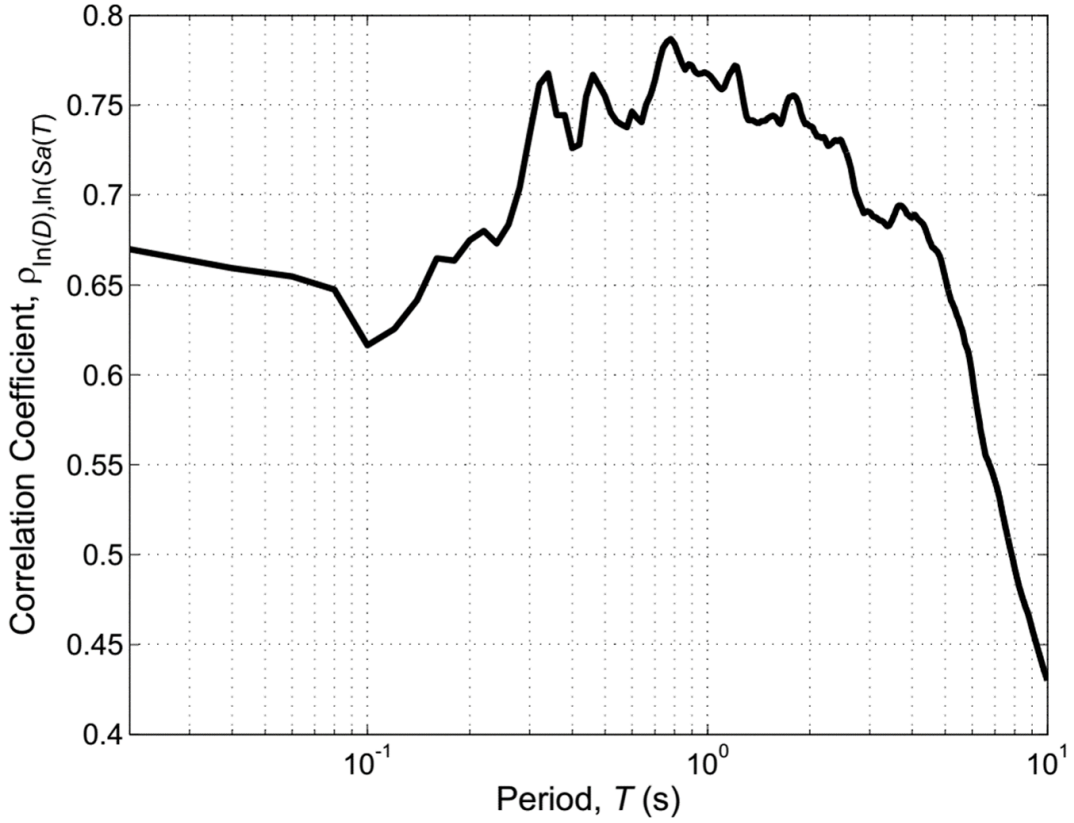

Figure 7.9: Variation of correlation coefficient between spectral accelerations and permanent displacements with respect to period; results based on sliding block analyses from a suite of 90 ground motions

As a result, Olson and Johnson's criteria for selecting ground motions produced higher uncertainty in the Newmark-based relationships between yield acceleration and permanent displacement (Figures 7.10 and 7.11). For the Wildlife site, the mean $a_y - D_H$ curves developed from the OJ08 suite of motions had a residual mean square of 0.974, corresponding to a $\sigma_{\ln D}$ of 0.987. The corresponding curve estimated from the NGA ground motion suite had a $\sigma_{\ln D}$ of 0.652. For the Moss Landing sites, the OJ08 curve had a $\sigma_{\ln D}$ of 0.973, compared with the $\sigma_{\ln D}$ of 0.564 from the corresponding NGA curves. Once again revisiting the box-and-whisker plots in Figure 7.2 and the response spectra in Figures 7.3 and 7.4, it is clear that the greater uncertainty in the OJ08-based $a_y - D_H$ curves stems from the greater variability in characteristics of their suite of ground motions.

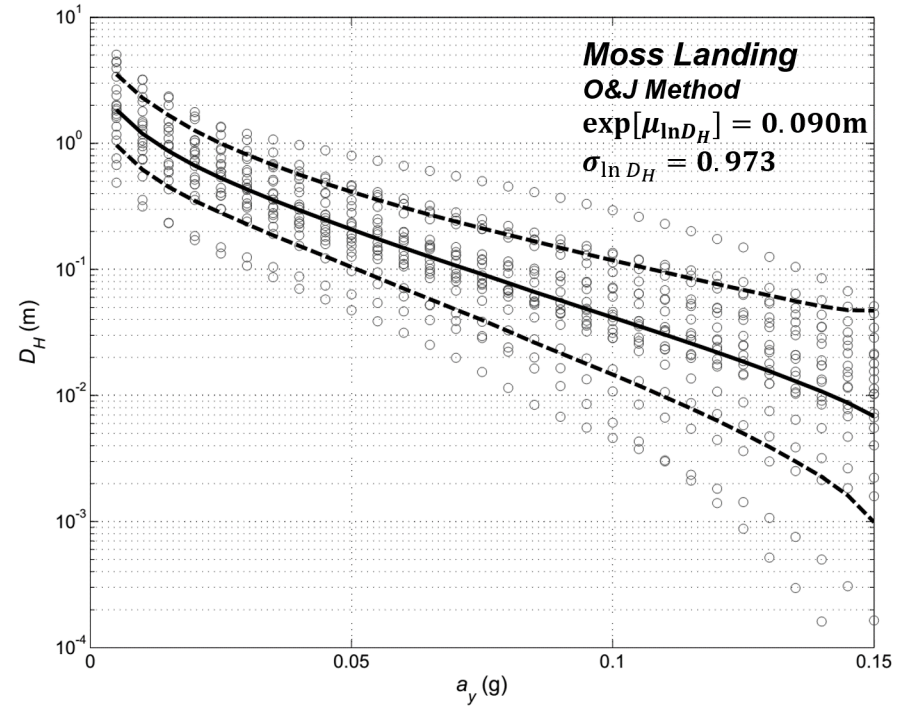

(a)

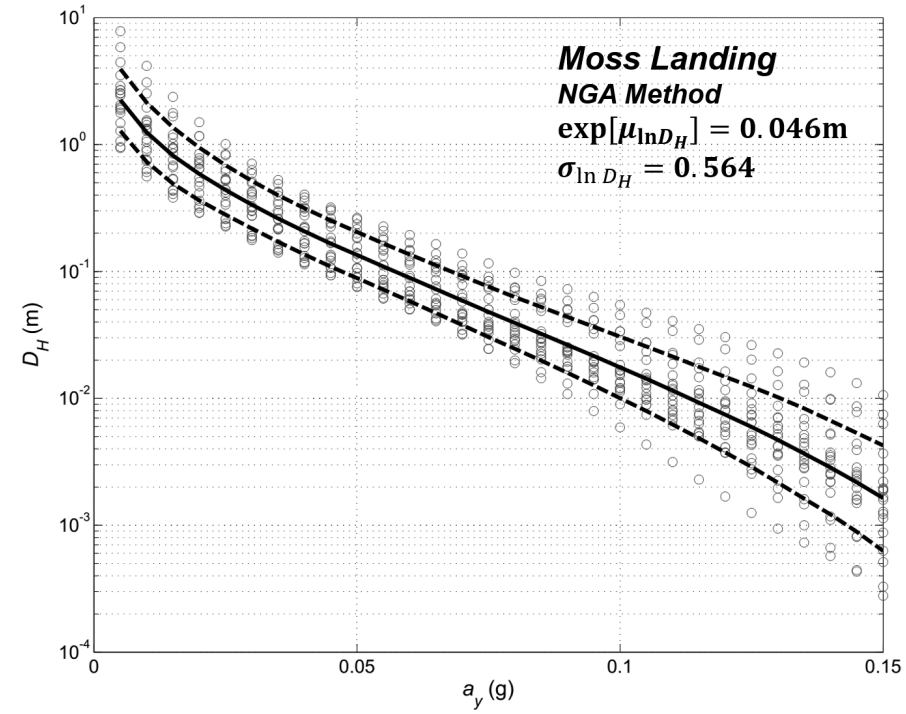

(b)

Figure 7.10: Mean and standard deviation sliding block-based relationships between yield acceleration and permanent displacement, using ground motions obtained from (a) OJ08 and (b) NGA methods for selecting ground motions, for the Moss Landing lateral spreading sites

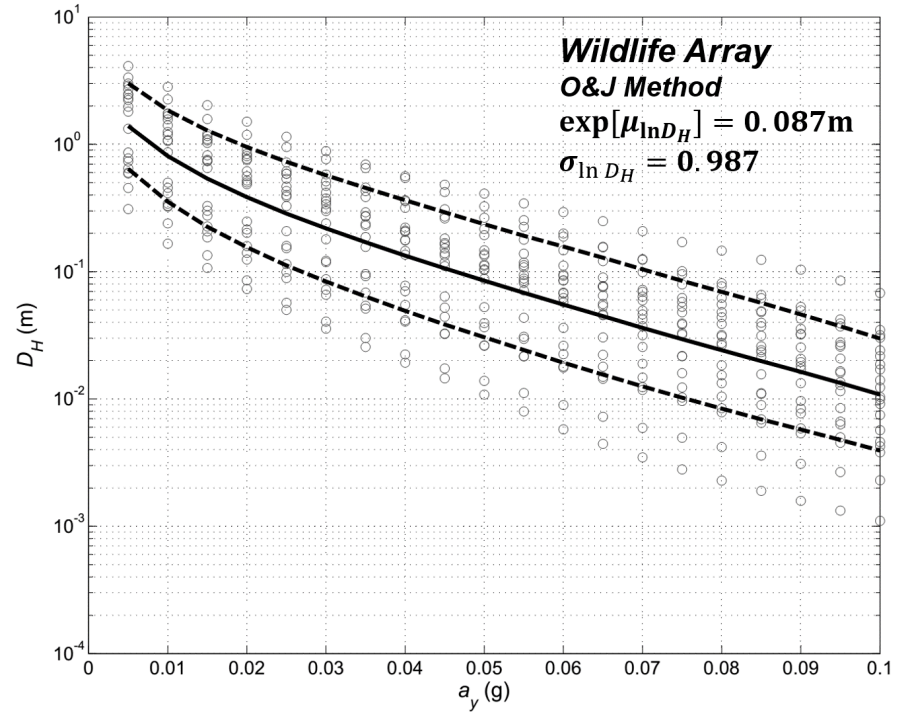

(a)

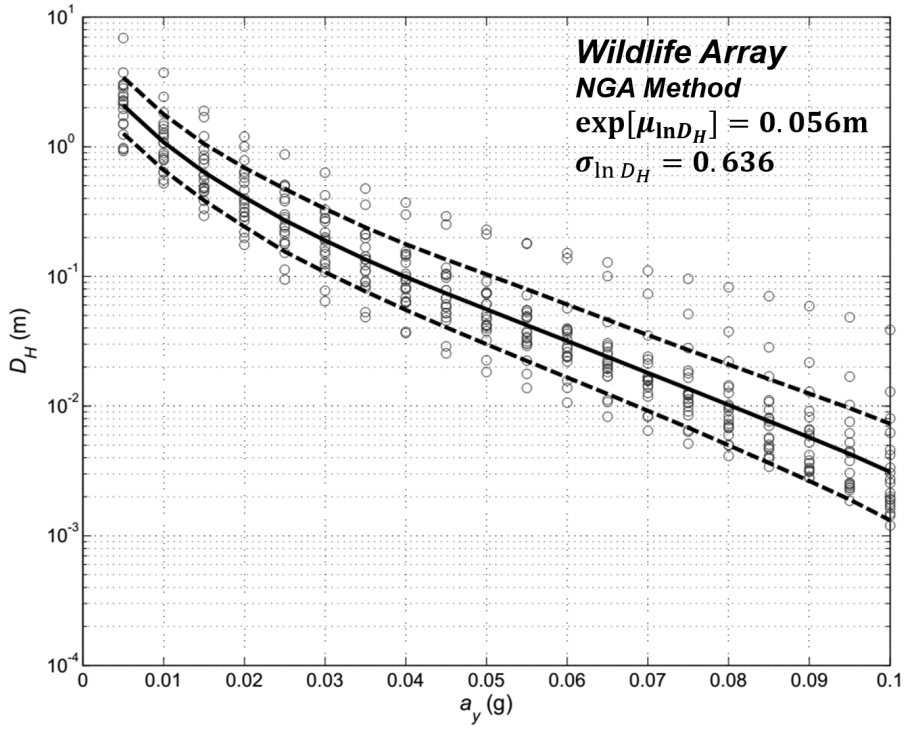

(b)

Figure 7.11: Mean and standard deviation sliding block-based relationships between yield acceleration and permanent displacement, using ground motions obtained from (a) OJ08 and (b) NGA methods for selecting ground motions, for the Wildlife Array lateral spreading site

Bias and Uncertainty in Back-Analysis

It is now instructive to examine how the discrepancies seen above might influence the back-calculated horizontal yield acceleration that is crucial to the employment of Olson and Johnson's method. Using the observed displacements at the Wildlife site and the four Moss Landing sites, the $a_y - D_H$ curves presented in the previous section were utilized to determine the mean and standard deviation of the yield acceleration, which was found to be lognormally distributed conditional upon a given displacement.

The results in Table 7.4 indicate that the differences between the OJ08- and NGA-based $a_y - D_H$ relationships can lead to significantly different estimates of the yield acceleration. The bias introduced by the higher scaling factors in the OJ08 ground motion records resulted in yield acceleration estimates that were between 20 and 45% higher than the NGA-based estimates for the four Moss Landing cases. Furthermore, the uncertainty in the yield acceleration estimates was significantly higher when using the OJ08 curves, with $\sigma_{\ln a_y}$ averaging above 0.5 for the five case histories, compared to an average of 0.34 for the NGA curves.

Table 7.4: Median and standard deviation of back-calculated yield acceleration from sliding block-based $a_y - D_H$ curves, using ground motion suites obtained using OJ08 and NGA selection methods, for the Wildlife Array and Moss Landing lateral spreading sites

Site	Observed D_H (m)	Estimated Median Yield Acceleration (g)			
		$\exp(\mu_{\ln a_y})$ (g)		$\sigma_{\ln a_y}$ (g)	
		OJ08	NGA	OJ08	NGA
Wildlife Array	0.18	0.032	0.031	0.583	0.274
MBARI 4	0.30	0.038	0.031	0.537	0.288
MBARI 3	0.25	0.043	0.035	0.501	0.265
MLML East	0.80	0.019	0.015	0.486	0.439
MLML West	0.70	0.021	0.016	0.543	0.410

7.2.3 Conclusions

In order to back-analyze the lateral spread case histories in the procedure developed by Olson and Johnson, it is critical to use suites of ground motions that closely match the conditions believed to have been observed at those sites of interest. The search criteria used by O&J are certainly effective to a degree in achieving this goal; it generates suites of acceleration records that come from earthquakes of similar magnitudes and styles of faulting at sites of similar stiffnesses. Similar intensities are produced by scaling all motions to the *PGA* believed to have been experienced at the site of interest.

However, *PGA* may not be the optimum intensity measure for the prediction of lateral spreading displacements; as shown in Figure 7.9, displacements are more closely correlated to longer period components of ground motions than *PGA*. There are other methods of selecting ground motions that, while having more restrictive search criteria, may produce more refined estimates of the sliding block-based relationship between observed horizontal displacement and yield acceleration. The alternative NGA method generates mean response spectrum likely experienced at the site, and uses this spectrum as a target for both finding candidate ground motion records and optimizing scaling factors. In most cases, the spectrum is based on the combination of four empirical ground motion prediction equations. It has been shown that, for the sites at the Wildlife Array and Moss Landing, the NGA method produced suites of ground motions with significantly less characteristic variability than the corresponding OJ08 ground motions suites.

For the cases analyzed in this section, the O&J ground motion suites generated $a_y - D_H$ relationships with significantly higher scatter than their NGA-based counterparts, resulting in less precise estimates of the back-calculated yield acceleration. The OJ08 method also produced much higher permanent displacement estimates, mainly due to the application of higher *PGA* scaling factors, which result from discrepancies between the reported *PGA* (used in O&J's method), and the GMPE-estimated *PGA* (NGA method). Of the 39 cases analyzed by Olson and Johnson, 32 featured an observed PGA that was at least 5% higher than the GMPE estimate. On average, the observed *PGA* was about 35% higher than the GMPE estimate, suggesting that this bias may be systematic in their analysis procedure. Whether or not the actual estimated *PGA* for a particular site is more accurate than the GMPE estimate (that is, whether or not the bias between the two D_H–a_y curves favors the OJ08 method) is naturally dependent on the reliability of the *PGA* estimate itself. For cases with reasonably large source-site distances (above about 15 km) and an abundance of neighboring ground motion data or event-specific attenuation relationships (e.g. Heber Road, Moss Landing, Wildlife), the estimated *PGA* may be more reliable than GMPE estimates, which are often obfuscated by large standard deviations.

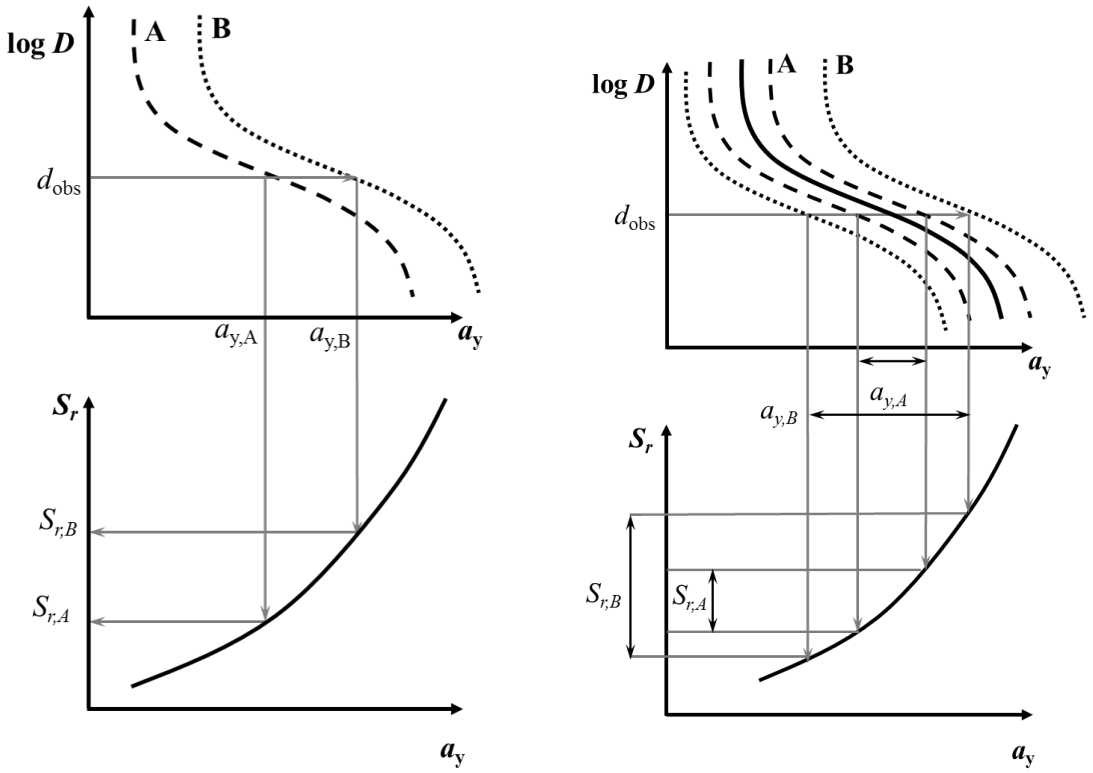

(a) Bias Effects **(b)** Uncertainty Effects

Figure 7.12: Schematic illustration of effects of using different ground motion selection methods on back-calculation procedure of yield acceleration and shear strength

Cases with sparse ground motion data (Whiskey Springs, Whakatane, Dagupan City) or near-fault sites (Northridge, Wufeng, and Kocaeli) carry significantly more uncertain estimates that may be difficult to evaluate formally. Cases like these may be better suited for using GMPE-based estimates for the back-analysis procedure.

The effects of using different methods to obtain ground motion suites for use in sliding block analyses are illustrated schematically in Figure 7.12. Differences in the mean ground motion intensity of the respective suites can result in significantly different $a_y - D_H$ curves, which in turn lead to differing estimates of the yield acceleration for a given observed displacement. Larger record-to-record variability in one ground motion suite compared to another is shown to result in larger variability in the back-calculated yield acceleration, which in turn results in less precision in the back-calculated shear strength.

In general, it appears that using the method employed by Olson and Johnson for selecting and scaling ground motions results in, on average, a suite of higher-intensity ground motion records than those obtained using the more traditional NGA method. The use of the O&J method would at the very least result in an unconservative estimate of the

liquefied shear strength within the pseudo-static back-analysis framework. From a probabilistic standpoint, the less rigorous ground motion selection criteria used by Olson and Johnson (compared to the NGA method) generally led to a wider probability distribution of yield acceleration estimates for each case. This uncertainty would produce less precision in the final estimate of the mobilized shear strength of the liquefied material.

7.3 Directionality and Dimensionality of Ground Motions

In Section 6.3, the practical implications of the different ways that ground motion acceleration records can be applied to Newmark analyses were discussed, based on the results of Kramer and Lindwall (2004). It was found that using the as-recorded ground motions, unresolved into downslope and normal components (pseudo-tangential), as direct inputs into sliding block analyses, could result in under-predicted displacements when compared to the "true-tangential" or "true two-dimensional" application of ground motions. It is presently unclear how, if at all, Olson and Johnson considered ground motion dimensionality in their Newmark analyses. In any event, given the shallow sloping sites they considered in their database, the effects of directionality are unlikely to have been particularly significant.

It is additionally important to consider the direction of the applied ground motion relative to the orientation of the sloping site. Using only a single component as an input for sliding block analyses assumes that the slope dips in that same direction. However, relative orientation of the seismograph instrumentation to the slope dip is almost an entirely random occurrence for most sites. Using the geometric mean of the two horizontal component motions represents a slight improvement for predicting sliding block displacements, but still remains generally smaller than the average of all azimuthal angles, by an amount that increases with decreasing yield acceleration. For the 137 1994 Northridge ground motions that K&L used in their analysis of azimuthal variability, it was shown that for $a_y/a_{max} = 0.5$, the rotated mean ground motions predicted average displacements that were approximately 30-35% higher than the two-component mean. From a back analysis standpoint, the results in KL04 suggest that at sites with higher observed displacements, the use of single component or two-component averages could significantly under-estimate the back-calculated yield acceleration. It is unclear whether or not O&J used single component, two-component averages, or rotated acceleration records in their back-analyses. It should be noted, however, that the 39 case histories in their database had an average observed displacement of about 0.80 m, with a single standard deviation range of 0.25 to 2.4 m. For reference, using Jibson's 2007 update of Ambraseys and Menu's 1988 sliding block empirical model, this range of observed displacements corresponds to a_y/a_{max}

values on the order of 0.03 to 0.35, which are low enough such that single component or two-component mean ground motions would result in significantly lower estimates of the "actual" back-calculated yield accelerations.

7.4 Sliding Mass Compliance

As discussed in Section 6.4, the assumption of a rigid mass can often introduce significant biases into the design process when sliding block analyses are used to model deformable, compliant sites. Wartman et al. (2003) showed that the rigid mass assumption can be unconservative for cases where the ratio of the natural period (T_s) to the mean period of the motion (T_p) is between about 0.4 and 1.3, with particular under-prediction seen between ratios of 0.5 and 0.7. In the context of the back-analysis procedure, un-conservative rigid block displacements would result in lower estimates of yield acceleration and shear strength than what could be reasonably expected from an appropriate de-coupled or fully coupled compliant block analysis.

It is generally unclear how, if at all, the assumption of rigid mass compliance may have impacted the results of Olson and Johnson's analyses. An very approximate estimate of the tuning ratios of each of the 39 case histories, using the peak of the GMPE-generated response spectrum for each case as a proxy for mean period, showed that the tuning ratios were largely much higher than 1.0. However, these estimated tuning ratios represented the initial site conditions and initial input ground motions, and do not take into account the fact that pore pressure generation and softening can significantly alter the frequency content of the ground motion, generally by lengthening the mean period of the ground motion, which may reduce the tuning ratio at the site significantly.

7.5 Assumption of Discrete Plane of Deformation

The use of Newmark sliding block analyses to back-calculate a yield acceleration for the 39 lateral spreading case histories that comprise the Olson and Johnson database implies that the lateral deformations occurred along a single, discrete surface at each of the sites. It has been shown in numerous cases that lateral deformations during ground shaking at sites of liquefaction are generally distributed throughout the liquefied stratum, and not along a single surface. A practical example of this principle can be found in the Moss Landing sites (1989 Loma Prieta), where slope inclinometer data showed a broad distribution of deformations throughout the liquefied sand and silty sand (see Section

5.4.6). In Section 6.6, dynamic analyses showed that strain distribution has a significant effect on permanent displacements that is not captured by Newmark analyses. Rigid block analyses tend to be particularly unconservative in sites underlain by weak material of practically any significant thickness, and further under-predict the actual displacements as the weak layer thickness increases.

The lateral spreading case histories used by O&J to develop their back-calculated shear strengths featured liquefied strata that were, on average, about 3.5 m thick; based on the results of the analyses in Section 6.6, rigid block analyses tended to predict displacements on the order of about 50% lower than the actual continuum displacements. 33 of the 39 cases had more than 1.0 m of liquefied material, 11 were greater than 5.0 m. Thus, nearly all of O&J's case histories likely experienced deformations that were distributed to some degree throughout the liquefied strata; this mechanism is not accounted for using Newmark analyses, and potentially results in significant bias in the predicted displacements, and thus much lower estimates of back-calculated yield acceleration and shear strength ratios.

7.6 Restriction of Sliding to the Downslope Direction

The Newmark sliding block analyses utilized by Olson and Johnson to back-calculate the yield acceleration for the 39 lateral spreading case histories were performed with a restriction of the movement of the block to the downslope direction (C. Johnson, personal communication, 2015). For many seismic slope stability applications, particularly when steeper slopes and embankments are involved, the assumption that sliding occurs in only the downslope direction is generally sound. However Section 6.5 showed that this assumption may potentially result in inaccurate (specifically, much larger) estimates of permanent deformations for gently sloping sites such as those often susceptible to lateral spreading.

In most situations, lateral spreading occurs on very gently sloping, or nearly flat ground, since the liquefied soil is quite weak. Youd et al. (2002) indicated that lateral spreading can occur on ground slopes ranging from roughly level to 3.5°. Referring back to Figure 6.10, it is clear that for this range of values, the restriction of sliding to the downslope direction in a Newmark-type analysis may over-predict the estimate of permanent relative displacements. Of the 39 case histories back-analyzed by Olson and Johnson, only 11 (Table 7.5) had ground slopes within the range of 0 to 3.5°, while three of the cases featured ground slopes significantly greater than 3.5°. Of the remaining 25 cases classified as free face sites, 16 of them featured free face ratios significantly higher than the 20% limit recommended by Youd et al. (2002). The distribution of ground slopes and

free faces used by O&J is therefore biased towards steeper slopes (or free faces with higher shear stresses), which may support the assumption of one-way sliding; however, it is inconsistent with the conditions under which lateral spreading failures have most commonly been observed to occur in the field, which calls into question its applicability to the type of failure it purports to predict.

Table 7.5: Summary of back-analyzed lateral spreading sites with ground slopes below the 3.5° upper limit recommended by Youd et al. (2002)

Case No.	Earthquake	Site	Displacement, D_H (m)	Slope Angle, β (degrees)	a_{max} (g)
1	1971 San Fernando	Juvenile Hall	1.50	0.7	0.50
10	1989 Loma Prieta	Moss Landing, MLML Bldg East Spread	0.80	3.8	0.25
12	1989 Loma Prieta	Miller Farm	0.16	0.3	0.36
13	1989 Loma Prieta	Farris Farm	0.30	0.1	0.36
14	1989 Loma Prieta	Leonardini Farm	0.23	0.2	0.21
15	1989 Loma Prieta	Sea Mist Farm	0.47	0.2	0.21
25	1994 Northridge	Balboa Blvd.	0.50	0.9	0.84
26	1994 Northridge	Wynne Ave.	0.15	0.7	0.51
34	1999 Kocaeli, Turkey	Hotel Sapanca	2.00	2.3	0.40
38	2003 San Simeon	Norswing Drive	0.25	2.9	0.25
39	2003 San Simeon	Juanita Ave	0.25	0.1	0.25

In order to determine whether the one-directional sliding restriction had a significant effect on the back-analyzed yield acceleration, the plots of displacement error and dispalcement ratio versus a_y/a_{max} for a series of ground slope angles that were generated in Section 6.5 (see Figure 6.11) were referred to for each of the cases in Table 7.5. It has been previously shown that from a forward-prediction standpoint, the one-way sliding restriction assumption is, at the very least, conservative, if not overly so. However, since this procedure was originally employed by O&J in order to *back-calculate* the mobilized shear strength of the liquefied material, it is possible that the one-way restriction could have produced unconservative estimates of the shear strength.

7.6.1 Effects on Back-Analysis Procedure

For each ground slope case, the median downslope yield acceleration calculated by Olson and Johnson was "corrected" to account for two-way sliding using the curves in Figure 7.13, which were obtained from the geometric mean of the displacements from the suite of 90 ground motions for a series of ground slope angles, as well as the one-way sliding restriction case.

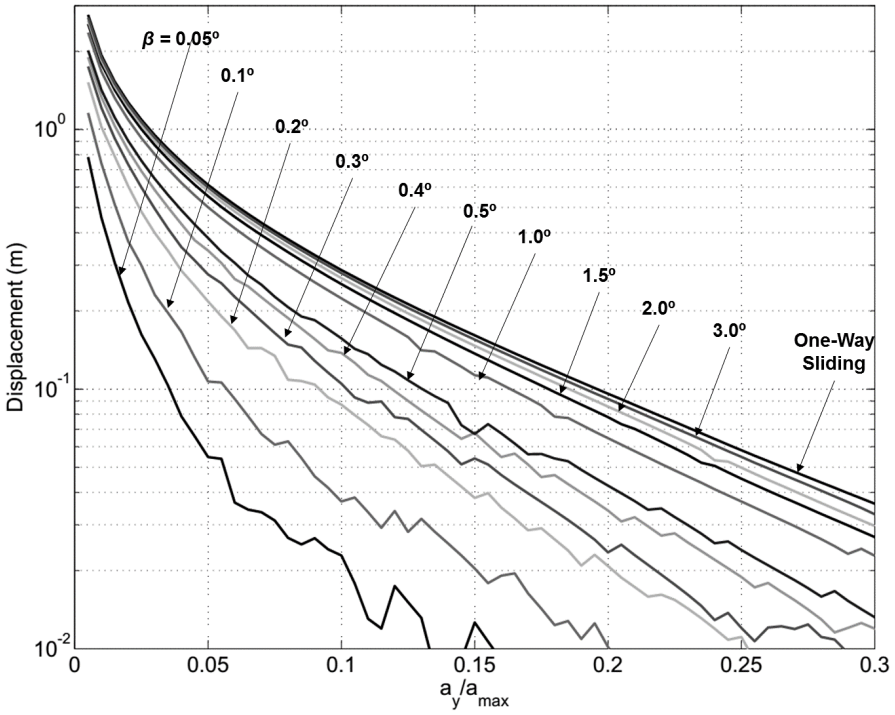

Figure 7.13: Curves relating normalized permanent displacement to normalized yield acceleration for a range of ground slope conditions

The relationship betweem $\log D_H$ and a_y/a_{max} takes the general form of Ambraseys and Menu's 1988 (and later, Jibson's 2007) rigid block model:

$$\log D_H = b_1 + \log\left[\left(1 - \frac{a_y}{a_{max}}\right)^{b_2}\left(\frac{a_y}{a_{max}}\right)^{b_3}\right] \tag{7.1}$$

where b_1, b_2, and b_3 are regression parameters. It can be assumed that differences in the ground motion suites used to develop the form of Equation 7.1 will be reflected largely in changes to the b_1 coefficient. In other words, the displacements from two separate curves (A and B) will be proportional for the same value of a_y/a_{max} according to:

$$\frac{D_A}{D_B} = \exp\left(b_{1,A} - b_{1,B}\right) \tag{7.2}$$

and the overall shape of the log $D_H - a_y/a_{max}$ curve is generally consistent regardless of the suite of ground motions used. Therefore, relative a_y/a_{max} values of different ground slope angles for a given displacement value is unlikely to be affected by the actual magnitude of the displacement (Figure 7.14). For the purposes in this section, this assumption is generally a reasonable one, since the differences in displacements, and thus adjustments to be made to the back-calculated yield accelerations, are relatively small.

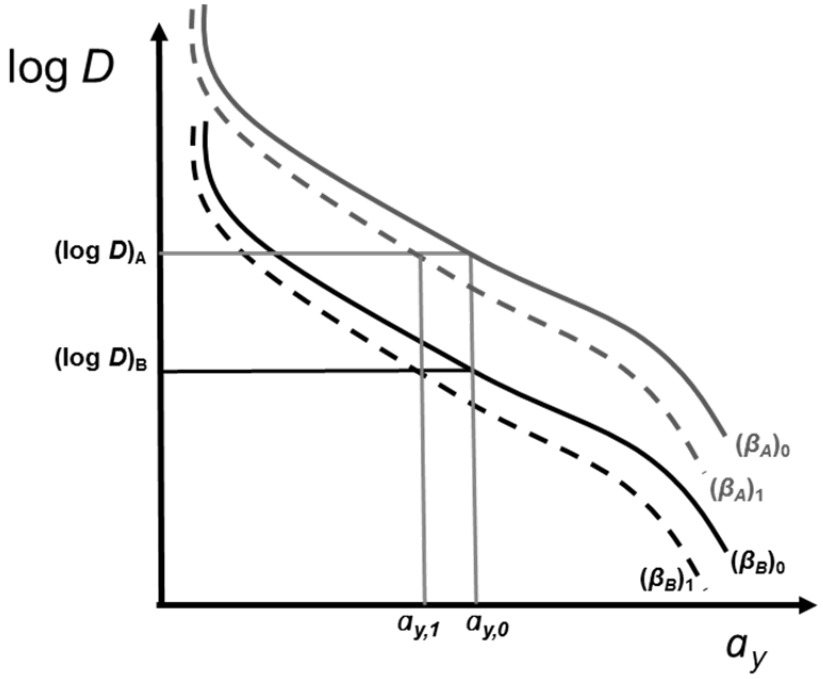

Figure 7.14: Consistency of relative yield accelerations for different ground slopes between curves developed from different ground motion suites

For example, the yield acceleration for the Wynne Avenue lateral spread (Case no. 26, Northridge 1994) was determined by Olson and Johnson to be 0.15 g ($a_y/a_{max} = 0.29$), assuming one-way sliding. By interpolating the data in Figure 7.13, it can be shown that for $a_y/a_{max} = 0.29$ and a ground slope of 0.7°, the corresponding two-way sliding curve would have a back-calculated a_y/a_{max} of 0.23, corresponding to a yield acceleration of 0.12 g. Using the linear relationship between a_y and $s_u(mob)/\sigma'_{v0}$ provided by the authors for this case history:

$$\frac{s_u(mob)}{\sigma'_{v0}} = 1.27a_y - 0.031 \tag{7.3}$$

The corrected strength ratio was determined to be 0.12, as opposed to the ratio 0.16 that was originally back-calculated by the authors. This procedure was repeated for each of the 11 ground slope cases, with the results illustrated in Figure 7.15 and summarized in

Table 7.6.

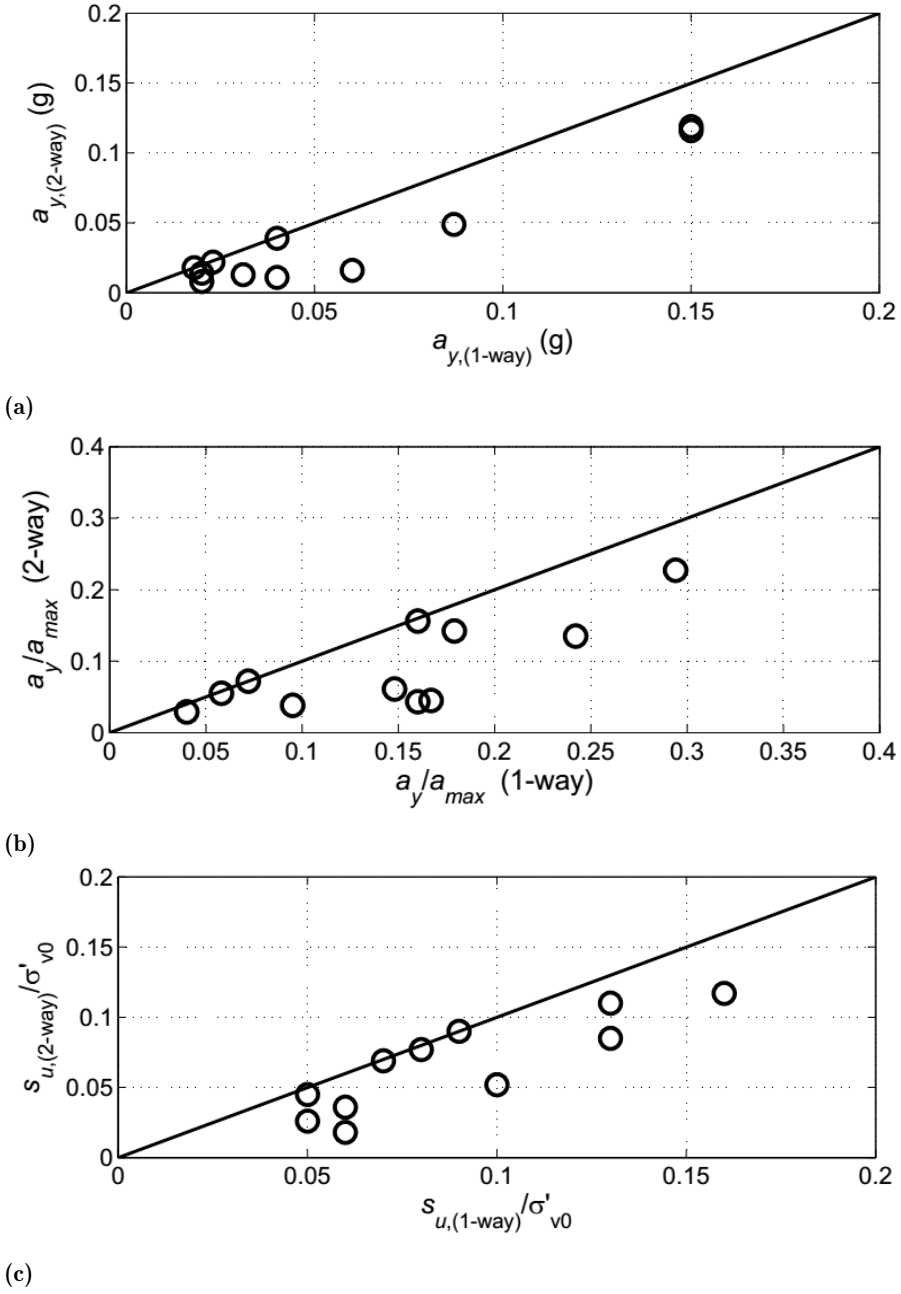

Figure 7.15: Comparison of one-way and two-way sliding block analyses with respect to back-calculated (a) yield accelerations, (b) normalized yield accelerations, and (c) mobilized strength ratios

Comparing the one-way and two-way sliding analyses, we see a general trend towards overprediction of a_y, a_y/a_{max}, and the mobilized strength ratio when the one-way sliding

Table 7.6: Summary of corrected back-analyzed yield acceleration and mobilized strength ratios for lateral spreading case histories with ground slopes below the 3.5° upper limit recommended by Youd et al. (2002)

Case No.	D_H (m)	β (deg)	a_{max} (g)	a_y (g)		a_y/a_{max}		$s_u(mob)/\sigma'_{v0}$		
				1-way (O&J)	2-way	1-way (O&J)	2-way	1-way (O&J)	2-way	Percent Diff.
1	1.50	0.7	0.50	0.020	0.014	0.040	0.029	0.050	0.045	-10.5%
10	0.80	3.8	0.25	0.018	0.018	0.072	0.072	0.090	0.090	-0.1%
12	0.16	0.3	0.36	0.087	0.049	0.242	0.135	0.130	0.085	-53.7%
13	0.30	0.1	0.36	0.060	0.016	0.167	0.045	0.100	0.052	-91.3%
14	0.23	0.2	0.21	0.031	0.013	0.148	0.061	0.060	0.036	-68.1%
15	0.47	0.2	0.21	0.020	0.008	0.095	0.038	0.050	0.026	-92.3%
25	0.50	0.9	0.84	0.150	0.119	0.179	0.142	0.130	0.110	-187%
26	0.15	0.7	0.51	0.150	0.116	0.294	0.227	0.160	0.117	-37.3%
34	2.00	2.3	0.40	0.023	0.022	0.058	0.055	0.080	0.077	-4.3%
38	0.25	2.9	0.25	0.040	0.039	0.160	0.156	0.070	0.069	-1.0%
39	0.25	0.1	0.25	0.040	0.011	0.160	0.043	0.0606	0.018	-229%

restriction is imposed. The differences between the original and corrected back-calculated shear strength ratios range from relatively insignficant, particularly at sites with steep slopes and/or large observed lateral deformations; to corrected strength ratios that were over 70% lower than the original back-calculated values, mostly at gently sloping sites that experienced relatively moderate displacements. It is important to note that all cases had corrected strength ratios that were less than the original estimates; thus, the one-way restriction actually results in an *unconservative* estimate of the back-calculated shear strength ratio.

The assumption of one-way sliding introduced the most bias for sites where moderate displacements were observed (0.5 m or less) on very gently sloping ground (less than approximately 1.0°). It has already been shown that permanent sliding block displacements in shallow slopes are heavily influenced by whether or not sliding has been restricted to the downslope direction. Similarly, it is clear that for D_H values below 0.5 m, the back-calculated a_y/a_{max} is highly sensitive to the ground slope angle, and estimates for a_y/a_{max} differ significantly between the one-way and two-way sliding assumptions for shallow slopes. For sites with ground slope angles above about 1.5°, which constitute about 8% of the case history database, the assumption of one-way sliding introduces relatively little error in the estimate of mobilized strength ratio.

7.6.2 Relationship Between Mobilized Strength Ratio and Penetration Resistance

For the 11 cases analyzed, the back-calculated mobilized strength ratios for both the one- and two-way sliding conditions (see Table 7.6 were plotted against the reported CPT and SPT penetration resistances (Figures 7.16 and 7.17) and compared to the limits of the relationship proposed by Olson and Stark (2002) for flow failures. Six of the 11 ground slope case histories showed significantly lower mobilized shear strength ratios when corrected for two-way sliding. Of those six, four had corrected strength ratios that dropped significantly below the lower bounds of Olson and Stark's equation for liquefaction flow failures. Each of these cases featured very low ground slope inclinations and moderate observed displacements, and it can be seen that the median general trend of the corrected data for ground slope cases plots much closer to (or possibly even below) the lower bound of the flow failure equations. Thus, the conclusion that mobilized strength ratios back-calculated from lateral spreads are essentially identical to liquefied shear strength ratios back-calculated from flow failures is not strongly supported by about 30% of the ground slope cases that were back-analyzed, and about 10% of the total cases back-analyzed by the authors. If the Olson and Johnson database had featured a similar proportion of gently sloping sites to the Youd et al. database, it is likely that an even larger percentage of cases would plot below the Olson and Stark limits, thus further illustrating the potential differences between lateral spread and flow liquefaction strenth ratios.

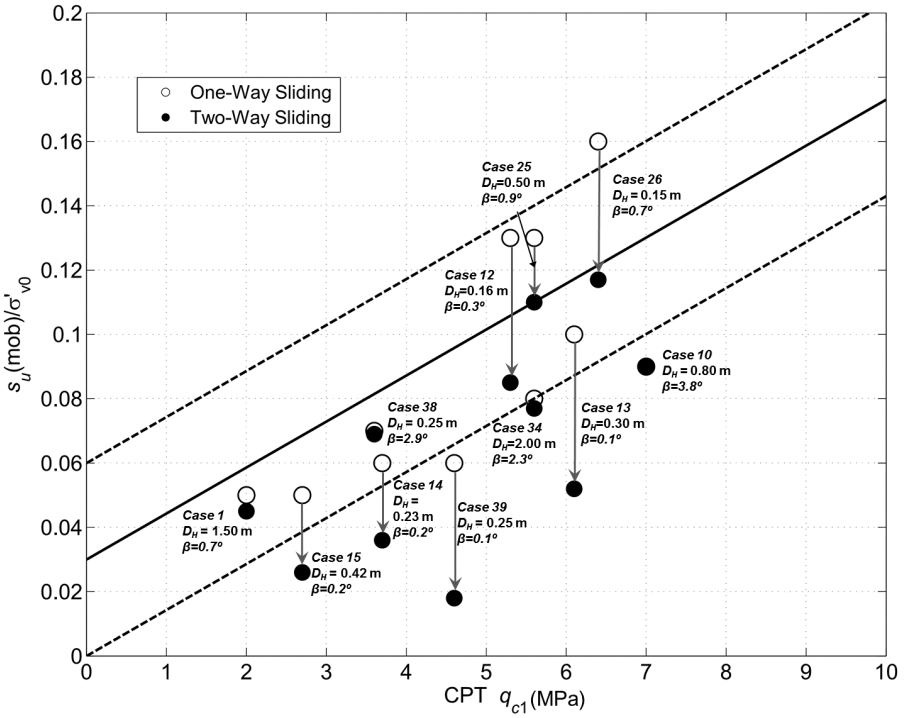

Figure 7.16: Relationships between corrected mobilized strength ratio and CPT tip resistance, plotted against Olson and Stark (2002) relationship for liquefaction flow failures

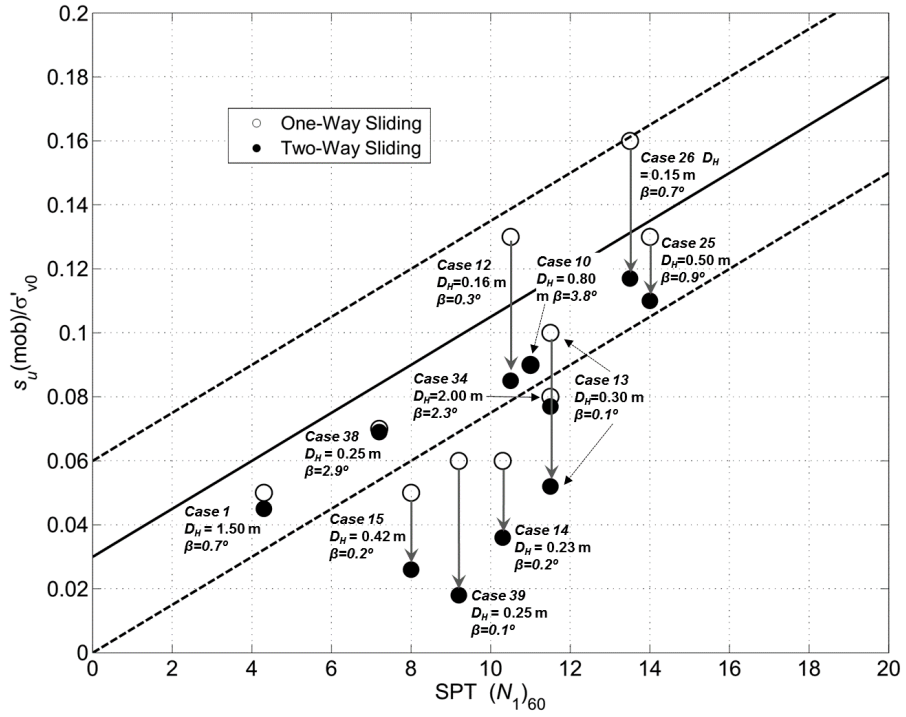

Figure 7.17: Relationships between corrected mobilized strength ratio and SPT N-value, plotted against Olson and Stark (2002) relationship for liquefaction flow failures

7.6.3 Conclusions

When used to predict lateral spreading displacements, the one-way restriction can result in overly conservative estimates of the permanent deformations. However, the effects of this bias on the back-analysis framework developed by Olson and Johnson are quite significant: for case history sites with ground slopes below about 1°, most of which had sustained moderate permanent displacements (0.10 to 0.50 m), the one-way assumption significantly over-estimated the sliding block yield accelerations, which resulted in higher estimates of the pseudostatic-based mobilized strength ratio.

The back-calculated strength ratio estimates, when corrected for two-way sliding, showed that the general relationship between strength ratios and *in situ* penetration resistances plots significantly lower than the Olson and Stark relationship for liquefaction flow failures. As a result, the link between mobilized strength ratios from liquefaction-induced lateral spreads and liquefied strength ratios from liquefaction flow failures does not appear to be as clear as was intially suggested by Olson and Johnson.

The results of the issues analyzed in this chapter, and their general effects on both forward prediction and back-calculation analyses, are presented in Table 7.7. Potential negative biases in the predicted displacements (and thus the back-calculated yield acceleration and residual shear strength) result from the use of single-component ground motions (at near-fault sites), and the assumptions of a rigid mass and a discrete failure plane. A source of potential positive bias in sites on shallow sloping ground comes from the restriction of sliding to the downslope direction. The procedure used to select ground motions has the potential to significantly increase the variability in the predicted or back-calculated values, particularly if candidate motions are scaled to a single PGA value.

7.7 Probabilistic Back-Analysis of Mobilized Shear Strength Ratios

The back-analysis procedure used by Olson and Johnson to estimate mobilized strength ratios from lateral spreading case histories, which is detailed in detail in Section 4.3.4, was developed largely within a deterministic framework by. The authors did include maximum, minimum, and median estimates for the yield acceleration, mobilized strength, and initial effective stresses for each case history. However, the bases for these ranges of estimates were not described, nor were distributions of values of the back-analyzed parameters about their median values.

In this section, the back-analysis procedure is repeated probabilistically for two lat-

Table 7.7: Summary of some of the issues with rigid block analyses as they pertain to analyzing lateral spreading displacements.

Issue	Effect on:		
	Displacement Prediction	Back-Calculated Yield Acceleration	Back-Calculated Residual Strength
Ground Motion Selection (scaling to PGA)	Higher Uncertainty	Higher Uncertainty	Higher Uncertainty
Directionality of Ground Motions (single component)	Decreased Magnitude (Near-fault sites only)	Decreased Magnitude (Near-fault sites only)	Decreased Magnitude (Near-fault sites only)
Rigid Mass Assumption	Decreased Magnitude (T_m/T_s close to 1)	Decreased Magnitude (T_m/T_s close to 1)	Decreased Magnitude (T_m/T_s close to 1)
Discrete Failure Surface Assumption	Decreased Magnitude	Decreased Magnitude	Decreased Magnitude
Downslope Sliding Restriction	Increased Magnitude (sites on 2° or smaller slope)	Increased Magnitude (sites on 2° or smaller slope)	Increased Magnitude (sites on 2° or smaller slope)

eral spread case histories: the Wildlife Liquefaction Array (1987 Superstition Hills) and the Monterey Bay Aquarium Research Facility (MBARI 3) in Moss Landing (1989 Loma Prieta). Using multiple Newmark analyses to characterize the aleatory uncertainty in sliding block predictions, in conjunction with a series of pseudo-static slope stability analyses to account for variability in site characterization, a site-specific probability distribution function (PDF) for the mobilized shear strength ratio in the liquefied material was computed for each case history. The resulting probabilistic characterizations of mobilized shear strength ratio were then evaluated to ascertain the degree to which the conclusion that strength ratios mobilized in lateral spreads coincided with those back-calculated from liquefaction flow failures.

7.7.1 Back-Analysis Framework

The probabilistic form of O&J's back-analysis procedure involves using the results of multiple Newmark sliding block analyses to obtain the probability distribution for the back-calculated yield acceleration (Figure 7.18). Each acceleration time history in the suite of ground motions is used to compute a curve relating horizontal displacement (D_H) to horizontal yield acceleration (a_Y).

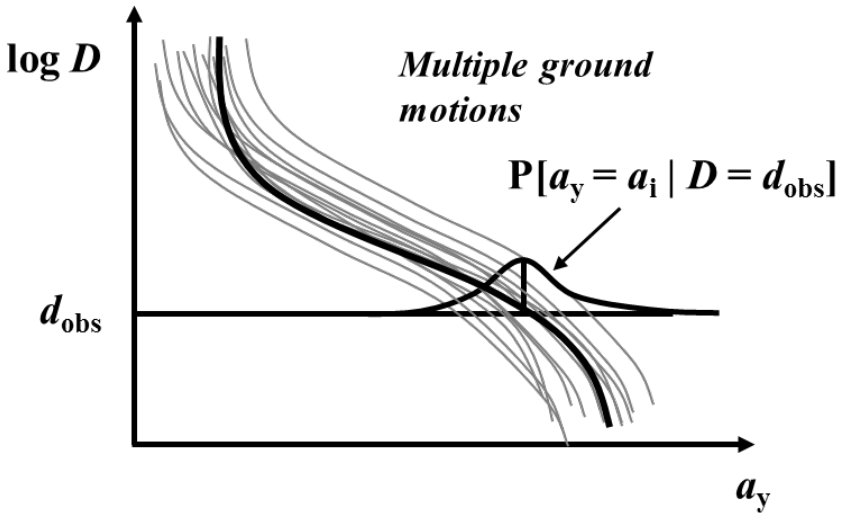

Figure 7.18: Schematic showing how the yield acceleration is back-calculated probabilistically from the results of Newmark sliding block analyses on multiple ground motions

Each a_y–D_H curve was used to determine the yield acceleration corresponding to the observed horizontal displacement, resulting in a series of estimates for the yield acceleration. By taking the median ($\hat{a}_y$) and standard deviation ($\sigma_{\ln a_y}$ of the set of yield acceleration estimates, the lognormal distribution of the yield acceleration , $P[\ln a_y = \ln a_i | D_H = d_{obs}]$, is obtained by calculating the standard score z for each value of a_y:

$$z_{\ln a_y} = \frac{(\ln a_i - \mu_{\ln a_y})}{\sigma_{\ln a_y}} \tag{7.4}$$

In the deterministic O&J procedure, the yield acceleration was used to determine the residual strength of the liquefied soil. Therefore, the probability density function that describes $P[\ln a_y = \ln a_i | D_H = d_{obs}]$ must then be combined with a probabilistic relationship between the yield acceleration and the normalized strength ratio S_r/σ'_{v0} (denoted here as NSR) of the liquefied soil. The relationship can be expressed in the form of a cumulative distribution function (CDF), F_{NSR}:

$$F_{NSR}(nsr_i) = 1 - P\big[NSR > nsr_i | a_y = a_i\big] \tag{7.5}$$

where F is the cumulative distribution function, a_y is the horizontal yield acceleration, and NSR is the normalized shear strength ratio of the liquefied soil.

The CDF in Equation 7.5 can be obtained through the use of a pseudo-static slope

stability analysis in a probabilistic framework. The case study sites were modeled using SLIDE 6.0, a commercial limit equilibrium slope stability analysis program. However, rather than the deterministic analysis performed by O&J using mean values for input soil parameters, the slope stability was evaluated, for a range of applied horizontal acceleration values, using SLIDE's "probabilistic" functionality. For the probabilistic portion of the analysis, probability distributions were generated for each input soil parameter (i.e. unit weight, friction angle, and cohesion) in the soil profile. Thus, for a given horizontal acceleration, a series of analyses in SLIDE generated CDFs in the form of Equation 7.5 for the range of shear strengths sampled in the sensitivity analysis (Figure 7.19).

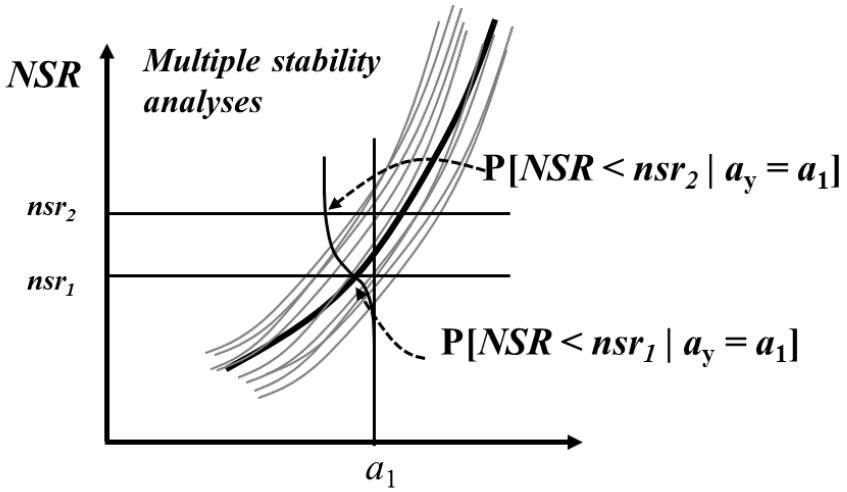

Figure 7.19: Schematic showing how normalized strength ratio is back-calculated probabilistically from the results of a series of pseudostatic slope stability analyses

Combining Probability Distributions

The probability of non-exceedance a particular strength ratio given the observed lateral spreading displacement can be obtained by taking the product of the strength ratio CDF for a particular yield acceleration and the probability density value of that yield acceleration given the observed displacement; the product is then summed over all sampled yield accelerations:

$$P\big[NSR < nsr_j | D_H = d_{obs}\big] = \sum_{i=1}^{N_a} P\big[NSR < nsr_i | a_y = a_i\big] P[\big[a_y = a_i | D_H = d_{obs}\big] \quad (7.6)$$

This process was repeated for each uniformly sampled value of liquefied shear strength ratio. The resulting relationship between $P\big[NSR = nsr | D_H = d_{obs}\big]$ and NSR was then

used to produce the CDF of the normalized strength ratio for each case history (Figure 7.20).

Uncertainty in Observed Displacements

The process of measuring and reporting permanent ground deformations was discussed in Section 5.2.1, and is a highly relevant component to the back-analysis framework. Uncertainty in observed displacement was not accounted for in the probabilistic back-analyses here, but its importance and contribution to the variability in back-calculated strengths cannot be understated. Sites with highly variable reported displacements, or displacements obtained using relatively crude methods, will have back-calculated shear strengths that should be interpreted to be less precise than more well-constrained lateral spreading cases.

Uncertainty in Yield Acceleration

Newmark siding block analyses require time histories of acceleration as inputs. Ground motions should have characteristics that are very similar to those expected to have occurred at the site in the earthquake of interest. Olson and Johnson used the criteria for ground motion selection described in Section 7.2

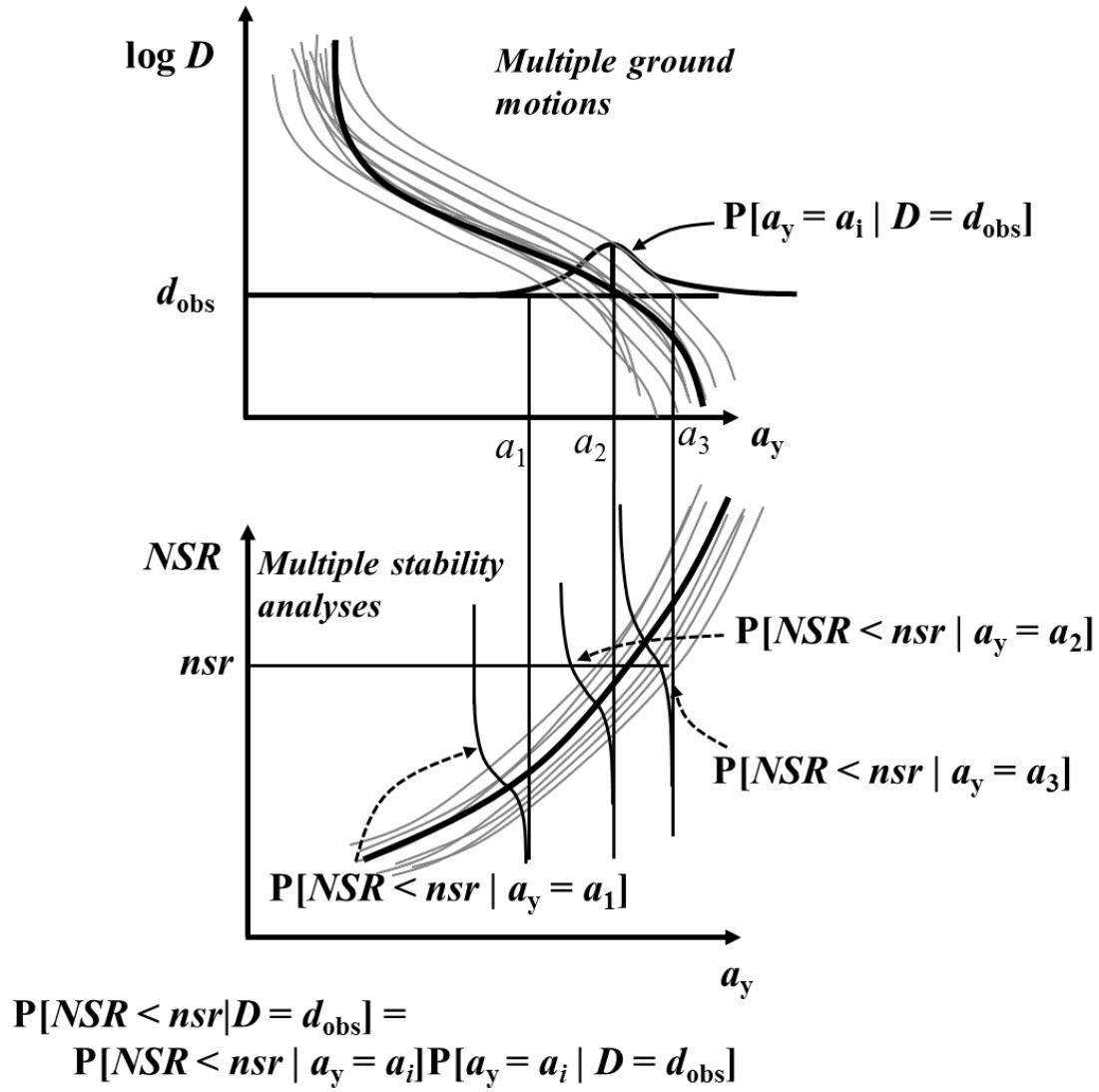

Figure 7.20: Graphical representation of procedure used to calculate the probability of non-exceedance for particular normalized strength ratio, from a distribution of yield accelerations, given the observed displacement

These criteria were used to select a suite of motions for use in the probabilistic back-analysis. The resulting ground motion suites (Table 7.8) are then scaled to the recorded or estimated site *PGA* in the same manner as O&J's deterministic procedure. Note the significant variation with respect to intensity, frequency content, and duration in the ground motion records; this occurs despite the fact that all ground motions in a given suite are scaled to the same peak ground acceleration value.

Table 7.8: Summary of ground motion suites for Moss Landing and Wildlife case histories; means, coefficients of variation, and range values are included for four ground motion parameters.

	Moss Landing, MBARI 3				Wildlife Array			
	No. of motions	39	Scaled PGA	0.25 g	No. of Motions	36	Scaled PGA	0.21 g
	Mean	C.o.V.	Min.	Max.	Mean	C.o.V.	Min.	Max.
v_{max} (cm/s)	0.328	31.8%	0.128	0.525	0.241	58.4%	0.063	0.615
Significant Duration (s)	18.2	51.0%	4.8	42.8	13.9	49.4%	4.5	35.6
Arias Intensity (m/s)	1.03	41.3%	0.29	2.61	0.58	48.4%	0.22	1.26
Mean Period (s)	0.85	35.9%	0.36	1.55	0.62	58.8%	0.22	1.38

The ground motion suites were then applied to a series of one-way, Newmark sliding block analyses for a range of yield acceleration values, thus producing the relationship between ay and permanent displacement for each ground motion (Figure 7.21).

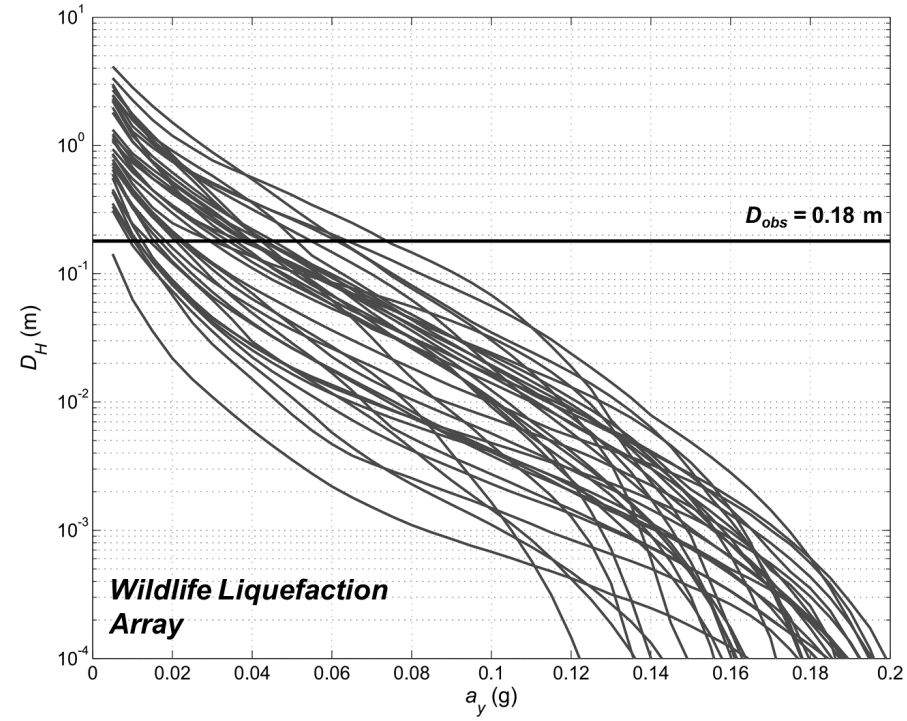

(a)

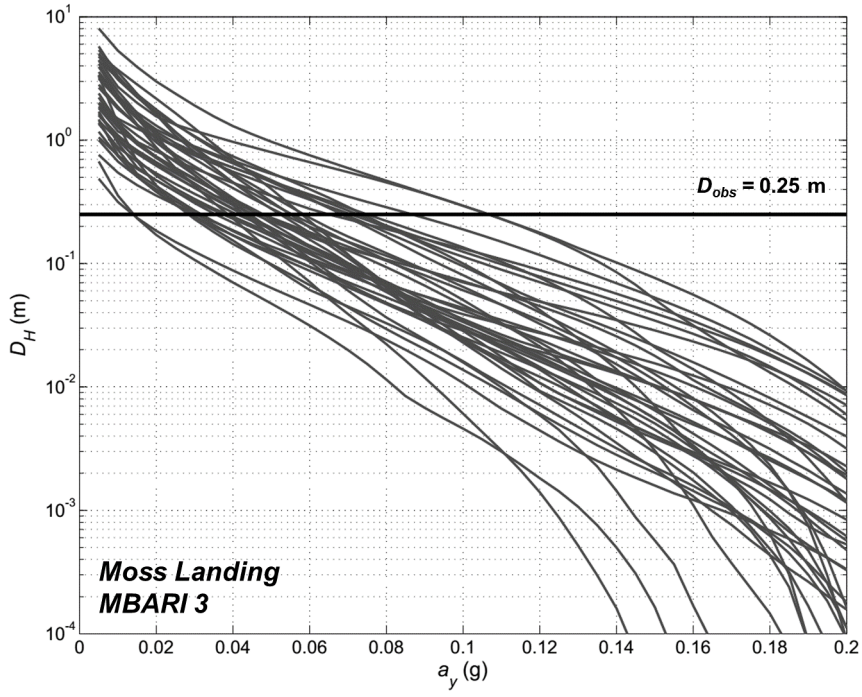

(b)

Figure 7.21: a) Sliding block-based relationships between yield acceleration and permanent horizontal displacement for (a) Wildlife Array and (b) Moss Landing MBARI 3 lateral spreading sites.

Table 7.9: Summary of Newmark-based back-calculated yield accelerations for the Wildlife and Moss Landing lateral spreading sites

Site	Estimated Yield Acceleration (g)				
	Median	16th Percentile	84th Percentile	Low	High
Wildlife	0.034	0.013	0.051	0.009	0.0737
Moss Landing	0.046	0.031	0.071	0.014	0.107

The ranges of back-calculated yield accelerations were relatively broad for both cases (Table 7.9); the high estimates of a_y for the Wildlife and Moss Landing sites were close to eight times larger than the low estimates. The geometric mean and standard deviations obtained from the sliding block-based estimates were used to produce the lognormal distributions for the back-calculated yield acceleration shown in Figure 7.22 .

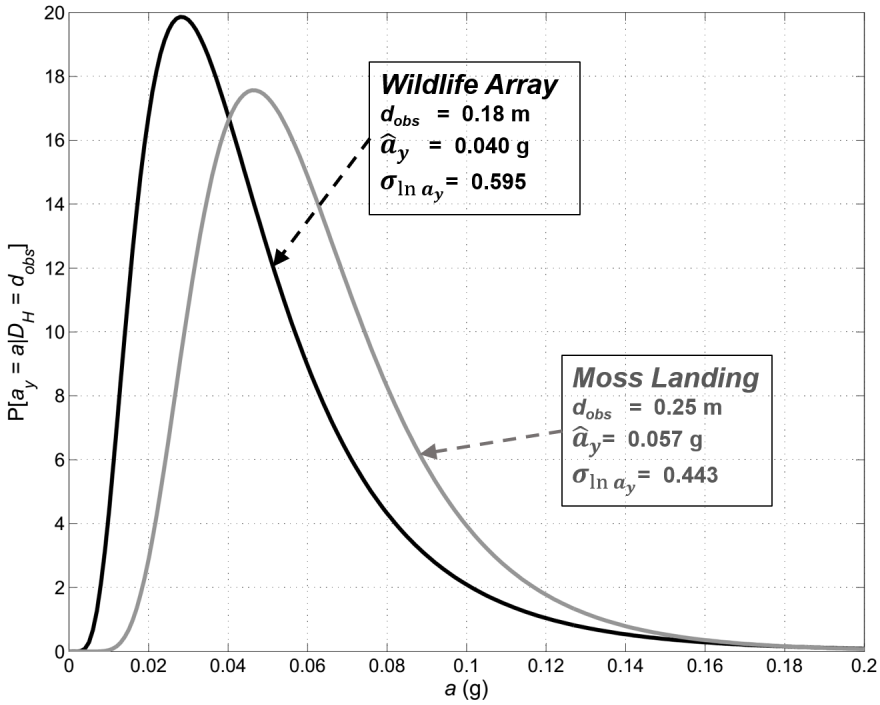

Figure 7.22: Lognormal probability distribution functions of back-calculated yield acceleration for Moss Landing MBARI 3 and Wildlife Array lateral spreading sites.

Uncertainty in Residual Shear Strength

The soil profiles for the two back-analyzed cases were generated from site data obtained from available literature. Ground slope dimensions, soil classification and stratification, and mean soil parameters for the Wildlife Array (Figure 7.23a) were estimated from site investigation data provided by Bennett et al. (1984), while MBARI 3 site at Moss Landing (Figure 7.23b) profile was developed using reconnaissance data from Boulanger et al. (1997) and Mejia (1998). Characterization of the uncertainty of the soil parameters was based on compiled data of the spatial variability of parameters in various soil types from Jones et al. (2002) as well as measured variability between adjacent penetration resistance measurements. Determination of the liquefied layer was based primarily on reports from the case literature mentioned above; factor-of-safety analyses for liquefaction susceptibility (Idriss and Boulanger 2008) were performed to verify the reported data, and in the case of MBARI 3, to estimate the horizontal extent of the liquefied layer.

Selection of Failure Surface

The failure surfaces for each site were determined by combining certain characteristics of the failure surface that are consistent across the range of applied seismic coefficients with any available knowledge in the literature about the limits of the lateral spread areas. At the Wildlife Array site, we see that in general, the failure surfaces of minimum stability tend to pass along the bottom of the liquefied silty sand layer. An examination of the available literature (Holzer et al., 1989) indicates that the lateral spread extended at least to the location of the of the instrumental array, the center of which was approximately 23 m east of the Alamo River channel. Based on this information, a reasonable failure surface can be inferred and specified as shown in Figure 7.24a, for the purposes of the consistent application of the pseudo-static back-analysis procedures. At the Moss Landing MBARI 3 site, surficial evidence of ground cracking was reported to extend as far inland as the centerline of Sandholdt Rd. The left endpoint of the failure surface in Figure7.24 reflects this extent.

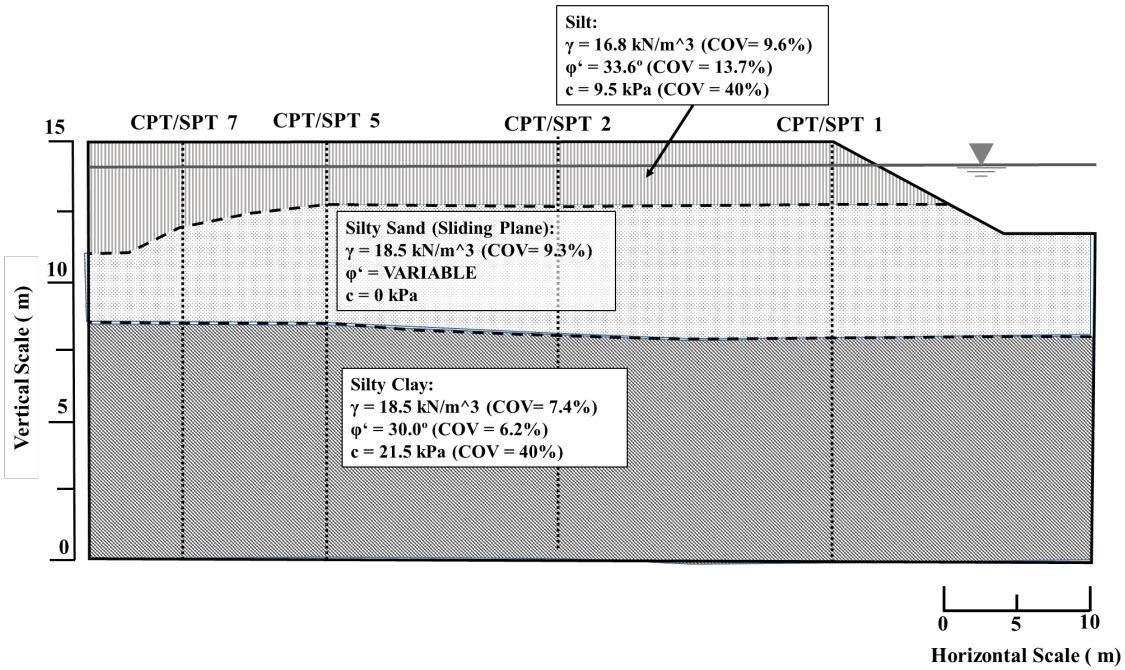

(a)

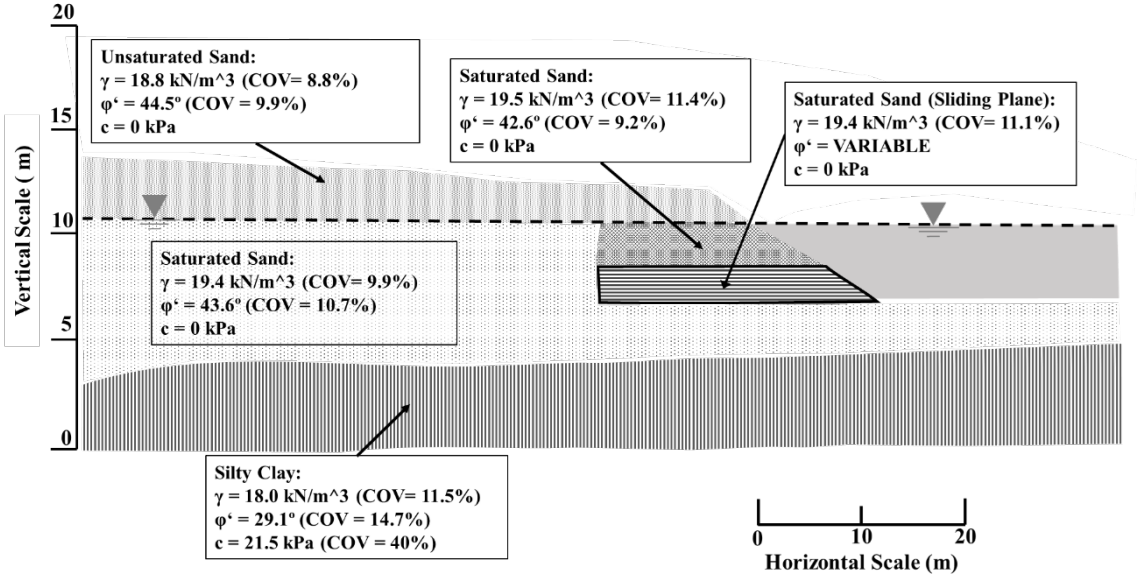

(b)

Figure 7.23: Subsurface profile of the (a) Wildlife Array and (b) Moss Landing MBARI 3 lateral spreading sites, including probabilistic input soil parameters, for use in SLIDE analyses.

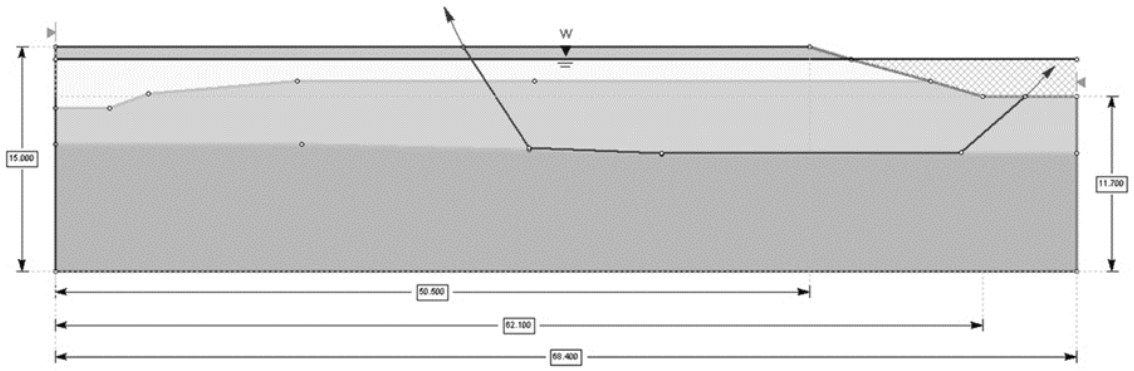

(a)

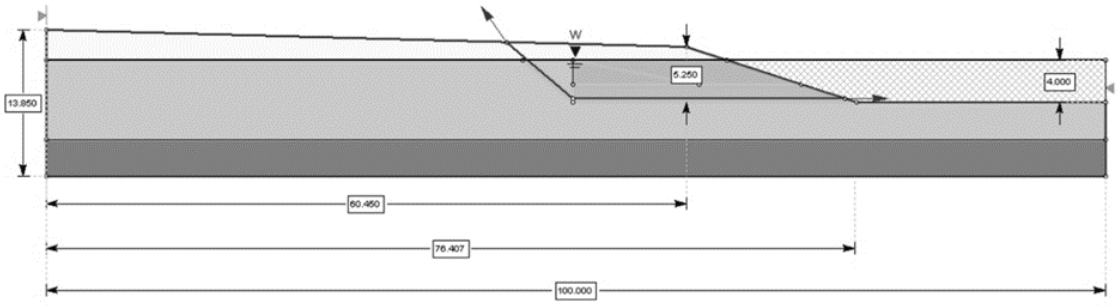

(b)

Figure 7.24: SLIDE input profiles, with specified failure surfaces for (a) Wildlife Array and (b) Moss Landing MBARI 3

Relationship Between Liquefied Shear Strength and Yield Acceleration

For a particular horizontal acceleration value, a probabilistic slope stability analysis was performed with the input soil parameters summarized in Tables 7.10 and 7.11. The Latin Hypercube sampling method (LHS) was used to generate 100,000 samples of combinations of the variable soil parameters. The LHS can be initially described by the sampling of points from a two-dimensional joint probability distribution (e.g., a single distribution comprised of the distributions of parameters a and b). The distributions of a and b can be assembled to form a square grid of parameter combinations, divided into M intervals of equal width. The sampling of this grid is therefore considered a *Latin square* if and only if there is one sample from each grid cell. The two-dimensional concept of the Latin square can be similarly extended to an arbitrary number of dimensions (seven, in the case of these analyses), with the number of subdivisions M controlled by the total number of samples specified by the user. In comparison to traditional random sampling, in which a new sample point is taken with no "memory" of the prior sample points, the LHS offers a distinct advantage in that it better represents the actual variability of the input soil parameters, for a given number of samples. Alternatively, LHS allows representation of

variability with a smaller number of samples than random sampling.

The probabilistic slope stability analyses were performed for the range of horizontal seismic coefficients (a_i) specified by the probability distributions in Figure 7.22. For each sampled value of a_i, a series of probabilistic analyses was performed for a range of friction ratios of the liquefied soil layer. The friction angle input for the sensitivity analysis can be directly converted to NSR for a cohesionless ($c = 0$) material via:

$$S_{u,mob} = c + \sigma'_{v0} + \tan\phi = \sigma'_{v0} \tan\phi \tag{7.7}$$

$$\tan\phi' = \frac{S_{u,mob}}{\sigma'_{v0}} = NSR \tag{7.8}$$

Table 7.10: Summary of statistical soil inputs to probabilistic pseudo-static slope stability analyses in SLIDE for the Wildlife Site

Wildlife Array			
Material	Property	Mean	C.o.V.
Silt	γ (kN/m^3)	16.8	9.6%
Silt	ϕ' (deg)	33.6	13.7%
Silt	c (kPa)	9.5	40.0%
Liquefied Silty Sand	γ (kN/m^3)	18.5	7.4%
Silty Clay	γ (kN/m^3)	18.5	7.4%
Silty Clay	ϕ' (deg)	30	6.2%
Silty Clay	c (kPa)	21.5	40.0%

Table 7.11: Summary of statistical soil inputs to probabilistic pseudo-static slope stability analyses in SLIDE for the Moss Landing Site

Material	Moss Landing, MBARI 3 Property	Mean	C.o.V.
Unsaturated Sand	γ (kN/m^3)	18.8	8.8%
Unsaturated Sand	ϕ' (deg)	44.5	9.9%
Saturated Sand (above liquefied soil)	γ (kN/m^3)	19.5	11.4%
Saturated Sand (above liquefied soil)	ϕ' (deg)	42.6	9.2%
Liquefied Sand	γ (kN/m^3)	19.4	11.1%
Saturated Sand (below liquefied soil)	(kN/m^3))	19.4	9.9%
Saturated Sand (below liquefied soil)	ϕ' (deg)	43.6	10.7%

7.7.2 Analysis Results

The results of a set of analyses for a given a_i can be summarized in SLIDE by the example histogram in Figure 7.25 from the Wildlife Array back-analysis.

Processing of Raw Data

For an applied horizontal acceleration and a given value of the friction ratio, the results of the probabilistic SLIDE analyses are characterized by a probability of failure (P_F), which is simply the ratio of samples with a pseudostatic factor of safety less than unity to the total number of samples:

$$P\big[FS < 1 | NSR = nsr\big] = \frac{N_{FS<1}}{N_{tot}} \tag{7.9}$$

A series of $P_F - NSR$ curves were obtained for the range of sampled horizontal accelerations (Figure 7.26). For a given a_i, the probability of failure decreases quite rapidly with increasing *NSR*. It is also clear that as a_i increases, the decrease in P_F as *NSR* increases is less rapid.

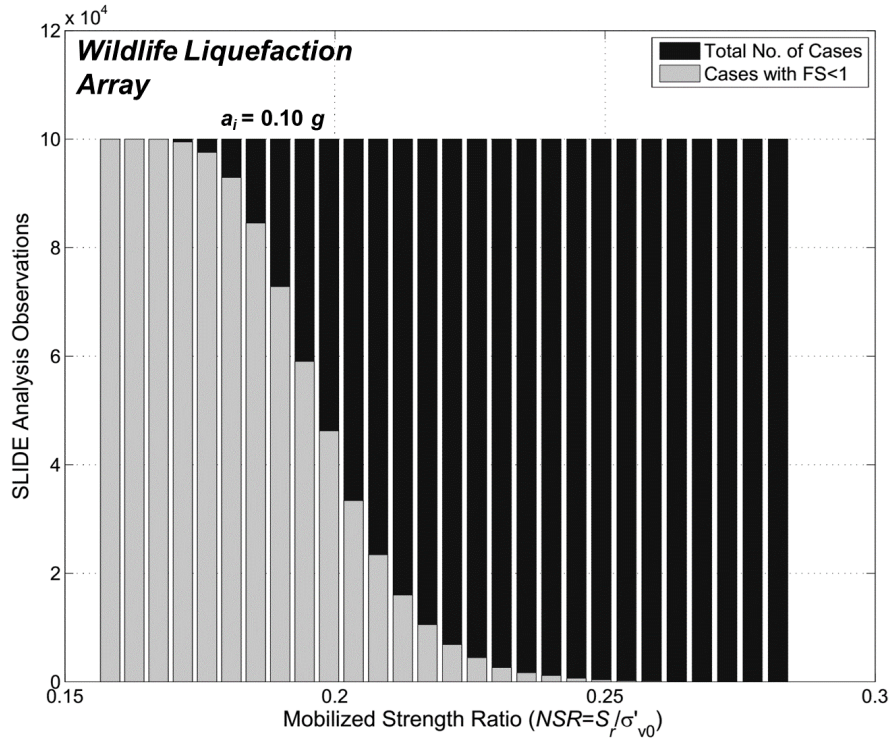

Figure 7.25: Frequency histogram obtained from a series of pseudo-static slope stability analyses, performed using the Latin Hybercube sampling method, for a horizontal seismic coefficient of 0.10 g

It is relatively straightforward to show that the probability of failure given specific values of *NSR* and a_i can be directly related to the probability of exceedance of *NSR*. For example, if we examine the curve in Figure 7.26 for $a = 0.20g$, the probability of failure at $NSR = 0.35$ is roughly 20%. This corresponds to a 20% likelihood that the *NSR* of the liquefied silty sand at Wildlife was less than or equal to 0.35, given the fact that failure did occur and that $a_i = 0.2g$. This probability of non-exceedance, or $P\big[NSR < nsr_i\big]$, can be directly converted to a point on a cumulative distribution curve. The cumulative distribution for a given nsr_i for a given a_j is thus described by:

$$P\big[NSR < nsr_i | a = a_j\big] = 1 - P\big[FS < 1 | NSR = nsr_i\big] \tag{7.10}$$

The raw data obtained from the SLIDE analyses can thus be directly interpreted as probability of non-exceedance curves for *NSR*, and by fitting the data to known probability distributions, cumulative distribution functions (CDFs) for *NSR* can be obtained for each yield acceleration. Note that as a_i increases, the curves become less steep, corresponding to higher variability in the back-calculated *NSR*.

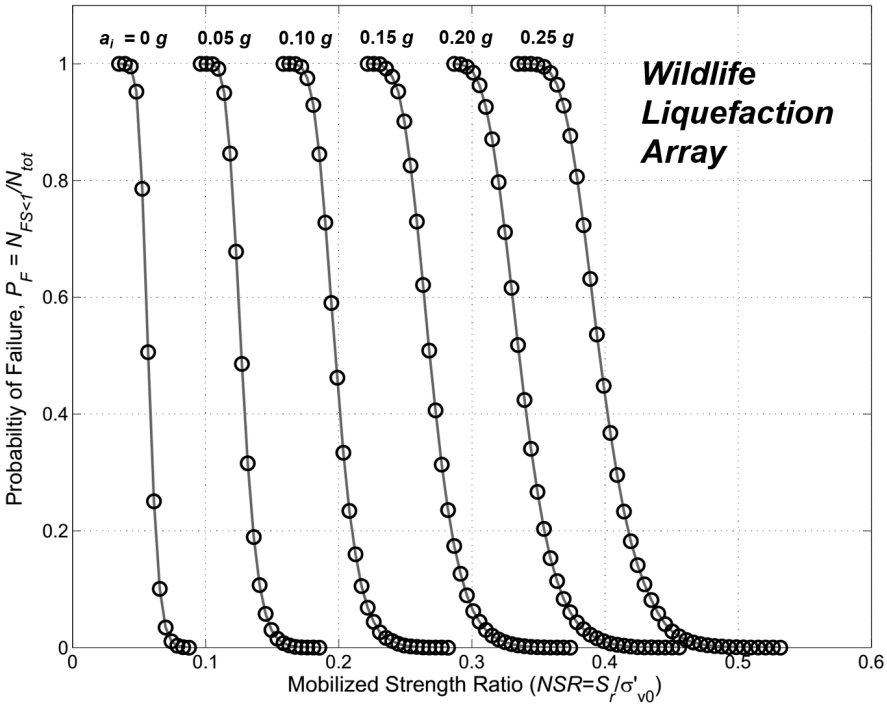

Figure 7.26: Probability-of-failure data, plotted against normalized strength ratio, obtained from the results of pseudostatic slope stability analyses on the Wildlife case history for six applied horizontal accelerations

Fitting Known Distributions to Data

The data obtained from the pseudostatic analyses in SLIDE are, at their most fundamental level, a series of "success" and "failure" observations, corresponding to cases where the pseudostatic factor of safety is less than unity (failure) or greater than unity (success). The probability of failure depends on a predictor variable, in this case represented by *NSR*. We can expect (and have observed) that as *NSR* is increased, the probability of failure will decrease. This form of data observation is characterized most appropriately using regression models that involve binary response variables. The binary response variable, Y_i, depends on the pseduostatic factor of safety F_i:

$$Y_i = \begin{cases} 1, & F_i > 1.0 \\ 0, & F_i \leq 1.0 \end{cases} \tag{7.11}$$

The factor of safety can be expressed as a function of strength, S_i, by a simple linear regression model with an error term ε_i:

$$F_i = \beta_0 + \beta_1 S_i + \varepsilon_i \tag{7.12}$$

For binary response, the expected value of Y_i is equal to the probability that Y_i is equal to 1, or equivalently, that the factor of safety will be greater than unity.

The form of the mean response function depends on the assumed distribution of ε_i. The simplest case to consider is one which assumes that the errors are normally distributed with zero mean and σ standard deviation, known as the *probit response function*. Combining Equations 7.11 and 7.12, and noting that the standard normal variable $Z = \varepsilon_i/\sigma$:

$$\begin{aligned} P\big[Y_i = 1\big] &= P\big[F_i > 1\big] \\ &= P\big[\beta_0 + \beta_1 S_i + \varepsilon_1 > 1\big] \\ &= P\left[\frac{\varepsilon_i}{\sigma} < \frac{1-\beta_0}{\sigma} - \frac{\beta_1}{\sigma} S_i\right] \\ &= P\big[Z < \beta_0^* + \beta_1^* S_i\big] \end{aligned} \tag{7.13}$$

Thus, the probability of non-failure follows a standard normal distribution, and the probit mean response function for Y_i takes the form of:

$$E\big[Y_i\big] = \Phi(\beta_0^* + \beta_1^* S_i) \tag{7.14}$$

The second mean response function that was fitted to the results was the *logistic function*, which assumes an alternative, logistic distribution for the error term. For a logistic random variable ε with zero mean and $\sigma = \pi/\sqrt{3}$, the probability density (f) and cumulative distribution (F) functions are, respectively:

$$f(\varepsilon) = \frac{\exp \varepsilon}{[1 + \exp(\varepsilon)]^2} \tag{7.15}$$

$$F(\varepsilon) = \frac{\exp \varepsilon}{1 + \exp(\varepsilon)} \tag{7.16}$$

The expected value of Y_i is expressed as:

$$E[Y_i] = F(\beta_0 + \beta_1 S_i) = \frac{\exp(\beta_0 + \beta_1 S_i)}{1 + \exp(\beta_0 + \beta_1 S_i)} \tag{7.17}$$

where $\beta_0 = (\pi/\sqrt{3})\beta_0^*$ and $\beta_1 = (\pi/\sqrt{3})\beta_1^*$.

The third response function tested was the complementary log-log response function, which assumed the errors are distributed according to extreme value or Gumbel distributions, which are slightly skewed. The mean response function takes the form of:

$$E[Y_i] = 1 - \exp\big[-\exp(\beta_0 + \beta_1 S_i)\big] \tag{7.18}$$

The three mean response functions were fitted to the raw data using the `glmfit` function in MATLAB. It was found that all three functions fit the data far better when regression was performed with respect to the logarithm of the predictor variable (NSR). The logistic and probit functions closely fit the raw data for both case histories (Figure 7.27), while the complementary log-log fit was generally too shallow to capture the response at the tails of the data.

The goodness-of-fit of the three mean response functions was evaluated in terms of three criteria: the residual sum of squares, deviance, and Kolmogorov-Smirnov test statistic. The residual sum of squares compares the fitted probability of non-exceedance function (P_{fit}) with the probability function derived from the raw data (P_{raw}), for a set of n predictor variables:

$$RSS = \sum_{i=1}^{n} (P_{fit,i} - P_{raw,i})^2 \tag{7.19}$$

The deviance is a natural extension of the residual sum of squares, and is generally described as the binomial analog to the chi square test statistic normally used for linear regression.

$$dev = -2 \sum_{i}^{n} \Big(\Big[\log P_{raw,i} - \log P_{fit,i} \Big] \tag{7.20}$$

The Kolmogorov-Smirnov (KS) test compares the raw (empirical) CDF, $C_{raw}(x)$, with a fitted (hypothetical) distribution, $C_{fit}(x)$, from the sample data. The KS test statistic is simply the maximum difference between the hypothetical and the empirical CDFs (Figure 7.28):

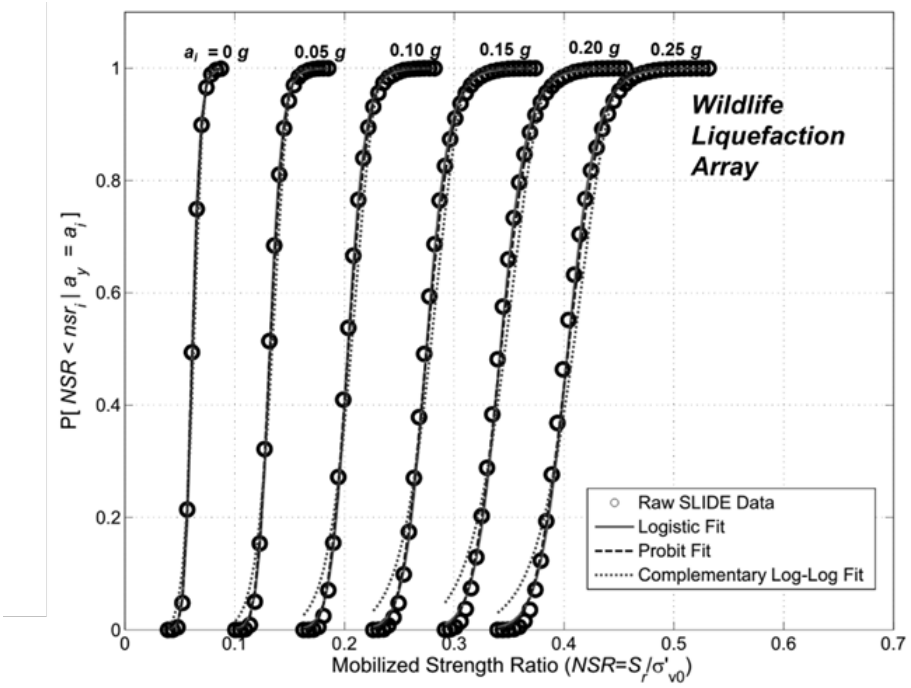

(a)

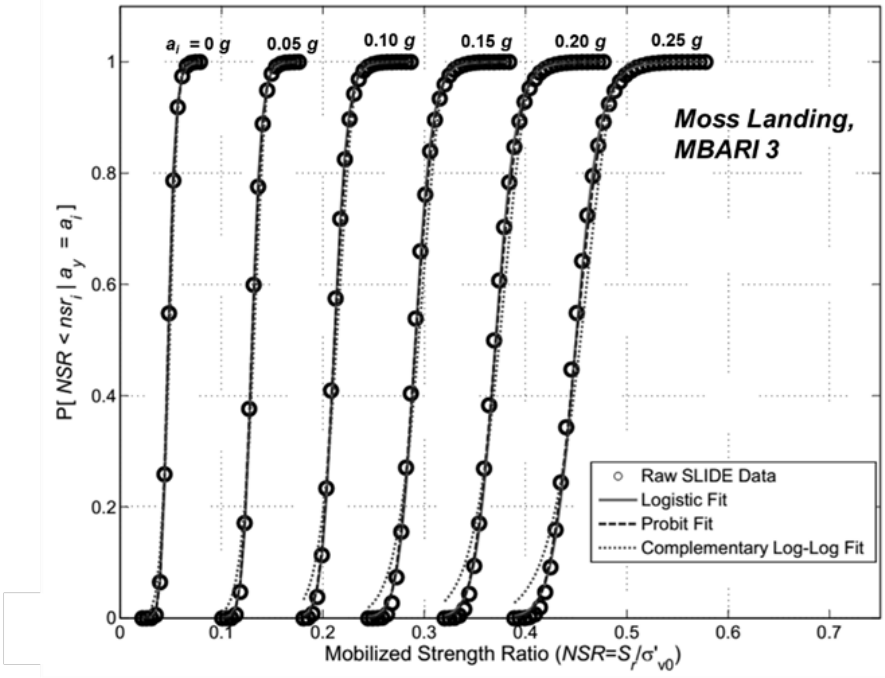

(b)

Figure 7.27: Raw probability-of-failure data and best-fit curves for logistic, probit, and complementary log-log mean response functions for (a) Wildlife and (b) Moss Landing case histories

$$KS = \max|C_{fit}(x) - C_{raw}(x)| \tag{7.21}$$

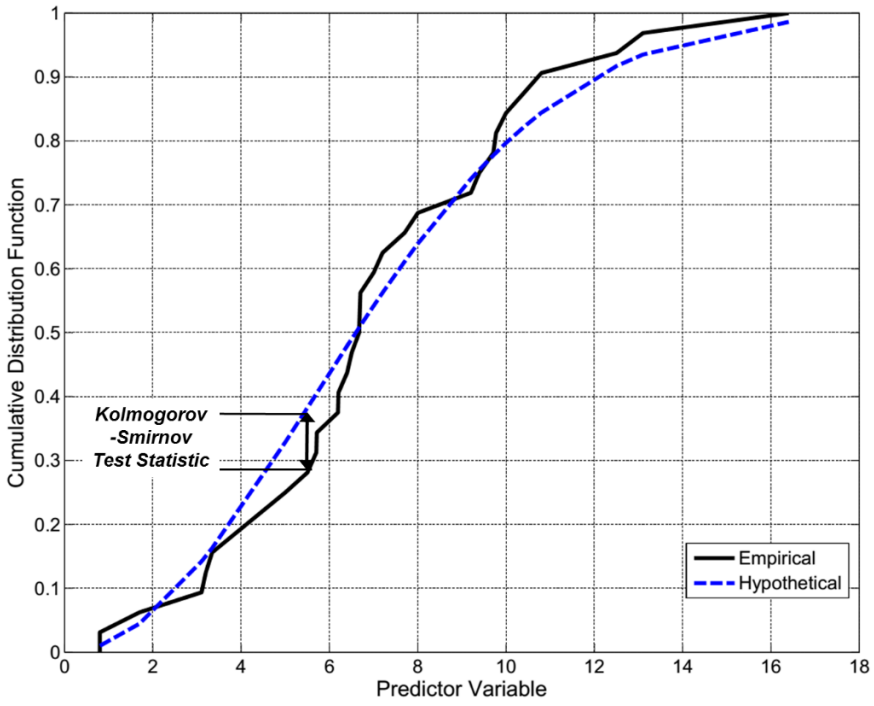

Figure 7.28: Schematic illustration of Kolmogorov-Smirnov test statistic

The goodness-of-fit test results (Tables 7.12 and 7.13) indicate that the logistic function provides a slightly better fit than the probit function for Moss Landing, and a significantly better fit for the Wildlife Site. Based on these results, the NSR data obtained from the SLIDE analyses is assumed to follow a logistic distribution.

Table 7.12: Goodness-of-fit test statistics for logistic, probit, and complementary log-log best fit functions for raw probability-of-failure data at Wildife Array site

Goodness of Fit Test Statistic	Wildlife Liquefaction Array		
	Logistic	Probit	Comp. Log-Log
Residual Sum of Squares	0.0068	0.0081	0.0768
Deviance/N_{tot}	0.1133	0.1239	1.0162
Kolmogorov-Smirnov	0.0418	0.0423	0.1161

The logistic fit for the full relationship between $P[NSR < nsr_i]$, NSR, and a_i can be visualized using the surface plot Figure 7.29, as well as the plot of median, 16th, and 84th percentile NSR with respect to horizontal acceleration in Figure 7.30. We can see that the median NSR value increases in a roughly linear fashion with respect to yield acceleration. The variance of the back-calculated NSR also increases with increasing

Table 7.13: Goodness-of-fit test statistics for logistic, probit, and complementary log-log best fit functions for raw probability-of-failure data at Moss Landing MBARI 3 Site

Goodness of Fit Test Statistic	Moss Landing MBARI 3		
	Logistic	Probit	Comp. Log-Log
Residual Sum of Squares	0.0051	0.0053	0.0612
Deviance/N_{tot}	0.0858	0.0898	0.8684
Kolmogorov-Smirnov	0.0387	0.376	0.1143

acceleration, however the overall variance remains generally low, with a coefficient of variation on the order of about 5 to 10% for all horizontal acceleration values.

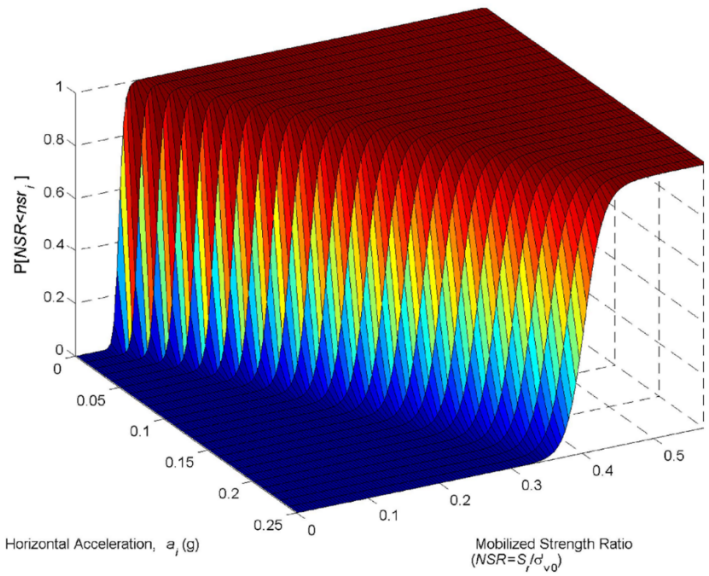

Figure 7.29: Surface mesh plot of logistic-fitted probability of failure plotted against horizontal acceleration and mobilized strength ratio for the Wildlife Array case history

Combining Probability Distributions

The probabilistic pseudostatic analyses produced a series of CDFs describing the probability distribution of *NSR* as a function of yield acceleration. To obtain the overall distribution of the normalized strength ratio of the liquefied soil, each CDF of *NSR* given a_y must then be multiplied by the corresponding probability mass of a_y (Figure 7.31), which was obtained from the Newmark sliding block analyses (see Figure 7.22). In the example shown in Figure 7.31 for the Wildlife case, the four curves reach plateaus that

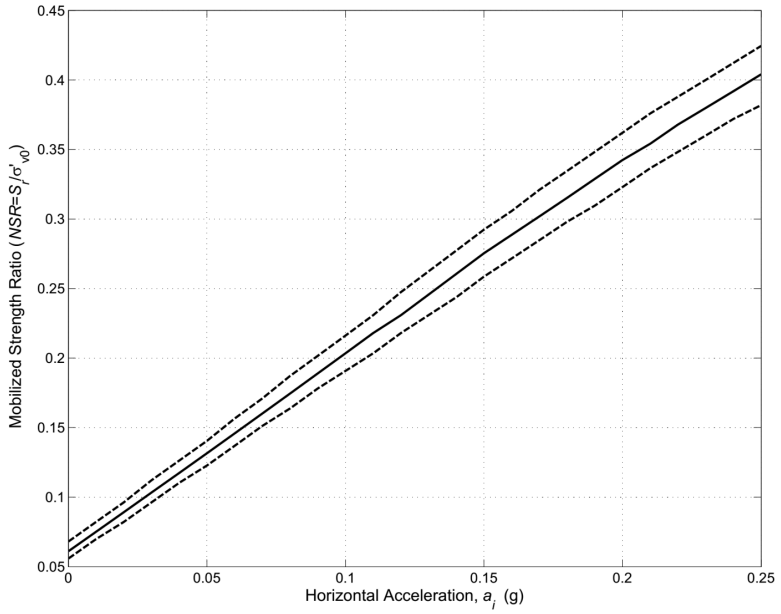

Figure 7.30: Median, 16th, ad 84th percentile of logistic-fitted mobilized strength ratio, plotted against horizontal acceleration for the Wildlife Array case history

correspond to their respective horizontal acceleration probability mass. Certain distributions of $NSR|a_i$ contribute more significantly than others to the final distribution of *NSR*. For instance, the joint probability curves associated with $a_i = 0$ and $a_i = 0.12$ have very low plateau values, due to the fact that each of these values have a very low probability of having been the back-calculated yield accelerations (see Figure 7.22). Conversely, the curve for $a_i = 0.04$, which is the median value for the back-calculated yield acceleration distribution, has the highest plateau.

The total distribution of *NSR* is calculated by integrating the individual values of $P[NSR|a_{y,j}]$ over the full range of a_y. The integration can be approximated numerically as:

$$P\big[NSR < nsr_i\big] = \sum_{j=1}^{m} P\big[NSR < nsr_i | a_y = a_i\big] P[a_y = a_i] \tag{7.22}$$

The corresponding probability distribution, $P[NSR = nsr_i]$ is obtained by differentiating the CDF calculated in Equation 7.22. The results for each case are illustrated in Figure 7.32 and Figure 7.33. The localized variations in probability density for both cases are due simply to the rough discretization interval for horizontal acceleration ($\Delta a_i = 0.01$) used in the SLIDE analyses.

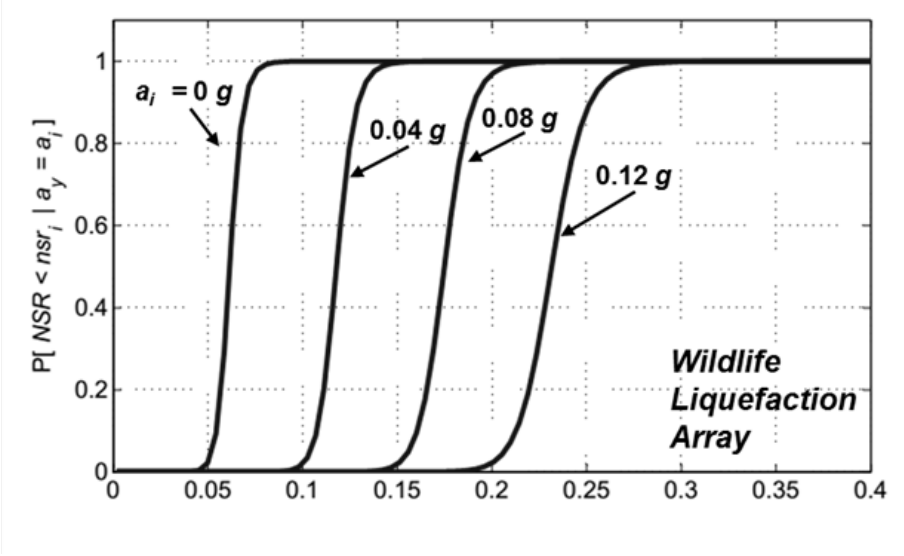

(a)

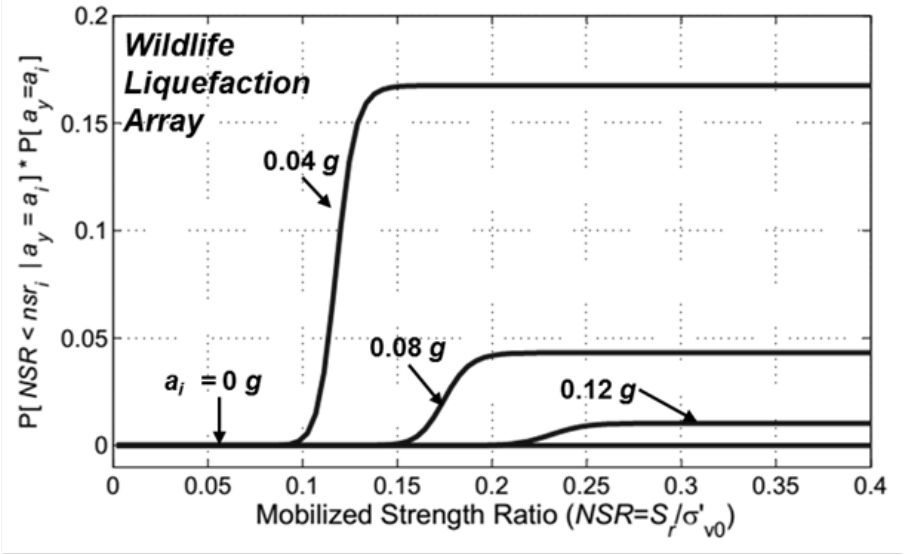

(b)

Figure 7.31: (a) Back-calculated CDFs of mobilized strength ratio given various yield acceleration values for Wildlife case history; (b) CDFs are multiplied by their corresponding probability density of yield acceleration

The PDFs suggest significant positive skew for both cases, with an exceptionally sharp increase in probability density at the lower tail. This behavior does have some physical basis; at very low strengths, the sites that were modelled in this section would have been more likely to experience static slope failure, thus corresponding to a yield acceleration at or near zero. The sliding block analyses indicate that such yield accelerations were highly unlikely, and thus the lower end of the *NSR* distribution acts as a "threshold" value for which lateral spreading is likely to occur, and below which static failure, and by extension

flow liquefaction, would become the dominating mechanism.

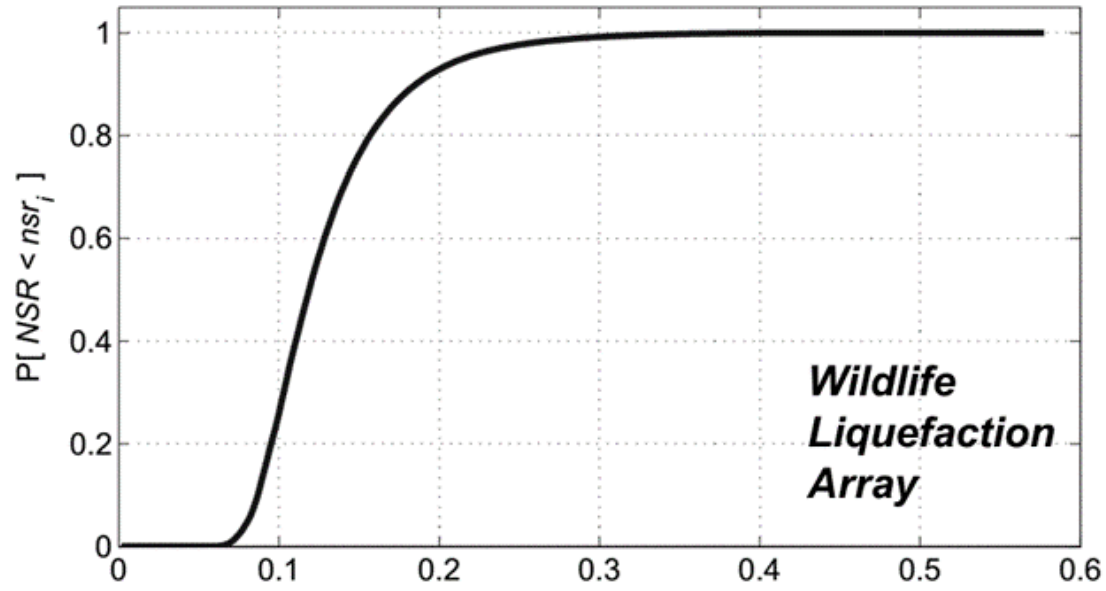

(a)

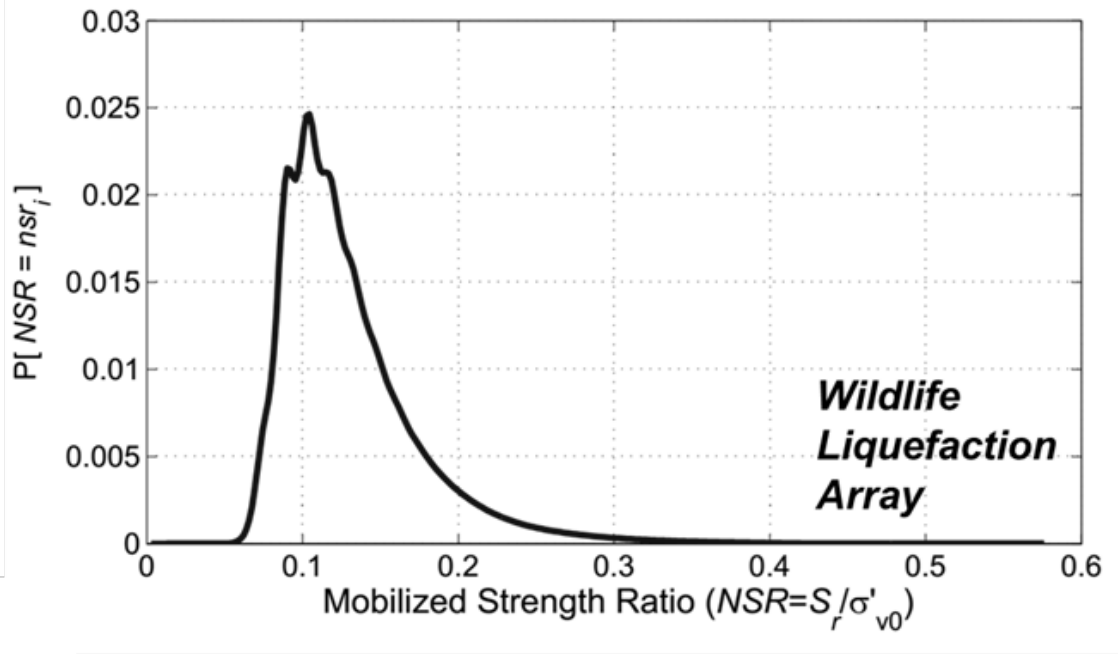

(b)

Figure 7.32: Calculated (a) CDF and (b) PDF of back-calculated mobilized strength ratio for Wildlife Array case history

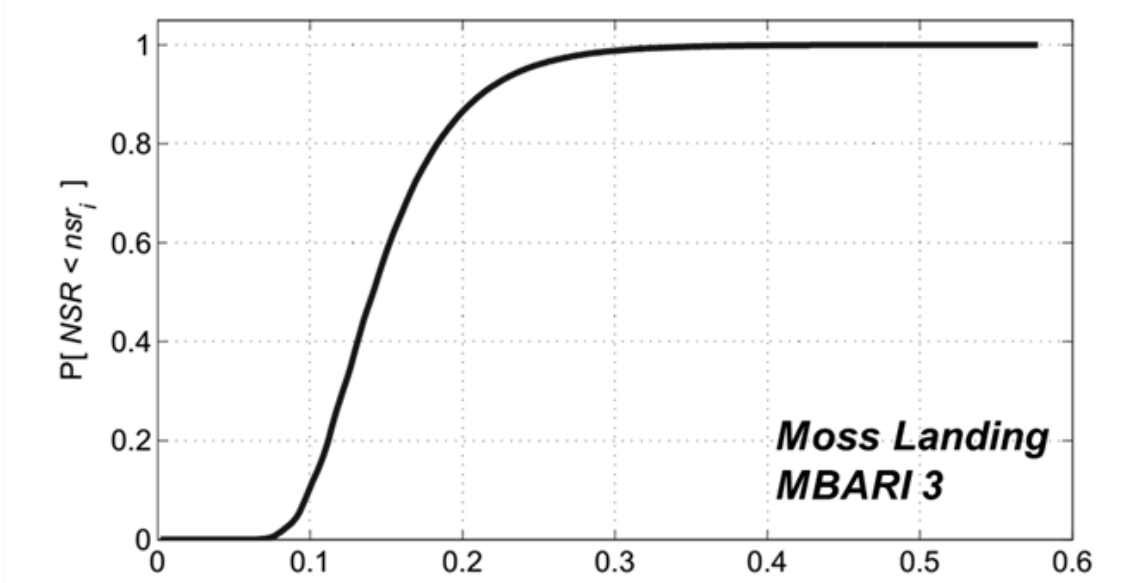

(a)

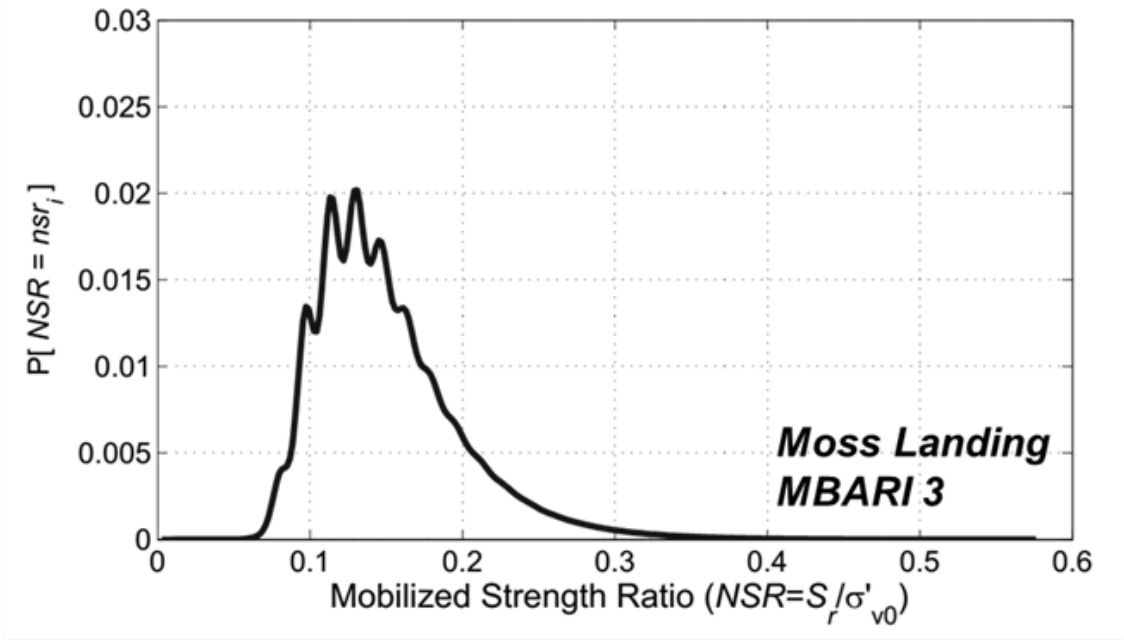

(b)

Figure 7.33: Calculated (a) CDF and (b) PDF of back-calculated mobilized strength ratio for Moss Landing case history

Fitting Known Distributions to NSR Data

The probability distributions shown in Figures 7.32 and 7.33 were converted to "theoretical" raw datasets of observed *NSR* values. The resulting theoretical data set was obtained simply by multiplying the probability distribution by the desired sample size (100,000 samples, in this case), thus converting the probability density into an integer-valued histogram of *NSR* observations. Hypothetical distributions were then fit to these theoretical datasets using the `fitdist` function in MATLAB, which uses maximum likelihood estimation to determine the parameters of each hypothetical distribution. Noting the overall skewness and extreme behavior at the lower tails of both distributions, three distributions were identified as possible candidates for regression: lognormal, log-logistic, and generalized extreme value. A visual comparison of the fitted hypothetical distributions with the probability density histogram (Figures 7.34 and 7.35) suggests that the generalized extreme value (GEV) distribution seems to provide the strongest fit to the raw data.

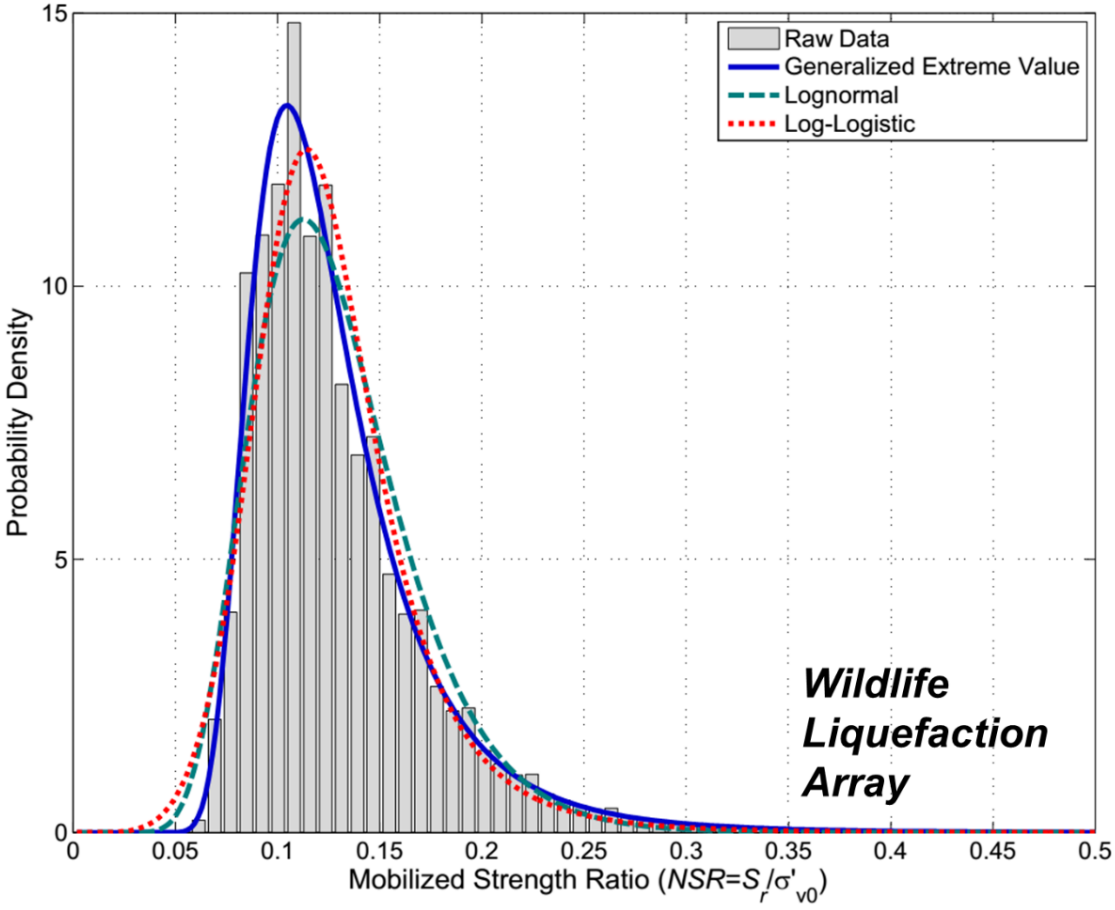

Figure 7.34: Theoretical probability density histogram of back-calculated *NSR*, with best-fit curves for generalized extreme value, lognormal, and log-logistic distributions for the Wildlife Array case history

The goodness-of–fit of each distribution was formally evaluated using the residual sum

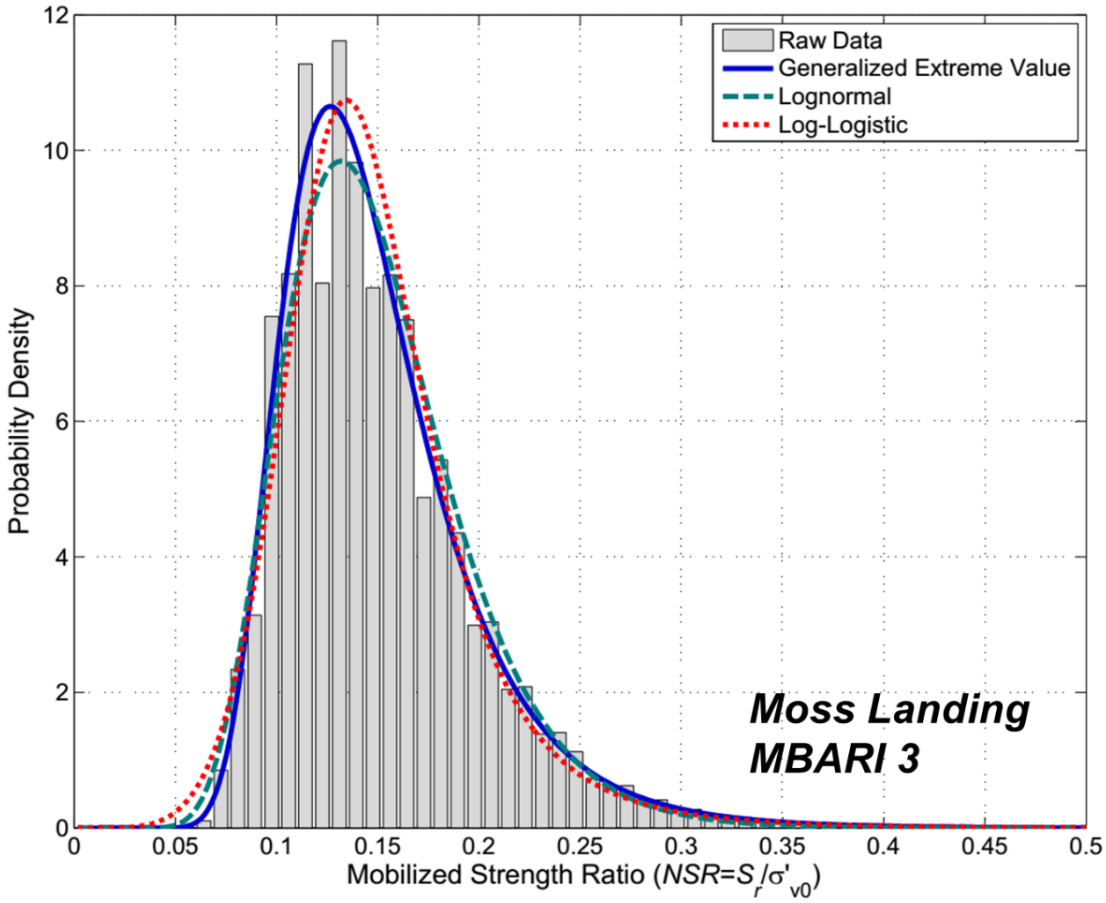

Figure 7.35: Theoretical probability density histogram of back-calculated *NSR*, with best-fit curves for generalized extreme value, lognormal, and log-logistic distributions for the Wildlife Array case history

of squares (see Equation 7.19) and the Kolmogorov-Smirnov test statistic (see Equation 7.21). The test results confirm that the GEV distribution provides a significantly better fit to the observed *NSR* data for each case than do either the lognormal or log-logistic distributions (Tables 7.12 and 7.13).

The generalized extreme value distribution has applications in civil engineering, when the system performance is heavily dependent on its response at the largest or smallest values in a distribution of a random variables (Benjamin and Cornell, 1970), and not just the typical values. In the cases studied in this section, the behavior of the sites at low strength values is critical. It has been shown that there is a threshold value of *NSR* for which flow liquefaction becomes the more likely deformation mechanism as opposed to lateral spreading. From the back-analysis standpoint, it is known *a priori* that lateral spreading was the actual mechanism of failure at both sites, and thus strength values low enough to have caused flow liquefaction would have been highly unlikely to be observed.

Table 7.14: Goodness-of-fit statistics for generalized extreme value, lognormal, and log-logistic functions for back-calculated NSR distribution at Wildlife Array site

Goodness of Fit Test Statistic	Wildlife Liquefaction Array		
	Generalized Extreme Value	Lognormal	Log-Logistic
Residual Sum of Squares	14.57	46.75	42.81
Kolmogorov-Smirnov	0.0186	0.0597	0.0412
Goodness of Fit Test Statistic	**Moss Landing MBARI 3**		
	Generalized Extreme Value	Lognormal	Log-Logistic
Residual Sum of Squares	15.35	21.52	27.15
Kolmogorov-Smirnov	0.0171	0.0345	0.0304

Thus, the use of the GEV distribution to fit the NSR data has a strong theoretical basis.

The final, fitted PDFs for the back-calculated normalized strength ratios are shown, along with their corresponding mean (μ), standard deviation (σ), and skewness (γ_1), in Figure 7.36. The corresponding CDFs are shown in Figure 7.37; the 25th and 75th percentile lines are included for comparison with O&J's reported 25th and 75th percentile estimates. The 11.5 and 88.5 percentile lines correspond roughly to the lower and upper bounds of the Olson and Stark's 2002 model for estimating *NSR* in flow liquefaction cases.

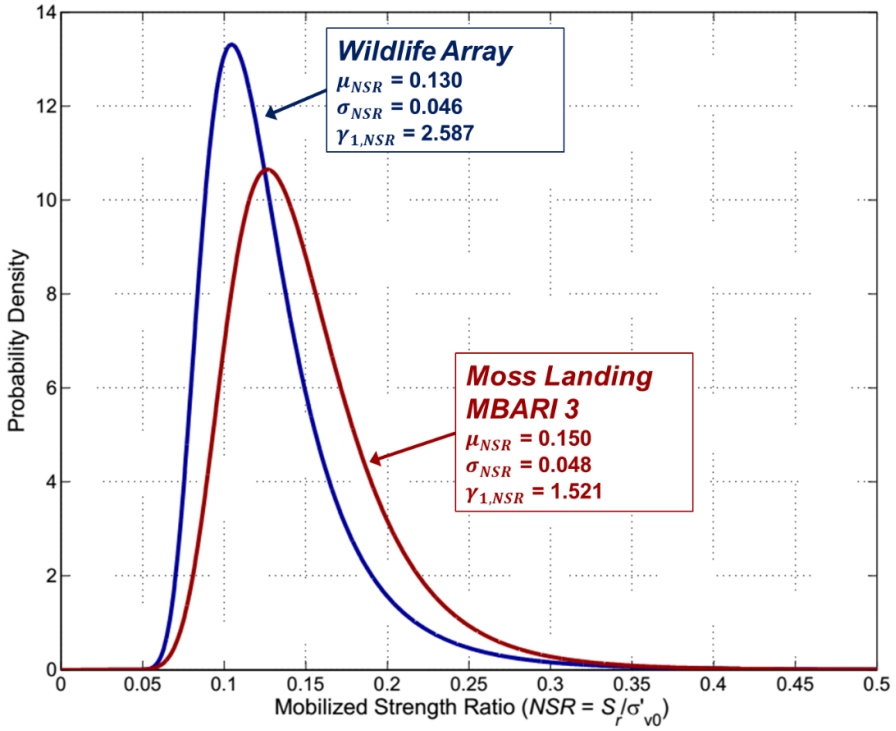

Figure 7.36: Fitted GEV probability density functions of *NSR* for Wildlife Array and Moss Landing case histories

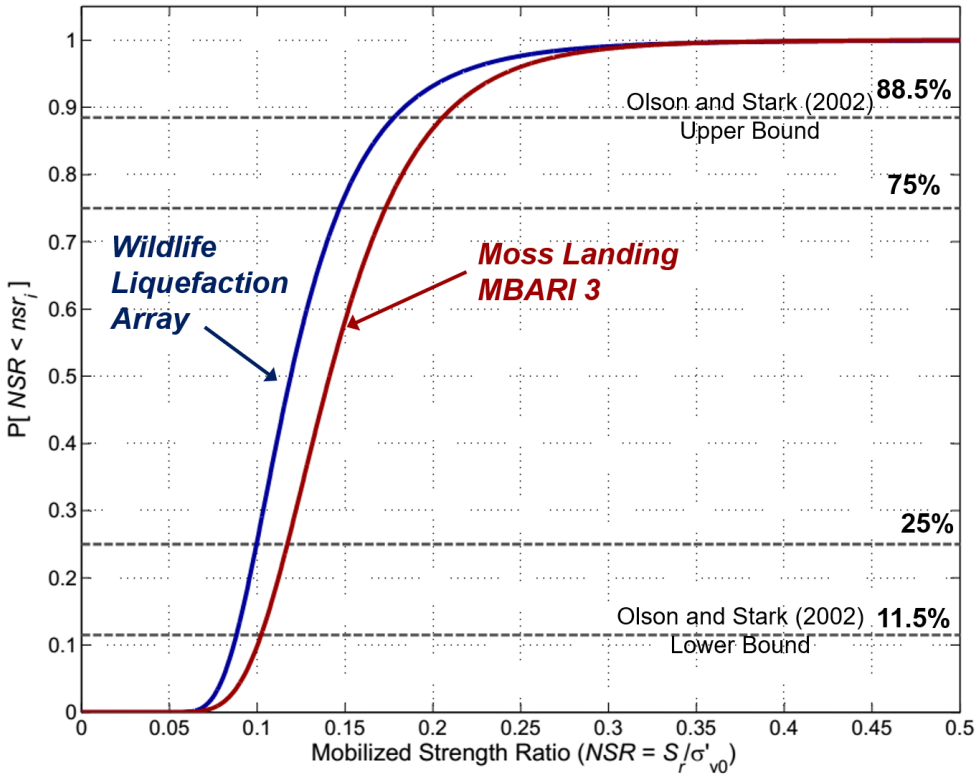

Figure 7.37: Fitted cumulative distribution functions of *NSR* for Wildlife Array and Moss Landing case histories.

7.7.3 Discussion

The data obtained from the probabilistic back-analyses of a_y and *NSR* were compared to the deterministic back-analysis data obtained from the O&J analyses by comparing their medians, 25th, and 75th percentiles (Tables 7.15 and 7.16). The differences between the $a_y - D_H$ relationships obtained from the two methods were also visualized by taking the mean relationship developed from the sliding block analyses in this section, and, assuming that the shape of the curves are roughly the same, applying a simple horizontal shift equal to the difference between the mean a_y back-calculated in this section and the median back-calculated A_y reported by O&J. The result is an "inferred" $D_H - a_y$ curve from O&J's analyses (Figure 7.38a and Figure 7.39a). Similarly, the results of the pseudo-static analyses from both methods were compared by plotting the mean *NSR* with respect to a_y (the relationship is linear) from the probabilistic method, and by plotting a linear best-fit line of the three value pairs of *NSR* and a_y (median, 25th, and 75th percentiles) reported by O&J from their deterministic analyses (Figure 7.38b and Figure 7.39b).

Table 7.15: Median, 25th and 75th percentile estimates for back-calculated *yield acceleration*; obtained from probabilistic back-analyses performed in this section, and compared with estimates reported from Olson and Johnson (2008) for the Wildlife Array and Moss Landing case histories

	Wildlife		Moss Landing	
a_y estimates	Probabilistic	Deterministic (O&J)	Probabilistic	Deterministic (O&J)
Median	0.028	0.048	0.047	0.043
25th pctile	0.027	0.023	0.042	0.039
75th pctile	0.060	0.050	0.076	0.079

Table 7.16: Mean/median, 25th and 75th percentile estimates for back-calculated *NSR*; obtained from probabilistic back-analyses performed in this section, and compared with estimates reported from Olson and Johnson (2008) for the Wildlife Array and Moss Landing case histories

NSR estimates	Wildlife		Moss Landing	
	Probabilistic	Deterministic (O&J)	Probabilistic	Deterministic (O&J)
Mean (or Median)	0.130	0.090	0.150	0.140
25th pctile	0.100	0.060	0.117	0.130
75th pctile	0.147	0.100	0.173	0.190

Bias in back-calculated values of a_y and NSR – Wildlife Array

There were significant differences between the analysis results of two methods for the Wildlife site. The probabilistic Newmark back-analyses produced a mean yield acceleration estimate that was more than 40% lower than the O&J median estimate; however the probabilistic analyses produced a 40% higher mean normalized strength ratio. A lower estimated yield acceleration should, all other factors being equal, result in a lower strength value obtained from pseudo-static analyses. Not only is the source of the bias between probabilistic and deterministic methods not limited to just the sliding block analyses, it is just as significant in the pseudo-static relationship between a_y and *NSR* (Figure 7.38).

The source of the bias, while not entirely clear, may be related to the significant differences in the location of the liquefied material that Olson and Johnson studied at the site, as well as their interpretation of the subsurface CPT and SPT data (see Section 5.4.5). The prefailure vertical effective stress estimates reported by O&J suggest the material being analyzed may have been located directly below the river channel, and not under the area behind the slope crest where ground cracks had been observed. Coupled with the different interpretation of SPT and CPT, the probabilistic and deterministic back-analyses may have effectively been considering two completely different soil deposits.

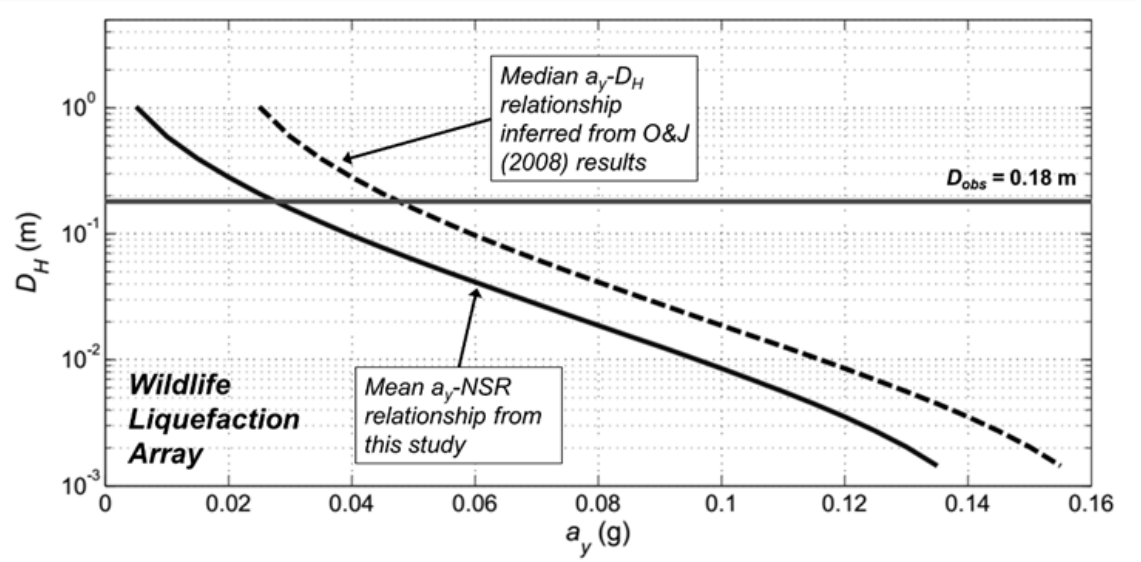

(a)

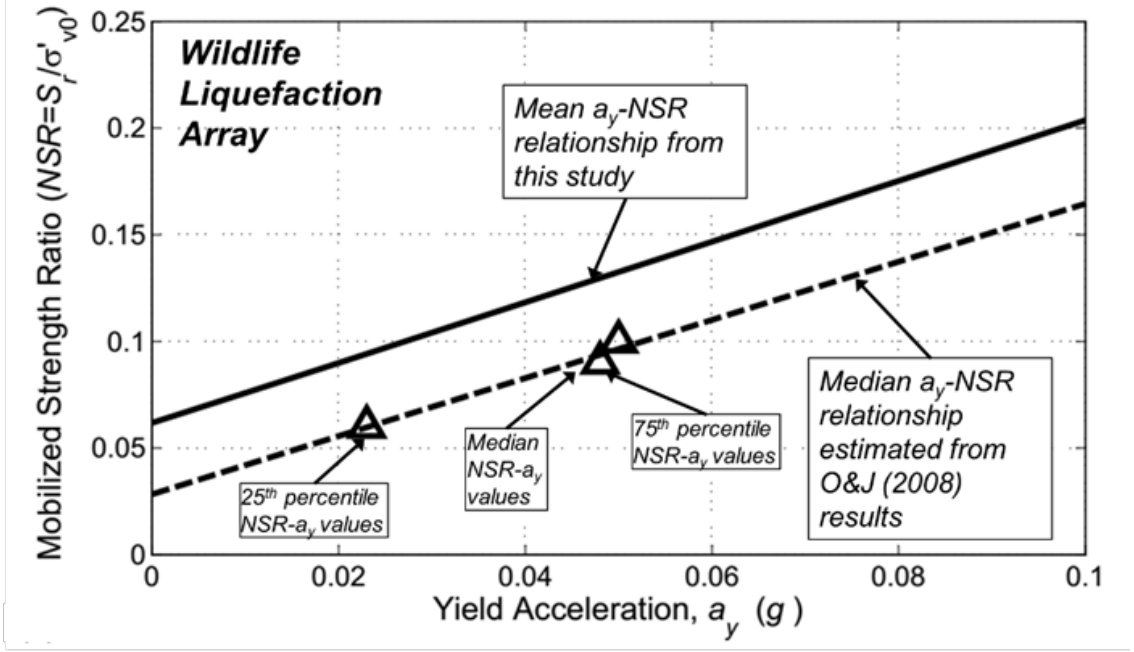

(b)

Figure 7.38: Illustration of differences in (a) D_H–a_y and (b) NSR–a_y relationships between probabilistic analyses performed in this section and deterministic analyses performed by Olson and Johnson (2008), for the Wildlife Array case history

Bias in back-calculated values of a_y and NSR – Moss Landing

The results of the probabilistic and pseudostatic analyses were far more consistent for the case of Moss Landing MBARI 3. The probabilistic estimates of a_y and NSR were approximately 8% and 7% higher, respectively, than the median estimates reported by O&J.

Comparison of the two $NSR - a_y$ lines (Figure 7.39b) shows only moderate discrepancies between the pseudo-static results of the two methods; while the slope of the probabilistic line is about 14% higher than the corresponding deterministic line, the differences in NSR are relatively small in the range of statistically significant yield accelerations.

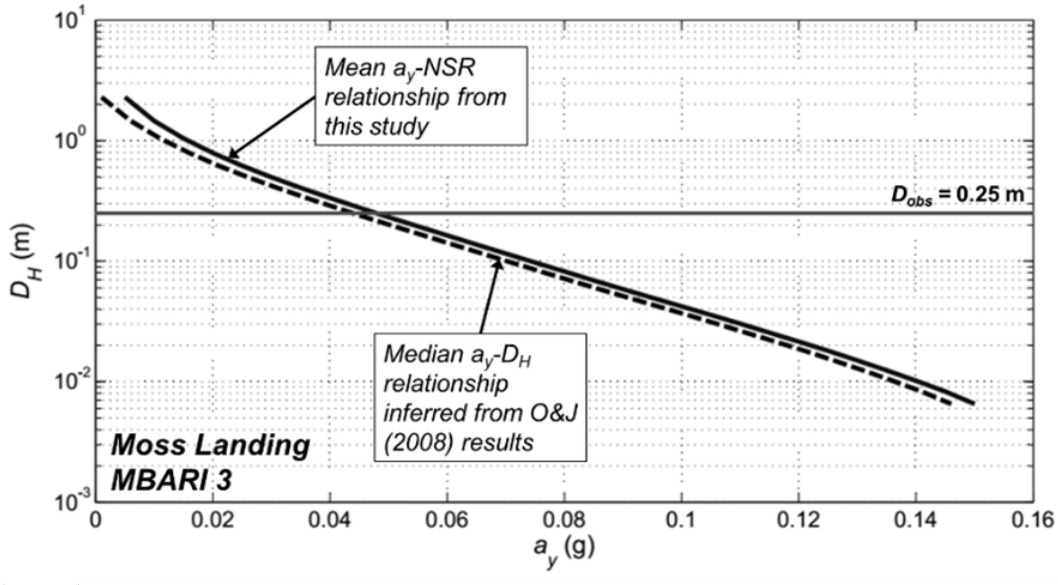

(a)

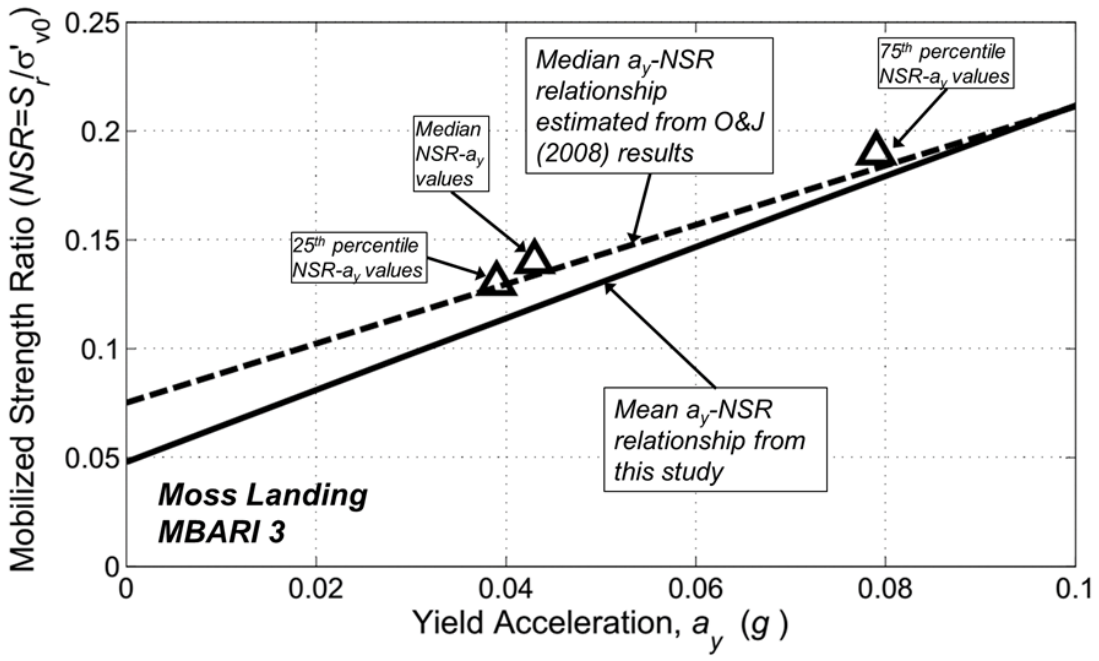

(b)

Figure 7.39: Illustration of differences in (a) D_H–a_y and (b) NSR–a_y relationships between probabilistic analyses performed in this section and deterministic analyses performed by Olson and Johnson (2008), for the Moss Landing case history

Analysis of results in relation to flow failure strength ratios (Olson and Stark 2002)

One of the significant conclusions presented by Olson and Johnson was that the mobilized strength ratios they back-calculated from the lateral spreading case histories plotted consistently within the bounds of Olson and Stark's 2002 equation for liquefaction flow failures (Figure 7.40):

$$\frac{S_r}{\sigma_0'} = \begin{cases} 0.03 + 0.0143(q_{c1}) \pm 0.03, & q_{c1} \leq\sim 10MPa \\ 0.03 + 0.0075(N_1)_{60} \pm 0.03, & (N_1)_{60} \leq\sim 16 \end{cases} \tag{7.23}$$

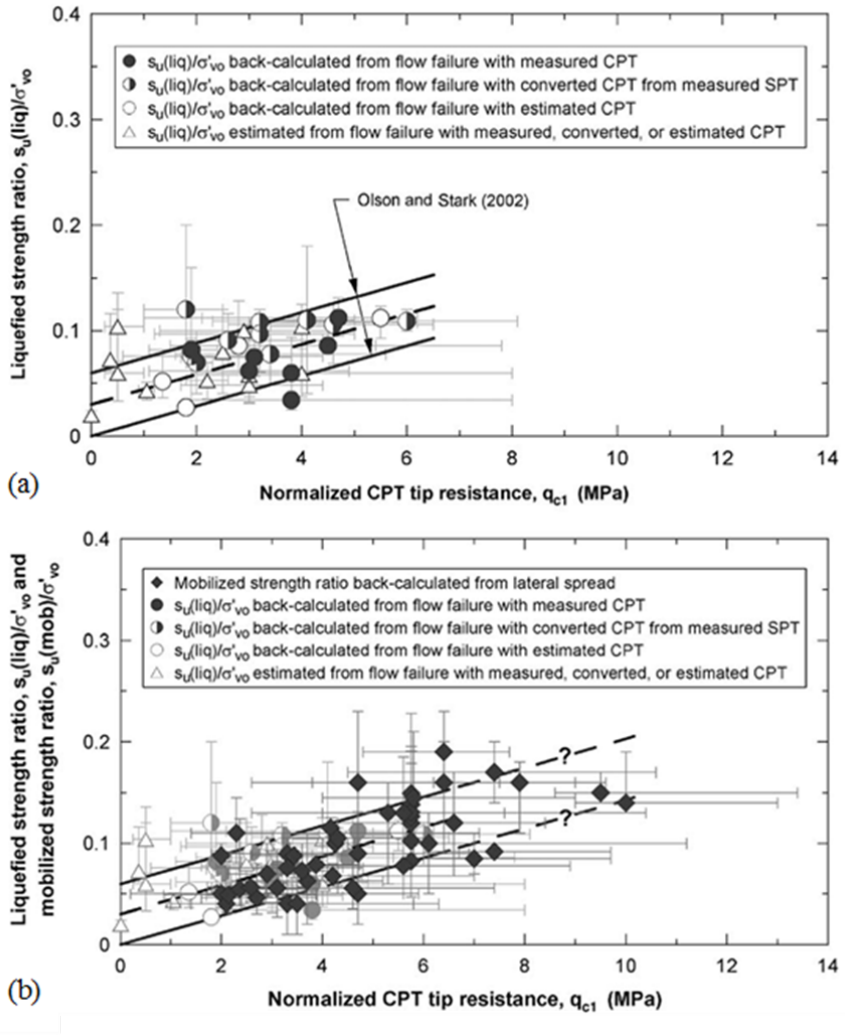

Figure 7.40: Relationships between CPT tip resistance and a) liquefied shear strength ratio back-calculated from liquefaction flow failures (Olson and Stark 2002) and b) mobilized strength ratio back-calculated from lateral spreads (Olson and Johnson 2008) plotted against the bounds from Olson and Stark's linear correlation. (Olson and Johnson 2008)

Note that O&J included 25th and 75th percentile estimates of their back-calculated *NSR*, as well as upper and lower bound values for the representative penetration resistances; these are represented visually by the vertical and horizontal error bars in Figure 7.40. However, there was no formal evaluation of the actual likelihood that the back-calculated *NSR*s fell within the bounds of Olson and Stark's equations; the magnitude of the error bars seem to suggest that there was potentially significant uncertainty regarding the location of the $NSR - q_{c1}$ data points for lateral spreading cases relative to the Olson and Stark bounds.

A simple analysis was undertaken here to obtain an estimate of the probability that the back-calculated strength ratios obtained from the probabilistic analyses performed in this section coincided with the flow failure strength ratios back-calculated by Olson and Stark. For a given penetration resistance value r_i, the upper- and lower-bound *NSR* values, $nsr_{u,i}$ and $nsr_{L,i}$ are calculated from Equation 7.23. The probability that the *NSR* estimated from the Wildlife or Moss Landing cases falls within the Olson and Stark bounds, denoted as $P_{OS}(r_i)$, can be expressed as:

$$\begin{aligned} P_{OS}(r_i) &= P\big[nsr_{L,i} < NSR < nsr_{U,i} | R + r_i\big] \\ &= P\big[NSR < nsr_{U,i} | R = r_i\big] - P\big[NSR > nsr_{L,i} | R = r_i\big] \end{aligned} \tag{7.24}$$

The cumulative distribution functions of *NSR* obtained from the probabilistic analyses (see Figure 7.37) were used to determine the likelihood of *NSR* falling within the bounds of Olson and Stark's equation. Figure 7.41 illustrates this calculation procedure. If, for example, the analysis of penetration test data at the site resulted in a representative CPT qc1 value of 10 MPa, then the corresponding upper- and lower-bound strength ratios would be 0.20 and 0.14, respectively. Using the strength ratio CDF obtained from the back-analysis procedure, we see that these NSR values correspond to a probability of non-exceedance of roughly 86% for the upper-bound value and 50% for the lower-bound value. The lower-bound non-exceedance probability is subtracted from the upper-bound probability to calculate that the probability of *NSR* coinciding with Olson and Stark's equation for flow failures is roughly 36%.

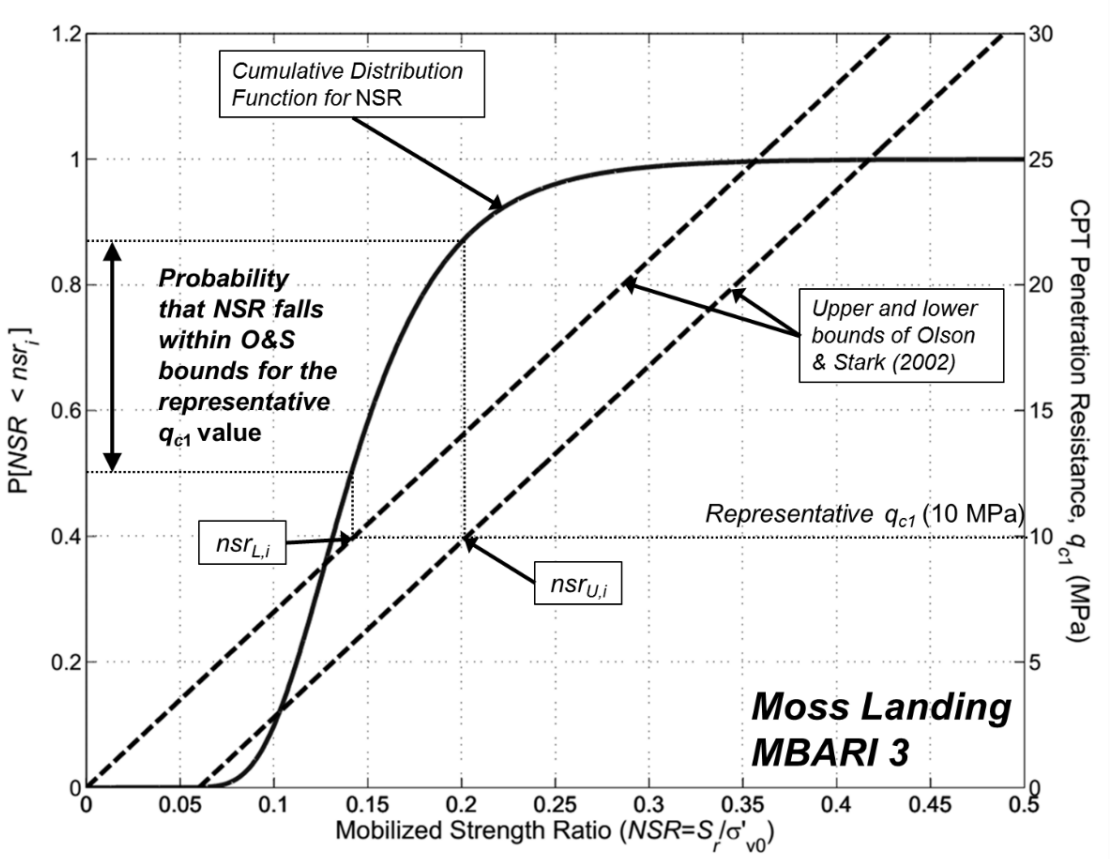

Figure 7.41: Example calculation procedure used to determine the probability that the back-calculated mobilized strength ratio for the Moss Landing case history falls within the bounds of Olson and Stark's 2002 equation for a given representative a_{c1}

To additionally account for the uncertainty in the representative penetration resistance values (i.e. the horizontal error bars in Figure 7.40), existing SPT and CPT data were reviewed for both case histories, and probability distributions were computed to characterize the representative penetration resistances (Figure 7.42). The methods used to obtain these distributions are presented in greater detail in Section 8.3.1.

The calculations outlined in Equation 9 and illustrated in Figure 7.41 were then repeated for a range of penetration resistance values. The calculated P_{OS} values given R_i were then multiplied by the probability density $P[R = r_i]$, and summed over m values of R to obtain the overall probability of NSR coinciding with Olson and Stark's equation.

$$P_{OS} = \sum_{i=1}^{m} P\big[nsr_{L,i} < NSR < nsr_{U,i} | R = r_i\big] P[R = r_i] \tag{7.25}$$

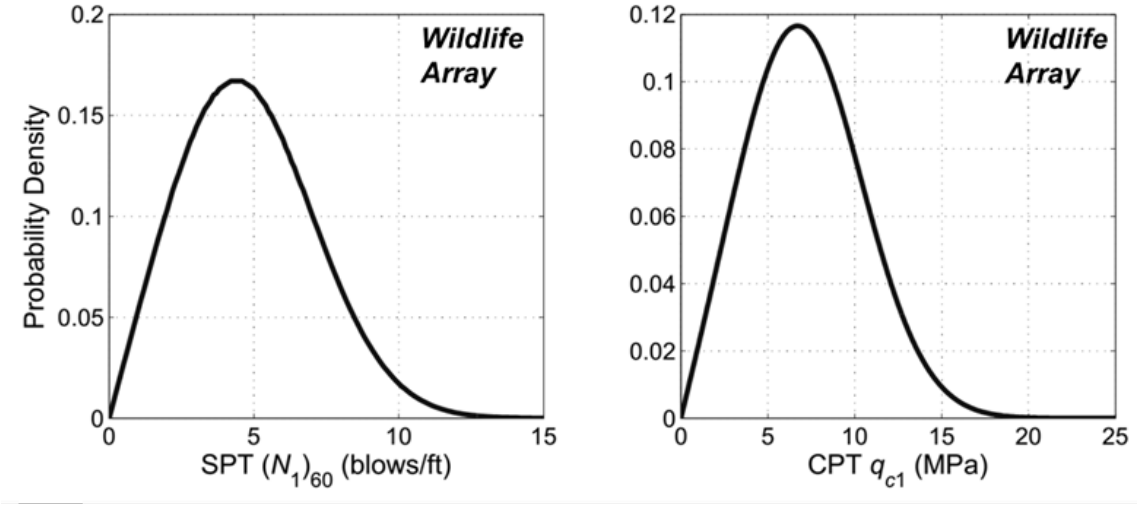

(a)

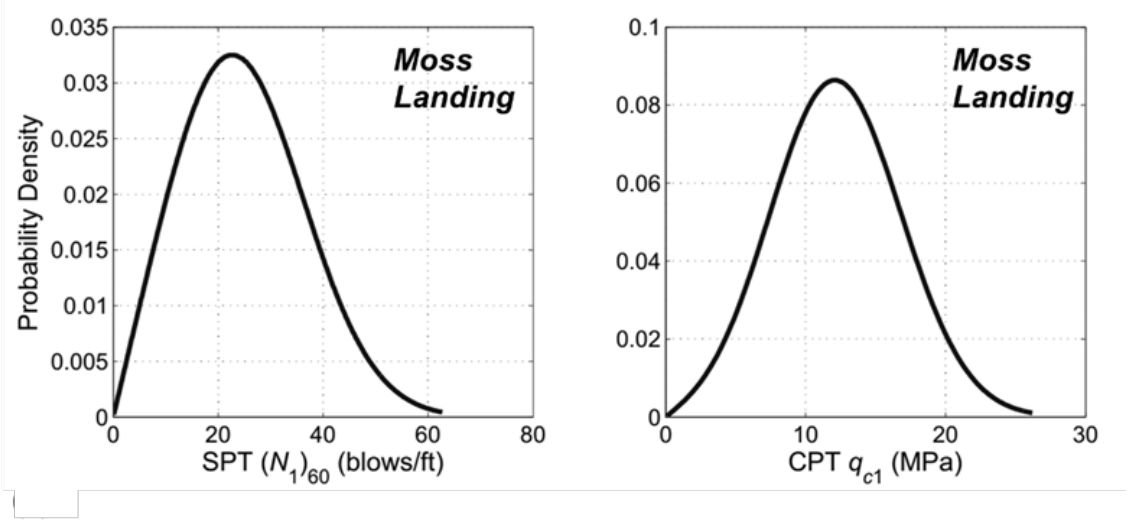

(b)

Figure 7.42: Probability density functions for representative SPT and CPT resistance values for the (a) Wildlife Array and (b) Moss Landing case histories

The results of the analyses are summarized in Table 7. Overall, the probability of *NSR* coinciding with Olson AND Stark's equation is quite low for both the Wildlife and Moss Landing case histories. For the Wildlife case, P_{OS} was estimated to be between 20 and 40%, with the discrepancy between the SPT- and CPT-based relationships largely due to seemingly disparate penetration resistance values. There was considerably more CPT data available for the Wildlife site, and thus the 38% probability associated with it may be the more significant estimate. The P_{OS} value for Moss Landing was between 20 and 25%, and was much more consistent between the CPT- and SPT-based analyses than for Wildlife.

Table 7.17: Overall, maximum, and mean probabilities of the back-calculated mobilized strength ratios coinciding with flow liquefaction strength ratios back-calculated by Olson and Stark (2002)

Probability of O&S Bounds	Wildlife		Moss Landing	
	CPT	SPT	CPT	SPT
P_{OS}	38%	23%	23%	20%
max $P_{OS}(r_i)$	66%	66%	57%	57%
Optimal r_i	5.7 MPa	11 bpf	7.2 MPa	14 bpf
mean r (μ_r)	7.2 MPa	5 bpf	12.3 MPa	25 bpf
$P_{OS}(\mu_r)$	54%	20%	18%	14%

In addition to the overall P_{OS} there are several other useful numbers to consider. The maximum P_{OS} given a certain r_i indicates the effective "best-case scenario" probability of *NSR* plotting within Olson and Stark's bounds. In other words, the maximum P_{OS} assumes that the relationship between the mean back-calculated *NSR* and penetration resistance corresponds perfectly to Olson and Stark's equation, and any remaining uncertainty is due solely to the variance of the back-calculated *NSR* estimate itself. The maximum $P_{OS}(r_i)$ for the Wildlife and Moss Landing cases were approximately 66% and 57%, respectively. It also may be useful to examine the P_{OS} value for the mean representative penetration resistance value, μ_r. These probabilities are largely a function of the differences between the mean and optimal penetration resistance values, and essentially indicate what the P_{OS} would be if the representative penetration resistance was evaluated in a purely deterministic fashion. The only case where P_{OS} was "improved" by the deterministic representation was the Wildlife CPT calculation, where the probability increased to about 54%. For the rest of the cases, P_{OS} decreased slightly.

7.7.4 Conclusions

The framework used by Olson and Johnson to back-analyze strength ratios from lateral spread was thoroughly investigated in this section. The goal was to examine the uncertainties inherent in the various methods used and to evaluate how they propagate through each stage of analyses to affect the back-calculated value of the normalized strength ratio of the liquefied soil. Furthermore, the uncertainty in the computed *NSR* values was used to assess the validity one of the key conclusions reached by Olson and Johnson, namely that the strength ratios mobilized during lateral spreads were essentially identical to those seen in liquefaction flow failures.

Uncertainties in the back-analysis procedure were found in each of its components, beginning with the use of the Newmark sliding block analyses, where significant variance was seen in the back-calculated yield acceleration when using a suite of ground motions; lognormal standard deviations for a_y were on the order of about 0.500. The uncertainty in the pseudostatic slope stability analyses stems from the inherent variability in soil properties, particularly those parameters that affected the weight of the failure mass and the strength along the non-liquefied failure surface (e.g. the surficial "crust"). Overall, the back-calculated *NSR* for the two cases was quite similar to the uncertainty reported by Olson and Johnson, based on comparison of the *NSR* distributions calculated here with the 25th and 75th percentile strength values reported by O&J. It is, however, unclear what the 25th and 75th percentile estimates reported by O&J were based on; it is possible that they are solely an extension of their 25th and 75th percentile a_y estimates, and there is no indication that the pseudostatic analyses were performed probabilistically or parametrically. The standard deviations of *NSR* were close to about 0.05 for both cases, which is quite significant given that back-calculated strength ratios from cases of liquefaction generally are on the order of 0 to 0.20.

In the context of Olson and Stark's 2002 relationship between liquefied strength ratio and penetration resistance for liquefaction flow failures, the relatively high variance in the back-calculated *NSR*, combined with the significant uncertainties inherent in selecting a representative penetration resistance, does not appear to strongly support the conclusion that mobilized strength ratios from lateral spreads coincide with those from liquefaction flow failures. For the two cases analyzed, the probability is approximately 20 to 40% that the back-calculated *NSR* would plot within the upper and lower bounds of Olson and Stark's bounds. Even if the characterization of the representative penetration resistance and its inherent uncertainties is removed, the variability in *NSR* alone results in a likelihood of about 50-65% that the two strength ratios are coincident; while an improvement on the original probability, this "best-case" scenario still does not support O&J's conclusion with overwhelming certainty.

While it is certainly possible that the relationships between initial relative density and strength ratio mobilized during liquefaction are one and the same for lateral spreads and flow failures, the results of Olson and Johnson's analyses do not clearly support such a conclusion with significant confidence. There are many sources of uncertainty at various stages in their back-analysis framework, all combining to obfuscate the final determination of strength ratio, and doing so to an extent that makes any sort of definitive conclusion about relationship between shear strengths mobilized during lateral spreads and flow failures difficult to justify.

7.8 Probabilistic Forward Analysis of Lateral Spreading Displacements

In order to characterize the method proposed by Olson and Johnson for estimating lateral spreading displacement probabilistically, the same two sites that were back-analyzed in the previous section, Wildlife Array and Moss Landing MBARI 3, were analyzed within the forward prediction framework. Particular attention was paid to characterizing the uncertainties involved in site characterization, estimating the normalized strength ratio of the liquefied material, the pseudo-static analyses used to determine the yield acceleration, and the sliding block-based relationship between yield acceleration and permanent displacement.

7.8.1 Site Characterization

The slope geometry, position of the phreatic surface, and the mean and uncertainty parameters of the non-liquefied soils were the same as those determined in the corresponding back-analysis procedure for the same sites outlined in the previous section (see Table 7.10 and 7.11).

The location of the failure surface was specified using the "Block Search" capability in SLIDE. The search limits were specified with a noncircular polyline passing through the bottom of the liquefiable material. The left-hand limit of the polyline was constrained such that any failure masses calculated by SLIDE had free face ratios (the ratio of crest height to distance from toe of slope) less than 20% (Figure 7.43). This restriction ensured that the mechanism being analyzed was closely related to lateral spreading by minimizing the number of cases where static failure would occur (for a horizontal seismic coefficient of zero). For the probabilistic analyses performed here, the failure surface search criteria in SLIDE was specified such that the failure surfaces were trilinear, with the bottom of the failure surface passing through the bottom of the liquefied materials. The distributions of failure surfaces for a typical analysis run are shown in Figure 7.44 for each case. In general, the pseudostatic factor of safety increased with increasing distance from the left-hand limit.

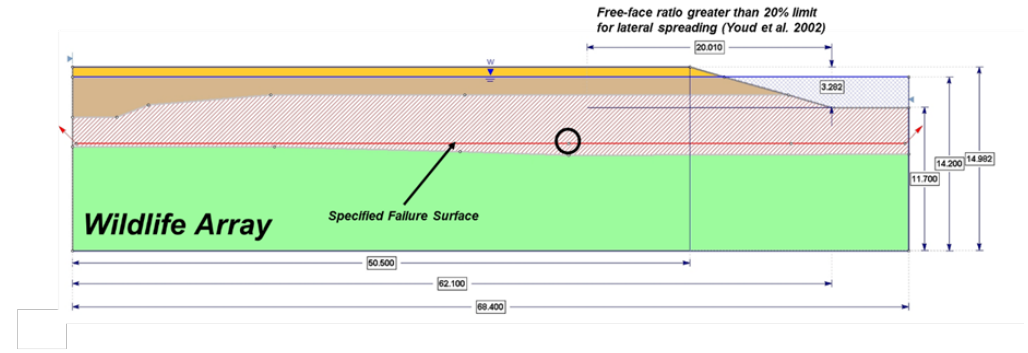

(a)

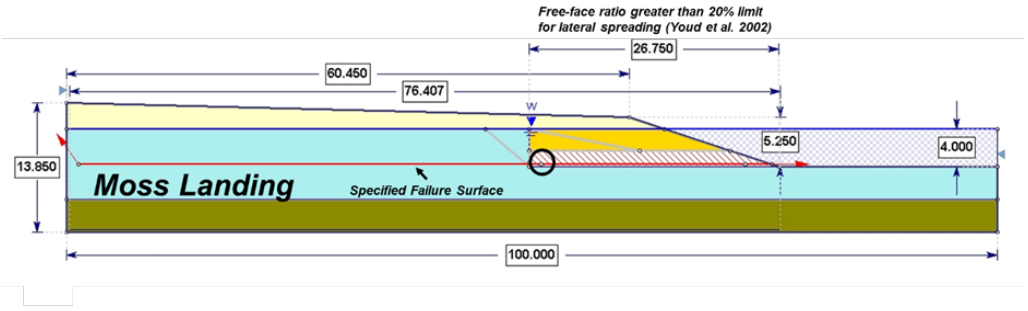

(b)

Figure 7.43: Specification of block search failure surface polyline in SLIDE for (a) Wildlife and (b) Moss Landing sites; limit of left-hand line segment location is circled

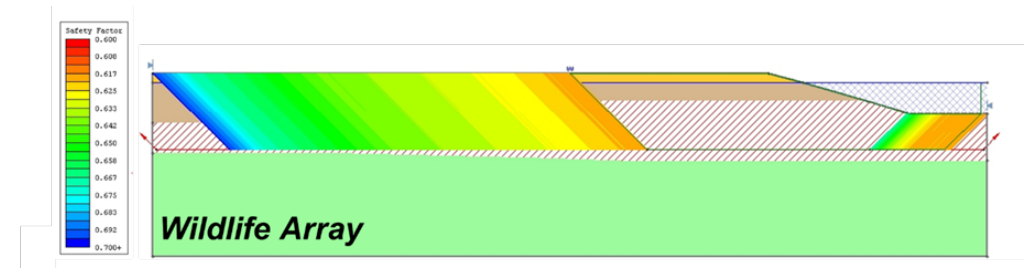

(a)

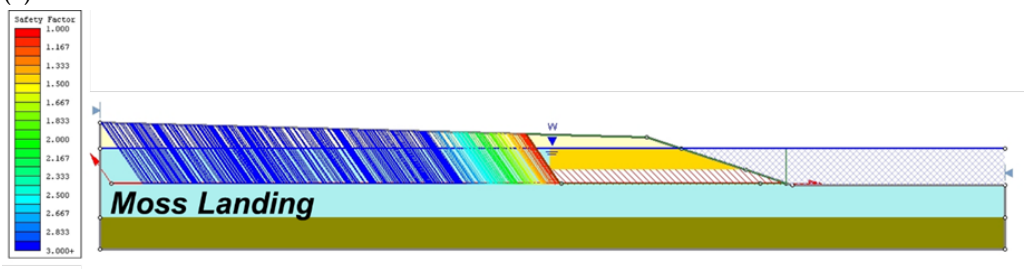

(b)

Figure 7.44: Distribution of failure surfaces and their associate pseudo-static factors of safety for a given series of pseudo-static SLIDE analyses, with varying horizontal seismic coefficient.

7.8.2 Determination of Representative Penetration Resistance

Wildlife Array

The characterization of *in situ* penetration data for the liquefied silty sand at the Wildlife site was based on the site investigation of Bennett et al. (1984), which consisted of four

CPT and two SPT borings at four locations spanning up to 70 m from the toe of the slope (see Figure 5.13). The CPT q_{c1} values for the liquefied silty sand were averaged by the author at 0.5 m depth intervals, and are plotted with respect to the distance from the toe of the slope (Figure 7.45), and exhibit relatively consistent median values across the four soundings. The median q_{c1} for the liquefied silty sand was about 7 MPa, with low and high recorded values of 0.8 MPa and 16.4 MPa, respectively.

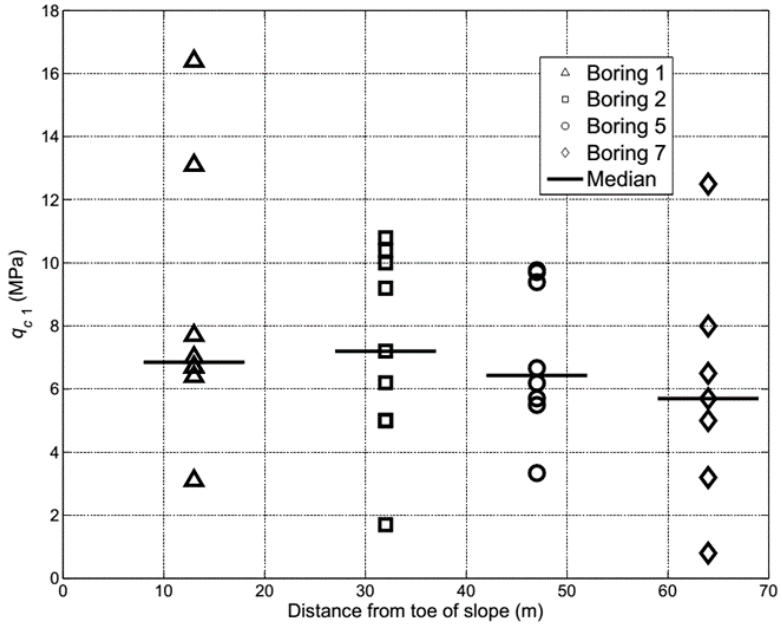

Figure 7.45: CPT q_{c1} data for the liquefied silty sand from four borings performed at the Wildlife liquefaction array

When plotted as a frequency histogram, the CPT data is seen to be slightly skewed about its median value. Coupled with the restriction of non-zero values of q_{c1}, the data qualitatively lends itself well to a number of potential distribution fits (Figure 7.46). The Rayleigh, Weibull, and Rician distributions were found to be superior fits to the initial lognormal distribution fit, and were identified as possible candidates in this case, and their goodness-of-fits were assessed with respect to the Kolmogorov-Smirnov test statistic (Table 7.18).

The results in Table 7.18 show that, for the 5% significance level, the K-S test result fails to reject the null hypothesis that the data belong to any of the test distributions. With the null hypothesis not rejected for any of known distributions, the Rician distribution was selected as the best fit on the basis of its minimum K-S test value of 0.114.

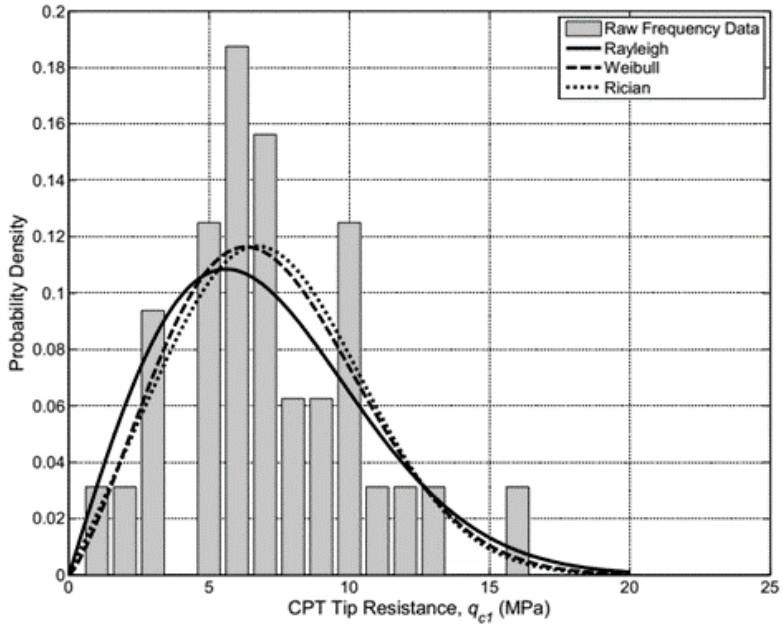

(a)

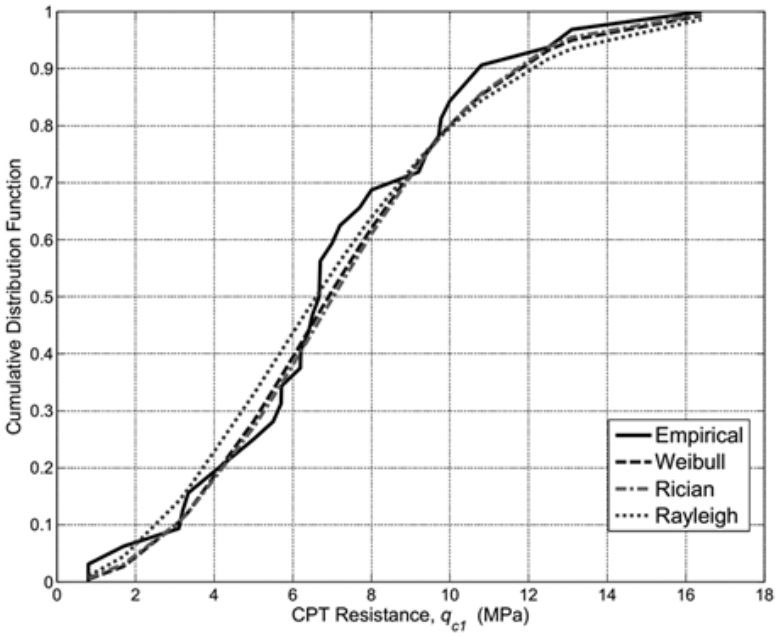

(b)

Figure 7.46: Weibull, Rician, and Rayleigh-fitted cumulative distribution functions, compared with the empirical cdf based on CPT resistance data at the Wildlife Site

Table 7.18: Results of Kolmogorov-Smirnov test on the distribution of CPT qc1 data, with significance level of 5%, for the three test distributions, for the Rayleigh, Rician, and Weibull test distributions

Distribution	Reject Null?	Significance Level (α)	p-value	KS Statistic	KS Critical Value
Rayleigh	No	0.05	0.265	0.172	0.234
Rician	No	0.05	0.754	0.114	0.234
Weibull	No	0.05	0.654	0.125	0.234

There was significantly less available SPT data for the Wildlife site; only seven values for $(N_1)_{60}$ were obtained from two borings for the liquefied silty sand, compared with 32 CPT qc1 values recorded in four soundings. The median $(N_1)_{60}$ was 4 blows per foot (Figure 7.47), with high and low values of 2 and 8 blows per foot, respectively. Due to the small sample size, the SPT data was assumed to have the same Rician distribution as the CPT data (Figure 7.48). It should be noted that these N-values may not be entirely consistent with the corresponding CPT values reported. If the correlation of Robertson et al. (1983) is used to convert the CPT data to SPT data, we would expect the SPT N-values to be on the order of 10-20, rather than 5-10. This may be due to significant inherent variability in SPT penetration resistances or uncertainty in hammer energy ratio.

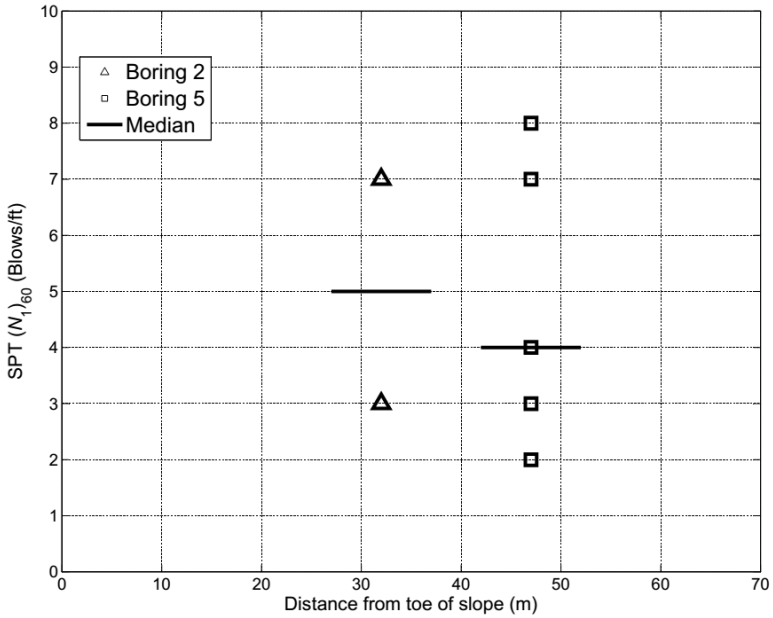

Figure 7.47: SPT $(N_1)_{60}$ data (after Bennett et al. 1984) from four borings performed at the Wildlife liquefaction array

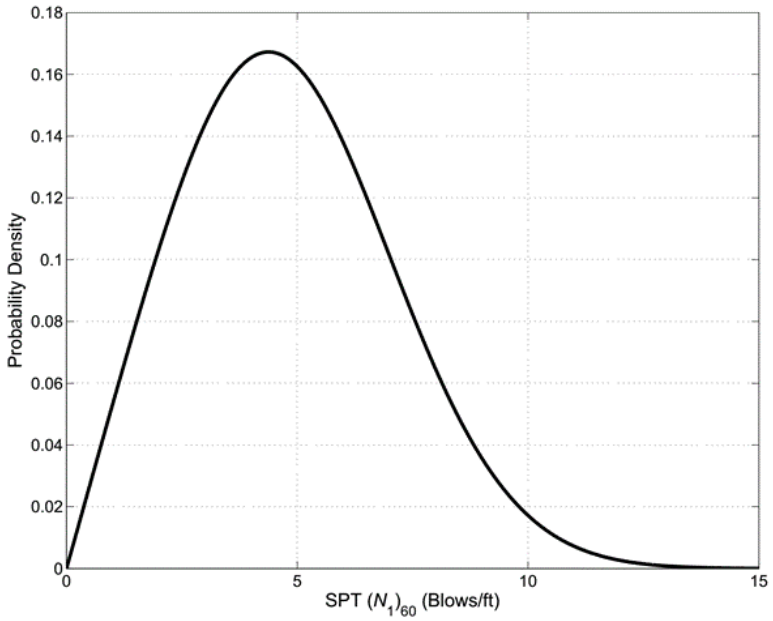

Figure 7.48: Rician distribution of representative SPT $(N_1)_{60}$ values at Wildlife Liquefaction array site

Moss Landing MBARI 3

The zone of liquefied material was less extensive (both vertically and horizontally) at the Moss Landing site than it was at Wildlife; as a result, there were far fewer SPT and CPT values from which to derive distributions (Table 7.19). Uncertainty parameters for q_{c1} and $(N_1)_{60}$ were therefore obtained from the more general (and not case-specific) literature. Phoon and Kulhawy (1999) reported that, for granular materials, the coefficient of variation (COV) for CPT tip resistance and SPT N-value measurements were about 38% and 54%, respectively.

Table 7.19: Penetration resistance values for the liquefied sand at the Moss Landing MBARI 3 site (Boulanger et al. 1997)

Type	Boring No.	Elevation (m)	Penetration Resistance (q_{c1} or $(N_1)_{60}$	C.o.V. (%)
CPT	RC-4	-2.75	14 MPa	38
CPT	RC-4	-3.25	10.5 MPa	38
SPT	EB-3	-3.25	20 bpf	54

These COV values were combined with the mean estimated values to produce initial

"theoretical" frequency histograms for the CPT and SPT data. In order to remove the probability of negative resistance values, and for the sake of consistency with the Wildlife site study, the Rician distribution was fit to both theoretical distributions (Figure 7.49).

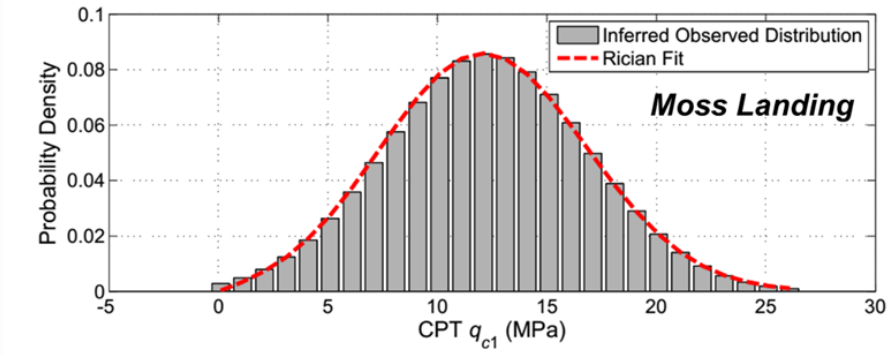

(a)

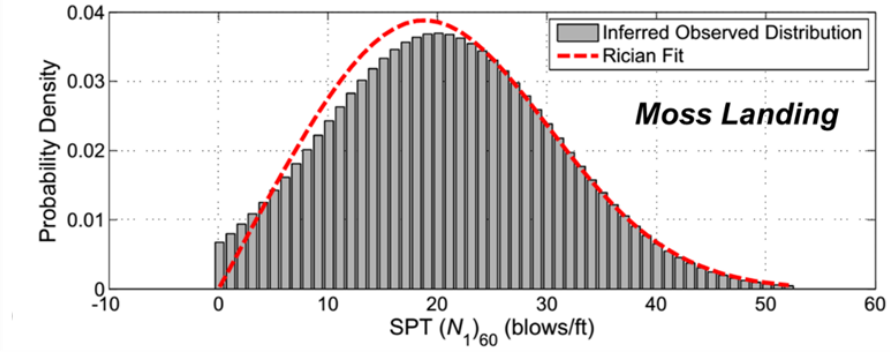

(b)

Figure 7.49: Theoretical distributions (a) CPT q_{c1} and (b) SPT $(N_1)_{60}$ and their fitted Rician distributions for the Moss Landing case history.

7.8.3 Characterization of Normalized Strength Ratio

To obtain statistical inputs for the friction angle of the liquefied material in the SLIDE pseudostatic analyses, mean and uncertainty estimates of normalized strength ratio (*NSR*) needed to be computed. The fitted distributions of q_{c1} and $(N_1)_{60}$ were applied to the linear relationship proposed by Olson and Stark (2002) between *NSR* and penetration resistance (see Equation 7.23. The equation be altered slightly to allow for a probabilistic characterization of *NSR* considering the centerline (i.e. the best-fit equation) as an expression for the mean value of *NSR*. Olson and Stark reported the standard deviation for *NSR* in their equation as 0.025 (upon which the 0.03 bounds are based), and the Olson and Stark relationship can be expressed as:

$$\mu_{NSR}(q_{c1}) = 0.03 + 0.0143(q_{c1}) \tag{7.26a}$$

$$\mu_{NSR}\big[(N_1)_{60}\big] = 0.03 + 0.0075(N_1)_{60} \tag{7.26b}$$

$$\sigma_{NSR} = 0.025 \tag{7.26c}$$

The symmetrical bounds indicated by Olson and Stark implies that they assumed the back-calculated *NSR* to distributed normally about the mean. This in turn implies that there is some non-zero probability of the strength being less than or equal to zero. The probability of exceedance for a given strength ratio nsr_i, given a particular resistance value (generalized here as r_j) can be expressed via:

$$P\big[NSR > nsr_i | r = rj\big] = 1 - \Phi\left(\frac{nsr_i - \mu_{nsr}(r_j)}{\sigma_{NSR}}\right) \tag{7.27}$$

where Φ is the standard normal cumulative distribution function. The expression in Equation 7.27 was evaluated for *NSR* values greater than zero. The probability of exceedance of nsr_i given r_j is then multiplied by the probability density of r_j , and subsequently summed for all r_j:

$$P\big[NSR > nsr_i\big] = \sum_{j=1}^{m} P\big[NSR > nsr_i | r = r_j\big] P\big[r = r_j\big] \tag{7.28}$$

These calculations were performed using the probability distributions in Figure 7.46, Figure 7.48 , and Figure 7.49; in combination with Equation 7.26 to obtain two PDFs for *NSR* for each case history, each respectively based on the CPT and SPT data. The two distributions were then combined using relative weights (w_{SPT} and w_{SPT}) between the two sources of data. For the Wildlife Array, weights of 0.9 and 0.1 were assigned to the CPT- and SPT-based distributions, respectively, to reflect the availability of over four times as many a_{c1} measurements as $(N_1)_{60}$ values, as well as the fact that the four CPT soundings represented twice the horizontal spatial extent as the two SPT borings. The CPT and SPT distributions were weighted equally for Moss Landing ($w_{SPT} = w_{CPT} = 0.5$). The final distributions of *NSR* were calculated via:

$$P\big[NSR > nsr_i\big] = w_{CPT} P_{CPT}\big[NSR > nsr_i\big] + w_{SPT} P_{SPT}\big[NSR > ns_i\big] \tag{7.29}$$

where P_{CPT} and P_{SPT} are the probability distributions based on CPT and SPT data,

respectively. The final distribution is shown, along with the two unweighted CPT- and SPT- based distributions, in Figure 7.50, and reflects the significantly stronger influence of the CPT data normalized strength ratio estimates.

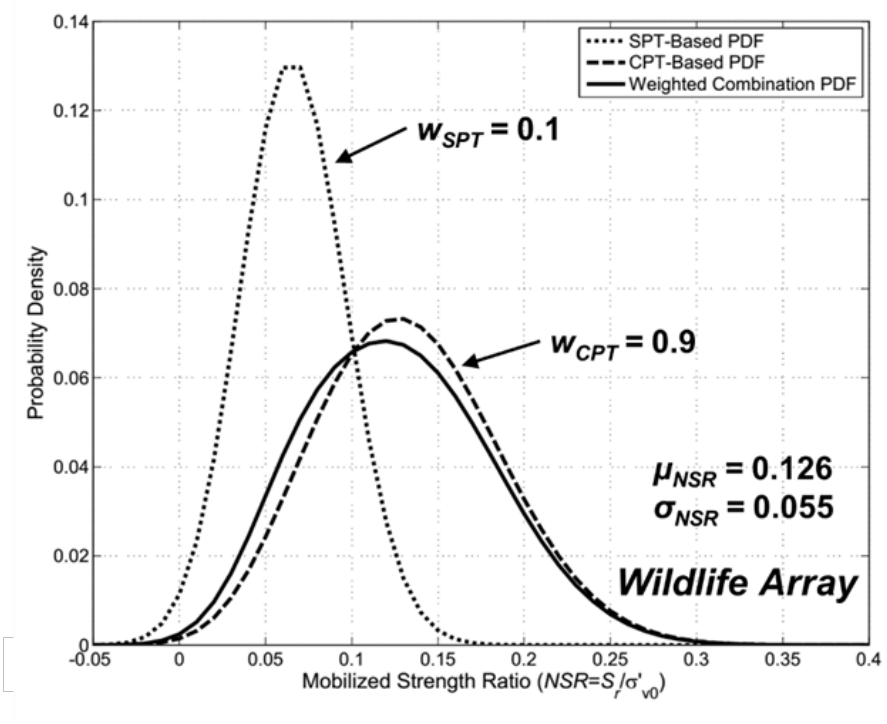

(a)

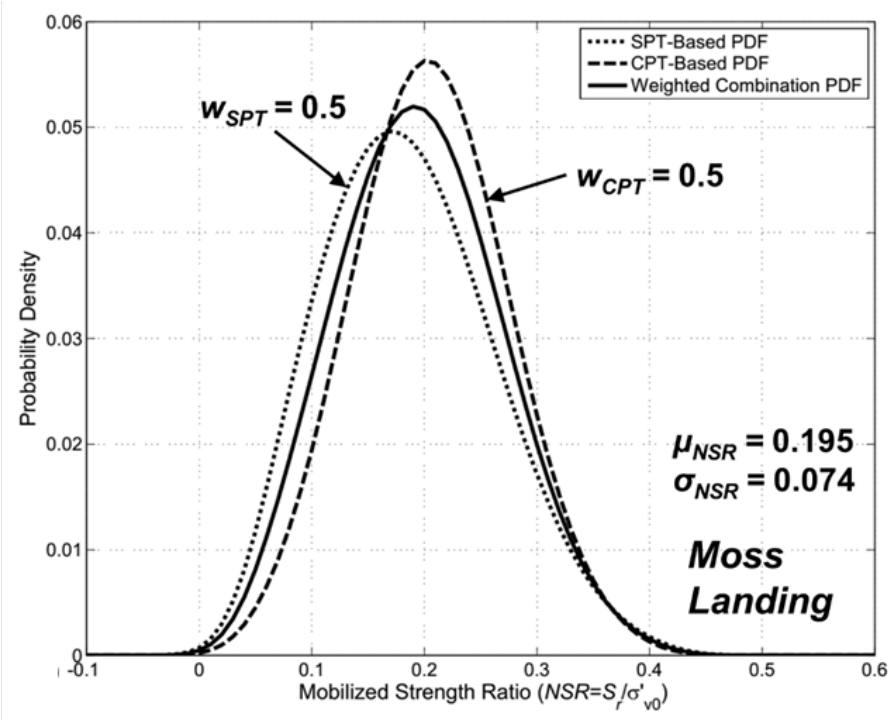

(b)

Figure 7.50: SPT-based, CPT-based, and combined weighted probability distributions for *NSR* for the liquefied material at (a) Wildlife Array and (b) Moss Landing Sites.

It should be noted that, due to the assumption of a normally distributed *NSR* implied by Olson and Stark's bounds, there exists a non-zero probability of negative *NSR* values for low penetration resistances. The statistical soil properties are implemented in SLIDE by specifying the mean, standard deviation, and relative minimum and maximum values (which are recommended to be three times the standard deviation). The issue of negative *NSR* was addressed directly in SLIDE by simply reducing the relative minimum so that minimum strength value was zero (negative values are rejected by SLIDE regardless), resulting in a truncated probability distribution, while the relative maximum remained three times the standard deviation.

7.8.4 Probabilistic Analysis of Yield Acceleration

With the soil parameters fully characterized and the failure surface search limits specified, the pseudostatic probabilistic analyses were performed in SLIDE using the Latin Hypercube Sampling method (LHS), with 1000 samples, for a series of applied horizontal seismic coefficients (a_i). The data from the set of analyses for the Wildlife site are presented as a histogram in Figure 7.51a, where the number cases where slope failure occurs (N_F), i.e. where the factor of safety is less than unity, is plotted over the total number of cases analyzed (N_{tot}) for each applied horizontal seismic coefficient. The probability of failure, P_F for a given horizontal acceleration can be determined via:

$$P_{F,i} = P\big[FS < 1 | a = a_i\big] = \frac{N_{F,i}}{N_{tot,i}} \tag{7.30}$$

Note from Figure 7.51a that the probability of failure for $a_i = 0$ (i.e. the static slope stability case) is relatively high at 16.3%, corresponding to 163 cases of flow failures (or static failures, in the context of SLIDE analyses). Since the focus of these analyses is pseudo-static stability within the context of lateral spreading (which is defined specifically by a *lack* of static failure), these static failure cases (denoted as N_{static}) were omitted from the dataset, and the values of N_F and N_{tot} were adjusted as follows:

$$P^*_{F,i} = \frac{N_{F,i} - N_{static}}{N_{tot,i} - N_{static}} \tag{7.31}$$

The adjusted data (Figure 7.51b) exhibits more reasonable behavior at the limits; the probability of failure is still 100% for very high horizontal accelerations, but is now more consistent with lateral spreading behavior in that the probability of failure is zero for the static case and very nearly zero for low values of a_i.

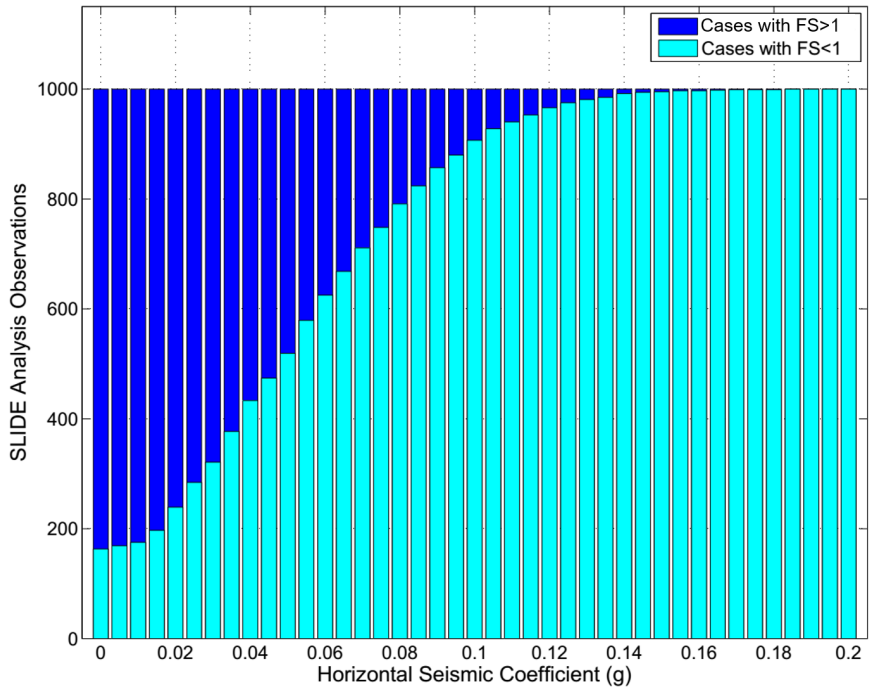

(a)

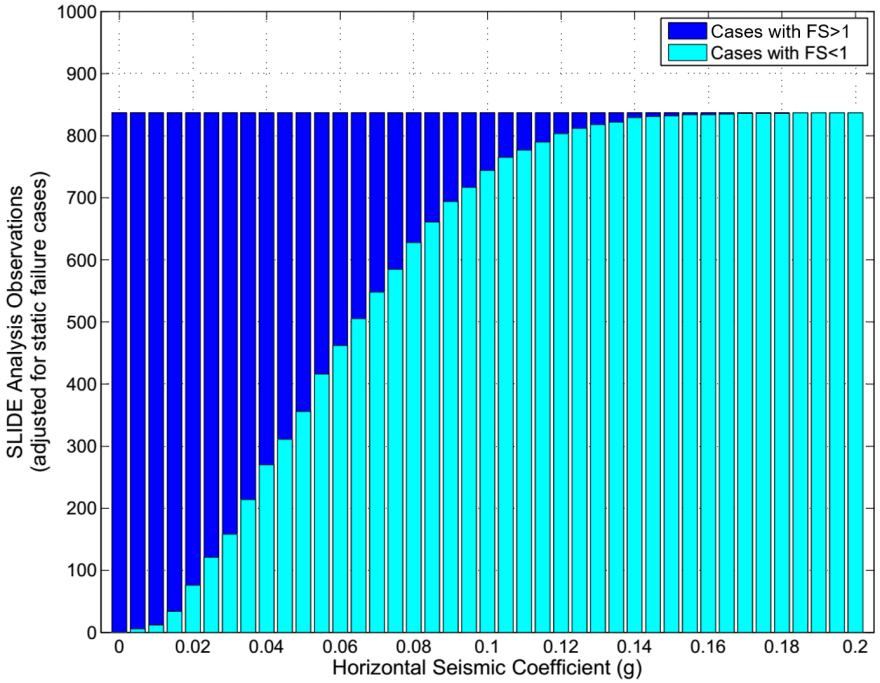

(b)

Figure 7.51: SLIDE output histograms showing (a) the number of failure observations over total observations, and (b) the same data, with cases of static failure removed; from a series of probabilistic pseudo-static SLIDE analyses with varying horizontal acceleration, for the Wildlife site.

Similar to the probabilistic back-analyses, the data obtained from the SLIDE analyses are of the binomial classification – that is, they consist of a set of "yes" and "no" observations (in this case, "failure" or "non-failure"), with a probability of failure that varies with respect to the predictor variable of interest (the horizontal acceleration, a_i). Initially, fitting of the data to a known distribution was attempted via binomial regression, using the logistic, probit, and complementary log-log link functions. The results (Figure 7.52) were clearly inadequate for all link functions. None of the fitted distributions captured the behavior of P_F for values of a_i below 0.02, and under-predicted P_F for large portions of a_i near the center of the distribution.

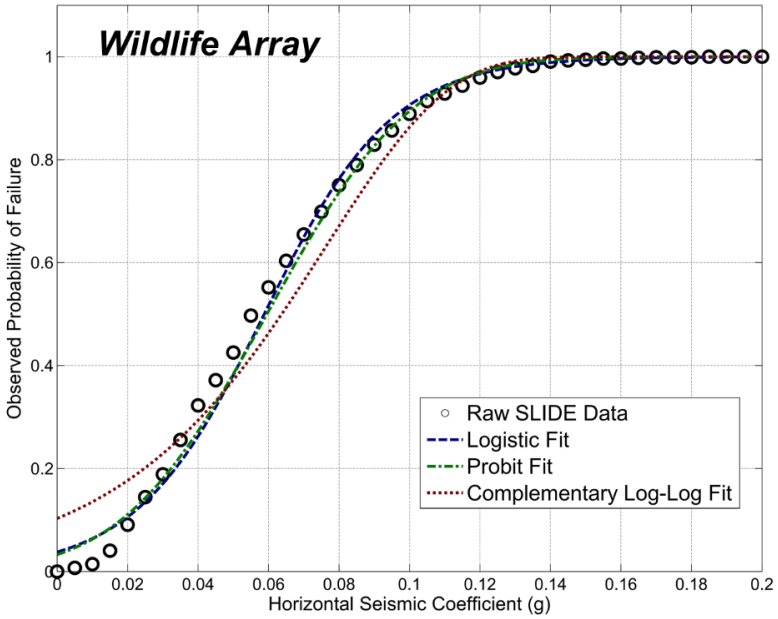

Figure 7.52: Observed probability of failure versus horizontal acceleration, plotted against binomial regression functions fitted with respect to a_i for the Wildlife Array site

A subsequent attempt was made to fit the data using a logarithmic transformation on a_i, with significant improvement in the results (Figure 7.53). The null hypothesis was not rejected for any of the three distributions, and the complementary log-log link function provided the best fit to the simulated data (Table 7.20).

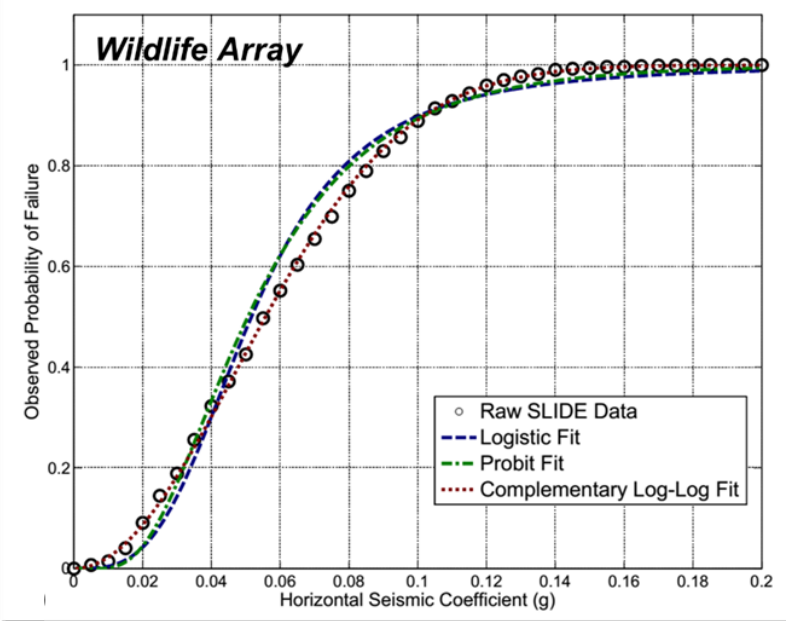

(a)

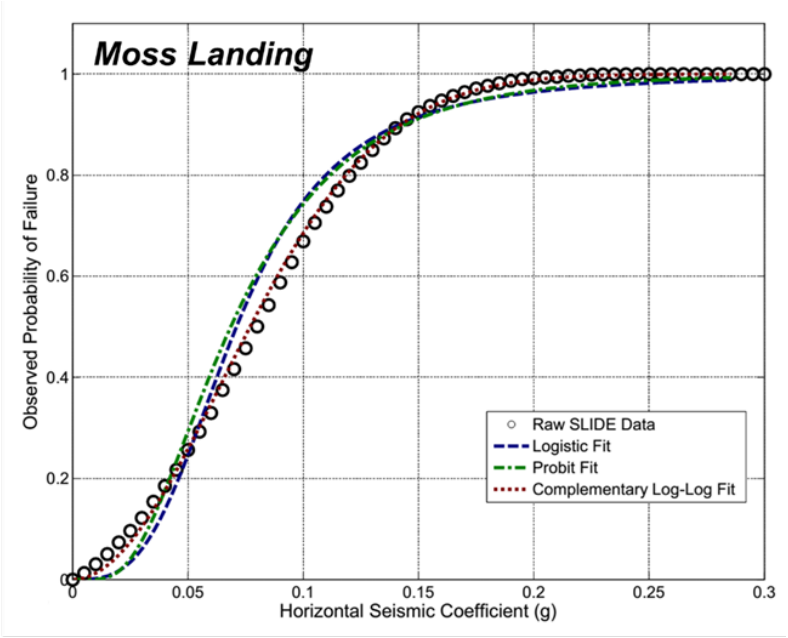

(b)

Figure 7.53: Observed probability of failure versus horizontal acceleration, plotted against binomial regression functions fitted with respect to the logarithm of a_i for the (a) Wildlife and (b) Moss Landing sites

Table 7.20: Kolmogorov-Smirnov test results for known distributions fit using binomial regression with respect to the logarithm of the predictor variable a_i for the Wildlife Array site

Distribution	Reject Null?	Significance Level (α)	KS Statistic	KS Critical Value
Logistic	No	0.05	0.0778	0.215
Probit	No	0.05	0.0732	0.215
Comp. Log-Log	No	0.05	0.021	0.215

It is easy to show that probability of pseudo-static failure given a horizontal acceleration a_i can be directly related to the probability of non-exceedance of the yield acceleration $a_{y,i}$ of the site. If, for example, the probability of pseudostatic failure is 60% for an applied acceleration of 0.06 g, this can be interpreted to mean that there is a 60% chance that the yield acceleration for the site is equal to or less than 0.06 g. The a_i–P_F curves in Figure 7.53 can therefore be considered as a cumulative distribution function (CDF) for a_y. The corresponding probability density function for the yield acceleration can then be obtained by differentiating the CDF with respect to a_i (Figure 7.54).

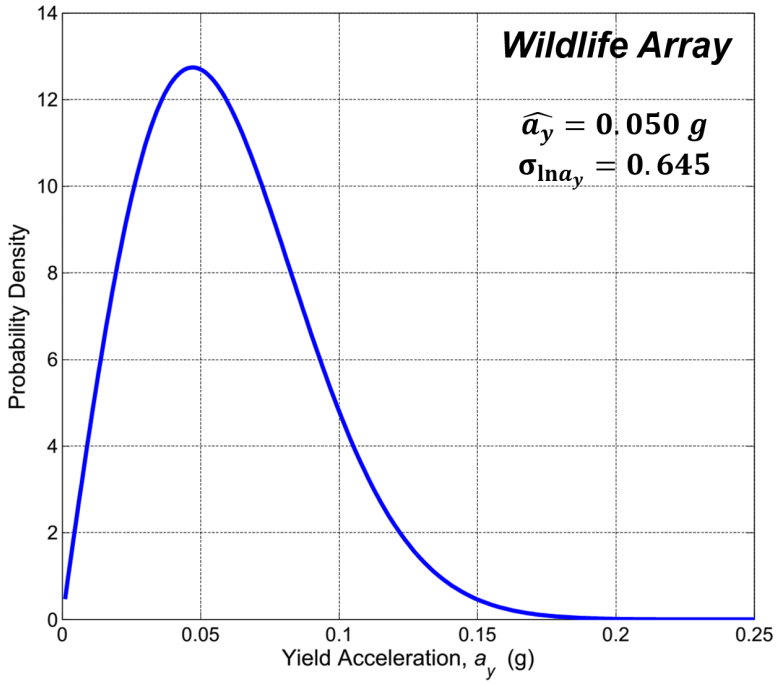

(a)

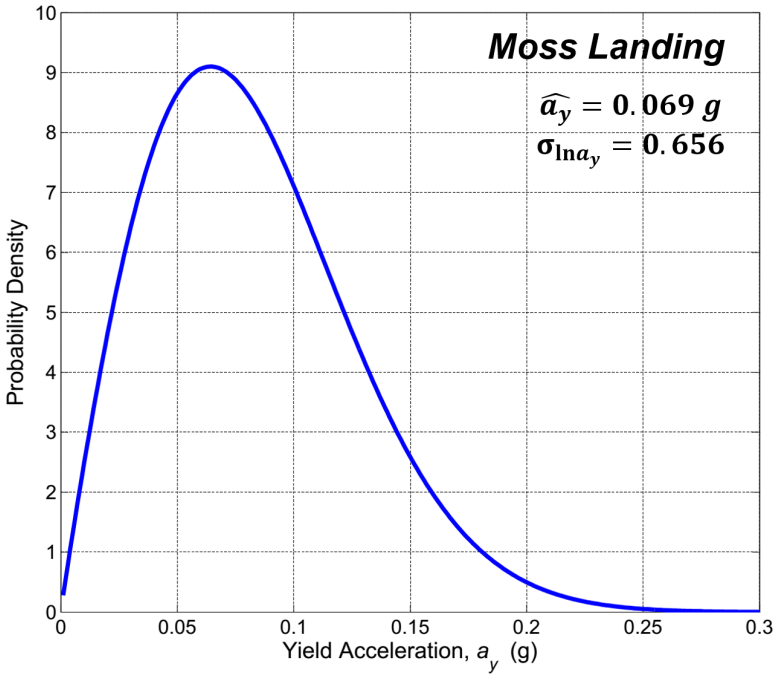

(b)

Figure 7.54: Probability density function for the yield acceleration at the Wildlife Site, obtained via binomial regression with respect to the logarithm of a_y for the (a) Wildlife and (b) Moss Landing sites

7.8.5 Probabilistic Analysis of Permanent Displacements

Once the yield acceleration for the site is characterized, a relationship between yield acceleration and permanent horizontal displacement can be obtained. This was achieved via a series of Newmark sliding block analyses, using the same ground motion selection framework employed in the back-analysis section. The resulting $D_H - a_y$ curves (Figure 7.56) were used to model the permanent displacement as a random variable related to the yield acceleration. The sliding block displacement was modeled as a mixed random variable (Bray and Travasarou 2007), where the probability of zero displacement is taken into account in addition to the probability distribution for nonzero displacements (Figure 7.55). The probability of zero displacement is first determined, and then subtracted from unity to adjust the area under the probability density function for nonzero displacements.

Generally speaking, permanent displacements less than or equal to 1 cm have little practical significance, and can be treated as negligible, zero-displacement cases (Bray and Travasarou, 2007); this minimum threshold displacement value is denoted as d_0. For the sliding block data, all displacements below d_0. were assumed to be equal to 1 cm. The probability of zero displacement was modeled a probit regression as a function of the logarithm of yield acceleration (Figure 7.57).

The permanent displacements for cases with nonzero displacement ($P\big[D_H > d_0 | a_y = a_i\big]$) were initially modeled using lognormal distributions, of the form:

$$P\big[D_H > d_i | a_y = a_{y,j}\big] = 1 - \Phi\left(\frac{\ln d_i - \mu_{\ln D}}{\sigma_{\ln D}}\right) \tag{7.32}$$

where $\mu_{\ln D}$ and $\sigma_{\ln D}$ are the mean and standard deviation, respectively, of the logarithm of the set of permanent displacements for a given yield acceleration. In order to account for the minimum displacement value of 1 cm, the lognormal distributions were then adjusted using truncated regression (Greene 2003, Bray and Travasarou 2007). A distribution can be truncated at a particular threshold value (in this case, d_0) simply by assigning zero probability density below the threshold value, and adjusting the scale of the nonzero probability density curve above the threshold value such that the total area under the curve remains unity (Figure 7.58). The truncated probability density can be expressed as:

$$P\big[D_H = d_i | D_H > d_0\big] = \begin{cases} 0, & d_i \le d_0 \\ \dfrac{P\big[D_H = d_i\big]}{1 - P\big[D_H = d_0\big]} \end{cases} \tag{7.33}$$

where $P[D_H > d_0]$ is determined from the probit model curves in Figure 7.53. The truncated distribution is useful for fitting to data where zero observations (or observations below a certain value) should be discarded (Greene 2003).

The total probability density function of permanent displacement, defined as a mixed random variable, is expressed as:

$$P[D_H = d_i] = P[D_H = d_0](\delta(d_i - d_0) + (1 - P[D_H = d_0])P[D_H = d_i | D_H > d_0] \quad (7.34)$$

where $\delta(d_i – d_0)$ is the Dirac delta function, which is equal to 1.0 for $d_i = d_0$ and equal to 0.0 for all other cases.

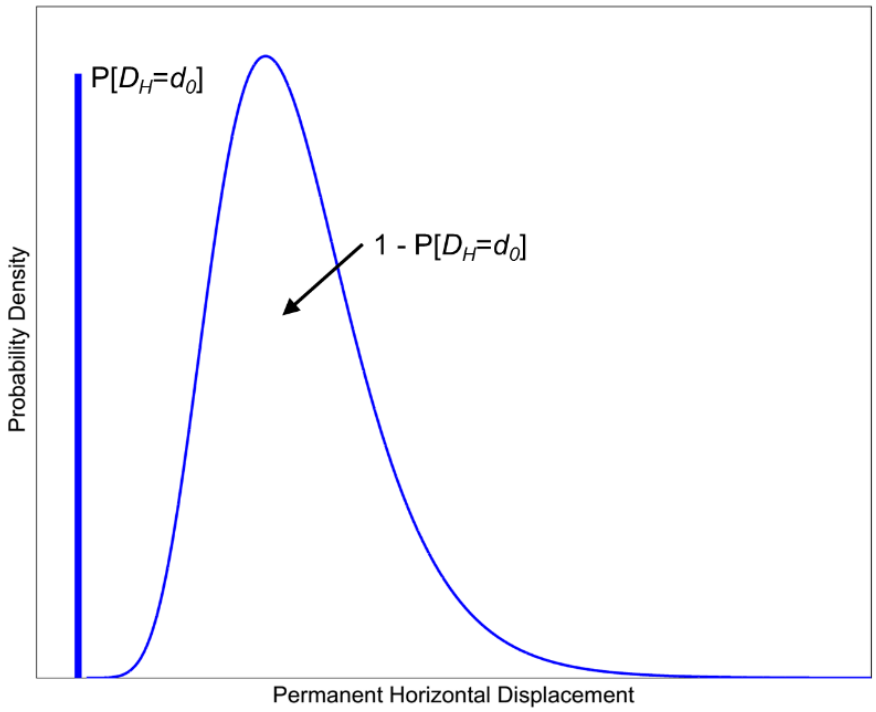

Figure 7.55: Probability density function for a mixed random variable (after Bray and Travasarou 2007)

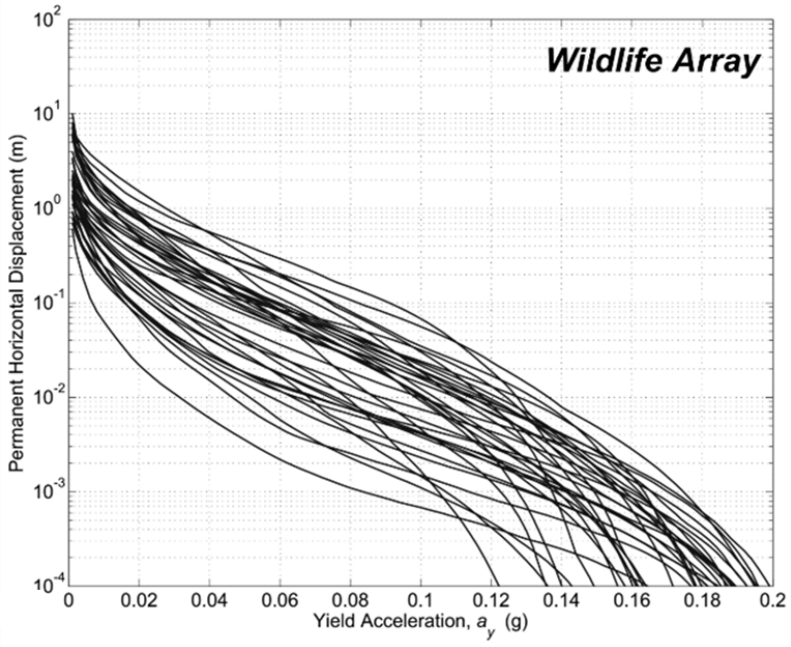

(a)

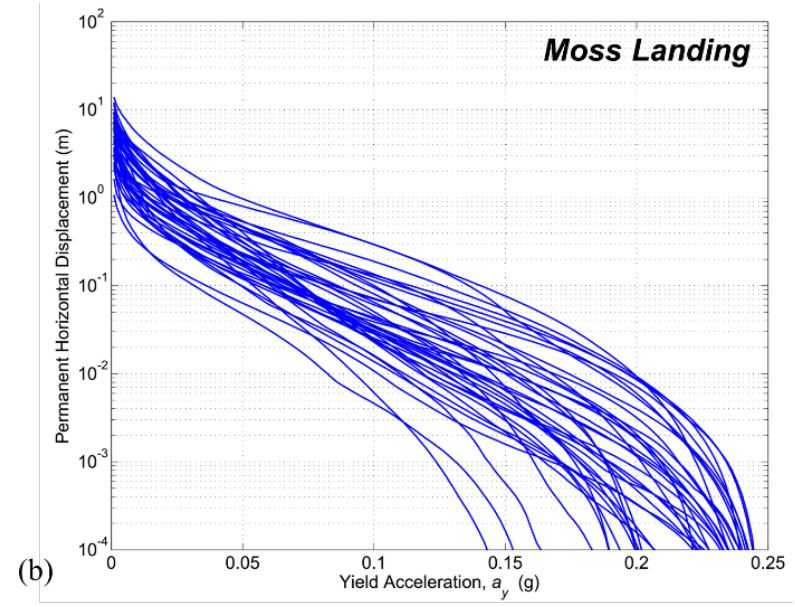

(b)

Figure 7.56: Relationship between permanent displacement and yield acceleration, obtained from Newmark sliding block analyses performed from 36 ground motion time histories for the (a) Wildlife Array and (b) Moss Landing sites

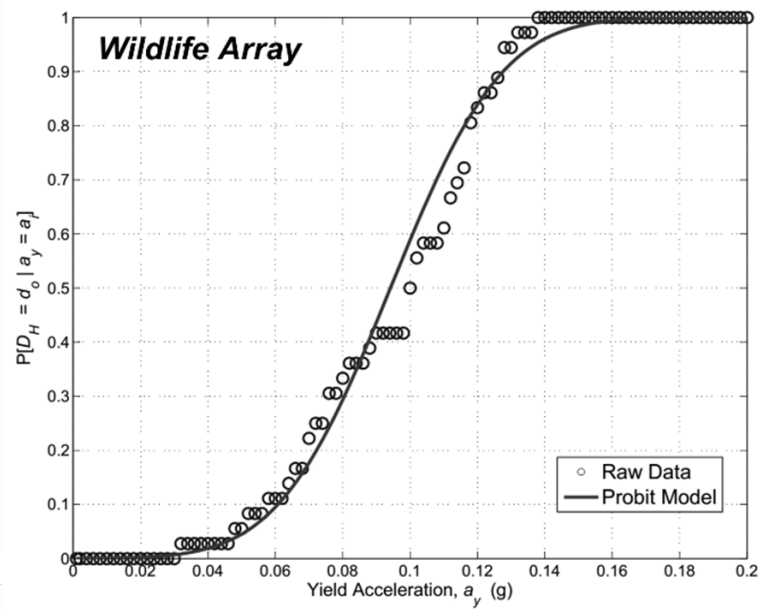

(a)

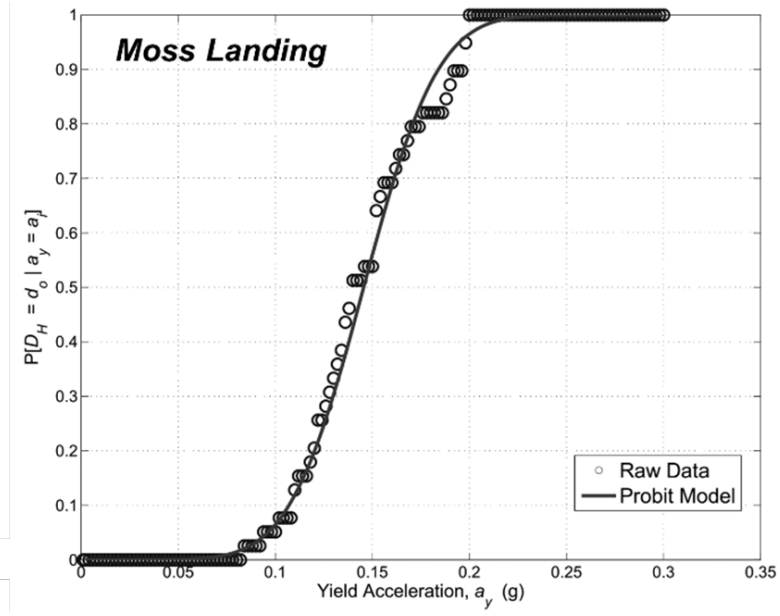

(b)

Figure 7.57: Comparison of predicted probability of zero displacement (using a log-transformed probit regression model) with simulated data from sliding block analyses, as a function of yield acceleration, for the (a) Wildlife and (b) Moss Landing sites

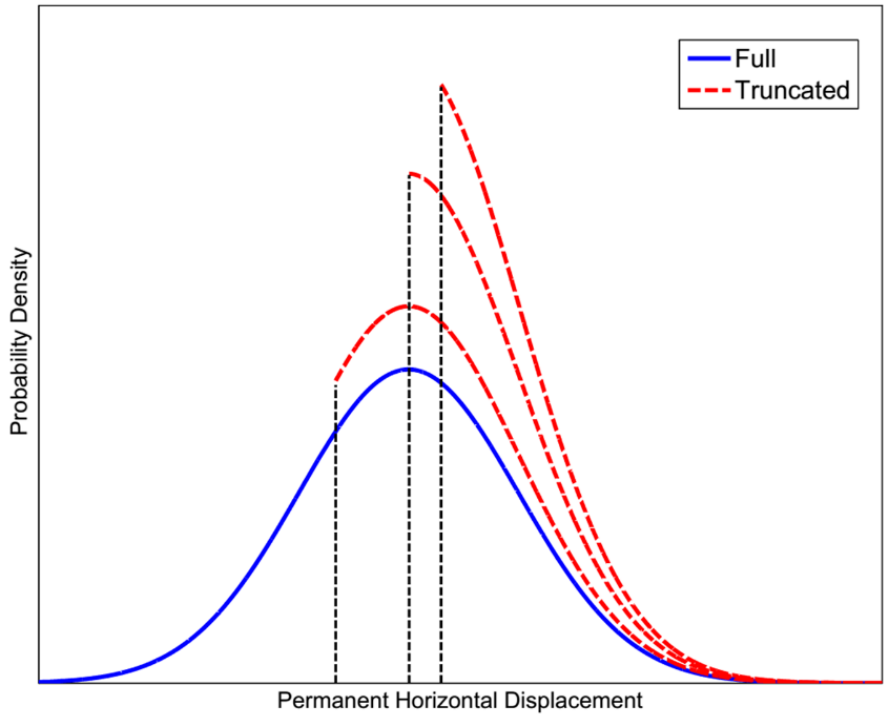

Figure 7.58: Probability density function of a normally distributed variable, truncated at various threshold values (after Greene 2003)

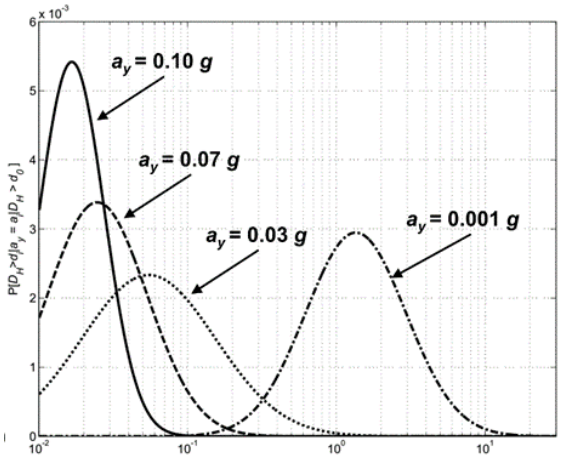

(a)

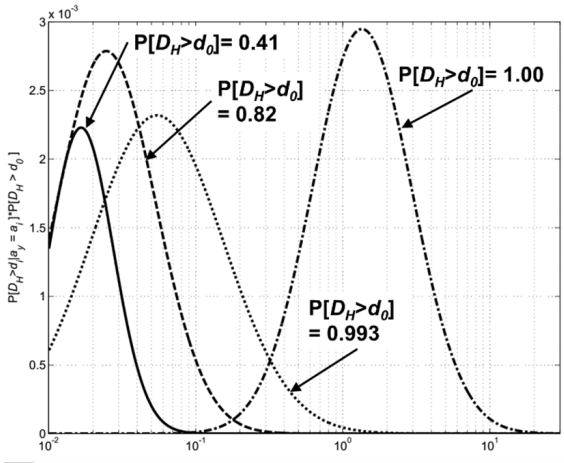

(b)

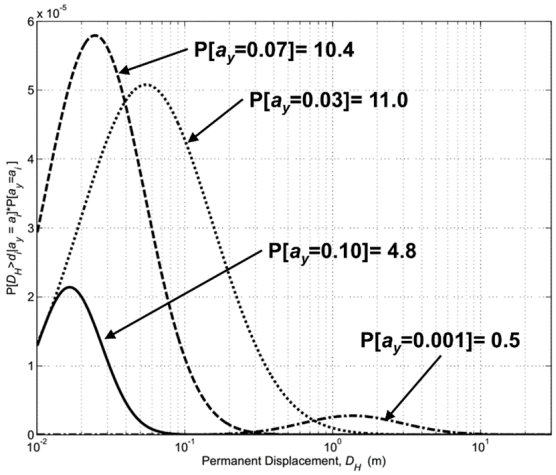

(c)

Figure 7.59: (a) Lognormal PDFs of sliding block displacements for various yield accelerations; (b) PDFs are multiplied by their respective probability of nonzero displacement; (c) PDFs from (b) are multiplied by the probability density of their respective yield accelerations

7.8.6 Results and Discussion

The full mixed-variable distribution for the displacements can be represented by cumulative distribution functions (Figure 7.60). These curves illustrate the discrete probability of "zero" displacements (e.g. displacements below 1 cm) as well as the calculated probability of non-exceedance curves, and allows visualization of specific percentile displacement values (such as the 25th, 50th, and 75th percentile values).

The probability distributions of permanent displacement for D_H greater than zero are shown in Figure 7.61 and Figure 7.62 for the Wildlife and Moss Landing sites. By applying Olson and Johnson's framework probabilistically, mean permanent horizontal displacements of 2.5 and 5.8 cm were predicted for Wildlife and Moss Landing, respectively; lognormal standard deviations ($\sigma_{\ln D}$) were 1.42 and 1.52. While the mean estimated displacements are relatively small, their standard deviations are extremely high. For the Wildlife site, the estimated displacements corresponding to one standard deviation from the mean range from negligible (less than 1 cm) to about 11 cm. For the Moss Landing case, the corresponding displacements range from about 1.5 cm to approximately 27 cm.

For comparison, probabilistic analyses of the lateral spreading displacements for these two sites were carried out using Youd's empirical model. Uncertainty in the equivalent thickness parameter T_{15} was characterized through a set of 1000 simulations. In each simulation the liquefiable stratum was divided into 0.1 m sublayers, and randomly assigned an SPT N-value from the probability distributions defined in Figures 7.48 and 7.49. T_{15} was then determined for that particular realization by summing up the sublayers with N less than 15. A normal probability distribution for $P[T_{15} = t_{15,i}]$ was fitted from the simulation results. The total probability of exceedance for the displacements using Youd's equation was then obtained by:

$$P[D > d_i] = \sum_{j=1}^{N} P[D > d_i | T_{15} = t_{15,j}] P[T_{15} = t_{15,j}] \tag{7.35}$$

where $P[D > d_i | T_{15} = t_{15,j}]$ is lognormally distributed, with the median obtained via Youd's equation and standard deviation $\sigma_{\ln D_H} = 0.464$.

For the Wildlife case, the standard deviation $\sigma_{\ln D_H}$ was about 0.465, indicating that the uncertainty in N-values added practically no variability to the overall estimation of D_H. This is not an unexpected result, as the probability of $N < 15$ for the Wildlife site was very small, resulting in a coefficient of variation of about 4% in the T_{15} parameter. The T_{15} parameter at the Moss Landing site had a C.o.V of about 14%, corresponding

to displacements predicted with a lognormal standard deviation of 0.470. These standard deviations obtained from Youd's empirical method are roughly one-third the standard deviations obtained using Olson and Johnson's model, the differences of which can be illustrated schematically in Figure 7.63.

The high levels of uncertainty seen in the O&J displacement predictions can be explained by examining the statistical uncertainties involved in estimating the intermediate parameters needed to calculate D_H (Table 7.21). It is clear that high coefficients of variation exist in all the estimated parameters, and it has been shown that these uncertainties propagate through the analysis procedure to ultimately contribute to the very wide range of predicted displacements seen in this section.

Table 7.21: Predicted median and uncertainty values of penetration resistances, normalized strength ratio, yield acceleration, and permanent lateral displacement using O&J method for estimating lateral spreading displacements probabilistically.

Wildlife Array			
Parameter	Median	Standard Deviation	C.o.V.
q_{c1} (MPa)	7.2	3.3	45.8%
$(N_1)_{60}$	4.8	2.3	47.9%
NSR	0.126	0.055	43.7%
a_y (g)	0.054	0.031	57.4%
D_H (m)	0.025	1.42	-

Moss Landing MBARI 3			
Parameter	Median	Standard Deviation	C.o.V.
q_{c1} (MPa)	12.3	4.6	37.4%
$(N_1)_{60}$	20.8	9.8	47.1%
NSR	0.195	0.074	37.9%
a_y (g)	0.082	0.044	53.7%
D_H (m)	0.058	1.52	-

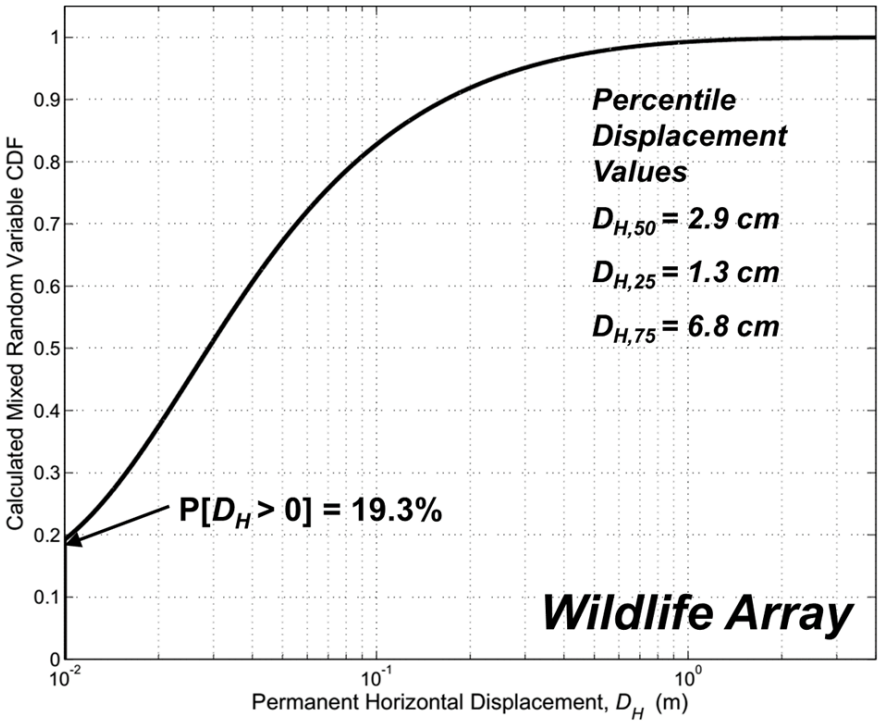

(a)

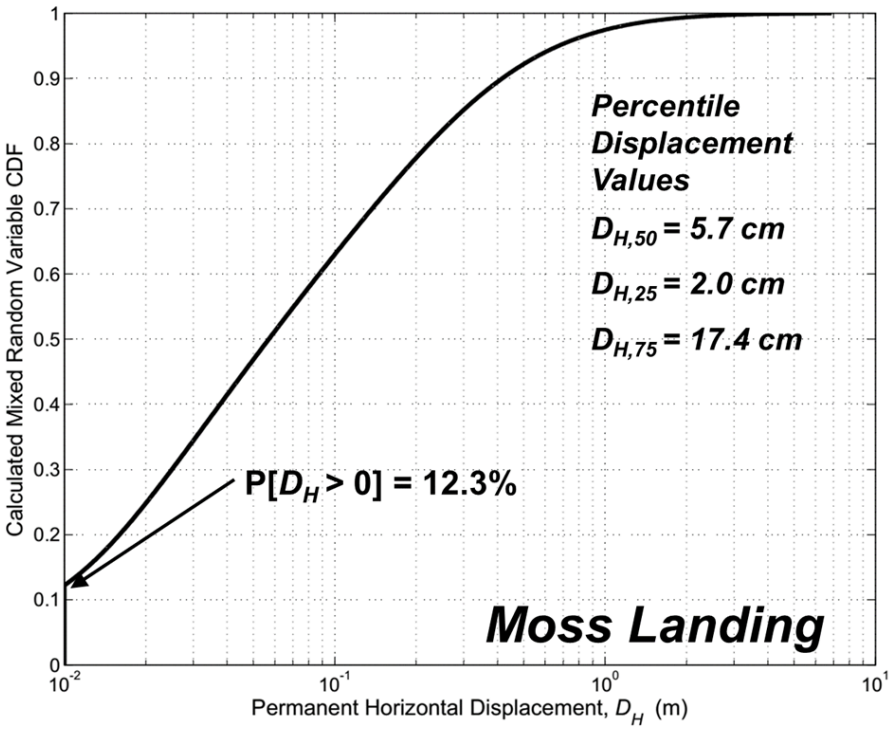

(b)

Figure 7.60: Cumulative distribution function of predicted permanent displacements at (a) Wildlife Array and (b) Moss Landing MBARI 3 sites, with D_H expressed as a mixed random variable

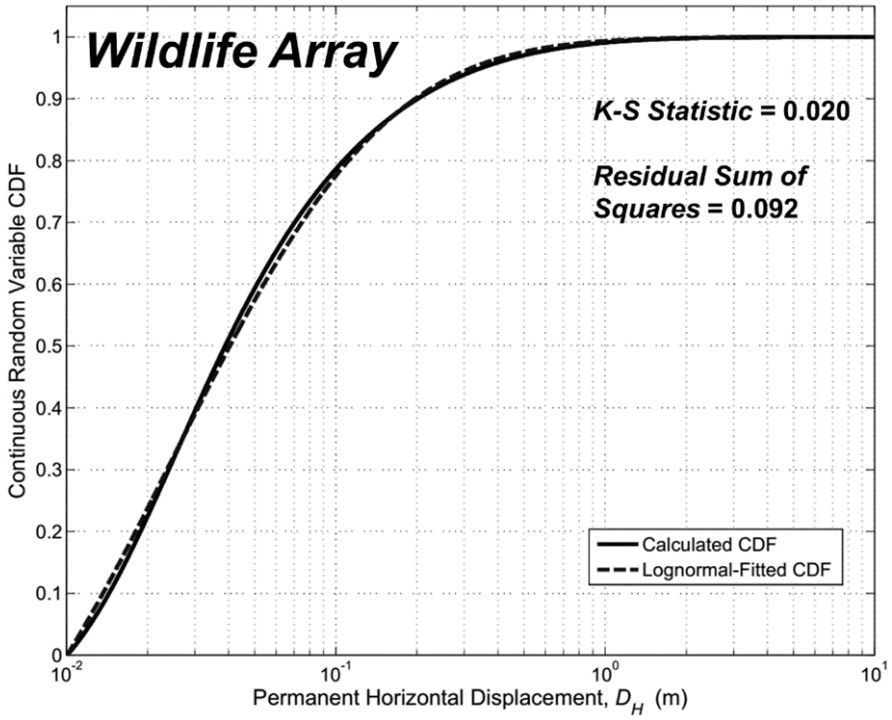

(a)

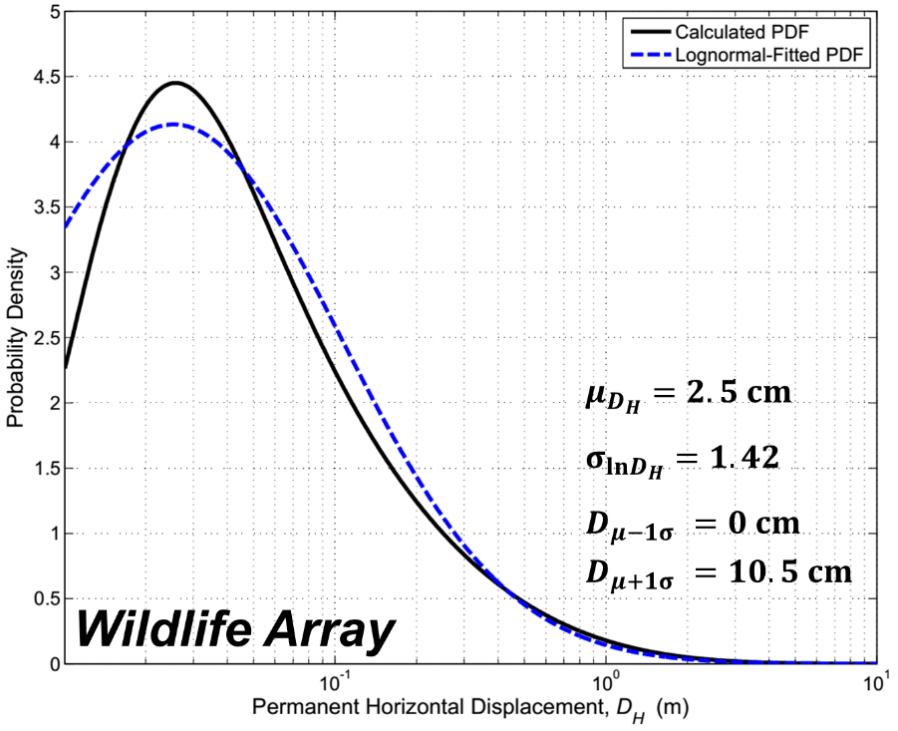

(b)

Figure 7.61: Calculated and fitted (a) cumulative distribution functions and (b) probability density functions of predicted permanent displacement, given D_H greater than zero, at the Wildlife Array site, with DH expressed as a continuous random variable

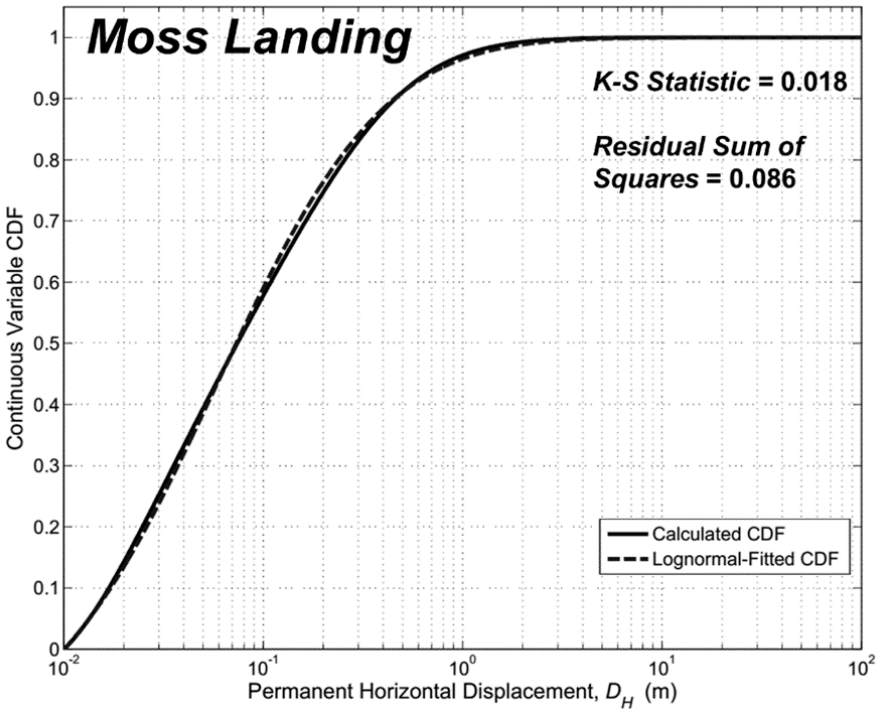

(a)

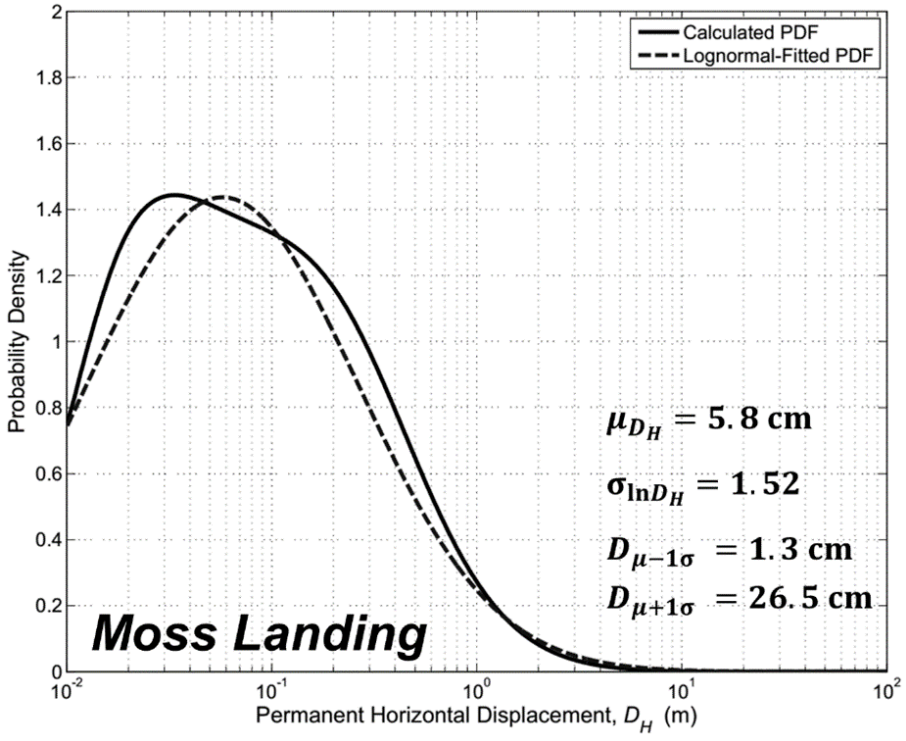

(b)

Figure 7.62: Calculated and fitted (a) cumulative distribution functions and (b) probability density functions of predicted permanent displacement, given D_H greater than zero, at the Moss Landing MBARI site, with D_H expressed as a continuous random variable

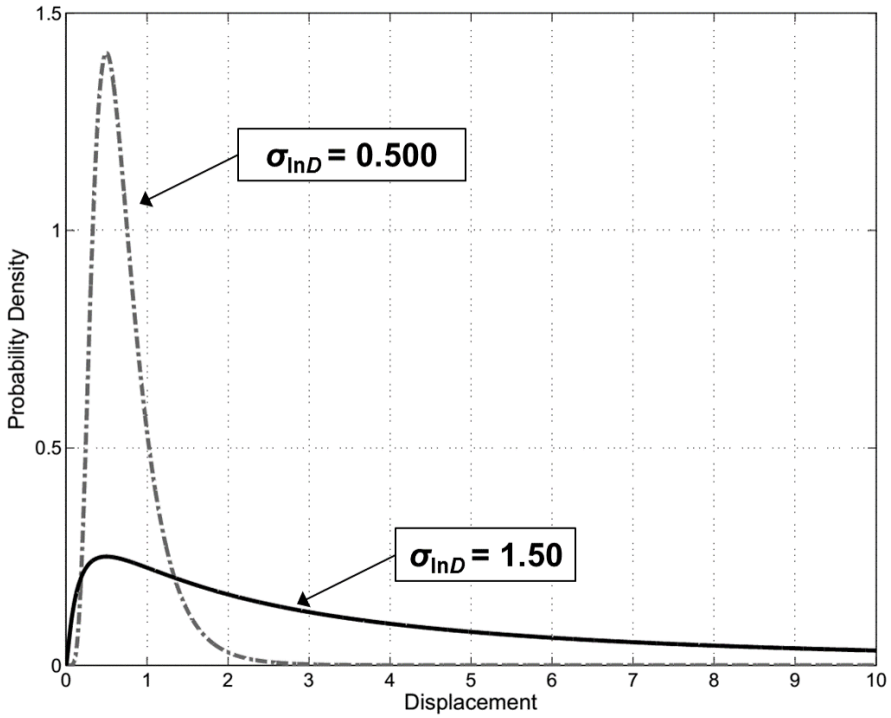

Figure 7.63: Comparison of two lognormal probability density functions for a given median displacement, with lognormal standard deviations of 0.464 and 1.5.

The initial determination of a representative penetration resistance can be hampered by several factors, the most fundamental of which is the fact that soil properties vary spatially, even within a relatively homogeneous layer of liquefiable sand. These variations are amplified through the use of SPT and CPT tests to characterize the initial relative density of the soil; as indicated earlier, SPT N-values carry a C.o.V. of over 50%, while CPT q measurements can vary by up to 40%. Furthermore, there remains no current consensus on what exactly defines the "representative" penetration resistance, with various researchers taking it to be a mean or median resistance value, while others have used values closer to the minimum (i.e. the "weakest link" approach [Wride et al. 1999]) as representative values (Kramer and Wang 2015). The probability distributions for q_{c1} and $(N_1)_{60}$ (see Figures 7.46, 7.48 7.49) reflect all of these uncertainties to a degree.

The determination of the normalized strength ratio using Olson and Stark's 2002 model and the estimated q_{c1} and $(N_1)_{60}$ distributions further introduces variability to the prediction procedure. This is largely due to the scatter in the data used by Olson and Stark to correlate *NSR* with penetration resistance for liquefaction flow failures, which resulted in a standard deviation of about 0.025. The C.o.V for the mean NSRs, which is an indicator for the variation added solely by using Olson and Stark's equation, is relatively low compared to the variation in the penetration resistances, at less than 20% for both cases (Table 7.22).

The pseudo-static analyses employed to estimate the yield acceleration a_y added further variability in the analysis procedure in the form of uncertainty in site characterization. This was comprised largely of uncertainty in the weight of the failure mass (i.e. the unit weight of the overlying material) and the location of the failure surface. Alternate SLIDE analyses performed with the mean deterministic *NSR*, rather than a distribution of *NSR*, produced C.o.V.'s in the range of about 5 to 20% (see Table 7.22). In other words, when removing the uncertainty obtained from the preceding analysis steps, the pseudo-static analyses introduce a similar level of uncertainty as Olson and Stark's equation, and a significantly lower level of uncertainty when compared to the determination of representative penetration resistance.

The final sources of uncertainty were the suites of ground motions used in the sliding block analyses to estimate the permanent displacements. It has been shown that O&J's selection method tends to produce more scatter in D_H estimates than the more restrictive NGA selection criteria (see Section 7.2). Similar to the previous steps in the analysis procedure, the sliding block results were analyzed for the mean estimated a_y; the resulting $\sigma_{\ln D}$ were 0.964 and 0.772 for Wildlife and Moss Landing, respectively (see Table 7.22). These are much lower, of course, than the standard deviations obtained for the full prob-

abilistic analyses, but still significantly above the standard deviation of 0.464 associated with Youd's empirical procedure.

Table 7.22: Predicted median and uncertainty values of penetration resistances, normalized strength ratio, yield acceleration, and permanent lateral displacement using O&J method for estimating lateral spreading displacements deterministically (using mean intermediate values)

Wildlife Array			
Parameter	Median	Standard Deviation	C.o.V.
q_{c1} (MPa)	7.2	3.3	45.8%
$(N_1)_{60}$	4.8	2.3	47.9%
NSR	0.126	0.025	19.8%
a_y (g)	0.035	0.006	17.1%
D_H (m)	0.14	0.964	-

Moss Landing MBARI 3			
Parameter	Median	Standard Deviation	C.o.V.
q_{c1} (MPa)	12.3	4.6	37.4%
$(N_1)_{60}$	20.8	9.8	47.1%
NSR	0.195	0.025	12.8%
a_y (g)	0.086	0.007	8.1%
D_H (m)	0.071	0.772	-

7.8.7 Conclusion

The intent of this section was to apply Olson and Johnson's procedure for estimating lateral spread displacements in a probabilistic fashion for two sites, and to characterize the level of precision that this procedure is capable of achieving. The forward-prediction procedure is made up of four distinct, sequential components, each introducing some level of uncertainty into the prediction of displacements. First is the characterization of the representative in situ penetration resistances, q_{c1} and $(N_1)_{60}$; which introduces variability in the form of spatial soil variations, uncertainty in measured SPT and CPT resistance values, and how "representative" is defined by researchers and practitioners. It has been

shown that these factors account for a significant portion of the uncertainty in the overall prediction of D_H. The second source of uncertainty comes from the application of Olson and Stark's 2002 relationship between penetration resistance and liquefied strength ratio for flow failures. Assuming that strength ratios mobilized in lateral spreading coincide with those seen in liquefaction flow failures, the use of Olson and Stark's model produces an added level of variation in the estimation of *NSR* related to the upper and lower bounds provided in their equation. Thirdly, it has been shown that the use of probabilistic pseudo-static analyses to estimate the yield acceleration involves some scatter related to the variability in the weight of the sliding mass and the position of the failure surface; the contributions from these factors to the overall prediction uncertainty, however, are relatively small. Finally, the use of sliding block analyses to obtain the final prediction of displacement sees a significant amount of uncertainty in the use of a suite of multiple ground motions to compute the relationship between a_Y and D_H, with a $\sigma_{\ln D}$ on the order of 0.75 to 1.00.

All of these factors suggest that while the forward prediction procedures may produce mean displacement estimates that appear to be reasonable, their extremely high standard deviations result in very wide range of plausible predicted values. For both of the analysis sites, displacement estimates, when considered in terms of plus or minus one standard deviation from the mean, ranged from nearly negligible to over 25 cm. In a practical sense, this type of scatter renders the mean estimate largely meaningless. Furthermore, there are very few ways the overall uncertainty can be reduced. While using a more restrictive ground motion selection method can reduce the deterministic $\sigma_{\ln D}$ from about 1.00 to about 0.600 (see Section 7.2), the bounds of Olson and Stark's equation are concrete, and, more critically, the selection of a representative penetration resistance remains a highly uncertain process.

It should be noted that the sites analyzed in this section were relatively well-constrained cases. There was a plethora of subsurface data for both the Wildlife and Moss Landing sites, their geometries were well-defined, and their failure surface terminals (and thus, the weight of the sliding mass) had consistent locations as defined by SLIDE (see Figure 7.44). Despite all of these factors, the final displacement predictions were about three times more uncertain than displacements that would be obtained from the Youd et al. (2002) empirical model. Based on the results obtained in this section, the method proposed by Olson and Johnson, from a purely probabilistic standpoint, does not appear to have strong precision in predicting lateral spreading displacements, and it should be recognized that a purely deterministic use of this procedure could result in significant under-prediction of the lateral spreading hazard.

7.9 Summary and Conclusions

The use of sliding block analyses in the characterization of lateral spreading displacements is an intriguing concept, due largely to its ability to mimic the ratcheting-like deformation often observed during ground shaking at lateral spreading sites, and to do so in a computationally efficient and simple manner. Beyond that, however, it has been shown that there are significant sources of structural biases and aleatory uncertainties in modeling lateral spreads within a Newmark-type framework, and that these factors have combined to largely obfuscate the results of the Olson and Johnson's 2008 back-analysis procedure, as well as the applicability of their proposed forward-prediction model.

The structural biases are a result of a number of different mechanisms. The first has to do largely with the manner in which the ground motions are applied to the sliding block. In particular, that the use of single-component or two-component average ground motion records tends to significantly under-predict displacements when compared to using the average motion of all directional components, particularly for sites in which observed displacements were very high. Olson and Johnson made no indication that their ground motions were rotated averages, and simply stated that they selected time histories based on their specific criteria, that were scaled to a particular PGA. If their input ground motions were indeed single-component time histories (or even two-component means), then the use of these time histories could have eventually resulted in significant under-prediction of the mobilized shear strength ratio for most of their lateral spreading sites. On the other hand, it was shown that O&J's restriction of sliding to the downslope direction likely resulted in a lower estimate of NSR than the more realistic case of two-directional sliding; however, this effect was only seen to be prominent in about six of the 39 case histories.

The other source of structural bias relates to simplification of the laterally spreading column of soil as a rigid block on a frictional, inclined plane. In reality, most sites underlain by low-stiffness materials do not move as rigid masses, and most lateral spreading sites do not experience deformation along just a single plane of failure. The effects of distributed deformations were significant for nearly all the cases analyzed by O&J, where rigid block estimates of displacements were seen to be as much as 60% lower than actual displacements, and on average about 40-50% lower for the 39 cases. There were additionally a handful of cases where the rigid mass assumption was deemed to be unconservative, with rigid block displacements on the order of 10 to 35% lower. The net result of these sources of bias and discrepancy is that the back-calculated yield accelerations, and by extension the back-calculated mobilized strength ratios, were likely much higher than those indicated by O&J in their analyses.

It is difficult, however, to say whether the bias in the back-calculated *NSR* due to the aforementioned factors, truly affects the conclusion proposed by Olson and Johnson that the lateral spread strength ratios are essentially coincident with flow liquefaction strength ratios, based on the bounds of Olson and Stark's 2002 equation. Due to the numerous sources of uncertainty– namely, their method for selecting ground motions, general record-to-record variability, and the complications involved in determining a representative penetration resistance – involved in the back-calculated procedure employed by O&J, any deterministic estimate of *NSR* are not very precise to begin with. These same factors also combine to render the use of O&J's forward prediction procedure largely ineffective within the context of lateral spreading, with standard deviations of permanent displacement significantly higher than those seen in Youd's empirical model.

The combination of all these factors allow for two relatively clear conclusions to emerge. One is that the Newmark sliding block method, which cannot capture mechanisms such as sliding mass compliance and distributed deformations, is a largely un-conservative simplification of lateral spreading. As a result, the mobilized strength ratios presented by Olson and Johnson are, in all likelihood, significantly lower than they would have been if these mechanism had been accounted for, even in some *post hoc* manner. The second is that there is far too much uncertainty in using sliding block analyses (as well as employing the concept of the "representative penetration resistance") to produce truly meaningful estimates of either the back-calculated *NSR* or forward-predicted displacement within a Newmark-type framework. Thus, the results of Olson and Johnson's 2008 work, while highly intriguing, should be used with extreme caution, with a proper acknowledgement of its potential un-conservatism as well as a thorough characterization of its high uncertainty.

Chapter 8

COMPARISON OF METHODS FOR PREDICTING LATERAL SPREADING DISPLACEMENTS

8.1 Introduction

Numerous models and methods have been proposed that can purportedly predict lateral spreading deformations. Most of these models were outlined in Section 4.3, and are based on various methodologies such as laboratory test data (Ishihara and Yoshimine 1992; Tokimatsu and Asaka 1998; Wu 2002), statistical regression of case histories (Youd et al. 2002; Kramer and Baska 2006), and sliding block analyses with consideration to a reduced yield acceleration (Olson and Johnson 2008). Thus far, little documented research has been performed to compare these procedures to one another across a wide range of site and source conditions. In this chapter three methods for evaluating lateral spreading are compared over a range of site conditions and earthquake source parameters: the empirical model developed by Youd et al. (2002), the Newmark-based method proposed by Olson and Johnson (2008), and dynamic analyses performed using the finite-element code FLIP.

These models were developed using three significantly contrasting frameworks; Youd's model is based on pure statistical regression of a large set of observed displacement vectors from 10 earthquakes (see Section 5.3). The Olson and Johnson (OJ08) model is based on the combination of two methods for evaluating inertial seismic slope stability (pseudostatic limit equilibrium and Newmark sliding block analyses), the Olson and Stark 2002 method for evaluating liquefied strength ratios, and a smaller database of lateral spreading case

histories. The FLIP analyses are largely based on the first principles and fundamentals of soil liquefaction; FLIP models the dynamic response of the soil continuum, the generation of excess pore pressure, and the associated loss of strength and shear strains of loose, saturated granular material. These vastly differing model frameworks may result in large differences in both the mean and variance of the predicted lateral spreading displacements for a given set of site conditions and source parameters, and it is therefore important to characterize how they differ with respect to both the accuracy and precision of their respective displacement predictions.

8.2 Analysis Framework

The range of conditions for which the comparative analyses were performed were based on varying site conditions and source parameters. The varying site parameters were defined as the ground slope angle of inclination, the thickness of the liquefiable material, and the strength of the liquefiable material (via the SPT N-value). The variable ground motion characteristics were defined in terms of source parameters, which varied according to moment magnitude and source-site distance. These parameters were applied to each of the analysis methods using the methodologies described in this section.

8.2.1 Site Parameter Characterization

36 idealized, infinite-slope soil profiles were defined and analyzed using each of the three methods. The profiles were a total of 11m thick with ground water at a depth of 2m, and consisted of a 2m-thick crust underlain by a layer of loose liquefiable fill, varying between 1 and 5m in thickness. The remainder of the soil profile consists of very dense sand, and a base of elastic bedrock (Figure 8.1). The ground slope inclination angle, thickness of the fill, and N-value of the fill were varied according to Table 8.1.

Table 8.1: Summary of variable soil profile parameters

Ground Slope Angle (degrees)	Thickness of Fill, T (m)	SPT N-value
0.5°, 1.5°, 3.5°	1.0 m, 3.0 m, 5.0 m	5, 10, 15, 20

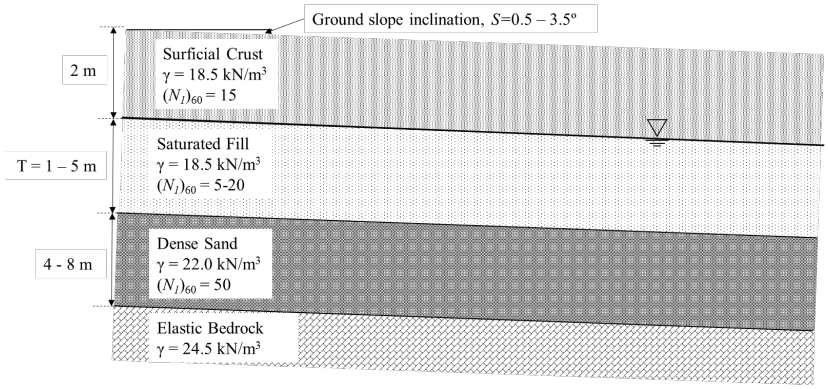

Figure 8.1: Idealized subsurface profile analyzed for lateral spreading displacements using FLIP, the Olson and Johnson (2008) method, and the Youd et al. (2002) empirical method (not to scale)

Implementation into Youd et al. (2002) model

A detailed discussion of the framework and implementation of the Youd model can be found in Section 4.3.2. The site parameters used in the equation are the slope angle (S), and the cumulative thickness (T_{15}), mean grain size ($D50_{15}$), and fines content (F_{15}) of the liquefiable material with N less than 15. For the profiles developed here, F_{15} was assumed to be zero (corresponding to a condition of clean sand), and $D50_{15}$ was assumed to be 1.75 mm (corresponding to a uniform, medium-grained sand). The variable site parameters were the slope angle S and the cumulative thickness parameter T_{15}. Note that the influence of the variable N-value (from 5 to 20) is reflected only as a step-function: in the 75% of soil profiles where the N-value is less than or equal to 15, displacements are expected to occur, and do not vary with respect to the N-value itself. In the remaining cases where $N = 20$, no displacements are expected to occur according to the model.

Implementation into Olson and Johnson (2008) model

The application of the OJ08 model first requires the liquefied shear strength ($s_u(liq)$) of the fill to be determined, which was estimated using the Olson and Stark (2002) relationship between $(N_1)_{60}$) and the normalized shear strength ratio $s_u(liq)/\sigma'_{v0}$ (see Equation 4.11 and Figure 4.18). Rather than estimating single mean values of the normalized strength ratio for each profile, normal probability distributions for $s_u(liq)/\sigma'_{v0}$ were obtained, using the mean relationship and the reported standard deviation of 0.025. Assuming zero cohesion, the corresponding distribution of an apparent friction angle was computed directly from the strength ratio via:

$$\tan \phi' = \frac{s_u(liq)}{\sigma'_{v0}} \tag{8.1}$$

The apparent friction angle in the liquefied fill was then used to calculate the static factor of safety for an infinite sloping condition and subsequently the horizontal yield acceleration, using the same framework outlined in Section 6.6.1 (specifically, Equations 6.16 through 6.21). For a given profile, the probability distribution of the yield acceleration was then used as the input for the sliding block analyses.

Implementation into FLIP Analyses

Creating a soil profile to analyze in FLIP requires the specification of a series of material parameters for each material type (or stratum). The parameters are:

- Model Type
- Indicator of liquefaction susceptibility (0 for non-liquefiable, 1 for liquefiable)
- Thickness of stratum (in meters)
- Number of subdivisions for each stratum
- Density (in kg/cm^3)
- Shear wave velocity (in m/s)
- Poisson's ratio
- Maximum damping parameter
- Clean-sand corrected SPT, $(N_1)_{60-cs}$
- Friction angle, ϕ

The soil profiles were divided into 1.0 m-thick sublayers. Fixed parameters were specified according to the summary in Table 8.2. The shear wave velocities were calculated using SPT-effective stress correlations for holocene sands proposed by Wair et al. (2012):

$$v_s = 27.0(N_{60})^{0.23}\sigma'^{0.25}_v \tag{8.2}$$

The friction angle was also estimated from the SPT N-value, using the SPT-overburden stress correlation of Kulhawy and Mayne (1990):

$$\tan\phi = \left[\frac{N_{60}}{(12.2 + 20.3\sigma'_v/p_A)}\right]^{0.34} \tag{8.3}$$

Table 8.2: Summary of material parameters for FLIP analyses

Material Type	Model	Liquefiable?	Density (kg/cm^3)	Poisson ratio	Maximum damping parameter
Crust	Cocktail	No	1.9	0.3	0.24
Fill	Cocktail	Yes	1.9	0.3	0.24
Dense Sand	Cocktail	No	2.25	0.3	0.24
Halfspace	Linear	No	2.5	0.3	N/A

Sensitivity FLIP Results to Input Parameters

As is the case with any numerical model, the relevant output (in this case, displacement) can be highly sensitive to how the input parameters are defined and interpreted. In the case of FLIP, defining the SPT N-value is critical, as the FLIP model is calibrated to this parameter in order to assess both the cyclic resistance of the fill and its post-liquefaction residual strength. Other important parameters to consider are the friction angle and the shear wave velocity. It is important to recognize that while using SPT N-values as the baseline by which ϕ and v_s are determined (see Equations 8.2 and 8.3), (a) these correlations contain a significant degree of variability, and (b) there are other possible ways a practitioner may define these parameters. Thus, a practical step to take before conducting a set of dynamic analyses is to vary the parameters about a particular "base case", and see how these small variations might affect the results.

The base case defined here is for a site sitting on a 1.5-degree slope inclination angle, underlain by a 1 m-thick layer of liquefiable fill with $N = 15$, $\phi = 38°$, and $v_s = 115$ m/s. The base profile, as well as the profiles with varying parameters (Table 8.3) were subjected to a suite of 20 ground motions from the $M_w = 7.5$ - $R = 50$ km bin.

Table 8.3: Parameter values used in sensitivity evaluation for FLIP analyses on a site with a 1.5-degree ground slope inclination angle underlain by a 1.0 m-thick stratum of liquefiable fill, subjected to ground motions from a magnitude-7.5 earthquake with a source 50 km from the site. Base case parameters are in bold

$T = 1.0$ m, $S = 1.5°$, $M_w = 7.5$, $R = 50$ m		
N (blows/ft)	ϕ (degree)	v_s (m/s)
10	34	100
12	35	105
14	36	110
15	37	**115**
16	**38**	120
18	39	125
20	40	130

The displacements are plotted with respect to each of the sensitivity parameters in Figures 8.2, 8.3, and 8.4. The base case analyses yielded a mean displacement of about 18 cm, and ranged between 12 and 29 cm. An interesting feature to note is that displacements tended to stabilize for values of N greater than 15. For values less than 15, displacements increased rapidly and dramatically. The effects of friction angle were somewhat similar, with displacements largely constant for ϕ greater than 35 degrees, and increasing dramatically as the friction angle dropped below that threshold value. Finally, we see that the displacements are largely insensitive to the initial stiffness of the liquefiable fill. For the values of v_s that were analyzed, displacements varied by only a few centimeters.

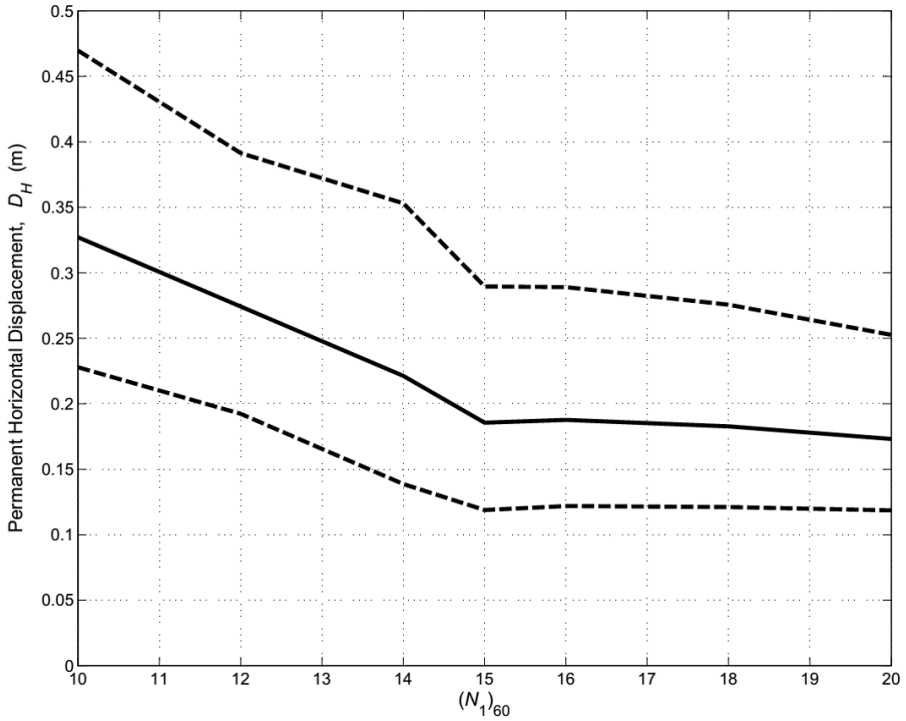

Figure 8.2: Sensitivity of median, 16th percentile, and 84th percentile computed displacements with respect to SPT N-value for FLIP analyses. Upper- and lower-bound displacements correspond to mean plus and minus one standard deviation, respectively.

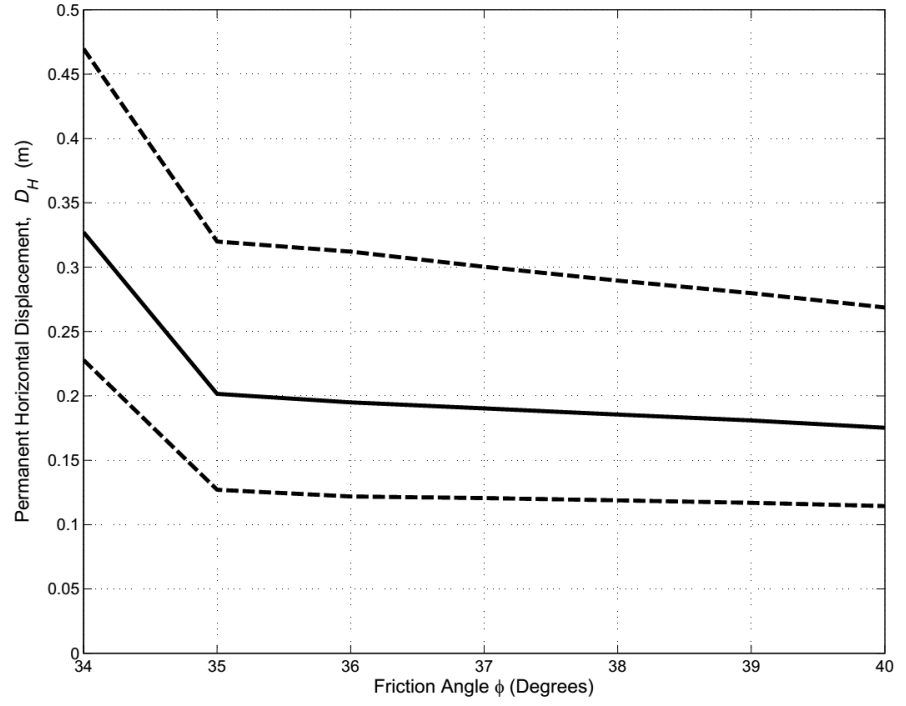

Figure 8.3: Sensitivity of median, 16th percentile, and 84th percentile computed displacements with respect to friction angle ϕ for FLIP analyses. Upper- and lower-bound displacements correspond to mean plus and minus one standard deviation, respectively.

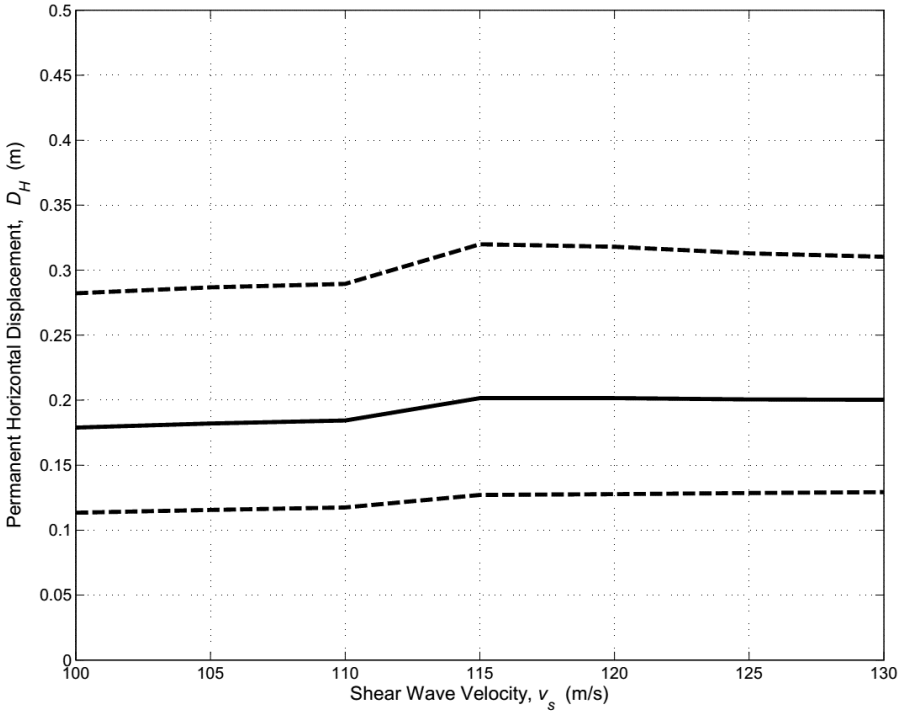

Figure 8.4: Sensitivity of median, 16th percentile, and 84th percentile computed displacements with respect to shear wave velocity v_s for FLIP analyses. Upper- and lower-bound displacements correspond to mean plus and minus one standard deviation, respectively.

8.2.2 Ground Motion Characterization

To generate ground motion inputs for the application of the FLIP and Newmark analyses, 35 suites of 20 ground motions each were obtained from the PEER NGA West-2 database, and scaled using the same spectrum-matching algorithm (minimizing the mean-square error) described in Section 6.2. The target spectra were similarly estimated for each suite using the same four GMPEs discussed in Section 6.2. The 35 suites were defined according to a series of pairs of moment magnitude and source-site distance (M-R), as shown in Table 8.4, for a site with shear wave velocity in the upper 30 m of 250 m/s.

The magnitude and source-site distance were the only two parameters that were varied in generating the target spectra. The rest of the GMPE-input parameters were assumed constant across all cases, the values of which are summarized in Table 8.5. To compute displacements using Youd's model, the M_w and R value pairs for each bin were simply used as inputs to the MLR equation.

Table 8.4: Moment magnitude and source-site distance bins used to estimate target spectra for the suite of ground motions for comparative FLIP dynamic analyses and Newmark sliding block analyses

R(km) / M_w	$M_w = 6.0$	$M_w = 6.5$	$M_w = 7.0$	$M_w = 7.5$	$M_w = 8.0$
$R = 10$ km	M1R1	M2R1	M3R1	M4R1	M5R1
$R = 20$ km	M1R2	M2R2	M3R2	M4R2	M5R2
$R = 30$ km	M1R3	M2R3	M3R3	M4R3	M5R3
$R = 40$ km	M1R4	M2R4	M3R4	M4R4	M5R4
$R = 50$ km	M1R5	M2R5	M3R5	M4R5	M5R5
$R = 70$ km	M1R6	M2R6	M3R6	M4R6	M5R6
$R = 100$ km	M1R7	M2R7	M3R7	M4R7	M5R7

Table 8.5: Constant input GMPE parameters used to estimate target spectra for the suite of ground motions for comparative FLIP dynamic analyses and Newmark sliding block analyses

Parameter	Value
Faulting Style	Strike-Slip
Shear Wave Velocity, v_{s30}	250 m/s
Dip Angle	90°
Rupture Depth	0 km (surface rupture)
Hypocentral Depth, Z_{hyp}	10.2 km
Depth to $v_s = 1.0$ km/s ($Z_{1.0}$)	0.48 km
Depth to $v_s = 2.5$ km/s ($Z_{2.5}$)	2.17 km
Rupture Width (W)	15 km

8.3 Analysis Results

To compute permanent displacement estimates using the FLIP and O&J methods for each of the 36 profiles, 20 accelerations were used as inputs from each of the 35 ground motion suites described previously. Thus, over 1260 combinations of soil profile and ground motion characteristics were analyzed using each of the three methods, with each case yielding data describing the probability of zero displacements, and the mean and variance of the predicted non-zero displacements. The probabilistic framework used to analyze

these results were slightly different for each method, and are described in detail herein.

8.3.1 Probabilistic Evaluation of Predicted Displacements

Due to the fact that numerous cases produced zero or negligible values, the displacement estimates for each method were characterized probabilistically as a mixed random variable (after Bray and Travasarou 2007), where the displacement is represented by the combination of a discrete probability of displacement below a certain minimum threshold value ($P[D \leq d_0]$, where d_0 was assumed to be 1 cm) and a continuous truncated probability distribution for the non-zero displacement ($P[D = d_i | D > d_0]$).

Analysis of Data from Olson & Johnson (2008) Method

Recall in Section 8.2.1 that the yield acceleration for each profile was in fact characterized in terms of a normal probability distribution, not as a single, deterministic value. Thus, for each combination of profile and $M - R$ pairing, the 20 sliding block analyses were run for a series of 40 a_y values, with each yield acceleration a_i having its own probability density. The discrete probability of zero displacement for a given yield acceleration ($P[D = d_0 | a_y = a_i]$), as well as the probability distribution of non-zero displacements ($P[D = d_i | a_y = a_i]$), were combined with the probability distribution of the yield acceleration ($P[a_y = a_i]$) using the exact same joint probability distribution formulation derived in Section 7.8.5.

Analysis of Data from FLIP Analyses

Processing of the FLIP data occurs in much the same way as the O&J data, however it is greatly simplified by the fact that there is no probability distribution for the yield acceleration to account for (because there is no yield acceleration to begin with). In other words, for each analysis case, $P[D = d_0]$ and $P[D = d_i | D > d_0]$ can be computed directly by fitting the displacement values obtained for the 20 acceleration records to a lognormal distribution, without any joint probability distribution computation.

Analysis of Data from the Youd et al. (2002) Method

The displacements obtained using Youd's method are even simpler to analyze. An initial cumulative distribution function $P[D > d_i]$ can be obtained via the lognormal mean and standard deviation for each case. $\mu_{\ln D}$ is simply the mean output of the empirical model

(for a given M, R, and site parameters) and $\sigma_{\ln D}$ is constant across all cases (0.464). $P[D = d_0]$ can be computed directly from this CDF, and the truncated probability distribution can be similarly derived from the estimates of $\mu_{\ln D}$ and $\sigma_{\ln D}$.

8.3.2 Results and Discussion: Representative Cases

16 of the 1260 analysis cases are presented in detail here, with the remaining results summarized in Appendix D. Note that due to an error in obtaining ground motions for the M_w=7.5-R=100 km case, the results are not included at this time. The 16 cases discussed here were for sites with a ground slope inclination angle of 1.5°, fill layer thicknesses of 1m or 5m, SPT N-values of 10 or 20, located 20 or 50 km from a magnitude-6.5 or -7.5 earthquake source (Table 8.6). Figures 8.5 through 8.8 show the continuous probability distribution of the *non-zero* displacement for each case, as well as summarize the probability of zero displacement, as predicted using each of the three methods. The accompanying Tables 8.7 through 8.10 also summarize the probabilities of zero displacement, and the means and standard deviations of the predicted displacements non-zero displacements for each case.

Probability of Zero Displacements

The predicted probabilities of zero displacements (or displacements less than 1cm), denoted here as P_{d_0}, differed considerably across the three methods for the representative cases. Using the dynamic analyses in FLIP, only two of the 16 cases featured non-zero P_{d_0} values, which occurred in the cases of the lowest intensity ground motions ($M_w = 6.5$ and $R = 50$ km), with N-values of 20. On the other hand, half the cases analyzed using Youd's method had 100% zero-displacement probabilities; this is not unexpected, since Youd's method assumes that no displacement occurs when N is greater than 15. For the other half of the cases (where $N = 10$), P_{d_0} was about 20% on average. Olson and Johnson's sliding block-based method yielded probabilities of negligible displacement of over 90%, on average, with only two cases where P_{d_0} was less than 80%.

Probability Distribution of Predicted Non-zero displacements

It is perhaps most informative to separate the cases where $N = 10$ and $N = 20$ in order to compare the means and standard deviations of their predicted displacements. For the eight cases where $N = 10$, the FLIP analyses yielded mean displacements of approximately 0.34 m on average, compared with just 0.0 7m and 0.03 m for the Youd and O&J models,

respectively. The lognormal standard deviations were similar on average between the FLIP and Youd models (0.500 and 0.464, respectively), and much higher in the O&J model (0.874, on average).

For the remaining eight cases in which $N = 20$, the FLIP analyses yielded predicted displacements that were about 12 cm on average, while the Youd and O&J models showed far more agreement, with median displacements of 0 and 1 cm, respectively.

Discussion

It is important to note several features about the Youd and O&J models that result in predicted displacements that do not vary with respect to certain factors, particularly site parameters that have been widely hypothesized and accepted to have an effect on lateral spreading displacements.

An extremely important component and point of discussion about the Youd model has been that it only accounts for the effects of initial relative density of the liquefiable material in a stepwise manner. It assumes that (a) liquefied soils with SPT N-values greater than 15 will result in practically *zero* deformations, and (b) for cases where N is indeed less than 15 bpf, that deformations are completely insensitive to the actual relative density of the liquefiable soil itself. The most conspicuous result of this is that the cases analyzed here for $N = 20$ predicted no displacements whatsoever. This sort of stepwise characteristic of the predicted displacements could be mitigated by instead characterizing the N-value as a probability distribution, from which a distribution of T_{15} can be obtained through some type of random assignment scheme (see Section 7.8.6). The other intriguing effect is that, for cases where all other parameters (ground slope, thickness, ground motion parameters, etc.) are held constant, the predicted displacements for sites with $N = 5$, 10, and 15 are *exactly the same*. As discussed in more detail in Section 4.3, there is a significant amount of theoretical, experimental, and empirical evidence that suggests that the degree to which shear strains manifest in liquefied soil depends fundamentally on its initial relative density.

The Olson and Johnson method, in its assumption of a single plane of failure, relies largely on evaluating the location of the minimum factor of safety for slope stability in order to calculate the corresponding yield acceleration. For the infinite slope conditions analyzed here, with a fully stress-dependent shear strength defined by ϕ' (see Equation 8.1 this inherently means that sites with different thicknesses of liquefied fill will have the exact same estimated yield accelerations (all other factors being equal). Thus, as it has been shown in the representative cases here, the displacements predicted using the O&J method are the same for both the 1m-thick cases and 5m-thick cases. This result

is generally inconsistent with both the theoretical principles governing lateral spreading (see Section 6.6), and what has generally been observed over a wide range of documented lateral spreading case histories in the field.

Table 8.6: Summary of site and ground motion parameters for 16 representative cases

Ground Slope Angle	Thickness (m)	N-value	Magnitude	Distance (km)
1.5°	1.0	10	6.5	20
1.5°	1.0	10	6.5	50
1.5°	1.0	10	7.5	20
1.5°	1.0	10	7.5	50
1.5°	1.0	20	6.5	20
1.5°	1.0	20	6.5	50
1.5°	1.0	20	7.5	20
1.5°	1.0	20	7.5	50
1.5°	5.0	10	6.5	20
1.5°	5.0	10	6.5	50
1.5°	5.0	10	7.5	20
1.5°	5.0	10	7.5	50
1.5°	5.0	20	6.5	20
1.5°	5.0	20	6.5	50
1.5°	5.0	20	7.5	20
1.5°	5.0	20	7.5	50

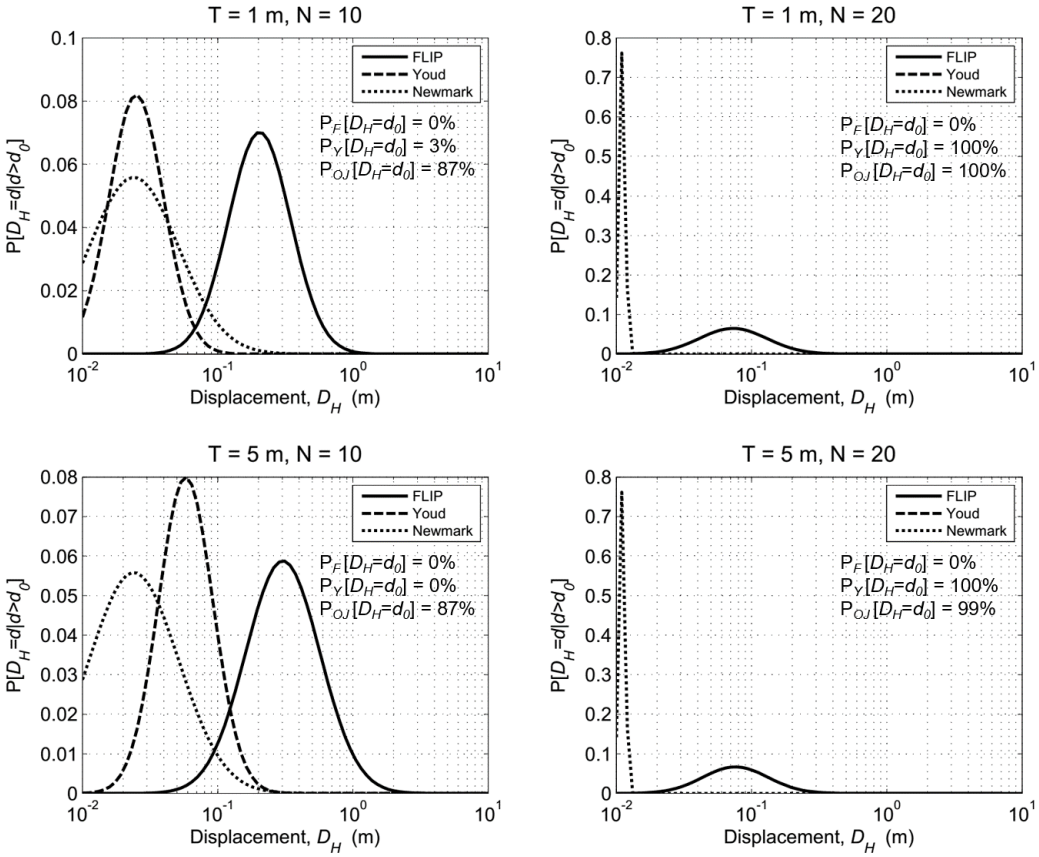

Figure 8.5: Predicted lateral spreading displacements, represented as mixed random variables, obtained using FLIP, Youd et al. (2002), and Olson & Johnson (2008) methods, for cases with $S = 1.5^{\circ}$, $M_w = 6.5$ and $R = 20$ km.

Table 8.7: Summary of analysis results, including probability of zero displacement, geometric mean, and lognormal standard deviations for selected soil profiles, obtained using FLIP, Youd et al. (2002), and Olson & Johnson (2008) methods, for $M_w = 6.5$ and $R = 20$ km.

T (m)	$(N_1)_{60}$	FLIP			Youd			OJ08		
		$P[D = d_0]$	μ_{D_H}	$\sigma_{\ln D_H}$	$P[D = d_0]$	μ_{D_H}	$\sigma_{\ln D_H}$	$P[D = d_0]$	μ_{D_H}	$\sigma_{\ln D_H}$
1	10	0	0.204	0.529	0.03	0.025	0.464	0.87	0.024	0.759
1	20	0	0.073	0.574	1.00	0	0	0.99	0.011	0.052
5	10	0	0.303	0.631	0	0.058	0.464	0.87	0.024	0.759
5	20	0	0.076	0.554	1.00	0	0	0.99	0.011	0.052

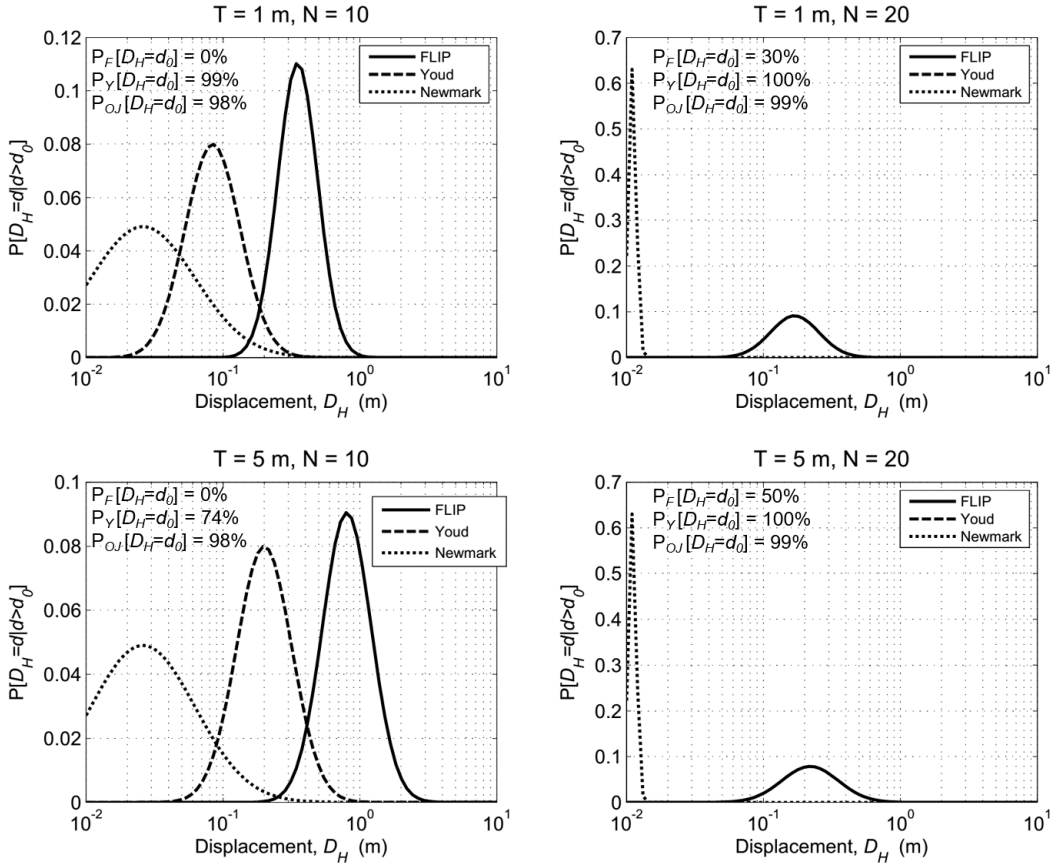

Figure 8.6: Predicted lateral spreading displacements, represented as mixed random variables, obtained using FLIP, Youd et al. (2002), and Olson & Johnson (2008) methods, for cases with $S = 1.5^{\circ}$, $M_w = 6.5$ and $R = 50$ km.

Table 8.8: Summary of analysis results, including probability of zero displacement, geometric mean, and lognormal standard deviations for selected soil profiles, obtained using FLIP, Youd et al. (2002), and Olson & Johnson (2008) methods, for $M_w = 6.5$ and $R = 50$ km.

T (m)	$(N_1)_{60}$	FLIP			Youd			OJ08		
		$P[D = d_0]$	μ_{D_H}	$\sigma_{\ln D_H}$	$P[D = d_0]$	μ_{D_H}	$\sigma_{\ln D_H}$	$P[D = d_0]$	μ_{D_H}	$\sigma_{\ln D_H}$
1	10	0	0.129	0.603	0.99	0.003	0.464	0.98	0.031	1.021
1	20	0.30	0.044	0.525	1.00	0	0	0.99	0.011	0.052
5	10	0	0.163	0.472	0.74	0.007	0.464	0.98	0.031	1.021
5	20	0.50	0.046	0.637	1.00	0	0	0.99	0.011	0.052

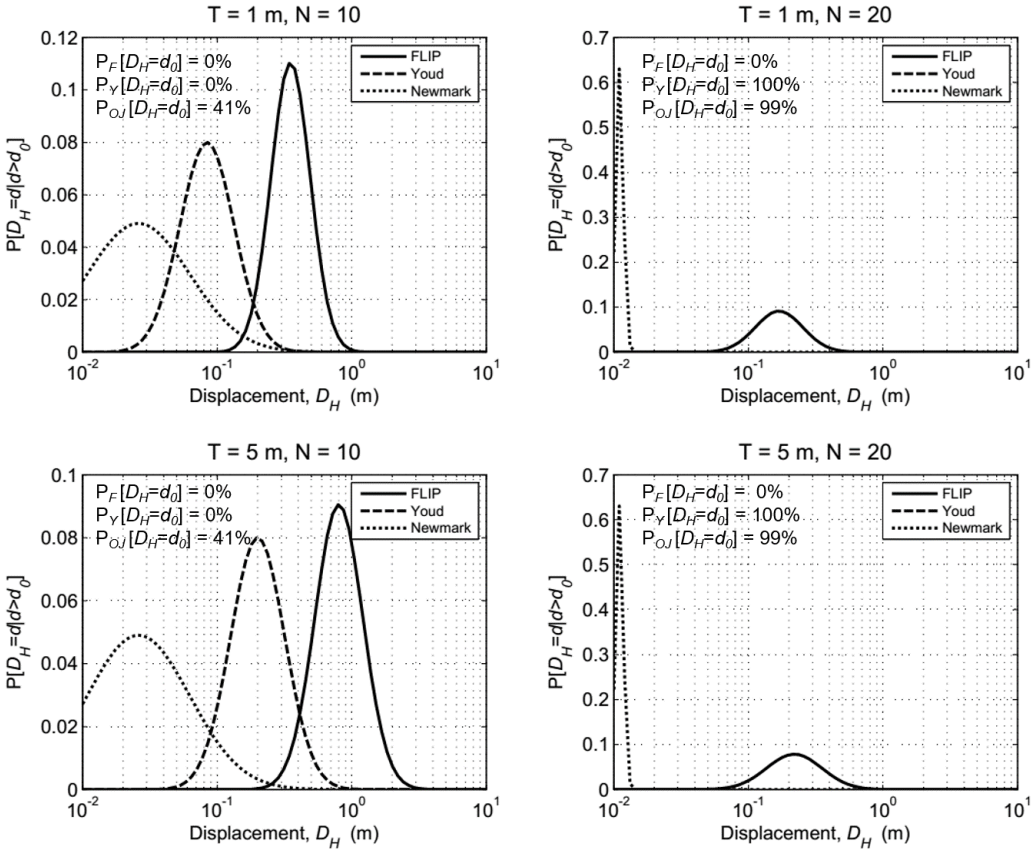

Figure 8.7: Predicted lateral spreading displacements, represented as mixed random variables, obtained using FLIP, Youd et al. (2002), and Olson & Johnson (2008) methods, for cases with $S = 1.5^{\circ}$, $M_w = 7.5$ and $R = 20$ km.

Table 8.9: Summary of analysis results, including probability of zero displacement, geometric mean, and lognormal standard deviations for selected soil profiles, obtained using FLIP, Youd et al. (2002), and Olson & Johnson (2008) methods, for $M_w = 7.5$ and $R = 20$ km.

T (m)	$(N_1)_{60}$	FLIP			Youd			OJ08		
		$P[D = d_0]$	μ_{D_H}	$\sigma_{\ln D_H}$	$P[D = d_0]$	μ_{D_H}	$\sigma_{\ln D_H}$	$P[D = d_0]$	μ_{D_H}	$\sigma_{\ln D_H}$
1	10	0	0.413	0.373	0	0.499	0.464	0.41	0.031	0.869
1	20	0	0.191	0.482	1.00	0	0	0.99	0.013	0.276
5	10	0	1.18	0.555	0	1.19	0.464	0.41	0.031	0.869
5	20	0	0.443	0.733	1.00	0	0	0.99	0.014	0.276

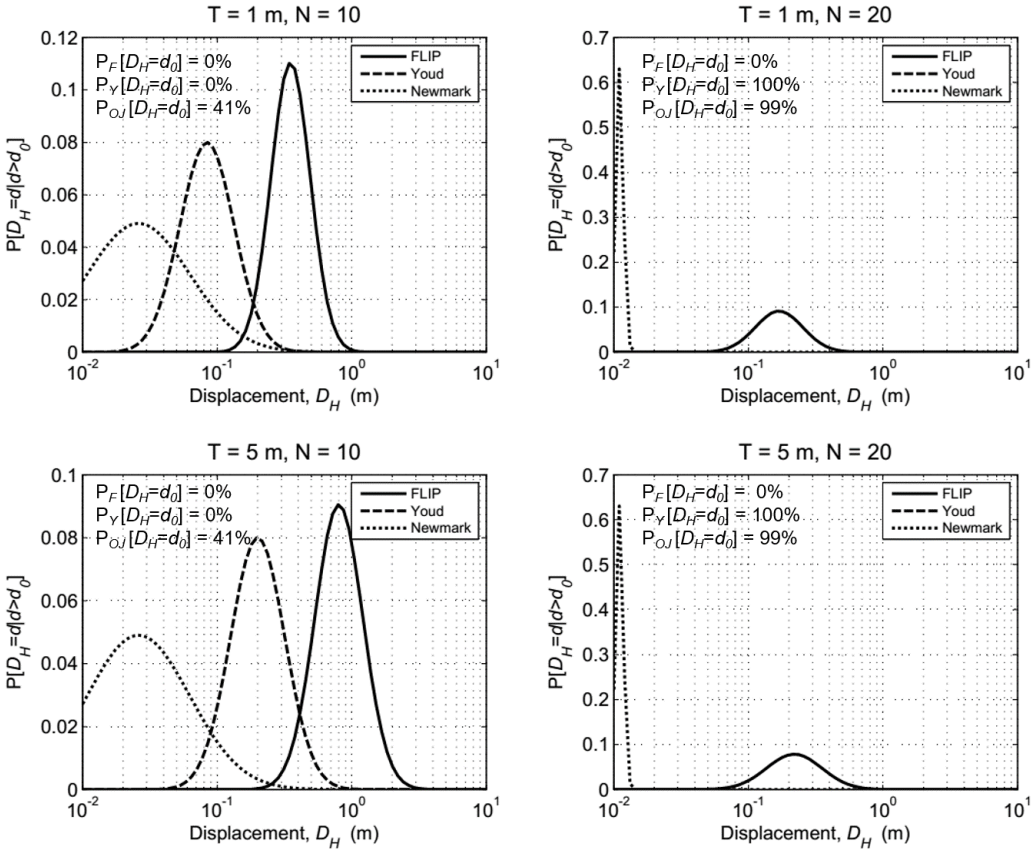

Figure 8.8: Predicted lateral spreading displacements, represented as mixed random variables, obtained using FLIP, Youd et al. (2002), and Olson & Johnson (2008) methods, for cases with $S = 1.5^{\circ}$, $M_w = 7.5$ and $R = 50$ km.

Table 8.10: Summary of analysis results, including probability of zero displacement, geometric mean, and lognormal standard deviations for selected soil profiles, obtained using FLIP, Youd et al. (2002), and Olson & Johnson (2008) methods, for $M_w = 7.5$ and $R = 50$ km.

T (m)	$(N_1)_{60}$	FLIP			Youd			OJ08		
		$P[D = d_0]$	μ_{D_H}	$\sigma_{\ln D_H}$	$P[D = d_0]$	μ_{D_H}	$\sigma_{\ln D_H}$	$P[D = d_0]$	μ_{D_H}	$\sigma_{\ln D_H}$
1	10	0	0.351	0.336	0	0.084	0.464	0.81	0.026	0.878
1	20	0	0.169	0.406	1.00	0	0	0.99	0.011	0.066
5	10	0	0.802	0.410	0	0.200	0.464	0.81	0.026	0.868
5	20	0	0.219	0.472	1.00	0	0	0.99	0.011	0.066

8.4 Summary and Conclusions

In this chapter, three different methods for analyzing lateral spreading were used to predict displacements for a wide range of site and ground motion conditions. The models

developed by Youd et al. (2002) and Olson and Johnson (2008) were based on significantly different frameworks, formulations, and assumptions; Youd's empirical model was based on multiple linear regression on a database of lateral spreading case histories, while the OJ08 model uses rigid block analyses to simplify the dynamic behavior of the laterally spreading mass. The simplifying assumptions that models such as these make - particularly with regard to factors such as dynamic site behavior, distribution of strains, dependence on initial density, and ground motion variability - certainly have the benefit of enhancing the speed and simplicity with which lateral spreading hazards can be characterized, but have the potential to do so at the expense of both accuracy (due to inherent bias) and precision.

When these methods were compared to a numerical model such as FLIP, it was clear that both the Youd and OJ08 models under-predicted the permanent displacements for a wide range of cases. More importantly, the Newmark-based method proposed by Olson and Johnson, simply put, does not seem to predict substantial displacements for very many realistic cases. Across the entire database, Newmark-based predictions were largely on the order of zero to 10 cm. By comparison, the Youd et al. method yielded displacement predictions between about 0 to 20 cm, and the FLIP analyses predicted displacements on the order of about 10 to 80 cm. Furthermore, when considering cases with large permanent displacements (greater than about 1 meter), about 11% of FLIP cases were greater than 1.0m, compared with about 6% for Youd's model, and less than 1% using the OJ08 model. Overall, the results seem to indicate that, while there may be a few conditions where the Olson and Johnson's model has the ability to predict accurate lateral spreading displacements (particularly for cases with thinner liquefiable layers), sliding block-based methods are largely unconservative over a broad range of lateral spreading conditions when compared to more advanced, computationally-intensive dynamic analyses.

Chapter 9

SUMMARY AND CONCLUSIONS

9.1 Introduction

The difficulties involved in characterizing lateral spreading-related hazards are well-known. The effects of various factors including the dynamic response of the system, post-liquefaction phenomena such as dilation pulses and void redistribution, and complex two-dimensional or three-dimensional topographic features, make lateral spreading extremely challenging to describe within a unified framework. Established approaches for dealing with lateral spreading, such as empirical methods and strain potential models, capture some of these complexities, but have their own inherent limitations, particularly with respect to the manner in which the earthquake loading is characterized. The Youd et al. (2002) model, for instance, only accounts for the magnitude and source-site distance of the event and site, while models based on shear strain potential usually account for the loading using the peak ground acceleration and magnitude. With the exception of Zhang et al.'s 2004 strain potential model, which uses "surface acceleration" to characterize the loading, each of these approaches neglect important factors, such as site effects and ground motion frequency content that can affect site displacements significantly.

On the surface, it would appear that using Newmark-type rigid block analyses to model lateral spreads is an attractive alternative to the aforementioned methods. The motion of a sliding block on an inclined, frictional plane has the potential to approximate the ratcheting-type displacements observed in lateral spreading case histories. Furthermore, the earthquake loading is accounted for more directly, by obtaining a suite of ground motions that accurately represent source, path, and site conditions of interest and capturing the effects of record-specific characteristics such as significant duration and Arias intensity. Theoretically, if the effects of pore pressure generation on the stiffness and

strength of the soil are accounted for adequately and reflected in the specification of the yield acceleration, a concept initially discussed by Baziar et al. in 1992 and developed more thoroughly by Olson and Johnson in 2008, rigid block analyses could be a viable alternative to the current methods used in practice today.

However, as is the case with any method that purports to model lateral spreading (or any other naturally-occurring phenomenon), it is important to consider what characteristics of lateral spreading the rigid block analysis represents, as well as what characteristics it does not. The focus of this thesis was to assess the applicability of sliding block analyses in two ways. The first was to evaluate any potential structural limitations of the sliding block analysis, i.e. how the rigid block assumption fundamentally differs from the conditions that exist in a typical lateral spread, and how those limitations might affect the accuracy or precision of the model's results. The second was to examine the utility of Newmark-based models in practice, particularly with the Olson and Johnson (2008) method, with respect to how well it represents a broad database of lateral spreading conditions, how precisely and accurately it predicts lateral spreading displacements, and how accurate and precise its back-calculated shear strengths are.

9.2 Structural Limitations of Rigid Block Analyses

One of the earliest critiques of rigid block analyses was that a rigid failure mass was rarely representative of most soil sites on sloping ground, thus spurring significant research efforts aimed at developing compliant block models. Wartman et al. (2003) established that the relationship between the natural period of the site and the predominant or mean period of the ground motion could significantly affect the accuracy of the rigid mass assumption. In particular, it was shown that tuning ratios close to unity could result in un-conservative displacement estimates using the Newmark analysis. It is difficult to estimate what portion of all potential lateral spreading cases might be applicable to this situation; the Olson and Johnson (2008) database may be a possible indicator, with about 15% of cases featuring tuning ratios close to unity, and most of the remaining cases with moderately higher values. It should be noted, however, that these tuning ratios were computed for the initial site and ground motion conditions; the onset of liquefaction generally results in a lengthening of the predominant ground motion period, which may reduce the tuning ratio; thus rigid block analyses could potentially under-predict displacements for a significantly higher proportion of potential lateral spreading cases.

It is also important to note that sliding block analyses evaluate only the *inertial* seismic instability of site. In other words, the strength of the material along the failure

surface (and thus the yield acceleration) is specified *a priori*, and is assumed not to change throughout the duration of the ground motion. The effects of this simplification are somewhat difficult to isolate; theoretically, if the strength is specified as a residual liquefied strength, then the sliding block analysis would be accurate in this regard, and possibly even *overly* conservative, since actual liquefied shear strengths are not mobilized until well into the duration of the ground motion. Therefore, the structural biases associated with neglecting the effects of weakening instability could potentially be counteracted by assigning a sufficiently low yield acceleration.

Perhaps the most significant source of structural bias lies in the assumption of a discrete failure surface. It is well-established that lateral spreading deformations generally do not develop along a single, discrete surface, but are instead distributed throughout the layer of liquefied soil, with varying degrees of uniformity. This result of this simplification is that sliding block analyses tend to significantly underpredict displacements for sites where liquefied soil exists in relatively thick strata. Naturally, these discrepancies in predicted displacements are amplified as the thickness of the weak material increases. For sites underlain by 5 meters of liquefied material, which are representative of a typical case analyzed in the Youd et al. (2002) database, the assumption of a discrete failure surface can result in predicted displacements that are about 50% lower on average than the displacements computed from dynamic finite-difference analyses, and can be as high as 70% lower. Overall, based on the analyses performed in Section 6.6, the key feature of sliding block analyses that displacements occur on a single plane within the liquefied material, an assumption which is inconsistent with observed lateral spreading behavior, is a largely and significantly un-conservative one. It should also be noted that sliding block-based displacements are largely insensitive to the thickness of the weak layer, which is also inconsistent with observed lateral spreading behavior.

To summarize, three main sources of potential structural bias were identified in the use of the Newmark sliding block analysis. The first, that a rigid failure mass is generally not representative of the true dynamic behavior of a laterally spreading site, has the potential to result in un-conservatively biased displacement predictions, depending on how close the natural period of the site and the predominant ground motion period are to each other. The second, that no weakening of the soil along the failure surface occurs during the ground motion event, could theoretically be an overly conservative assumption, but only if the initial strength is estimated accurately and appropriately. The final source of structural bias, that lateral spreading displacements occur along a single failure surface, has been shown to be consistently un-conservative to a significant degree. The combination of these three factors suggests that rigid block analyses may be, overall, an un-conservative representation of the true behavior of lateral spreading.

9.3 Practical Implications

The analyses presented in Chapter 6 showed that, when evaluating solely the effects of discrete versus distributed deformations, sliding block analyses predicted displacements that were on the order of 30 to 70% lower than displacements predicted using simple dynamic analyses of a soil continuum. Chapter 8 showed, however, that rigid block analyses are even more unconservative for predicting actual lateral spreading displacements (using the Olson and Johnson 2008 method). When compared to more advanced numerical methods that specifically account for the nonlinear dynamics of the site response, pore pressure generation, and post-liquefaction softening, the OJ08 method largely failed to predict substantial displacements; for the broad range of conditions defined in Chapter 8, the OJ08 predicted nearly an 80% probability of zero displacement. Comparable analyses performed using FLIP yielded a corresponding probability of less than 2%, with a mean nonzero displacement of about 40 cm, and calculated displacements of greater than 1m in about 10% of cases . The implication here is that, in addition to the discrete failure surface bias, the effects of weakening instability are inadequately accounted for by Olson and Johnson's strength ratio estimates to a significant degree.

On a related note, the methodology used by Olson and Johnson to estimate strength ratios from laterally spreading soils, as well as their conclusion that those strength ratios are consistent with flow liquefaction strength ratios, warrants some further discussion. The case history database upon which they were based is largely well-representative of a wide range of lateral spreading conditions. The one clear exception to this is that the database is heavily biased towards cases where displacements have occurred in close proximity to the crest of a free face. It has been well established that these areas of the lateral spread can be highly unstable, in which case deformations can be heavily influenced by slumping, toppling, or raveling of the soil. These types of ground failures, in addition to the six cases from the 1990 Luzon event that were classified by investigators as flow failures, represent an even further divergence from the rigid block simplification, and it can be argued that using sliding block analyses to back-analyze such cases is a wholly inadequate strategy given the additional aforementioned structural limitations that already exist.

Aside from the potential issues with the case history database, the back-analysis framework itself was evaluated in Chapters 6 and 7. In addition to the probable overestimation of strength ratios (due to assuming one-way sliding) in about one-quarter of the case histories, it was shown that the back-analysis framework is influenced by many uncertain parameters and relationships. The combination of record-to-record variability (which can be exacerbated by selection methods that scale only to single PGA values), variability in soil parameters, significant uncertainty in determining a single failure surface,

and significant uncertainty involved in selecting a representative penetration resistance, all combine to produce highly uncertain back-calculated estimates of shear strengths. The probabilistic back-analyses performed in Chapter 7 showed that, even for two cases as well-constrained as Moss Landing and Wildlife, there was no strong evidence to support the notion that liquefied strength ratios mobilized in lateral spreads are identical to those calculated in flow failures.

Overall, the combination of the various inherent biases associated with rigid block analyses discussed in this thesis, along with the practical issues involved with their implementation in the OJ08 analysis framework, result in a method that has the potential to extremely under-predict displacement for a wide rang of actual lateral spreading conditions. Additionally, it seems likely that back-calculated shear strength estimates are not representative of actual lateral spreading cases; many are based on cases influenced by failure modes not associated with cyclic mobility, which complicates the formulation of any definitive statement about how they relate to liquefied flow failures.

9.4 Concluding Remarks and Possible Future Work

Characterizing lateral spreading hazards and predicting displacements is by no means an easy task. The numerous competing factors that vary from site to site and ground motion to ground motion have made the application of the various models and methods difficult to apply with any precision on a site-specific basis. Rather than relying on a collection of methods that only partially account for some of the mechanisms that drive lateral spreading to predict displacements, the author advocates a more rigorous approach when possible, arguing that empirical methods, strain potential models, and sliding block analyses all have certain deficiencies that can result in significant inaccuracies in estimating lateral spreading hazards. Recognizing that lateral spreading displacements depend strongly on how the system behaves after the onset of liquefaction, the use of numerical methods to more accurately assess weakening instability (and the resulting dynamic response of the system), as well as two- or three-dimensional site effects, should produce more reliable results.

With this in mind, there is certainly potential for future models to predict lateral spreading more accurately. It is the author's opinion that such models could be, in the same vein as Kramer and Baska's 2006 model, based on large databases of numerical simulations, which allow for a more controlled way to test the effects of various source and site factors on lateral displacements. Such models should, in theory account for seismic loading in a manner that recognizes the importance of evolutionary ground motion

parameters such as Arias Intensity or cumulative absolute velocity, as well as other site-specific complexities such as void redistribution, post-liquefaction dynamics of the system, and complex topographic effects. Finally, we should recognize that, while displacements occurring near free faces do not necessarily fall under the traditional classification of lateral spreading, they do often occur at sites where lateral spread-type deformations have occurred further inland, and these types of slumping or toppling failures are generally what developers and public agencies are most concerned about. Thus, future research could also be focused on establishing a connection between the lateral deformations predicted further away from the crest of a free face with potential hazard characterization at the free face itself. Such research efforts could have the potential to greatly improve seismic hazard assessment and risk mitigation at liquefaction-susceptible sites near rivers, levees, and embankments.

Appendix A

Summary of Lateral Spreading Case Histories

Table A.1: Summary of case histories in Olson & Johnson database, and potential sources of bias or uncertainty

Earthquake	Case No.	Location	Site Characterization	Ground Motion Characterization	Selection of Failure Surface	Observed Displacements	Selection of Representative $(N_1)_{60}$ and q_{c1}
1971 San Fernando	1	Juvenile Hall			Reports of horizontal continuity of lateral deformations are inconsistent (Youd 1973; Bennett 1989)		
1979 Imperial Valley	2	Heber Road		Discrepancy between O&J-estimated *PGA* (0.47g) and other estimates (0.25-0.3g); v_{s30} estimated using SPT correlations			
1983 Borah Peak	3	Whiskey Springs Fan	Liquefaction occurred in gravelly soils	*PGA* estimates are highly uncertain due to lack of ground motion data; O&J erroneously reported Richter magnitude (6.9) instead of M_w (7.3)			
1987 Edgecumbe, New Zealand	4	Landing Rd. Bridge	Pre-earthquake channel depth unknown	-v_{s30} estimated from SPT data		Location of displacement vector not reported by O&J	

Table A.1 (Continued): Summary of case histories in Olson & Johnson database, and potential sources of bias or uncertainty

Earthquake	Case No.	Location	Site Characterization	Ground Motion Characterization	Selection of Failure Surface	Observed Displacements	Selection of Representative $(N_1)_{60}$ and q_{c1}
1987 Edgecumbe, New Zealand	5	James St. Loop		v_{s30} estimated from SPT data	Multiple possible failure surfaces	Location of displacement vector not reported by O&J ; Displ. measurements uncertain due to quality of photogrammetric measurements; High scatter in magnitude & direction of ground cracks	N-value calculated from Eq. 5.1
	6	Whakatane Pony Club	Lagoon depth unclear	v_{s30} estimated from SPT data	Multiple possible failure surfaces	High scatter in magnitude & direction of ground cracks	N-value estimated from Eq. 5.1
1987 Superstition Hills	7	Wildlife Array			Only shallow sandy silt directly below river channel was back-analyzed by O&J for strength ratio		
1989 Loma Prieta	8	Moss Landing MBARI Bldg 4		v_{s30} estimated from SPT and CPT data	Multiple possible failure surfaces		Mejia (1998) estimated lower N-value (10) than O&J (16.5)
	9	Moss Landing MBARI Bldg 3		v_{s30} estimated from SPT and CPT data			N-value possibly estimated from Eq. 5.1; Mejia (1998) estimated higher N-value (20) than O&J (15)

Table A.1 (Continued): Summary of case histories in Olson & Johnson database, and potential sources of bias or uncertainty

Earthquake	Case No.	Location	Site Characterization	Ground Motion Characterization	Selection of Failure Surface	Observed Displacements	Selection of Representative $(N_1)_{60}$ and q_{c1}
1989 Loma Prieta	10	Moss Landing MLML Bldg East3		v_{s30} estimated from SPT and CPT data	Extent of liquefied material uncertain		Mejia (1998) estimated higher N-value (17) than O&J (11)
	11	Moss Landing, MLML Bldg East	Geometry of spread is unclear	v_{s30} estimated from SPT and CPT data		Location of displacement vector not reported by O&J	Mejia (1998) estimated higher N-value (17.5) than O&J (11.5)
	12	Miller Farm		v_{s30} estimated from SPT and CPT data		Representative displacement at low end of reported range; Location of displacement vector not reported by O&J	Wide range of SPT/CPT values reported in liquefied strata
	13	Farris Farm		v_{s30} estimated from SPT and CPT data		Representative displacement at low end of reported range; Location of displacement vector not reported by O&J	Holzer (1994) estimated higher N-value (18) than O&J (11.5);Wide range of SPT/CPT values reported in liquefied strata
	14	Leonardini Farm		O&J-estimated *PGA* (0.21 g) higher than Charlie et al. (1998) estimate (0.16 g); v_{s30} estimated from SPT and CPT data		Representative displacement at low end of reported range; Location of displacement vector not reported by O&J	

Table A.1 (Continued): Summary of case histories in Olson & Johnson database, and potential sources of bias or uncertainty

Earthquake	Case No.	Location	Site Characterization	Ground Motion Characterization	Selection of Failure Surface	Observed Displacements	Selection of Representative $(N_1)_{60}$ and q_{c1}
1989 Loma Prieta	15	Sea Mist Farm	Horizontal extent of liquefiable material uncertain	O&J-estimated *PGA* (0.21 g) higher than Charlie et al. (1998) estimate (0.16 g); v_{s30} estimated from SPT and CPT data		Location of displacement vector not reported by O&J	
	16	Marina District; St. Francis Yacht Club		v_{s30} estimated from SPT & CPT data	Existence of seawall may complicate failure surface selection		Relatively sparse SPT data for liquefiable fill; N-values are highly variable (1-12 bpf)
	17	Treasure Island, 4th & N St.					q_{c1} estimated from Eq. 5.1; Representative N-values are highly variable (4-15 bpf)
1990 Luzon, Philippines	18	Magsaysay Bridge, E. Bank (A-A)		v_{s30} estimated from SPT & CPT data		Large observed displacements attributed to flow-like deformations (Ishihara 1993)	q_{c1} estimated from Eq. 5.1
	19	Nable St. West (B-B)		v_{s30} estimated from SPT & CPT data		Large observed displacements attributed to flow-like deformations (Ishihara 1993)	q_{c1} estimated from Eq. 5.1

Table A.1 (Continued): Summary of case histories in Olson & Johnson database, and potential sources of bias or uncertainty

Earthquake	Case No.	Location	Site Characterization	Ground Motion Characterization	Selection of Failure Surface	Observed Displacements	Selection of Representative $(N_1)_{60}$ and q_{c1}
1990 Luzon, Philippines	20	Nable St. East (C-C)		v_{s30} estimated from SPT & CPT data		Large observed displacements attributed to flow-like deformations (Ishihara 1993)	q_{c1} estimated from Eq. 5.1
	21	Magsaysay Bridge, E. Bank (D-D)		v_{s30} estimated from SPT & CPT data		Large observed displacements attributed to flow-like deformations (Ishihara 1993)	q_{c1} estimated from Eq. 5.1
	22	Magsaysay Bridge, W. Bank (E-E)		v_{s30} estimated from SPT & CPT data		Large observed displacements attributed to flow-like deformations (Ishihara 1993)	q_{c1} estimated from Eq. 5.1
	23	Pogo Chico, West Bank		v_{s30} estimated from SPT & CPT data		Large observed displacements attributed to flow-like deformations (Ishihara 1993)	N-values estimated from Swedish Cone test data; q_{c1} estimated from Eq. 5.1
1990 Manjil, Iran	24	Rudbaneh Town Canal	Reports of canal depth are inconsistent (4 or 15 m)	v_{s30} estimated from SPT & CPT data		Representative displacement at low end of reported range; Location of displacement vector not reported by O&J	q_{c1} estimated from Eq. 5.1
1994 Northridge, CA	25	Balboa Blvd.		Near-fault site, high PGA variability; v_{s30} estimated from SPT & CPT data	High FC fluvial deposits, multiple potential failure planes		

Table A.1 (Continued): Summary of case histories in Olson & Johnson database, and potential sources of bias or uncertainty

Earthquake	Case No.	Location	Site Characterization	Ground Motion Characterization	Selection of Failure Surface	Observed Displacements	Selection of Representative $(N_1)_{60}$ and q_{c1}
1994 Northridge, CA	26	Wynne Ave.		Near-fault site, high *PGA* variability; v_{s30} estimated from SPT & CPT data			
	27	Potero Canyon	Unclear which cross section used for back-analysis	Near-fault site, high *PGA* variability; v_{s30} estimated from SPT & CPT data	Multiple possible failure planes	Location of displacement vector not reported by O&J	
1999 Chi-Chi, Taiwan	28	Wufeng Site C (A-A')	Near-fault site, high *PGA* variability; v_{s30} estimated from SPT & CPT data		Maximum displacement vector used by O&J, high FF ratio (50%)		
	29	Wufeng Site C (B-B')		Near-fault site, high *PGA* variability; v_{s30} estimated from SPT & CPT data		Maximum displacement vector used by O&J, high FF ratio (21%)	
	30	Wufeng Site C1		Near-fault site, high *PGA* variability; v_{s30} estimated from SPT & CPT data		Maximum displacement vector used by O&J, high FF ratio (58%)	

Table A.1 (Continued): Summary of case histories in Olson & Johnson database, and potential sources of bias or uncertainty

Earthquake	Case No.	Location	Site Characterization	Ground Motion Characterization	Selection of Failure Surface	Observed Displacements	Selection of Representative $(N_1)_{60}$ and q_{c1}
1999 Chi-Chi, Taiwan	31	Wufeng Site B		Near-fault site, high *PGA* variability; v_{s30} estimated from SPT & CPT data		Maximum displacement vector used by O&J, high FF ratio (31%)	SPT highly variable w/ in liquefied material
	32	Wufeng Site M		Near-fault site, high *PGA* variability; v_{s30} estimated from SPT & CPT data		Maximum displacement vector used by O&J, high FF ratio (24%)	SPT highly variable w/ in liquefied material
	33	Nantou Site N		Near-fault site, high *PGA* variability; v_{s30} estimated from SPT & CPT data		Observed displacements not directly measured, not as reliable at this site	SPT data sparse and highly variable w/ in liquefied material
1999 Kocaeli, Turkey	34	Hotel Sapanca		v_{s30} estimated from SPT & CPT data		"Accumulated" displacement at free face used by O&J	SPT & CPT data highly vvariable w/ in liquefied material
	35	Police Station	Discrepancy in median $D50$ between O&J and Cetin et al. (2004b)	v_{s30} estimated from SPT & CPT data	Multiple potential failure planes	"Accumulated" displacement at free face used by O&J	

Table A.1 (Continued): Summary of case histories in Olson & Johnson database, and potential sources of bias or uncertainty

Earthquake	Case No.	Location	Site Characterization	Ground Motion Characterization	Selection of Failure Surface	Observed Displacements	Selection of Representative $(N_1)_{60}$ and q_{c1}
1999 Kocaeli, Turkey	36	Soccer Field	No grain size data reported by O&J despite available data from Cetin et al. (2004b)	v_{s30} estimated from SPT & CPT data			Highly variable CPT data in liquefiable material; SPT data is very sparse
	37	Yalova Harbor		v_{s30} estimated from SPT & CPT data		Maximum displacement vector used by O&J, high FF ratio (75%)	
2003 San Simeon	38	Norwsing Dr.			Multiple potential failure planes		N-value calculated from Eq. 5.1
	39	Juanita Ave.					N-value calculated from Eq. 5.1

Appendix B

Selection of 90 Ground Motions Based on Target Response Spectra

The ground motions that were used as inputs in the sliding block and continuum dynamic analyses performed in this chapter were obtained from Astaneh-Asl (personal communication) using teh following method. 16 total bin combinations of magnitude and source-site distance were selected (based on table B.1). For each bin a target response spectra were created based on GMPE 2008 relations for a magnitude and distance of the bin, $(V_s)_{30} = 760m/s$ and strike slip fault. For each bin, the 5 best matching motions to the target spectra were selected. 10 near fault motions were also added to the input data, for a total of 90 motions. The response spectra for the motions in each bin are shown below.

Table B.1: Moment magnitude and source-site distance bins used to formulate target spectra for the generation of the suite of ground motions for PSNL dynamic analyses and Newmark sliding block analyses.

M / R(km)	$0 < R < 10$	$10 < R < 20$	$20 < R < 40$	$40 < R < 80$
$6.5 < M < 7.0$	M1R1	M1R2	M1R3	M1R4
$7.0 < M < 7.5$	M2R1	M2R2	M2R3	M2R4
$7.5 < M < 8.0$	M3R1	M3R2	M3R3	M3R4
$M > 8.0$	M4R1	M4R2	M4R3	M4R4

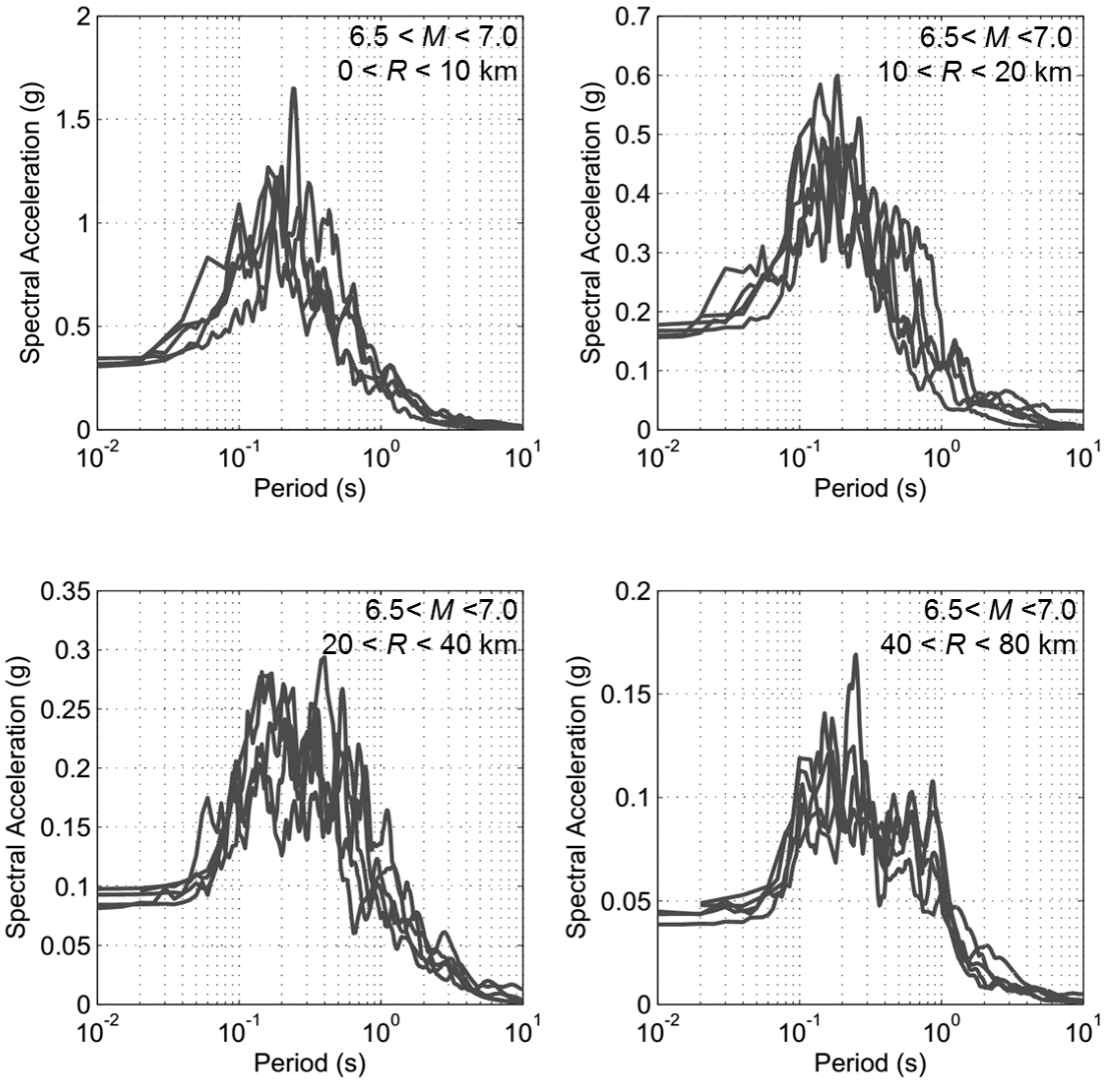

Figure B.1: Response spectra for selected ground motions in Bins 1 through 4

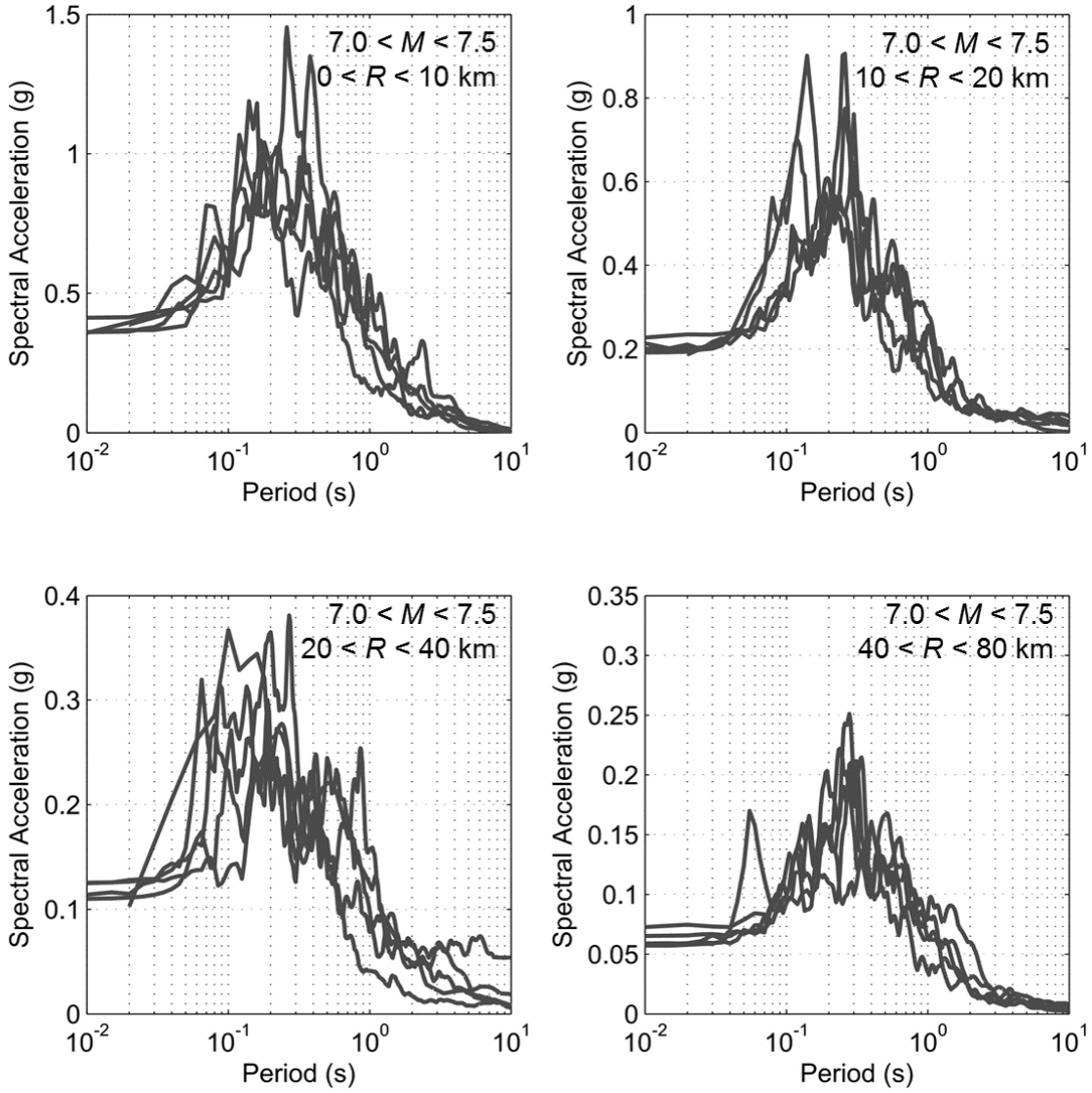

Figure B.2: Response spectra for selected ground motions in Bins 5 through 8

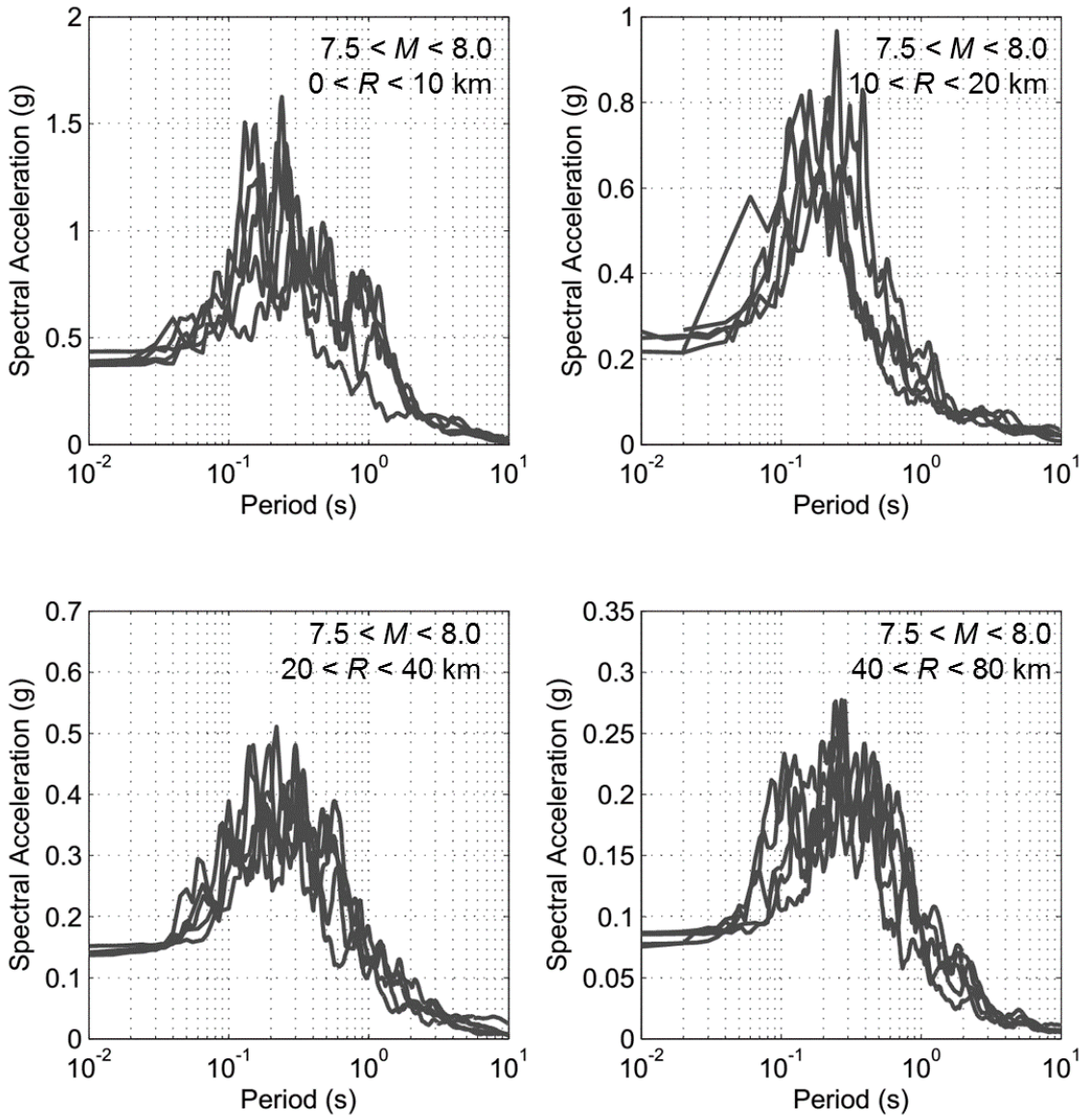

Figure B.3: Response spectra for selected ground motions in Bins 9 through 12

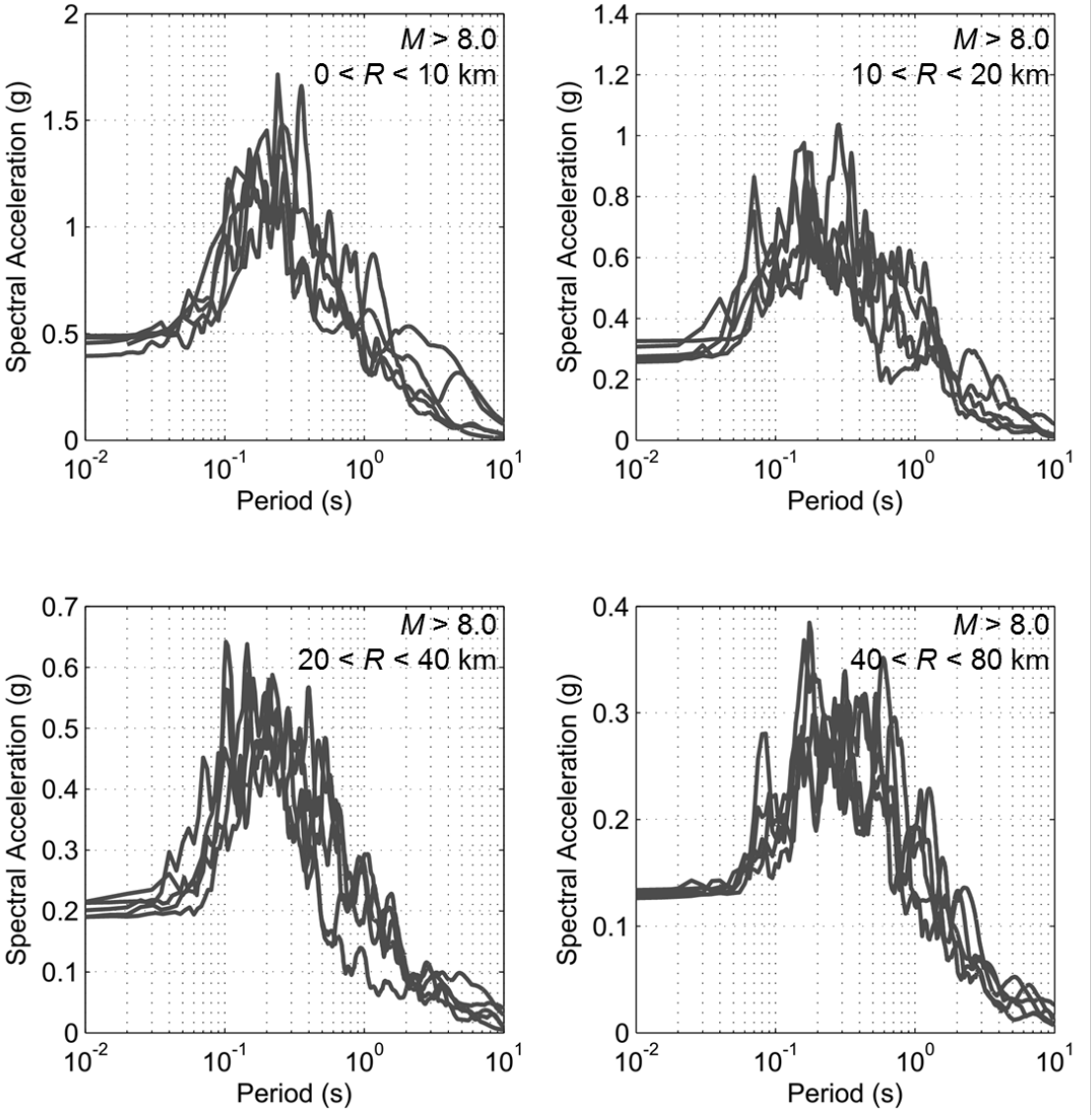

Figure B.4: Response spectra for selected ground motions in Bins 13 through 16

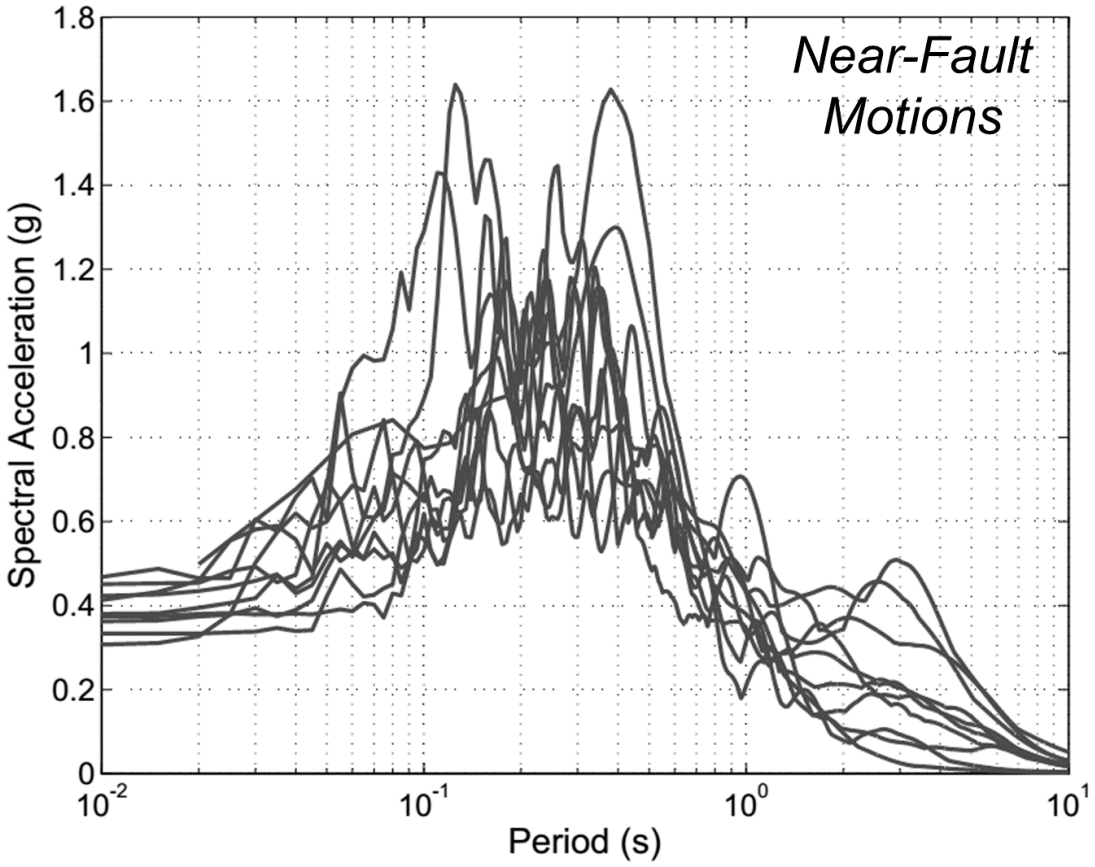

Figure B.5: Response spectra for selected near-fault ground motions

Appendix C

Summary of Newmark Sliding Block and PSNL Analysis Data

Table C.1: Summary of dynamic analysis results, using Newmark and PSNL analyses, on "Low Strength" sites

T_w (m)	$\beta = 0.5^\circ$						$\beta = 1.0^\circ$					
	$D_{C,m}$ (cm)	r_D	$W_{C,m}$ (kPa)	r_W	$r_{W,D}$	η	$D_{C,m}$ (cm)	r_D	$W_{C,m}$ (kPa)	r_W	$r_{W,D}$	η
0.1	5.4	0.89	0.86	0.95	0.89	0	10.2	0.85	0.72	0.83	0.93	0
0.2	6.0	0.82	0.89	0.94	0.88	0.53	10.6	0.83	0.78	0.80	0.90	0.55
0.3	5.3	0.81	0.86	0.94	0.83	0.54	11.2	0.79	0.79	0.80	0.86	0.54
0.5	5.8	0.73	0.82	0.87	0.89	0.58	10.6	0.76	0.76	0.82	0.86	0.53
1.0	6.0	0.63	0.86	0.70	0.84	0.66	11.8	0.69	0.96	0.69	0.84	0.63
2.0	6.0	0.60	1.14	0.58	0.78	0.75	12.6	0.64	1.27	0.59	0.83	0.72
3.0	6.0	0.62	1.34	0.57	0.80	0.84	11.7	0.63	1.29	0.67	0.80	0.80
4.0	7.3	0.50	1.54	0.55	0.75	0.87	13.0	0.56	1.52	0.59	0.75	0.84
5.0	7.5	0.42	1.63	0.55	0.70	0.89	14.9	0.50	1.78	0.57	0.68	0.87

T_w (m)	$\beta = 2.0^\circ$						$\beta = 3.0^\circ$					
	$D_{C,m}$ (cm)	r_D	$W_{C,m}$ (kPa)	r_W	$r_{W,D}$	η	$D_{C,m}$ (cm)	r_D	$W_{C,m}$ (kPa)	r_W	$r_{W,D}$	η
0.1	20.6	0.80	0.90	0.84	0.92	0.00	45.5	0.69	1.67	0.80	0.94	0.00
0.2	20.9	0.80	0.96	0.82	0.90	0.52	48.4	0.66	1.78	0.74	0.91	0.56
0.3	21.0	0.81	0.99	0.81	0.89	0.54	52.4	0.62	1.98	0.69	0.90	0.50
0.5	21.4	0.70	0.87	0.80	0.88	0.53	51.7	0.63	1.98	0.72	0.88	0.48
1.0	25.3	0.62	1.14	0.70	0.86	0.57	57.7	0.60	2.42	0.70	0.86	0.51
2.0	25.7	0.62	1.40	0.66	0.86	0.60	58.1	0.64	2.95	0.72	0.85	0.39
3.0	28.2	0.58	1.79	0.61	0.82	0.65	72.1	0.55	4.18	0.61	0.80	0.43
4.0	30.2	0.56	2.05	0.62	0.78	0.70	84.4	0.48	5.28	0.57	0.81	0.42
5.0	32.5	0.53	2.32	0.62	0.74	0.74	96.6	0.43	6.80	0.50	0.76	0.41

Table C.2: Summary of dynamic analysis results, using Newmark and PSNL analyses, on "Medium Strength" sites

T_w (m)	$\beta = 0.5^\circ$						$\beta = 1.0^\circ$					
	$D_{C,m}$ (cm)	r_D	$W_{C,m}$ (kPa)	r_W	$r_{W,D}$	η	$D_{C,m}$ (cm)	r_D	$W_{C,m}$ (kPa)	r_W	$r_{W,D}$	η
0.1	4.3	0.95	0.86	0.98	0.94	0.00	7.1	0.87	0.88	0.92	0.91	0
0.2	4.6	0.79	0.91	0.85	0.93	0.61	6.8	0.79	0.89	0.90	0.84	0.57
0.3	4.5	0.84	0.98	0.83	0.90	0.63	7.2	0.83	0.97	0.88	0.85	0.58
0.5	5.2	0.75	1.09	0.78	0.89	0.58	6.7	0.72	1.05	0.82	0.84	0.63
1.0	5.5	0.68	1.22	0.76	0.87	0.68	6.4	0.56	1.19	0.59	0.82	0.72
2.0	5.2	0.68	1.40	0.72	0.85	0.78	7.4	0.46	1.13	0.62	0.83	0.79
3.0	6.2	0.60	1.62	0.55	0.82	0.81	8.1	0.42	1.51	0.53	0.81	0.86
4.0	6.8	0.47	1.74	0.49	0.77	0.89	9.0	0.39	1.82	0.47	0.74	0.88
5.0	6.7	0.40	2.04	0.48	0.65	0.91	10.1	0.36	2.07	0.34	0.69	0.90

T_w (m)	$\beta = 2.0^\circ$						$\beta = 3.0^\circ$					
	$D_{C,m}$ (cm)	r_D	$W_{C,m}$ (kPa)	r_W	$r_{W,D}$	η	$D_{C,m}$ (cm)	r_D	$W_{C,m}$ (kPa)	r_W	$r_{W,D}$	η
0.1	10.8	0.91	0.98	0.90	0.90	0.00	18.3	0.74	1.02	0.77	0.89	0.00
0.2	19.1	0.95	1.69	0.92	0.87	0.57	19.4	0.71	1.05	0.77	0.87	0.43
0.3	11.8	0.71	0.79	0.81	0.86	0.55	19.5	0.71	1.15	0.73	0.85	0.57
0.5	12.4	0.69	0.87	0.77	0.84	0.56	17.5	0.61	1.00	0.67	0.83	0.55
1.0	14.3	0.60	1.08	0.64	0.81	0.65	21.9	0.54	1.36	0.61	0.83	0.59
2.0	14.6	0.49	1.40	0.45	0.82	0.75	25.0	0.50	1.90	0.53	0.84	0.60
3.0	15.9	0.48	1.69	0.44	0.78	0.79	24.1	0.47	1.91	0.54	0.80	0.71
4.0	17.7	0.42	1.81	0.45	0.74	0.82	27.7	0.43	2.39	0.52	0.77	0.72
5.0	18.2	0.42	2.15	0.43	0.70	0.86	29.3	0.43	2.87	0.50	0.74	0.78

Table C.3: Summary of dynamic analysis results, using Newmark and PSNL analyses, on "High Strength" sites

T_w (m)	$\beta = 0.5^\circ$						$\beta = 1.0^\circ$					
	$D_{C,m}$ (cm)	r_D	$W_{C,m}$ (kPa)	r_W	$r_{W,D}$	η	$D_{C,m}$ (cm)	r_D	$W_{C,m}$ (kPa)	r_W	$r_{W,D}$	η
0.1	2.8	0.84	1.01	0.92	0.88	0.00	4.7	0.95	0.86	0.98	1.03	0.00
0.2	3.0	0.68	0.95	0.88	0.71	0.57	1.8	0.75	0.97	0.82	0.87	0.59
0.3	3.1	0.71	1.01	0.86	0.69	0.62	5.0	0.68	0.95	0.89	0.83	0.60
0.5	3.2	0.66	1.15	0.78	0.67	0.66	5.2	0.66	1.03	0.75	0.90	0.61
1.0	3.9	0.51	1.20	0.82	0.63	0.70	6.2	0.55	1.19	0.70	0.73	0.70
2.0	4.0	0.48	1.44	0.66	0.69	0.79	4.8	0.56	1.50	0.40	0.71	0.81
3.0	4.5	0.43	1.77	0.56	0.70	0.83	5.6	0.50	1.68	0.44	0.75	0.87
4.0	4.8	0.43	2.07	0.56	0.70	0.88	6.5	0.40	1.98	0.42	0.68	0.89
5.0	5.6	0.34	2.21	0.41	0.55	0.91	7.3	0.33	2.10	0.43	0.58	0.91

T_w (m)	$\beta = 2.0^\circ$						$\beta = 3.0^\circ$					
	$D_{C,m}$ (cm)	r_D	$W_{C,m}$ (kPa)	r_W	$r_{W,D}$	η	$D_{C,m}$ (cm)	r_D	$W_{C,m}$ (kPa)	r_W	$r_{W,D}$	η
0.1	8.1	0.86	0.92	0.94	0.87	0.00	11.9	0.82	1.06	0.85	0.89	0.00
0.2	8.8	0.74	0.94	0.81	0.81	0.69	12.9	0.79	1.15	0.81	0.81	0.48
0.3	8.9	0.74	0.96	0.80	0.81	0.62	14.1	0.67	1.28	0.74	0.82	0.58
0.5	10.1	0.67	1.13	0.84	0.84	0.57	14.5	0.67	1.38	0.73	0.80	0.59
1.0	9.4	0.57	1.31	0.61	0.76	0.68	14.0	0.52	1.16	0.62	0.80	0.65
2.0	10.2	0.48	1.65	0.52	0.77	0.79	15.7	0.43	1.55	0.46	0.78	0.76
3.0	11.5	0.46	2.08	0.55	0.73	0.83	18.6	0.33	2.15	0.34	0.74	0.78
4.0	13.7	0.38	2.22	0.51	0.67	0.87	19.5	0.34	2.57	0.34	0.72	0.82
5.0	16.0	0.34	2.64	0.49	0.61	0.89	22.0	0.32	3.05	0.34	0.67	0.86

Appendix D

Summary of Lateral Spreading Analysis Results

Table D.1: Compiled results of lateral spreading analysis for a site with T = 1m, N = 5, and $S = 0.5^{\circ}$

T_{liq} = 1 m, N = 5 blows/ft, Slope= 0.5°										
		FLIP			Youd et al.			Olson and Johnson		
M_w	R (km)	$P[D = d_0]$	μ_{D_H}	$\sigma_{\ln D_H}$	$P[D = d_0]$	μ_{D_H}	$\sigma_{\ln D_H}$	$P[D = d_0]$	μ_{D_H}	$\sigma_{\ln D_H}$
6.0	10	5%	0.072	0.531	47%	0.010	0.464	41%	0.028	0.829
6.0	20	10%	0.057	0.956	99%	0.003	0.464	71%	0.027	0.874
6.0	30	5%	0.031	0.833	100%	0.001	0.464	91%	0.027	0.922
6.0	40	25%	0.032	0.747	100%	0.001	0.464	96%	0.032	0.980
6.0	50	45%	0.019	0.418	100%	0.000	0.464	98%	0.031	0.989
6.0	70	80%	0.015	0.211	100%	0.000	0.464	99%	0.040	1.009
6.0	100	100%	0.000	0.000	100%	0.000	0.464	100%	0.042	0.991
6.5	10	0%	0.184	0.855	0%	0.054	0.464	37%	0.037	0.964
6.5	20	0%	0.101	1.015	13%	0.017	0.464	70%	0.030	0.956
6.5	30	0%	0.119	0.919	73%	0.007	0.464	75%	0.033	1.081
6.5	40	0%	0.062	0.692	98%	0.004	0.464	93%	0.035	1.152
6.5	50	5%	0.066	0.762	100%	0.002	0.464	92%	0.036	1.142
6.5	70	10%	0.033	0.623	100%	0.001	0.464	96%	0.040	1.186
6.5	100	65%	0.024	0.400	100%	0.000	0.464	99%	0.051	1.214
7.0	10	5%	0.392	0.357	0%	0.239	0.464	3%	0.106	1.091
7.0	20	0%	0.313	0.570	0%	0.084	0.464	29%	0.045	1.115
7.0	30	0%	0.201	0.526	0%	0.039	0.464	72%	0.035	1.128
7.0	40	0%	0.236	0.354	6%	0.021	0.464	71%	0.035	1.131
7.0	50	0%	0.188	0.589	36%	0.012	0.464	81%	0.035	1.161
7.0	70	10%	0.055	0.915	96%	0.004	0.464	96%	0.042	1.191
7.5	10	5%	0.416	0.438	0%	0.788	0.464	7%	0.107	1.203
7.5	20	0%	0.354	0.477	0%	0.344	0.464	33%	0.041	1.076
7.5	30	0%	0.366	0.475	0%	0.176	0.464	32%	0.044	1.158
7.5	40	0%	0.314	0.379	0%	0.098	0.464	49%	0.036	1.107
7.5	50	0%	0.254	0.424	0%	0.058	0.464	61%	0.036	1.123
7.5	70	0%	0.186	0.532	4%	0.022	0.464	80%	0.041	1.168
7.5	100	5%	0.124	0.685	84%	0.006	0.464	91%	0.041	1.232
8.0	10	0%	0.394	0.686	0%	1.824	0.464	4%	0.151	1.315
8.0	20	5%	0.401	0.403	0%	1.013	0.464	9%	0.090	1.242
8.0	30	0%	0.343	0.341	0%	0.595	0.464	36%	0.044	1.161
8.0	40	0%	0.387	0.330	0%	0.364	0.464	18%	0.060	1.160
8.0	50	0%	0.301	0.349	0%	0.229	0.464	29%	0.046	1.127
8.0	70	0%	0.241	0.449	0%	0.096	0.464	48%	0.040	1.101
8.0	100	0%	0.242	0.432	1%	0.029	0.464	78%	0.042	1.240

Table D.2: Compiled results of lateral spreading analysis for a site with T = 1m, N = 5, and $S = 1.5^{\circ}$

T_{liq} = 1 m, N = 5 blows/ft, Slope= 1.5°

		FLIP			Youd et al.			Olson and Johnson		
M_w	R (km)	$P[D = d_0]$	μ_{D_H}	$\sigma_{\ln D_H}$	$P[D = d_0]$	μ_{D_H}	$\sigma_{\ln D_H}$	$P[D = d_0]$	μ_{D_H}	$\sigma_{\ln D_H}$
6.0	10	0%	0.166	0.620	19%	0.015	0.464	8%	0.053	1.070
6.0	20	0%	0.186	0.721	96%	0.004	0.464	43%	0.038	1.066
6.0	30	0%	0.105	0.825	100%	0.002	0.464	75%	0.034	1.013
6.0	40	0%	0.083	0.963	100%	0.001	0.464	87%	0.036	1.023
6.0	50	5%	0.050	0.969	100%	0.001	0.464	93%	0.037	0.981
6.0	70	30%	0.040	0.816	100%	0.000	0.464	96%	0.041	1.001
6.0	100	90%	0.024	0.807	100%	0.000	0.464	98%	0.043	0.927
6.5	10	0%	0.445	0.304	0%	0.078	0.464	10%	0.071	1.214
6.5	20	0%	0.285	0.635	3%	0.025	0.464	42%	0.044	1.161
6.5	30	0%	0.310	0.568	43%	0.011	0.464	45%	0.050	1.242
6.5	40	0%	0.232	0.569	90%	0.006	0.464	79%	0.045	1.231
6.5	50	0%	0.209	0.650	99%	0.003	0.464	77%	0.044	1.229
6.5	70	0%	0.136	0.711	100%	0.001	0.464	88%	0.048	1.217
6.5	100	5%	0.068	0.689	100%	0.000	0.464	95%	0.056	1.214
7.0	10	0%	0.637	0.323	0%	0.346	0.464	0%	0.410	0.998
7.0	20	0%	0.586	0.319	0%	0.122	0.464	4%	0.112	1.339
7.0	30	0%	0.473	0.456	0%	0.057	0.464	41%	0.054	1.312
7.0	40	0%	0.521	0.390	1%	0.030	0.464	41%	0.055	1.333
7.0	50	0%	0.505	0.365	13%	0.017	0.464	55%	0.048	1.336
7.0	70	0%	0.176	1.097	84%	0.006	0.464	89%	0.049	1.225
7.5	10	5%	0.660	0.395	0%	1.142	0.464	0%	0.445	1.163
7.5	20	5%	0.597	0.303	0%	0.499	0.464	6%	0.099	1.309
7.5	30	5%	0.608	0.308	0%	0.255	0.464	6%	0.108	1.374
7.5	40	0%	0.584	0.298	0%	0.142	0.464	18%	0.069	1.353
7.5	50	0%	0.555	0.295	0%	0.084	0.464	30%	0.061	1.348
7.5	70	0%	0.495	0.314	1%	0.032	0.464	56%	0.059	1.329
7.5	100	0%	0.391	0.402	58%	0.009	0.464	77%	0.055	1.329
8.0	10	5%	0.677	0.608	0%	2.645	0.464	0%	0.752	1.148
8.0	20	5%	0.632	0.275	0%	1.468	0.464	1%	0.359	1.259
8.0	30	5%	0.394	0.951	0%	0.863	0.464	11%	0.099	1.400
8.0	40	15%	0.589	0.329	0%	0.527	0.464	4%	0.152	1.358
8.0	50	0%	0.428	0.876	0%	0.332	0.464	9%	0.101	1.365
8.0	70	0%	0.522	0.282	0%	0.140	0.464	20%	0.073	1.343
8.0	100	0%	0.476	0.195	0%	0.042	0.464	51%	0.065	1.406

Table D.3: Compiled results of lateral spreading analysis for a site with T = 1m, N = 5, and $S = 3.5^{\circ}$

T_{liq} = 1 m, N = 5 blows/ft, Slope= 3.5°										
		FLIP			Youd et al.			Olson and Johnson		
M_w	R (km)	$P[D = d_0]$	μ_{D_H}	$\sigma_{\ln D_H}$	$P[D = d_0]$	μ_{D_H}	$\sigma_{\ln D_H}$	$P[D = d_0]$	μ_{D_H}	$\sigma_{\ln D_H}$
6.0	10	0%	0.339	0.322	7%	0.020	0.464	0%	0.153	1.119
6.0	20	0%	0.360	0.386	87%	0.006	0.464	11%	0.078	1.252
6.0	30	0%	0.238	0.439	100%	0.003	0.464	35%	0.051	1.119
6.0	40	0%	0.210	0.585	100%	0.001	0.464	55%	0.045	1.076
6.0	50	0%	0.148	0.715	100%	0.001	0.464	69%	0.040	0.995
6.0	70	0%	0.120	1.000	100%	0.000	0.464	83%	0.042	0.958
6.0	100	30%	0.067	0.923	100%	0.000	0.464	91%	0.039	0.883
6.5	10	0%	0.595	0.212	0%	0.104	0.464	1%	0.226	1.275
6.5	20	0%	0.468	0.355	1%	0.033	0.464	10%	0.104	1.325
6.5	30	0%	0.491	0.304	21%	0.014	0.464	10%	0.122	1.368
6.5	40	0%	0.396	0.347	74%	0.007	0.464	40%	0.074	1.297
6.5	50	0%	0.377	0.347	97%	0.004	0.464	38%	0.073	1.314
6.5	70	0%	0.308	0.410	100%	0.002	0.464	58%	0.064	1.240
6.5	100	0%	0.255	0.232	100%	0.000	0.464	77%	0.056	1.200
7.0	10	0%	0.804	0.257	0%	0.461	0.464	0%	1.171	0.987
7.0	20	0%	0.720	0.190	0%	0.163	0.464	0%	0.443	1.299
7.0	30	0%	0.615	0.318	0%	0.076	0.464	8%	0.146	1.474
7.0	40	0%	0.640	0.245	0%	0.040	0.464	8%	0.149	1.523
7.0	50	0%	0.596	0.269	4%	0.023	0.464	16%	0.110	1.527
7.0	70	0%	0.372	0.495	65%	0.008	0.464	58%	0.060	1.273
7.5	10	0%	0.886	0.174	0%	1.521	0.464	0%	1.447	1.051
7.5	20	0%	0.743	0.188	0%	0.665	0.464	0%	0.372	1.311
7.5	30	0%	0.762	0.171	0%	0.340	0.464	0%	0.433	1.379
7.5	40	0%	0.714	0.172	0%	0.189	0.464	2%	0.242	1.498
7.5	50	0%	0.689	0.189	0%	0.112	0.464	5%	0.186	1.530
7.5	70	0%	0.670	0.221	0%	0.043	0.464	16%	0.123	1.517
7.5	100	0%	0.573	0.237	34%	0.012	0.464	38%	0.090	1.439
8.0	10	0%	0.974	0.167	0%	3.523	0.464	0%	2.403	1.000
8.0	20	0%	0.853	0.191	0%	1.955	0.464	0%	1.283	1.088
8.0	30	0%	0.732	0.157	0%	1.149	0.464	1%	0.394	1.415
8.0	40	0%	0.773	0.146	0%	0.702	0.464	0%	0.610	1.295
8.0	50	0%	0.704	0.166	0%	0.442	0.464	1%	0.388	1.368
8.0	70	0%	0.697	0.164	0%	0.186	0.464	3%	0.247	1.430
8.0	100	0%	0.636	0.164	0%	0.056	0.464	13%	0.162	1.544

Table D.4: Compiled results of lateral spreading analysis for a site with T = 1m, N = 10, and $S = 0.5^{\circ}$

T_{liq} = 1 m, N = 10 blows/ft, Slope= 0.5°										
		FLIP			Youd et al.			Olson and Johnson		
M_w	R (km)	$P[D = d_0]$	μ_{D_H}	$\sigma_{\ln D_H}$	$P[D = d_0]$	μ_{D_H}	$\sigma_{\ln D_H}$	$P[D = d_0]$	μ_{D_H}	$\sigma_{\ln D_H}$
6.0	10	5%	0.063	0.582	47%	0.010	0.464	76%	0.021	0.550
6.0	20	5%	0.050	0.844	99%	0.003	0.464	97%	0.020	0.527
6.0	30	15%	0.027	0.709	100%	0.001	0.464	100%	0.019	0.524
6.0	40	45%	0.029	0.456	100%	0.001	0.464	100%	0.020	0.498
6.0	50	75%	0.017	0.152	100%	0.000	0.464	100%	0.017	0.387
6.0	70	100%	0.000	0.000	100%	0.000	0.464	100%	0.012	0.016
6.0	100	100%	0.000	0.000	100%	0.000	0.464	100%	0.012	0.016
6.5	10	5%	0.160	0.492	0%	0.054	0.464	78%	0.021	0.554
6.5	20	5%	0.086	0.811	13%	0.017	0.464	97%	0.020	0.567
6.5	30	0%	0.094	0.735	73%	0.007	0.464	98%	0.019	0.625
6.5	40	10%	0.052	0.591	98%	0.004	0.464	100%	0.021	0.647
6.5	50	10%	0.051	0.706	100%	0.002	0.464	100%	0.022	0.660
6.5	70	15%	0.025	0.552	100%	0.001	0.464	100%	0.024	0.552
6.5	100	100%	0.000	0.000	100%	0.000	0.464	100%	0.016	0.269
7.0	10	0%	0.318	0.301	0%	0.239	0.464	17%	0.038	0.795
7.0	20	5%	0.266	0.508	0%	0.084	0.464	72%	0.020	0.602
7.0	30	10%	0.178	0.590	0%	0.039	0.464	98%	0.020	0.632
7.0	40	0%	0.181	0.602	6%	0.021	0.464	98%	0.020	0.625
7.0	50	5%	0.164	0.646	36%	0.012	0.464	99%	0.021	0.671
7.0	70	45%	0.046	0.953	96%	0.004	0.464	100%	0.020	0.562
7.5	10	5%	0.325	0.394	0%	0.788	0.464	21%	0.042	0.838
7.5	20	0%	0.265	0.501	0%	0.344	0.464	78%	0.021	0.586
7.5	30	0%	0.280	0.493	0%	0.176	0.464	79%	0.020	0.638
7.5	40	0%	0.265	0.365	0%	0.098	0.464	91%	0.020	0.601
7.5	50	0%	0.212	0.501	0%	0.058	0.464	96%	0.021	0.646
7.5	70	0%	0.162	0.616	4%	0.022	0.464	99%	0.023	0.728
7.5	100	0%	0.089	0.889	84%	0.006	0.464	100%	0.024	0.713
8.0	10	5%	0.331	0.510	0%	1.824	0.464	14%	0.052	0.979
8.0	20	5%	0.307	0.393	0%	1.013	0.464	30%	0.033	0.818
8.0	30	10%	0.288	0.357	0%	0.595	0.464	82%	0.021	0.625
8.0	40	10%	0.281	0.402	0%	0.364	0.464	60%	0.024	0.668
8.0	50	10%	0.233	0.404	0%	0.229	0.464	74%	0.022	0.601
8.0	70	0%	0.201	0.533	0%	0.096	0.464	90%	0.022	0.580
8.0	100	0%	0.190	0.411	1%	0.029	0.464	99%	0.024	0.740

Table D.5: Compiled results of lateral spreading analysis for a site with T = 1m, N = 10, and $S = 1.5^{\circ}$

T_{liq} = 1 m, N = 10 blows/ft, Slope= 1.5°										
		FLIP			Youd et al.			Olson and Johnson		
M_w	R (km)	$P[D = d_0]$	μ_{D_H}	$\sigma_{\ln D_H}$	$P[D =_0]$	μ_{D_H}	$\sigma_{\ln D_H}$	$P[D = d_0]$	μ_{D_H}	$\sigma_{\ln D_H}$
6.0	10	5%	0.137	0.486	19%	0.015	0.464	38%	0.024	0.681
6.0	20	0%	0.140	0.578	96%	0.004	0.464	87%	0.023	0.695
6.0	30	0%	0.068	0.658	100%	0.002	0.464	98%	0.024	0.802
6.0	40	10%	0.056	0.859	100%	0.001	0.464	99%	0.027	0.920
6.0	50	40%	0.038	0.765	100%	0.001	0.464	100%	0.028	0.955
6.0	70	95%	0.038	0.000	100%	0.000	0.464	100%	0.043	0.983
6.0	100	100%	0.000	0.000	100%	0.000	0.464	100%	0.049	0.982
6.5	10	0%	0.203	0.778	0%	0.078	0.464	48%	0.027	0.770
6.5	20	0%	0.204	0.529	3%	0.025	0.464	87%	0.024	0.759
6.5	30	0%	0.223	0.480	43%	0.011	0.464	90%	0.024	0.862
6.5	40	0%	0.132	0.592	90%	0.006	0.464	99%	0.031	1.035
6.5	50	0%	0.129	0.603	99%	0.003	0.464	98%	0.031	1.021
6.5	70	0%	0.086	0.695	100%	0.001	0.464	99%	0.041	1.109
6.5	100	70%	0.021	0.535	100%	0.000	0.464	100%	0.048	1.231
7.0	10	0%	0.422	0.374	0%	0.346	0.464	1%	0.118	0.920
7.0	20	5%	0.335	0.745	0%	0.122	0.464	34%	0.033	0.890
7.0	30	0%	0.319	0.480	0%	0.057	0.464	88%	0.026	0.876
7.0	40	0%	0.338	0.392	1%	0.030	0.464	88%	0.025	0.885
7.0	50	0%	0.293	0.423	13%	0.017	0.464	94%	0.026	0.940
7.0	70	10%	0.107	0.847	84%	0.006	0.464	99%	0.035	1.127
7.5	10	0%	0.473	0.255	0%	1.142	0.464	1%	0.119	1.035
7.5	20	0%	0.413	0.373	0%	0.499	0.464	41%	0.031	0.869
7.5	30	0%	0.433	0.358	0%	0.255	0.464	42%	0.031	0.907
7.5	40	0%	0.389	0.304	0%	0.142	0.464	68%	0.027	0.849
7.5	50	0%	0.351	0.336	0%	0.084	0.464	81%	0.026	0.878
7.5	70	0%	0.323	0.504	1%	0.032	0.464	94%	0.030	0.981
7.5	100	0%	0.238	0.519	58%	0.009	0.464	98%	0.033	1.098
8.0	10	0%	0.530	0.217	0%	2.645	0.464	1%	0.206	1.064
8.0	20	0%	0.472	0.197	0%	1.468	0.464	5%	0.085	1.055
8.0	30	0%	0.364	0.548	0%	0.863	0.464	52%	0.030	0.905
8.0	40	0%	0.450	0.224	0%	0.527	0.464	29%	0.039	0.945
8.0	50	0%	0.393	0.245	0%	0.332	0.464	45%	0.031	0.879
8.0	70	0%	0.347	0.301	0%	0.140	0.464	70%	0.027	0.856
8.0	100	0%	0.306	0.325	0%	0.042	0.464	92%	0.029	1.010

Table D.6: Compiled results of lateral spreading analysis for a site with T = 1m, N = 10, and $S = 3.5^{\circ}$

T_{liq} = 1 m, N = 10 blows/ft, Slope= 3.5°										
			FLIP			Youd et al.			Olson and Johnson	
M_w	R (km)	$P[D = d_0]$	μ_{D_H}	$\sigma_{\ln D_H}$	$P[D = d_0]$	μ_{D_H}	$\sigma_{\ln D_H}$	$P[D = d_0]$	μ_{D_H}	$\sigma_{\ln D_H}$
6.0	10	0%	0.219	0.338	7%	0.020	0.464	6%	0.054	1.059
6.0	20	0%	0.206	0.349	87%	0.006	0.464	46%	0.036	1.041
6.0	30	0%	0.148	0.408	100%	0.003	0.464	78%	0.034	1.002
6.0	40	0%	0.121	0.559	100%	0.001	0.464	88%	0.035	1.018
6.0	50	0%	0.071	0.822	100%	0.001	0.464	94%	0.036	0.978
6.0	70	45%	0.073	0.541	100%	0.000	0.464	97%	0.042	0.993
6.0	100	100%	0.000	0.000	100%	0.000	0.464	99%	0.045	0.909
6.5	10	0%	0.323	0.229	0%	0.104	0.464	11%	0.067	1.192
6.5	20	0%	0.256	0.363	1%	0.033	0.464	45%	0.042	1.134
6.5	30	0%	0.283	0.358	21%	0.014	0.464	49%	0.048	1.216
6.5	40	0%	0.210	0.370	74%	0.007	0.464	81%	0.042	1.225
6.5	50	0%	0.208	0.369	97%	0.004	0.464	79%	0.042	1.216
6.5	70	0%	0.165	0.316	100%	0.002	0.464	90%	0.046	1.214
6.5	100	15%	0.096	0.406	100%	0.000	0.464	96%	0.056	1.213
7.0	10	0%	0.527	0.237	0%	0.461	0.464	0%	0.445	0.946
7.0	20	0%	0.464	0.226	0%	0.163	0.464	4%	0.112	1.285
7.0	30	0%	0.363	0.297	0%	0.076	0.464	44%	0.051	1.284
7.0	40	0%	0.388	0.245	0%	0.040	0.464	44%	0.051	1.309
7.0	50	0%	0.349	0.296	4%	0.023	0.464	60%	0.047	1.303
7.0	70	0%	0.183	0.670	65%	0.008	0.464	90%	0.047	1.225
7.5	10	0%	0.587	0.238	0%	1.521	0.464	0%	0.534	1.031
7.5	20	0%	0.440	0.236	0%	0.665	0.464	6%	0.095	1.279
7.5	30	0%	0.468	0.199	0%	0.340	0.464	6%	0.102	1.345
7.5	40	0%	0.458	0.180	0%	0.189	0.464	20%	0.064	1.325
7.5	50	0%	0.420	0.211	0%	0.112	0.464	33%	0.057	1.319
7.5	70	0%	0.405	0.208	0%	0.043	0.464	59%	0.054	1.311
7.5	100	0%	0.312	0.212	34%	0.012	0.464	80%	0.052	1.321
8.0	10	0%	0.642	0.248	0%	3.523	0.464	0%	0.899	1.039
8.0	20	0%	0.546	0.304	0%	1.955	0.464	0%	0.395	1.162
8.0	30	0%	0.446	0.191	0%	1.149	0.464	12%	0.092	1.376
8.0	40	0%	0.465	0.206	0%	0.702	0.464	3%	0.141	1.346
8.0	50	0%	0.447	0.183	0%	0.442	0.464	10%	0.094	1.339
8.0	70	0%	0.400	0.295	0%	0.186	0.464	23%	0.068	1.317
8.0	100	0%	0.380	0.241	0%	0.056	0.464	55%	0.060	1.383

Table D.7: Compiled results of lateral spreading analysis for a site with T = 1m, N = 15, and $S = 0.5^{\circ}$

T_{liq} = 1 m, N = 15 blows/ft, Slope= 0.5°										
			FLIP			Youd et al.			Olson and Johnson	
M_w	R (km)	$P[D = d_0]$	μ_{D_H}	$\sigma_{\ln D_H}$	$P[D = d_0]$	μ_{D_H}	$\sigma_{\ln D_H}$	$P[D = d_0]$	μ_{D_H}	$\sigma_{\ln D_H}$
6.0	10	0%	0.037	0.570	47%	0.010	0.464	95%	0.019	0.488
6.0	20	30%	0.039	0.745	99%	0.003	0.464	100%	0.018	0.435
6.0	30	80%	0.013	0.295	100%	0.001	0.464	100%	0.018	0.444
6.0	40	90%	0.018	0.139	100%	0.001	0.464	100%	0.018	0.444
6.0	50	100%	0.000	0.000	100%	0.000	0.464	100%	0.018	0.444
6.0	70	100%	0.000	0.000	100%	0.000	0.464	100%	0.018	0.444
6.0	100	100%	0.000	0.000	100%	0.000	0.464	100%	0.018	0.444
6.5	10	5%	0.065	0.702	0%	0.054	0.464	97%	0.017	0.393
6.5	20	5%	0.042	0.760	13%	0.017	0.464	100%	0.019	0.478
6.5	30	5%	0.057	0.712	73%	0.007	0.464	100%	0.013	0.169
6.5	40	70%	0.024	0.347	98%	0.004	0.464	100%	0.013	0.124
6.5	50	50%	0.023	0.401	100%	0.002	0.464	100%	0.013	0.124
6.5	70	100%	0.000	0.000	100%	0.001	0.464	100%	0.013	0.124
6.5	100	100%	0.000	0.000	100%	0.000	0.464	100%	0.013	0.124
7.0	10	10%	0.153	0.764	0%	0.239	0.464	44%	0.023	0.559
7.0	20	15%	0.160	0.623	0%	0.084	0.464	96%	0.013	0.318
7.0	30	0%	0.104	0.778	0%	0.039	0.464	100%	0.014	0.235
7.0	40	0%	0.116	0.735	6%	0.021	0.464	100%	0.013	0.192
7.0	50	10%	0.083	0.639	36%	0.012	0.464	100%	0.011	0.024
7.0	70	100%	0.000	0.000	96%	0.004	0.464	100%	0.011	0.024
7.5	10	5%	0.222	0.358	0%	0.788	0.464	48%	0.025	0.597
7.5	20	5%	0.155	0.587	0%	0.344	0.464	98%	0.015	0.326
7.5	30	5%	0.173	0.571	0%	0.176	0.464	98%	0.013	0.347
7.5	40	0%	0.149	0.574	0%	0.098	0.464	100%	0.015	0.302
7.5	50	0%	0.125	0.638	0%	0.058	0.464	100%	0.014	0.244
7.5	70	0%	0.083	0.862	4%	0.022	0.464	100%	0.013	0.175
7.5	100	50%	0.033	0.982	84%	0.006	0.464	100%	0.013	0.175
8.0	10	5%	0.210	0.337	0%	1.824	0.464	30%	0.032	0.732
8.0	20	5%	0.172	0.524	0%	1.013	0.464	64%	0.021	0.542
8.0	30	0%	0.148	0.731	0%	0.595	0.464	98%	0.016	0.357
8.0	40	5%	0.161	0.558	0%	0.364	0.464	92%	0.017	0.388
8.0	50	0%	0.150	0.501	0%	0.229	0.464	96%	0.017	0.352
8.0	70	0%	0.124	0.469	0%	0.096	0.464	99%	0.016	0.309
8.0	100	0%	0.088	0.447	1%	0.029	0.464	100%	0.014	0.185

Table D.8: Compiled results of lateral spreading analysis for a site with T = 1m, N = 15, and $S = 1.5^{\circ}$

T_{liq} = 1 m, N = 15 blows/ft, Slope= 1.5°										
			FLIP			Youd et al.			Olson and Johnson	
M_w	R (km)	$P[D = d_0]$	μ_{D_H}	$\sigma_{\ln D_H}$	$P[D = d_0]$	μ_{D_H}	$\sigma_{\ln D_H}$	$P[D = d_0]$	μ_{D_H}	$\sigma_{\ln D_H}$
6.0	10	5%	0.076	0.380	19%	0.015	0.464	79%	0.019	0.467
6.0	20	0%	0.059	0.647	96%	0.004	0.464	99%	0.018	0.436
6.0	30	55%	0.027	0.496	100%	0.002	0.464	100%	0.013	0.227
6.0	40	80%	0.029	0.769	100%	0.001	0.464	100%	0.013	0.207
6.0	50	100%	0.000	0.000	100%	0.001	0.464	100%	0.013	0.207
6.0	70	100%	0.000	0.000	100%	0.000	0.464	100%	0.013	0.207
6.0	100	100%	0.000	0.000	100%	0.000	0.464	100%	0.013	0.207
6.5	10	0%	0.124	0.394	0%	0.078	0.464	89%	0.019	0.460
6.5	20	0%	0.080	0.597	3%	0.025	0.464	99%	0.019	0.463
6.5	30	0%	0.102	0.583	43%	0.011	0.464	100%	0.016	0.369
6.5	40	30%	0.041	0.609	90%	0.006	0.464	100%	0.013	0.109
6.5	50	15%	0.042	0.690	99%	0.003	0.464	100%	0.014	0.222
6.5	70	85%	0.016	0.342	100%	0.001	0.464	100%	0.014	0.222
6.5	100	100%	0.000	0.000	100%	0.000	0.464	100%	0.014	0.222
7.0	10	5%	0.236	0.402	0%	0.346	0.464	10%	0.040	0.778
7.0	20	0%	0.236	0.437	0%	0.122	0.464	81%	0.018	0.492
7.0	30	0%	0.147	0.524	0%	0.057	0.464	100%	0.017	0.418
7.0	40	0%	0.163	0.510	1%	0.030	0.464	100%	0.017	0.398
7.0	50	0%	0.128	0.489	13%	0.017	0.464	100%	0.015	0.366
7.0	70	95%	0.128	0.000	84%	0.006	0.464	100%	0.010	0.036
7.5	10	0%	0.298	0.415	0%	1.142	0.464	9%	0.042	0.817
7.5	20	0%	0.217	0.470	0%	0.499	0.464	87%	0.018	0.482
7.5	30	0%	0.244	0.399	0%	0.255	0.464	88%	0.018	0.498
7.5	40	0%	0.209	0.380	0%	0.142	0.464	97%	0.017	0.469
7.5	50	0%	0.188	0.422	0%	0.084	0.464	99%	0.017	0.475
7.5	70	0%	0.153	0.514	1%	0.032	0.464	100%	0.017	0.436
7.5	100	20%	0.047	1.015	58%	0.009	0.464	100%	0.013	0.175
8.0	10	0%	0.339	0.267	0%	2.645	0.464	6%	0.072	0.911
8.0	20	0%	0.248	0.462	0%	1.468	0.464	27%	0.033	0.740
8.0	30	0%	0.217	0.388	0%	0.863	0.464	91%	0.018	0.489
8.0	40	0%	0.227	0.424	0%	0.527	0.464	75%	0.020	0.545
8.0	50	0%	0.213	0.344	0%	0.332	0.464	87%	0.019	0.468
8.0	70	0%	0.181	0.499	0%	0.140	0.464	97%	0.018	0.437
8.0	100	0%	0.150	0.369	0%	0.042	0.464	100%	0.017	0.424

Table D.9: Compiled results of lateral spreading analysis for a site with T = 1m, N = 15, and $S = 3.5^{\circ}$

T_{liq} = 1 m, N = 15 blows/ft, Slope= 3.5°										
			FLIP			Youd et al.			Olson and Johnson	
M_w	R (km)	$P[D = d_0]$	μ_{D_H}	$\sigma_{\ln D_H}$	$P[D = d_0]$	μ_{D_H}	$\sigma_{\ln D_H}$	$P[D = d_0]$	μ_{D_H}	$\sigma_{\ln D_H}$
6.0	10	0%	0.108	0.306	7%	0.020	0.464	36%	0.024	0.679
6.0	20	0%	0.099	0.346	87%	0.006	0.464	89%	0.022	0.670
6.0	30	10%	0.047	0.609	100%	0.003	0.464	98%	0.023	0.780
6.0	40	60%	0.052	0.729	100%	0.001	0.464	99%	0.025	0.918
6.0	50	95%	0.052	0.000	100%	0.001	0.464	100%	0.029	0.951
6.0	70	100%	0.000	0.000	100%	0.000	0.464	100%	0.043	0.998
6.0	100	100%	0.000	0.000	100%	0.000	0.464	100%	0.036	1.102
6.5	10	0%	0.155	0.281	0%	0.104	0.464	49%	0.026	0.750
6.5	20	0%	0.116	0.345	1%	0.033	0.464	89%	0.022	0.733
6.5	30	0%	0.136	0.356	21%	0.014	0.464	92%	0.024	0.840
6.5	40	5%	0.072	0.686	74%	0.007	0.464	99%	0.029	1.020
6.5	50	5%	0.086	0.516	97%	0.004	0.464	99%	0.029	0.999
6.5	70	40%	0.031	0.789	100%	0.002	0.464	100%	0.039	1.105
6.5	100	100%	0.000	0.000	100%	0.000	0.464	100%	0.046	1.238
7.0	10	0%	0.275	0.328	0%	0.461	0.464	0%	0.135	0.876
7.0	20	0%	0.256	0.334	0%	0.163	0.464	31%	0.032	0.878
7.0	30	0%	0.181	0.309	0%	0.076	0.464	89%	0.025	0.848
7.0	40	0%	0.193	0.242	0%	0.040	0.464	90%	0.024	0.851
7.0	50	0%	0.177	0.302	4%	0.023	0.464	95%	0.026	0.919
7.0	70	65%	0.048	0.791	65%	0.008	0.464	100%	0.034	1.116
7.5	10	0%	0.339	0.327	0%	1.521	0.464	0%	0.162	0.910
7.5	20	0%	0.230	0.388	0%	0.665	0.464	41%	0.030	0.853
7.5	30	0%	0.255	0.302	0%	0.340	0.464	43%	0.030	0.887
7.5	40	0%	0.229	0.292	0%	0.189	0.464	71%	0.026	0.816
7.5	50	0%	0.212	0.293	0%	0.112	0.464	84%	0.026	0.850
7.5	70	0%	0.191	0.301	0%	0.043	0.464	95%	0.029	0.956
7.5	100	5%	0.089	0.732	34%	0.012	0.464	99%	0.032	1.077
8.0	10	0%	0.411	0.265	0%	3.523	0.464	0%	0.266	0.997
8.0	20	0%	0.328	0.305	0%	1.955	0.464	2%	0.094	1.050
8.0	30	0%	0.229	0.289	0%	1.149	0.464	55%	0.029	0.884
8.0	40	0%	0.262	0.270	0%	0.702	0.464	29%	0.037	0.934
8.0	50	0%	0.248	0.205	0%	0.442	0.464	47%	0.029	0.857
8.0	70	0%	0.215	0.272	0%	0.186	0.464	72%	0.026	0.815
8.0	100	0%	0.186	0.262	0%	0.056	0.464	94%	0.030	0.975

Table D.10: Compiled results of lateral spreading analysis for a site with T = 1m, N = 20, and $S = 0.5^{\circ}$

T_{liq} = 1 m, N = 20 blows/ft, Slope= 0.5°										
			FLIP			Youd et al.			Olson and Johnson	
M_w	R (km)	$P[D = d_0]$	μ_{D_H}	$\sigma_{\ln D_H}$	$P[D = d_0]$	μ_{D_H}	$\sigma_{\ln D_H}$	$P[D = d_0]$	μ_{D_H}	$\sigma_{\ln D_H}$
6.0	10	5%	0.032	0.425	100%	0.000	0.464	99%	0.019	0.459
6.0	20	25%	0.037	0.661	100%	0.000	0.464	100%	0.018	0.449
6.0	30	85%	0.015	0.399	100%	0.000	0.464	100%	0.018	0.449
6.0	40	100%	0.000	0.000	100%	0.000	0.464	100%	0.018	0.449
6.0	50	100%	0.000	0.000	100%	0.000	0.464	100%	0.018	0.449
6.0	70	100%	0.000	0.000	100%	0.000	0.464	100%	0.018	0.449
6.0	100	100%	0.000	0.000	100%	0.000	0.464	100%	0.018	0.449
6.5	10	0%	0.057	0.730	100%	0.000	0.464	100%	0.013	0.266
6.5	20	5%	0.037	0.761	100%	0.000	0.464	100%	0.011	0.049
6.5	30	5%	0.052	0.765	100%	0.000	0.464	100%	0.011	0.049
6.5	40	70%	0.021	0.382	100%	0.000	0.464	100%	0.011	0.049
6.5	50	55%	0.019	0.398	100%	0.000	0.464	100%	0.011	0.049
6.5	70	100%	0.000	0.000	100%	0.000	0.464	100%	0.011	0.049
6.5	100	100%	0.000	0.000	100%	0.000	0.464	100%	0.011	0.049
7.0	10	15%	0.163	0.447	100%	0.000	0.464	74%	0.019	0.405
7.0	20	10%	0.141	0.695	100%	0.000	0.464	100%	0.012	0.158
7.0	30	5%	0.108	0.730	100%	0.000	0.464	100%	0.011	0.046
7.0	40	5%	0.117	0.724	100%	0.000	0.464	100%	0.011	0.046
7.0	50	10%	0.079	0.627	100%	0.000	0.464	100%	0.011	0.046
7.0	70	100%	0.000	0.000	100%	0.000	0.464	100%	0.011	0.046
7.5	10	5%	0.186	0.361	100%	0.000	0.464	75%	0.019	0.439
7.5	20	10%	0.157	0.578	100%	0.000	0.464	100%	0.014	0.249
7.5	30	10%	0.177	0.531	100%	0.000	0.464	100%	0.012	0.088
7.5	40	0%	0.143	0.640	100%	0.000	0.464	100%	0.011	0.071
7.5	50	0%	0.121	0.633	100%	0.000	0.464	100%	0.011	0.071
7.5	70	0%	0.082	0.806	100%	0.000	0.464	100%	0.011	0.071
7.5	100	60%	0.041	0.901	100%	0.000	0.464	100%	0.011	0.071
8.0	10	10%	0.191	0.301	100%	0.000	0.464	52%	0.024	0.587
8.0	20	10%	0.170	0.497	100%	0.000	0.464	90%	0.016	0.351
8.0	30	10%	0.160	0.532	100%	0.000	0.464	100%	0.017	0.367
8.0	40	10%	0.157	0.501	100%	0.000	0.464	100%	0.015	0.263
8.0	50	5%	0.146	0.484	100%	0.000	0.464	100%	0.015	0.224
8.0	70	0%	0.108	0.571	100%	0.000	0.464	100%	0.014	0.198
8.0	100	0%	0.083	0.472	100%	0.000	0.464	100%	0.014	0.198

Table D.11: Compiled results of lateral spreading analysis for a site with T = 1m, N = 20, and $S = 1.5^{\circ}$

T_{liq} = 1 m, N = 20 blows/ft, Slope= 1.5°										
			FLIP			Youd et al.			Olson and Johnson	
M_w	R (km)	$P[D = d_0]$	μ_{D_H}	$\sigma_{\ln D_H}$	$P[D = d_0]$	μ_{D_H}	$\sigma_{\ln D_H}$	$P[D = d_0]$	μ_{D_H}	$\sigma_{\ln D_H}$
6.0	10	5%	0.069	0.370	100%	0.000	0.464	97%	0.018	0.422
6.0	20	0%	0.057	0.634	100%	0.000	0.464	100%	0.017	0.412
6.0	30	65%	0.025	0.548	100%	0.000	0.464	100%	0.017	0.412
6.0	40	90%	0.056	0.115	100%	0.000	0.464	100%	0.017	0.412
6.0	50	100%	0.000	0.000	100%	0.000	0.464	100%	0.017	0.412
6.0	70	100%	0.000	0.000	100%	0.000	0.464	100%	0.017	0.412
6.0	100	100%	0.000	0.000	100%	0.000	0.464	100%	0.017	0.412
6.5	10	0%	0.112	0.478	100%	0.000	0.464	99%	0.015	0.349
6.5	20	0%	0.073	0.574	100%	0.000	0.464	100%	0.011	0.052
6.5	30	0%	0.093	0.589	100%	0.000	0.464	100%	0.011	0.052
6.5	40	45%	0.039	0.610	100%	0.000	0.464	100%	0.011	0.052
6.5	50	30%	0.044	0.525	100%	0.000	0.464	100%	0.011	0.052
6.5	70	95%	0.044	0.000	100%	0.000	0.464	100%	0.011	0.052
6.5	100	100%	0.000	0.000	100%	0.000	0.464	100%	0.011	0.052
7.0	10	0%	0.210	0.444	100%	0.000	0.464	39%	0.021	0.524
7.0	20	0%	0.218	0.399	100%	0.000	0.464	98%	0.014	0.278
7.0	30	0%	0.132	0.590	100%	0.000	0.464	100%	0.012	0.148
7.0	40	0%	0.150	0.495	100%	0.000	0.464	100%	0.012	0.148
7.0	50	0%	0.120	0.486	100%	0.000	0.464	100%	0.012	0.148
7.0	70	95%	0.120	0.000	100%	0.000	0.464	100%	0.012	0.148
7.5	10	0%	0.236	0.745	100%	0.000	0.464	36%	0.023	0.558
7.5	20	0%	0.191	0.482	100%	0.000	0.464	99%	0.014	0.276
7.5	30	0%	0.211	0.438	100%	0.000	0.464	99%	0.014	0.265
7.5	40	0%	0.195	0.393	100%	0.000	0.464	100%	0.012	0.203
7.5	50	0%	0.169	0.406	100%	0.000	0.464	100%	0.011	0.066
7.5	70	0%	0.143	0.537	100%	0.000	0.464	100%	0.011	0.066
7.5	100	40%	0.052	0.923	100%	0.000	0.464	100%	0.011	0.066
8.0	10	0%	0.301	0.354	100%	0.000	0.464	19%	0.035	0.737
8.0	20	0%	0.246	0.499	100%	0.000	0.464	66%	0.019	0.498
8.0	30	0%	0.192	0.425	100%	0.000	0.464	100%	0.015	0.295
8.0	40	0%	0.202	0.418	100%	0.000	0.464	98%	0.016	0.324
8.0	50	0%	0.192	0.319	100%	0.000	0.464	99%	0.016	0.285
8.0	70	5%	0.171	0.382	100%	0.000	0.464	100%	0.014	0.222
8.0	100	0%	0.132	0.368	100%	0.000	0.464	100%	0.013	0.180

Table D.12: Compiled results of lateral spreading analysis for a site with T = 1m, N = 20, and $S = 3.5^{\circ}$

T_{liq} = 1 m, N = 20 blows/ft, Slope= 3.5°										
		FLIP			Youd et al.			Olson and Johnson		
M_w	R (km)	$P[D = d_0]$	μ_{D_H}	$\sigma_{\ln D_H}$	$P[D = d_0]$	μ_{D_H}	$\sigma_{\ln D_H}$	$P[D = d_0]$	μ_{D_H}	$\sigma_{\ln D_H}$
6.0	10	0%	0.061	0.424	100%	0.000	0.464	79%	0.019	0.469
6.0	20	15%	0.050	0.768	100%	0.000	0.464	99%	0.018	0.421
6.0	30	95%	0.050	0.000	100%	0.000	0.464	100%	0.014	0.236
6.0	40	100%	0.000	0.000	100%	0.000	0.464	100%	0.014	0.236
6.0	50	100%	0.000	0.000	100%	0.000	0.464	100%	0.014	0.236
6.0	70	100%	0.000	0.000	100%	0.000	0.464	100%	0.014	0.236
6.0	100	100%	0.000	0.000	100%	0.000	0.464	100%	0.014	0.236
6.5	10	0%	0.109	0.508	100%	0.000	0.464	89%	0.018	0.460
6.5	20	0%	0.056	0.820	100%	0.000	0.464	100%	0.018	0.437
6.5	30	0%	0.077	0.853	100%	0.000	0.464	100%	0.016	0.347
6.5	40	95%	0.077	0.000	100%	0.000	0.464	100%	0.011	0.088
6.5	50	90%	0.012	0.098	100%	0.000	0.464	100%	0.011	0.088
6.5	70	100%	0.000	0.000	100%	0.000	0.464	100%	0.011	0.088
6.5	100	100%	0.000	0.000	100%	0.000	0.464	100%	0.011	0.088
7.0	10	0%	0.200	0.409	100%	0.000	0.464	6%	0.044	0.793
7.0	20	0%	0.201	0.339	100%	0.000	0.464	81%	0.018	0.493
7.0	30	0%	0.128	0.609	100%	0.000	0.464	100%	0.016	0.399
7.0	40	0%	0.147	0.510	100%	0.000	0.464	100%	0.016	0.368
7.0	50	0%	0.102	0.610	100%	0.000	0.464	100%	0.016	0.314
7.0	70	100%	0.000	0.000	100%	0.000	0.464	100%	0.012	0.035
7.5	10	0%	0.205	0.758	100%	0.000	0.464	4%	0.054	0.830
7.5	20	0%	0.177	0.495	100%	0.000	0.464	88%	0.018	0.485
7.5	30	0%	0.194	0.414	100%	0.000	0.464	89%	0.018	0.499
7.5	40	0%	0.183	0.407	100%	0.000	0.464	98%	0.017	0.459
7.5	50	0%	0.170	0.381	100%	0.000	0.464	99%	0.016	0.448
7.5	70	20%	0.115	0.623	100%	0.000	0.464	100%	0.017	0.406
7.5	100	100%	0.000	0.000	100%	0.000	0.464	100%	0.012	0.096
8.0	10	0%	0.275	0.261	100%	0.000	0.464	2%	0.086	0.944
8.0	20	0%	0.223	0.516	100%	0.000	0.464	19%	0.033	0.769
8.0	30	0%	0.180	0.368	100%	0.000	0.464	93%	0.018	0.483
8.0	40	0%	0.185	0.393	100%	0.000	0.464	77%	0.020	0.534
8.0	50	0%	0.186	0.324	100%	0.000	0.464	89%	0.019	0.453
8.0	70	5%	0.171	0.343	100%	0.000	0.464	98%	0.018	0.425
8.0	100	10%	0.118	0.548	100%	0.000	0.464	100%	0.018	0.357

Table D.13: Compiled results of lateral spreading analysis for a site with T = 3m, N = 5, and $S = 0.5^{\circ}$

T_{liq} = 3 m, N = 5 blows/ft, Slope= 0.5°										
			FLIP			Youd et al.			Olson and Johnson	
M_w	R (km)	$P[D = d_0]$	μ_{D_H}	$\sigma_{\ln D_H}$	$P[D = d_0]$	μ_{D_H}	$\sigma_{\ln D_H}$	$P[D = d_0]$	μ_{D_H}	$\sigma_{\ln D_H}$
6.0	10	0%	0.167	0.597	9%	0.019	0.464	41%	0.028	0.829
6.0	20	0%	0.092	0.914	90%	0.006	0.464	71%	0.027	0.874
6.0	30	5%	0.044	0.790	100%	0.002	0.464	91%	0.027	0.922
6.0	40	20%	0.037	0.781	100%	0.001	0.464	96%	0.032	0.980
6.0	50	45%	0.025	0.520	100%	0.001	0.464	98%	0.031	0.989
6.0	70	65%	0.015	0.258	100%	0.000	0.464	99%	0.040	1.009
6.0	100	100%	0.000	0.000	100%	0.000	0.464	100%	0.042	0.991
6.5	10	0%	0.371	0.509	0%	0.098	0.464	37%	0.037	0.964
6.5	20	0%	0.156	0.873	1%	0.031	0.464	70%	0.030	0.956
6.5	30	0%	0.201	0.812	26%	0.014	0.464	75%	0.033	1.081
6.5	40	0%	0.082	0.699	78%	0.007	0.464	93%	0.035	1.152
6.5	50	0%	0.083	0.887	98%	0.004	0.464	92%	0.036	1.142
6.5	70	5%	0.040	0.654	100%	0.001	0.464	96%	0.040	1.186
6.5	100	40%	0.021	0.560	100%	0.000	0.464	99%	0.051	1.214
7.0	10	0%	0.844	0.452	0%	0.432	0.464	3%	0.106	1.091
7.0	20	0%	0.601	0.512	0%	0.153	0.464	29%	0.045	1.115
7.0	30	0%	0.335	0.480	0%	0.071	0.464	72%	0.035	1.128
7.0	40	0%	0.373	0.344	0%	0.037	0.464	71%	0.035	1.131
7.0	50	0%	0.290	0.444	5%	0.021	0.464	81%	0.035	1.161
7.0	70	10%	0.068	0.885	70%	0.008	0.464	96%	0.042	1.191
7.5	10	0%	0.959	0.382	0%	1.425	0.464	7%	0.107	1.203
7.5	20	0%	0.579	0.502	0%	0.623	0.464	33%	0.041	1.076
7.5	30	0%	0.635	0.461	0%	0.318	0.464	32%	0.044	1.158
7.5	40	0%	0.509	0.331	0%	0.178	0.464	49%	0.036	1.107
7.5	50	0%	0.425	0.340	0%	0.105	0.464	61%	0.036	1.123
7.5	70	0%	0.293	0.529	0%	0.040	0.464	80%	0.041	1.168
7.5	100	0%	0.162	0.631	40%	0.011	0.464	91%	0.041	1.232
8.0	10	0%	1.110	0.286	0%	3.302	0.464	4%	0.151	1.315
8.0	20	0%	0.921	0.405	0%	1.833	0.464	9%	0.090	1.242
8.0	30	0%	0.623	0.291	0%	1.077	0.464	36%	0.044	1.161
8.0	40	0%	0.685	0.298	0%	0.658	0.464	18%	0.060	1.160
8.0	50	0%	0.525	0.313	0%	0.414	0.464	29%	0.046	1.127
8.0	70	0%	0.432	0.379	0%	0.174	0.464	48%	0.040	1.101
8.0	100	0%	0.372	0.293	0%	0.053	0.464	78%	0.042	1.240

Table D.14: Compiled results of lateral spreading analysis for a site with T = 3m, N = 5, and $S = 1.5^{\circ}$

T_{liq} = 3 m, N = 5 blows/ft, Slope= 1.5°										
			FLIP			Youd et al.			Olson and Johnson	
M_w	R (km)	$P[D = d_0]$	μ_{D_H}	$\sigma_{\ln D_H}$	$P[D = d_0]$	μ_{D_H}	$\sigma_{\ln D_H}$	$P[D = d_0]$	μ_{D_H}	$\sigma_{\ln D_H}$
6.0	10	0%	0.414	0.484	2%	0.027	0.464	8%	0.053	1.070
6.0	20	0%	0.342	0.646	68%	0.008	0.464	43%	0.038	1.066
6.0	30	0%	0.146	0.773	99%	0.004	0.464	75%	0.034	1.013
6.0	40	0%	0.108	0.925	100%	0.002	0.464	87%	0.036	1.023
6.0	50	0%	0.061	0.957	100%	0.001	0.464	93%	0.037	0.981
6.0	70	10%	0.038	0.924	100%	0.000	0.464	96%	0.041	1.001
6.0	100	75%	0.021	0.698	100%	0.000	0.464	98%	0.043	0.927
6.5	10	0%	0.845	0.370	0%	0.142	0.464	10%	0.071	1.214
6.5	20	0%	0.539	0.595	0%	0.044	0.464	42%	0.044	1.161
6.5	30	0%	0.640	0.546	7%	0.020	0.464	45%	0.050	1.242
6.5	40	0%	0.331	0.537	49%	0.010	0.464	79%	0.045	1.231
6.5	50	0%	0.324	0.585	89%	0.006	0.464	77%	0.044	1.229
6.5	70	0%	0.176	0.620	100%	0.002	0.464	88%	0.048	1.217
6.5	100	0%	0.077	0.761	100%	0.001	0.464	95%	0.056	1.214
7.0	10	0%	1.686	0.250	0%	0.626	0.464	0%	0.410	0.998
7.0	20	0%	1.457	0.363	0%	0.222	0.464	4%	0.112	1.339
7.0	30	0%	0.917	0.493	0%	0.103	0.464	41%	0.054	1.312
7.0	40	0%	1.054	0.337	0%	0.054	0.464	41%	0.055	1.333
7.0	50	0%	0.913	0.360	1%	0.031	0.464	55%	0.048	1.336
7.0	70	0%	0.229	0.998	39%	0.011	0.464	89%	0.049	1.225
7.5	10	0%	1.765	0.330	0%	2.066	0.464	0%	0.445	1.163
7.5	20	0%	1.406	0.403	0%	0.903	0.464	6%	0.099	1.309
7.5	30	0%	1.510	0.367	0%	0.462	0.464	6%	0.108	1.374
7.5	40	0%	1.320	0.311	0%	0.257	0.464	18%	0.069	1.353
7.5	50	0%	1.152	0.294	0%	0.152	0.464	30%	0.061	1.348
7.5	70	0%	0.871	0.394	0%	0.059	0.464	56%	0.059	1.329
7.5	100	0%	0.576	0.423	14%	0.016	0.464	77%	0.055	1.329
8.0	10	0%	1.929	0.222	0%	4.786	0.464	0%	0.752	1.148
8.0	20	0%	1.734	0.324	0%	2.657	0.464	1%	0.359	1.259
8.0	30	0%	1.418	0.300	0%	1.561	0.464	11%	0.099	1.400
8.0	40	0%	1.551	0.276	0%	0.954	0.464	4%	0.152	1.358
8.0	50	0%	1.298	0.303	0%	0.600	0.464	9%	0.101	1.365
8.0	70	0%	1.081	0.340	0%	0.253	0.464	20%	0.073	1.343
8.0	100	0%	0.903	0.219	0%	0.076	0.464	51%	0.065	1.406

Table D.15: Compiled results of lateral spreading analysis for a site with T = 3m, N = 5, and $S = 3.5^{\circ}$

T_{liq} = 3 m, N = 5 blows/ft, Slope= 3.5°										
			FLIP			Youd et al.			Olson and Johnson	
M_w	R (km)	$P[D = d_0]$	μ_{D_H}	$\sigma_{\ln D_H}$	$P[D = d_0]$	μ_{D_H}	$\sigma_{\ln D_H}$	$P[D = d_0]$	μ_{D_H}	$\sigma_{\ln D_H}$
6.0	10	0%	0.831	0.388	0%	0.036	0.464	0%	0.153	1.119
6.0	20	0%	0.747	0.473	44%	0.011	0.464	11%	0.078	1.252
6.0	30	0%	0.399	0.565	95%	0.005	0.464	35%	0.051	1.119
6.0	40	0%	0.316	0.734	100%	0.002	0.464	55%	0.045	1.076
6.0	50	0%	0.208	0.665	100%	0.001	0.464	69%	0.040	0.995
6.0	70	0%	0.141	0.929	100%	0.000	0.464	83%	0.042	0.958
6.0	100	30%	0.072	0.994	100%	0.000	0.464	91%	0.039	0.883
6.5	10	0%	1.406	0.268	0%	0.189	0.464	1%	0.226	1.275
6.5	20	0%	1.013	0.457	0%	0.059	0.464	10%	0.104	1.325
6.5	30	0%	1.128	0.393	2%	0.026	0.464	10%	0.122	1.368
6.5	40	0%	0.713	0.484	26%	0.013	0.464	40%	0.074	1.297
6.5	50	0%	0.690	0.483	73%	0.008	0.464	38%	0.073	1.314
6.5	70	0%	0.492	0.269	100%	0.003	0.464	58%	0.064	1.240
6.5	100	0%	0.268	0.226	100%	0.001	0.464	77%	0.056	1.200
7.0	10	0%	2.111	0.207	0%	0.834	0.464	0%	1.171	0.987
7.0	20	0%	1.913	0.264	0%	0.295	0.464	0%	0.443	1.299
7.0	30	0%	1.600	0.425	0%	0.137	0.464	8%	0.146	1.474
7.0	40	0%	1.775	0.300	0%	0.072	0.464	8%	0.149	1.523
7.0	50	0%	1.646	0.347	0%	0.041	0.464	16%	0.110	1.527
7.0	70	0%	0.672	0.592	18%	0.015	0.464	58%	0.060	1.273
7.5	10	0%	2.244	0.217	0%	2.753	0.464	0%	1.447	1.051
7.5	20	0%	1.935	0.232	0%	1.203	0.464	0%	0.372	1.311
7.5	30	0%	2.023	0.223	0%	0.615	0.464	0%	0.433	1.379
7.5	40	0%	1.948	0.283	0%	0.343	0.464	2%	0.242	1.498
7.5	50	0%	1.832	0.307	0%	0.202	0.464	5%	0.186	1.530
7.5	70	0%	1.670	0.290	0%	0.078	0.464	16%	0.123	1.517
7.5	100	0%	1.188	0.407	5%	0.022	0.464	38%	0.090	1.439
8.0	10	0%	2.359	0.206	0%	6.376	0.464	0%	2.403	1.000
8.0	20	0%	2.247	0.180	0%	3.539	0.464	0%	1.283	1.088
8.0	30	0%	1.933	0.231	0%	2.080	0.464	1%	0.394	1.415
8.0	40	0%	2.046	0.183	0%	1.271	0.464	0%	0.610	1.295
8.0	50	0%	1.934	0.233	0%	0.799	0.464	1%	0.388	1.368
8.0	70	0%	1.770	0.265	0%	0.336	0.464	3%	0.247	1.430
8.0	100	0%	1.547	0.197	0%	0.102	0.464	13%	0.162	1.544

Table D.16: Compiled results of lateral spreading analysis for a site with T = 3m, N = 10, and $S = 0.5^{\circ}$

T_{liq} = 3 m, N = 10 blows/ft, Slope= 0.5°										
		FLIP			Youd et al.			Olson and Johnson		
M_w	R (km)	$P[D = d_0]$	μ_{D_H}	$\sigma_{\ln D_H}$	$P[D = d_0]$	μ_{D_H}	$\sigma_{\ln D_H}$	$P[D = d_0]$	μ_{D_H}	$\sigma_{\ln D_H}$
6.0	10	0%	0.132	0.568	9%	0.019	0.464	76%	0.021	0.550
6.0	20	5%	0.061	0.908	90%	0.006	0.464	97%	0.020	0.527
6.0	30	20%	0.028	0.814	100%	0.002	0.464	100%	0.019	0.524
6.0	40	40%	0.028	0.531	100%	0.001	0.464	100%	0.020	0.498
6.0	50	60%	0.017	0.388	100%	0.001	0.464	100%	0.017	0.387
6.0	70	100%	0.000	0.000	100%	0.000	0.464	100%	0.012	0.016
6.0	100	100%	0.000	0.000	100%	0.000	0.464	100%	0.012	0.016
6.5	10	0%	0.201	0.775	0%	0.098	0.464	78%	0.021	0.554
6.5	20	5%	0.101	0.805	1%	0.031	0.464	97%	0.020	0.567
6.5	30	0%	0.126	0.732	26%	0.014	0.464	98%	0.019	0.625
6.5	40	5%	0.054	0.641	78%	0.007	0.464	100%	0.021	0.647
6.5	50	5%	0.053	0.696	98%	0.004	0.464	100%	0.022	0.660
6.5	70	15%	0.028	0.588	100%	0.001	0.464	100%	0.024	0.552
6.5	100	95%	0.028	0.000	100%	0.000	0.464	100%	0.016	0.269
7.0	10	0%	0.685	0.392	0%	0.432	0.464	17%	0.038	0.795
7.0	20	0%	0.434	0.608	0%	0.153	0.464	72%	0.020	0.602
7.0	30	0%	0.205	0.622	0%	0.071	0.464	98%	0.020	0.632
7.0	40	0%	0.248	0.466	0%	0.037	0.464	98%	0.020	0.625
7.0	50	0%	0.191	0.549	5%	0.021	0.464	99%	0.021	0.671
7.0	70	25%	0.039	0.884	70%	0.008	0.464	100%	0.020	0.562
7.5	10	0%	0.687	0.536	0%	1.425	0.464	21%	0.042	0.838
7.5	20	0%	0.447	0.629	0%	0.623	0.464	78%	0.021	0.586
7.5	30	0%	0.519	0.483	0%	0.318	0.464	79%	0.020	0.638
7.5	40	0%	0.398	0.365	0%	0.178	0.464	91%	0.020	0.601
7.5	50	0%	0.312	0.409	0%	0.105	0.464	96%	0.021	0.646
7.5	70	0%	0.207	0.638	0%	0.040	0.464	99%	0.023	0.728
7.5	100	5%	0.105	0.723	40%	0.011	0.464	100%	0.024	0.713
8.0	10	5%	0.912	0.328	0%	3.302	0.464	14%	0.052	0.979
8.0	20	0%	0.741	0.347	0%	1.833	0.464	30%	0.033	0.818
8.0	30	0%	0.412	0.620	0%	1.077	0.464	82%	0.021	0.625
8.0	40	0%	0.519	0.361	0%	0.658	0.464	60%	0.024	0.668
8.0	50	0%	0.408	0.381	0%	0.414	0.464	74%	0.022	0.601
8.0	70	0%	0.306	0.454	0%	0.174	0.464	90%	0.022	0.580
8.0	100	0%	0.222	0.418	0%	0.053	0.464	99%	0.024	0.740

Table D.17: Compiled results of lateral spreading analysis for a site with T = 3m, N = 10, and $S = 1.5^{\circ}$

T_{liq} = 3 m, N = 10 blows/ft, Slope= 1.5°										
			FLIP			Youd et al.			Olson and Johnson	
M_w	R (km)	$P[D = d_0]$	μ_{D_H}	$\sigma_{\ln D_H}$	$P[D = d_0]$	μ_{D_H}	$\sigma_{\ln D_H}$	$P[D = d_0]$	μ_{D_H}	$\sigma_{\ln D_H}$
6.0	10	0%	0.259	0.468	2%	0.027	0.464	38%	0.024	0.681
6.0	20	0%	0.187	0.718	68%	0.008	0.464	87%	0.023	0.695
6.0	30	0%	0.073	0.667	99%	0.004	0.464	98%	0.024	0.802
6.0	40	0%	0.055	0.815	100%	0.002	0.464	99%	0.027	0.920
6.0	50	25%	0.034	0.827	100%	0.001	0.464	100%	0.028	0.955
6.0	70	75%	0.024	0.772	100%	0.000	0.464	100%	0.043	0.983
6.0	100	100%	0.000	0.000	100%	0.000	0.464	100%	0.049	0.982
6.5	10	0%	0.519	0.414	0%	0.142	0.464	48%	0.027	0.770
6.5	20	0%	0.276	0.625	0%	0.044	0.464	87%	0.024	0.759
6.5	30	0%	0.339	0.574	7%	0.020	0.464	90%	0.024	0.862
6.5	40	0%	0.153	0.514	49%	0.010	0.464	99%	0.031	1.035
6.5	50	0%	0.137	0.518	89%	0.006	0.464	98%	0.031	1.021
6.5	70	0%	0.087	0.638	100%	0.002	0.464	99%	0.041	1.109
6.5	100	55%	0.025	0.665	100%	0.001	0.464	100%	0.048	1.231
7.0	10	0%	1.081	0.317	0%	0.626	0.464	1%	0.118	0.920
7.0	20	0%	0.924	0.411	0%	0.222	0.464	34%	0.033	0.890
7.0	30	0%	0.554	0.638	0%	0.103	0.464	88%	0.026	0.876
7.0	40	0%	0.624	0.496	0%	0.054	0.464	88%	0.025	0.885
7.0	50	0%	0.510	0.490	1%	0.031	0.464	94%	0.026	0.940
7.0	70	10%	0.120	0.900	39%	0.011	0.464	99%	0.035	1.127
7.5	10	0%	1.239	0.292	0%	2.066	0.464	1%	0.119	1.035
7.5	20	0%	0.852	0.480	0%	0.903	0.464	41%	0.031	0.869
7.5	30	0%	0.921	0.468	0%	0.462	0.464	42%	0.031	0.907
7.5	40	0%	0.768	0.406	0%	0.257	0.464	68%	0.027	0.849
7.5	50	0%	0.685	0.429	0%	0.152	0.464	81%	0.026	0.878
7.5	70	0%	0.507	0.495	0%	0.059	0.464	94%	0.030	0.981
7.5	100	0%	0.255	0.571	14%	0.016	0.464	98%	0.033	1.098
8.0	10	0%	1.371	0.206	0%	4.786	0.464	1%	0.206	1.064
8.0	20	0%	1.139	0.335	0%	2.657	0.464	5%	0.085	1.055
8.0	30	0%	0.839	0.422	0%	1.561	0.464	52%	0.030	0.905
8.0	40	0%	0.909	0.395	0%	0.954	0.464	29%	0.039	0.945
8.0	50	0%	0.745	0.399	0%	0.600	0.464	45%	0.031	0.879
8.0	70	0%	0.653	0.408	0%	0.253	0.464	70%	0.027	0.856
8.0	100	0%	0.453	0.401	0%	0.076	0.464	92%	0.029	1.010

Table D.18: Compiled results of lateral spreading analysis for a site with T = 3m, N = 10, and $S = 3.5^{\circ}$

T_{liq} = 3 m, N = 10 blows/ft, Slope= 3.5°										
			FLIP			Youd et al.			Olson and Johnson	
M_w	R (km)	$P[D = d_0]$	μ_{D_H}	$\sigma_{\ln D_H}$	$P[D = d_0]$	μ_{D_H}	$\sigma_{\ln D_H}$	$P[D = d_0]$	μ_{D_H}	$\sigma_{\ln D_H}$
6.0	10	0%	0.487	0.338	0%	0.036	0.464	6%	0.054	1.059
6.0	20	0%	0.365	0.506	44%	0.011	0.464	46%	0.036	1.041
6.0	30	0%	0.169	0.477	95%	0.005	0.464	78%	0.034	1.002
6.0	40	0%	0.132	0.572	100%	0.002	0.464	88%	0.035	1.018
6.0	50	0%	0.081	0.728	100%	0.001	0.464	94%	0.036	0.978
6.0	70	40%	0.075	0.794	100%	0.000	0.464	97%	0.042	0.993
6.0	100	90%	0.032	1.128	100%	0.000	0.464	99%	0.045	0.909
6.5	10	0%	0.797	0.307	0%	0.189	0.464	11%	0.067	1.192
6.5	20	0%	0.516	0.526	0%	0.059	0.464	45%	0.042	1.134
6.5	30	0%	0.595	0.430	2%	0.026	0.464	49%	0.048	1.216
6.5	40	0%	0.274	0.434	26%	0.013	0.464	81%	0.042	1.225
6.5	50	0%	0.258	0.391	73%	0.008	0.464	79%	0.042	1.216
6.5	70	0%	0.168	0.289	100%	0.003	0.464	90%	0.046	1.214
6.5	100	15%	0.104	0.456	100%	0.001	0.464	96%	0.056	1.213
7.0	10	0%	1.268	0.289	0%	0.834	0.464	0%	0.445	0.946
7.0	20	0%	1.215	0.292	0%	0.295	0.464	4%	0.112	1.285
7.0	30	0%	0.845	0.513	0%	0.137	0.464	44%	0.051	1.284
7.0	40	0%	0.900	0.386	0%	0.072	0.464	44%	0.051	1.309
7.0	50	0%	0.727	0.419	0%	0.041	0.464	60%	0.047	1.303
7.0	70	0%	0.197	0.717	18%	0.015	0.464	90%	0.047	1.225
7.5	10	0%	1.501	0.233	0%	2.753	0.464	0%	0.534	1.031
7.5	20	0%	1.151	0.348	0%	1.203	0.464	6%	0.095	1.279
7.5	30	0%	1.257	0.257	0%	0.615	0.464	6%	0.102	1.345
7.5	40	0%	1.075	0.310	0%	0.343	0.464	20%	0.064	1.325
7.5	50	0%	0.967	0.352	0%	0.202	0.464	33%	0.057	1.319
7.5	70	0%	0.867	0.374	0%	0.078	0.464	59%	0.054	1.311
7.5	100	0%	0.457	0.450	5%	0.022	0.464	80%	0.052	1.321
8.0	10	0%	1.606	0.226	0%	6.376	0.464	0%	0.899	1.039
8.0	20	0%	1.456	0.232	0%	3.539	0.464	0%	0.395	1.162
8.0	30	0%	1.190	0.220	0%	2.080	0.464	12%	0.092	1.376
8.0	40	0%	1.286	0.203	0%	1.271	0.464	3%	0.141	1.346
8.0	50	0%	1.143	0.249	0%	0.799	0.464	10%	0.094	1.339
8.0	70	0%	0.974	0.305	0%	0.336	0.464	23%	0.068	1.317
8.0	100	0%	0.768	0.273	0%	0.102	0.464	55%	0.060	1.383

Table D.19: Compiled results of lateral spreading analysis for a site with T = 3m, N = 15, and $S = 0.5^{\circ}$

T_{liq} = 3 m, N = 15 blows/ft, Slope= 0.5°										
		FLIP			Youd et al.			Olson and Johnson		
M_w	R (km)	$P[D = d_0]$	μ_{D_H}	$\sigma_{\ln D_H}$	$P[D = d_0]$	μ_{D_H}	$\sigma_{\ln D_H}$	$P[D = d_0]$	μ_{D_H}	$\sigma_{\ln D_H}$
6.0	10	0%	0.056	0.651	9%	0.019	0.464	95%	0.019	0.488
6.0	20	25%	0.035	0.782	90%	0.006	0.464	100%	0.018	0.435
6.0	30	75%	0.019	0.449	100%	0.002	0.464	100%	0.018	0.444
6.0	40	85%	0.017	0.199	100%	0.001	0.464	100%	0.018	0.444
6.0	50	100%	0.000	0.000	100%	0.001	0.464	100%	0.018	0.444
6.0	70	100%	0.000	0.000	100%	0.000	0.464	100%	0.018	0.444
6.0	100	100%	0.000	0.000	100%	0.000	0.464	100%	0.018	0.444
6.5	10	5%	0.082	0.742	0%	0.098	0.464	97%	0.017	0.393
6.5	20	10%	0.048	0.690	1%	0.031	0.464	100%	0.019	0.478
6.5	30	10%	0.062	0.629	26%	0.014	0.464	100%	0.013	0.169
6.5	40	60%	0.024	0.346	78%	0.007	0.464	100%	0.013	0.124
6.5	50	40%	0.023	0.417	98%	0.004	0.464	100%	0.013	0.124
6.5	70	100%	0.000	0.000	100%	0.001	0.464	100%	0.013	0.124
6.5	100	100%	0.000	0.000	100%	0.000	0.464	100%	0.013	0.124
7.0	10	0%	0.349	0.572	0%	0.432	0.464	44%	0.023	0.559
7.0	20	0%	0.267	0.653	0%	0.153	0.464	96%	0.013	0.318
7.0	30	0%	0.112	0.864	0%	0.071	0.464	100%	0.014	0.235
7.0	40	0%	0.125	0.757	0%	0.037	0.464	100%	0.013	0.192
7.0	50	10%	0.086	0.674	5%	0.021	0.464	100%	0.011	0.024
7.0	70	100%	0.000	0.000	70%	0.008	0.464	100%	0.011	0.024
7.5	10	0%	0.419	0.536	0%	1.425	0.464	48%	0.025	0.597
7.5	20	10%	0.267	0.704	0%	0.623	0.464	98%	0.015	0.326
7.5	30	10%	0.326	0.543	0%	0.318	0.464	98%	0.013	0.347
7.5	40	0%	0.195	0.680	0%	0.178	0.464	100%	0.015	0.302
7.5	50	0%	0.150	0.603	0%	0.105	0.464	100%	0.014	0.244
7.5	70	5%	0.099	0.856	0%	0.040	0.464	100%	0.013	0.175
7.5	100	35%	0.035	0.911	40%	0.011	0.464	100%	0.013	0.175
8.0	10	0%	0.504	0.436	0%	3.302	0.464	30%	0.032	0.732
8.0	20	0%	0.414	0.500	0%	1.833	0.464	64%	0.021	0.542
8.0	30	10%	0.224	0.703	0%	1.077	0.464	98%	0.016	0.357
8.0	40	5%	0.274	0.742	0%	0.658	0.464	92%	0.017	0.388
8.0	50	5%	0.210	0.578	0%	0.414	0.464	96%	0.017	0.352
8.0	70	0%	0.142	0.621	0%	0.174	0.464	99%	0.016	0.309
8.0	100	0%	0.090	0.411	0%	0.053	0.464	100%	0.014	0.185

Table D.20: Compiled results of lateral spreading analysis for a site with T = 3m, N = 15, and $S = 1.5^{\circ}$

T_{liq} = 3 m, N = 15 blows/ft, Slope= 1.5°										
		FLIP			Youd et al.			Olson and Johnson		
M_w	R (km)	$P[D = d_0]$	μ_{D_H}	$\sigma_{\ln D_H}$	$P[D = d_0]$	μ_{D_H}	$\sigma_{\ln D_H}$	$P[D = d_0]$	μ_{D_H}	$\sigma_{\ln D_H}$
6.0	10	0%	0.124	0.542	2%	0.027	0.464	79%	0.019	0.467
6.0	20	0%	0.067	0.677	68%	0.008	0.464	99%	0.018	0.436
6.0	30	35%	0.026	0.665	99%	0.004	0.464	100%	0.013	0.227
6.0	40	75%	0.046	0.438	100%	0.002	0.464	100%	0.013	0.207
6.0	50	95%	0.046	0.000	100%	0.001	0.464	100%	0.013	0.207
6.0	70	100%	0.000	0.000	100%	0.000	0.464	100%	0.013	0.207
6.0	100	100%	0.000	0.000	100%	0.000	0.464	100%	0.013	0.207
6.5	10	0%	0.209	0.495	0%	0.142	0.464	89%	0.019	0.460
6.5	20	0%	0.096	0.698	0%	0.044	0.464	99%	0.019	0.463
6.5	30	0%	0.122	0.654	7%	0.020	0.464	100%	0.016	0.369
6.5	40	25%	0.045	0.690	49%	0.010	0.464	100%	0.013	0.109
6.5	50	5%	0.045	0.728	89%	0.006	0.464	100%	0.014	0.222
6.5	70	75%	0.022	0.428	100%	0.002	0.464	100%	0.014	0.222
6.5	100	100%	0.000	0.000	100%	0.001	0.464	100%	0.014	0.222
7.0	10	0%	0.565	0.417	0%	0.626	0.464	10%	0.040	0.778
7.0	20	0%	0.414	0.646	0%	0.222	0.464	81%	0.018	0.492
7.0	30	0%	0.212	0.518	0%	0.103	0.464	100%	0.017	0.418
7.0	40	0%	0.222	0.577	0%	0.054	0.464	100%	0.017	0.398
7.0	50	0%	0.139	0.510	1%	0.031	0.464	100%	0.015	0.366
7.0	70	90%	0.024	0.515	39%	0.011	0.464	100%	0.010	0.036
7.5	10	0%	0.701	0.345	0%	2.066	0.464	9%	0.042	0.817
7.5	20	0%	0.415	0.639	0%	0.903	0.464	87%	0.018	0.482
7.5	30	0%	0.506	0.481	0%	0.462	0.464	88%	0.018	0.498
7.5	40	0%	0.371	0.540	0%	0.257	0.464	97%	0.017	0.469
7.5	50	0%	0.273	0.532	0%	0.152	0.464	99%	0.017	0.475
7.5	70	0%	0.175	0.678	0%	0.059	0.464	100%	0.017	0.436
7.5	100	10%	0.061	0.925	14%	0.016	0.464	100%	0.013	0.175
8.0	10	0%	0.825	0.269	0%	4.786	0.464	6%	0.072	0.911
8.0	20	0%	0.643	0.422	0%	2.657	0.464	27%	0.033	0.740
8.0	30	0%	0.412	0.524	0%	1.561	0.464	91%	0.018	0.489
8.0	40	0%	0.496	0.427	0%	0.954	0.464	75%	0.020	0.545
8.0	50	0%	0.403	0.457	0%	0.600	0.464	87%	0.019	0.468
8.0	70	0%	0.293	0.485	0%	0.253	0.464	97%	0.018	0.437
8.0	100	0%	0.164	0.381	0%	0.076	0.464	100%	0.017	0.424

Table D.21: Compiled results of lateral spreading analysis for a site with T = 3m, N = 15, and $S = 3.5^{\circ}$

T_{liq} = 3 m, N = 15 blows/ft, Slope= 3.5°										
		FLIP			Youd et al.			Olson and Johnson		
M_w	R (km)	$P[D = d_0]$	μ_{D_H}	$\sigma_{\ln D_H}$	$P[D = d_0]$	μ_{D_H}	$\sigma_{\ln D_H}$	$P[D = d_0]$	μ_{D_H}	$\sigma_{\ln D_H}$
6.0	10	0%	0.194	0.400	0%	0.036	0.464	36%	0.024	0.679
6.0	20	0%	0.119	0.464	44%	0.011	0.464	89%	0.022	0.670
6.0	30	10%	0.055	0.539	95%	0.005	0.464	98%	0.023	0.780
6.0	40	40%	0.048	0.716	100%	0.002	0.464	99%	0.025	0.918
6.0	50	75%	0.046	0.616	100%	0.001	0.464	100%	0.029	0.951
6.0	70	100%	0.000	0.000	100%	0.000	0.464	100%	0.043	0.998
6.0	100	100%	0.000	0.000	100%	0.000	0.464	100%	0.036	1.102
6.5	10	0%	0.304	0.406	0%	0.189	0.464	49%	0.026	0.750
6.5	20	0%	0.161	0.493	0%	0.059	0.464	89%	0.022	0.733
6.5	30	0%	0.185	0.456	2%	0.026	0.464	92%	0.024	0.840
6.5	40	5%	0.080	0.553	26%	0.013	0.464	99%	0.029	1.020
6.5	50	0%	0.088	0.534	73%	0.008	0.464	99%	0.029	0.999
6.5	70	30%	0.044	0.596	100%	0.003	0.464	100%	0.039	1.105
6.5	100	90%	0.016	0.429	100%	0.001	0.464	100%	0.046	1.238
7.0	10	0%	0.666	0.386	0%	0.834	0.464	0%	0.135	0.876
7.0	20	0%	0.588	0.385	0%	0.295	0.464	31%	0.032	0.878
7.0	30	0%	0.307	0.511	0%	0.137	0.464	89%	0.025	0.848
7.0	40	0%	0.335	0.451	0%	0.072	0.464	90%	0.024	0.851
7.0	50	0%	0.247	0.449	0%	0.041	0.464	95%	0.026	0.919
7.0	70	50%	0.051	0.782	18%	0.015	0.464	100%	0.034	1.116
7.5	10	0%	0.821	0.349	0%	2.753	0.464	0%	0.162	0.910
7.5	20	0%	0.523	0.481	0%	1.203	0.464	41%	0.030	0.853
7.5	30	0%	0.590	0.395	0%	0.615	0.464	43%	0.030	0.887
7.5	40	0%	0.497	0.399	0%	0.343	0.464	71%	0.026	0.816
7.5	50	0%	0.418	0.437	0%	0.202	0.464	84%	0.026	0.850
7.5	70	0%	0.289	0.453	0%	0.078	0.464	95%	0.029	0.956
7.5	100	0%	0.118	0.513	5%	0.022	0.464	99%	0.032	1.077
8.0	10	0%	0.974	0.323	0%	6.376	0.464	0%	0.266	0.997
8.0	20	0%	0.792	0.369	0%	3.539	0.464	2%	0.094	1.050
8.0	30	0%	0.493	0.473	0%	2.080	0.464	55%	0.029	0.884
8.0	40	0%	0.603	0.353	0%	1.271	0.464	29%	0.037	0.934
8.0	50	0%	0.521	0.371	0%	0.799	0.464	47%	0.029	0.857
8.0	70	0%	0.415	0.397	0%	0.336	0.464	72%	0.026	0.815
8.0	100	0%	0.257	0.422	0%	0.102	0.464	94%	0.030	0.975

Table D.22: Compiled results of lateral spreading analysis for a site with T = 3m, N = 20, and $S = 0.5^{\circ}$

T_{liq} = 3 m, N = 20 blows/ft, Slope= 0.5°										
		FLIP			Youd et al.			Olson and Johnson		
M_w	R (km)	$P[D = d_0]$	μ_{D_H}	$\sigma_{\ln D_H}$	$P[D = d_0]$	μ_{D_H}	$\sigma_{\ln D_H}$	$P[D = d_0]$	μ_{D_H}	$\sigma_{\ln D_H}$
6.0	10	5%	0.046	0.689	100%	0.000	0.464	99%	0.019	0.459
6.0	20	35%	0.035	0.642	100%	0.000	0.464	100%	0.018	0.449
6.0	30	90%	0.016	0.190	100%	0.000	0.464	100%	0.018	0.449
6.0	40	100%	0.000	0.000	100%	0.000	0.464	100%	0.018	0.449
6.0	50	100%	0.000	0.000	100%	0.000	0.464	100%	0.018	0.449
6.0	70	100%	0.000	0.000	100%	0.000	0.464	100%	0.018	0.449
6.0	100	100%	0.000	0.000	100%	0.000	0.464	100%	0.018	0.449
6.5	10	15%	0.087	0.650	100%	0.000	0.464	100%	0.013	0.266
6.5	20	5%	0.038	0.754	100%	0.000	0.464	100%	0.011	0.049
6.5	30	5%	0.053	0.772	100%	0.000	0.464	100%	0.011	0.049
6.5	40	90%	0.022	0.110	100%	0.000	0.464	100%	0.011	0.049
6.5	50	85%	0.020	0.150	100%	0.000	0.464	100%	0.011	0.049
6.5	70	100%	0.000	0.000	100%	0.000	0.464	100%	0.011	0.049
6.5	100	100%	0.000	0.000	100%	0.000	0.464	100%	0.011	0.049
7.0	10	0%	0.328	0.525	100%	0.000	0.464	74%	0.019	0.405
7.0	20	0%	0.210	0.930	100%	0.000	0.464	100%	0.012	0.158
7.0	30	5%	0.110	0.749	100%	0.000	0.464	100%	0.011	0.046
7.0	40	10%	0.131	0.569	100%	0.000	0.464	100%	0.011	0.046
7.0	50	15%	0.074	0.593	100%	0.000	0.464	100%	0.011	0.046
7.0	70	100%	0.000	0.000	100%	0.000	0.464	100%	0.011	0.046
7.5	10	0%	0.370	0.406	100%	0.000	0.464	75%	0.019	0.439
7.5	20	5%	0.221	0.801	100%	0.000	0.464	100%	0.014	0.249
7.5	30	5%	0.265	0.647	100%	0.000	0.464	100%	0.012	0.088
7.5	40	0%	0.172	0.657	100%	0.000	0.464	100%	0.011	0.071
7.5	50	0%	0.129	0.595	100%	0.000	0.464	100%	0.011	0.071
7.5	70	10%	0.077	0.811	100%	0.000	0.464	100%	0.011	0.071
7.5	100	100%	0.000	0.000	100%	0.000	0.464	100%	0.011	0.071
8.0	10	0%	0.450	0.408	100%	0.000	0.464	52%	0.024	0.587
8.0	20	0%	0.402	0.372	100%	0.000	0.464	90%	0.016	0.351
8.0	30	15%	0.214	0.800	100%	0.000	0.464	100%	0.017	0.367
8.0	40	10%	0.263	0.615	100%	0.000	0.464	100%	0.015	0.263
8.0	50	0%	0.188	0.705	100%	0.000	0.464	100%	0.015	0.224
8.0	70	5%	0.131	0.537	100%	0.000	0.464	100%	0.014	0.198
8.0	100	0%	0.081	0.460	100%	0.000	0.464	100%	0.014	0.198

Table D.23: Compiled results of lateral spreading analysis for a site with T = 3m, N = 20, and $S = 1.5^{\circ}$

T_{liq} = 3 m, N = 20 blows/ft, Slope= 1.5°										
		FLIP			Youd et al.			Olson and Johnson		
M_w	R (km)	$P[D = d_0]$	μ_{D_H}	$\sigma_{\ln D_H}$	$P[D = d_0]$	μ_{D_H}	$\sigma_{\ln D_H}$	$P[D = d_0]$	μ_{D_H}	$\sigma_{\ln D_H}$
6.0	10	0%	0.099	0.692	100%	0.000	0.464	97%	0.018	0.422
6.0	20	15%	0.057	0.710	100%	0.000	0.464	100%	0.017	0.412
6.0	30	80%	0.028	0.493	100%	0.000	0.464	100%	0.017	0.412
6.0	40	100%	0.000	0.000	100%	0.000	0.464	100%	0.017	0.412
6.0	50	100%	0.000	0.000	100%	0.000	0.464	100%	0.017	0.412
6.0	70	100%	0.000	0.000	100%	0.000	0.464	100%	0.017	0.412
6.0	100	100%	0.000	0.000	100%	0.000	0.464	100%	0.017	0.412
6.5	10	0%	0.177	0.548	100%	0.000	0.464	99%	0.015	0.349
6.5	20	5%	0.068	0.585	100%	0.000	0.464	100%	0.011	0.052
6.5	30	5%	0.093	0.600	100%	0.000	0.464	100%	0.011	0.052
6.5	40	75%	0.029	0.743	100%	0.000	0.464	100%	0.011	0.052
6.5	50	55%	0.025	0.699	100%	0.000	0.464	100%	0.011	0.052
6.5	70	95%	0.025	0.000	100%	0.000	0.464	100%	0.011	0.052
6.5	100	100%	0.000	0.000	100%	0.000	0.464	100%	0.011	0.052
7.0	10	0%	0.470	0.415	100%	0.000	0.464	39%	0.021	0.524
7.0	20	0%	0.377	0.639	100%	0.000	0.464	98%	0.014	0.278
7.0	30	0%	0.143	0.631	100%	0.000	0.464	100%	0.012	0.148
7.0	40	0%	0.157	0.578	100%	0.000	0.464	100%	0.012	0.148
7.0	50	0%	0.114	0.499	100%	0.000	0.464	100%	0.012	0.148
7.0	70	100%	0.000	0.000	100%	0.000	0.464	100%	0.012	0.148
7.5	10	0%	0.598	0.408	100%	0.000	0.464	36%	0.023	0.558
7.5	20	0%	0.330	0.723	100%	0.000	0.464	99%	0.014	0.276
7.5	30	0%	0.395	0.614	100%	0.000	0.464	99%	0.014	0.265
7.5	40	0%	0.294	0.587	100%	0.000	0.464	100%	0.012	0.203
7.5	50	0%	0.210	0.475	100%	0.000	0.464	100%	0.011	0.066
7.5	70	10%	0.144	0.495	100%	0.000	0.464	100%	0.011	0.066
7.5	100	100%	0.000	0.000	100%	0.000	0.464	100%	0.011	0.066
8.0	10	0%	0.692	0.283	100%	0.000	0.464	19%	0.035	0.737
8.0	20	0%	0.555	0.398	100%	0.000	0.464	66%	0.019	0.498
8.0	30	0%	0.347	0.582	100%	0.000	0.464	100%	0.015	0.295
8.0	40	0%	0.423	0.544	100%	0.000	0.464	98%	0.016	0.324
8.0	50	0%	0.346	0.462	100%	0.000	0.464	99%	0.016	0.285
8.0	70	0%	0.198	0.800	100%	0.000	0.464	100%	0.014	0.222
8.0	100	0%	0.134	0.407	100%	0.000	0.464	100%	0.013	0.180

Table D.24: Compiled results of lateral spreading analysis for a site with T = 3m, N = 20, and $S = 3.5^{\circ}$

T_{liq} = 3 m, N = 20 blows/ft, Slope= 3.5°										
		FLIP			Youd et al.			Olson and Johnson		
M_w	R (km)	$P[D = d_0]$	μ_{D_H}	$\sigma_{\ln D_H}$	$P[D = d_0]$	μ_{D_H}	$\sigma_{\ln D_H}$	$P[D = d_0]$	μ_{D_H}	$\sigma_{\ln D_H}$
6.0	10	0%	0.141	0.476	100%	0.000	0.464	79%	0.019	0.469
6.0	20	0%	0.071	0.709	100%	0.000	0.464	99%	0.018	0.421
6.0	30	75%	0.048	0.539	100%	0.000	0.464	100%	0.014	0.236
6.0	40	95%	0.048	0.000	100%	0.000	0.464	100%	0.014	0.236
6.0	50	100%	0.000	0.000	100%	0.000	0.464	100%	0.014	0.236
6.0	70	100%	0.000	0.000	100%	0.000	0.464	100%	0.014	0.236
6.0	100	100%	0.000	0.000	100%	0.000	0.464	100%	0.014	0.236
6.5	10	0%	0.219	0.463	100%	0.000	0.464	89%	0.018	0.460
6.5	20	0%	0.096	0.560	100%	0.000	0.464	100%	0.018	0.437
6.5	30	0%	0.118	0.592	100%	0.000	0.464	100%	0.016	0.347
6.5	40	50%	0.048	0.630	100%	0.000	0.464	100%	0.011	0.088
6.5	50	45%	0.057	0.396	100%	0.000	0.464	100%	0.011	0.088
6.5	70	90%	0.021	0.455	100%	0.000	0.464	100%	0.011	0.088
6.5	100	100%	0.000	0.000	100%	0.000	0.464	100%	0.011	0.088
7.0	10	0%	0.558	0.339	100%	0.000	0.464	6%	0.044	0.793
7.0	20	0%	0.503	0.390	100%	0.000	0.464	81%	0.018	0.493
7.0	30	0%	0.206	0.536	100%	0.000	0.464	100%	0.016	0.399
7.0	40	0%	0.212	0.456	100%	0.000	0.464	100%	0.016	0.368
7.0	50	0%	0.145	0.393	100%	0.000	0.464	100%	0.016	0.314
7.0	70	100%	0.000	0.000	100%	0.000	0.464	100%	0.012	0.035
7.5	10	0%	0.698	0.324	100%	0.000	0.464	4%	0.054	0.830
7.5	20	0%	0.393	0.670	100%	0.000	0.464	88%	0.018	0.485
7.5	30	0%	0.470	0.488	100%	0.000	0.464	89%	0.018	0.499
7.5	40	0%	0.364	0.549	100%	0.000	0.464	98%	0.017	0.459
7.5	50	0%	0.305	0.508	100%	0.000	0.464	99%	0.016	0.448
7.5	70	0%	0.162	0.574	100%	0.000	0.464	100%	0.017	0.406
7.5	100	65%	0.066	0.712	100%	0.000	0.464	100%	0.012	0.096
8.0	10	0%	0.823	0.312	100%	0.000	0.464	2%	0.086	0.944
8.0	20	0%	1.034	0.754	100%	0.000	0.464	19%	0.033	0.769
8.0	30	0%	1.933	0.231	100%	0.000	0.464	93%	0.018	0.483
8.0	40	0%	2.046	0.183	100%	0.000	0.464	77%	0.020	0.534
8.0	50	0%	1.934	0.233	100%	0.000	0.464	89%	0.019	0.453
8.0	70	0%	1.770	0.265	100%	0.000	0.464	98%	0.018	0.425
8.0	100	0%	0.178	0.446	100%	0.000	0.464	100%	0.018	0.357

Table D.25: Compiled results of lateral spreading analysis for a site with T = 5m, N = 5, and $S = 0.5^{\circ}$

T_{liq} = 5 m, N = 5 blows/ft, Slope= 0.5°										
		FLIP			Youd et al.			Olson and Johnson		
M_w	R (km)	$P[D = d_0]$	μ_{D_H}	$\sigma_{\ln D_H}$	$P[D = d_0]$	μ_{D_H}	$\sigma_{\ln D_H}$	$P[D = d_0]$	μ_{D_H}	$\sigma_{\ln D_H}$
6.0	10	0%	0.206	0.522	3%	0.025	0.464	41%	0.028	0.829
6.0	20	0%	0.116	0.868	75%	0.007	0.464	71%	0.027	0.874
6.0	30	0%	0.051	0.841	99%	0.003	0.464	91%	0.027	0.922
6.0	40	5%	0.041	0.805	100%	0.002	0.464	96%	0.032	0.980
6.0	50	25%	0.026	0.621	100%	0.001	0.464	98%	0.031	0.989
6.0	70	50%	0.017	0.300	100%	0.000	0.464	99%	0.040	1.009
6.0	100	95%	0.017	0.000	100%	0.000	0.464	100%	0.042	0.991
6.5	10	0%	0.466	0.475	0%	0.129	0.464	37%	0.037	0.964
6.5	20	0%	0.191	0.864	0%	0.040	0.464	70%	0.030	0.956
6.5	30	0%	0.230	0.805	11%	0.018	0.464	75%	0.033	1.081
6.5	40	0%	0.099	0.560	57%	0.009	0.464	93%	0.035	1.152
6.5	50	0%	0.103	0.664	92%	0.005	0.464	92%	0.036	1.142
6.5	70	0%	0.058	0.707	100%	0.002	0.464	96%	0.040	1.186
6.5	100	15%	0.024	0.518	100%	0.000	0.464	99%	0.051	1.214
7.0	10	0%	1.096	0.488	0%	0.569	0.464	3%	0.106	1.091
7.0	20	0%	0.763	0.484	0%	0.201	0.464	29%	0.045	1.115
7.0	30	0%	0.402	0.472	0%	0.093	0.464	72%	0.035	1.128
7.0	40	0%	0.433	0.378	0%	0.049	0.464	71%	0.035	1.131
7.0	50	0%	0.367	0.368	1%	0.028	0.464	81%	0.035	1.161
7.0	70	5%	0.082	0.886	47%	0.010	0.464	96%	0.042	1.191
7.5	10	0%	1.272	0.417	0%	1.878	0.464	7%	0.107	1.203
7.5	20	0%	0.752	0.494	0%	0.821	0.464	33%	0.041	1.076
7.5	30	0%	0.828	0.450	0%	0.420	0.464	32%	0.044	1.158
7.5	40	0%	0.634	0.337	0%	0.234	0.464	49%	0.036	1.107
7.5	50	0%	0.507	0.339	0%	0.138	0.464	61%	0.036	1.123
7.5	70	0%	0.375	0.499	0%	0.053	0.464	80%	0.041	1.168
7.5	100	0%	0.200	0.535	20%	0.015	0.464	91%	0.041	1.232
8.0	10	0%	1.528	0.381	0%	4.350	0.464	4%	0.151	1.315
8.0	20	0%	1.145	0.408	0%	2.415	0.464	9%	0.090	1.242
8.0	30	0%	0.728	0.331	0%	1.419	0.464	36%	0.044	1.161
8.0	40	0%	0.844	0.346	0%	0.867	0.464	18%	0.060	1.160
8.0	50	0%	0.640	0.346	0%	0.545	0.464	29%	0.046	1.127
8.0	70	0%	0.516	0.347	0%	0.230	0.464	48%	0.040	1.101
8.0	100	0%	0.408	0.312	0%	0.069	0.464	78%	0.042	1.240

Table D.26: Compiled results of lateral spreading analysis for a site with T = 5m, N = 5, and $S = 1.5^{\circ}$

T_{liq} = 5 m, N = 5 blows/ft, Slope= 1.5°										
		FLIP			Youd et al.			Olson and Johnson		
M_w	R (km)	$P[D = d_0]$	μ_{D_H}	$\sigma_{\ln D_H}$	$P[D = d_0]$	μ_{D_H}	$\sigma_{\ln D_H}$	$P[D = d_0]$	μ_{D_H}	$\sigma_{\ln D_H}$
6.0	10	0%	0.502	0.531	0%	0.036	0.464	8%	0.053	1.070
6.0	20	0%	0.409	0.552	45%	0.011	0.464	43%	0.038	1.066
6.0	30	0%	0.176	0.693	95%	0.005	0.464	75%	0.034	1.013
6.0	40	0%	0.142	0.888	100%	0.002	0.464	87%	0.036	1.023
6.0	50	0%	0.077	0.930	100%	0.001	0.464	93%	0.037	0.981
6.0	70	10%	0.057	0.873	100%	0.000	0.464	96%	0.041	1.001
6.0	100	65%	0.024	0.687	100%	0.000	0.464	98%	0.043	0.927
6.5	10	0%	1.066	0.411	0%	0.187	0.464	10%	0.071	1.214
6.5	20	0%	0.604	0.582	0%	0.058	0.464	42%	0.044	1.161
6.5	30	0%	0.696	0.555	2%	0.026	0.464	45%	0.050	1.242
6.5	40	0%	0.359	0.482	27%	0.013	0.464	79%	0.045	1.231
6.5	50	0%	0.368	0.588	74%	0.007	0.464	77%	0.044	1.229
6.5	70	0%	0.219	0.516	100%	0.003	0.464	88%	0.048	1.217
6.5	100	0%	0.109	0.747	100%	0.001	0.464	95%	0.056	1.214
7.0	10	0%	2.351	0.347	0%	0.825	0.464	0%	0.410	0.998
7.0	20	0%	2.031	0.438	0%	0.292	0.464	4%	0.112	1.339
7.0	30	0%	1.096	0.513	0%	0.136	0.464	41%	0.054	1.312
7.0	40	0%	1.235	0.406	0%	0.071	0.464	41%	0.055	1.333
7.0	50	0%	1.060	0.340	0%	0.041	0.464	55%	0.048	1.336
7.0	70	0%	0.297	0.823	19%	0.015	0.464	89%	0.049	1.225
7.5	10	0%	2.611	0.382	0%	2.723	0.464	0%	0.445	1.163
7.5	20	0%	1.879	0.453	0%	1.190	0.464	6%	0.099	1.309
7.5	30	0%	2.079	0.375	0%	0.608	0.464	6%	0.108	1.374
7.5	40	0%	1.657	0.355	0%	0.339	0.464	18%	0.069	1.353
7.5	50	0%	1.428	0.333	0%	0.200	0.464	30%	0.061	1.348
7.5	70	0%	1.062	0.433	0%	0.077	0.464	56%	0.059	1.329
7.5	100	0%	0.638	0.426	5%	0.022	0.464	77%	0.055	1.329
8.0	10	0%	2.908	0.353	0%	6.307	0.464	0%	0.752	1.148
8.0	20	0%	2.575	0.369	0%	3.501	0.464	1%	0.359	1.259
8.0	30	0%	1.798	0.375	0%	2.057	0.464	11%	0.099	1.400
8.0	40	0%	2.050	0.308	0%	1.257	0.464	4%	0.152	1.358
8.0	50	0%	1.619	0.355	0%	0.791	0.464	9%	0.101	1.365
8.0	70	0%	1.404	0.368	0%	0.333	0.464	20%	0.073	1.343
8.0	100	0%	1.055	0.300	0%	0.101	0.464	51%	0.065	1.406

Table D.27: Compiled results of lateral spreading analysis for a site with T = 5m, N = 5, and $S = 3.5^{\circ}$

T_{liq} = 5 m, N = 5 blows/ft, Slope= 3.5°										
		FLIP			Youd et al.			Olson and Johnson		
M_w	R (km)	$P[D = d_0]$	μ_{D_H}	$\sigma_{\ln D_H}$	$P[D = d_0]$	μ_{D_H}	$\sigma_{\ln D_H}$	$P[D = d_0]$	μ_{D_H}	$\sigma_{\ln D_H}$
6.0	10	0%	1.042	0.449	0%	0.048	0.464	0%	0.153	1.119
6.0	20	0%	0.879	0.566	23%	0.014	0.464	11%	0.078	1.252
6.0	30	0%	0.460	0.457	85%	0.006	0.464	35%	0.051	1.119
6.0	40	0%	0.366	0.632	99%	0.003	0.464	55%	0.045	1.076
6.0	50	0%	0.240	0.601	100%	0.002	0.464	69%	0.040	0.995
6.0	70	0%	0.172	0.756	100%	0.001	0.464	83%	0.042	0.958
6.0	100	25%	0.088	0.961	100%	0.000	0.464	91%	0.039	0.883
6.5	10	0%	1.971	0.349	0%	0.249	0.464	1%	0.226	1.275
6.5	20	0%	1.293	0.560	0%	0.078	0.464	10%	0.104	1.325
6.5	30	0%	1.465	0.504	0%	0.034	0.464	10%	0.122	1.368
6.5	40	0%	0.757	0.490	11%	0.018	0.464	40%	0.074	1.297
6.5	50	0%	0.759	0.514	51%	0.010	0.464	38%	0.073	1.314
6.5	70	0%	0.507	0.309	99%	0.004	0.464	58%	0.064	1.240
6.5	100	0%	0.304	0.233	100%	0.001	0.464	77%	0.056	1.200
7.0	10	0%	3.301	0.248	0%	1.100	0.464	0%	1.171	0.987
7.0	20	0%	3.136	0.316	0%	0.389	0.464	0%	0.443	1.299
7.0	30	0%	2.164	0.504	0%	0.181	0.464	8%	0.146	1.474
7.0	40	0%	2.428	0.392	0%	0.095	0.464	8%	0.149	1.523
7.0	50	0%	2.224	0.410	0%	0.054	0.464	16%	0.110	1.527
7.0	70	0%	0.717	0.625	7%	0.020	0.464	58%	0.060	1.273
7.5	10	0%	3.583	0.263	0%	3.627	0.464	0%	1.447	1.051
7.5	20	0%	3.039	0.301	0%	1.586	0.464	0%	0.372	1.311
7.5	30	0%	3.229	0.271	0%	0.810	0.464	0%	0.433	1.379
7.5	40	0%	2.960	0.317	0%	0.452	0.464	2%	0.242	1.498
7.5	50	0%	2.623	0.385	0%	0.266	0.464	5%	0.186	1.530
7.5	70	0%	2.187	0.386	0%	0.103	0.464	16%	0.123	1.517
7.5	100	0%	1.434	0.418	1%	0.029	0.464	38%	0.090	1.439
8.0	10	0%	3.771	0.263	0%	8.401	0.464	0%	2.403	1.000
8.0	20	0%	3.580	0.235	0%	4.663	0.464	0%	1.283	1.088
8.0	30	0%	2.991	0.251	0%	2.740	0.464	1%	0.394	1.415
8.0	40	0%	3.247	0.205	0%	1.675	0.464	0%	0.610	1.295
8.0	50	0%	2.939	0.266	0%	1.053	0.464	1%	0.388	1.368
8.0	70	0%	2.476	0.375	0%	0.443	0.464	3%	0.247	1.430
8.0	100	0%	2.072	0.289	0%	0.134	0.464	13%	0.162	1.544

Table D.28: Compiled results of lateral spreading analysis for a site with T = 5m, N = 10, and $S = 0.5^{\circ}$

T_{liq} = 5 m, N = 10 blows/ft, Slope= 0.5°										
		FLIP			Youd et al.			Olson and Johnson		
M_w	R (km)	$P[D = d_0]$	μ_{D_H}	$\sigma_{\ln D_H}$	$P[D = d_0]$	μ_{D_H}	$\sigma_{\ln D_H}$	$P[D = d_0]$	μ_{D_H}	$\sigma_{\ln D_H}$
6.0	10	0%	0.165	0.575	3%	0.025	0.464	76%	0.021	0.550
6.0	20	15%	0.085	0.739	75%	0.007	0.464	97%	0.020	0.527
6.0	30	5%	0.030	0.762	99%	0.003	0.464	100%	0.019	0.524
6.0	40	15%	0.032	0.661	100%	0.002	0.464	100%	0.020	0.498
6.0	50	55%	0.020	0.470	100%	0.001	0.464	100%	0.017	0.387
6.0	70	85%	0.013	0.155	100%	0.000	0.464	100%	0.012	0.016
6.0	100	100%	0.000	0.000	100%	0.000	0.464	100%	0.012	0.016
6.5	10	0%	0.315	0.480	0%	0.129	0.464	78%	0.021	0.554
6.5	20	10%	0.132	0.768	0%	0.040	0.464	97%	0.020	0.567
6.5	30	10%	0.182	0.489	11%	0.018	0.464	98%	0.019	0.625
6.5	40	0%	0.064	0.568	57%	0.009	0.464	100%	0.021	0.647
6.5	50	10%	0.066	0.579	92%	0.005	0.464	100%	0.022	0.660
6.5	70	5%	0.030	0.619	100%	0.002	0.464	100%	0.024	0.552
6.5	100	80%	0.017	0.558	100%	0.000	0.464	100%	0.016	0.269
7.0	10	0%	0.901	0.511	0%	0.569	0.464	17%	0.038	0.795
7.0	20	0%	0.562	0.596	0%	0.201	0.464	72%	0.020	0.602
7.0	30	0%	0.261	0.584	0%	0.093	0.464	98%	0.020	0.632
7.0	40	0%	0.306	0.429	0%	0.049	0.464	98%	0.020	0.625
7.0	50	0%	0.223	0.518	1%	0.028	0.464	99%	0.021	0.671
7.0	70	15%	0.050	0.957	47%	0.010	0.464	100%	0.020	0.562
7.5	10	0%	0.993	0.502	0%	1.878	0.464	21%	0.042	0.838
7.5	20	0%	0.497	0.703	0%	0.821	0.464	78%	0.021	0.586
7.5	30	0%	0.587	0.522	0%	0.420	0.464	79%	0.020	0.638
7.5	40	0%	0.458	0.355	0%	0.234	0.464	91%	0.020	0.601
7.5	50	0%	0.355	0.403	0%	0.138	0.464	96%	0.021	0.646
7.5	70	0%	0.249	0.575	0%	0.053	0.464	99%	0.023	0.728
7.5	100	0%	0.110	0.778	20%	0.015	0.464	100%	0.024	0.713
8.0	10	0%	1.185	0.496	0%	4.350	0.464	14%	0.052	0.979
8.0	20	0%	0.917	0.398	0%	2.415	0.464	30%	0.033	0.818
8.0	30	0%	0.453	0.602	0%	1.419	0.464	82%	0.021	0.625
8.0	40	5%	0.601	0.447	0%	0.867	0.464	60%	0.024	0.668
8.0	50	0%	0.420	0.484	0%	0.545	0.464	74%	0.022	0.601
8.0	70	0%	0.359	0.449	0%	0.230	0.464	90%	0.022	0.580
8.0	100	0%	0.280	0.351	0%	0.069	0.464	99%	0.024	0.740

Table D.29: Compiled results of lateral spreading analysis for a site with T = 5m, N = 10, and $S = 1.5^{\circ}$

T_{liq} = 5 m, N = 10 blows/ft, Slope= 1.5°										
		FLIP			Youd et al.			Olson and Johnson		
M_w	R (km)	$P[D = d_0]$	μ_{D_H}	$\sigma_{\ln D_H}$	$P[D = d_0]$	μ_{D_H}	$\sigma_{\ln D_H}$	$P[D = d_0]$	μ_{D_H}	$\sigma_{\ln D_H}$
6.0	10	0%	0.319	0.476	0%	0.036	0.464	38%	0.024	0.681
6.0	20	0%	0.208	0.652	45%	0.011	0.464	87%	0.023	0.695
6.0	30	0%	0.094	0.595	95%	0.005	0.464	98%	0.024	0.802
6.0	40	0%	0.071	0.766	100%	0.002	0.464	99%	0.027	0.920
6.0	50	10%	0.042	0.669	100%	0.001	0.464	100%	0.028	0.955
6.0	70	70%	0.048	0.508	100%	0.000	0.464	100%	0.043	0.983
6.0	100	100%	0.000	0.000	100%	0.000	0.464	100%	0.049	0.982
6.5	10	0%	0.599	0.506	0%	0.187	0.464	48%	0.027	0.770
6.5	20	0%	0.303	0.631	0%	0.058	0.464	87%	0.024	0.759
6.5	30	0%	0.384	0.611	2%	0.026	0.464	90%	0.024	0.862
6.5	40	0%	0.174	0.440	27%	0.013	0.464	99%	0.031	1.035
6.5	50	0%	0.163	0.472	74%	0.007	0.464	98%	0.031	1.021
6.5	70	0%	0.102	0.552	100%	0.003	0.464	99%	0.041	1.109
6.5	100	35%	0.036	0.635	100%	0.001	0.464	100%	0.048	1.231
7.0	10	0%	1.572	0.375	0%	0.825	0.464	1%	0.118	0.920
7.0	20	0%	1.262	0.510	0%	0.292	0.464	34%	0.033	0.890
7.0	30	0%	0.633	0.611	0%	0.136	0.464	88%	0.026	0.876
7.0	40	0%	0.693	0.516	0%	0.071	0.464	88%	0.025	0.885
7.0	50	0%	0.551	0.488	0%	0.041	0.464	94%	0.026	0.940
7.0	70	10%	0.157	0.639	19%	0.015	0.464	99%	0.035	1.127
7.5	10	0%	1.710	0.377	0%	2.723	0.464	1%	0.119	1.035
7.5	20	0%	1.178	0.555	0%	1.190	0.464	41%	0.031	0.869
7.5	30	0%	1.297	0.529	0%	0.608	0.464	42%	0.031	0.907
7.5	40	0%	0.952	0.427	0%	0.339	0.464	68%	0.027	0.849
7.5	50	0%	0.802	0.410	0%	0.200	0.464	81%	0.026	0.878
7.5	70	0%	0.580	0.567	0%	0.077	0.464	94%	0.030	0.981
7.5	100	0%	0.290	0.565	5%	0.022	0.464	98%	0.033	1.098
8.0	10	0%	1.971	0.359	0%	6.307	0.464	1%	0.206	1.064
8.0	20	0%	1.703	0.315	0%	3.501	0.464	5%	0.085	1.055
8.0	30	0%	1.112	0.419	0%	2.057	0.464	52%	0.030	0.905
8.0	40	0%	1.251	0.468	0%	1.257	0.464	29%	0.039	0.945
8.0	50	0%	1.004	0.403	0%	0.791	0.464	45%	0.031	0.879
8.0	70	0%	0.767	0.474	0%	0.333	0.464	70%	0.027	0.856
8.0	100	0%	0.573	0.377	0%	0.101	0.464	92%	0.029	1.010

Table D.30: Compiled results of lateral spreading analysis for a site with T = 5m, N = 10, and $S = 3.5^{\circ}$

T_{liq} = 5 m, N = 10 blows/ft, Slope= 3.5°										
		FLIP			Youd et al.			Olson and Johnson		
M_w	R (km)	$P[D = d_0]$	μ_{D_H}	$\sigma_{\ln D_H}$	$P[D = d_0]$	μ_{D_H}	$\sigma_{\ln D_H}$	$P[D = d_0]$	μ_{D_H}	$\sigma_{\ln D_H}$
6.0	10	0%	0.570	0.456	0%	0.048	0.464	6%	0.054	1.059
6.0	20	0%	0.431	0.534	23%	0.014	0.464	46%	0.036	1.041
6.0	30	0%	0.193	0.519	85%	0.006	0.464	78%	0.034	1.002
6.0	40	0%	0.148	0.525	99%	0.003	0.464	88%	0.035	1.018
6.0	50	0%	0.106	0.547	100%	0.002	0.464	94%	0.036	0.978
6.0	70	20%	0.082	0.762	100%	0.001	0.464	97%	0.042	0.993
6.0	100	90%	0.027	0.525	100%	0.000	0.464	99%	0.045	0.909
6.5	10	0%	1.051	0.386	0%	0.249	0.464	11%	0.067	1.192
6.5	20	0%	0.607	0.581	0%	0.078	0.464	45%	0.042	1.134
6.5	30	0%	0.725	0.573	0%	0.034	0.464	49%	0.048	1.216
6.5	40	0%	0.304	0.466	11%	0.018	0.464	81%	0.042	1.225
6.5	50	0%	0.303	0.457	51%	0.010	0.464	79%	0.042	1.216
6.5	70	0%	0.186	0.288	99%	0.004	0.464	90%	0.046	1.214
6.5	100	10%	0.116	0.358	100%	0.001	0.464	96%	0.056	1.213
7.0	10	0%	1.957	0.327	0%	1.100	0.464	0%	0.445	0.946
7.0	20	0%	1.753	0.384	0%	0.389	0.464	4%	0.112	1.285
7.0	30	0%	1.123	0.574	0%	0.181	0.464	44%	0.051	1.284
7.0	40	0%	1.261	0.501	0%	0.095	0.464	44%	0.051	1.309
7.0	50	0%	0.887	0.523	0%	0.054	0.464	60%	0.047	1.303
7.0	70	0%	0.220	0.527	7%	0.020	0.464	90%	0.047	1.225
7.5	10	0%	2.285	0.285	0%	3.627	0.464	0%	0.534	1.031
7.5	20	0%	1.643	0.454	0%	1.586	0.464	6%	0.095	1.279
7.5	30	0%	1.839	0.390	0%	0.810	0.464	6%	0.102	1.345
7.5	40	0%	1.624	0.464	0%	0.452	0.464	20%	0.064	1.325
7.5	50	0%	1.380	0.466	0%	0.266	0.464	33%	0.057	1.319
7.5	70	0%	1.107	0.526	0%	0.103	0.464	59%	0.054	1.311
7.5	100	0%	0.519	0.453	1%	0.029	0.464	80%	0.052	1.321
8.0	10	0%	2.497	0.269	0%	8.401	0.464	0%	0.899	1.039
8.0	20	0%	2.260	0.225	0%	4.663	0.464	0%	0.395	1.162
8.0	30	0%	1.714	0.373	0%	2.740	0.464	12%	0.092	1.376
8.0	40	0%	1.902	0.294	0%	1.675	0.464	3%	0.141	1.346
8.0	50	0%	1.667	0.356	0%	1.053	0.464	10%	0.094	1.339
8.0	70	0%	1.363	0.425	0%	0.443	0.464	23%	0.068	1.317
8.0	100	0%	1.003	0.345	0%	0.134	0.464	55%	0.060	1.383

Table D.31: Compiled results of lateral spreading analysis for a site with T = 5m, N = 15, and $S = 0.5^{\circ}$

T_{liq} = 5 m, N = 15 blows/ft, Slope= 0.5°										
		FLIP			Youd et al.			Olson and Johnson		
M_w	R (km)	$P[D = d_0]$	μ_{D_H}	$\sigma_{\ln D_H}$	$P[D = d_0]$	μ_{D_H}	$\sigma_{\ln D_H}$	$P[D = d_0]$	μ_{D_H}	$\sigma_{\ln D_H}$
6.0	10	5%	0.078	0.579	3%	0.025	0.464	95%	0.019	0.488
6.0	20	15%	0.036	0.814	75%	0.007	0.464	100%	0.018	0.435
6.0	30	60%	0.022	0.343	99%	0.003	0.464	100%	0.018	0.444
6.0	40	80%	0.016	0.227	100%	0.002	0.464	100%	0.018	0.444
6.0	50	100%	0.000	0.000	100%	0.001	0.464	100%	0.018	0.444
6.0	70	100%	0.000	0.000	100%	0.000	0.464	100%	0.018	0.444
6.0	100	100%	0.000	0.000	100%	0.000	0.464	100%	0.018	0.444
6.5	10	10%	0.105	0.617	0%	0.129	0.464	97%	0.017	0.393
6.5	20	5%	0.061	0.653	0%	0.040	0.464	100%	0.019	0.478
6.5	30	5%	0.064	0.653	11%	0.018	0.464	100%	0.013	0.169
6.5	40	40%	0.026	0.433	57%	0.009	0.464	100%	0.013	0.124
6.5	50	25%	0.025	0.439	92%	0.005	0.464	100%	0.013	0.124
6.5	70	100%	0.000	0.000	100%	0.002	0.464	100%	0.013	0.124
6.5	100	100%	0.000	0.000	100%	0.000	0.464	100%	0.013	0.124
7.0	10	0%	0.473	0.543	0%	0.569	0.464	44%	0.023	0.559
7.0	20	0%	0.323	0.617	0%	0.201	0.464	96%	0.013	0.318
7.0	30	0%	0.114	0.931	0%	0.093	0.464	100%	0.014	0.235
7.0	40	0%	0.137	0.692	0%	0.049	0.464	100%	0.013	0.192
7.0	50	5%	0.100	0.636	1%	0.028	0.464	100%	0.011	0.024
7.0	70	95%	0.100	0.000	47%	0.010	0.464	100%	0.011	0.024
7.5	10	10%	0.663	0.509	0%	1.878	0.464	48%	0.025	0.597
7.5	20	10%	0.317	0.606	0%	0.821	0.464	98%	0.015	0.326
7.5	30	10%	0.377	0.531	0%	0.420	0.464	98%	0.013	0.347
7.5	40	0%	0.212	0.658	0%	0.234	0.464	100%	0.015	0.302
7.5	50	0%	0.167	0.603	0%	0.138	0.464	100%	0.014	0.244
7.5	70	5%	0.107	0.865	0%	0.053	0.464	100%	0.013	0.175
7.5	100	15%	0.041	0.794	20%	0.015	0.464	100%	0.013	0.175
8.0	10	10%	0.828	0.417	0%	4.350	0.464	30%	0.032	0.732
8.0	20	0%	0.494	0.795	0%	2.415	0.464	64%	0.021	0.542
8.0	30	5%	0.214	0.896	0%	1.419	0.464	98%	0.016	0.357
8.0	40	5%	0.302	0.956	0%	0.867	0.464	92%	0.017	0.388
8.0	50	0%	0.218	0.651	0%	0.545	0.464	96%	0.017	0.352
8.0	70	0%	0.179	0.508	0%	0.230	0.464	99%	0.016	0.309
8.0	100	0%	0.088	0.423	0%	0.069	0.464	100%	0.014	0.185

Table D.32: Compiled results of lateral spreading analysis for a site with T = 5m, N = 15, and $S = 1.5^{\circ}$

T_{liq} = 5 m, N = 15 blows/ft, Slope= 1.5°										
		FLIP			Youd et al.			Olson and Johnson		
M_w	R (km)	$P[D = d_0]$	μ_{D_H}	$\sigma_{\ln D_H}$	$P[D = d_0]$	μ_{D_H}	$\sigma_{\ln D_H}$	$P[D = d_0]$	μ_{D_H}	$\sigma_{\ln D_H}$
6.0	10	0%	0.147	0.532	0%	0.036	0.464	79%	0.019	0.467
6.0	20	0%	0.073	0.623	45%	0.011	0.464	99%	0.018	0.436
6.0	30	20%	0.031	0.613	95%	0.005	0.464	100%	0.013	0.227
6.0	40	50%	0.028	0.747	100%	0.002	0.464	100%	0.013	0.207
6.0	50	90%	0.019	0.424	100%	0.001	0.464	100%	0.013	0.207
6.0	70	100%	0.000	0.000	100%	0.000	0.464	100%	0.013	0.207
6.0	100	100%	0.000	0.000	100%	0.000	0.464	100%	0.013	0.207
6.5	10	0%	0.229	0.515	0%	0.187	0.464	89%	0.019	0.460
6.5	20	0%	0.105	0.585	0%	0.058	0.464	99%	0.019	0.463
6.5	30	0%	0.134	0.564	2%	0.026	0.464	100%	0.016	0.369
6.5	40	10%	0.050	0.692	27%	0.013	0.464	100%	0.013	0.109
6.5	50	5%	0.058	0.499	74%	0.007	0.464	100%	0.014	0.222
6.5	70	60%	0.028	0.235	100%	0.003	0.464	100%	0.014	0.222
6.5	100	100%	0.000	0.000	100%	0.001	0.464	100%	0.014	0.222
7.0	10	0%	0.809	0.446	0%	0.825	0.464	10%	0.040	0.778
7.0	20	0%	0.554	0.653	0%	0.292	0.464	81%	0.018	0.492
7.0	30	0%	0.213	0.541	0%	0.136	0.464	100%	0.017	0.418
7.0	40	0%	0.230	0.631	0%	0.071	0.464	100%	0.017	0.398
7.0	50	0%	0.152	0.521	0%	0.041	0.464	100%	0.015	0.366
7.0	70	55%	0.027	0.574	19%	0.015	0.464	100%	0.010	0.036
7.5	10	0%	1.029	0.443	0%	2.723	0.464	9%	0.042	0.817
7.5	20	0%	0.515	0.708	0%	1.190	0.464	87%	0.018	0.482
7.5	30	0%	0.627	0.582	0%	0.608	0.464	88%	0.018	0.498
7.5	40	0%	0.420	0.541	0%	0.339	0.464	97%	0.017	0.469
7.5	50	0%	0.289	0.538	0%	0.200	0.464	99%	0.017	0.475
7.5	70	0%	0.196	0.716	0%	0.077	0.464	100%	0.017	0.436
7.5	100	5%	0.089	0.684	5%	0.022	0.464	100%	0.013	0.175
8.0	10	0%	1.182	0.449	0%	6.307	0.464	6%	0.072	0.911
8.0	20	0%	0.966	0.403	0%	3.501	0.464	27%	0.033	0.740
8.0	30	0%	0.503	0.518	0%	2.057	0.464	91%	0.018	0.489
8.0	40	0%	0.633	0.479	0%	1.257	0.464	75%	0.020	0.545
8.0	50	0%	0.450	0.532	0%	0.791	0.464	87%	0.019	0.468
8.0	70	0%	0.326	0.537	0%	0.333	0.464	97%	0.018	0.437
8.0	100	0%	0.172	0.355	0%	0.101	0.464	100%	0.017	0.424

Table D.33: Compiled results of lateral spreading analysis for a site with T = 5m, N = 15, and $S = 3.5^{\circ}$

T_{liq} = 5 m, N = 15 blows/ft, Slope= 3.5°										
		Youd et al.			Olson and Johnson					
M_w	R (km)	$P[D = d_0]$	μ_{D_H}	$\sigma_{\ln D_H}$	$P[D = d_0]$	μ_{D_H}	$\sigma_{\ln D_H}$	$P[D = d_0]$	μ_{D_H}	$\sigma_{\ln D_H}$
6.0	10	0%	0.236	0.503	0%	0.048	0.464	36%	0.024	0.679
6.0	20	0%	0.125	0.470	23%	0.014	0.464	89%	0.022	0.670
6.0	30	5%	0.061	0.500	85%	0.006	0.464	98%	0.023	0.780
6.0	40	15%	0.043	0.699	99%	0.003	0.464	99%	0.025	0.918
6.0	50	70%	0.055	0.360	100%	0.002	0.464	100%	0.029	0.951
6.0	70	100%	0.000	0.000	100%	0.001	0.464	100%	0.043	0.998
6.0	100	100%	0.000	0.000	100%	0.000	0.464	100%	0.036	1.102
6.5	10	0%	0.367	0.478	0%	0.249	0.464	49%	0.026	0.750
6.5	20	0%	0.170	0.507	0%	0.078	0.464	89%	0.022	0.733
6.5	30	0%	0.228	0.519	0%	0.034	0.464	92%	0.024	0.840
6.5	40	0%	0.084	0.488	11%	0.018	0.464	99%	0.029	1.020
6.5	50	0%	0.095	0.466	51%	0.010	0.464	99%	0.029	0.999
6.5	70	20%	0.056	0.479	99%	0.004	0.464	100%	0.039	1.105
6.5	100	90%	0.025	0.067	100%	0.001	0.464	100%	0.046	1.238
7.0	10	0%	0.979	0.453	0%	1.100	0.464	0%	0.135	0.876
7.0	20	0%	0.819	0.507	0%	0.389	0.464	31%	0.032	0.878
7.0	30	0%	0.345	0.536	0%	0.181	0.464	89%	0.025	0.848
7.0	40	0%	0.362	0.505	0%	0.095	0.464	90%	0.024	0.851
7.0	50	0%	0.250	0.462	0%	0.054	0.464	95%	0.026	0.919
7.0	70	35%	0.073	0.581	7%	0.020	0.464	100%	0.034	1.116
7.5	10	0%	1.300	0.354	0%	3.627	0.464	0%	0.162	0.910
7.5	20	0%	0.723	0.554	0%	1.586	0.464	41%	0.030	0.853
7.5	30	0%	0.864	0.443	0%	0.810	0.464	43%	0.030	0.887
7.5	40	0%	0.669	0.457	0%	0.452	0.464	71%	0.026	0.816
7.5	50	0%	0.501	0.508	0%	0.266	0.464	84%	0.026	0.850
7.5	70	0%	0.322	0.547	0%	0.103	0.464	95%	0.029	0.956
7.5	100	0%	0.140	0.457	1%	0.029	0.464	99%	0.032	1.077
8.0	10	0%	1.507	0.308	0%	8.401	0.464	0%	0.266	0.997
8.0	20	0%	1.198	0.389	0%	4.663	0.464	2%	0.094	1.050
8.0	30	0%	0.721	0.482	0%	2.740	0.464	55%	0.029	0.884
8.0	40	0%	0.882	0.387	0%	1.675	0.464	29%	0.037	0.934
8.0	50	0%	0.753	0.404	0%	1.053	0.464	47%	0.029	0.857
8.0	70	0%	0.527	0.529	0%	0.443	0.464	72%	0.026	0.815
8.0	100	0%	0.299	0.446	0%	0.134	0.464	94%	0.030	0.975

Table D.34: Compiled results of lateral spreading analysis for a site with T = 5m, N = 20, and $S = 0.5^{\circ}$

T_{liq} = 5 m, N = 20 blows/ft, Slope= 0.5°										
		FLIP			Youd et al.			Olson and Johnson		
M_w	R (km)	$P[D = d_0]$	μ_{D_H}	$\sigma_{\ln D_H}$	$P[D = d_0]$	μ_{D_H}	$\sigma_{\ln D_H}$	$P[D = d_0]$	μ_{D_H}	$\sigma_{\ln D_H}$
6.0	10	0%	0.055	0.706	100%	0.000	0.464	99%	0.019	0.459
6.0	20	25%	0.039	0.724	100%	0.000	0.464	100%	0.018	0.449
6.0	30	85%	0.016	0.202	100%	0.000	0.464	100%	0.018	0.449
6.0	40	95%	0.016	0.000	100%	0.000	0.464	100%	0.018	0.449
6.0	50	100%	0.000	0.000	100%	0.000	0.464	100%	0.018	0.449
6.0	70	100%	0.000	0.000	100%	0.000	0.464	100%	0.018	0.449
6.0	100	100%	0.000	0.000	100%	0.000	0.464	100%	0.018	0.449
6.5	10	5%	0.087	0.721	100%	0.000	0.464	100%	0.013	0.266
6.5	20	0%	0.044	0.726	100%	0.000	0.464	100%	0.011	0.049
6.5	30	0%	0.059	0.749	100%	0.000	0.464	100%	0.011	0.049
6.5	40	75%	0.028	0.373	100%	0.000	0.464	100%	0.011	0.049
6.5	50	65%	0.028	0.350	100%	0.000	0.464	100%	0.011	0.049
6.5	70	100%	0.000	0.000	100%	0.000	0.464	100%	0.011	0.049
6.5	100	100%	0.000	0.000	100%	0.000	0.464	100%	0.011	0.049
7.0	10	0%	0.444	0.572	100%	0.000	0.464	74%	0.019	0.405
7.0	20	0%	0.281	0.664	100%	0.000	0.464	100%	0.012	0.158
7.0	30	0%	0.119	0.811	100%	0.000	0.464	100%	0.011	0.046
7.0	40	0%	0.129	0.768	100%	0.000	0.464	100%	0.011	0.046
7.0	50	5%	0.086	0.788	100%	0.000	0.464	100%	0.011	0.046
7.0	70	100%	0.000	0.000	100%	0.000	0.464	100%	0.011	0.046
7.5	10	0%	0.526	0.632	100%	0.000	0.464	75%	0.019	0.439
7.5	20	5%	0.273	0.697	100%	0.000	0.464	100%	0.014	0.249
7.5	30	5%	0.323	0.581	100%	0.000	0.464	100%	0.012	0.088
7.5	40	0%	0.197	0.586	100%	0.000	0.464	100%	0.011	0.071
7.5	50	0%	0.145	0.617	100%	0.000	0.464	100%	0.011	0.071
7.5	70	15%	0.121	0.626	100%	0.000	0.464	100%	0.011	0.071
7.5	100	70%	0.034	0.722	100%	0.000	0.464	100%	0.011	0.071
8.0	10	5%	0.665	0.666	100%	0.000	0.464	52%	0.024	0.587
8.0	20	0%	0.536	0.536	100%	0.000	0.464	90%	0.016	0.351
8.0	30	10%	0.232	0.717	100%	0.000	0.464	100%	0.017	0.367
8.0	40	10%	0.298	0.746	100%	0.000	0.464	100%	0.015	0.263
8.0	50	0%	0.206	0.669	100%	0.000	0.464	100%	0.015	0.224
8.0	70	5%	0.165	0.544	100%	0.000	0.464	100%	0.014	0.198
8.0	100	0%	0.085	0.444	100%	0.000	0.464	100%	0.014	0.198

Table D.35: Compiled results of lateral spreading analysis for a site with T = 5m, N = 20, and $S = 1.5^{\circ}$

T_{liq} = 5 m, N = 20 blows/ft, Slope= 1.5°										
		FLIP			Youd et al.			Olson and Johnson		
M_w	R (km)	$P[D = d_0]$	μ_{D_H}	$\sigma_{\ln D_H}$	$P[D = d_0]$	μ_{D_H}	$\sigma_{\ln D_H}$	$P[D = d_0]$	μ_{D_H}	$\sigma_{\ln D_H}$
6.0	10	0%	0.113	0.595	100%	0.000	0.464	97%	0.018	0.422
6.0	20	10%	0.061	0.700	100%	0.000	0.464	100%	0.017	0.412
6.0	30	75%	0.031	0.563	100%	0.000	0.464	100%	0.017	0.412
6.0	40	90%	0.037	0.553	100%	0.000	0.464	100%	0.017	0.412
6.0	50	100%	0.000	0.000	100%	0.000	0.464	100%	0.017	0.412
6.0	70	100%	0.000	0.000	100%	0.000	0.464	100%	0.017	0.412
6.0	100	100%	0.000	0.000	100%	0.000	0.464	100%	0.017	0.412
6.5	10	0%	0.193	0.555	100%	0.000	0.464	99%	0.015	0.349
6.5	20	0%	0.076	0.554	100%	0.000	0.464	100%	0.011	0.052
6.5	30	0%	0.098	0.556	100%	0.000	0.464	100%	0.011	0.052
6.5	40	60%	0.038	0.793	100%	0.000	0.464	100%	0.011	0.052
6.5	50	50%	0.046	0.637	100%	0.000	0.464	100%	0.011	0.052
6.5	70	95%	0.046	0.000	100%	0.000	0.464	100%	0.011	0.052
6.5	100	100%	0.000	0.000	100%	0.000	0.464	100%	0.011	0.052
7.0	10	0%	0.700	0.481	100%	0.000	0.464	39%	0.021	0.524
7.0	20	5%	0.481	0.693	100%	0.000	0.464	98%	0.014	0.278
7.0	30	0%	0.169	0.631	100%	0.000	0.464	100%	0.012	0.148
7.0	40	0%	0.170	0.612	100%	0.000	0.464	100%	0.012	0.148
7.0	50	0%	0.123	0.476	100%	0.000	0.464	100%	0.012	0.148
7.0	70	100%	0.000	0.000	100%	0.000	0.464	100%	0.012	0.148
7.5	10	0%	0.894	0.420	100%	0.000	0.464	36%	0.023	0.558
7.5	20	0%	0.443	0.733	100%	0.000	0.464	99%	0.014	0.276
7.5	30	0%	0.547	0.555	100%	0.000	0.464	99%	0.014	0.265
7.5	40	0%	0.327	0.591	100%	0.000	0.464	100%	0.012	0.203
7.5	50	0%	0.219	0.472	100%	0.000	0.464	100%	0.011	0.066
7.5	70	5%	0.152	0.820	100%	0.000	0.464	100%	0.011	0.066
7.5	100	55%	0.052	0.845	100%	0.000	0.464	100%	0.011	0.066
8.0	10	0%	1.033	0.331	100%	0.000	0.464	19%	0.035	0.737
8.0	20	0%	0.828	0.396	100%	0.000	0.464	66%	0.019	0.498
8.0	30	0%	0.377	0.668	100%	0.000	0.464	100%	0.015	0.295
8.0	40	0%	0.573	0.420	100%	0.000	0.464	98%	0.016	0.324
8.0	50	0%	0.380	0.493	100%	0.000	0.464	99%	0.016	0.285
8.0	70	0%	0.249	0.673	100%	0.000	0.464	100%	0.014	0.222
8.0	100	0%	0.150	0.389	100%	0.000	0.464	100%	0.013	0.180

Table D.36: Compiled results of lateral spreading analysis for a site with T = 5m, N = 20, and $S = 3.5^{\circ}$

T_{liq} = 5 m, N = 20 blows/ft, Slope= 3.5°										
		FLIP			Youd et al.			Olson and Johnson		
M_w	R (km)	$P[D = d_0]$	μ_{D_H}	$\sigma_{\ln D_H}$	$P[D = d_0]$	μ_{D_H}	$\sigma_{\ln D_H}$	$P[D = d_0]$	μ_{D_H}	$\sigma_{\ln D_H}$
6.0	10	0%	0.158	0.551	100%	0.000	0.464	79%	0.019	0.469
6.0	20	0%	0.080	0.620	100%	0.000	0.464	99%	0.018	0.421
6.0	30	60%	0.037	0.729	100%	0.000	0.464	100%	0.014	0.236
6.0	40	80%	0.048	0.295	100%	0.000	0.464	100%	0.014	0.236
6.0	50	100%	0.000	0.000	100%	0.000	0.464	100%	0.014	0.236
6.0	70	100%	0.000	0.000	100%	0.000	0.464	100%	0.014	0.236
6.0	100	100%	0.000	0.000	100%	0.000	0.464	100%	0.014	0.236
6.5	10	0%	0.240	0.500	100%	0.000	0.464	89%	0.018	0.460
6.5	20	0%	0.101	0.380	100%	0.000	0.464	100%	0.018	0.437
6.5	30	0%	0.126	0.379	100%	0.000	0.464	100%	0.016	0.347
6.5	40	40%	0.046	0.894	100%	0.000	0.464	100%	0.011	0.088
6.5	50	40%	0.062	0.652	100%	0.000	0.464	100%	0.011	0.088
6.5	70	85%	0.031	0.189	100%	0.000	0.464	100%	0.011	0.088
6.5	100	100%	0.000	0.000	100%	0.000	0.464	100%	0.011	0.088
7.0	10	0%	0.841	0.437	100%	0.000	0.464	6%	0.044	0.793
7.0	20	0%	0.664	0.509	100%	0.000	0.464	81%	0.018	0.493
7.0	30	0%	0.208	0.573	100%	0.000	0.464	100%	0.016	0.399
7.0	40	0%	0.220	0.478	100%	0.000	0.464	100%	0.016	0.368
7.0	50	0%	0.165	0.422	100%	0.000	0.464	100%	0.016	0.314
7.0	70	100%	0.000	0.000	100%	0.000	0.464	100%	0.012	0.035
7.5	10	0%	1.050	0.361	100%	0.000	0.464	4%	0.054	0.830
7.5	20	0%	0.541	0.703	100%	0.000	0.464	88%	0.018	0.485
7.5	30	0%	0.662	0.532	100%	0.000	0.464	89%	0.018	0.499
7.5	40	0%	0.415	0.600	100%	0.000	0.464	98%	0.017	0.459
7.5	50	0%	0.333	0.505	100%	0.000	0.464	99%	0.016	0.448
7.5	70	0%	0.198	0.596	100%	0.000	0.464	100%	0.017	0.406
7.5	100	40%	0.094	0.516	100%	0.000	0.464	100%	0.012	0.096
8.0	10	0%	1.235	0.324	100%	0.000	0.464	2%	0.086	0.944
8.0	20	0%	0.993	0.425	100%	0.000	0.464	19%	0.033	0.769
8.0	30	0%	0.475	0.597	100%	0.000	0.464	93%	0.018	0.483
8.0	40	0%	0.703	0.449	100%	0.000	0.464	77%	0.020	0.534
8.0	50	0%	0.542	0.419	100%	0.000	0.464	89%	0.019	0.453
8.0	70	0%	0.361	0.462	100%	0.000	0.464	98%	0.018	0.425
8.0	100	0%	0.190	0.507	100%	0.000	0.464	100%	0.018	0.357

Bibliography

Abrahamson, N. A., Silva, W. J., and Kamai, R. (2013). "Update of the AS08 Ground-Motion Prediction equations based on the NGA-west2 data set." *Pacific Engineering Research Center Report, 4.*

Ambraseys, N. N., and Menu, J. M. (1988). "Earthquake-induced ground displacements." *Earthquake engineering and structural dynamics*, 16(7), 985-1006.

Andrus, R. D., and Youd, T. L. (1987). *Subsurface Investigation of a Liquefaction-Induced Lateral Spread, Thousand Springs Valley, Idaho.* Brigham Young University, Provo UT, Dept Of Civil Engineering.

Baker, J. W. (2008). "An introduction to probabilistic seismic hazard analysis (PSHA)." Version 1

Bartlett, S. F., and Youd, T. L. (1995). "Empirical prediction of liquefaction-induced lateral spread." *Journal of Geotechnical Engineering*, 121(4), 316-329.

Baziar, M. H., Dobry, R., and Elgamal, A.-W. M. (1992). "Engineering evaluation of permanent ground deformations due to seismically induced liquefaction." *Technical Rep. No. NCEER-92-0007*, National Center for Earthquake Engineering Research, State Univ. of New York at Buffalo, Buffalo, N.Y.

Baziar, M. H., Jafarian, Y., Shahnazari, H., Movahed, V., Tutunchian, M. A. (2011). "Prediction of strain energy-based liquefaction resistance of sand-silt mixtures: An evolutionary approach." *Computers and Geosciences*, 37(11), 1883-1893.

Been, K., and Jeffries, M. G. (1985). "A state parameter for sands." *Geotechnique* 35(2), 99-112.

Benjamin, J. R., & Cornell, C. A. (1970). *Probability, statistics, and decision for civil engineers*. Courier Corporation.

Bennett, M. J. (1989). "Liquefaction analysis of the 1971 ground failure at the San Fernando Valley Juvenile Hall, California." *Bulletin of the Association of Engineering Geologists*, 26(2), 209-226.

Bennett, M. J. (1990). "Effects of the Loma Prieta earthquake on the Marina District San Francisco, California." *USGS Open-File Rep. No. 90-253*, Washington, D.C.

Bennett, M. J., and Tinsley, J. C. (1995). "Geotechnical data from surface and subsurface samples outside of and within liquefaction-related ground failures caused by the October 17, 1989, Loma Prieta earthquake, Santa Cruz and Monterey counties, California." *USGS OpenFile Rep. No. 95-663*, Washington, D.C.

Bennett, M. J., Youd, T. L., Harp, E. L., and Wieczorek, G. F. (1981). "Subsurface investigation of liquefaction, Imperial Valley earthquake, California, October 15, 1979." *USGS Open-File Rep. No. 81-502*, Washington, D.C.

Bennett, M. J., McLaughlin, P. V., Sarmiento, J. S., and Youd, T. L. (1984). *Geotechnical investigation of liquefaction sites, Imperial Valley, California* (No. 84-252). US Geological Survey.

Bennett, M. J., Ponti, D. J., Tinsley, J. C., Holzer, T. L., and Conaway, C. H. (1998). "Subsurface geotechnical investigations near sites of ground deformation caused by the January 17, 1994, Northridge, California, earthquake." *USGS Open-File Rep. No. 98-373*, Washington, D.C.

Berrill, J. B., Christensen, S. A., Keenan, R. P., Okada, W., and Pettinga, J. R. (2001). "Case study of lateral spreading forces on a piled foundation." *Geotechnique*, 51(6), 501-518.

Bolton, M. D. (1986). "The strength and dilatancy of sands." *Geotechnique* 36(1), 65-78.

Boore, D. M. (2010). "Orientation-independent, nongeometric-mean measures of seismic intensity from two horizontal components of motion." *Bulletin of the Seismological Society of America* 100(4):1830-1835

Boore, D. M., Stewart, J. P., Seyhan, E., and Atkinson, G. M. (2014). "NGA-West2 equations for predicting PGA, PGV, and 5% damped PSA for shallow crustal earthquakes." *Earthquake Spectra* August 2014, Vol. 30, No. 3, pp. 1057-1085.

Boulanger, R. W. (2003a). "Relating K_α to relative state parameter index." *J. Geotech. Geoenviron. Eng.* 129(8), 770-773.

Boulanger, R. W. (2003b). "High overburden stress effects in liquefaction analyses." *J. Geotech. Geoenviron. Eng.*, 129(12), 1071-1082.

Boulanger, R. W., and Truman, S. P. (1996). "Void redistribution in sand under post-earthquake loading." *Canadian geotechnical journal*, 33(5), 829-834.

Boulanger, R. W., and Ziotopoulou, K. (2012). "PM4Sand (Version 2): a sand plasticity model for earthquake engineering applications." *Rep. UCD/CGM-12, 1.*

Boulanger, R. W., Mejia, L. H., and Idriss, I. M. (1997). "Liquefaction at moss landing during Loma Prieta earthquake." *J. Geotech. Geoenviron. Eng*, 123(5), 453-467.

Bray, J. D., and Travasarou, T. (2007). "Simplified procedure for estimating earthquake-induced deviatoric slope displacements." *J. Geotech. Geoenviron. Eng*, 133(4), 381-392.

Campbell, K. W., and Bozorgnia, Y. (2014). "NGA-West2 ground motion model for the average horizontal components of PGA, PGV, and 5% damped linear acceleration response spectra." *Earthquake Spectra*, 30(3), 1087-1115.

Castro, G. (1969). *Liquefaction of sands.* Harvard Univ., Division of Engineering and Applied Mechanics.

Castro, G. (1995). "Empirical methods in liquefaction evaluation." *Proc., 1st Annual Leonardo Zeevaert Int. Conf.*, Vol. 1, National Autonomous University of Mexico, Mexico City, Mexico, 1–41.

Cetin, K. O., Seed, R. B., Der Kiureghian, A., Tokimatsu, K., Harder Jr, L. F., Kayen, R. E., and Moss, R. E. (2004). "Standard penetration test-based probabilistic and deterministic assessment of seismic soil liquefaction potential." *J. Geotech. Geoenviron. Eng*, 130(12), 1314-1340.

Cetin, K. O., Youd, T. L., Seed, R. B., Bray, J. D., Sancio, R., Lettis, W., Yilmaz, M. T., and Durgunoglu, H. T. (2002). "Liquefaction-induced ground deformations at Hotel Sapanca during Kocaeli Izmit, Turkey earthquake." *Soil Dyn. Earthquake Eng.*, 22, 1083–1092.

Cetin, K. O., Youd, T. L., Seed, R. B., Bray, J. D., Stewart, J. P., Durgunoglu, H. T., Lettis, W., and Yilmaz, M. T. (2004b). "Liquefaction-induced lateral spreading at Izmit Bay during the Kocaeli Izmit-Turkey earthquake." *J. Geotech. Geoenviron. Eng.*, 13012, 1300–1313.

Charlie, W. A., Doehring, D. O., Brislawn, J. P., and Hassen, H. (1998). "Direct measurement of liquefaction potential in soils of Monterey County, California." *The Loma Prieta, California, Earthquake of October 17, 1989—Liquefaction*, T. L. Holzer, ed., USGS, Washington, D.C., Professional Paper No. 1551-B, B181–B221.

Chiou, B. S. J., and Youngs, R. R. (2014). "Update of the Chiou and Youngs NGA model for the average horizontal component of peak ground motion and response spectra." *Earthquake Spectra*, 30(3), 1117-1153.

Christensen, S. A. (1995). *Liquefaction of cohesionless soils in the March 2, 1987 Edgecumbe earthquake, Bay of Plenty, New Zealand, and other earthquakes.* Department of Civil Engineering, University of Canterbury.

Chu, D. B., Stewart, J. P., Youd, T. L., and Chu, B. L. (2006). "Liquefaction-induced lateral spreading in near-fault regions during the 1999 Chi-Chi, Taiwan earthquake." *J. Geotech. Geoenviron. Eng.*, 132(12), 1549–1565.

Davis, R.O., and Berrill, J.B. (1982). "Energy dissipation and seismic liquefaction in sands." *Earthquake Engineering and Structural Dynamics*, 10(1), 59–68.

Davis, A. P., Jr., Poulos, S. J., and Castro, G. (1988). "Strengths backfigured from liquefaction case histories." *Proc., 2nd Int. Conf. on Case Histories in Geotechnical Engineering*, Rolla, Mo., 1693–1701.

Davis, R. O., and Berrill, J. B. (1998). "Rational approximation of stress and strain based on downhole acceleration measurements." *Int. J. Numerical and Analytical Methods in Geomechanics*, 22(8), 603-619.

Davis, R. O., and Berrill, J. B. (2001). "Pore Pressure and Dissipated Energy inEarthquakes-Field Verification." *J. Geotech. Geoenviron. Eng*, 127(3), 269-274.

Dobry, R. (1985). *Pore pressure model for cyclic straining of sand.* Department of Civil Engineering, Rensselaer Polytechnic Institute, 1985.

Faris, A. T., Seed, R. B., Kayen, R. E., and Wu, J. (2006). "A semi-empirical model for the estimation of maximum horizontal displacement due to liquefaction-induced lateral spreading." *Proc. 8th US Conference on Earthquake Engineering*, Vol. 3, 1584-1593

Franke, K. W., and Kramer, S. L. (2014). "Procedure for the empirical evaluation of lateral spread displacement hazard curves." *J. Geotech. Geoenviron. Eng.*, 140(1), 110-120.

Golesorkhi, R. (1989). *Factors influencing the computational determination of earthquake-induced shear stresses in sandy soils*. Ph.D. thesis, University of California, Berkeley.

Green, R. A., Cubrinovski, M., Cox, B., Wood, C., Wotherspoon, L., Bradley, B., and Maurer, B. (2014). "Select liquefaction case histories from the 2010-2011 Canterbury earthquake sequence." *Earthquake Spectra*, 30(1), 131-153.

Greene, W. H. (2003). *Econometric analysis*. Pearson Education India.

Harding-Lawson Associates (1977). "Soil and foundation investigation, St. Francis Yacht Club reconstruction. San Francisco, California." Geotechnical Report, HLA Job no. 9201,001.04

Holzer, T. L., Hanks, T. C., and Youd, T. L. (1989). "Dynamics of liquefaction during the 1987 Superstition Hills, California, earthquake." *Science*, 244(4900), 56-59.

Holzer, T. L., Tinsley, J. C., Bennett, M. J., and Mueller, C. S. (1994). "Observed and predicted ground deformation—Miller Farm lateral spread, Watsonville, California." *Proc., 5th US–Japan Workshop on Earthquake Resistant Design of Lifeline Facilities and Countermeasures for Soil Liquefaction*, Technical Rep. NCEER-94-0026 79 (Vol. 99).

Holzer, T. L., Bennett, M. J., Ponti, D. J., and Tinsley, J. C. (1998). "Liquefaction and soil failure during 1994 Northridge earthquake." *J. Geotech. Geoenviron. Eng.*, 125(6), 438–452.

Holzer, T. L., Noce, T. E., Bennett, M. J., Di Alessandro, C., Boatwright, J., Tinsley, J. C., Sell, R. W., and Rosenberg, L. I. (2004). "Liquefaction-induced lateral spreading in Oceano, California during the 2003 San Simeon earthquake." *USGS Open-File Rep. No. 2004- 1269*, Washington, D.C.

Hryciw, R. D., Shewbridge, S. E., Kropp, A., and Homolka, M. (1998). "Postearthquake investigations at liquefaction sites in Santa Cruz and on Treasure Island." *The Loma Prieta, California, Earthquake of October 17, 1989—Liquefaction*, T. L. Holzer, ed., USGS, Washington, D.C., Professional Paper No. 1551-B, B165–B180.

Idriss, I. M. (1999). "An update to the Seed-Idriss simplified procedure for evaluating liquefaction potential." *Proc., TRB Worshop on New Approaches to Liquefaction*, Publication No. FHWA-RD-99-165, Federal Highway Administation.

Idriss, I. M., and Boulanger, R. W. (2006). "Semi-empirical procedures for evaluating liquefaction potential during earthquakes." *Soil Dynamics and Earthquake Engineering*, 26(2), 115-130.

Idriss, I. M., and Boulanger, R. W. (2007). "SPT-and CPT-based relationships for the residual shear strength of liquefied soils." *Earthquake geotechnical engineering* (pp. 1-22). Springer Netherlands.

Idriss, I. M., and Boulanger, R. W. (2008). *Soil Liquefaction During Earthquakes*, Earthquake Engineering Research Institute, Berkeley, California.

Ishihara, K. (1993). "Liquefaction and flow failure during earthquakes." *Geotechnique* 43(3), 351-415.

Ishihara, K., and Yoshimine, M. (1992). "Evaluation of settlements in sand deposits following liquefaction during earthquakes." *Soils and Foundations*, 32(1), 173-188.

Ishihara, K., Haeri, S. M., Moinfar, A. A., Towhata, I., and Tsujino, S. (1992). "Geotechnical aspects of the June 20, 1990 Manjil earthquake in Iran." *Soils and Foundations*, 323, 61–78.

Ishihara, K., Acacio, A. A., and Towhata, I. (1993). "Liquefaction-induced ground damage in Dagupan in the July 16, 1990 Luzon earthquake." *Soils and Foundations*, 33(1), 133–154.

Jackson, S. M., and Boatwright, J. (1987). "Strong ground motion in the 1983 Borah Peak, Idaho, earthquake and its aftershocks." *Bulletin of the Seismological Society of America*, 77(3), 724-738.

Jibson, R. W. (2007). "Regression models for estimating coseismic landslide displacement." *Engineering Geology*, 91(2), 209-218.

Kokusho, T. (1999). "Water film in liquefied sand and its effect on lateral spread." *J. Geotech. Geoenviron. Eng.*, 125(10), 817-826.

Konrad, J.-M. (1988). "Interpretation of flat plate dilatometer tests in sands in terms of the state parameter." *Geotechnique* 38(2), 263-277.

Koza, J.R. (1992). *Genetic Programming: On the Programming of Computers by Means of Natural Selection.* MIT Press, Cambridge, MA.

Kramer, S. L. (1996) *Geotechnical Earthquake Engineering*, Prentice Hall, Upper Saddle River, New Jersey.

Kramer, S.L. (2009). "Evaluation of Liquefaction Hazards in Washington State," Washington State Transportation Center, Final Report.

Kramer, S. L., and Smith, M. W. (1997). "Modified Newmark model for seismic displacements of compliant slopes." *J. Geotech. Geoenviron. Eng.*, 123(7), 635-644.

Kramer, S.L. and Wang, C.H. (2004). "Residual Strength of Liquefied Soil," *PEER Report* 2005/xx, in press

Kramer, S.L. and Baska, D.A. (2009). "Estimation of permanent displacement due to lateral spreading," *Journal of Geotechnical and Geoenvironmental Engineering*, ASCE, accepted pending revisions.

Lee, K. L., and Seed, H.B. (1967). "Drained strength characteristics of sands." *J. Soil Mech. Found. Engrg. Div.*, 93(SM6), 117-141.

Makdisi, F. I., and Seed, H. B. (1977). *A simplified procedure for estimating earthquake-induced deformations in dams and embankments.* Earthquake Engineering Research Center, College of Engineering, University of California.

Malvick, E. J., Kutter, B. L., and Boulanger, R. W. (2008). "Postshaking shear strain localization in a centrifuge model of a saturated sand slope." *J. Geotech. Geoenviron. Eng.*, 134(2), 164-174.

Mejia, L. H. (1998). "Liquefaction at Moss Landing." *The Loma Prieta, California, Earthquake of October 17, 1989 — Liquefaction*, (1551-B), B129-B150.

Monastersky, R. (1999). "Taiwan quake floods scientists with data." *Science News*, 156(14), 213-213.

Moss, R. E., and Hollenback, J. C. (2009). "Discussion of 'Analyzing Liquefaction-Induced Lateral Spreads Using Strength Ratios' by SM Olson and CI Johnson." *J. Geotech. Geoenviron. Eng.*, 135(12), 2006-2008.

Murphy, L. M., Benfer, N. A., and Coffman, J. L. (1973). *San Fernando, California, Earthquake of February 9, 1971: Geological and geophysical studies* (Vol. 3). Environmental Research Laboratories.

O'Rourke, T. D., Pease, J. W., and Stewart, H. E. (1992). "Lifeline performance and ground deformation during the earthquake." *The Loma Prieta, California, Earthquake of October 17, 1989—Marina District*, T. D. O'Rourke, ed., T.L. Holzer, coord., USGS, Washington, D.C., Professional Paper 1551-F, F155–F179.

Olson, S. M., and Stark, T. D. (2002). "Liquefied strength ratio from liquefaction flow failure case histories." *Canadian Geotechnical Journal*, 39(3), 629-647.

Olson, S. M., and Johnson, C. I. (2008). "Analyzing liquefaction-induced lateral spreads using strength ratios." *J. Geotech. Geoenviron. Eng.*, 134(8), 1035-1049.

Park, D., and Kutter, B. L. (2009). "Discussion of 'Analyzing Liquefaction-Induced Lateral Spreads Using Strength Ratios' by SM Olson and CI Johnson." *J. Geotech. Geoenviron. Eng.*, 135(12), 2008-2010.

Poulos, H. G. (1985). "Ultimate Lateral Pile Capacity in Two-Layer Soil." *Geotechnical Engineering*, 16(1), 25-37.

Power, M. S., Egan, J. A., Shewbridge, S. E., deBecker, J., and Faris, J. R. (1998). "Analysis of liquefaction-induced damage on Treasure Island." *The Loma Prieta, California, Earthquake of October 17, 1989—Liquefaction*, T. L. Holzer, ed., USGS, Washington, D.C., Professional Paper 1551-B, B87–B119.

Rathje, E. M., and Bray, J. D. (2000). "Nonlinear coupled seismic sliding analysis of earth structures. " J. Geotech. Geoenviron. Eng., 126(11), 1002-1014.

Rathje, E. M., and Saygili, G. (2009). "Probabilistic assessment of earthquake-induced sliding displacements of natural slopes." *Bulletin of the New Zealand Society for Earthquake Engineering*, 42(1), 18.

Robertson, P. K., and Campanella, R. G. (1983). "Interpretation of cone penetration tests. Part I: Sand." *Canadian geotechnical journal*, 20(4), 718-733.

Rollins, K. M., and McHood, M. D. 1998. "Comparison of computed and measured liquefaction-induced settlements in the Marina District, San Francisco." *The Loma Prieta, California, Earthquake of October17, 1989—Liquefaction*, T. L. Holzer, ed., USGS, Washington, D.C., Professional Paper 1551-B, B223–B239.

Salgado, R. (2008). *The Engineering of Foundations*. McGraw Hill, New York.

Seed, H. B. (1987). "Design problems in soil liquefaction." *J. Geotech. Eng.*, 113(8), 827-845.

Seed, H.B., and Idriss, I. M. (1971). "Simplified procedure for evaluating soil liquefaction potential." *J. Soil Mech. Found. Engrg. Div.*, 107 (SM9) 1249-1274

Seed, H. B., Idriss, I. M., Lee, K. L., and Makdisi, F. I. (1975). "Dynamic analysis of the slide in the Lower San Fernando dam during the earthquake of February 9, 1971." *J. Soil Mech. Found. Engrg. Div.*, 101(9), 889-912.

Seed, R. B., and Harder, L. F. (1990). "SPT-based analysis of cyclic pore pressure generation and undrained residual strength." *H. Bolton Seed Memorial Symposium Proceedings*, Vol. 2, 351-376.

Shamoto, Y., Zhang, J. M., and Tokimatsu, K. (1998). "Methods for evaluating residual post-liquefaction ground settlement and horizontal displacement." *Soils and Foundations*, 38(1), 69-84.

Stark, T. D., and Mesri, G. (1992). "Undrained shear strength of liquefied sands for stability analysis." *Journal of Geotechnical Engineering,* 118(11), 1727-1747.

Taylor, H. T., Cameron, J. T., Vahdani, S., and Yap, H. (1992). "Behavior of the seawalls and shoreline during the earthquake." *The Loma Prieta, California, Earthquake of October 17, 1989—Marina District*, T. D. O'Rourke, ed., T.L. Holzer, coord., USGS, Washington, D.C., Professional Paper 1551-F, F141–F153.

Tokimatsu, K., and Seed, H. B. (1987). "Evaluation of settlements in sands due to earthquake shaking." *Journal of Geotechnical Engineering*, 113(8), 861-878.

Tokimatsu, K., and Asaka, Y. (1998). "Effects of liquefaction-induced ground displacements on pile performance in the 1995 Hyogoken-Nambu earthquake." *Soils and Foundations*, Special Issue, (2), 163-177.

Tokimatsu, K., Kojima, H., Kuwayama, S., Abe, A., and Midorikawa, S. (1994). "Liquefaction-induced damage to buildings in 1990 Luzon earthquake." *Journal of Geotechnical Engineering*, 120(2), 290-307.

Toprak, S., Holzer, T. L., Bennett, M. J., and Tinsley, J. C. (1999). "CPT-and SPT-based probabilistic assessment of liquefaction potential." *Proc., 7th US–Japan Workshop on Earthquake Resistant Design of Lifeline Facilities and Countermeasures against Liquefaction.*

Wair, B. R., DeJong, J. T., and Shantz, T. (2012). "Guidelines for estimation of shear wave velocity profiles." *Pacific Earthquake Engineering Research Center*, PEER Report, 8.

Wartman, J., Bray, J. D., and Seed, R. B. (2003). "Inclined plane studies of the Newmark sliding block procedure." *J. Geotech. Geoenviron. Eng.*, 129(8), 673-684

Wride, C. E., McRoberts, E. C., and Robertson, P. K. (1999). "Reconsideration of case histories for estimating undrained shear strength in sandy soils." *Canadian geotechnical journal*, 36(5), 907-933.

Wu, J. (2002). *Liquefaction Triggering and Post-Liquefaction Deformation of Monterey 0/30 Sand Under Uni-Directional Cyclic Simple Shear Loading.* Ph.D. Thesis, University of California, Berkeley.

Yegian, M. K., Ghahraman, V. G., Nogole-Sadat, M. A. A., and Daraie, H. (1995a). "Liquefaction during the 1990 Manjil, Iran, earthquake, I: Case history data." *Bull. Seismol. Soc. Am.*, 851, 66–82.

Yegian, M. K., Ghahraman, V. G., Nogole-Sadat, M. A. A., and Daraie, H. (1995b). "Liquefaction during the 1990 Manjil, Iran, earthquake, II: Case history analysis." *Bull. Seismol. Soc. Am.*, 851, 83–92.

Yoshida, N., Tazoh, T., Wakamatsu, K., Towhata, I., Nakazawa, H., and Kiku, H. (2007). "Causes of Showa Bridge collapse in the 1964 Niigata earthquake based on eyewitness testimony." *Soil and Foundations* 47(6), 1075-1087

Yoshimine, M., *and Ishihara, K. (1998). "Flow potential of sand during liquefaction." Soils and Foundations*, 38(3), 189-198.

Youd, T. L. (1971). "Landsliding in the vicinity of the Van Norman Lakes." *The San Fernando, California, Earthquake of February 9,1971,* USGS Professional Paper 733, U.S. Department of the Interior, U.S. Government Printing Office, Washington, D.C., 105–109.

Youd, T. L. (1972). "Compaction of sands by repeated shear straining." *J. Soil Mech. Found. Engrg. Div.*, 98(7), 709-725.

Youd, T. L. (1973). "Ground movements in Van Norman Lake vicinity during San Fernando earthquake." *San Fernando, California, Earthquake of February 9, 1971*, L. M. Murphy, ed., Vol. 3, U.S. Dept. of Commerce, U.S. Government Printing Office, Washington, D.C., 197–206.

Youd, T. L., and Bennett, M. J. (1983). "Liquefaction sites, Imperial Valley, California." *J. Geotech. Engrg.*, 109(3), 440–457.

Youd, T. L., Idriss, I. M., Andrus, R. D., Arango, I., Castro, G., Christian, J. T., Dobry, R., Finn, W. D. L., Harder, L. F., Hynes, M. E., Ishihara, K., Koester, J. P., Liao, S. S. C., Marcuson, W. F., Martin, G. R., Mitchell, J. K., Moriwaki, Y., Power, M. S., Rovertson, P. K., Seed, R. B., and Stokoe, K. H. (2001). "Liquefaction resistance of soils: summary report from the 1996 NCEER and 1998 NCEER/NSF workshops on evaluation of liquefaction resistance of soils." *J. Geotech. Geoenviron. Eng.* 127(10), 817-833.

Youd, T. L., Hansen, C. M., and Bartlett, S. F. (2002). "Revised multilinear regression equations for prediction of lateral spread displacement." *J. Geotech. Geoenviron. Eng.*, 128(12), 1007-1017.

Zhang, G., Robertson, P. K., and Brachman, R. W. I. (2004). "Estimating liquefaction-induced lateral displacements using the standard penetration test or cone penetration test." *J. Geotech. Geoenviron. Eng.*, 130(8), 861-871.

Zeghal, M., and Elgamal, A. W. (1994). "Analysis of site liquefaction using earthquake records." *Journal of Geotechnical Engineering.* 120(6), 996-1017.